

Proceedings

AD641921
Vol. I



13 TH ANNUAL AIR FORCE SCIENCE & ENGINEERING SYMPOSIUM

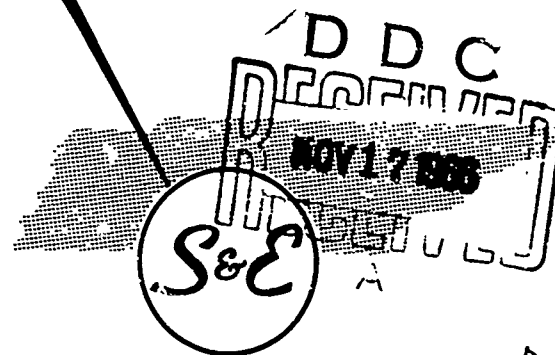
Arnold Engineering Development Center
Arnold AFS, Tennessee

University of Tennessee Space Institute
Tullahoma, Tennessee

Sponsored by
Air Force Systems Command
Office of Aerospace Research

27-29 September 1966

CLEARINGHOUSE FOR FEDERAL SCIENTIFIC AND TECHNICAL INFORMATION		
Hardcopy	Microfiche	611
1 ARCHIVE COPY		



PROCEEDINGS
of the
13th ANNUAL AIR FORCE SCIENCE & ENGINEERING SYMPOSIUM

27-28-29 September 1966

ARNOLD ENGINEERING DEVELOPMENT CENTER
ARNOLD AIR FORCE STATION, TENNESSEE

VOLUME I
UNCLASSIFIED, UNCONTROLLED DISTRIBUTION VOLUME

Sponsored by
AIR FORCE SYSTEMS COMMAND
and
OFFICE OF AEROSPACE RESEARCH

PREFACE

This 13th Annual Air Force Science and Engineering Symposium continues the purpose of illustrating and further stimulating Air Force in-house accomplishment and capability in research, development, test and evaluation vital to the Air Force mission and to national security.

Contributing to this purpose the symposium provides:

- a. For our audience a view of a representative cross section of the many significant scientific and engineering programs being carried out by Air Force personnel in Air Force facilities.
- b. For our own military and civilian scientists and engineers a forum for the presentation and critique of original work, a stimulation to continued effort and a recognition of achievement.
- c. For all participants a close look at one of our major facilities, a broader understanding of the scope and importance of Air Force technical programs, and an occasion to become better acquainted and to exchange ideas in areas of mutual interest.

It is particularly intended to emphasize the overall in-house capabilities of the Air Force Systems Command (AFSC) and the Office of Aerospace Research (OAR) and to demonstrate the effectiveness of the Air Force laboratories.

The Symposium program presents the spectrum of science and engineering activity as carried out by AFSC and OAR. This activity includes research, exploratory development, engineering development, advanced development, test, and evaluation. Toward this end, the program consists of a selection of the best "contributed" papers submitted in competition for the Air Force Association Aerospace Education Foundation Awards, the Patricia Kayes Glass Award, the AFSC Awards for Scientific Achievement, and the AFSC Technical Management Council Award. The scientific and technical papers to be presented will provide a representative sample of the scope and depth of the Air Force research, development, technology and engineering program, and of the program's value to the national defense.

TABLE OF CONTENTS

VOLUME I

UNCLASSIFIED, UNCONTROLLED DISTRIBUTION

	Paper Number
Adaptive Bang-Bang Control of an Unstable Mechanical System Containing an Unknown Parameter Captain John F. Schaefer Frank J. Seiler Research Laboratory Office of Aerospace Research	1
Rotation/Go-Around Instrument Guidance System Paul A. Rauschelbach Systems Engineering Group (RTD) Air Force Systems Command	2
Accelerations on Aircraft Induced by the Earth's Rotation Everett W. Dunlap 1/Lt Milton B. Porter Air Force Flight Test Center Air Force Systems Command	3
A Tandem Mass Spectrometer for the Study of Ion-Molecule Reactions Jean H. Futrell Larry I. Bone Fred P. Abramson Aerospace Research Laboratories Office of Aerospace Research	4
A New Technique for the Direct Determination of Vibrational Transition Probabilities Alva T. Stair, Jr. Marshall H. Bruce Air Force Cambridge Research Laboratories Office of Aerospace Research	5
Experimental and Theoretical f-Values for λ 3076 Zn I, λ 3261 Cd I and λ 2537 Hg I Thomas M. Bieniewski Thomas K. Krueger Stanley J. Czyzak Aerospace Research Laboratories Office of Aerospace Research	6

<ul style="list-style-type: none"> Studies of Surface Layer Transport and Its Contributions to the Properties of Ceramic Materials <ul style="list-style-type: none"> Henry C. Graham Norman M. Tallan Aerospace Research Laboratories Office of Aerospace Research 	7
<ul style="list-style-type: none"> Impulse Facilities for Scramjet Research and Development <ul style="list-style-type: none"> Forrest B. Smith, Jr. Arnold Engineering Development Center Air Force Systems Command 	8
<ul style="list-style-type: none"> Supersonic Combustion Simulation for High Mach Number Flight <ul style="list-style-type: none"> Robert G. Dunn Emil J. Walk Aerospace Research Laboratories Office of Aerospace Research 	9
<ul style="list-style-type: none"> Hydrocarbon Fuels for Hypersonic Vehicles <ul style="list-style-type: none"> Herbert R. Lander, Jr. Alan E. Zengel Air Force Aero Propulsion Laboratory (RTD) Air Force Systems Command 	10
<ul style="list-style-type: none"> Real Time Tem-Mode Analysis of He-Ne Lasers <ul style="list-style-type: none"> Ferdinand F. Kuhn Air Force Missile Development Center Air Force Systems Command 	11
<ul style="list-style-type: none"> Lasing Potential of II-VI Compounds <ul style="list-style-type: none"> Donald C. Reynolds Aerospace Research Laboratories Office of Aerospace Research 	12
<ul style="list-style-type: none"> Laser Brightness Gain and Mode Control by Compensation for Thermal Distortion <ul style="list-style-type: none"> C. Martin Stickley Air Force Cambridge Research Laboratories Office of Aerospace Research 	13
<ul style="list-style-type: none"> Laboratory Investigations of Plasma Interactions with a Dipole Magnetic Field <ul style="list-style-type: none"> Morton A. Levine Allen G. Rubin Air Force Cambridge Research Laboratories Office of Aerospace Research 	14

Rapid Remote Sensing by Spectrum Matching Technique:
Application in the Laboratory and in Lunar Observations ; 15
Graham R. Hunt
John W. Salisbury
John W. Reed
Air Force Cambridge Research Laboratories
Office of Aerospace Research

Environmental System Development for Rapid
Decompression of Chimpanzees to Pressures Less
than Two Torr ; 16
Tommy L. Dobson
Air Force Missile Development Center
Air Force Systems Command

Filament Wound Aircraft Tires ; 17
Theodore J. Reinhart, Jr.
Air Force Materials Laboratory (RTD)
Air Force Systems Command

Use of Tuned Viscoelastic Dampers for Reduction
of Vibrations in Aerospace Structures ; 18
David I. G. Jones
John P. Henderson
1/Lt George H. Bruns
Air Force Materials Laboratory (RTD)
Air Force Systems Command

Progress Report - Development of Advanced
Composite Structures ; 19
Maj Loris D. Whipple
Air Force Materials Laboratory (RTD)
Air Force Systems Command

Ultrasonic Studies of 1060 and 6061-T6 Aluminum ; 20
James R. Asay
Arthur H. Guenther
Air Force Weapons Laboratory (RTD)
Air Force Systems Command

VOLUME II
UNCLASSIFIED, UNCONTROLLED DISTRIBUTION

	Paper Number
Confronting the Heat Protection Problem in Hypersonic Nozzles Using High Enthalpy Air Lt Col Gordon M. Gray Arnold Engineering Development Center Air Force Systems Command	21
The Use of Flightpath Accelerometers in Performance Flight Testing Willie L. Allen L/Lt Robert H. Weight Air Force Flight Test Center Air Force Systems Command	22
Application of Nucleonic Mass Measurement Techniques for Measurement of Two-Phase Fluid Conditions Existing in Aircraft Fluid Systems Harry W. Schmidt Systems Engineering Group (RTD) Air Force Systems Command	23
Thin Film Heat Transfer Gages Capt. John W. Frye, Jr. Milton E. Franke Air Force Institute of Technology	24
Performance Analysis of Aircraft Subsystems Based on Automatic Airborne Data Acquisition Donald M. Caldwell, Jr. Lee Winograd Air Force Flight Test Center Air Force Systems Command	25
An Analysis of Radioisotope Dynamic Power Systems for Future Military Space Programs Lt David Kauffman Lt John T. Piker Space Systems Division Air Force Systems Command	26
Gemini Performance Optimization Capt John D. Regenhardt Space Systems Division Air Force Systems Command	27

Design, Fabrication and Testing of a Prototype Fly-Away Satellite Triangulation System	28
Lt Col Martin Selinfreund George P. Musante Military Airlift Command	
Current and Light Storage Effects in Lithium and Sodium Doped Crystals of ZnO	29
Yoon Soo Park Cole W. Litton Aerospace Research Laboratories Office of Aerospace Research	
Electrical and Magnetic Properties of Single Crystals of Rare Earth Tungsten Bronzes and Uranium Tungsten Bronzes	30
Capt Charles V. Collins Air Force Institute of Technology	
Dielectric Resonators	31
James C. Sethares Martin R. Stiglitz Air Force Cambridge Research Laboratories Office of Aerospace Research	
Solid State Display Techniques	32
Capt Carlton J. Peterson Air Force Flight Dynamics Laboratory (RTD) Air Force Systems Command	
Using the Electronic Computer to Define and Implement Policy	33
Raymond E. Christal Aerospace Medical Division Air Force Systems Command	
A Study of Job Preferences of Government and Non-Government Personnel	34
Robinette E. McCabe Air Force Contract Management Division Air Force Systems Command	
Maximizing Protection from EOQ Safety Levels	35
Irving Katz Victor J. Presutti, Jr. Air Force Logistics Command	

Electromagnetic Pulse (EMP) Generation and Measurement	36
Lt George R. Riling	
Lt Stephen T. Negler	
Air Force Special Weapons Center	
Air Force Systems Command	
Blast Wave Effects on the Pitching of Blunt Cones	37
1/Lt Brian P. Quinn	
Aerospace Research Laboratories	
Office of Aerospace Research	
Development of a Unique Mobile Integrated Support System for Tactical Electronics	38
Maurice N. Scheiderich	
Anthony N. Cioncio	
Rome Air Development Center	
Air Force Systems Command	
Machines that Communicate and Designers Who Don't	39
J. Albert Southern	
Systems Engineering Group (RTD)	
Air Force Systems Command	
Photographic Display Systems - Typical USAF Applications	40
Leon McDowell	
Rome Air Development Center (RTD)	
Air Force Systems Command	
Analysis of Digital Communication Systems on Tropospheric Scatter	41
1/Lt Robert G. McLaughlin	
Rome Air Development Center (RTD)	
Air Force Systems Command	
Evolution of Computer Systems to Perform Parallel Processing	42
Morris A. Knapp	
Rome Air Development Center (RTD)	
Air Force Systems Command	
Validating Vela Satellite Orbit Determination Procedures Using Observed Eclipse Entrance Times	43
1/Lt Charles B. Huelman, III	
Air Force Satellite Control Facility	
Air Force Systems Command	

Adaptive Bang-Bang Control of an Unstable Mechanical System
Containing an Unknown Parameter

Captain John F. Schaefer
Research Associa
Frank J. Seiler Research Laboratory
USAF Academy, Colorado 80840



Capt John F. Schaefer

Biography

Captain John F. Schaefer reported to the Aerospace Mechanics Division of the Frank J. Seiler Research Laboratory in April of 1965, after completing his studies at Stanford University.

Captain Schaefer was born 8 November 1936 in Cuero, Texas, and spent his early years in Meyersville, later in Vanderbilt, Texas. He was appointed to West Point as a member of the Class of 1958 following graduation from Industrial High School at Vanderbilt in 1954. On 4 June 1958, he was graduated and commissioned, and married Merrill Johnson of Western Springs, Illinois.

Following schooling at Keesler AFB, Mississippi, Captain Schaefer was assigned as Assistant Maintenance Officer for Flight Test Radar at Wright-Patterson AFB in August 1959. After eight months in this capacity, he became a Flight Test Engineer at Wright-Patterson AFB and was involved in the in-flight testing of newly developed radar, navigation, and electronic countermeasures equipment.

Captain Schaefer was assigned to AFIT in June 1961, and reported to Stanford University at that time as an Electrical Engineering graduate student. He took the M.S. degree in 1963 and the Ph.D. in June 1965. He is a member of Sigma Xi and the Institute of Electrical and Electronic Engineers.

Abstract

Adaptive Bang-Bang Control of an Unstable Mechanical System Containing an Unknown Parameter (U)

An adaptive control scheme is formulated for a slowly time-varying unstable mechanical system driven by a bounded controller. The control law is constrained to be of the "bang-bang" type. The adaptive control law is shown to result in stable operation for all system initial conditions lying within the region of controllability (the region of controllability is a function only of the plant and the maximum available control effort).

The mechanical system analyzed consists of a rigid rod hinged at its base to a motorized cart. A movable mass is positioned arbitrarily on the rod, and it is assumed that the mass location cannot be directly measured. This constitutes a fourth-order unstable plant with a single unknown parameter. The problem is thus to design a controller which switches the cart motor so as to drive the cart back and forth in the proper fashion to both balance the rod and maintain the cart near its zero position, regardless of the position on the rod of the movable mass.

The evolved controller operates in two modes, only the first of which is discussed in the paper. In the first, or "adapt", mode of operation, the bang-bang controller is forced to chatter. The resulting average control effort is measured and implemented to cause certain controller parameters to vary. In the second mode, the entire cart-rod assembly is returned to the equilibrium.

A. Introduction

Techniques for designing feedback controllers for linear dynamical systems whose parameters are known are well established and widely understood. When the system's parameters are unknown, however, the above statement must be modified considerably. Most frequently special techniques must be developed during the course of the control synthesis procedure for systems whose elements are unknown or are time-varying in some random fashion.

The use of special techniques was required in the investigation reported in this paper. The dynamical system, a mechanical device, was chosen to be investigated more for its illustrative character than its utility. The relatively simple mechanical model is unstable when unforced (uncontrolled), and it imposes stringent requirements on control sophistication. The constraint that the maximum available control effort (force) is limited was also imposed. For this reason, only "bang-bang" control laws were considered ("bang-bang" implies the controller is always full on, in either the positive or negative direction, and that it reverses between these states instantaneously).

The desired outcome of this study was simple: design a controller (control logic) which will stabilize the device, in spite of an uncertainty in certain system parameters.

B. System Description

The mechanical system for which the controller is to be designed is shown in Figure 1. The device consists of a motor-driven cart, free to translate horizontally (in the plane of the paper). A rigid rod, of length l and mass m , is pinned to the cart bed and is free to rotate about the pin. A point mass q is positioned somewhere along the rod a distance r from the pin. It is assumed that r is unknown, but that $\dot{r} = dr/dt$ is so small that it does not influence system dynamics. Additional system parameters are m_c ¹, the cart mass, and U' , the

¹ The parameter m_c includes terms due to motor and gear train rotational inertia.

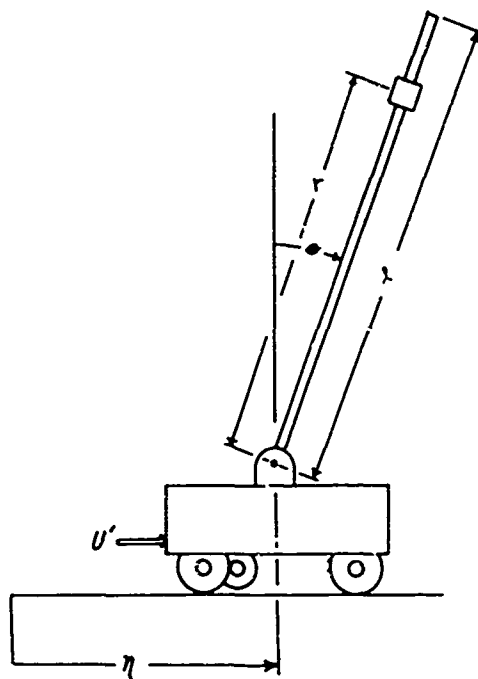


Figure 1 Unstable mechanical model. The dimension r is assumed to be unknown.

horizontal floor reaction due to cart motor torque. The constraint on U' is $|U'| \leq U'_{\max}$. Coordinates describing the system are η , the displacement of the cart from some inertial reference, and θ , the angle the rod forms with the vertical (these coordinates, and their velocities, are assumed measurable). Assumptions to be employed are that θ and $\dot{\theta}$ are small, and that negligible damping exists.

The assembly shown in Figure 1 constitutes (when unforced) a fourth-order, unstable dynamical system. When the control U' is properly chosen within its bounds $|U'| \leq U'_{\max}$, it is apparent that the device can be stabilized (i.e., forced to a resting position $\theta=0$, $\eta = \text{arbitrary}$), but only for some range of values of θ and $\dot{\theta}$ near zero. When U' is improperly chosen, the actual range of initial values of θ and $\dot{\theta}$ which will be driven to the equilibrium can only decrease in size, even though U'_{\max} is held fixed. It can easily be anticipated that when r , the lumped-mass position, is unknown, it is more likely than not that the control logic governing U' will result in such a smaller region of controllability.²

² Region of controllability is defined to be that volume of $\theta, \dot{\theta}$ and η space from the interior of which a control of maximum possible amplitude U'_{\max} can drive the system to the equilibrium $\theta = 0, \dot{\theta} = 0, \eta = \text{arbitrary}$. It is thus determined by available control effort, and not by control logic.

As analysis of the equations of motion verified this anticipation, the following approach was followed: It was decided to synthesize a dual-mode controller. In the first mode of operation, the control logic attempts only to maintain the rod in some controllable configuration, paying no regard to cart position and velocity. Simultaneously, a secondary loop takes certain measurements in order to update the control computer's estimate of r . Once \hat{r} (the estimate of r) is determined this phase is terminated and the entire assembly is taken to the equilibrium under second mode control.

In the following only Mode One, or Adaptive Mode, logic will be discussed. The logic chosen to control the entire assembly, in Mode Two, has essentially been discussed elsewhere [Reference 1]. Before proceeding it should be noted that extensive use is made of the phenomenon of chatter motion of the prescribed bang-bang controller. A description of such motion, which consists essentially of high frequency reversals of the relay element switching the control (motor), can be found in Reference 2. Also, inasmuch as a complete treatment would tend to detract from the following development, the approach will be to outline the steps taken and, when appropriate, explain the reasons for them, and to present the results. In addition, results of an extensive digital simulation will be presented.

C. Equations of Motion and the Control Law

The equations of motion governing the unstable system are straightforward to obtain, and their derivation is omitted. Due to the assumption of small θ and $\dot{\theta}$ they are linear:

$$\ddot{\theta} = \lambda^2 \theta - \frac{\lambda^2}{g} U \quad (1A)$$

$$\ddot{\eta} = -c \lambda^2 \theta + \left(1 + \frac{c \lambda^2}{g} \right) U \quad (1B)$$

The parameters c and λ^2 are functions of r and are thus themselves unknown; c increases linearly with r while λ^2 is a non-monotonic, rather complicated function. The new control U is just U'/m_T , m_T being total system mass, and g is gravitational acceleration.

The first step is to define two new variables, y_1 and y_2 . They will be used directly by the control computer during the adapt mode, and are given by

$$y_1 = 0.5 (\theta + \dot{\theta} / \hat{\lambda}) \quad (2A)$$

$$y_2 = 0.5 (\theta - \dot{\theta} / \hat{\lambda}) \quad (2B)$$

The variable $\hat{\lambda}$ is the computer's estimate of λ ; since physical constraints place bounds on λ , $\hat{\lambda}$ will always lie in the range

$$\lambda_{\min \text{ expected}} \leq \hat{\lambda} \leq \lambda_{\max \text{ expected}}$$

If $\hat{\lambda}$ and λ are identical, it is found that y_1 and y_2 obey the equations

$$\dot{y}_1 = \lambda y_1 - \frac{\lambda}{2g} U \quad (3A)$$

$$\dot{y}_2 = -\lambda y_2 + \frac{\lambda}{2g} U \quad (3B)$$

Note that the y_i 's are uncoupled. A further feature is that a determination of the extent of the region of controllability can be made from analysis of equation (3A) alone, for it describes the time behavior of the single unstable mode of the system. From (3A) it can be seen that if $|y_1| > \frac{U_{\max}}{2g}$ then y_1 and \dot{y}_1 will always be of identical sign

regardless of the choice of U . If the above inequality is reversed, however, proper choice of U can force y_1 arbitrarily within the range $|y_1| < \frac{U_{\max}}{2g}$. Thus the region of controllability of this

mechanical system is given by $|y_1| < \frac{U_{\max}}{2g}$, or, in terms of θ and $\dot{\theta}$,

by

$$|\theta + \dot{\theta} / \lambda| < \frac{U_{\max}}{g} \quad (4)$$

Note that cart position and velocity do not influence this region of potentially controllable initial conditions.

The situation just discussed is shown in Figure 2, the $\theta, \dot{\theta}$ phase plane. The region of controllability is the infinite-extent strip enclosed by the lines $\theta = \dot{\theta} / \lambda = \pm U_{\max} / g$. In addition, the y_1, y_2 axes

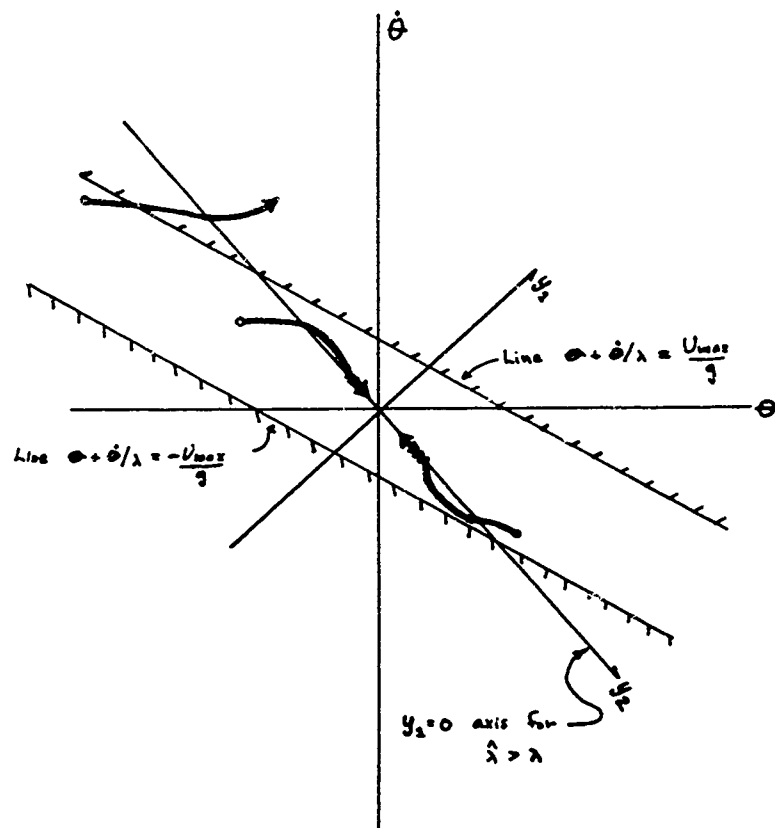


Figure 2 Region of controllability in the phase plane, showing typical trajectories for the control law $U = U_{\max} \operatorname{sgn} y_1$.

are shown for the case $\hat{\lambda} > \lambda$ (when $\hat{\lambda} = \lambda$, the $y_1 = 0$ axis forms the centerline of the region of controllability). The heavy lines are $\theta, \dot{\theta}$ trajectories and will be discussed later.

The control law to be employed during the adapt mode is simple:

$$U = U_{\max} \operatorname{sgn} y_1 \quad (5)$$

Under the influence of such a control the state point will always be forced toward the line $y_1 = 0$ (which is the equation for the switching surface in the y_1, y_2 space). The sample trajectories in Figure 2 show this. Note

especially the one trajectory which departs the region of controllability before it strikes the surface (the rod configuration associated with it is no longer controllable). Had $\hat{\lambda}$ more nearly matched λ , this eventuality would not have occurred.

D. The Adaptive Scheme

To prevent such an occurrence as that just discussed, the adapt mode has itself two phases of operation. In the first phase, the computer chooses $\hat{\lambda}$ ($t = 0$) such that $\theta + \dot{\theta}/\hat{\lambda} \equiv 0$ ($y_1 \equiv 0$). If this results in a value of $\hat{\lambda}$ such that

$$\lambda_{\min \text{ expected}} > \hat{\lambda} > \lambda_{\max \text{ expected}},$$

then $\hat{\lambda}$ ($t = 0$) is taken to equal $\lambda_{\min \text{ expected}}$. It will be stated without proof that such a choice will insure that a potentially controllable initial condition remains controllable under the action of the control law (5).

Regardless of the value of $\hat{\lambda}$ resulting from the above logic, at some point near the y_1, y_2 origin the controller will enter the chatter mode.³ At this time the second phase of the adaptive process is initiated (t_{ch} designates the time of inception of chatter motion). A chatter detector activates a secondary process which varies $\hat{\lambda}$ according to the law

$$\dot{\hat{\lambda}} = \frac{k\bar{U}}{gy_2}. \quad (6)$$

It is difficult to explain the wherewithal of (6), but its use is easily justified. In short, (6), which governs the dynamics of $\hat{\lambda}$, is employed because it results in attainment of the condition $\hat{\lambda} \equiv \lambda$ during the chatter phase of Mode One. In addition, the stability of the overall process can be proven. Finally, all variables in (6) are readily obtainable

³ The only case in which chatter will not exist is when $\hat{\lambda}$ ($t = 0$) is taken to be $\lambda_{\min \text{ expected}}$ and the state trajectory passes through the origin.

[k is a positive constant, an "adapt gain constant"; \bar{U} is the time-average-value of the control effort during chatter motion.

$$(\bar{U}(t) = \frac{1}{t-t_{ch}} \int_{t_{ch}}^t U(t) dt).$$

Two steps are involved in the proof of overall adaptive-process stability. First, it must be shown that chatter motion, once it commences, must be continuous. The results of this step establish a necessary upper bound on k , the gain constant, which is

$$k \leq \lambda_{\min}^2 \text{ expected} \quad (7)$$

The second step is to show that the only possible equilibrium of the variables y_2 and $\hat{\lambda}$ is the point $(0, \lambda)$. The particular technique employed to establish this fortunately imposed the same constraint (7) on k for stability. Thus a k chosen to satisfy (7) is both necessary and sufficient for stability of the overall adaptive process.

A significant amount of algebra plus use of many of the techniques of Reference 2 enables one to eliminate \bar{U} and y_2 from (6), permitting a solution in closed form. It shows that, if k satisfies (7), then

$$\hat{\lambda}(\tau) = \frac{\hat{\lambda}(0) - \lambda + [\hat{\lambda}(0) + \lambda] e^{\frac{2kg\lambda}{\lambda^2 - k} \tau}}{1 - \frac{\hat{\lambda}(0)}{\lambda} + [1 + \frac{\hat{\lambda}(0)}{\lambda}] e^{\frac{2kg\lambda}{\lambda^2 - k} \tau}} \quad (8)$$

(here $\tau = t - t_{ch}$). Also, it can be shown that the mode y_2 decays according to

$$y_2(\tau) = y_2(0) e^{-\int_0^\tau \hat{\lambda}(\tau) d\tau} \quad (9)$$

Since $y_1 \equiv 0$ at the inception of chatter motion, the rod assembly approaches the vertical at the rate $\theta(\tau) = y_2(\tau)/2 \hat{\lambda}(\tau)$.

During the entire Mode One operation the cart is forced at will, since η and $\dot{\eta}$ are not involved in the adapt mode feedback path. Thus some

criterion must be established for terminating Mode One and initiating Mode Two, in which the entire system is controlled. This is discussed below.

E. Simulation Results

During the course of this study, both analog and digital simulations were conducted. The generally-substantiating results presented here are those of a digital simulation of a system with parameters

$$\begin{aligned} m &= 1.0 \text{ slugs} & g &= 30.0 \text{ ft/sec}^2 \\ m_c &= 1.0 \text{ slugs} & U_{\max} &= 15.0 \text{ ft/sec}^2 \\ q &= 10.0 \text{ slugs} & r &= 5.0 \text{ feet} \\ l &= 10.0 \text{ feet} \end{aligned}$$

The length r was assumed to lie between the limits $4.13 < r < 10.0$ feet, giving $\lambda_{\min} \text{ expected} = 5.23 \text{ sec}^{-1}$, $\lambda_{\max} \text{ expected} = 7.39 \text{ sec}^{-1}$.

The relay imperfection allowing chatter motion was assumed to be hysteresis; the width of the hysteresis zone simulated was taken as 1/500 the amplitude of the maximum (normalized) input signal.

One important difficulty in mechanization was encountered: It was decided to extract \bar{U} , the average control effort during chatter motion, by passing the control output through a single-time-constant low-pass filter. This, of course, introduced additional dynamics not considered in the analysis. The equation governing \bar{U} was of the form

$$\dot{\bar{U}} = \alpha(U - \bar{U}) . \quad (10)$$

The time-constant α was initially taken to be $\alpha = 5\lambda$, but with $k = 25$ (near its theoretical limit of 27.45) overshoots in $\hat{\lambda}$ and discontinuities in chatter motion resulted. Also as $|y_2|$ approached zero additional instabilities developed. Both phenomena are shown in Figures 3. The overshoot in α was cured by increasing α to $\alpha = 10\lambda$, but post-adaption instability persisted. [Figure 4B shows this. Note $\hat{\lambda} \approx \lambda$ after only 0.6 secs has elapsed, but diverges as $|y_2| \rightarrow 0$ (at $t \approx 1.05 \text{ sec}$).] This instability near $|y_2| = 0$ was anticipated, for even though [see equation (6)] division by a time variable (y_2) approaching zero gives desirable

theoretical results, embarrassment can be expected (indeed, deserved) in application. The analog work, not discussed, added a small constant in the denominator of (6) to preclude division by zero, with successful results. A termination criterion at $|y_2| \leq \epsilon$, ϵ small, eliminated the difficulty in the digital work.

The series of Figures 5 show time histories of the various variables during the adapt mode. These are for parameter values $\alpha = 5\lambda$, $k = 15$, and initial conditions

$$\begin{aligned}\theta(0) &= 0.3 \text{ rad} \\ \dot{\theta}(0) &= -0.8 \text{ rad/sec} \\ \eta(0) &= 0 \\ \dot{\eta}(0) &= 0.\end{aligned}$$

For such an initial configuration $\hat{\lambda}(0)$, Figure 6b, is chosen by the Mode One controller to be $\lambda_{\min} \text{ expected} = 5.23 \text{ sec}^{-1}$. Note the near-perfect adaption to the correct value $\lambda = 7.266$.

F. Conclusion

Although the majority of the derivations and proofs involved in this investigation have been omitted, it is clear that a solution to the "unknown" portion of the problem goal has been obtained. In short, a controller has been synthesized which will maintain the system in a controllable state while simultaneously preparing other controller parameters for proper operation in Mode Two. It is felt that the closed-loop adaptive mechanism, which utilizes the average control effort during chatter motion as its stimulus, is itself adaptable to other applications.

References

1. D.T. Higdon, "Automatic Control of Inherently Unstable Systems with Bounded Control Inputs", PhD Dissertation, SUDAER Report #176, Department of Aeronautics and Astronautics, Stanford University, Stanford, California, December 1963.
2. J.F. Schaefer, "On the Bounded Control of Some Unstable Mechanical Systems", PhD Dissertation, SUDAER Report #223, Department of Aeronautics and Astronautics, Stanford University, Stanford, California, April 1965.

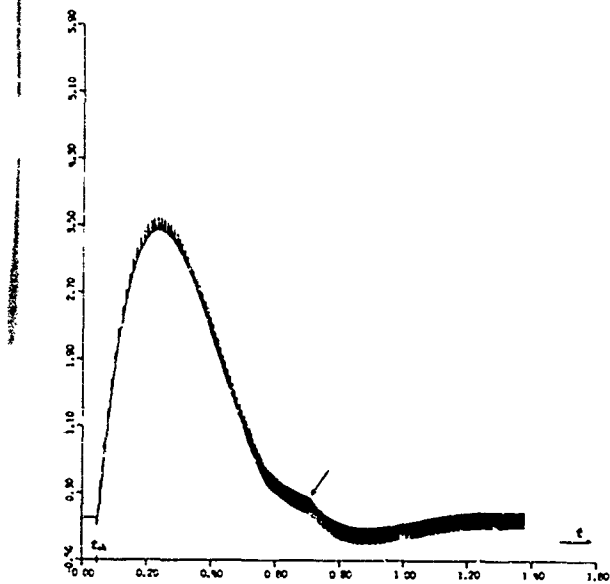


Figure 5A Average control effort \bar{u} for the case $b = 25 \text{ sec}^{-2}$, $q = 51 \text{ sec}^{-1}$. The arrow indicates the start of the discontinuous chatter motion.

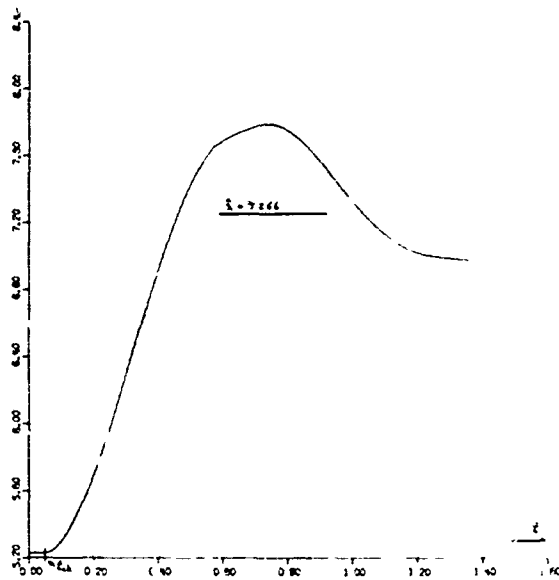


Figure 5B Time history of λ for the case $b = 25 \text{ sec}^{-2}$, $q = 51 \text{ sec}^{-1}$. The actual λ is 7.466 sec^{-1} .

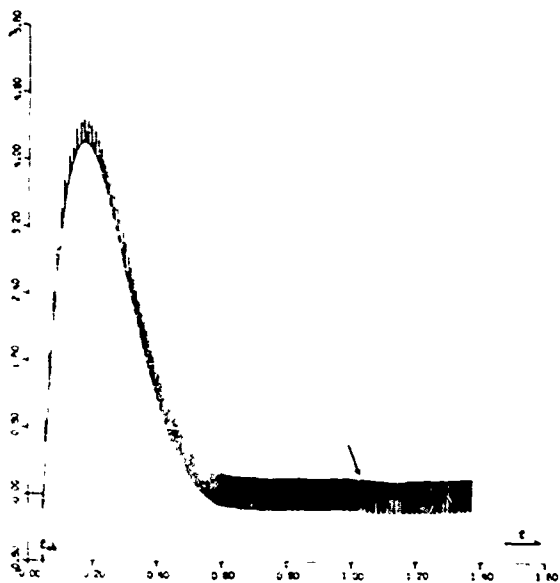


Figure 6A Average control effort \bar{u} for the case $b = 25 \text{ sec}^{-2}$, $q = 101 \text{ sec}^{-1}$. The arrow indicates the start of the discontinuous chatter motion.

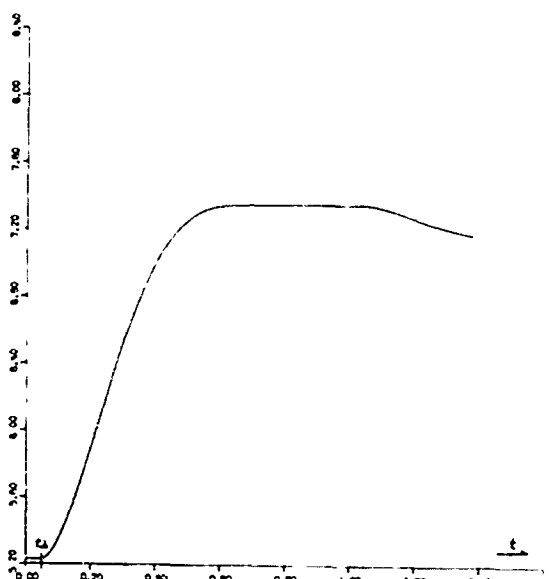


Figure 6B Time history of λ for the case $b = 25 \text{ sec}^{-2}$, $q = 101 \text{ sec}^{-1}$. The actual λ is 7.466 sec^{-1} .

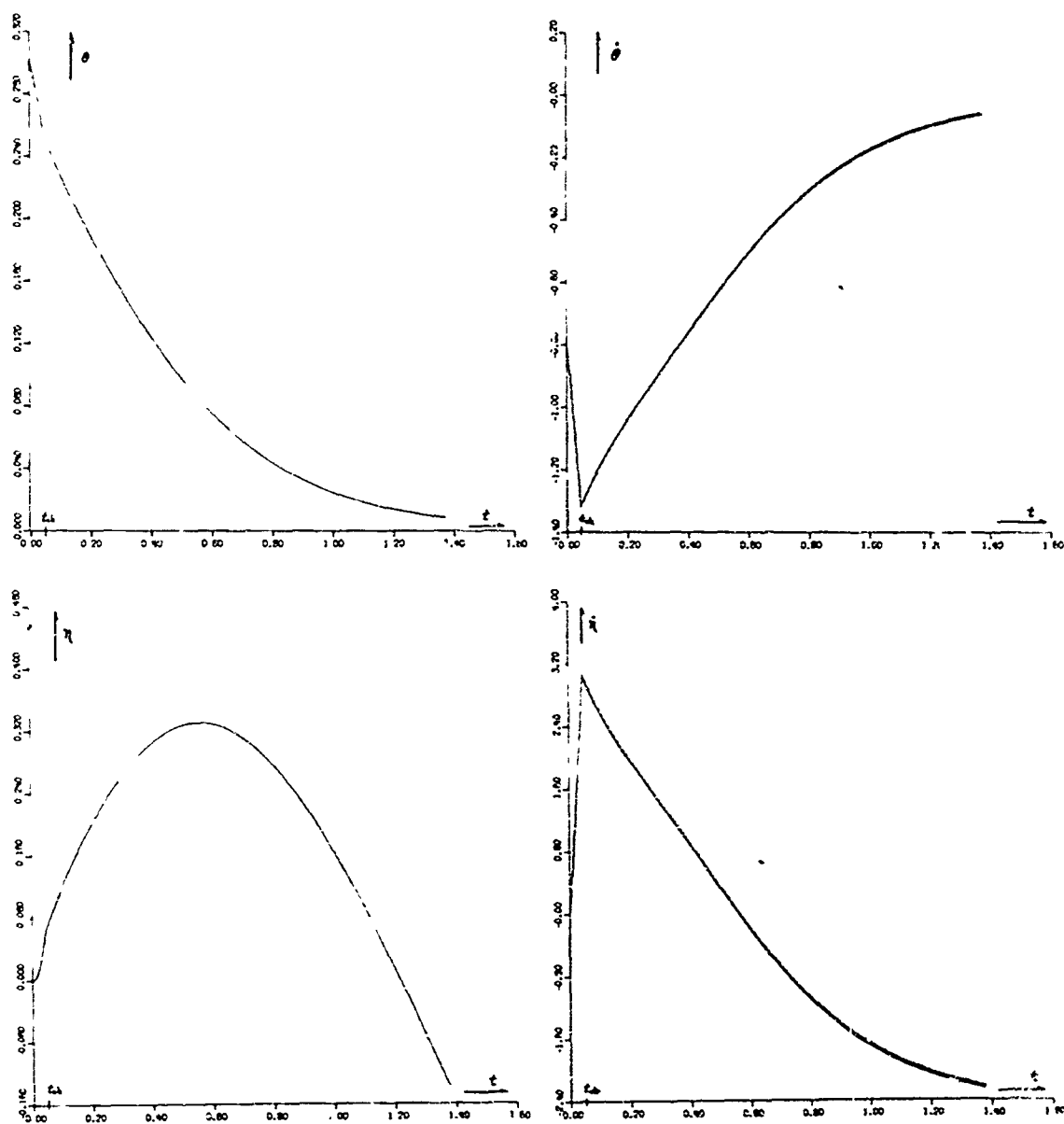


Figure 5 Time histories of the physical variables for the case $h = 25 \text{ cm}$, $a = 51 \text{ cm}^{-1}$.

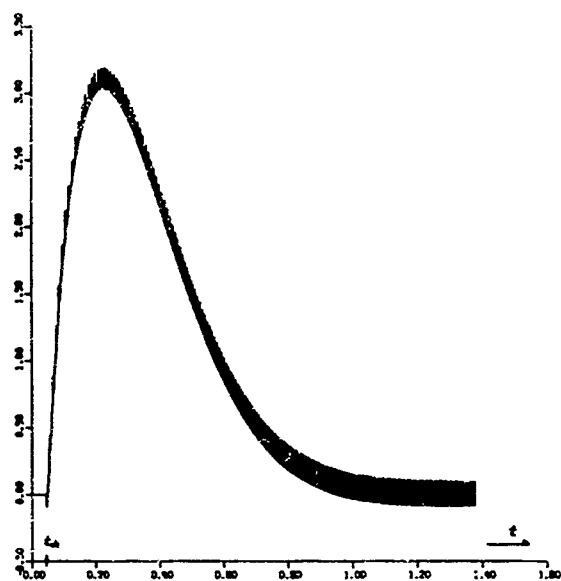


Figure 4b Average control effort \bar{u} for the initial conditions of Figure 5.

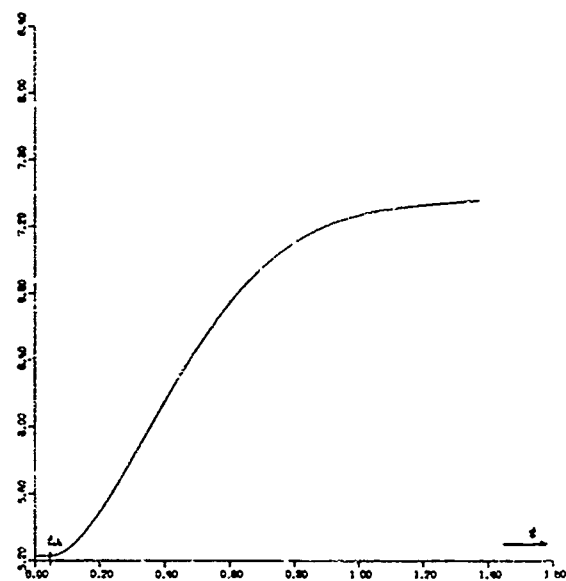


Figure 5a The history of x for the initial conditions of Figure 5.

ROTATION/GO-AROUND INSTRUMENT GUIDANCE SYSTEM (U)

by

Paul A. Rauschelbach

**Systems Engineering Group
Research and Technology Division
Wright-Patterson AFB, Ohio**



Paul A. Rauschelbach

BIOGRAPHY

Mr. Paul A. Rauschelbach
Electronic Engineer
Systems Engineering Group
Wright Patterson AFB, Ohio

Born in New York City, New York, 26 July 1941, Mr. Rauschelbach was graduated from Duke University, Durham, North Carolina, in 1963 with a Bachelor of Science Degree in Electrical Engineering.

Since graduation he has been employed by the Air Force at Wright Field, working in the flight instrument area for much of his tenure, and specializing in flight director computers and display systems. He more recently has been project engineer on the C-141 All Weather Landing System Development being conducted by SEG, and the C/KC-135 rotation/go-around instrument guidance system development.

In 1965, he received an Air Force Sustained Superior Performance Award for his efforts in the field of Flight Instrumentation.

ABSTRACT

This paper presents the accomplishments of the Systems Engineering Group in developing an instrument system for improved rotation, climb-out, approach and go-around guidance under all weight variations, all aerodynamic configurations and all thrust levels for the C/KC-135 aircraft. The system includes a rotation/go-around (R/GA) computer, a flight director system, and a majority logic monitoring computer.

The first phase of the program called for a study of the guidance required for takeoff, approach and go-around flight regimes and the development of a guidance system for the C/KC-135. During rotation, climb-out and go-around, it was determined that the primary longitudinal-axis parameter to be controlled is angle of attack. A command angle-of-attack term for optimum angle of attack throughout the takeoff and go-around regimes can be generated from altitude rate without the need for switching or mechanical gain changing. Effective phugoid damping is provided by use of altitude rate and longitudinal acceleration. An angle-of-attack command system was determined to yield optimum guidance during a condition of reduced thrust or engines out.

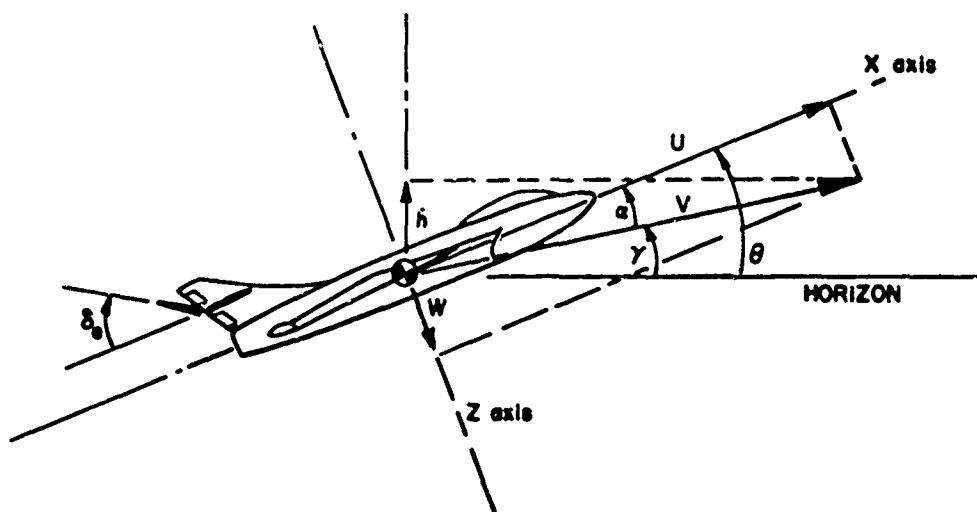
The system integration and hardware development phase included the design of the total system for flight test. A flight director computer and display system are used to compute and display the signals from the R/GA computer and flight control guidance during approach. The critical flight regimes in which the R/GA command system is used demands proper monitoring and back-up to provide continuation of the flight control maneuver. A microelectronic monitoring computer was fabricated to provide fail safe operation of the system.

SYMBOLS

A_L	longitudinal acceleration from accelerometer
A_N	normal acceleration from accelerometer
ADI	attitude director indicator
C_L	coefficient of lift
C_D	coefficient of drag
D	drag
E_{loc}	angular deviation from localizer path
FDC	flight director computer
g	gravity constant = 3.2 ft/sec^2
GCA	ground controlled approach
HSI	horizontal situation indicator
h	altitude
\dot{h}	altitude rate
ILS	instrument landing system
L	lift
p	path distance to transmitter
q	dynamic pressure
S_A	wing area
T	thrust
U	aircraft velocity component along x axis
\dot{U}	longitudinal acceleration along x axis
V	total aircraft velocity
V_S	stall velocity
V_{TO}	takeoff velocity
V_{VC}	complemented vertical speed
W	aircraft gross weight

α	angle of attack
α_A	augmented angle of attack
α_P	programmed angle of attack
γ	flight path angle
δ_e	elevator position
δ_F	flap position
$\epsilon ()$	error ()
θ	pitch attitude
θ_T	pitch trim
ϕ	roll attitude
ψ	heading
$\dot{\psi}$	heading rate

DEFINITION OF ANGLES



SECTION I

INTRODUCTION

Guidance of an aircraft during takeoff, climb-out and landing portions of the flight profile must be accurate to achieve flight safety. This is especially true for the C-135 and KC-135 (C/KC-135) aircraft. For example, an error in lift-off attitude of only two degrees can extend the required runway length for the C/KC-135 by 3200 ft.

It is believed that several C/KC-135 accidents which have occurred during takeoff were due in part to inadequate instrument guidance offered the pilot. Recognizing the deficiency with the present flight instrument system in the C/KC-135, both the Military Airlift Command (MAC) and the Strategic Air Command (SAC) have requested that an improved instrument system be provided for their aircraft. Specifically, they requested that improved guidance be provided for the takeoff and approach phases of flight and that improvements be made to the attitude indicating system.

This report presents the system being provided by the Systems Engineering Group (SEG) to meet the requirements of MAC and SAC for the C-135 and KC-135, respectively. This instrument guidance system is comprised of several newly developed subsystems which were developed both on contract and in house, and flight tested during their development.

To aid in understanding present takeoff and approach guidance problems of the C/KC-135, Section II presents an analysis of the KC-135 takeoff. Section III is an overview of the total instrument guidance system being developed. Sections IV, V, and VI discuss the theoretical basis and implementation of the rotation/go-around computer (R/GA), the flight director system, and the monitoring system, respectively.

The data presented in this report applies specifically to the KC-135 aircraft. However, the overall analysis holds true for both the C-135 and KC-135 aircraft.

SECTION II

ANALYSIS OF THE KC-135 TAKEOFF

A. TAKEOFF PROCEDURES

The takeoff maneuver of an aircraft may be divided into three distinct phases: (1) ground roll, (2) rotation, and (3) climb-out.

1. Ground-Roll Phase

Ground roll begins when an aircraft starts the takeoff and ends when the aircraft has sufficient speed to rotate. During ground roll, it is necessary to accelerate the aircraft to required lift-off velocity as soon as possible to reduce the ground-roll distance. Table I illustrates the ground roll required for a KC-135A to become airborne. No longitudinal guidance is necessary during the ground-roll phase since the aircraft must only be maintained on the runway.

TABLE I
KC-135 TAKEOFF CONDITIONS

Four Engines Weight in 1000 lb	30° Flap Setting Unstick Speed kt	Ground-Roll	Zero Altitude Unstick Time sec
100	102.23	958	10.98
120	111.99	1404	14.66
140	120.96	1946	18.76
160	129.32	2590	23.28
180	137.16	3340	28.23
200	144.58	4204	33.61
220	151.64	5189	39.42
240	158.38	6301	45.69
260	164.85	7548	52.42
280	171.07	8940	59.63
300	177.07	10485	67.34

2. Rotation Phase

The rotation phase of takeoff occurs when an aircraft reaches takeoff velocity, V_{TO} . The aircraft is rotated by raising the nose to a pitch attitude required for lift-off. The attitude to which an aircraft is rotated depends upon takeoff conditions but is usually an attitude which will result in a lift-off velocity of approximately $1.2 V_S$. This value of velocity is a compromise between operating too close to the stall speed and using excessive runway distance prior to lift-off. By rotating the aircraft, lift is increased sufficiently to overcome the force of gravity and the aircraft becomes airborne.

3. Climb-Out Phase

The climb-out phase begins when an aircraft leaves the ground. In this phase of the takeoff maneuver it is of prime importance to properly utilize excess thrust (thrust not being used to overcome drag forces.) The optimum climb-out performance recommended for the KC-135 is flight at a constant pitch attitude until a speed of $V_{TO} + 10$ knots is reached. At this point a constant speed climb is initiated to gain altitude prior to flap retraction and acceleration.

During a typical KC-135 takeoff maneuver, the aircraft is accelerated on the runway to required rotation speed. As the aircraft approaches required takeoff speed during ground roll, the pilot begins rotating his aircraft to a pitch attitude of 8° . As pitch increases to 8° , so does the angle of attack (α) increase, since α equals pitch during ground-roll and rotation phases. As angle of attack and speed of the aircraft increase, lift increases ($L \approx \alpha U^2$), causing the KC-135 to leave the runway (Figure 1). Using standard operating procedures the KC-135 is maintained at a constant pitch attitude from lift-off until completion of the initial climb-out.

At the moment of initial lift-off, excess thrust produces a positive acceleration (\dot{U}) and an increase in the flight-path angle (γ). The basic aircraft equation describing how extra thrust may be used is shown below. This simplified equation is derived from the longitudinal-axis equations of motion by disregarding short term pitch changes and assuming small angles.

$$\frac{T-D}{W} \approx \gamma + \frac{\dot{U}}{g} \quad (1)$$

The equation states that thrust minus drag (thrust available), divided by aircraft weight, equals flight-path angle plus acceleration divided by the gravity constant. Therefore, energy (thrust) available at takeoff can be used either to increase the rate of climb (γ) or to increase airspeed (\dot{U}) or both. Since pitch is held constant in the KC-135 and γ is increasing, α must decrease. Although α decreases, lift continues to increase because velocity (U) has increased.

B. DISADVANTAGES OF CONSTANT PITCH TAKEOFF PROCEDURES

Two major problems exist with the use of a constant pitch takeoff procedure on the KC-135: (1) inaccuracy of the attitude system during takeoff; and (2)

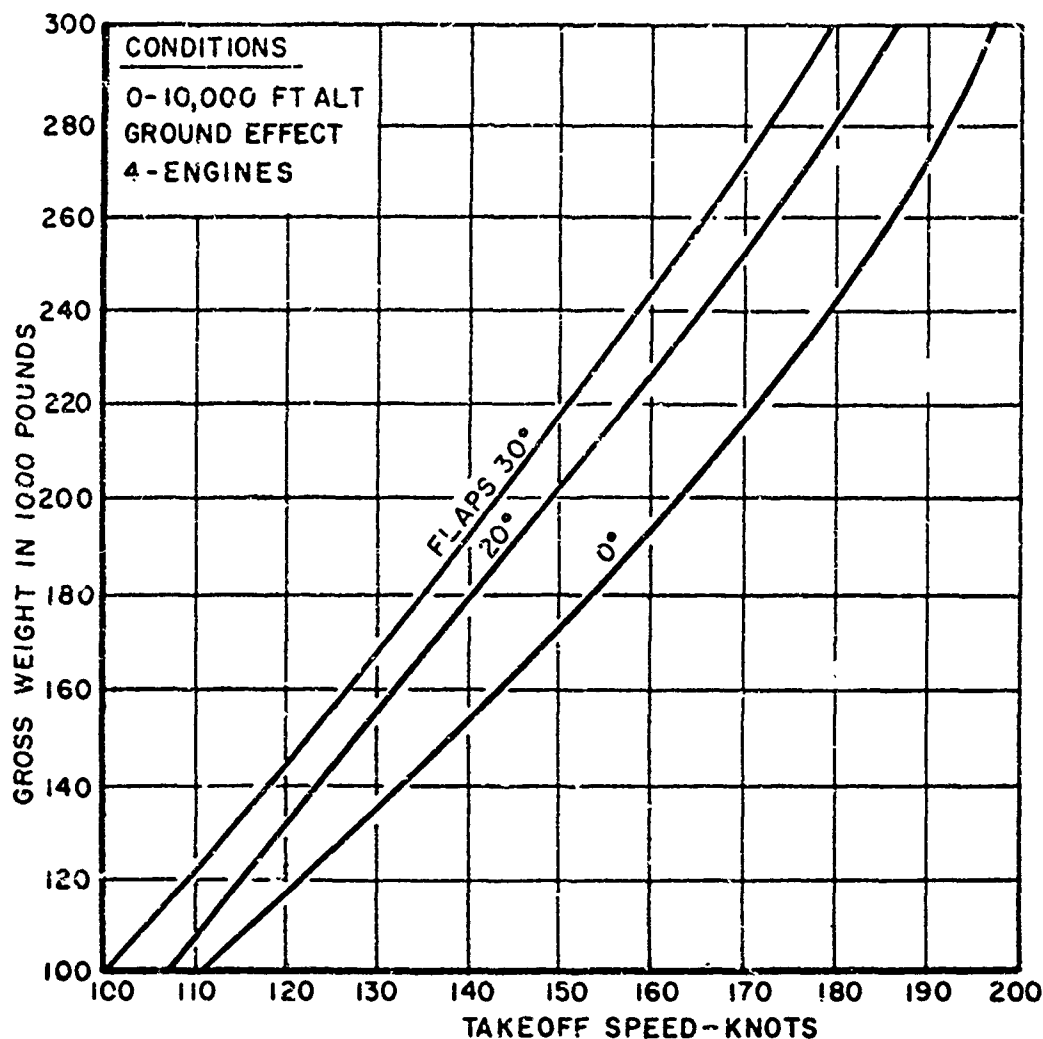


Figure 1. KC-135 Takeoff Speed vs Gross Weight

less than optimum instrument guidance given the pilot, particularly during high gross weight and reduced thrust takeoff conditions.

1. Attitude System

The vertical gyroscope installed in the KC-135 gives accurate pitch information to the attitude indicator under the majority of flight conditions. During the takeoff maneuver, high longitudinal accelerations are experienced which can precess the gyro indication off the actual pitch of the aircraft by as much as seven degrees. The precession is due to longitudinal acceleration acting on the electrolytic switch which controls verticality of the gyro. Figure 2 shows the configuration of the vertical gyro electrolytic erection switch. The purpose of the switch is to sense the free drift of the gyro, erecting the gimbal by switching on the torque motor when the gyro drifts off vertical. When the glass tube which is tied to the gimbal tilts off due to gyro drift, the mercury level rolls to one end of the tube completing an electrical path for the torque motor current. When the electrolytic

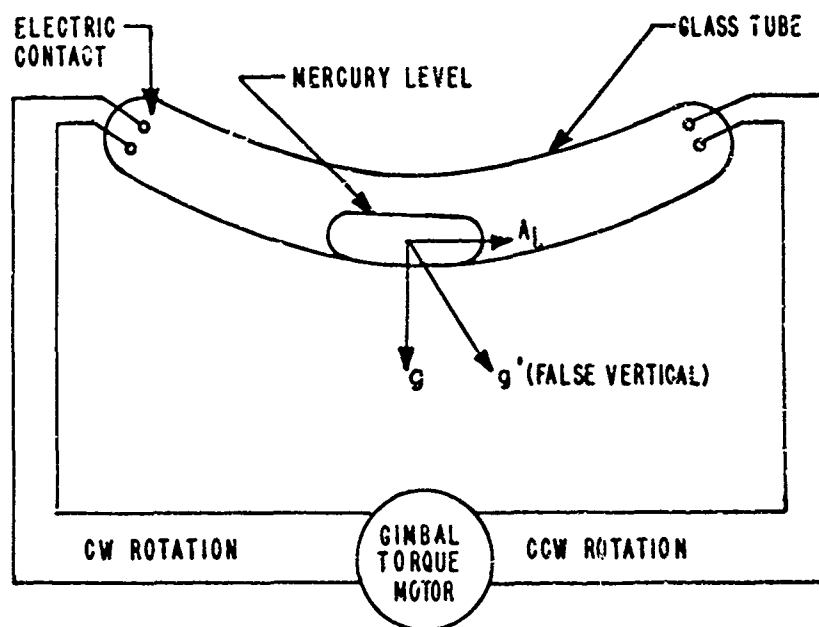


Figure 2. Vertical Gyro Electrolytic Erection Switch

switch senses a false vertical, g' , due to the longitudinal acceleration vector, the pitch gimbal is torqued to the angle of the resultant of acceleration and gravitation forces. The error is in the safe direction, that is, pitch displayed on the attitude indicator is greater than the actual pitch of the aircraft. However, it is impossible to obtain accurate aircraft pitch by mentally adding pitch error due to gyro precession to the indicated pitch because the amount of precession varies with the length and magnitude of ground-roll acceleration.

A second difficulty in using the attitude indicating system to guide rotation during takeoff is that if the aircraft attitude is increased beyond a limit of 10 to 12 degrees, drag on the aircraft becomes so great that the aircraft cannot lift off. Figure 3 illustrates the rapid increase in drag at rotation with an increase in pitch. If the pilot rotates the aircraft to an excessive pitch attitude due to his inability to accurately read small increments of pitch or to interpolate the gyro precession, the increased drag must be overcome by increased velocity, which requires more thrust and results in a larger runway ground roll. This increased drag is an important consideration during an engine-out condition on the KC-135, since excess thrust at takeoff during this condition is marginal compared with other aircraft.

2. Constant Pitch Performance

For jet aircraft, the angle of attack which maximizes flight-path angle (maximum climb) is approximately equal to the angle of attack corresponding to the maximum lift-to-drag ratio. (This is discussed in detail in Section IV.) This angle of attack will not support the aircraft in the air at lift-off speed since lift-off speed must be kept low to minimize ground roll. Therefore, rotation at takeoff must be made to a higher initial angle of attack to give the aircraft some climb or vertical speed. Maintaining this pitch attitude does not result in the best performance during climb-out because climb is not optimized. When additional vertical speed is obtained, the aircraft flight path can be modified to result in a maximum rate of climb. Since the

constant pitch attitude is optimized to provide best lift-off angle of attack, once vertical speed is obtained, this attitude no longer provides the best aircraft flight path. When thrust is reduced due to an engine-out and the weight of the aircraft is high, the thrust available is marginal and optimum use of the available energy becomes important.

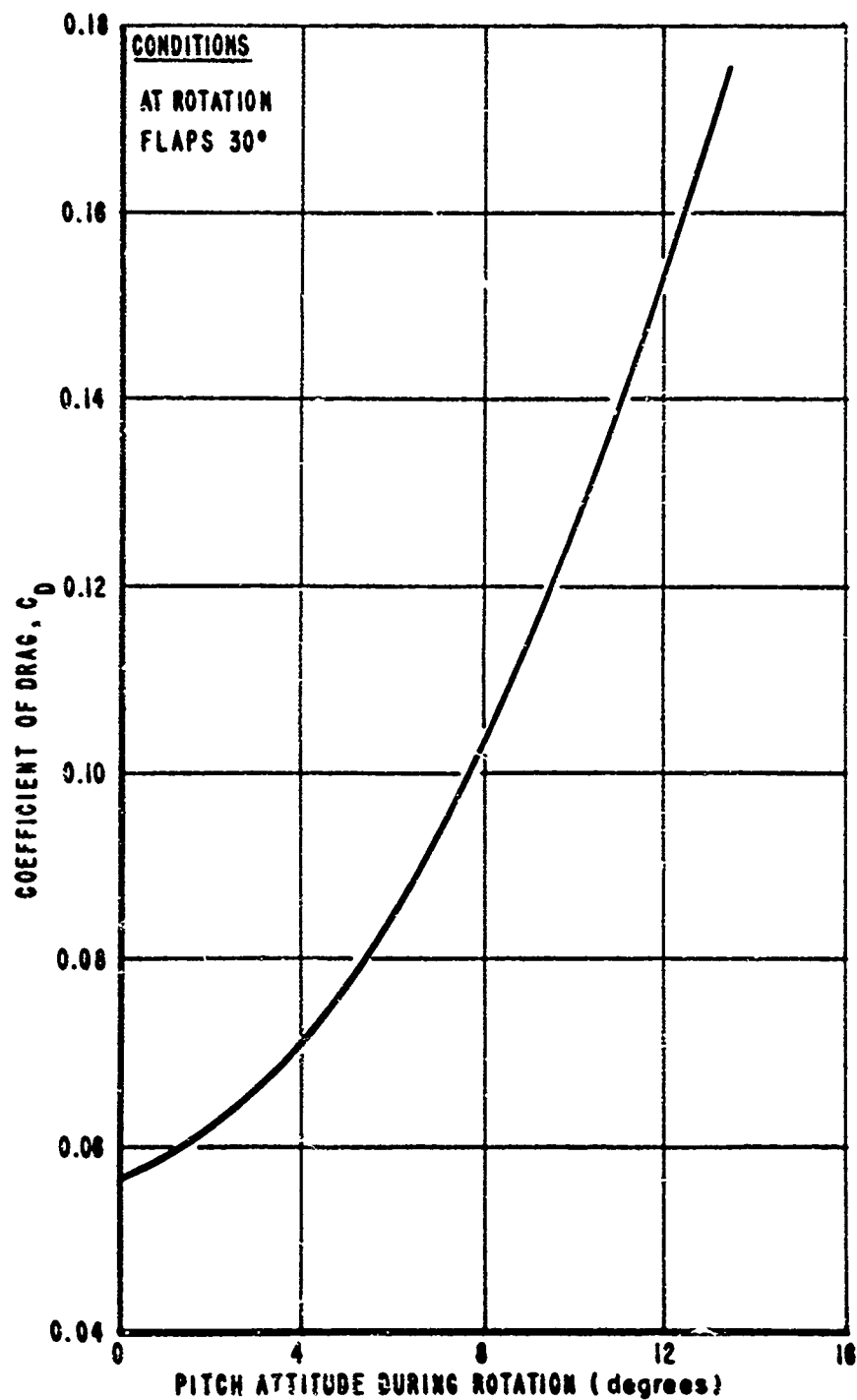


Figure 3. Coefficient of Drag vs Pitch During Rotation

SECTION III

ROTATION/GO-AROUND FLIGHT DIRECTOR SYSTEM

As indicated in Section II the constant pitch procedure for controlling a KC-135 takeoff and go-around has serious limitations. Recognizing these limitations the SEG developed an instrument guidance system to improve the takeoff and approach capabilities of the C-135 and the KC-135 (C/KC-135) based on requests from both the MAC and the SAC. The following capabilities were development requirements:

- (1) Optimum control guidance for rotation, climb-out and go-around;
- (2) Improved approach guidance;
- (3) Instrument display of the control guidance;
- (4) Improvement in the existing attitude system;
- (5) Monitoring essential parameters for fail-safe operation of the improved guidance.

To provide these capabilities an instrument system was developed employing advanced component design and utilizing subsystems which had been shown to be airworthy for production installation.

The relationship of the various elements in the system is shown in Figure 4. The system installation will be dual providing separate, independent systems for both pilot and copilot.

A. ROTATION/GO-AROUND COMPUTER

As a part of the program to provide a rotation, climb-out and go-around instrument guidance system for the KC-135 several guidance schemes were investigated. Since this program was initiated to provide a total system that will be considered for retrofit, the subsystems chosen had to be sufficiently developed to be ready for production.

The R/GA computer chosen for the system had been developed as a part of the C-141 all-weather landing system program conducted by the SEG. It provides an angle-of-attack guidance signal to the flight director system for display on the horizontal pointer of the attitude director indicator (ADI). This angle-of-attack guidance signal commands an optimum rotation and climb-out for the aircraft based on weight, drag and thrust available. During takeoff, the R/GA mode will be selected prior to the beginning of runway acceleration. When proper rotation speed is reached, the pilot will rotate his aircraft to center the horizontal pointer of the ADI. By maintaining this centered position, the aircraft will achieve optimum climb-out.

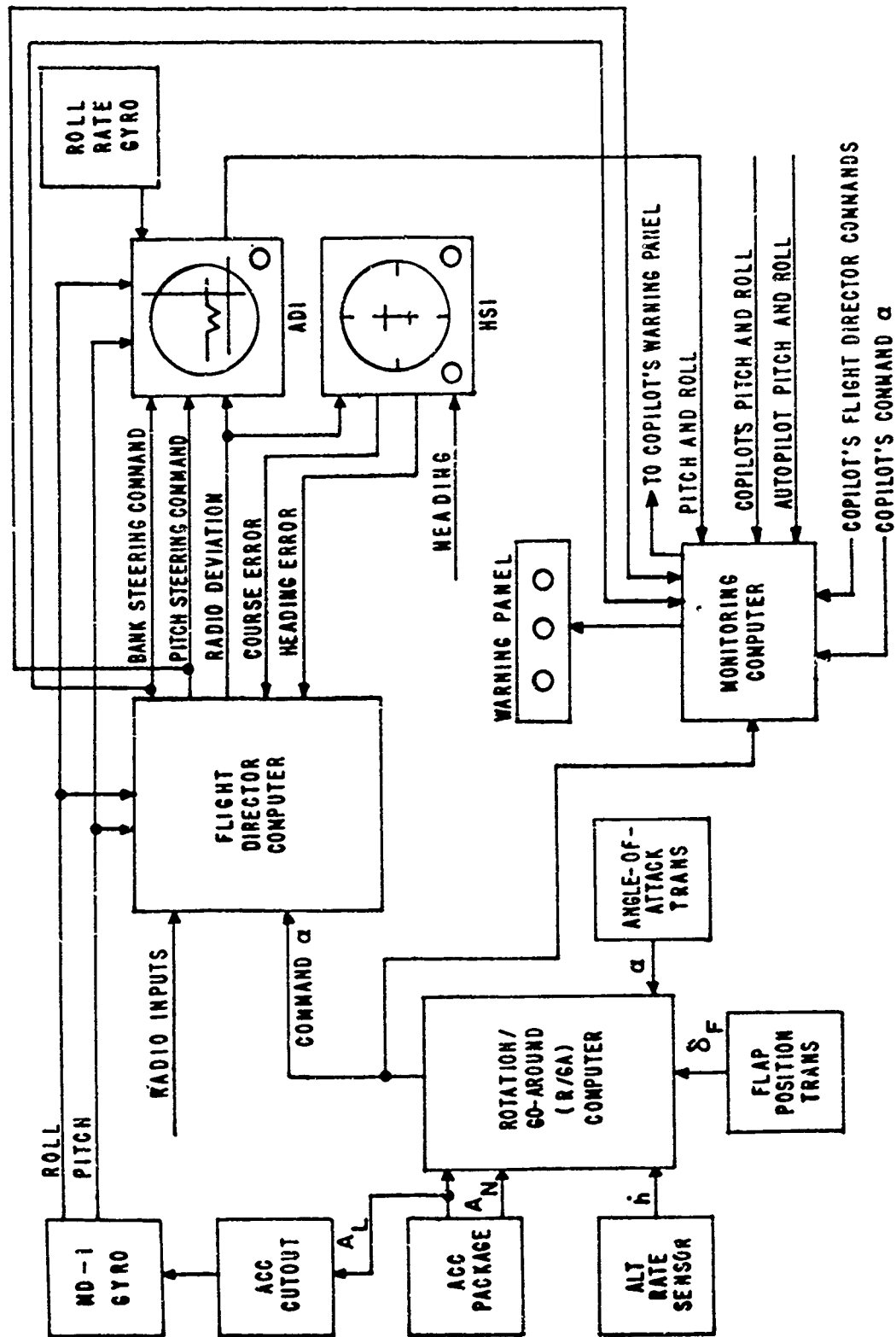


Figure 4. C/KC-135 Rotation/Go-Around Flight Director System - Pilot's System

It is to be noted that the R/GA computers do not tell the pilot when to rotate at takeoff, but rather how much to rotate. The pilot disregards the pitch steering bar of the ADI until rotation speed is attained; he then rotates the aircraft until the steering bar is nulled.

B. FLIGHT DIRECTOR COMPUTER SYSTEM

The flight director computer system includes the flight director computer (FDC), the ADI and the horizontal situation indicator (HSI). This system displays flight control information including roll, pitch, heading, radio deviation and flight director computer steering commands in an integrated, easily interpreted format. This basic system is installed in all the newer generation Air Force aircraft.

In addition to processing the input of the R/GA computer for display, the FDC presents pitch and bank steering commands to the pilot during many other phases of the flight profile including enroute navigation (VOR, TACAN, and Doppler) and landing (ILS and ILS Approach). The computer to be used in the system is a newly designed unit which extensively utilizes microcircuitry.

C. GYRO PITCH ERECTION CUT-OUT

One of the problems which has been prevalent with the vertical gyro is the pitch error which develops during high longitudinal acceleration. This error is due to the gyro pitch erection circuit seeking a false vertical due to longitudinal acceleration.

As discussed in Section II, the purpose of the erection circuit is to correct the verticality of the gyro for free drift. Since the free drift of the gyro is 0.25 degrees per minute and the gimbal erection motor rate is 1.5 degrees per minute, the erection motor can be turned off during periods of high acceleration reducing the gyro error rate by 1.25 degrees per minute. This technique is used to improve the accuracy of the gyro indicating system.

The erection cut-out unit senses longitudinal acceleration, A_L , which has been corrected for pitch errors from the R/GA computer. When acceleration reaches a level which adversely affects the pitch erection circuit of the vertical gyro, the circuit is switched off and the gyro becomes free, minimizing the short term pitch errors due to acceleration.

D. SYSTEM MONITORING

Monitoring is provided for the attitude system, the R/GA computers and the flight director computers to assure not only flight safety but proper operation of the guidance system as well.

1. Flight Director and R/GA Computer Monitoring System

Monitoring of the flight director computers and the R/GA computers is accomplished by comparison of the outputs. The two outputs from the R/GA computers are compared and if a disparity exists a monitor circuit detects the difference and indicates a malfunction to the pilot. The two outputs from the pilot's flight director computer, bank command and pitch command, are compared with the

respective outputs from the copilot's flight director computer in a method identical to the R/GA computer comparison. This monitoring method indicates if a failure has occurred in either system but does not indicate which system has failed.

2. Attitude Monitoring System

The attitude monitoring system provides a continuous check on the condition of the three attitude reference systems (pilot's, copilot's and autopilot's) warning the pilot of a failure if a discrepancy exists between the systems. The monitor indicates the system and axis (roll and pitch) that has failed. The monitoring technique used is majority logic which is discussed in detail in Section VI.

SECTION IV

ROTATION/GO-AROUND COMPUTER

A. THEORETICAL DISCUSSION OF ROTATION, CLIMB-OUT AND GO-AROUND GUIDANCE

The R/GA computer provides an angle-of-attack output which commands optimum guidance throughout the critical rotation, climb-out and go-around regimes. This command is based on the aircraft weight, drag and available thrust.

1. Thrust/Drag Characteristics

A typical thrust/drag curve for a four-engine jet transport like the KC-135 is illustrated in Figure 5. As indicated in the figure, there are three drag components which can be present during the takeoff and go-around regimes. The bottom area on the thrust/drag graph represents the basic drag of the aircraft. Basic drag increases with airspeed because of increasing dynamic pressure and also increases at low airspeeds because of the increased angle of attack required to give sufficient lift. The second drag force operating on the aircraft can exist due to application of rudder to counteract the moment caused by loss of an engine. The remaining drag force is due to the landing gear.

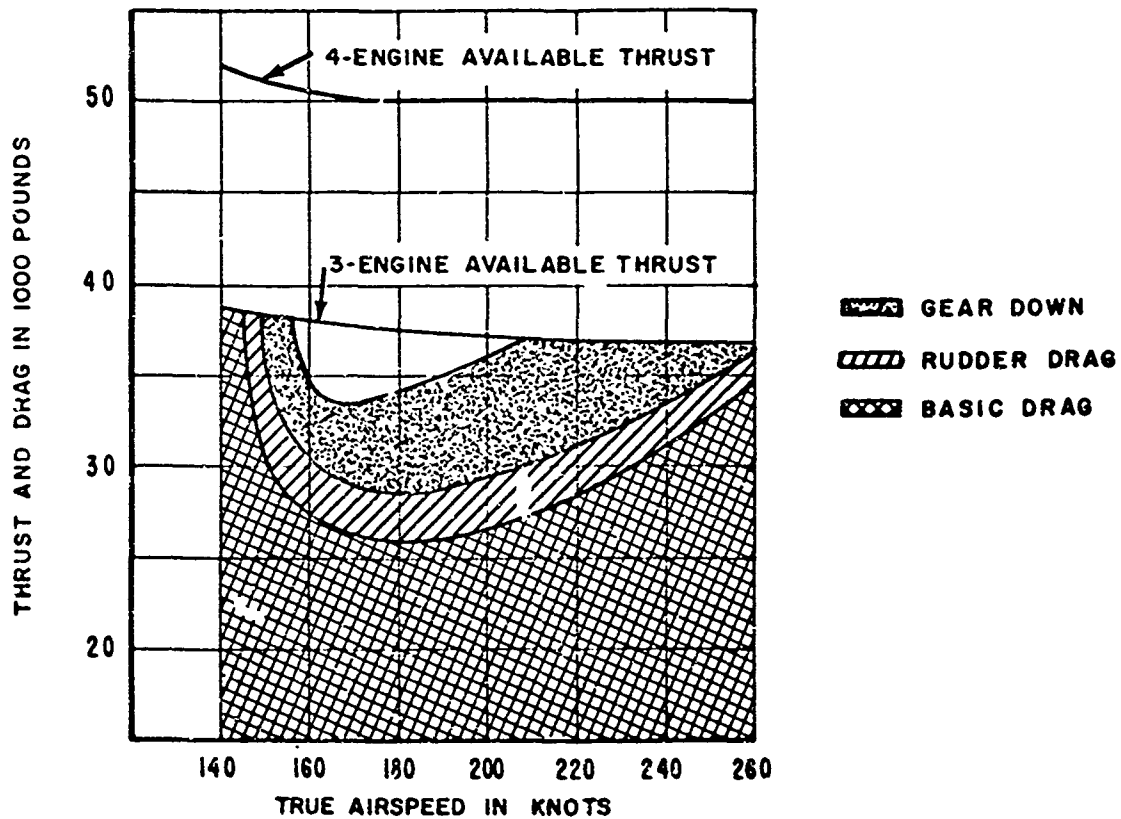


Figure 5. Thrust and Drag vs Airspeed

The available thrust curves for four engines and three engines are also plotted in Figure 5 as a function of airspeed. Available thrust for jet engines is seen to be relatively constant with airspeed. The difference between the total drag curve and engine thrust plot indicates the thrust available to accelerate or climb. Note that if an aircraft loses an engine after it becomes airborne, available thrust can be less than drag if airspeed is too low or too high, causing the aircraft to come back down.

The thrust drag curves have been plotted as a function of airspeed for a fully loaded jet. These curves when plotted for a lighter aircraft move downward and to the left along the airspeed axis. However, if these curves are plotted as a function of angle of attack, they do not shift along the angle-of-attack axis as a function of aircraft weight. This points to angle of attack as the desirable longitudinal-axis parameter for controlling aircraft pitch attitude during takeoff and go-around, since for different aircraft weights the same angle of attack will give minimum drag and maximize the extra thrust available for acceleration or climb.

2. Utilization of Extra Thrust

As stated in Section II, Equation 1 is the basic aircraft equation that describes how for a jet aircraft, extra thrust can be utilized in controlling the airframe.

$$\frac{T-D}{W} = \gamma + \frac{\dot{U}}{g}$$

Starting with this basic equation it will be shown that for a jet aircraft the angle of attack which maximizes the flight-path angle (or minimizes drag) is approximately equal to the angle of attack corresponding to the maximum lift-to-drag ratio.

Since $W = L$ at take off

$$\frac{T}{W} - \frac{D}{L} = \gamma + \frac{\dot{U}}{g} \quad (2)$$

Since thrust is relatively constant at takeoff with power settings and is independent of airspeed, flight-path angle, γ , or acceleration, \dot{U} , can be maximized for a given weight and total thrust by minimizing the term D/L or by maximizing the lift-to-drag ratio, L/D .

$$\frac{L}{D} = \frac{C_L q S_A}{C_D q S_A} = \frac{C_L}{C_D} \quad (3)$$

Equation 3 states that the maximum lift-to-drag ratio also corresponds to the maximum coefficient of lift/coefficient of drag quotient C_L/C_D . Since γ can be defined by

$$\gamma = \sin^{-1} \left(\frac{L}{D} \right) \quad (4)$$

maximum climb will correspond to the maximum L/D ratio. Using a polar plot of C_L/C_D , this point can be identified as the tangent to a C_L/C_D curve drawn from the origin. Figure 6 illustrates the KC-135 C_L vs C_D plotted for 30° flaps which are used during takeoff with the maximum C_L/C_D point calculated. To relate this ratio to angle of attack the curve of C_L vs α is also drawn in Figure 6. On this curve the maximum C_L/C_D quotient has been transferred from the C_L vs C_D curve to identify it in terms of angle of attack.

3. Angle-of-Attack Requirements During Rotation, Climb-Out, and Go-Around

Although it has been shown that maximum climb angle is obtained at the angle of attack corresponding to maximum lift-to-drag ratio, this angle of attack will not support the aircraft in the air at lift-off speeds. Lift-off speed must be kept low to minimize the ground roll required for initial acceleration. Rotation at takeoff must, therefore, be made to a higher initial angle of attack to lift-off giving the aircraft some climb or vertical speed. Since forward acceleration should be maintained until a safer airspeed is reached, maximum angle of attack before stall should not be used at takeoff. When sufficient airspeed is attained, the aircraft should be pitched to an angle of attack corresponding to maximum lift-to-drag ratio to maximize the steady-state climb angle. Climb angle rather than rate of climb should be maximized to clear an impending obstacle during climb-out. If full engine power is available after initial climb, the pilot can subsequently reduce angle of attack still further after sufficient airspeed and vertical speed are reached to allow a faster climb-out. This final climb-out at a lesser angle of attack and at a higher airspeed is a luxury that the pilot can afford if ample thrust is available and climb angle is sufficiently large.

In a go-around maneuver, the first concern of the pilot is to stop the descent with minimum altitude loss after the decision is made to abort the approach and landing. Since the aircraft has had adequate airspeed during the approach phase, minimum altitude loss during the go-around maneuver can best be accomplished by assuming the maximum angle of attack which will give a safe margin above stall angle of attack. This will give maximum safe lift and quickly reduce rate of descent to zero after which the pilot can again fly an angle of attack similar to that for climb-out after rotation. By utilizing angle-of-attack information instead of airspeed, maneuvers near stall can be made more safely since, during transient conditions, airspeed is not always an immediate indication of the margin available before the stall condition is reached.

4. Programmed Angle of Attack

Now that the angle-of-attack requirements have been established, optimum angle-of-attack command can be defined throughout rotation/climb-out and go-around

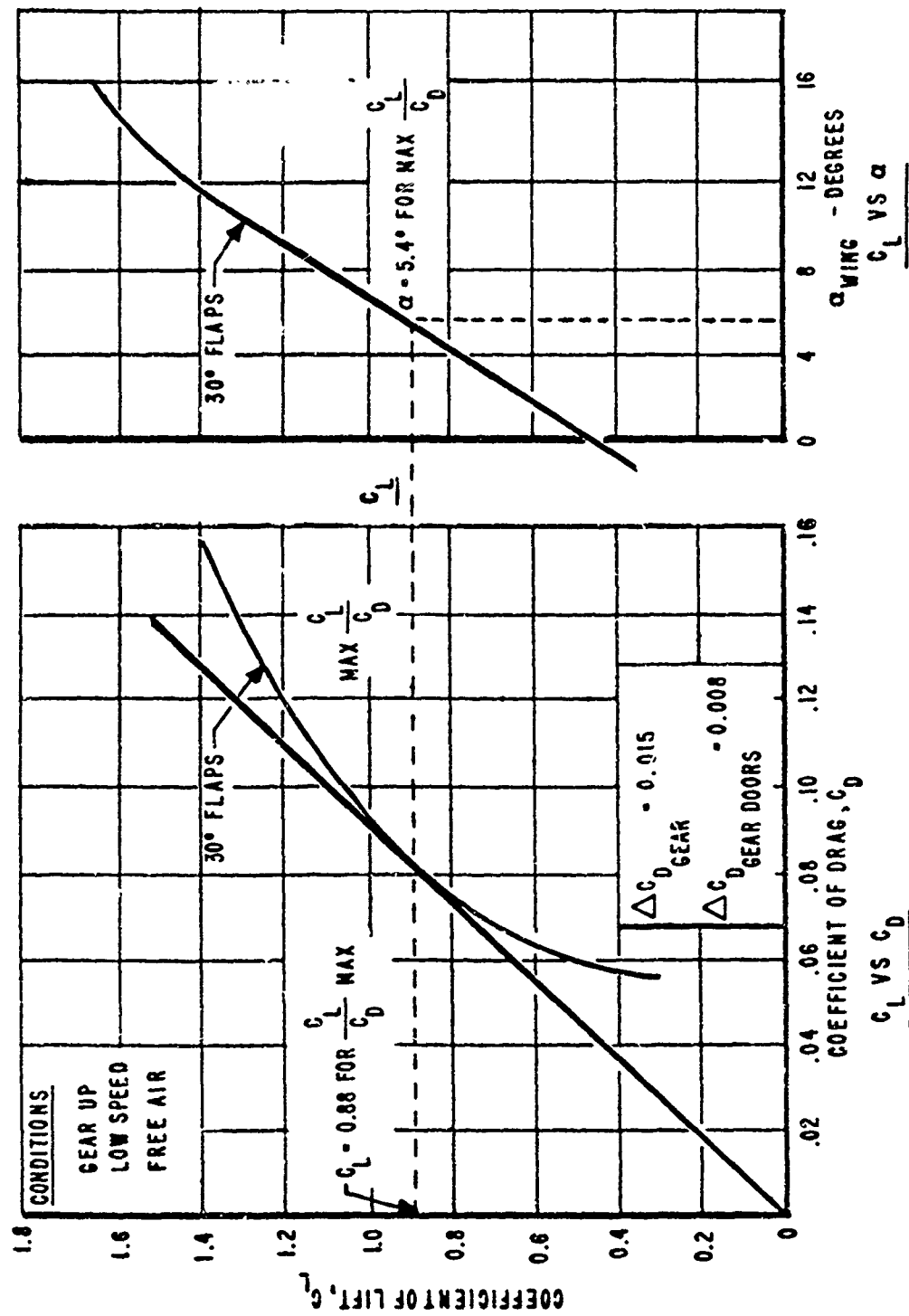


Figure 6. Polar Plot, C_L vs C_D and C_L vs α_{WING} for KC-135A

regimes as a programmed function of vertical speed. This nonlinear programmed angle-of-attack function as computed in the R/GA computer is shown in Figure 7. As is mentioned in the block diagram discussion of the R/GA computer, Subsection B, programmed angle of attack is combined with augmented angle-of-attack feedback to give a nulled pitch steering bar when optimum angle of attack is achieved.

Referring to Figure 7, when vertical speed is zero at rotation an angle of attack is commanded to give lift-off and attain some vertical speed. As vertical speed builds up, the aircraft quickly reaches the angle of attack corresponding to the maximum lift-to-drag ratio. This angle of attack allows the aircraft to accelerate to a higher airspeed while continuing to pick up additional vertical speed. As the rate of climb continues to increase due to extra available thrust, the angle of attack is further decreased to a value which gives a fast climb-out at a desired combination of airspeed and rate of climb. In the event of an engine failure, the loss of thrust would result in reduced rate of climb and the aircraft would migrate back to the angle of attack corresponding to minimum drag and optimum climb-out angle.

In a go-around situation, assume the airplane has been descending down the glide-slope beam with a descent rate of approximately 600 feet per minute. Upon initiation of a go-around, a maximum safe angle of attack is commanded as shown on the left side of Figure 7. This angle is maintained until the sink rate is essentially reduced to zero after which the airplane migrates to the same programmed angle of attack used for climb-out.

The programmed angle-of-attack function described above provides safety during loss of an engine. When power is marginal, the aircraft is directed to a maximum

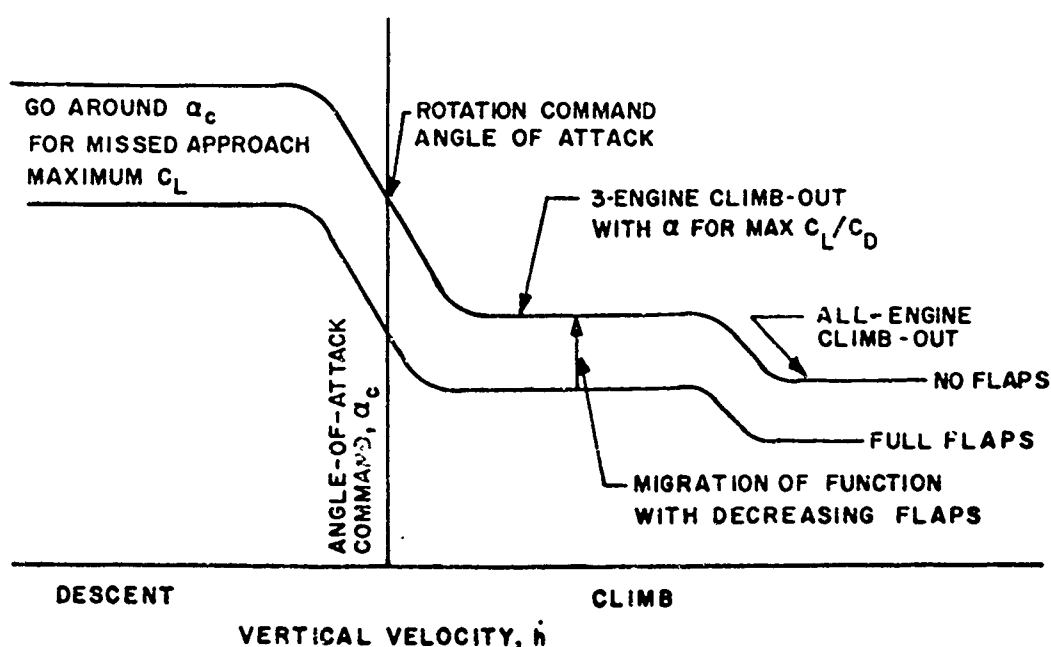


Figure 7. Programmed Angle-of-Attack Command

climb angle $\left(\frac{C_L}{C_D} \right)_{MAX}$ which is represented by the first plateau of the angle-of-attack command curve, Figure 7.

Since the C_D vs C_L plot is modified by flap position, this must be considered in computing the programmed angle-of-attack term. The amount of modification for each portion of the curve is dependent on the effects of flaps during that portion of the takeoff or go-around. The modification in the programmed angle-of-attack (α_p) function is illustrated in Figure 7 as shifting of the α_p curve as a function of flaps, about the α_p axis.

5. Phugoid Damping

When angle of attack is the only controlling longitudinal axis parameter, aircraft phugoiding may result. Phugoiding is a cycling in vertical speed and airspeed with negligible change in angle of attack. Various sources of phugoid damping signals were studied during the development of the R/GA computer. The sources include vertical velocity, longitudinal acceleration, Mach rate and pitch. These various phugoid damping parameters have been compared by simulation studies which showed that vertical speed and longitudinal acceleration were most effective in preventing phugoiding. The implementation of these terms is discussed in the block diagram description.

B. BLOCK DIAGRAM DISCUSSION

The system block diagram of the R/GA computer is shown in Figure 8. There are three basic computations performed by the computer: (1) vertical speed, (2) augmented angle of attack, and (3) programmed angle of attack which are discussed separately for clarification. Each area of computation is indicated on the block diagram.

1. Vertical Speed Computation

The source of altitude rate is a remote altitude rate sensor with an input of static pressure. Barometric altitude rate, \dot{h} , is brought into the computer through a quadrature rejection circuit and then is filtered to remove higher frequency aerodynamic and mechanical noise. The R/GA computer computes vertical speed by complementing the filtered altitude rate with normal (vertical) acceleration. Normal acceleration is obtained from an accelerometer mounted externally. The output of the accelerometer consists of the acceleration signal, A_N , plus an error signal, $\epsilon \phi$, due to gravity effects of aircraft banking, ϕ . A bank signal, $\sin \phi$, from the vertical gyro is passed through a shaping network which gives it the same characteristic as the accelerometer error signal, $\epsilon \phi$. This error signal can be shown to equal $g \left(\frac{1 - \cos \phi}{\cos \phi} \right)$. Signals, $A_N + \epsilon \phi$ from the accelerometer and $\epsilon \phi$ from the shaping network, are combined to yield A_N . The banking signal thus is used to eliminate the accelerometer bank errors. The normal acceleration signal A_N is passed through a band-pass filter. The band-pass filter integrates the acceleration to provide normal velocity in the band-pass region. The filter also attenuates the high-frequency errors due to vibrations and eliminates low-frequency errors caused by stand-off and the gravity constant. The filtered altitude rate from the \dot{h} sensor and the normal velocity derived from the accelerometer are summed together and amplified. The resulting complemented vertical speed signal,

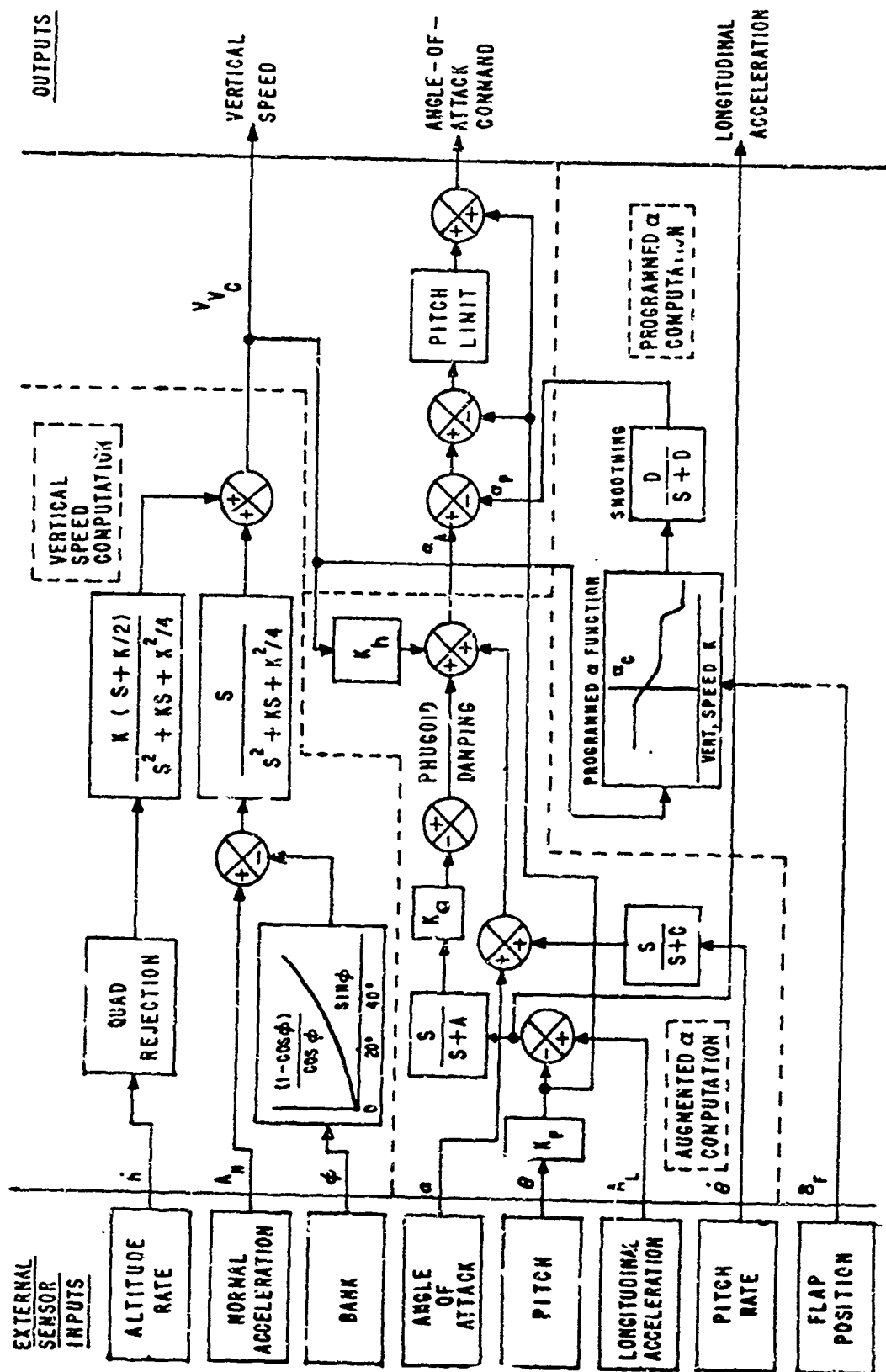


Figure 8. Block Diagram of Rotation/Go-Around Computer

V_{VC} is used for phugoid damping and for programmed angle-of-attack signal computation. The signal is also delivered to the FDC for use in computations.

2. Programmed Angle of Attack

Programmed angle of attack, α_P , is the optimum angle of attack to be commanded. It is a function of both complemented vertical speed, V_{VC} , and flap position. Complemented vertical speed is passed through the function generating network. This network has the transfer characteristic illustrated in Figure 7 discussed previously. The function generator is modified with the flap position signal, δ_F , which is obtained from an external flap transducer. In the event go-around is required because of a missed approach, V_{VC} is negative. The R/GA computer then commands a maximum safe angle of attack. For three-engine climb-out, the climb rate is moderate and an angle of attack corresponding to maximum lift-to-drag ratio is commanded. With sufficient thrust, a greater altitude rate is sensed and angle of attack giving a high-speed climb-out is commanded.

3. Augmented Angle of Attack

Local angle of attack is supplied by an angle-of-attack transmitter located on the aircraft. This angle of attack is different from the actual angle of attack of the wing due to the position of the sensor on the fuselage. A separate flight test was conducted to determine the difference between the actual angle of attack and the local angle of attack at the sensor. The plot of this relationship is illustrated in Figure 9. The error in the local versus true angle-of-attack is removed by compensating the programmed angle-of-attack function generator for the difference.

The angle-of-attack signal from the sensor is augmented with the pitch rate for damping. An external longitudinal accelerometer provides an acceleration signal, $A_L + \epsilon \theta$. This signal contains an error term, $\epsilon \theta$, which results from gravitation effects due to aircraft pitch, θ . A pitch signal from the vertical gyro, $\sin \theta$, is summed with the accelerometer signal so that it is just equal to the accelerometer error term, $\epsilon \theta$, cancelling this error from accelerometer output. The result, A_L , (which is available as an output for gyro erection cutout) is summed with the complemented vertical altitude rate signal, V_{VC} , providing phugoid damping of the augmented angle-of-attack signal. Since the R/GA computer commands the maximum climb angle, an unnaturally high pitch will be commanded when the weight of the aircraft is low and full thrust is used. Therefore, the commanded angle of attack, $\alpha_A + \alpha_P$, is pitch limited to prevent this condition. This pitch limit is of sufficient magnitude that it will affect the commanded output during conditions of high gross weight or reduced thrust.

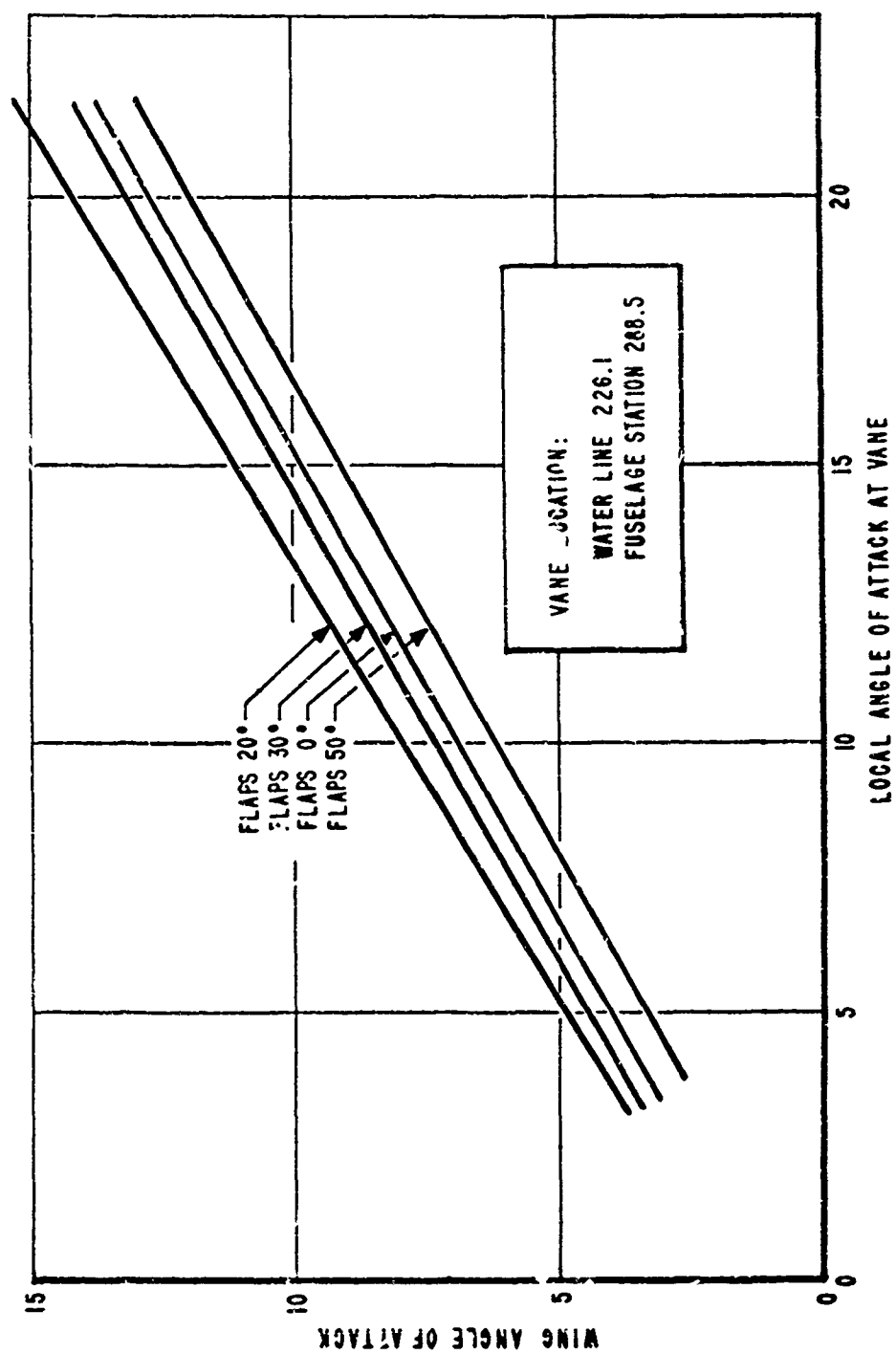


Figure 9. Angle of Attack of Vane vs Angle of Attack of Wing - KC-135

SECTION V

FLIGHT DIRECTOR COMPUTER SYSTEM

The flight director computer steering commands provide an accurate, highly responsive display of aircraft control action during ILS, VOR, TACAN, VOR/TACAN Approach, R/GA and Heading Modes. Of these modes, the R/GA and ILS modes are the most important because they involve aircraft control during critical portions of a mission (takeoff and landing). The role of the flight director in the R/GA mode is to provide an input with the proper scale factor to the horizontal pointer for display. The ILS mode, considerably more complex, involves computation of the command signals. The localizer lateral guidance is identical to VOR and TACAN modes for the purposes of this discussion.

The FDC is designed to provide the capability of operating to Category II landing minimums. Table II is an outline of the definition and requirements for the flight director for Category II landing minimums. For the flight director to meet these requirements, accuracy, stability, and the effect of external forces (winds) on the aircraft must be considered. The following is a discussion of the techniques used in meeting the improved ILS guidance requirements.

A. CROSSWIND FILTER

To minimize the effects of crosswinds, adequate crosswind compensation must be provided by the flight director so that proper rate damping can be included in the command signal. Yet, extreme care must be taken in implementing the crosswind filter so that windshear does not cause beam standoff errors.

Figure 10 shows the crosswind filter technique used to generate the composite rate signal in which the localizer noise is heavily filtered by using localizer, lagged localizer, and lagged roll angle. No heading or course error signal is used; therefore, there is no beam standoff error in the presence of crosswind or windshear. Furthermore, there is no possibility of hunting in roll because the need for high heading gain has been eliminated.

The transfer function of the rate generating system of Figure 10 can be derived as follows:

- E_{loc} = angular deviation of the aircraft from the localizer path.
- ϕ = aircraft roll attitude
- ψ = aircraft heading
- ρ = path distance to transmitter

where $\dot{\psi} = K\phi$.

TABLE II
FLIGHT DIRECTOR REQUIREMENTS FOR CATEGORY II

1. Definition of Category II
 - a. MDA (minimum decision altitude) 100 feet
 - b. RVR (runway visibility range) 1200 feet
2. Category II Criteria
 - a. Wind Conditions (maximum)
 - (1) Surface crosswind component 15 knots
 - (2) Surface downwind component 10 knots
 - (3) Windshear - 4 knots per 100 feet starting at 500 feet
 - b. Localizer Performance
 - (1) Stabilized before outer marker
 - (2) Tracking from outer marker to 300 feet within $\pm 35 \mu$ amp (95% probability)
 - (3) Tracking from 300 feet to decision altitude (100 feet) within $\pm 25 \mu$ amp (95% probability)
 - c. Glideslope Performance
 - (1) Stability before a altitude of 700 feet
 - (2) Tracking from 700 feet altitude to decision altitude (100 feet) within $\pm 35 \mu$ amp or ± 12 feet, whichever is larger.

$$\begin{aligned}
E_o &= K_{loc} E_{loc} \left(1 - \frac{1}{Ts + 1} \right) + K_{\phi} p s^2 E_{loc} \left(\frac{-1}{Ts + 1} \right) \\
E_o &= \frac{K_{loc} E_{loc} Ts - K_{\phi} p s^2 E_{loc}}{Ts + 1} \\
E_o &= s E_{loc} \frac{-K_{\phi} p s + K_{loc} T}{Ts + 1} \\
E_o &= K_{loc} T s E_{loc} \frac{\left(\frac{-K_{\phi} p}{K_{loc} T} \right) s + 1}{Ts + 1} \quad (5)
\end{aligned}$$

It can be seen from Equation 5 that E_o is proportional to localizer rate and the rate gain is proportional to T and K_{loc} . For proper damping, it is only necessary to maintain the term $K_{\phi} p / K_{loc}$ approximately equal to T over the operating range of p . Proper selection of T can maintain this equality.

B. TRACKING ACCURACY

As indicated in Table II localizer tracking must be maintained within ± 25 microamps of beam center and glideslope tracking must be maintained with ± 35 microamps of beam center. This requires computer nulls and parallax errors in reading the steering pointers to be minimum. Also, the error washout must be minimum so that an aircraft that is mistrimmed 1 or 2 degrees in bank will not cause an error. The following is an error analysis of both the glideslope and localizer accuracy of the flight director system.

1. Localizer Error

Function	LOC Error μ amps	(Error) ²
Roll trim error	4.0	16.0
Error due to heading not cancelling	2.0	4.0
Windshear of 5 knots per 100 ft	6.9	47.6
Modulator or demodulator unbalance	3.8	14.5
Visual dead zone of indicator	10.0	100.0
Total		182.1

Root Sum Square Calculation to Total Errors (rss):

$$rss = \sqrt{(\text{Error})^2}$$

$$rss = \sqrt{182.1} = 13.5 \mu a$$

Calculated tracking accuracy = $\pm 13.5 \mu a$

Required tracking accuracy = $\pm 25 \mu a$

2. Glideslope Error

Function	Glideslope Error μ amps	(Error) ²
Glideslope error for pitch washout	6.75	45.5
Modulator or demodulator unbalance	3.8	14.5
Visual dead zone of indicator	10.0	100.0
Windshear of 5 knots per 100 ft (along runway)	6.9	47.6
	Total	207.6

$$rss = \sqrt{207.6}$$

$$rss = 14.4 \mu a$$

Calculated tracking accuracy = $\pm 14.4 \mu a$

Required tracking accuracy = $\pm 35 \mu a$

From the above calculations of flight director system errors, it is shown that the system adequately meets the glideslope and localizer tracking requirements for Category II operation.

C. GLIDESLOPE EXTENSION

1. Gain Programming

The glideslope gain selected for the ILS mode will maintain stability at altitudes down to 200 feet above the runway elevation. Below 200 feet it is necessary to reduce the gain as a function of altitude because of beam convergence. The FDC provides this reduction program as a function of time after passing the middle marker. Gain is reduced continuously to one-fourth initial value in 15 seconds after passing the middle marker. Figure 11 illustrates the effect of gain programming in keeping the flight director commands accurate and stable.

2. Rate Damping

Because the glideslope beam becomes noisy below approximately 200 feet, rate damping is required to stabilize the pitch steering command. During the initial

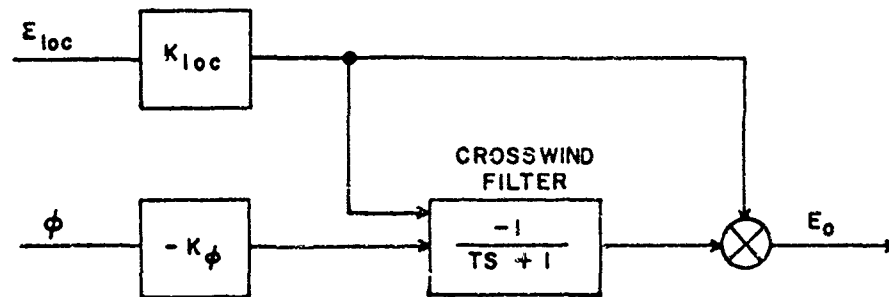


Figure 10. Composite Beam Rate Generation

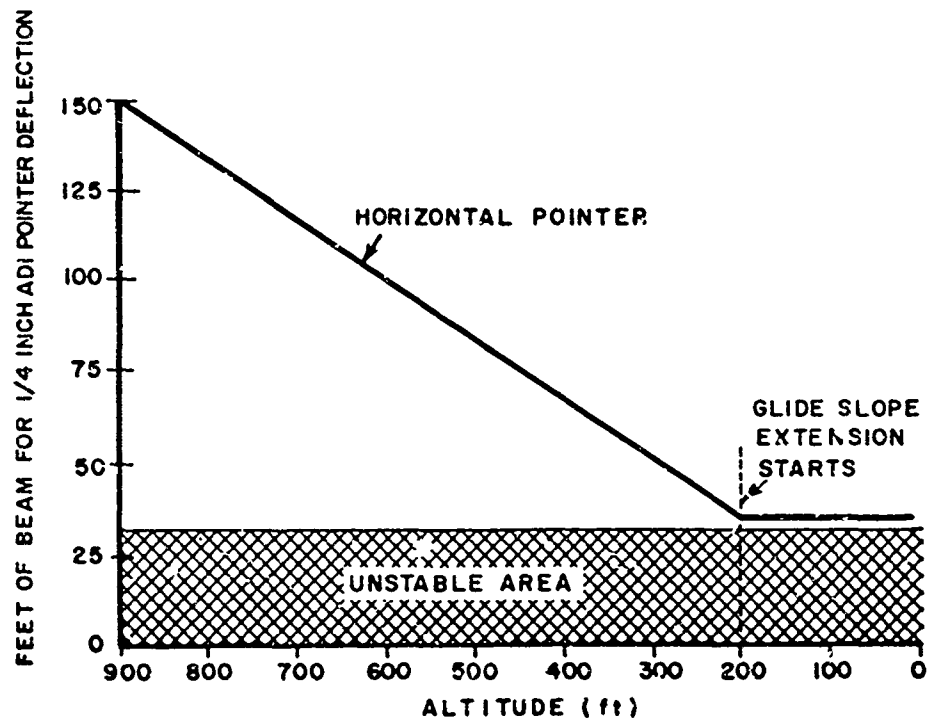


Figure-11. Glideslope Gain Programming

approach phase, a washout filter memorizes instantaneous rate of descent (\dot{h}) from the R/GA computer. When glideslope extension is engaged at the middle marker, the output of the washout filter (memorized \dot{h} error) is added to the reduced glideslope signal. The addition of vertical rate makes it possible to reduce glideslope gain to a level where glideslope bends and noise are insignificant while maintaining a high degree of directional gain.

D. MISSED APPROACH

If at any time during a landing approach using either ILS or GCA, the pilot must go around, selection of the R/GA modes will remove the ILS commands from the flight director display and present go-around commands as discussed in Section IV.

This command provides control guidance resulting in a minimum loss of altitude and a smooth transition from ILS to climb-out.

SECTION VI

ATTITUDE MONITORING SYSTEM

A. SYSTEM THEORY

The remote attitude monitoring system, employing the principle of majority logic, monitors the condition of the three attitude reference systems by receiving and comparing inputs of roll and pitch from the pilot's ADI, the copilot's ADI and the autopilot gyro. Figure 12 shows the total system relationship. Each ADI has synchro transmitters tied directly to the roll and pitch axes of the display sphere. These synchros provide output signals to the monitoring computer which are proportional to the display position. By monitoring the output of the display sphere, a check is provided on every element of the attitude system, the gyro, the cabling between components, the amplifier and the indicator, since a failure in any of these components would affect the display sphere position. The third source of attitude information, the autopilot gyro, is fed to the monitoring computer to be compared with the indicator sphere positions. The analog output of the indicators is made identical to the autopilot gyro output to simplify the majority logic.

Since the two ADIs can be individually trimmed in pitch by the pilot and copilot, the pitch outputs to the computer can be different due to the difference in pitch trim. Therefore, the pitch trim signals, θ_T , are also fed to the monitoring computer to remove the pitch trim component present in the total pitch input signal, $\theta + \theta_T$.

B. COMPUTER THEORY

The logic diagram of the pitch channel of the computer is illustrated in Figure 13. The roll channel is identical except for the pitch trim and pitch erection cutout monitor inputs.

The three pitch inputs are summed as indicated in Figure 13. If the input signals are equal, which is the normal condition, the output of each summing amplifier is zero. In the case of a failure, the outputs will not be zero. This can be restated by saying that a nonzero at the output of a summing amplifier is an indication that one of the input systems has failed. (Assume for now that two systems cannot fail simultaneously.) As an example, assume that System A has failed, its input to the computer being different than B or C. The output of summing amplifier 1 will indicate that either System A or System B, (A+B), has failed and the output of summing amplifier will indicate that either System A or System C (A+C) has failed. The output of summing amplifier 2 will be zero. This example can be expanded to show that outputs from summing amplifier 1, 2 or 3 is an indication of a system failure and is represented, in logic form, by (A+B), (B+C) or (A+C), respectively. If these three outputs are applied to the "AND" gates as illustrated, the output of each gate will indicate a particular system failure, represented in logic form, by Equation 6 developed below.

To complete the example of System A failure, the inputs to gate 1 are (A+B) and (A+C). The output of the gate is

$$\text{Output} = (A+B) + (A+C)$$

$$\text{Output} = A+BC$$

6)

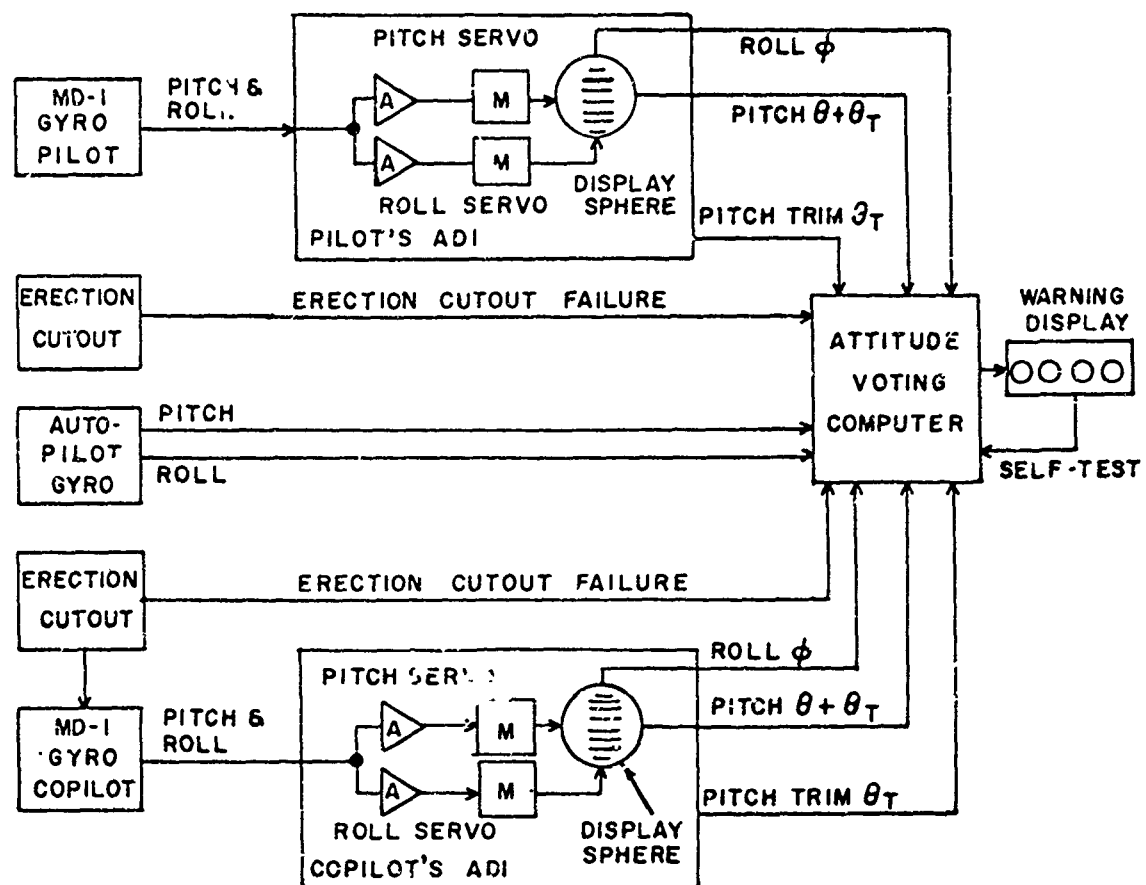


Figure 12. Remote Attitude Monitoring System

This states that if System A is in error or both Systems B and C are in error, there will be an output from gate 1. The probability of any two systems failing simultaneously is remote; also, if two systems do fail simultaneously, outputs will be present at all three gates; therefore, the "AND" term of the output expression can be ignored ($BC = 0$). Expansion of this example will show the logic outputs of gates 1, 2 and 3 to be A, B, and C, respectively. The outputs of each of the gates are used to switch the failure annunciation on the instrument panel.

It is mandatory for any monitoring device to have a high reliability and for the operator to know that the device is operating correctly. Therefore, microcircuitry has been used extensively in the design of the computer and a self-test capability has been included in this device to completely test its operation. As indicated in Figure 13, self-test is accomplished by applying calibrated error signal to each of the summing amplifiers. Using this technique more than 90 percent of the computer circuitry is tested.

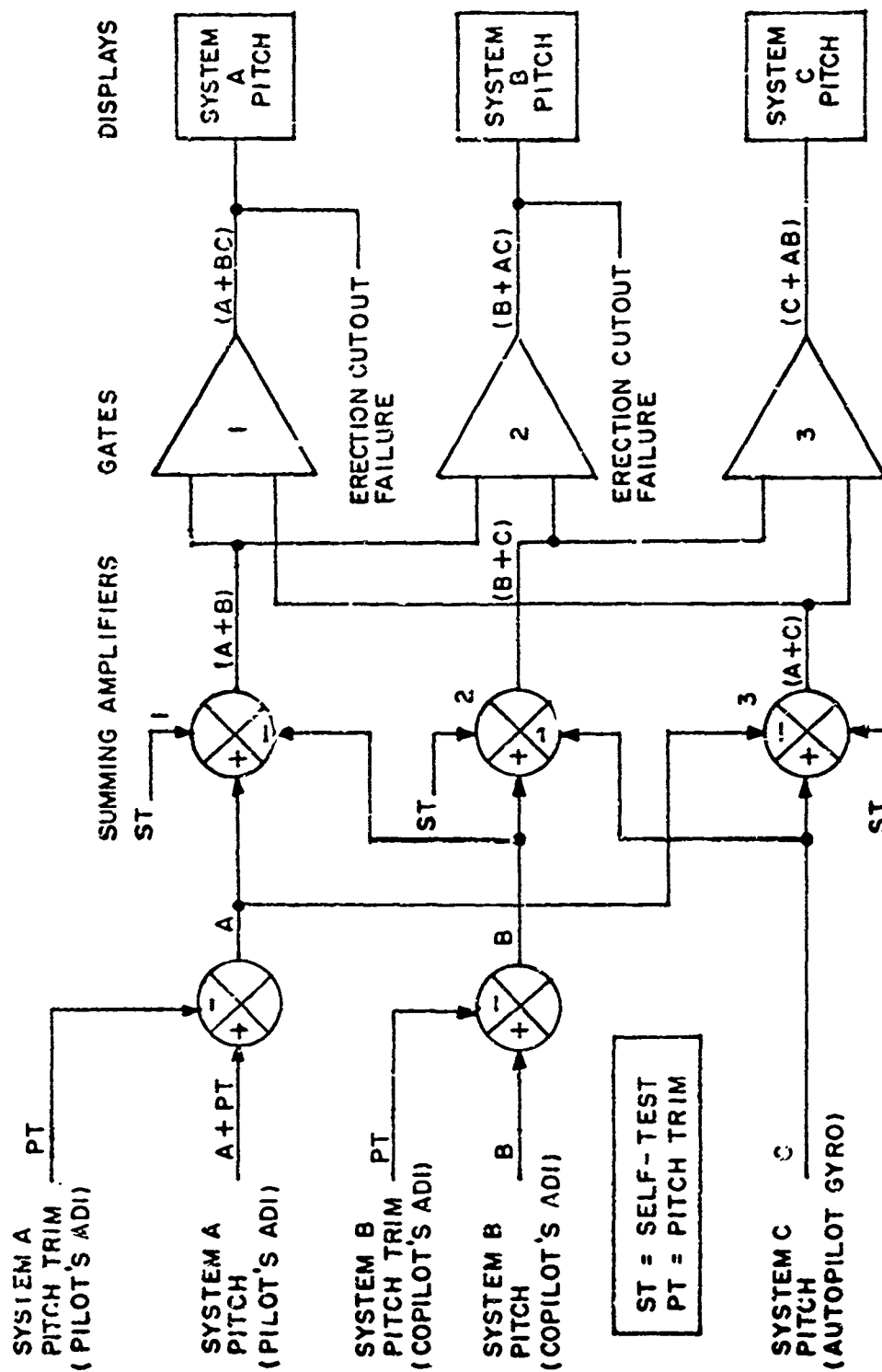


Figure 13. Remote Attitude Monitoring Computer - Block Diagram Pitch Channel

SECTION VII

CONCLUSIONS

The R/GA instrument guidance system described in this paper is presently being developed for flight test on a KC-135 prior to production retrofit. At this time simulation studies of the R/GA computer and the flight director computer are being conducted to optimize the system parameter for the KC-135. Results of these studies are not available for inclusion in this report. Simulator studies conducted during the initial development of the R/GA computer are presented in the Appendix. These studies illustrate the effectiveness of controlling an aircraft takeoff and go-around with optimum angle-of-attack guidance provided by the R/GA computer and flight director system.

APPENDIX

LOW APPROACH-NAVIGATION DIRECTOR SYSTEM (LANDS) SIMULATION

During the latter part of 1962 Air Force Contract 33 (657)-9639 was awarded to the Collins Radio Co. to develop a Low Approach-Navigation Director System (LANDS) which was to be integrated with the existing C-141 instrument system. The rotation/go-around computer was developed as a part of this contract. The flight test of the LANDS system was conducted on a T-39 and therefore the simulation studies prior to flight test were conducted with a T-39 model.

The final simulation of the angle-of-attack control system was accomplished at the time of the overall LAND system simulation. Actual hardware, including the R/GA computer and cockpit instruments, was used with an actual pilot within the control loop. Figures 14, 15, and 16 show recordings of this simulation. Figure 14 shows a go-around which was initiated with the simulated T-39 in the approach configuration. Figure 15 shows takeoffs with one engine and two engines operating. Altitude rate on the rotation/climb-out recordings is seen to go negative initially at rotation. This is to be disregarded since the simulation was not accurate until the aircraft became airborne. Figure 16 shows a two-engine takeoff with an engine being lost shortly after lift-off. Each of these recordings shows how angle of attack becomes adjusted to a value appropriate for the power available.

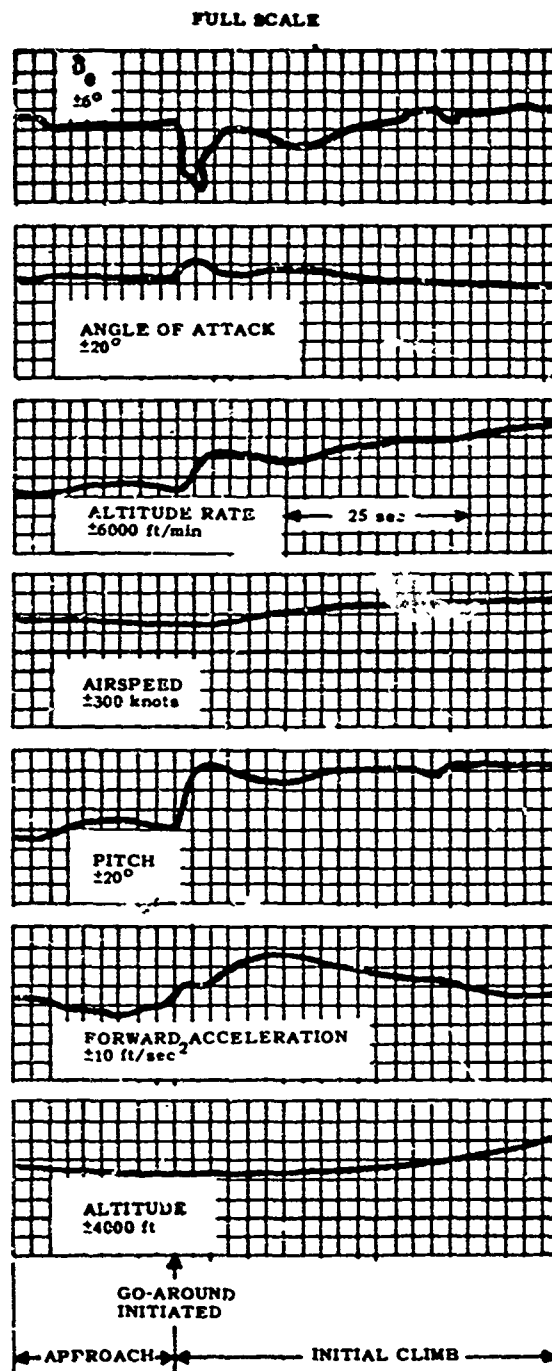


Figure 14. Go-Around Using Programmed Angle of Attack for Flight Director Steering - Simulated T-39 Aircraft

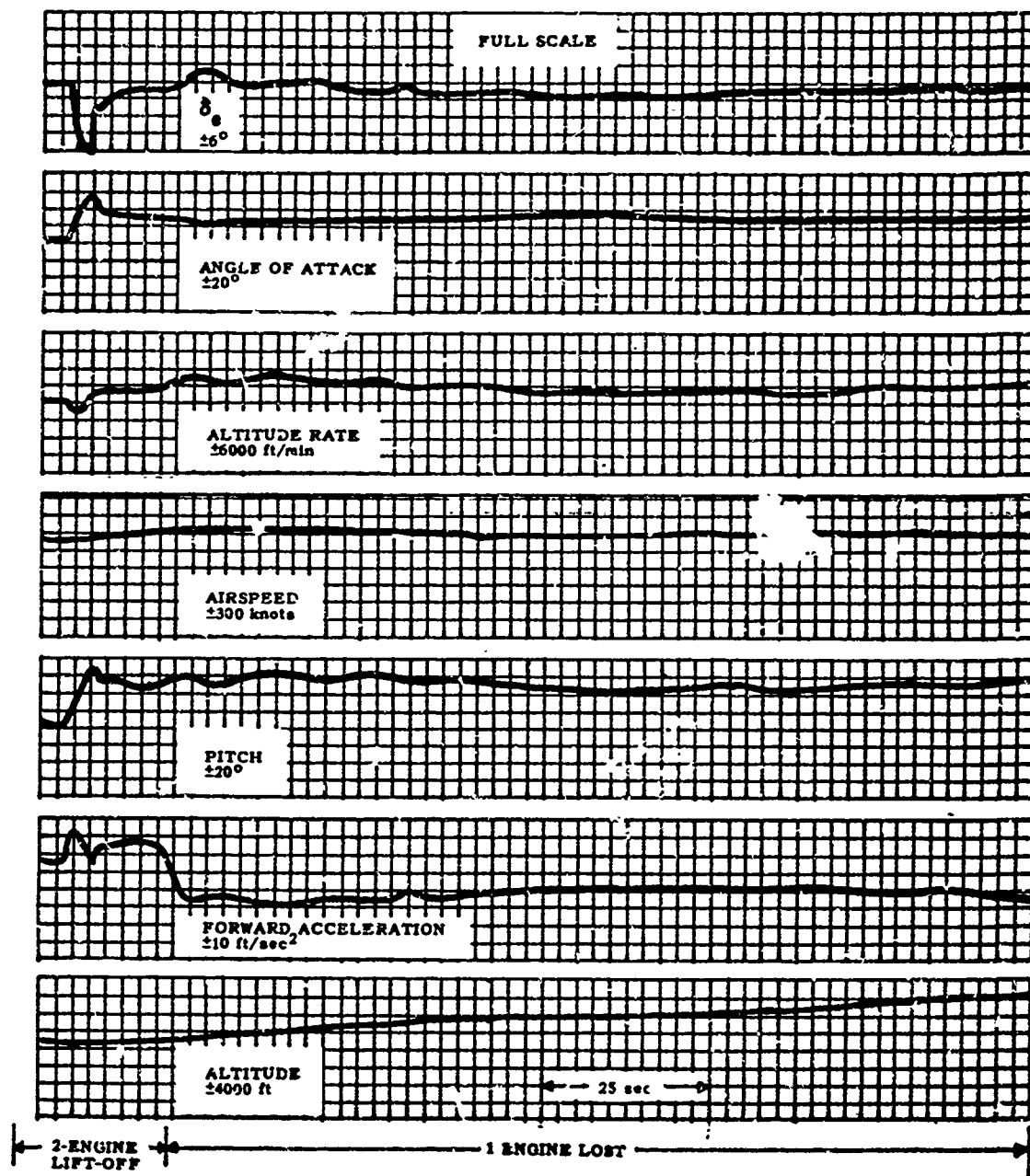


Figure 15. Rotation and Climb-Out Using Programmed Angle of Attack for Flight Director Steering - Simulated T-39 Aircraft With One and Two Engines Operating

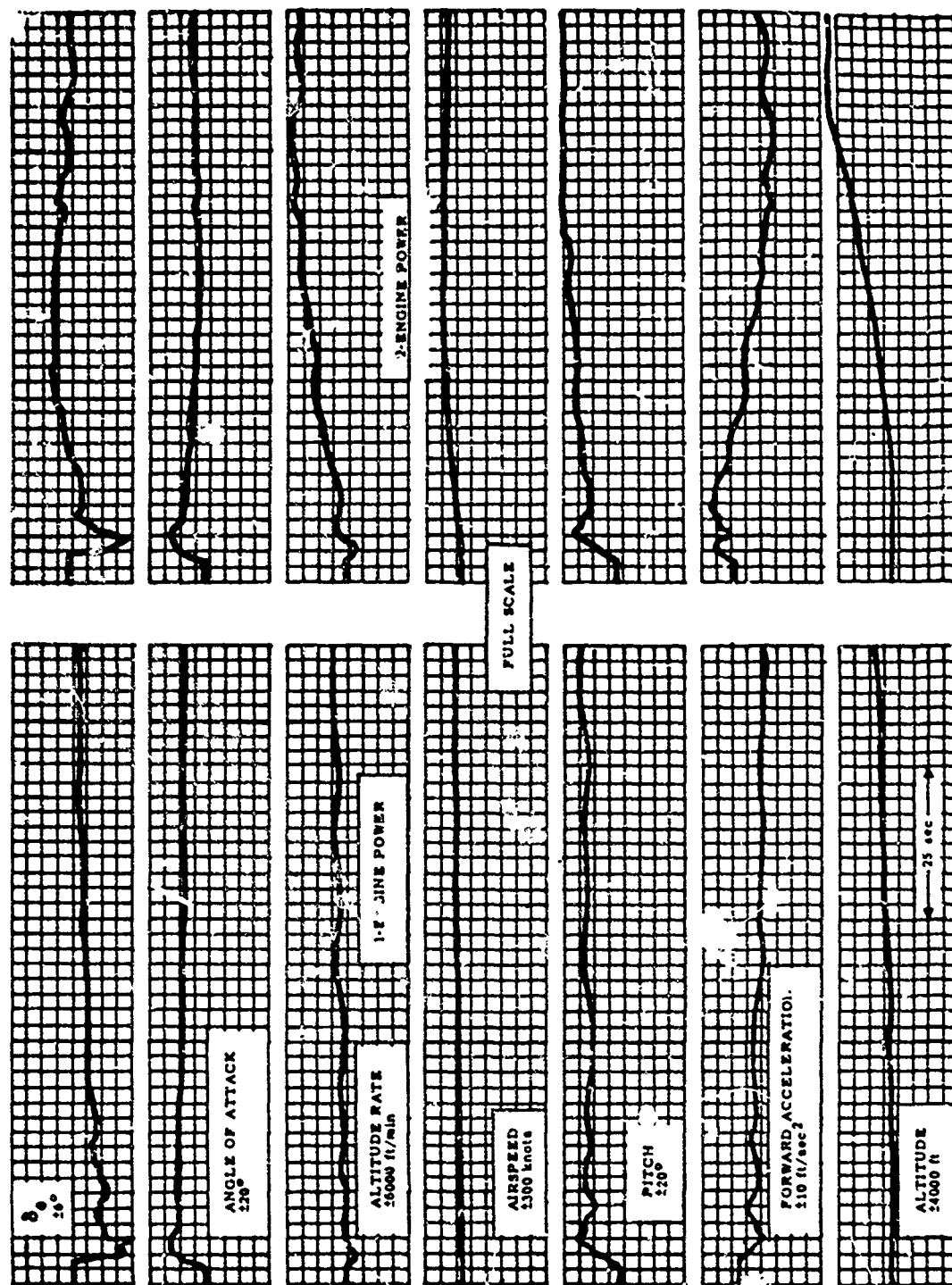


Figure 16. Rotation and Climb-Out Using Programmed Angle of Attack for Flight Director Steering - Simulated T-39 Aircraft With One and Two Engines Operating

BIBLIOGRAPHY

Air Force Flight Tester Center, "KC-135A Heavy Weight Takeoff Performance Test," AFFTC-TR-58-26, ASTIA No. AD-152303, Edwards Air Force Base, California, October 1958.

Boeing Airplane Company, "Substantiating Data Report KC-135," Document No. D-5599, Seattle, Washington, July 1960.

Collins Radio Company, "Analysis Task No. 9 Vertical Speed Sensor Studies," Interim Report, Contract No. AF 33(657)-9639, 1962.

Dommasch, D., Sherby, S., and Connolly, T., Airplane Aerodynamics, Pitman Publishing Co. New York, 1957.

Hattendorf, E. R., "An Angle-of-Attack Guidance System for Rotation/Climb-out and Go-Around," International Convention on Military Electronics, Conference Proceedings, 8:450-454, 1964.

Moretti, W. G. and Neuendorf, C. A., Design and Analysis of a Maximum Performance Take-off Director as applied to a Heavily-Loaded KC-135, Air Force Institute of Technology, GGC-61, Wright-Patterson Air Force Base, Ohio, March 1961.

Technical Order 1C-135(K)A-1-1, "USAF Series KC-135 Aircraft Flight Manual, Appendix I - Performance Data," 15 January 1964.

ACCELERATIONS ON AIRCRAFT
INDUCED BY THE EARTH'S ROTATION (U)

By

Everett W. Dunlap

and

Milton B. Porter
1st Lt., USAF

Flight Research Division
Directorate of Flight Test Engineering
Air Force Flight Test Center
Edwards AFB, California



Everett W. Dunlap

EVERETT W. DUNLAP
Air Force Flight Test Center

Mr Everett W. Dunlap has been engaged in aircraft flight testing since 1948 at Wright Field and at the AFFTC. He has acted as project engineer on a large variety of aircraft projects, conduction performance, stability and contract tests. He has been active in the area of space flight, completing studies in the flight mechanics of space vehicles.

Currently he conducts and supervises applied research studies in aircraft performance, handling qualities, and subsystem analysis. Previous experience was gained during employment by the NACA at Langley Field, Virginia, following graduation from Worcester Polytechnic Institute.



Milton B. Porter

MILTON B. PORTER, JR.
1st Lt, USAF
Air Force Flight Test Center

1st Lt Milton B. Porter, Jr., received his BS Degree in Aerospace Engineering in 1963 from the University of Texas where he became a member of Sigma Gamma Tau, Tau Beta Pi, and Sigma Xi. He received his reserve commission as a distinguished military graduate and is now a member of the regular Air Force. He was graduated from AFIT in 1964 with a MS Degree in Aerospace-Mechanical Engineering and assigned to the Flight Research Division of the Air Force Flight Test Center.

There he is working with analog and digital flight path simulators, optimization of flight paths, and improved procedures for standardizing aircraft performance measurements.

ABSTRACT

A mathematical analysis is made of the accelerations which act on vehicles flying within the atmosphere. From this analysis, equations are extracted which describe the accelerations induced by the earth's rotational velocity. Factors which influence the magnitude of the effect of these accelerations on performance are: heading angle, latitude, weight, aerodynamic characteristics, and, most importantly, speed. While the effect on performance of most aircraft currently in the inventory is of small consequence, it will be of considerable significance to vehicles projected for the future which will have higher operating weights and, in particular, will be flown at higher speeds. As speeds are increased into the hypersonic flight regime, accelerations caused by the earth's rotation must be considered for adequate flight planning.

Equations are developed to evaluate the consequence of varying heading angle and latitude on two performance parameters which are related to range (payload) and to the standardization of flight data. First, the equilibrium cruise weight for constant engine thrust is expressed as a function of latitude and heading; then the correction to excess thrust (or engine thrust) is found for constant weight. Since generalizations are not possible because of the dependence on weight and aerodynamic characteristics, sample calculations are included for a 300,000 pound airplane flying at Mach 3. As an example, the maximum variation in equilibrium cruise weight with latitude and heading angle is 8,800 pounds. For the same cruise conditions at 300,000 pounds and at 45 degrees latitude, the maximum variation in excess thrust with heading is 1400 pounds.

TABLE OF CONTENTS

	<u>Page</u>
Abstract	
List of Symbols	ii
Introduction	1
Equations for Inertial Accelerations in the Wind-Axes System ...	2
Axes Systems	2
Development of General Acceleration Equations	5
Inertial Accelerations for Horizontal Unbanked Flight	7
Accelerations Caused by the Earth's Rotation	7
Application of Equations	10
Cruise Weight Variation	10
Standardization of Flight Test Data	11
Sources of Flight Test Data	14
Discussion and Sample Calculations	15
Sample Calculations of Excess Thrust Variation	17
Sample Calculations of Cruise Weight Variation	17
Conclusions	22
References	23
Appendix I - Derivation of Equations for Inertial Accelerations in the Wind-Axes System	24
Inertial Velocity in Wind-Axes System	24
Accelerations in Inertial System	26
Appendix II - Variation of Excess Thrust with Load Factors	37

LIST OF SYMBOLS

<u>Symbol</u>	<u>Definition</u>	<u>Unit</u>
\bar{a}_I	inertial acceleration	ft per sec ²
a_X, a_Y, a_Z	components of inertial acceleration in wind-axes system	ft per sec ²
$a_{X_{\omega}}, a_{Y_{\omega}}$	components of acceleration caused by the earth's rotation only	ft per sec ²
$a_{\omega_X}, a_{\omega_Y}, a_{\omega_Z}$	components of acceleration caused by rotation of wind-axes system	ft per sec ²
B	roll angle about the velocity vector	radians
C_D	drag coefficient	dimensionless
C_L	lift coefficient	dimensionless
F	engine thrust	lb
F_{ex}	excess thrust	lb
g	local acceleration of gravity	ft per sec ²
g_{ref}	reference acceleration of gravity	ft per sec ²
h	altitude	ft
$\bar{i}, \bar{j}, \bar{k}$	unit vectors in wind-axes system	----
$\bar{i}_g, \bar{j}_g, \bar{k}_g$	unit vectors in north, east, down system	----
K_i	induced drag parameter, dC_D/dC_L^2	----
L	lift	lb
M	Mach number	----
m	mass of aircraft	slugs
n_X	load factor tangent to the flight path	dimensionless
n_Z	load factor normal to the flight path	dimensionless
P	atmospheric pressure	lb per ft ²
r	radius of the earth	ft
T	atmospheric temperature	degrees Kelvin
V_g	horizontal component of aircraft speed relative to the ground	ft per sec
V_t	speed of aircraft relative to local air mass	ft per sec
V_I	inertial speed	ft per sec
V_X, V_Y, V_Z	components of inertial velocity in wind-axes system	ft per sec

<u>Symbol</u>	<u>Definition</u>	<u>Unit</u>
W	weight ($W = mg_{ref}$)	lb
α	angle of attack	radians
γ	vertical flight path angle measured from horizontal plane	radians
δ	latitude	radians
λ	longitude	radians
π	power setting	
σ	heading angle measure from north	radians
ψ	wind direction from north	radians
ω_{\bullet}	earth's rotation rate	radians per sec
$\bar{\omega}_w$	rotational velocity of wind-axes system	radians per sec
$\omega_{wX}, \omega_{wY}, \omega_{wZ}$	components of rotational velocity of wind-axes system	radians per sec
$(\dot{})$	dot indicates time derivative	per sec
$(\bar{})$	bar indicates a vector quantity	----

Subscripts

s	standard
t	test

INTRODUCTION

All vehicles flying within the atmosphere are subjected to accelerations induced by the earth's rotation. These accelerations are of considerable importance at orbital and sub-orbital speeds. They are accounted for as a matter of course in the trajectory analysis of reentry vehicles, launch vehicles, and intercontinental ballistic missiles. The magnitude of these accelerations experienced by aircraft in the past, however, has not usually been sufficient to warrant accounting for their effects on performance. This is not true of some aircraft which will be tested and put into service in the future because of improvements in the precision with which accelerations on test aircraft are measured, and because of increases in operating speeds and weights. As an example, the payload of a supersonic transport will be significantly different depending on whether it is traveling eastward or westward. Further, as vehicle speeds are increased into the hypersonic regime, accelerations caused by the earth's rotation become of such importance that they cannot be ignored.

Equations are derived from which components of acceleration along conventional wind-axes may be computed. Of concern are the tangential acceleration (x-component in the direction of the flight path) and the normal acceleration (z-component normal to the flight path). Precise derivations are first made. The equations are then simplified to the straight and level condition, and results are shown graphically in Figures 4 and 5. These figures are presented to serve two purposes. First, they can be used together with an aircraft's aerodynamic characteristics and equations developed in this report to estimate the effect of latitude and heading angle on that aircraft's range and payload. That the effect can be of considerable importance has been demonstrated by the following means. With data representative of a Mach 3 airplane, the weight required for equilibrium flight has been computed as a function of latitude and heading angle (Figure 8); also, excess thrust* at constant weight has been computed for similar cruise conditions (Figures 6 and 7). Second, for flight test applications it can be decided, based on data in Figures 4 and 5, if corrections should be made for a particular aircraft. If they are to be made it is suggested that a latitude and a heading angle (perhaps a latitude of 45 degrees and a heading of true north) be adopted as standard and that test data be corrected to these conditions. Further, it may be desirable to publish in technical reports, together with standardized data, correction factors for range and/or other performance parameters as a function of speed, heading, and latitude.

*Excess thrust is the vectorial sum of the thrust and drag in the direction of the velocity vector.

EQUATIONS FOR INERTIAL ACCELERATIONS

IN THE WIND-AXES SYSTEM

In the following paragraphs the axes systems used in this report are described. Also, general equations which define inertial accelerations and equations for special flight conditions are presented.

Axes Systems

Aircraft performance parameters are generally presented in the wind-axes system; however, the wind velocity and earth-related linear and angular velocities are more simply expressed in an earth-oriented axes system. These two axes systems are described in this section. Also, the wind-axes forces, accelerations, and load factors are shown in their relation to the aircraft.

The earth-referenced axes system chosen is shown in Figure 1.

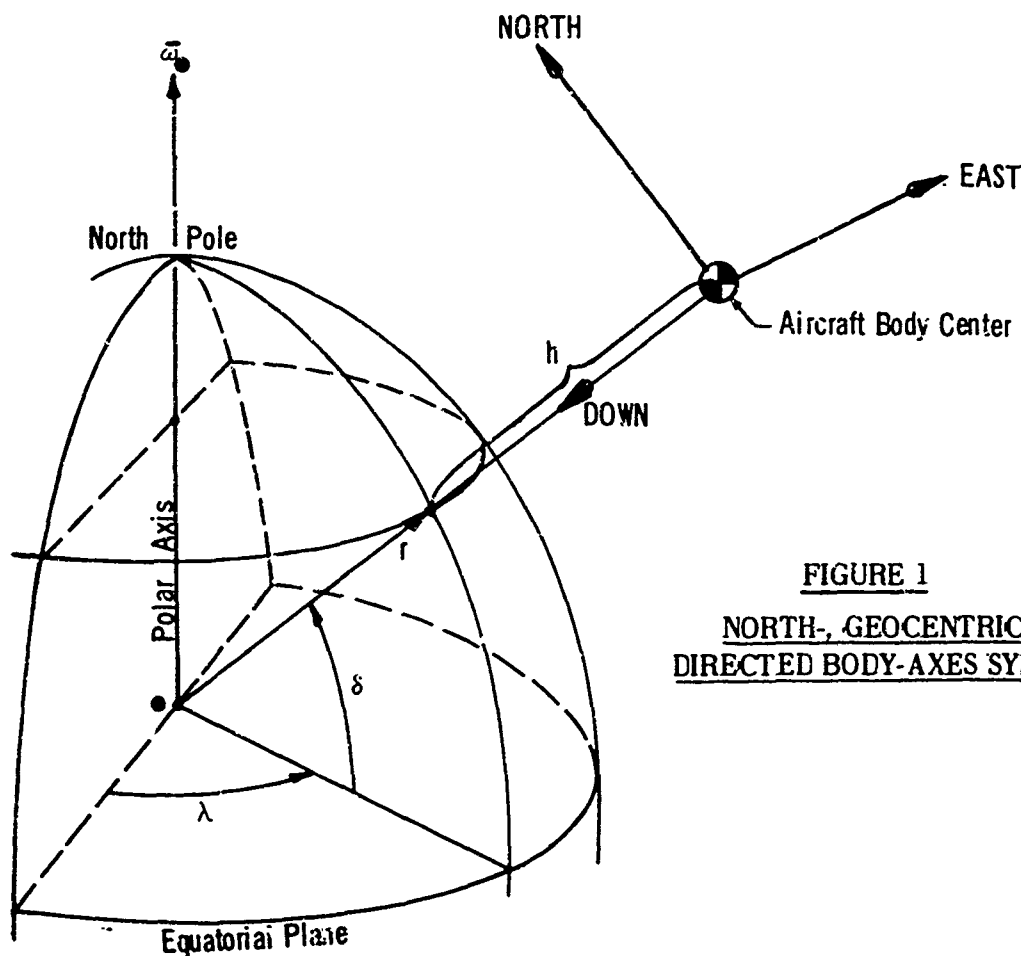


FIGURE 1
NORTH-, GEOCENTRICALLY-
DIRECTED BODY-AXES SYSTEM

It has one axis always directed north, one axis directed east, and one directed down toward the center of the earth, and its origin is at the aircraft body center. This system is termed the north-, geocentrically-directed body-axes system.

The wind-axes system as it is related to north-, geocentrically-directed axes is shown in Figure 2. The orientation of the wind axes with respect to the north-, geocentrically-directed axes is obtained by the following

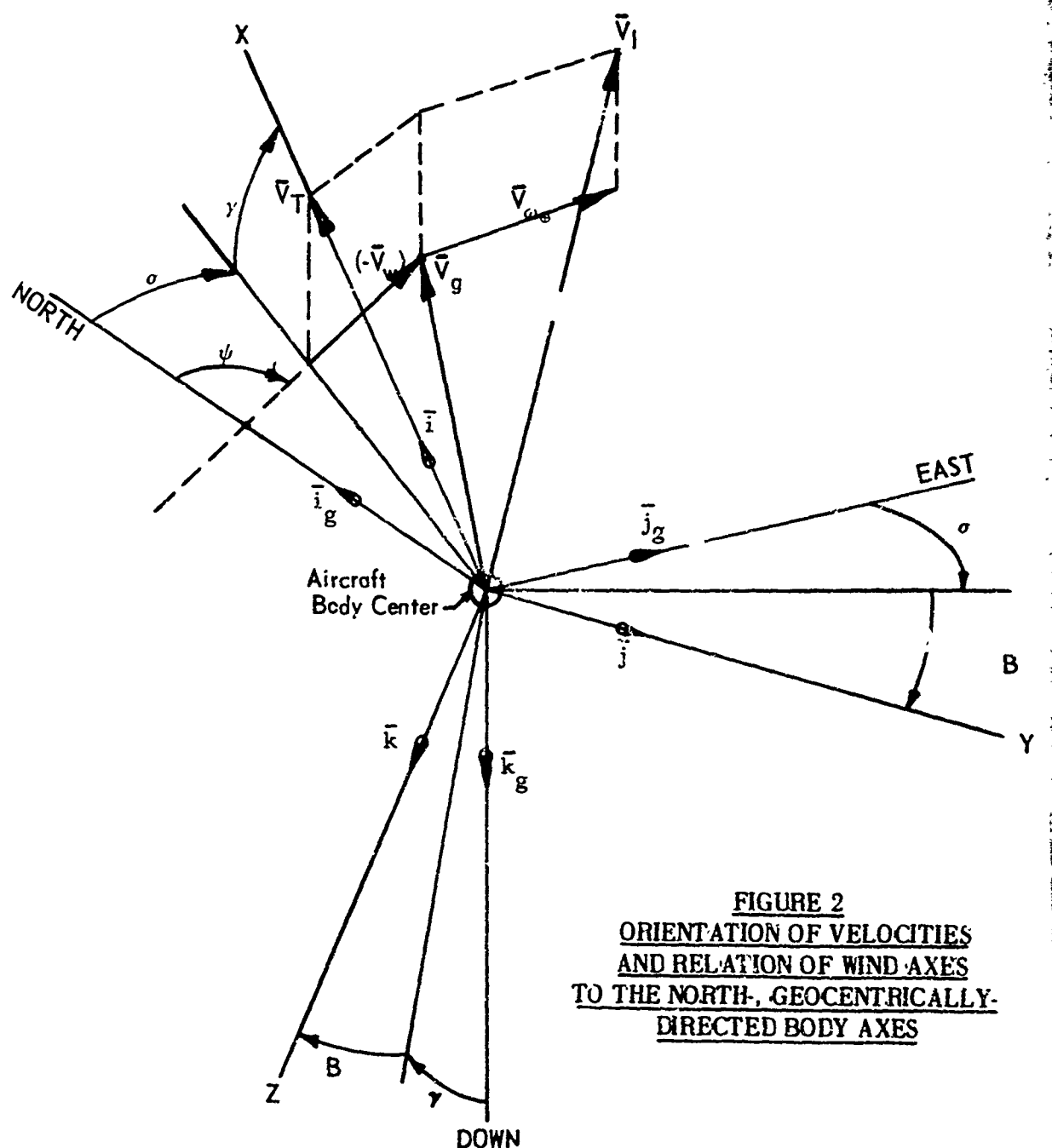


FIGURE 2
ORIENTATION OF VELOCITIES
AND RELATION OF WIND AXES
TO THE NORTH-, GEOCENTRICALLY-
DIRECTED BODY AXES

transformation: rotation through the heading angle, σ , about the down-axis; rotation through the vertical flight path angle, γ , about the newly oriented east-axis; and rotation through the angle, B , about the wind X-axis. The velocity vector of the aircraft with respect to the airmass is by definition coincident with the wind X-axis. The wind velocity vector is oriented with respect to the north-axis by the angle ψ . This angle is the angle from which the wind blows, and a negative sign must be attached to the wind speed. The horizontal projection of the aircraft's velocity with respect to the earth's surface is defined as the ground speed. At a point above the earth's surface an aircraft has an additional velocity along the east-axis induced by the earth's rotation. These velocities are shown in Figure 2.

Figure 3 shows the relation to the aircraft of the wind-axes forces, accelerations, and load factors.

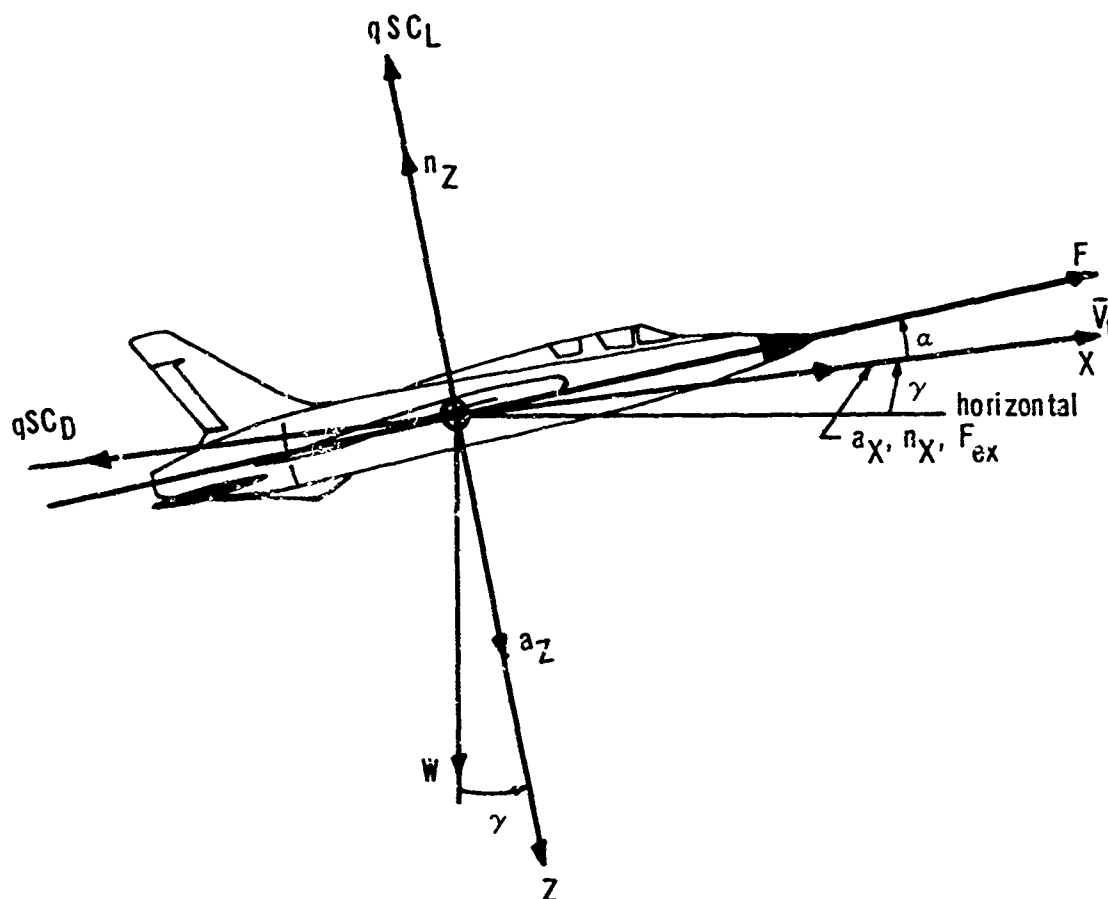


FIGURE 3
WIND-AXES FORCES, ACCELERATIONS, AND LOAD FACTORS
IN THE X-Z PLANE RELATED TO THE AIRCRAFT

Development of General Acceleration Equations

To find the effect of the earth's rotation on aircraft performance it is convenient to relate the acceleration produced by the earth's rotation to a change in excess thrust. The changes in excess thrust can then be easily related to other performance parameters. Inertial accelerations must, therefore, be found to permit conversion to excess thrust. This is done by first expressing the inertial velocity in the conventional wind-axes system and then differentiating using the following basic equation for differentiation of a vector expressed in a moving coordinate system.

$$\bar{a}_I = \frac{d\bar{V}_I}{dt} \Big|_W + \omega_W \times \bar{V}_I \quad (1)$$

Accelerations caused by the earth's rotation are determined by performing the operations indicated by the relationship expressed in equation (1) and expanding the resulting equation to find acceleration components in the wind-axes system. This has been carried out in detail in Appendix I. Equations defining the acceleration components along the velocity vector and normal to it in the Z-direction appear as (46)A and (47)A and are repeated below as equations (2) and (3).

$$\begin{aligned} a_X = & \dot{V}_t - \frac{1}{2} \frac{dV_w}{dh} V_t \sin 2\gamma \cos(\psi - \sigma) + \frac{1}{2} \frac{d\psi}{dh} V_w V_t \sin 2\gamma \sin(\psi - \sigma) \\ & + \omega_e \cos \delta \cos \gamma \sin \sigma \left[V_t \sin \gamma - \frac{20.92647 \times 10^6 V_g \cos \sigma (.003366988 \sin 2\delta - .000014196 \sin 4\delta)}{r + h} \right] \\ & - \frac{1}{2} \omega_e V_g \sin 2\sigma \sin \delta \cos \gamma + \frac{V_w V_g \cos \sigma \sin \gamma \cos \psi}{r + h} - V_w \left[\omega_e + \frac{V_g \sin \sigma}{(r + h) \cos \delta} \right] \left[\cos \gamma \sin(\psi - \sigma) \sin \delta \right. \\ & \left. - \sin \gamma \cos \delta \sin \psi \right] + \left[\omega_e^2 (r + h) + \frac{\omega_e V_g \sin \sigma}{\cos \delta} \right] \left[\frac{1}{2} \sin 2\delta \cos \gamma \cos \sigma - \cos^2 \delta \sin \gamma \right] \end{aligned} \quad (2)$$

$$\begin{aligned}
a_z = & -V_t \dot{\gamma} \cos B + \frac{V_t V_g \cos \sigma}{r+h} (\sin \gamma \sin \sigma \sin B + \cos \sigma \cos B) - V_t \dot{\sigma} \cos \gamma \sin B \\
& - V_t \left[\omega_{\bullet} + \frac{V_g \sin \sigma}{(r+h) \cos \delta} \right] \left[\sin \gamma \cos \sigma \cos \delta \sin B - \sin \sigma \cos \delta \cos B - \cos \gamma \sin \delta \sin B \right] \\
& - \frac{dV_w}{dh} V_t \sin \gamma \left[\sin \gamma \cos(\psi - \sigma) \cos B - \sin(\psi - \sigma) \sin B \right] + V_w \frac{d\psi}{dh} V_t \sin \gamma \cdot \\
& \cdot \left[\sin \gamma \sin(\psi - \sigma) \cos B + \cos(\psi - \sigma) \sin B \right] - V_w \left[\omega_{\bullet} + \frac{V_g \sin \sigma}{(r+h) \cos \delta} \right] \cdot \\
& \cdot \left[\cos \gamma \sin \psi \cos \delta \cos B + \cos(\psi - \sigma) \sin \delta \sin B + \sin \gamma \sin(\psi - \sigma) \sin \delta \cos B \right] \\
& + \omega_{\bullet} \left[V_t \sin \gamma - \frac{20.92647 \times 10^6 V_g \cos \sigma (.003366988 \sin 2\delta - .000014196 \sin 4\delta)}{r+h} \right] \cdot \\
& \cdot \cos \delta (\sin \gamma \sin \sigma \cos B - \cos \sigma \sin B) - \omega_{\bullet} V_g \cos \sigma \sin \delta (\sin \gamma \sin \sigma \cos B - \cos \sigma \sin B) \\
& + \left[\omega_{\bullet}^2 (r+h) + \frac{\omega_{\bullet} V_g \sin \sigma}{\cos \delta} \right] \cos \delta (\cos \gamma \cos \delta \cos B + \sin \sigma \sin \delta \sin B \\
& + \sin \gamma \cos \sigma \sin \delta \cos B) - \frac{V_w V_g \cos \sigma}{r+h} \cos \gamma \cos \psi \cos B
\end{aligned} \tag{3}$$

The lateral acceleration, a_y , is omitted from consideration since it produces only a negligible change in aircraft performance.

Inertial Accelerations for Horizontal Unbanked Flight

If the flight path angle is equal to zero and unbanked flight is also assumed, equations (2) and (3) reduce to

$$\begin{aligned}
 a_X = \dot{V}_t - \omega_{\bullet} \cos \delta \sin \sigma & \left[\frac{20.92647 \times 10^6 V_g \cos \sigma}{r+h} \right. \\
 & \cdot (.003366988 \sin 2\delta - .000014196 \sin 4\delta) - V_w \left[\omega_{\bullet}^2 + \frac{V_g \sin \sigma}{(r+h) \cos \delta} \right] \cdot \\
 & \cdot \left[\sin(\psi - \sigma) \sin \delta \right] + \frac{1}{2} \omega_{\bullet}^2 (r+h) \sin 2\delta \cos \sigma \quad (4)
 \end{aligned}$$

$$\begin{aligned}
 \text{and } a_Z = V_t \left(\omega_{\bullet} \sin \sigma \cos \delta + \frac{V_g}{r+h} \right) - V_w & \left[\omega_{\bullet} + \frac{V_g \sin \sigma}{(r+h) \cos \delta} \right] \sin \psi \cos \delta \\
 + \left[\omega_{\bullet}^2 (r+h) + \frac{\omega_{\bullet} V_g \sin \sigma}{\cos \delta} \right] \cos^2 \delta - \frac{V_w V_g \cos \sigma \cos \psi}{r+h} \quad (5)
 \end{aligned}$$

Accelerations Caused by the Earth's Rotation

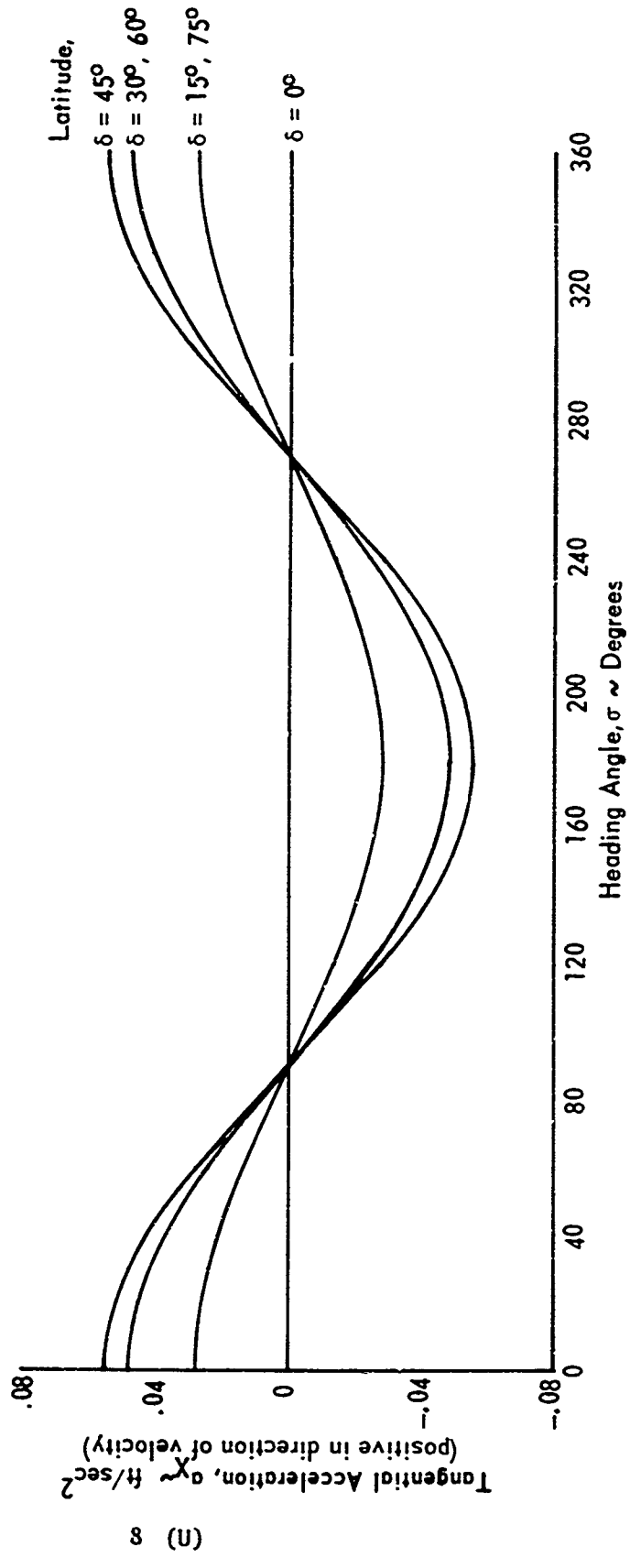
If the same restrictions are retained as in the preceding analysis, as well as no wind, an examination of equations (4) and (5) shows that the accelerations caused by the earth's rotation only are

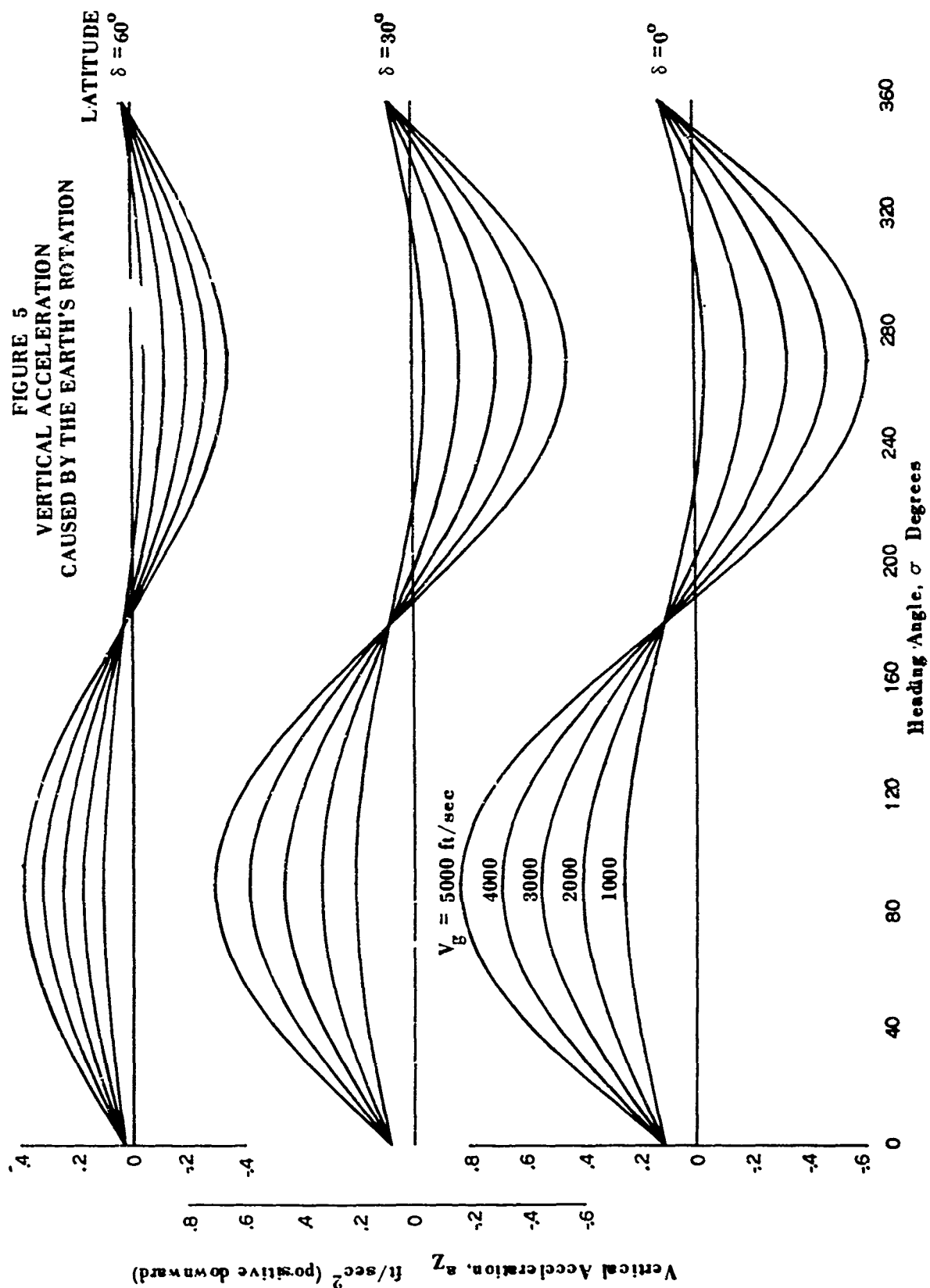
$$\begin{aligned}
 a_{X\omega_{\bullet}} = -\omega_{\bullet} \cos \delta \sin \sigma & \left[\frac{20.92647 \times 10^6 V_g \cos \sigma}{r+h} \right. \\
 & \cdot (.003366988 \sin 2\delta - .000014196 \sin 4\delta) + \frac{1}{2} \omega_{\bullet}^2 (r+h) \sin 2\delta \cos \sigma \quad (6)
 \end{aligned}$$

$$\text{and } a_{Z\omega_{\bullet}} = 2 V_g \omega_{\bullet} \sin \sigma \cos \delta + \omega_{\bullet}^2 (r+h) \cos^2 \delta \quad (7)$$

Results from equations (6) and (7) are shown in Figures 4 and 5.

FIGURE 4
TANGENTIAL ACCELERATION
CAUSED BY THE EARTH'S ROTATION





Application of Equations

The acceleration equations which were introduced in the preceding section are applied to two major aircraft performance problems. These problems are the determination of the allowable cruise weight (or payload) for a given range and cruise condition and the determination of an aircraft's standard day performance from test day flight data. The second problem is peculiar to the area of aircraft flight testing, but the first problem is of general interest to flight test engineers and others concerned with aircraft performance.

Cruise Weight Variation

We first consider the problem of determining cruise weight using the aircraft equations of motion and the acceleration equations. At a given speed the accelerations induced by the earth's rotation vary as a function of latitude and heading angle. If horizontal flight is to be maintained at that speed, then to satisfy the longitudinal and normal equations of motion the aircraft weight or the weight and engine thrust must be varied. If it is assumed that the thrust is aligned with the velocity vector, then the longitudinal and normal equations of motion for horizontal unbanked flight become

$$F - qS C_D = W \frac{a_x}{g_{ref}} \quad (8)$$

$$qS C_L = \frac{W}{g_{ref}} (g - a_z) \quad (9)$$

Under the additional conditions of constant airspeed and zero wind velocity the accelerations become

$$a_x = -\omega \cos \delta \sin \sigma \left[\frac{20.92647 \times 10^6 V \cos \sigma}{r+h} \right] \cdot \left[(.003366988 \sin 2\delta - .000014196 \sin 4\delta) \right] + \frac{1}{2} \omega^2 (r+h) \sin 2\delta \cos \sigma \quad (10)$$

$$a_z = \frac{V^2}{r+h} + 2V \omega \sin \sigma \cos \delta + \omega^2 (r+h) \cos^2 \delta \quad (11)$$

For a constant cruise speed and altitude the dynamic pressure and the Mach number are constant (assuming uniform atmospheric conditions at

the specified altitude). The lift and drag coefficients are then functions of angle of attack. When a latitude and heading angle are specified, a_x and a_z are determined by equations (10) and (11). If the engine thrust is held constant, then equations (8) and (9) become a set of two simultaneous equations in two unknowns, weight and angle of attack. The cruise weight is obtained by solution of this set of equations.

If it is desired to include wind effects on cruise weight, equations (4) and (5) can be used to compute a_x and a_z .

Standardization of Flight Test Data

Aircraft flight test data must be reduced to a set of standard conditions since it is recorded under widely varying test day conditions that make difficult any direct comparison or prediction of performance capabilities. One method of correcting test data to standard conditions makes use of the quantity excess thrust, from which aircraft performance parameters can be calculated using the equations of motion. This standardization method is described in the following paragraphs.

The longitudinal equation of motion can be arranged to provide two equivalent expressions for the excess thrust

$$F_{ex} = F \cos \alpha - qSC_L = Wn_x \quad (12)$$

where the load factor tangent to the flight path is defined as

$$n_x = \frac{1}{g_{ref}} (g \sin \gamma + a_x) \quad (13)$$

The normal equation of motion provides a constraint on the variables in the excess thrust equations. It takes the form

$$qSC_L = n_z W - F \sin \alpha \quad (14)$$

where the load factor normal to the flight path is defined in general as

$$n_z = \frac{1}{g_{ref}} (g \cos \gamma \cos \beta - a_z) \quad (15)$$

For a fixed wing jet or rocket engine aircraft the quantities in equations (12) through (15) are uniquely determined when the following variables are known from measurement or calculation: Mach number, temperature, pressure,

engine power setting, weight, and the load factors tangent and normal to the flight path. In terms of these variables the functional expression for the excess thrust is

$$F_{ex} = F_{ex}(M, T, P, \pi, W, n_X, n_Z) \quad (16)$$

A set of standard day flight conditions may be defined specifying the variables in equation (16). For example, the U. S. Standard Atmosphere, 1962, specifies temperature, pressure, density, and zero wind velocity as a function of altitude. In addition to a standard atmosphere, for a given aircraft and flight condition a standard Mach number, engine power setting (e.g., maximum after-burner), and weight are specified or calculated. Since for high speed aircraft the load factors will vary significantly with latitude and heading angle, standard values of these load factors must be established by choosing a standard latitude and heading angle.

An equation for the standard excess thrust is obtained with a Taylor series expansion as follows

$$\begin{aligned} F_{exs} = & F_{ext} + \left(\frac{\partial F_{ex}}{\partial M} \right)_t (M_s - M_t) + \left(\frac{\partial F_{ex}}{\partial T} \right)_t (T_s - T_t) \\ & + \left(\frac{\partial F_{ex}}{\partial P} \right)_t (P_s - P_t) + \left(\frac{\partial F_{ex}}{\partial \pi} \right)_t (\pi_s - \pi_t) + \left(\frac{\partial F_{ex}}{\partial W} \right)_t (W_s - W_t) \\ & + \left(\frac{\partial F_{ex}}{\partial n_X} \right)_t (n_{Xs} - n_{Xt}) + \left(\frac{\partial F_{ex}}{\partial n_Z} \right)_t (n_{Zs} - n_{Zt}) \\ & + \text{higher order terms} \end{aligned} \quad (17)$$

The values of the partial derivatives of excess thrust with respect to each of the test variables are obtained by differentiation of equation (12) using equation (14) to evaluate the derivatives of the angle of attack which result. The partials with respect to the load factors are developed in Appendix II. For a development of the remaining partials see reference 2.

Considering only the first order tangential and normal load factor terms of the series, equation (17) is approximated as follows

$$F_{ex_s} = F_{ex_t} + W(n_{X_s} - n_{X_t}) - 2K_i C_L W(n_{Z_s} - n_{Z_t}) \quad (16)$$

The acceleration equations derived in this report along with equations (13) and (15) are used to evaluate the test and standard load factors in equation (18).

Under standard conditions the wind velocity is zero, and the acceleration equations (2) and (3) become

$$\begin{aligned} a_{X_s} = & \dot{V}_t + \omega \cos \delta \cos \gamma \sin \sigma \left[V_t \sin \gamma \right. \\ & - \frac{20.92647 \times 10^6 V_g \cos \sigma (.003366988 \sin 2\delta - .000014196 \sin 4\delta)}{r + h} \\ & - \frac{1}{2} \omega V_g \sin 2\sigma \sin \delta \cos \gamma + \left[\omega^2 (r + h) + \frac{\omega V_g \sin \sigma}{\cos \delta} \right] \cdot \\ & \left. \cdot \left[\frac{1}{2} \sin 2\delta \cos \gamma \cos \sigma - \cos^2 \delta \sin \gamma \right] \right] \quad (19) \end{aligned}$$

and

$$\begin{aligned} a_{Z_s} = & -V_t \dot{\gamma} \cos B + \frac{V_t V_g \cos \sigma}{r + h} (\sin \gamma \sin \sigma \sin B + \cos \sigma \cos B) - V_t \dot{\sigma} \cos \gamma \sin B \\ & - V_t \left[\omega + \frac{V_g \sin \sigma}{(r + h) \cos \delta} \right] \left[\sin \gamma \cos \sigma \cos \delta \sin B - \sin \sigma \cos \delta \cos B - \cos \gamma \sin \delta \sin B \right] \\ & + \omega \left[V_t \sin \gamma - \frac{V_g \cos \sigma (.003366988 \sin 2\delta - .000014196 \sin 4\delta)}{r + h} \right] \cdot \\ & \cdot \cos \delta (\sin \gamma \sin \sigma \cos B - \cos \gamma \sin B) - \omega V_g \cos \sigma \sin \delta (\sin \gamma \sin \sigma \cos B \\ & - \cos \sigma \sin B) + \left[\omega^2 (r + h) + \frac{\omega V_g \sin \sigma}{\cos \delta} \right] \cos \delta (\cos \gamma \cos \delta \cos B \\ & + \sin \sigma \sin \delta \sin B + \sin \gamma \cos \sigma \cos B) \quad (20) \end{aligned}$$

where each of the variables h , V_E , V_t , γ , $\dot{\gamma}$, B , σ , $\dot{\sigma}$, and δ are evaluated at the standard conditions. These equations can be combined with equations (13) and (15) to compute the standard load factors required in equation (18).

Sources of Flight Test Data

The method for computing test day load factors depends on the instrumentation system used to record the test variables. Three instrumentation systems are considered in the following paragraphs: airspeed-altitude instruments, on-board accelerometers and ground-based radar.

Airspeed-Altitude Instrument System: The test day values of tangential and normal load factors are often computed from airspeed and altitude values calculated from on-board pitot-static pressure measurements. The portions of the load factors which can be computed from these measurements are only the terms $(\sin \gamma)$ and $(\cos \gamma \cos B)$ appearing in equations (13) and (15) and the terms (\dot{V}_t) in equation (2) and $(-V_t \dot{\gamma} \cos B)$ in equation (3). To evaluate the remaining terms in the acceleration equations the wind velocity and test latitude and heading angle must also be measured.

Accelerometer System: Direct acceleration measurement systems such as flight path accelerometers, body-axes accelerometers, and inertial navigation systems measure the total test day load factors. These values may be used directly in equation (18). There is no requirement for measuring the wind velocity or test latitude and heading angle when an accelerometer system is used.

Ground-Based Radar System: A radar site located at a point on the earth's surface has an acceleration induced by the rotation of the earth. Addition of this value to aircraft acceleration measurements made with the radar yields the total test day inertial accelerations. A technique for computing inertial accelerations from radar trajectory measurements and transforming then to the wind-axes system is presented in reference 4. The wind velocity must be measured in order that the transformation to the wind axes can be made.

DISCUSSION AND SAMPLE CALCULATIONS

Based on the analysis contained in this report, aircraft performance may be significantly affected by the earth's rotational velocity. Factors which influence the magnitude of the effect on performance are: heading angle, latitude, weight, aerodynamic characteristics, and, most importantly, speed.

Expressed in a conventional wind-axes system the normal acceleration (in the Z-direction) depends on heading angle, latitude, and speed. The magnitude of this acceleration increases with speed, particularly with easterly or westerly headings. The tangential acceleration (component along the velocity vector) also depends on heading angle and latitude but is only very slightly dependent on speed. Values of this component are important in terms of the accuracy of flight path accelerometers in current use at the Air Force Flight Test Center.

Table 1 has been constructed using equations (6) and (7), which represent the zero wind, straight and level flight case, and referring accelerations to a heading of true north.

<u>Table 1</u> Variation of Acceleration Components with Heading Angle $\delta = 45^\circ$ $V = 2912 \text{ ft/sec}$ $h = 70,000$		
<u>Heading</u>	<u>$\Delta a_x \text{ (ft/sec}^2\text{)}$</u>	<u>$\Delta a_z \text{ (ft/sec}^2\text{)}$</u>
0	0	0
30	.0065	-.1497
60	.0279	-.2593
90	.0558	-.2995
120	.0837	-.2593
150	.1041	-.1497
180	.1116	0
210	.1041	.1497
240	.0837	.2593
270	.0558	.2995
300	.0279	.2593
330	.0065	.1497

It may be seen from Table 1 that maximum values of acceleration in the X-direction are at headings of north and south while maximum values in the Z-direction are at headings of east and west. Also, the maximum deviation in a_x of .1116 ft/sec² (approximately .0035 g's) is well within the accuracy of a sensitive accelerometer.

To show changes in acceleration with latitude, Figure 2 has been constructed also using equations (6) and (7) and referring accelerations to a latitude of 45 degrees.

Table 2 Variation of Acceleration Components with Latitude		
$\sigma = 0^\circ$ $V = 2912$ ft/sec $h = 70,000$ ft		
Latitude	Δa_x (ft/sec ²)	Δa_z (ft/sec ²)
0	.0558	.0560
15	.0279	.0485
30	.0074	.0280
45	0	0
60	.0075	-.0280
75	.0280	-.0483
90	.0550	-.0558

It may be seen that the sensitivity of acceleration to latitude is slight at the reference latitude of 45 degrees, indicating that accurate corrections may be made to excess thrust without a precise knowledge of latitude.

Since the effect of variation in a_z on performance depends on aerodynamic characteristics, it is not possible to generalize the effect of the earth's rotation on vehicle performance. Therefore, to illustrate the significance of the accelerations created by the earth's rotation, data representative of a Mach 3 aircraft have been selected and substituted in equations which appear in the preceding sections. Sample calculations are presented in the following paragraphs using the assumed values, listed below, of drag alone, zero lift drag, the product of dynamic pressure and wing area, and a cruise altitude for a Mach 3 aircraft at a weight of 300,000 pounds. A standard latitude of 45 degrees and a standard heading of true north are also assumed.

$$W = 300,000 \text{ lb}$$

$$h = 70,000 \text{ ft}$$

$$C_{D_0} = .02$$

$$K_i = .5$$

$$qS = 1.755 \times 10^6 \text{ lb}$$

$$V_t = 2912 \text{ ft/sec}$$

Two approaches have been taken. First, the change in excess thrust caused by a change in heading angle has been computed for the specified cruise condition; second, the variation in equilibrium weight for the same cruise condition has been computed as a function of heading angle and latitude.

Sample Calculations of Excess Thrust Variation

By substituting the assumed values and accelerations from Tables 1 and 2 in equation (18), values which make up Figures 6 and 7 are obtained. These values represent the correction to excess thrust which should be added if the heading of the aircraft were changed instantaneously to true north from the heading angles indicated in Figure 6, or to a latitude of 45 degrees from the values indicated in Figure 7. The maximum variation in excess thrust occurs between headings of 40 and 220 degrees and amounts to 1400 pounds.

Sample Calculations of Cruise Weight Variation

The effect of the earth's rotation is also demonstrated by permitting the equilibrium weight to vary while holding the Mach number, altitude, and thrust constant and using the same assumed data as in the preceding paragraph.

The equations of motion, equations (8) and (9), are solved simultaneously for weight after assuming lift and drag coefficients of the form

$$C_L = C_{L_\alpha} \alpha \quad (21)$$

$$\text{and } C_D = C_{D_0} + K_i C_L^2 \quad (22)$$

FIGURE 6
VARIATION IN EXCESS THRUST WITH HEADING

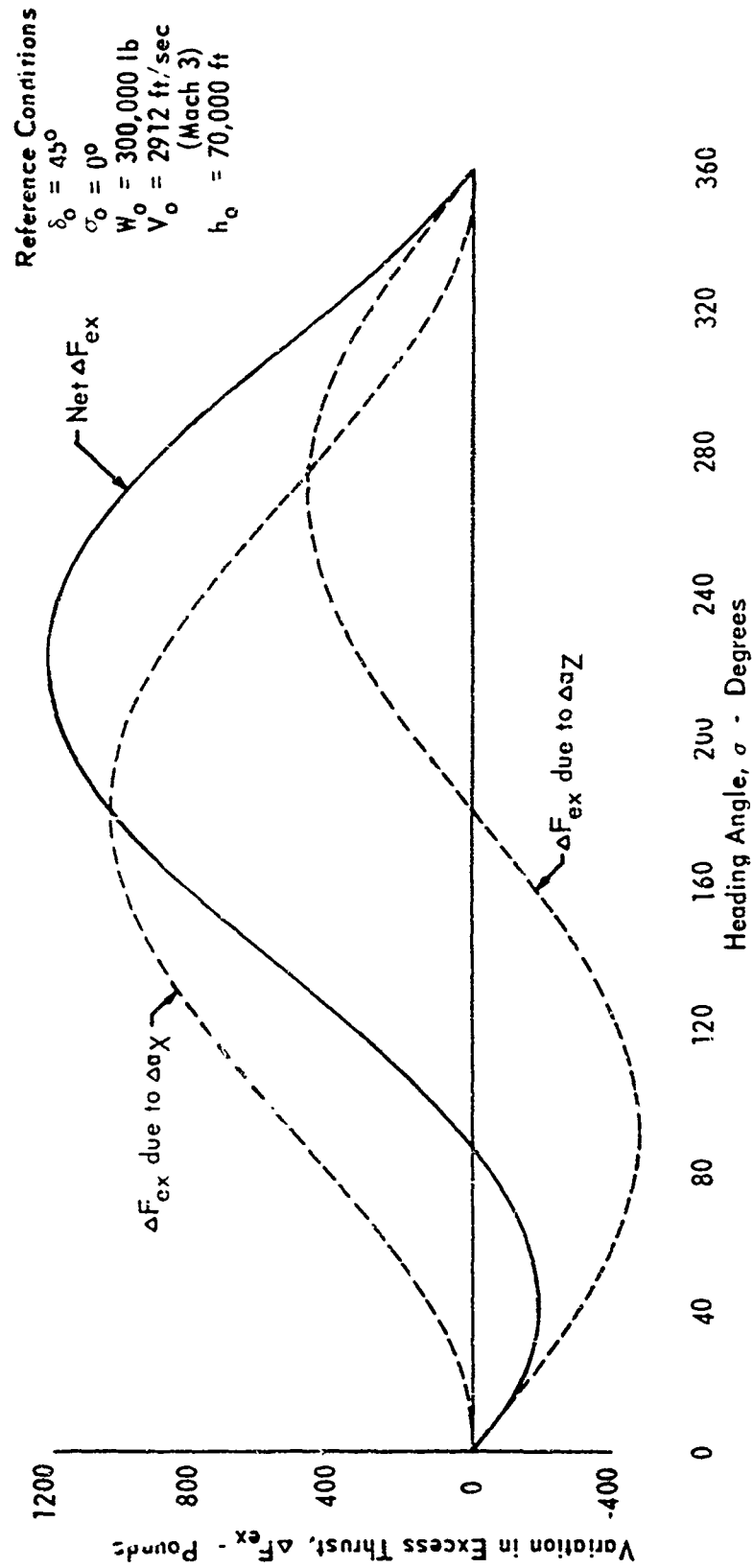
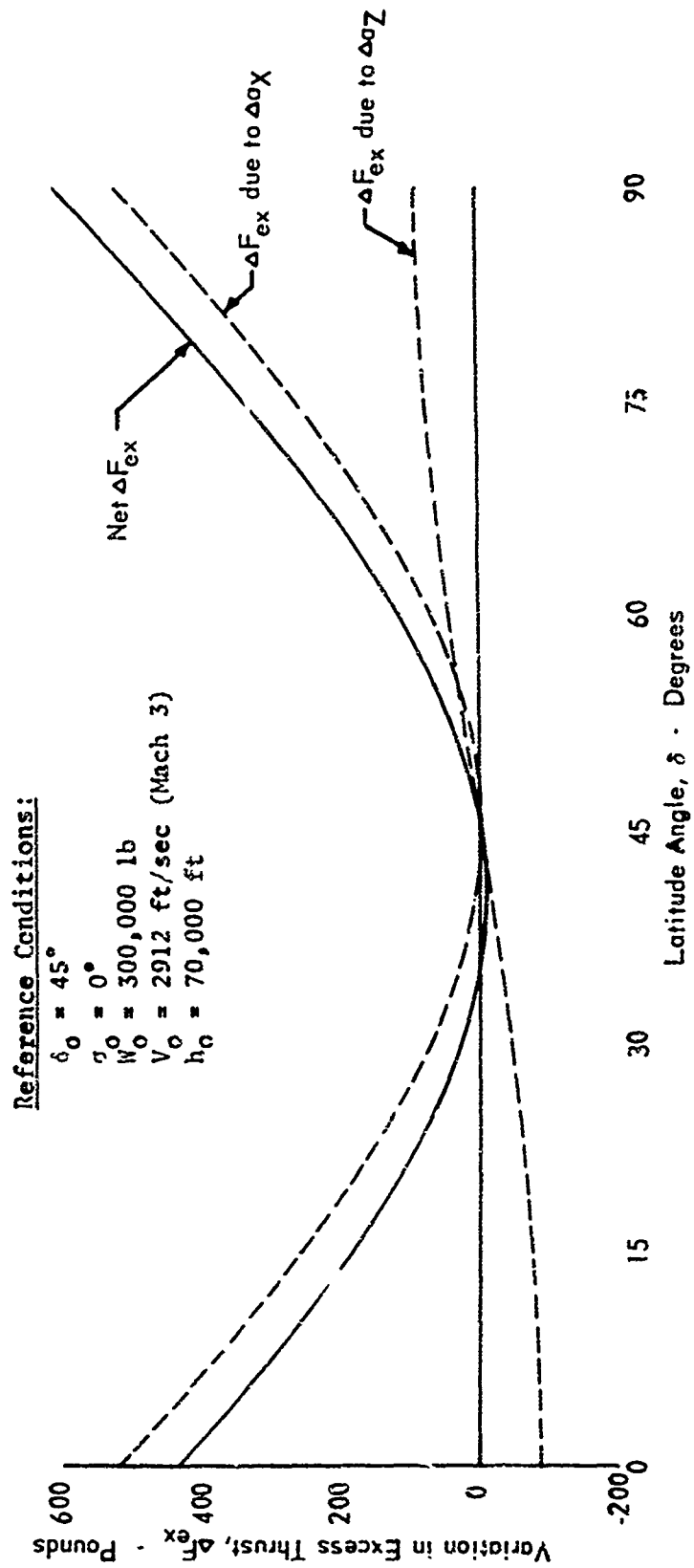


FIGURE 7
VARIATION IN EXCESS THRUST WITH LATITUDE



Solving for angle of attack in equation (9)

$$\alpha = \frac{W \left(\frac{g - a_z}{g_{ref}} \right)}{q S C_{L_\alpha}} \quad (23)$$

Substituting this value into equation (8) we obtain

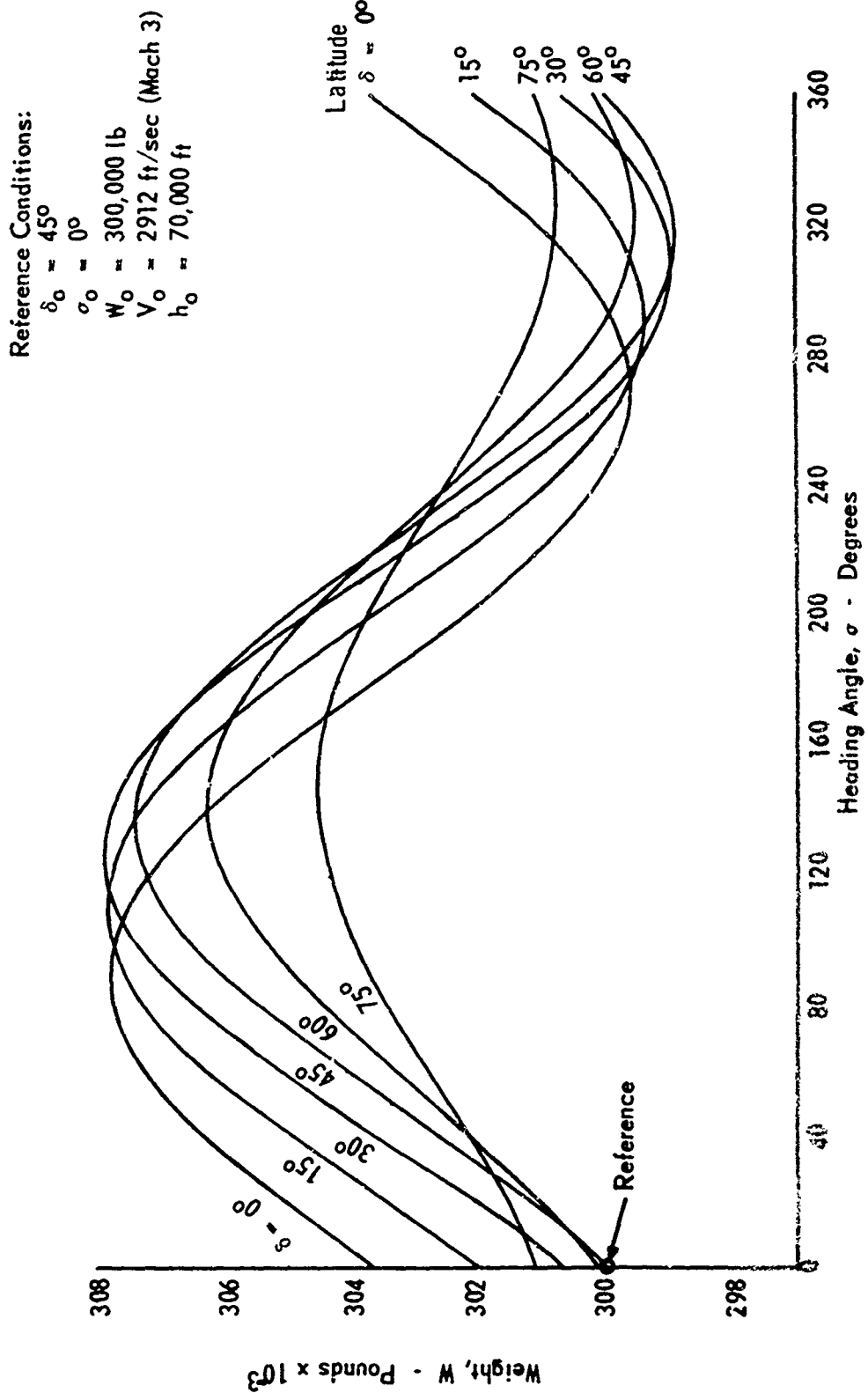
$$F - q S C_{D_0} - K_i \frac{\left(\frac{g - a_z}{g_{ref}} \right)^2}{q S} W^2 = W \frac{a_x}{g_{ref}} \quad (24)$$

Solving this quadratic equation for weight (and taking the positive root)

$$W = \frac{\frac{a_x}{g_{ref}} + \left[\left(\frac{a_x}{g_{ref}} \right)^2 + 4 K_i \frac{\left(\frac{g - a_z}{g_{ref}} \right)^2}{q S} (F - q S C_{D_0}) \right]^{1/2}}{2 K_i \frac{\left(\frac{g - a_z}{g_{ref}} \right)^2}{q S}} \quad (25)$$

This equation along with equations (10) and (11) is used to compute equilibrium cruise weight as a function of latitude and heading angle. The engine thrust is first computed at the standard latitude and heading for a weight of 300,000 pounds, then maintained constant as the latitude and heading are varied. A plot of the resulting weight values is shown in Figure 8. The maximum weight near $\delta = 30$ degrees and $\sigma = 120$ degrees is 307,800 pounds and the minimum weight near $\delta = 330$ degrees is 299,000 pounds. The difference, 8800 pounds, is a total change of approximately 2.9 percent.

FIGURE 8
VARIATION OF EQUILIBRIUM CRUISE WEIGHT
WITH LATITUDE AND HEADING ANGLE



CONCLUSIONS

The range (or payload) of any aircraft is affected to some degree by the earth's rotation. The effect is slight, in general, for currently operational aircraft; however, to make accurate estimates of range (or payload), account should be taken of the accelerations caused by the earth's rotational velocity for (1) aircraft which are operated at high supersonic speeds or for (2) very heavy aircraft operated at subsonic speeds for extended periods. The range of hypersonic vehicles which are to become operational will be markedly affected by the earth's rotation.

Adjustments to computed excess thrust for the earth's rotation should be included in a performance standardization procedure under the following circumstances:

1. In all cases where sensitive accelerometers capable of accuracies of $\pm .005g$'s or less are used to determine excess thrust.
2. When accelerometers are not used but the acceleration components incurred by the earth's rotation, as evidenced by Figures 4 and 5, approach the accuracy of the system used.

REFERENCES

1. Dunlap, E. W., Effect of Wind Gradients on the Climb Performance of Aircraft, Flight Research Division Office Memo, Air Force Flight Test Center, California, November 1964.
2. Walker, R. C., Determination of an Aircraft's Standard Climb and Level Acceleration Performance, FTC-TR-64-40, Air Force Flight Test Center, California, May 1965.
3. Porter, M. B., Flight Path Load Factor Correction for Aircraft Standard Climb and Level Acceleration Performance, FTC-TIM-65-1019, Air Force Flight Test Center, August 1965
4. Walker, R. C., Formulation of a Digital Computer Program to Determine Aircraft and Spacecraft Performance from Trajectory Data, FTC-TIM-64-1016, Air Force Flight Test Center, California, 1964.

APPENDIX I

DERIVATION OF EQUATIONS FOR INERTIAL ACCELERATIONS IN THE WIND-AXES SYSTEM

Inertial Velocity in Wind-Axes System

Referring to Figure 2 the inertial velocity may be expressed as

$$\mathbf{V}_I = \mathbf{V}_t + \mathbf{V}_{\omega_\bullet} + \mathbf{V}_w \quad (1)A$$

In the wind-axes system the airspeed, \mathbf{V}_t , is $V_t \mathbf{i}$. Performing transformations, first through the angle σ , then through γ and B , the velocity due to the earth's rotation is

$$\mathbf{V}_{\omega_\bullet} = [T] \begin{bmatrix} 0 \\ \omega_\bullet (r + h) \cos \delta \\ 0 \end{bmatrix} \quad (2)A$$

$$\text{where } [T] = \begin{bmatrix} 1 & 0 & 0 \\ 0 & \cos B & \sin B \\ 0 & -\sin B & \cos B \end{bmatrix} \begin{bmatrix} \cos \gamma & 0 & -\sin \gamma \\ 0 & 1 & 0 \\ \sin \gamma & 0 & \cos \gamma \end{bmatrix} \begin{bmatrix} \cos \sigma & \sin \sigma & 0 \\ -\sin \sigma & \cos \sigma & 0 \\ 0 & 0 & 1 \end{bmatrix}$$

In expanded form equation (2)A becomes

$$\begin{aligned} \mathbf{V}_{\omega_\bullet} = \omega_\bullet (r + h) \cos \delta [& \cos \gamma \sin \sigma \mathbf{i} + (\sin \gamma \sin \sigma \sin B + \cos \sigma \cos B) \mathbf{j} \\ & + (\sin \gamma \sin \sigma \cos B - \cos \sigma \sin B) \mathbf{k}] \end{aligned} \quad (3)A$$

The velocity due to local winds as obtained from rawinsonde data is found by making transformation through the angles σ , γ , and B , as above so that

$$\bar{V}_w = [T] \begin{bmatrix} -V_w \cos \psi \\ -V_w \sin \psi \\ 0 \end{bmatrix} \quad (4)A$$

Expanding as before

$$\begin{aligned} \bar{V}_w = & \left[-V_w \cos \psi \cos \gamma \cos \sigma - V_w \sin \psi \cos \gamma \sin \sigma \right] \bar{i} \\ & + \left[-V_w \cos \psi (\sin \gamma \cos \sigma \sin B - \sin \sigma \cos B) \right. \\ & \left. - V_w \sin \psi (\sin \gamma \sin \sigma \sin B + \cos \sigma \cos B) \right] \bar{j} \\ & + \left[-V_w \cos \psi (\cos \sigma \sin \gamma \cos B + \sin \sigma \sin B) \right. \\ & \left. - V_w \sin \psi (\sin \gamma \sin \sigma \cos B - \cos \sigma \sin B) \right] \bar{k} \end{aligned} \quad (5)A$$

Equation (5)A may be simplified to become

$$\begin{aligned} \bar{V}_w = & -V_w \left\{ \cos \gamma \cos(\psi - \sigma) \bar{i} + [\sin \gamma \sin B \cos(\psi - \sigma) + \cos B \sin(\psi - \sigma)] \bar{j} \right. \\ & \left. + [\sin \gamma \cos B \cos(\psi - \sigma) - \sin B \sin(\psi - \sigma)] \bar{k} \right\} \end{aligned} \quad (6)A$$

Adding terms as indicated by equation (1)A the inertial velocity in the wind-axes system becomes

$$\begin{aligned} \bar{V}_I = & \left[V_t - V_w \cos \gamma \cos(\psi - \sigma) + \omega_\bullet (r+h) \cos \delta \cos \gamma \sin \sigma \right] \bar{i} \\ & + \left\{ -V_w [\sin \gamma \sin B \cos(\psi - \sigma) + \cos B \sin(\psi - \sigma)] \right. \\ & \left. + \omega_\bullet (r+h) \cos \delta (\sin \gamma \sin \sigma \sin B + \cos \sigma \cos B) \right\} \bar{j} \\ & + \left\{ -V_w [\sin \gamma \cos B \cos(\psi - \sigma) - \sin B \sin(\psi - \sigma)] \right. \\ & \left. + \omega_\bullet (r+h) \cos \delta (\sin \gamma \sin \sigma \cos B - \cos \sigma \sin B) \right\} \bar{k} \end{aligned} \quad (7)A$$

where the earth's radius, r , may be found from

$$r = 20.92647 \times 10^6 (.998320047 + .001683494 \cos 2\delta - .000003549 \cos 4\delta) \quad (8)A$$

Accelerations in Inertial System

Since accelerations must be expressed in an inertial system so they can be related to changes in excess thrust, the following equation is used

$$\bar{a}_{\text{inertial system}} = \left. \frac{d\bar{V}}{dt} \right|_{\text{wind-axes system}} + \bar{\omega}_{\text{wind-axes system}} \times \bar{V} \quad (9)A$$

First, the term $\left. \frac{d\bar{V}}{dt} \right|_{\text{wind-axes system}}$ is evaluated by expressing the velocity in the wind-axes system as

$$\bar{V}_I = V_X \bar{i} + V_Y \bar{j} + V_Z \bar{k} \quad (10)A$$

The acceleration becomes

$$\left. \frac{d\bar{V}}{dt} \right|_w = \dot{V}_X \bar{i} + \dot{V}_Y \bar{j} + \dot{V}_Z \bar{k} \quad (11)A$$

which may be found by differentiating equation (7)A.

$$\begin{aligned} \dot{V}_X = & \dot{V}_t - \dot{V}_w \cos \gamma \cos(\psi - \sigma) + V_w [\dot{\gamma} \sin \gamma \cos(\psi - \sigma) \\ & + (\dot{\psi} - \dot{\sigma}) \cos \gamma \sin(\psi - \sigma)] + \omega_\bullet (r + h) \cos \delta \cos \gamma \sin \sigma \\ & + \omega_\bullet (r + h) (-\dot{\delta} \sin \delta \cos \gamma \sin \sigma - \dot{\gamma} \cos \delta \sin \gamma \sin \sigma + \dot{\sigma} \cos \delta \cos \gamma \cos \sigma \end{aligned} \quad (12)A$$

$$\begin{aligned}
\dot{V}_Y = & -\dot{V}_w [\sin\gamma \sin B \cos(\psi - \sigma) + \cos B \sin(\psi - \sigma)] \\
& -V_w [\dot{\gamma} \cos\gamma \sin B \cos(\psi - \sigma) + \dot{B} \sin\gamma \cos B \cos(\psi - \sigma) \\
& - (\dot{\psi} - \dot{\sigma}) \sin\gamma \sin B \sin(\psi - \sigma) - \dot{B} \sin B \sin(\psi - \sigma) \\
& + (\dot{\psi} - \dot{\sigma}) \cos B \cos(\psi - \sigma)] + \omega_\bullet (r + h) \cos\delta (\sin\gamma \sin\sigma \sin B \\
& + \cos\sigma \cos B) - \omega_\bullet (r + h) \dot{\delta} \sin\delta (\sin\gamma \sin\sigma \sin B + \cos\sigma \cos B) \\
& + \omega_\bullet (r + h) \cos\delta (\dot{\gamma} \cos\gamma \sin\sigma \sin B + \dot{\sigma} \sin\gamma \cos\sigma \sin B \\
& + \dot{B} \sin\gamma \sin\sigma \cos B - \dot{\sigma} \sin\sigma \cos B - \dot{B} \cos\sigma \sin B)
\end{aligned} \tag{13}A$$

$$\begin{aligned}
\dot{V}_Z = & -\dot{V}_w [\sin\gamma \cos B \cos(\psi - \sigma) - \sin B \sin(\psi - \sigma)] \\
& -V_w [\dot{\gamma} \cos\gamma \cos B \cos(\psi - \sigma) - \dot{B} \sin\gamma \sin B \cos(\psi - \sigma) \\
& - (\dot{\psi} - \dot{\sigma}) \sin\gamma \cos B \sin(\psi - \sigma) - \dot{B} \cos B \sin(\psi - \sigma) \\
& - (\dot{\psi} - \dot{\sigma}) \sin B \cos(\psi - \sigma)] + \omega_\bullet (r + h) \cos\delta (\sin\gamma \sin\sigma \cos B \\
& - \cos\sigma \sin B) - \omega_\bullet (r + h) \dot{\delta} \sin\delta (\sin\gamma \sin\sigma \cos B - \cos\sigma \sin B) \\
& + \omega_\bullet (r + h) \cos\delta (\dot{\gamma} \cos\gamma \sin\sigma \cos B + \dot{\sigma} \sin\gamma \cos\sigma \cos B \\
& - \dot{B} \sin\gamma \sin\sigma \sin B + \dot{\sigma} \sin\sigma \sin B - \dot{B} \cos\sigma \cos B)
\end{aligned} \tag{14}A$$

If no rate of roll exists,* as may be expected during performance flight testing, \dot{B} may be set equal to zero and equations (13)A and (14)A reduced to the following:

* \dot{B} has no influence on a_x , a_y , or a_z . This can be shown by retaining terms which contain B in equations (12) through (14) as well as in subsequent equations which define ω_\bullet . All terms containing \dot{B} then vanish due to cancellation of terms.

$$\begin{aligned}
\dot{V}_Y &= -\dot{V}_W [\sin\gamma \sin B \cos(\psi - \sigma) + \cos B \sin(\psi - \sigma)] \\
&- V_W [\dot{\gamma} \cos\gamma \sin B \cos(\psi - \sigma) - (\dot{\psi} - \dot{\sigma}) \sin\gamma \sin B \sin(\psi - \sigma) \\
&+ (\dot{\psi} - \dot{\sigma}) \cos B \cos(\psi - \sigma)] \\
&+ \omega_{\bullet}(r + h) \cos\delta (\sin\gamma \sin\sigma \sin B + \cos\sigma \cos B) \\
&- \omega_{\bullet}(r + h) \dot{\delta} \sin\delta (\sin\gamma \sin\sigma \sin B + \cos\sigma \cos B) \\
&+ \omega_{\bullet}(r + h) \cos\delta (\dot{\gamma} \cos\gamma \sin\sigma \sin B + \dot{\sigma} \sin\gamma \cos\sigma \sin B - \dot{\sigma} \sin\sigma \cos B) \quad (15)A
\end{aligned}$$

$$\begin{aligned}
\dot{V}_Z &= -\dot{V}_W [\sin\gamma \cos B \cos(\psi - \sigma) - \sin B \sin(\psi - \sigma)] \\
&- V_W [\dot{\gamma} \cos\gamma \cos B \cos(\psi - \sigma) - (\dot{\psi} - \dot{\sigma}) \sin\gamma \cos B \sin(\psi - \sigma) \\
&- (\dot{\psi} - \dot{\sigma}) \sin B \cos(\psi - \sigma)] \\
&+ \omega_{\bullet}(r + h) \cos\delta (\sin\gamma \sin\sigma \cos B - \cos\sigma \sin B) \\
&- \omega_{\bullet}(r + h) \dot{\delta} \sin\delta (\sin\gamma \sin\sigma \cos B - \cos\sigma \sin B) \\
&+ \omega_{\bullet}(r + h) \cos\delta (\dot{\gamma} \cos\gamma \sin\sigma \cos B + \dot{\sigma} \sin\gamma \cos\sigma \cos B \\
&+ \dot{\sigma} \sin\sigma \sin B) \quad (16)A
\end{aligned}$$

Next, referring back to equation (9)A, it is necessary to define the rotational velocity of the wind-axes system. This is first determined in the north, east, down system, denoted by the subscript g.

$$\bar{\omega}_g = [(\omega_\bullet + \dot{\lambda})\cos\delta - \dot{\gamma}\sin\delta]\bar{i}_g + (\dot{\gamma}\cos\delta - \dot{\delta})\bar{j}_g + [\dot{\sigma} - (\omega_\bullet + \dot{\lambda})\sin\delta]\bar{k}_g \quad (17)A$$

with the rotational velocity due to a rate of roll set equal to zero.

Transforming, as before, to the wind-axes system

$$\begin{bmatrix} \omega_{wX} \\ \omega_{wY} \\ \omega_{wZ} \end{bmatrix} = [T] \begin{bmatrix} (\omega_\bullet + \dot{\lambda})\cos\delta - \dot{\gamma}\sin\delta \\ \dot{\gamma}\cos\delta - \dot{\delta} \\ \dot{\sigma} - (\omega_\bullet + \dot{\lambda})\sin\delta \end{bmatrix} \quad (18)A$$

Performing the matrix multiplication

$$\begin{aligned} \omega_{wX} &= [(\omega_\bullet + \dot{\lambda})\cos\delta - \dot{\gamma}\sin\delta]\cos\gamma\cos\sigma + [\dot{\gamma}\cos\delta - \dot{\delta}]\cos\gamma\sin\sigma \\ &\quad - [\dot{\sigma} - (\omega_\bullet + \dot{\lambda})\sin\delta]\sin\gamma \end{aligned} \quad (19)A$$

$$\begin{aligned} \omega_{wY} &= [(\omega_\bullet + \dot{\lambda})\cos\delta - \dot{\gamma}\sin\delta](\sin\gamma\cos\sigma\sin B - \sin\sigma\cos B) \\ &\quad + (\dot{\gamma}\cos\delta - \dot{\delta})(\sin\gamma\sin\sigma\sin B + \cos\sigma\cos B) \\ &\quad + [\dot{\sigma} - (\omega_\bullet + \dot{\lambda})\sin\delta]\cos\gamma\sin B \end{aligned} \quad (20)A$$

$$\begin{aligned} \omega_{wZ} &= [(\omega_\bullet + \dot{\lambda})\cos\delta - \dot{\gamma}\sin\delta](\cos\sigma\sin\gamma\cos B + \sin\sigma\sin B) \\ &\quad + (\dot{\gamma}\cos\delta - \dot{\delta})(\sin\gamma\sin\sigma\cos B - \cos\sigma\sin B) \\ &\quad + [\dot{\sigma} - (\omega_\bullet + \dot{\lambda})\sin\delta]\cos\gamma\cos B \end{aligned} \quad (21)A$$

Simplifying equations (19)A, (20)A, and (21)A, we have

$$\omega_{wX} = (\omega_{\bullet} + \dot{\lambda})(\cos\delta\cos\gamma\cos\sigma + \sin\delta\sin\gamma) - \dot{\delta}\cos\gamma\sin\sigma - \dot{\sigma}\sin\gamma \quad (22)A$$

$$\begin{aligned} \omega_{wY} = & (\omega_{\bullet} + \dot{\lambda})(\cos\delta\sin\gamma\cos\sigma\sin B - \cos\delta\sin\sigma\cos B - \sin\delta\cos\gamma\sin B) \\ & + \dot{\gamma}\cos B - \dot{\delta}(\sin\gamma\sin\sigma\sin B + \cos\sigma\cos B) + \dot{\sigma}\cos\gamma\sin B \end{aligned} \quad (23)A$$

$$\begin{aligned} \omega_{wZ} = & (\omega_{\bullet} + \dot{\lambda})\cos\delta\cos\sigma\sin\gamma\cos B + \cos\delta\sin\sigma\sin B - \sin\delta\cos\gamma\cos B \\ & - \dot{\gamma}\sin B - \dot{\delta}(\sin\gamma\sin\sigma\cos B - \cos\sigma\sin B) + \dot{\sigma}\cos\gamma\cos B \end{aligned} \quad (24)A$$

Again referring back to equation (9)A, to evaluate the acceleration due to the rotation of the wind-axes system we have

$$\vec{\omega} \times \vec{V} = \begin{vmatrix} \vec{i} & \vec{j} & \vec{k} \\ \omega_{wX} & \omega_{wY} & \omega_{wZ} \\ V_X & V_Y & V_Z \end{vmatrix} \quad (25)A$$

Components of acceleration are, then

$$a_{\omega X} = \omega_{wY} V_Z - \omega_{wZ} V_Y \quad (26)A$$

$$a_{\omega Y} = \omega_{wZ} V_X - \omega_{wX} V_Z \quad (27)A$$

$$a_{\omega Z} = \omega_{wX} V_Y - \omega_{wY} V_X \quad (28)A$$

Substituting terms from equations (7)A, (19)A, (20)A, and (21)A we have

$$\begin{aligned}
a_{\omega_X} = & \omega_{\oplus}(\omega_{\oplus} + \dot{\lambda})(r + h)(\cos\delta\sin\delta\cos\gamma\cos\sigma - \cos^2\delta\sin\gamma) \\
& - V_w(\omega_{\oplus} + \dot{\lambda})[\cos\gamma\sin(\psi - \sigma)\sin\delta - \sin\gamma\cos\delta\sin\psi] \\
& + \dot{\gamma}\omega_{\oplus}(r + h)\cos\delta\sin\gamma\sin\sigma - \dot{\sigma}\omega_{\oplus}(r + h)\cos\delta\cos\gamma\cos\sigma \\
& - \dot{\gamma}V_w\sin\gamma\cos(\psi - \sigma) + \dot{\delta}V_w\sin\gamma\cos\psi + V_w\dot{\sigma}\cos\gamma\sin(\psi - \sigma)
\end{aligned}
\tag{29}A$$

$$\begin{aligned}
a_{\omega_Y} = & V_t(\omega_{\oplus} + \dot{\lambda})(\cos\delta\cos\sigma\sin\gamma\cos B + \cos\delta\sin\sigma\sin B - \sin\delta\cos\gamma\cos B) \\
& - V_t\dot{\gamma}\sin B - V_t\dot{\delta}(\sin\gamma\sin\sigma\cos B - \cos\sigma\sin B) + V_t\dot{\sigma}\cos\gamma\cos B \\
& + V_w(\omega_{\oplus} + \dot{\lambda})[\cos(\psi - \sigma)\sin\delta\cos B - \cos\gamma\cos\delta\sin\psi\sin B \\
& - \sin\gamma\sin(\psi - \sigma)\sin\delta\sin B] + V_w\dot{\gamma}\cos\gamma\cos(\psi - \sigma)\sin B \\
& - V_w\dot{\delta}\cos\gamma\cos\psi\sin B - V_w\dot{\sigma}[\cos(\psi - \sigma)\cos B - \sin\gamma\sin(\psi - \sigma)\sin B] \\
& + \omega_{\oplus}(\omega_{\oplus} + \dot{\lambda})(r + h)[- \sin\sigma\cos\delta\sin\delta\cos B + \cos\gamma\cos^2\delta\sin B \\
& + \sin\gamma\cos\sigma\cos\delta\sin\delta\sin B] - \dot{\gamma}\omega_{\oplus}(r + h)\cos\gamma\sin\sigma\cos\delta\sin B \\
& + \dot{\sigma}\omega_{\oplus}(r + h)(\sin\sigma\cos\delta\cos B - \sin\gamma\cos\sigma\cos\delta\sin B)
\end{aligned}
\tag{30}A$$

$$\begin{aligned}
a_{\omega_Z} = & - V_t[(\omega_{\oplus} + \dot{\lambda})(\cos\delta\sin\gamma\cos\sigma\sin B - \cos\delta\sin\sigma\cos B - \sin\delta\cos\gamma\sin B) \\
& + \dot{\gamma}\cos B - \dot{\delta}(\sin\gamma\sin\sigma\sin B + \cos\sigma\cos B) + \dot{\sigma}\cos\gamma\sin B] \\
& - V_w(\omega_{\oplus} + \dot{\lambda})[\cos\gamma\sin\psi\cos\delta\cos B + \cos(\psi - \sigma)\sin\delta\sin B \\
& + \sin\gamma\sin(\psi - \sigma)\sin\delta\cos B] + \omega_{\oplus}(\omega_{\oplus} + \dot{\lambda})(r + h)\cos\delta \cdot \\
& \cdot (\cos\gamma\cos\delta\cos B + \sin\sigma\sin\delta\sin B + \sin\gamma\cos\sigma\sin\delta\cos B) \\
& - V_w\dot{\delta}\cos\gamma\cos\psi\cos B + V_w\dot{\sigma}[\cos(\psi - \sigma)\sin B + \sin\gamma\sin(\psi - \sigma)\cos B] \\
& + V_w\dot{\gamma}\cos\gamma\cos(\psi - \sigma)\cos B - \dot{\gamma}\omega_{\oplus}(r + h)\cos\gamma\sin\sigma\cos\delta\cos B \\
& - \dot{\sigma}\omega_{\oplus}(r + h)\cos\delta(\sin\sigma\sin B + \sin\gamma\cos\sigma\cos B)
\end{aligned}
\tag{31}A$$

To obtain total accelerations in the \bar{i} , \bar{j} , and \bar{k} directions, as indicated by equation (9)A, we combine terms as follows:

$$a_X = \dot{V}_X + a_{\omega_X} \quad (32)A$$

$$a_Y = \dot{V}_Y + a_{\omega_Y} \quad (33)A$$

$$a_Z = \dot{V}_Z + a_{\omega_Z} \quad (34)A$$

From equations (11)A and (29)A

$$\begin{aligned} a_X = & \dot{V}_t - \dot{V}_w \cos \gamma \cos(\psi - \sigma) + V_w \dot{\psi} \cos \gamma \sin(\psi - \sigma) + \omega_e (r + h) \cos \delta \cos \gamma \sin \sigma \\ & - \omega_e (r + h) \dot{\delta} \sin \delta \cos \gamma \sin \sigma + V_w \dot{\delta} \sin \gamma \cos \psi - V_w (\omega_e + \dot{\lambda}) \cdot \\ & \cdot [\cos \gamma \sin(\psi - \sigma) \sin \delta - \sin \gamma \cos \delta \sin \psi] + \omega_e (\omega_e + \dot{\lambda}) (r + h) \cdot \\ & \cdot (\cos \delta \sin \delta \cos \gamma \cos \sigma - \cos^2 \delta \sin \gamma) \end{aligned} \quad (35)A$$

Combining equations (14)A and (30)A

$$\begin{aligned} a_Y = & V_t (\omega_e + \dot{\lambda}) (\cos \delta \cos \sigma \sin \gamma \sin B + \cos \delta \sin \sigma \sin B - \sin \delta \cos \gamma \cos B) \\ & - V_t \dot{\gamma} \sin B - V_t \dot{\delta} (\sin \gamma \sin \sigma \cos B - \cos \sigma \sin B) + V_t \dot{\sigma} \cos \gamma \cos B \\ & + V_w (\omega_e + \dot{\lambda}) [\cos(\psi - \sigma) \sin \delta \cos B - \cos \gamma \cos \delta \sin B \sin \psi \\ & - \sin \gamma \sin(\psi - \sigma) \sin \delta \sin B] - V_w \dot{\delta} \cos \gamma \cos \psi \sin B \\ & - \dot{V}_w [\sin \gamma \sin B \cos(\psi - \sigma) + \cos B \sin(\psi - \sigma)] \\ & + V_w \dot{\psi} [\sin \gamma \sin(\psi - \sigma) \sin B - \cos(\psi - \sigma) \cos B] + [\omega_e (r + h) \cos \delta \\ & - \omega_e (r + h) \dot{\delta} \sin \delta] \{ \sin \gamma \sin \sigma \sin B + \cos \sigma \cos B \} + \omega_e (\omega_e + \dot{\lambda}) (r + h) \cdot \\ & \cdot [-\sin \sigma \cos \delta \sin \delta \cos B + \cos \gamma \cos^2 \delta \sin B + \sin \gamma \cos \sigma \cos \delta \sin \delta \sin B] \end{aligned}$$

Equations (15)A and (31)A yield

$$\begin{aligned}
 a_z = & -V_t \dot{\gamma} \cos B + V_t \dot{\delta} (\sin \gamma \sin \sigma \sin B + \cos \sigma \cos B) - V_t \dot{\sigma} \cos \gamma \sin B \\
 & - V_t (\omega_e + \dot{\lambda}) (\sin \gamma \cos \sigma \cos \delta \sin B - \sin \sigma \cos \delta \cos B - \cos \gamma \sin \delta \sin B) \\
 & - \dot{V}_w [\sin \gamma \cos (\psi - \sigma) \cos B - \sin (\psi - \sigma) \sin B] + V_w \dot{\psi} [\sin \gamma \cos (\psi - \sigma) \cos B \\
 & + \cos (\psi - \sigma) \sin B] - V_w (\omega_e + \dot{\lambda}) [\cos \gamma \sin \psi \cos \delta \cos B + \cos (\psi - \sigma) \sin \delta \sin B \\
 & + \sin \gamma \sin (\psi - \sigma) \sin \delta \cos B] + \omega_e (r + h) \cos \delta (\sin \gamma \sin \sigma \cos B \\
 & - \cos \sigma \sin B) - \omega_e (r + h) \dot{\delta} \sin \delta (\sin \gamma \sin \sigma \cos B - \cos \sigma \sin B) \\
 & + \omega_e (\omega_e + \dot{\lambda}) (r + h) \cos \delta (\cos \gamma \cos \delta \cos B + \sin \sigma \sin \delta \sin B \\
 & + \sin \gamma \cos \sigma \sin \delta \cos B) - V_w \dot{\delta} \cos \gamma \cos \psi \cos B
 \end{aligned} \tag{37)A}$$

The lateral acceleration, a_y , will tend to produce a sideslip, the magnitude of which will depend on the aerodynamic characteristics of the airplane. The resulting increase in drag, even in extreme cases, will be slight, and the effect of a_y on aircraft performance can be safely ignored.

If accelerations in the X and Z directions based on on-board measurements of airspeed and altitude are desired, equations (35)A and (37)A may be modified to better suit that purpose. In this case the effects of wind gradients are accounted for together with the effects of the earth's rotation rate. First, wind data may be expressed as

$$\dot{V}_w = \frac{dV_w}{dh} h = \frac{dV_w}{dh} V_t \sin \gamma \tag{38)A}$$

$$\text{and } \dot{\psi} = \frac{d\psi}{dh} h = \frac{d\psi}{dh} V_t \sin \gamma \tag{39)A}$$

The ground speed may be expressed as

$$\bar{V}_g = (V_t \cos \gamma \cos \sigma - V_w \cos \psi) \bar{i}_g + (V_t \cos \gamma \sin \sigma - V_w \sin \psi) \bar{j}_g \quad (40)A$$

Then the rates-of-change of latitude and longitude become

$$\dot{\delta} = \frac{V_g \cos \sigma}{r + h} \quad (41)A$$

and

$$\dot{\lambda} = \frac{V_g \sin \sigma}{(r + h) \cos \delta} \quad (42)A$$

To find \dot{r} , equation (8)A is differentiated with respect to latitude to give

$$\frac{dr}{d\delta} = 20.92647 \times 10^6 (-.003366988 \sin 2\delta + .000014196 \sin 4\delta) \quad (43)A$$

Then from

$$\dot{r} = \frac{dr}{d\delta} \dot{\delta} \quad (44)A$$

and equations (41)A and (43)A we have

$$\dot{r} = - \frac{20.92647 \times 10^6 V_g \cos \sigma (.003366988 \sin 2\delta - .000014196 \sin 4\delta)}{r + h} \quad (45)A$$

Substituting equations (38)A through (45)A in equations (35)A and (37)A we have

$$\begin{aligned}
a_X = & \dot{V}_t - \frac{1}{2} \frac{dV_w}{dh} V_t \sin 2\gamma \cos(\psi - \sigma) + \frac{1}{2} \frac{d\psi}{dh} V_w V_t \sin 2\gamma \sin(\psi - \sigma) \\
& + \omega_\bullet \cos \delta \cos \gamma \sin \sigma \left[V_t \sin \gamma - \right. \\
& \left. - \frac{20.92647 \times 10^6 V_g \cos \sigma (.003366988 \sin 2\delta - .000014196 \sin 4\delta)}{r + h} \right] \\
& - \frac{1}{2} \omega_\bullet V_g \sin 2\sigma \sin \delta \cos \gamma + \frac{V_w V_g \cos \sigma \sin \gamma \cos \psi}{r + h} \\
& - V_w \left[\omega_\oplus + \frac{V_g \sin \sigma}{(r + h) \cos \delta} \right] \left[\cos \gamma \sin(\psi - \sigma) \sin \delta - \sin \gamma \cos \delta \sin \psi \right] \\
& + \left[\omega_\oplus^2 (r + h) + \frac{\omega_\bullet V_g \sin \sigma}{\cos \delta} \right] \left[\frac{1}{2} \sin 2\delta \cos \gamma \cos \sigma - \cos^2 \delta \sin \gamma \right] \quad (46)A
\end{aligned}$$

and

$$\begin{aligned}
 a_Z = & -V_t \dot{\gamma} \cos B + \frac{V_t V_g \cos \sigma}{r+h} (\sin \gamma \sin \sigma \sin B + \cos \sigma \cos B) \\
 & - V_t \dot{\sigma} \cos \gamma \sin B - V_t \left[\omega_{\oplus} + \frac{V_g \sin \sigma}{(r+h) \cos \delta} \right] \left[\sin \gamma \cos \sigma \cos \delta \sin B \right. \\
 & \left. - \sin \sigma \cos \delta \cos B - \cos \gamma \sin \delta \sin B \right] \\
 & - \frac{dV_w}{dh} V_t \sin \gamma \left[\sin \gamma \cos(\psi - \sigma) \cos B - \sin(\psi - \sigma) \sin B \right] \\
 & + V_w \frac{d\psi}{dh} V_t \sin \gamma \left[\sin \gamma \sin(\psi - \sigma) \cos B + \cos(\psi - \sigma) \sin B \right] \\
 & - V_w \left[\omega_{\oplus} + \frac{V_g \sin \sigma}{(r+h) \cos \delta} \right] \left[\cos \gamma \sin \psi \cos \delta \cos B + \cos(\psi - \sigma) \sin \delta \sin B \right. \\
 & \left. + \sin \gamma \sin(\psi - \sigma) \sin \delta \cos B \right] + \omega_{\oplus} \left[V_t \sin \gamma \right. \\
 & \left. - \frac{20.92647 \times 10^6 V_g \cos \sigma (.003366988 \sin 2\delta - .000014196 \sin 4\delta)}{r+h} \right] \cdot \\
 & \cdot \cos \delta (\sin \gamma \sin \sigma \cos B - \cos \sigma \sin B) \\
 & - \omega_{\oplus} V_g \cos \sigma \sin \delta (\sin \gamma \sin \sigma \cos B - \cos \sigma \sin B) \\
 & + \left[\omega_{\oplus}^2 (r+h) + \frac{\omega_{\oplus} V_g \sin \sigma}{\cos \delta} \right] \cos \delta (\cos \gamma \cos \delta \cos B + \sin \sigma \sin \delta \sin B \\
 & + \sin \gamma \cos \sigma \sin \delta \cos B) - \frac{V_w V_g \cos \sigma}{r+h} \cos \gamma \cos \psi \cos B \quad (47)A
 \end{aligned}$$

APPENDIX II

VARIATION OF EXCESS THRUST WITH LOAD FACTORS

Variation of Excess Thrust with n_X

From an examination of equations (12) and (17) of the main text it is seen that a change in load factor along an airplane's velocity vector due to the earth's rotation can be related directly to a change in excess thrust.

$$\frac{\partial F_{ex}}{\partial n_X} dn_X = W dn_Z \quad (48)A$$

Variation of Excess Thrust with n_Z

To find a general equation relating the change in excess thrust to a change in load factor normal to the flight path equation (12) of the main text is used to find the partial of excess thrust with normal load factor.

$$\frac{\partial F_{ex}}{\partial n_Z} = -F \sin \alpha \frac{\partial \alpha}{\partial n_Z} - q S \frac{\partial C_D}{\partial n_Z} \quad (49)A$$

Substituting

$$\frac{\partial \alpha}{\partial n_Z} = \frac{\partial \alpha}{\partial C_L} \frac{\partial C_L}{\partial n_Z} \quad (50)A$$

$$\text{and } \frac{\partial \alpha}{\partial C_L} = \frac{1}{C_{L_\alpha}} \quad (51)A$$

we have

$$\frac{\partial F_{ex}}{\partial n_Z} = -\frac{F \sin \alpha}{C_{L_\alpha}} \frac{\partial C_L}{\partial n_Z} - q S \frac{\partial C_D}{\partial n_Z} \quad (52)A$$

Differentiation of the normal equation of motion (equation (14)) yields

$$qS \frac{\partial C_L}{\partial n_Z} = W - F \cos \alpha \frac{\partial \alpha}{\partial n_Z} \quad (53)A$$

Making substitutions as before and rearranging

$$\frac{\partial C_L}{\partial n_Z} = \frac{W}{qS + \frac{F \cos \alpha}{C_{L\alpha}}} \quad (54)A$$

Substituting equation (54)A in equation (52)A

$$\frac{\partial F_{ex}}{\partial n_Z} = - \frac{W}{qS + \frac{F \cos \alpha}{C_{L\alpha}}} \left(\frac{F \sin \alpha}{C_{L\alpha}} + qS \frac{\partial C_D}{\partial C_L} \right) \quad (55)A$$

Equation (55)A may be simplified with little loss in accuracy to

$$\frac{\partial F_{ex}}{\partial n_Z} = - W \frac{\partial C_D}{\partial C_L} \quad (56)A$$

If a parabolic drag polar is assumed

$$C_D = C_{D_0} + K_i C_L^2 \quad (57)A$$

Partial differentiation yields

$$\frac{\partial C_D}{\partial C_L} = 2 K_i C_L \quad (58)A$$

so that equation (55) may be rewritten as

$$\frac{\partial F_{ex}}{\partial n_Z} = -2 K_i C_L W \quad (59)A$$

$$\text{or } \frac{\partial F_{ex}}{\partial n_Z} dn_Z = -2 K_i C_L W dn_Z \quad (60)A$$

From differentiation of equation (15) with γ and B constant

$$dn_Z = -d\left(\frac{a_Z}{g_{ref}}\right) \quad (61)A$$

which combined with equation (59)A gives as an alternate form of equation (60)A

$$\frac{\partial F_{ex}}{\partial n_Z} dn_Z = 2 K_i C_L W d\left(\frac{a_Z}{g_{ref}}\right) \quad (62)A$$

Total Variation of Excess Thrust with n_X and n_Z

The total change in excess thrust due to changes in load factors may be expressed as

$$dF_{ex} = \frac{\partial F_{ex}}{\partial n_X} dn_X + \frac{\partial F_{ex}}{\partial n_Z} dn_Z \quad (63)A$$

Summing equations (48)A and (60)A as indicated by equation (63)A we have

$$dF_{ex} = W dn_X - 2 K_i C_L W dn_Z \quad (64)A$$

which may be written in the form

$$F_{ex_s} = F_{ex_t} + W(n_{X_s} - n_{X_t}) - 2 K_i C_L W(n_{Z_s} - n_{Z_t}) \quad (65)A$$

(U) A TANDEM MASS SPECTROMETER
FOR THE STUDY OF ION-MOLECULE
REACTIONS

by

J.H. Futrell, L.I. Bone and F.P. Abramson

Chemistry Research Laboratory
Aerospace Research Laboratories
Wright-Patterson Air Force Base, Ohio



J. H. Futrell

BIOGRAPHY

DR. JEAN H. FUTRELL

Dr. Jean H. Futrell, Research Chemist, Chemistry Research Laboratory, Aerospace Research Laboratories, joined ARL in June, 1961. The Chemistry Research Laboratory conducts basic research in the general field of chemistry and, in particular, in areas of physical chemistry related to combustion, detonation, reaction kinetics, energy transfer, as well as polymer and fuel chemistry and analytical chemistry. As leader of the High Energy Kinetics group, Dr. Futrell is responsible for giving direction to research in radiation chemistry and mass spectrometry at ARL.

Dr. Futrell graduated first in his class at Louisiana Polytechnic Institute in 1955, receiving the degree of Bachelor of Science in Chemical Engineering summa cum laude. That year he was also one of three residents of Louisiana selected by the National Science Foundation to receive pre-doctoral fellowships at the universities of their choice. In September, 1955, he enrolled as a graduate student in the College of Chemistry of the University of California at Berkeley. For the academic year 1956-57, he served as a graduate teaching assistant in chemistry and was appointed the Allied Chemical and Dye Corporation fellow in physical chemistry at the University in 1957. He received his PhD. in chemistry in 1958 and worked briefly at the Lawrence Radiation Laboratory of the University of California from June to September 1958 as a research associate. In September, Dr. Futrell joined the Humble Oil & Refining Company research laboratory in Baytown, Texas, as a research chemist. In June, 1959, he was ordered to active duty in the Air Force and assigned to the Aeronautical Research Laboratory (predecessor to the Aerospace Research Laboratories) as a First Lieutenant.

Upon being released from extended active duty, Dr. Futrell continued his research at ARL in chemical kinetics in the areas which evolved into his present research program.



L. I. Bone

BIOGRAPHY

Capt Larry I. Bone

Capt Larry I. Bone is a native of Conrad, Iowa. He graduated from Conrad High School in 1953 and from Coe College, Cedar Rapids, Iowa in 1957, where he received a B.A. degree in chemistry and a reserve commission in the United States Air Force. He entered active duty in 1956 at Lackland AFB, Texas. In 1958 he received his wings after completing Navigator Training at Harlingen AFB, Texas. In 1959 he graduated first in his class from Radar Intercept School at James Connally AFB, Texas and was then assigned as a line radar observer with the 29th FIS Malmstrom AFB, Montana. In 1960 he completed Interceptor Weapons School at Maxwell AFB, Ala. In 1964 he received a M.S. degree in Physical Chemistry from the Ohio State University and was subsequently assigned to the Aerospace Research Laboratory, Wright-Patterson AFB, Ohio as a task scientist. In 1966 he received his PhD. from the Ohio State University.

Capt Bone is married to the former Marilyn Batz of Lytton, Iowa. They have two children, Bruce and Kimberly.



F. P. Abramson

BIOGRAPHY

DR. FRED P. ABRAMSON

Dr. Fred P. Abramson is currently working in the Chemistry Research Laboratory at the Aerospace Research Laboratories (ARL) on a National Academy of Sciences-National Science Council Post-doctoral Associateship.

A native of Columbus, Ohio, Dr. Abramson received his PhD. in radiation chemistry at Ohio State University in 1965. He received his A.B. degree in chemistry at the Western Reserve University in 1962.

Dr. Abramson is currently conducting research in the area of radiation chemistry of organic systems.

ABSTRACT

An instrument for the study of ion molecule reactions which is superior to conventional single stage instruments has been developed. It consists of a double-focusing mass spectrometer which serves as an ion source for a collision chamber connected to a second double-focusing mass spectrometer. This instrument allows one to study unambiguously the charged products produced by the reaction of a given ion at a given energy with a given neutral molecule. The in-line configuration maximizes collection of momentum transfer products and ion beams of useful intensity are produced over an energy range of the impacting ion of 0.2 - 100 eV with an energy spread of 0.3 eV.

Experimental results which exemplify this instrument's utility in identifying reaction partners are discussed. Examples are also given which demonstrate the value of this instrument for studying the kinetic effects of ion translational energy. Two general phenomena associated with ion translational energy are described. One is a change in mechanism with kinetic energy and the other is the conversion of translation energy into internal energy of the reaction complex. The possible significance of this work to basic science as well as current and future Air Force problems is also discussed.

INTRODUCTION

The study of ion-molecule reactions has long been of interest at the Aerospace Research Laboratory as well as at other laboratories throughout the world. Ion-molecule reactions can be described as interactions between molecules or atoms which bear an electrical charge (either positive or negative) and neutral molecular species such that a material particle either charged or uncharged is transferred from one reactant to the other. The particle transferred can simply be an electron, in which case it is common to refer to the reaction as charge transfer. At the other extreme it can involve the complete condensation of both particles into a single, charged aggregate.

The significance of this type of study to basic science as well as current and future Air Force problems is probably obvious. Ion-molecule reactions of various types are among the most important processes which account for the observed physical and chemical changes in materials produced by ionizing radiation, whether the materials are biological or inanimate. Thus the elucidation of these processes is of utmost importance in understanding radiation effects on both vehicles and personnel which will operate in an environment where ionizing radiation is present, whether the radiation be of cosmic origin or from nuclear devices. A less obvious application of this type of investigation is exemplified by a project which we are performing in conjunction with the Aerospace Medical Research Laboratories at Wright-Patterson. They are interested in a device which will electrostatically condense and collect contaminants in closed ecological systems such as space cabins. The process under investigation involves selectively condensing the various contaminants by ion-molecule reactions and subsequently removing them by ionic precipitation in a manner analogous to the well-established electrostatic precipitators used for smoke purification.

The most customarily applied, but often ambiguous, approach to the study of ion-molecule reactions is the use of a conventional mass spectrometer at elevated ion-source pressures. For this technique both the gas from which the desired ion is to be produced and the reactant molecule are expanded into the source region of the mass spectrometer and are then exposed to a beam of electrons. Ions are produced and because of the relatively high pressures undergo reactive collision before they are extracted from the source region and mass analyzed. By observing the initially produced fragment ions as well as the ion-molecule product ions, the reactions involved can be deduced. Except in certain special cases, however, a variety of ions are produced and it is often

difficult to determine which ions are responsible for the observed products. A number of techniques have been developed to simplify matters, but unfortunately there still are a large number of systems which cannot be studied by this technique.

The instrument which we describe consists of two double-focusing mass spectrometers connected in tandem. The basic idea is quite simple. Ions are produced in the first mass spectrometer. The desired ion is mass and energy selected and brought to focus in a reaction chamber containing the appropriate neutral molecule. The reactions take place and product ions are extracted and mass analyzed by the second mass spectrometer. We are thus able to select a given ion at a given energy and impact it on a given molecule and study the complete spectrum of product ions unambiguously.

Description of Instrument

The first instrument, or the ion gun section, consists of a gas handling system, an ion source, energy analyzer, mass analyzer, and various optical elements along with the necessary electronics and vacuum components. A room temperature, glass sample handling system of conventional design with a Granville-Phillips model 203 manually variable leak is used. A modified Consolidated 21-110 gas source, model D-136900 is used. The ion exit aperture has been enlarged to 5 mm x 0.62 mm to increase sensitivity of the source and the focus plates have been trimmed to an aperture width of 1.1 mm to make tuning less critical. At the higher ion intensities required for these studies, space charge effects caused severe loss of resolution with the object slit of the source-acceleration lens system at the theoretical focal point of the electric sector. The slit was therefore moved back 0.5 mm and mass resolution of the order of $M/\Delta M = 100$ for base line resolution was restored.

The mass spectrometer portion of the ion gun consists of a 90° electric sector and a 60° magnetic sector arranged geometrically so that the aberrations due to angular divergence and energy spread are corrected to second order. It corresponds to solution 9 of Table III in the treatment of Hintenberger and König (1) and its performance characteristics as a mass spectrometer have been described (2). The electric sector has a mean optic radius of 3.396" and is terminated by Herzog shunts (3) chosen to terminate the field and to transmit an ion beam of half angle of divergence, α , of 0.0126 radians, for the object slit width of 0.0036". An energy slit, designated β in Fig. 1, with an aperture of 0.004" establishes the energy band pass of the electric sector at 0.2 eV kinetic energy and serves as an object slit for the 3" radius, 60° magnetic sector.

The electric sector has a magnification of 1.125, which when multiplied by the object slit width of 0.0036" determines the β slit width of 0.004. At the characteristic ion energy chosen for the ion gun, 169.8 eV, the energy (velocity) dispersion is thereby set at 2.77×10^{-4} , or 0.188 eV for 169.8 eV ions. The electric sector potentials required are + and - 20.00 volts on the outer and inner field plates.

The magnetic sector field is also terminated by Herzog shunts (4) and limiting stops to restrict the ion beam height to 0.150 in. and prevent any ions from grazing the magnetic field plates. An electromagnet is used to produce and scan the magnetic field, and is coupled to the field plates through a gap in the vacuum chamber which provides electrical isolation. It is obvious that the first stage mass spectrometer must float at the accelerating voltage of the second stage, so that this electrical isolation of the magnetic field plates is essential. The potential of the final acceleration slit (object slit) is the reference voltage of the ion gun assembly and is referred to as source instrument ground in subsequent discussion.

The β slit is electrically isolated from source instrument ground and is used to locate and monitor the ion beam transmitted by the electric sector. An electrometer temporarily connected to these plates is used in tuning the ion optic elements of the source and electric sector for maximum transmission. Final tuning is achieved by maximizing the dip for balanced sectors to assure that the most intense portion of the ion beam is centered. The electrometer is disconnected and the β slit is then externally connected to source instrument ground.

Following the object slit of the ion source we have constructed as a Z-axis focusing element an Einzel lens (5) which is placed between the object slit and the electric sector as shown in Fig. 1. Asymmetric potentials are placed on the central lens element as required for steering the ion beam. Since the final optical configuration is so complicated, this element is normally used only for steering in tuning the first stage. The Z-axis focusing capability is used to optimize overall ion beam transmission once a signal is obtained at the final detector.

The mass resolving slit of 0.007" is placed 4" from the exit edge of the magnetic field. The ion beam at this point theoretically has a width of ca. 0.003" and a half angle of divergence of 0.0152 radians. The mass resolving slit serves as an object for the 60° turning electric sector shown in Fig. 1. This sector has an optic axis radius of 1.466", and by potentials of + and - 24.86 volts turns the beam and centers it in an aperture 0.004" wide which forms the object of the deceleration lens system. This plate also serves as a beam monitor and, when the sector voltages are unbalanced, serves as a total beam detector for the first stage mass spectrometer.

Deceleration Lens and Collision Chamber

The deceleration lens system is undoubtedly the most critical element in the application of the tandem mass spectrometer to the study of low energy ion-neutral interactions. The lens which we use was designed by Kuyatt and Simpson and is shown in Fig. 2. Nichrome V was chosen as construction material and sapphire rods and spacers were used for structural rigidity and electrical insulation.

The fixed points in the design are the location of the focal point of the turning electric sector and the object slit of the second stage mass analyzer, which in our apparatus are 2.25" apart. The design problem was therefore that of retarding ions of 169.8 eV kinetic energy to ca. 1-2 eV without defocusing the ion beam appreciably, injecting the ion beam into a collision chamber of sufficient length and accelerating and focusing product ions and unreacted primary ions on the object slit of the second spectrometer.

Achieving these objectives dictated the use of two stages for deceleration and a strong focusing system which maintains the slit geometry of the ion beam required for optimum performance of the mass spectrometers. For this purpose a "slot" lens system - i. e., thick slits which are long in the beam direction - was chosen. Since to the authors' knowledge this is the first application of slot lenses as an ion optical element, the design is presented in some detail.

The fact that slit lenses at the same voltage ratio are twice as strong focusing as circular aperture lenses is well-known (6). As a first approximation the same relationship will hold for other two dimensional lenses relative to three dimensional lenses of equivalent geometry. With this assumption the optical properties which have been worked out in detail for cylinder lenses may be used to design a slot lens system.

The design procedure may be accomplished most efficiently using P-Q curves given by Spangenberg (17). These parametric curves present the object and image distances for a two-cylinder lens as a function of voltage ratio and magnification. The latter quantities were chosen from a consideration of acceptance angle of the second mass spectrometer with due regard for the Helmholtz-Lagrange Law (17) where α is the

$$\alpha \cdot S \cdot \sqrt{E} = \text{Constant} \quad (1)$$

angle of divergence of the beam, S is beam size, and E is energy.

From the properties of the entering ion beam and the geometrical requirements of the second stage spectrometer, an overall magnification of 4 and final energy of 2.1 eV ($169.8/81 = 2.09$) was chosen for the present system.

This deceleration is accomplished in two stages, so for each lens a magnification of 2 and voltage ratio of 9 pertains. Since the curves in Spangenberg (7) are drawn for an accelerated electron (or ion) beam and we are concerned with a deceleration system we interchange P and Q, the object and image distances, in the figure. Similarly a magnification of 0.5 rather than 2 is used. Finally we take into account the stronger focusing properties of the slot lens by taking the parametric curve for a voltage ratio of 18 to represent our chosen ratio of 9. The ordinate and abscissa of the $M = 0.5$, $V_1/V_2 = 18$ curves (18) yield an object distance of 2.6 slot widths.

A slot width of 0.180" was used in our design, so the corresponding object and image distances are 0.288" and 0.468", respectively, as shown schematically in Fig. 2. The final image plane for the lens is the exit slit of the 0.170" long collision chamber, and a split slot for beam alignment is placed at the image plane of the first lens element. The exit slit width is 0.012", which is somewhat greater than the calculated beam width of 0.0096", and the entrance slit width is similarly somewhat larger than the beam width at that point. The exit slit of the chamber is electrically isolated from the body so that it can be used as an ion extraction slit or as a retarding potential device for measuring the kinetic energy of the impacting ion beam. For the reacceleration lens a standard lens originated by Soa (9) and described recently by Simpson (10) was selected. Both the deceleration and reacceleration lens systems are efficient, high transmission devices. Within experimental accuracy the total ion current collected by a collector placed behind the analyzer object slit was equal to the decrease in the current reading of electrometer D1 of Fig. 1 as the beam is swung into a centered position.

Since the lens system is held at the accelerating potential (1.8, 3.7, 7.5 KV) of the second mass spectrometer, it is necessary that it be carefully shielded from ground. This is accomplished by enclosing this assembly in a 90% transparency mesh box attached to the intermediate lens. This procedure provides a good electrical shield without greatly impeding gas flow from the chamber.

A separate gas handling system connects to the collision chamber via a large diameter (12 mm ID glass tube expanding to 22 mm) some 3 feet in length sealed to a Granville-Phillips motor driven leak. A static pressure tube tees into this line and connects to the measuring side

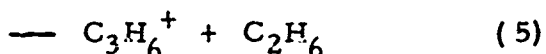
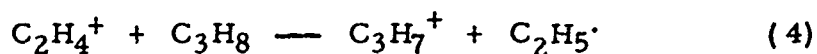
of MKS Baratron model 77-M-XRD pressure sensor head of 0-1 mm range. The signal generated by the Baratron is fed to a Granville-Phillips Automatic Pressure Controller which drives the leak to maintain a predetermined pressure in the chamber itself.

Contact potentials and space charge effects which alter the potential of the region from which ions are extracted from the source require occasional readjustment of repeller, focus plate, and acceleration potentials. Since the optical configuration of the ion gun transmits exactly 169.8 eV ions, however, it was possible to use a Deltron model A176 power supply and voltage divider for the retarding lens. Retarding potential analysis of the transmitted beam indicated that contact potentials in the lens and collision chamber region were negligible.

Product Ion Mass Analyzer

The second stage mass spectrometer was constructed from components of a Consolidated model 21-110 mass spectrometer and has geometry identical to the commercial instrument. To make the two mass spectrometers compatible, the object slit was enlarged to 0.008" and the electric sector termination slits were enlarged to 0.250". In addition the B slit which is located between the electric and magnetic sectors and which limits energy spread was removed to maximize ion transmission. A quadrupole lens scaled down by a factor of 0.8 from the design of Giese (11) was placed approximately mid-way between the object slit and the entrance slit of the electric sector. In our application the order of the potentials is approximately reversed. Giese used his lens to convert a rectangular beam into a tall, narrow beam which would match the object slit of his mass spectrometer. We use the lens to convert a tall, narrow beam to a shorter, rectangular beam which will be transmitted by the electric sector and by the rather narrow (0.100") magnet gap. In addition, asymmetric potentials are used for steering and for deflecting the beam onto electrometer collectors located in the drift spaces preceding the electric sector and between the electric and magnetic sectors.

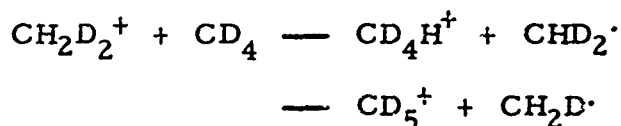
As a detector we use an EMI model 9642B eighteen stage multiplier. The anode signal is amplified by a conventional electrometer and displayed on a Varian G14 recorder. In addition, a signal from the anode is capacitively coupled via a 27 μ f capacitor and 50 ohm cable to a Johnston Laboratories PAD-1 pulse amplifier and discriminator which drives a Computer Measurements Corporation model 706C counter. Pulse counting is the customary mode for recording secondary ion signals.



the ratio of products from H^-/H_2^- transfer is 7/3 for low energy ions (14, 16) and changes to 3.5 ± 0.5 for a terminal ion energy of 1.1 eV. Since low energy reactions predominate in conventional single-stage instruments, this variation implied a strong dependence on kinetic energy. For ca. 4 eV C_2H_4^+ ions, only the H^- -transfer reaction is observed (17). Our results for this ratio are 2.3 at 0.3 eV, 4 at 0.7 eV and 10 at 4 eV nominal ion energy. The correspondence with data from single-stage instruments is therefore quite good, and we take this agreement as chemical evidence that ions have the low energy indicated by physical measurements.

Yet another application of this instrument is the study of the effect of kinetic energy on ion-molecule reactions. Since the kinetic energy of the impacting ion can be varied continuously from essentially thermal energies up to 100 eV, this instrument is well suited to such investigations. Two interesting phenomena which are observed are (i) change in reaction mechanism and (ii) conversion of ion kinetic energy into internal energy of the reaction complex.

Our studies have revealed numerous examples of such a change in mechanism. One is the proton transfer reaction



A study of isotope effects in this reaction indicates that at lower kinetic energies (< 4 eV) an intermediate "loose complex" is formed between the ion and the CD_4 molecule. This complex then decomposes such that the observed isotope effect reflects the difference between a C - D and a C - H bond. Above 4 eV, however, a "stripping" mechanism becomes operative and is exhibited as a very large kinetic isotope effect. In this mechanism the complex does not exist and a proton is stripped from the incoming ion as it passes near the acceptor molecule. Fig. 6 illustrates the transition from complex formation to a stripping mechanism. The relative kinetic energy where the large isotope effect becomes operative corresponds to an interaction time of 3.4×10^{-14} sec. or about 2 vibrational cycles of the methane molecule. This seems to be a useful criterion for a change in mechanism in many ion-molecule reaction

systems. If an ion-molecule reaction product persists at higher relative kinetic energies than those corresponding to interaction times of ca. two vibrational cycles, some form of stripping mechanism is operative.

A direct application of this instrument of immediate relevance to Air Force technology is involved in a collaborative effort with the Aerospace Medical Research Laboratory. A theoretical feasibility study monitored by Mr. W. H. Toliver, Sr. (13) suggested that the oxygen molecule-ion (O_2^+) could be used as a reagent for selective removal of contaminants from space cabin atmospheres. This obviously requires experimental verification before work can proceed to evolve a practical device based on this principle.

The availability of the tandem instrument made it possible to launch an experimental study of reactions of O_2^+ with typical contaminant molecules (formaldehyde, hydrogen sulfide, acetone, benzene), an undertaking which is not possible with conventional, commercially available instrumentation. In a heated chamber with high energy electrons and an incandescent filament, oxygen and hydrocarbons indeed undergo reactions in a conventional spectrometer, but it is far from obvious how that portion of the reactions resulting from ion-molecule interaction could be deduced. The happy coincidence of our development of the tandem mass spectrometer and the evolution of the AMRL requirement for such a study have made possible a cooperative effort which will undoubtedly be a credit to both laboratories.

In conclusion, we have developed an instrument at ARL with truly unique capabilities for fundamental studies of ion-molecule reactions. We have sketched some of the applications which have already been made in the 4 1/2 months it has been in operation. We are confident that it represents a significant breakthrough in such studies and that many significant experiments which we can now visualize in only very broad outline will be forthcoming.

Acknowledgments

The authors are greatly indebted to Drs. John Simpson and Chris Kuvatt of the Electron Physics Section of the National Bureau of Standards for the design of the deceleration lens system and for helpful discussion of ion optics problems. We also wish to acknowledge many helpful discussions of design and performance characteristics of double-focusing mass spectrometers with George Perkins and Dr. Charles Robinson of the Bell and Howell Research Center.

References

1. H. Hintenberger and L. A. Konig, in "Advances in Mass Spectrometry." H. Elliott, ed, Pergamon Press, London (1959), p. 16.
2. G. Perkins, presented at the Thirteenth Annual Conference on Mass Spectrometry, Am. Soc. for Testing Materials Committee E-14, St. Louis, Mo., May 1965.
3. R. Herzog, Zeitschrift Phys., 97, 596 (1935).
4. R. Herzog, Zeitschrift Naturforsch, 10a, 887 (1955).
5. K. R. Spangenberg, "Vacuum Tubes," New York, McGraw-Hill Book Co. (1948), p. 349.
6. J. R. Pierce, "Theory and Design of Electron Beams," p. 102, New York, D. Van Nostrand Co., Inc. (1949).
7. K. R. Spangenberg, *ibid.* p. 379.
8. The highest voltage ratio curve on the P-Q plot of reference 17 is $V_1/V_2 = 11$. However the curves may be calculated from the principles discussed in chapter 13 of that work. Dr. Kuyatt of the Electron Physics Section of the National Bureau of Standards, Washington, D.C., 20234, has continued the curves to $V_1/V_2 = 25$, and the P-Q parameters deduced here were interpolated from his curves.
9. E. A. Soa, Jenaer Jahrbuch 1959/1, (Carl Zeiss, Jena 1959).
10. J. A. Simpson, Rev. Sci. Instr., 32, 1283 (1961).
11. C. F. Giese, Rev. Sci. Instr., 30, 260 (1959).
12. E. Lindholm, Rev. Sci. Instr., 31, 210 (1960).
13. L. W. Sieck and J. H. Futrell, J. Chem. Phys. (in press, 1966).
14. L. W. Sieck and J. H. Futrell, unpublished results.
15. L. I. Bone, F. P. Abramson, and J. H. Futrell (to be published, J. Chem. Phys., 1966).

16. M. S. B. Munson, J. L. Franklin, and F. H. Field, J. Phys. Chem., 68, 3098 (1964).
17. K. R. Ryan and J. H. Futrell, J. Chem Phys., 42, 819 (1965).
18. G. J. Doyle and R. G. Caldwell "Feasibility Investigations of Electrostatic Precipitation for the Removal of Gaseous Trace Contaminants from Manned Cabin Atmospheres", final report, Contract AF33 (615)-2405 (to be published as AMRL report, 1966).

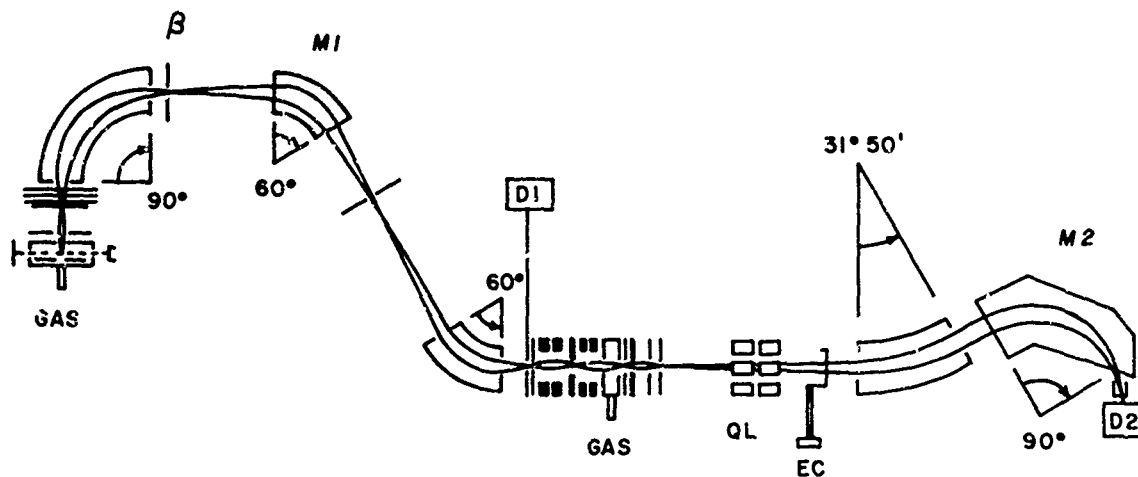


Fig Schematic of Tandem Mass Spectrometers. β is the energy resolving slit and M1 is magnet of ion gun spectrometer. D1 is the ion detector-monitor for the ion gun. QL is quadrupole lens, EC is a movable electrometer for total ion current measurement, M2 the mass analyzer, and D2 the final detector for the product ion analyzer.

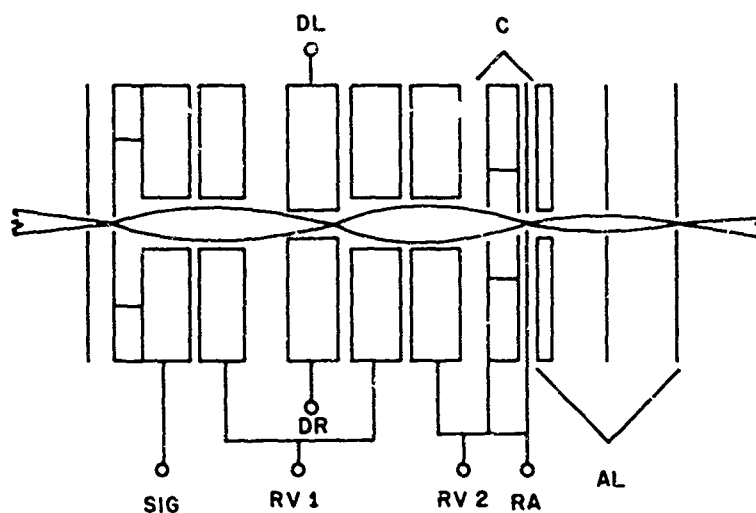


Fig. 2 Schematic of Deceleration Lens. Ion focal planes greatly exaggerated for clarity. SIG = source instrument ground, the reference potential for the ion gun. RV1, RV2 retarding voltage for first and second stages of deceleration. DL and DR are deflection plates for beam centering. C = collision chamber and RA = retarding analyzer for beam energy analysis. AL is the acceleration lens for the second stage mass spectrometer.

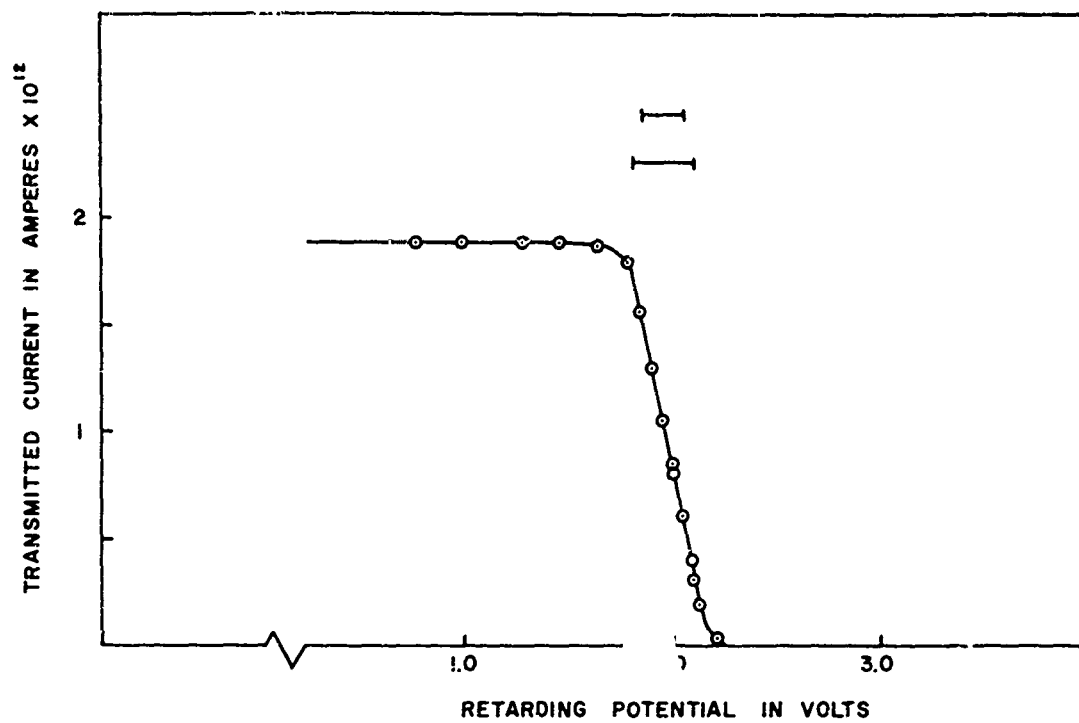


Fig. 3 Energy Spread of 2 eV Ion Beam. Horizontal bars indicate theoretical energy spread of 0.2 eV and the experimental value of 0.3 eV deduced from this curve.

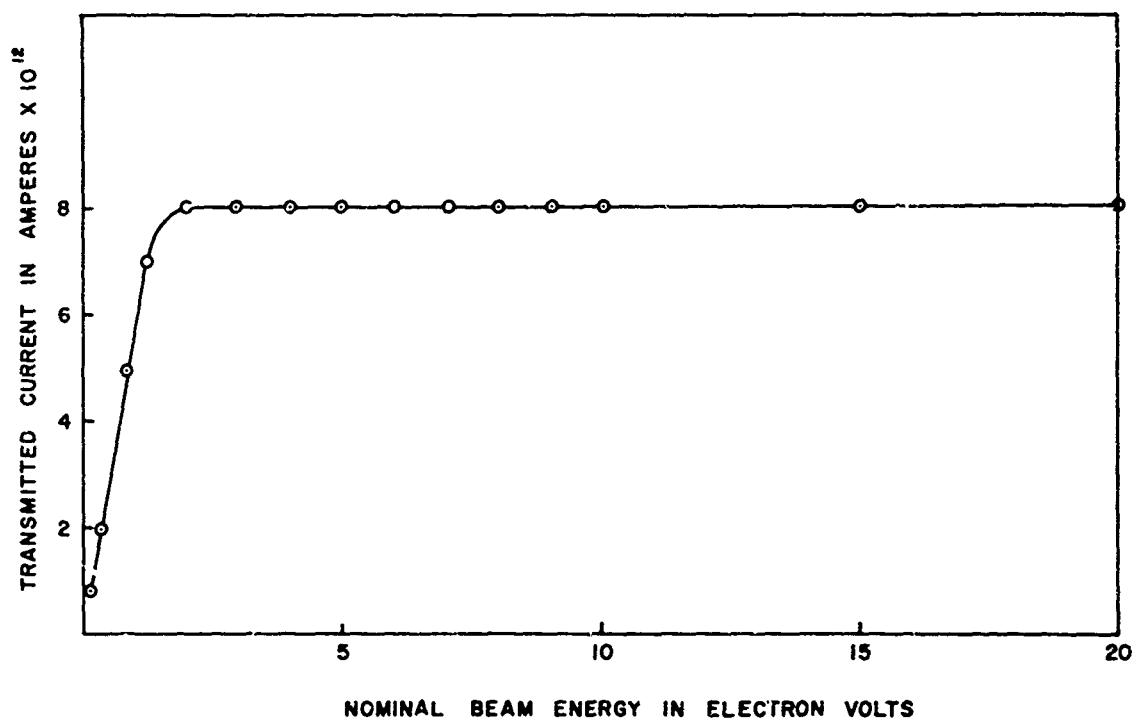


Fig. 4 Transmission Curve of Retarding Lens.

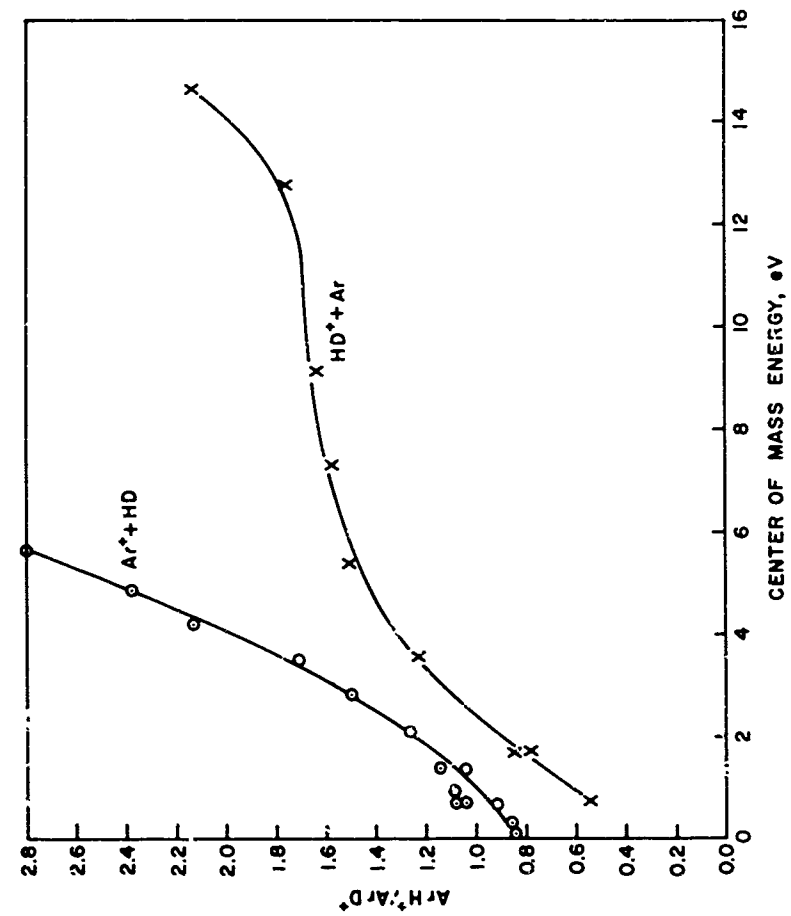


Fig. 5 Isotope effect in ion molecule reactions in the HD-argon system as a function of kinetic energy in the center of mass.

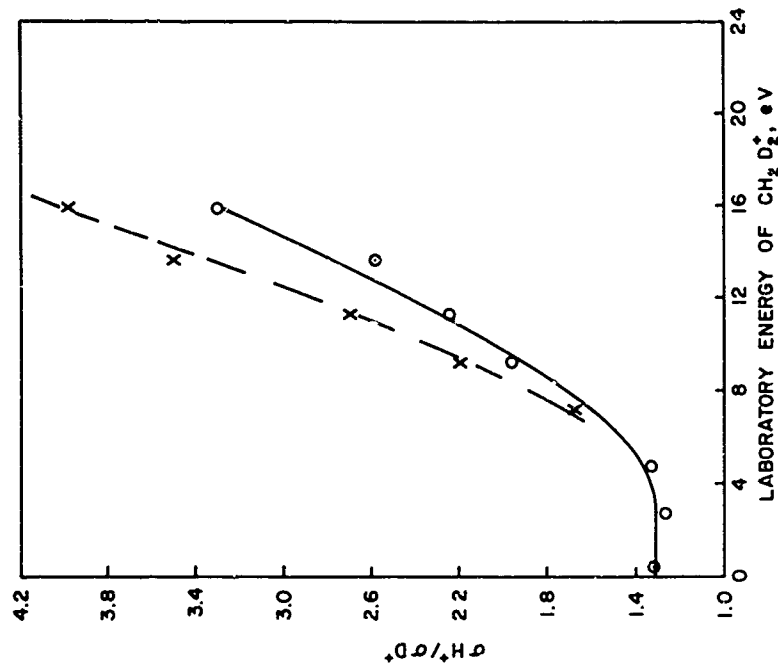


Fig. 6 Isotope effect in proton vs. deuteron transfer reaction as a function of kinetic energy.

A NEW TECHNIQUE WHICH DIRECTLY DETERMINES MOLECULAR-
VIBRATIONAL TRANSITION PROBABILITIES (U)

By

A. T. Stair, Jr. and M. H. Bruce

Air Force Cambridge Research Laboratories
Office of Aerospace Research
L. G. Hanscom Field, Mass.

Mr. Stair's photograph was not available.

ALVA T. STAIR, Jr., BS, Ph.D

Born 22 November 1930 in Oklahoma City, Oklahoma

Title: Research Physicist, Radiation Effects Branch, Optical Physics Laboratory, Air Force Cambridge Research Laboratories.

Education:

Dr. Stair attended the University of Oklahoma; in 1952 he received his B.S. in mathematics and in 1956 his Ph. D. in physics.

Previous Experience:

Dr. Stair served 18 months in the Air Force and in 1958 he joined the Air Force Cambridge Research Center as a civilian scientist. He designed and developed spectroscopic instrumentation for studying nuclear detonations and specialized in the interpretation of thermal radiation phenomena, particularly in the infrared spectral region. In 1961 he started a basic laboratory program on non-equilibrium radiative mechanisms. He has authored or co-authored more than 20 papers. One of his classified papers demonstrated a present day nuclear tactic wherein Russia has a serious advantage. He is a member of the Defense Atomic Support Agency's Thermal Panel and participates in the Bi-Partite meeting on nuclear weapons.

Current Work:

Dr. Stair is pursuing basic studies of inelastic collision processes producing infrared radiation. This includes neutral molecular beam techniques and energy exchange processes. Part of his interest is in the study of energy partition resulting from gas kinetic reactions. In this area he has developed advanced techniques for infrared chemiluminescence studies such as the use of Fourier Spectroscopy. These mechanisms are particularly important for studies of energy transfer for high temperature gases such as in re-entry physics and high altitude nuclear detonations and for studies of the upper atmosphere.

Professional Societies and Honors:

Optical Society of America, American Institute of Physics, RESA, Phi Beta Kappa.



Marshall H. Bruce

MARSHALL H. BRUCE

Born 31 December 1935 in Vermont.

Title: Research Physicist, Radiation Effects Branch, Optical Physics Laboratory, AFCRL.

Education: Mr. Bruce attended Clark University in 1957, received his BA in Physics, and has done Graduate work at UCLA.

Previous Experience:

Mr. Bruce joined AFCRL in 1958. From 1958-1963, his work was entirely centered about magneto-hydro dynamics where he developed a quiescent cesium plasma and studied the propagation, attenuation and excitation of Alfvén waves. The results of this laboratory study were used in formulating a theory of MHD existence in the earth's atmosphere.

Current Work:

Mr. Bruce has been working on the theoretical description of vibration-rotation bands of molecules such as CO, NO, and OH which play important roles in atmospheric energy balance processes. He recently co-authored an important classified paper interpreting the infrared spectra of a high altitude nuclear detonation in which the late time temperatures and electron densities were determined. The current paper is the result of a need to provide an independent technique for determining the radiant energy transfer and gas kinetic temperatures from infrared spectra.

ABSTRACT

A technique is developed for empirically obtaining the vibrational matrix elements of simple molecules. The approach is to obtain the infrared spectra of molecules excited to high vibrational states by either chemiluminescence (for example, $\text{H} + \text{O}_3 \rightarrow \text{OH}^\ddagger + \text{O}_2$) or vibrational luminescence (i. e. $\text{N}_2^\ddagger + \text{CO} \rightarrow \text{CO}_{hv}^\ddagger + \text{N}_2^\ddagger$). The gas kinetic conditions are controlled to produce a Boltzmann distribution of vibrational states with high temperatures, for example, $T_V = 5000^\circ \text{K}$ but with rotational temperatures of about 400°K . The spectrum of a sequence ($\Delta v = 1$ for the fundamental, 2 for the first overtone, etc.) are shown to be describable as a series of overlapping bands displaced by $2 \cdot \Delta v \cdot \omega_e \cdot x_e$ in some cases. The magnitude of each band is proportional to the vibrational transition probability and the population in the upper state or the Boltzmann factor, $N(v', T_V)$. Rotational and vibrational temperatures are determined and the magnitude of each band gives directly the transition probability. Vibrational matrix elements of the $\Delta v = 2$ sequence of CO are determined from low resolution spectra by successively subtracting the contribution of each band. Transitions up to 17-15 are observed. The transition probabilities are found to be much larger than previously predicted with the old approach using integrated absorption measurements.

I. INTRODUCTION

The intensities of the vibration-rotation bands of simple molecules are of fundamental importance for solving some of the most pressing problems in modern technology. Knowledge of vibrational transition probabilities is necessary, for example, in calculations of radiant-energy transfer, measurements of the temperature of hot gases, and in knowing the distribution of the radiating or absorbing molecules among their vibrational levels. These problems are basic to scientific areas ranging through missile technology, nuclear explosions, atmospheric physics, and molecular lasers. Extensive studies in recent years, both theoretical and experimental, have greatly increased our knowledge in this area; however, the near impossibility of making sufficiently accurate quantum mechanical calculations and the experimental difficulties of observing molecules in highly excited states are well known.

The present paper will demonstrate a new technique for obtaining the vibrational matrix elements (proportional to the transition probabilities) directly from experimental data. This represents a true breakthrough in this area and has come about by the recent developments of laboratory techniques for producing a steady state source of vibrationally hot ($1,000^\circ \text{ K} \leq T_{\text{vib}} \leq 10,000^\circ \text{ K}$) but rotationally and translationally cold (c. a. 400° K) molecules. These unusual gas kinetic conditions can be created by the release of some of the chemical energy of a reaction into internal excitation of the products which then radiate. This infrared chemiluminescent phenomena was first demonstrated with the $\text{H} + \text{O}_3 \rightarrow \text{OH}^* + \text{O}_2$ reaction by McKinley, Garvin, and Boudart² and in the $\text{H} + \text{Cl}_2 \rightarrow \text{HCl}^* + \text{H}$ reaction by Cashion and Polanyi³. Another mechanism is through the transfer of vibrational energy stored, for example, in the non-radiating specie N_2 with near-resonant molecules which can radiate, such as CO , CCl_2 and N_2O . This efficient energy transfer process, now known as infrared vibrational luminescence, was first demonstrated by Legay and Legay-Sommaire⁴ with the $\text{N}_2^* - \text{CO}$ system.

The disequilibrium between the vibrational temperature and the other degrees of freedom (which will be shown to be a valuable circumstance) is the result of the difference in efficiency of the various relaxation processes. Rotational-translational relaxation is very fast whereas the exchange of vibrational energy with rotational and kinetic modes is quite slow.

The intensity of an emission line of wavenumber ν_{nm} corresponding to the transition from a state n to a state m is given by⁵

$$I_{em}^{nm} = N_n hc \nu_{nm} A_{nm}^{nm}. \quad (1)$$

N_n is the number of molecules in the initial state n and A_{nm}^{nm} is the Einstein transition probability for emission which for dipole radiation is

$$A_{nm}^{nm} = \frac{64\pi^4 \nu_{nm}^3}{3c} \left| R_{nm}^{nm} \right|^2. \quad (2)$$

R_{nm}^{nm} is the matrix element of the dipole moment for the transition $n \rightarrow m$

$$R_{nm}^{nm} = \int \psi_n^* M \psi_m d\tau \quad (3)$$

where M is the dipole moment of the system and ψ_n and ψ_m are the eigenfunctions in the upper and lower state respectively. Thus, one can write for emission

$$I_{em}^{nm} \sim N_n \nu_{nm}^4 \left| R_{nm}^{nm} \right|^2. \quad (4)$$

Absorption is complicated by the effects of natural line widths but for thin absorbing layers one can write, similarly,

$$I_{abs}^{nm} \sim N_m \nu_{nm} \left| R_{nm}^{nm} \right|^2. \quad (5)$$

Thus, the primary problem can be seen to be the evaluation of equation (3). For vibration-rotation transitions of a diatomic molecule in the ground electronic state equation (3) becomes

$$R_{v'',j''}^{v',j'} = \int_0^\infty \psi_{v',j'}(r) M(r) \psi_{v'',j''}(r) dr \quad (6)$$

where v' and v'' are the vibrational quantum numbers of the upper and lower state respectively, j' and j'' are the rotational quantum numbers*, r is the internuclear distance, $M(r)$ is the electric dipole moment function, and the ψ 's are solutions of the radial Schrodinger equation. $R_{v'',j''}^{v',j'}$ is the vibration-rotation matrix element to be determined. This integral is evaluated by a two-fold process: first, one typically calculates Morse or perturbed harmonic oscillator wave functions and second, one expands M as a power series about the equilibrium internuclear distance, r_e , and attempts to experimentally determine the coefficients:

$$M(r) = \sum_n M_n (r-r_e)^n \quad (7)$$

where M_0 is the permanent electric moment.

More recently the use of computers has permitted the numerical solution of the radial Schrodinger equation for better wave functions^{6,7}; however, the solutions are still strongly dependent upon the accuracy of the potential function used. The most restrictive aspect of the problem, perhaps, has been the determination of $M(r)$. First, the Taylor expansion of equation (7) will give an adequate description only in the immediate neighborhood of the equilibrium distance. Second, the only method of obtaining the expansion coefficients M_1 , M_2 , etc. has been to measure the integrated intensity α_n of the n^{th} harmonic band or sequence^{8,9,10} ($n = \Delta v$, $n = 1$ for the fundamental, $n = 2$ for the first overtone, etc.), where

$$\alpha_n = \sum_{v=0}^{\infty} \alpha_v^{v+n} \sim \left| R_v^{v+n} \right|^2 \quad (8)$$

and α_v^{v+n} is the integrated intensity of the v^{th} vibrational band. Since even the most recent work using shock tube techniques¹¹ have obtained little data higher than the first overtone and since even these measurements determine only the magnitudes and not the algebraic signs of the matrix elements it has not been possible to determine, unambiguously, the expansion coefficients beyond the quadratic term. Furthermore, it has been demonstrated^{12,13} that, in order to obtain matrix elements of reasonable accuracy for the n^{th} band, the dipole moment expansion through $(r-r_e)^n$ must be used. From several theoretical studies^{12,13,14} the

*The authors find the use of single and double primes very bulky and unnecessary but this convention is used to agree with older work.

first approximation to the transition probabilities has been shown to have the simple algebraic form $\frac{(v'' + \Delta v)!}{v''! \Delta v!}$. The actual deviations from this expression are primarily the result of the anharmonic departure from a linear dipole. The various difficulties are clearly pointed out in the recent work of Young and Eachus¹⁵ on the CO molecule. These authors applied the predicted anharmonic vibration-rotation interaction¹⁶ which affects the relative intensities of the rotational lines in a single vibrational band to help choose among four possible theoretical solutions for the CO vibrational matrix elements. These authors made use of some recent data in absorption on the second overtone ($n = 3$)^{17, 18} of CO; however, the problem of analytic continuation of the dipole function to describe its functional form beyond the region experimentally measured ($v' \geq 4$) is still the basic difficulty.

II. NON-EQUILIBRIUM ($T_{\text{Vib}} \neq T_{\text{Rot}}$) INFRARED BAND SHAPES

For simplicity the case for diatomic molecules with CO ($X^2\Sigma^+$) as the example will be developed although the technique has wide applicability. The rotation-vibration spectrum of a molecule making transitions from only one vibrational level v' to level v'' will consist of a series of lines whose relative intensities as a function of J is given essentially by the thermal distribution of the rotational levels:⁵

$$I_{v'}(J') = \frac{(\text{const.})v^4}{Q_R} (J' + J'' + 1) \exp \left[\frac{-B_{v'} J'(J' + 1)hc}{k T_R} \right] . \quad (9)$$

Where Q_R is the rotational partition function, $B_{v'}$ is the rotational constant, and the constant term depends upon the particular vibrational transition probability and total number of molecules in the initial vibrational level. The above expression assumes that the rotational transition probability is the same for all lines of a band.

In practice, this 'true' spectrum is modified by the scanning function of the observing instrument. If one uses a triangular scanning function (typical for spectrometers) with a half width, λ_Q , that is much wider than the line widths then it is possible to predict the band profiles under moderate resolution as follows. Equation (9) for the intensity profile of any single vibrational band becomes

$$I_{v'}(J') = A_{v'}(J') + \sum_{i=1}^P \left\{ A_{v'}(J'+i) \left[1 - \frac{|\lambda(J') - \lambda(J'+i)|}{\lambda_{\alpha}} \right] \right\} \\ + \sum_{i=1}^P \left\{ A_{v'}(J'-i) \left[1 - \frac{|\lambda(J') - \lambda(J'-i)|}{\lambda_{\alpha}} \right] \right\} \quad (10)$$

where

$$A_{v'}(J') = J' \exp \left(- \frac{J'(J'+1)hc B_{v'}}{kT_R} \right) \quad J' = 1, 2, \dots, v' = 0, 1, \dots \\ = -(J'-1) \exp \left(- \frac{J'(J'-1)hc B_{v'}}{kT_R} \right) \quad J' = -1, -2, \dots, v' = 0, 1, \dots \\ = 0. \quad J' = 0, \quad v' = 0, 1, \dots$$

The line positions, as functions of J' and v' , are:

$$\frac{1}{\lambda_{v'}(J')} = \omega_e [2 - (6+4v')x_e] - 2\alpha_e v' + [2B_e - \alpha_e](J'-1) - 2\alpha_e J' + 2\alpha_e (J'-2)v', \quad J' > 0 \\ = \omega_e [2 - (6+4v')x_e] - 2\alpha_e v' + [2B_e - 3\alpha_e]J' + 2\alpha_e J'^2 - 2\alpha_e J'v', \quad J' < 0 \\ + \omega_e [2 - (6+4v')x_e] - 2\alpha_e v' \quad J' = 0 \quad (11)$$

and

$$B_{v'} = B_e - \alpha_e (v' + 1/2). \quad (12)$$

ω_e and x_e are the anharmonic constants of the molecule, for CO:

$\omega_e = 2170.21 \text{ cm}^{-1}$, $x_e = .00612$, $B_e = 1.9313 \text{ cm}^{-1}$ and α_e (correction for the rotational constant) = $.01896 \text{ cm}^{-1}$.

The effect of the width of the scanning function, λ_Q , is demonstrated by Figure 1 which shows an emission spectrum of the first overtone of 'vibrationally hot' carbon monoxide excited by vibrational exchange with nitrogen. The molecular nitrogen excitation was created by a microwave (2450 M Hz) discharge in a steady state flow system. A schematic of the apparatus is shown in Figure 2. The active nitrogen and carbon monoxide were mixed in a one liter sphere at a total pressure of about 300 mTorr.

The emission from a set of molecules making transitions only to the vibrational ground state from $v' = 2$ consists of a single series of lines designated as a "band". As soon as higher vibrational levels are populated new bands appear and are displaced from one another by $(2 \cdot \Delta v \cdot \omega_e \cdot x_e)$ where $\Delta v = 2$ for the first overtone, etc. The total effect is to create overlapping bands, each being proportional to both the transition probability for the vibrational transition and the Boltzmann factor, $N(v, T_V)$, provided, of course, that the vibrational population can be represented by a 'temperature', where

$$N(v, T_V) = \exp \left\{ \left[(x_e - 1) v + x_e v^2 \right] \frac{hc \omega_e}{k T_V} \right\}. \quad (13)$$

The overlapping can be seen in Figure 1 but is more clearly illustrated in Figure 3. The 2-0 band R branch ($\Delta J = +1$) is seen to be only partially overlapped by the 3-1 R branch whereas the 2-0 P branch ($\Delta J = 1$) and 3-1 R branch overlap strongly to produce the observed maxima at 2.36 microns. The relative magnitudes of the band peaks are a direct measurement of vibrational temperature.

It can be shown that the total intensity for the first overtone is given by the following expression:

$$I(\lambda) = \frac{\text{Const}}{\lambda^4} \sum_{v'=2} \left(1 - \exp \left\{ \frac{-hc}{k} \left[\frac{G(v') - G(v'')}{T_V} + \frac{F(J') - F(J'')}{T_R} \right] \right\} \right) \cdot I_{v'}(J') \exp \left\{ \left[(x_e - 1) v' + x_e v'^2 \right] \frac{hc \omega_e}{k T_V} \right\} P(v', \Delta v) \cdot H_{v'}(J') \quad (14)$$

where:

$\frac{P(v', \Delta v)}{\lambda^3}$ = transition probability

$H_{v'}(J')$ = vibration-rotation interaction term^{15, 16}.

$P(v, \Delta v)$ is used for convenient notation to represent the square of the vibrational matrix element. The effects of disequilibrium between the vibrational temperature and rotational temperature are thus conveniently separable as shown in the intensity formula (14). In general, induced emission could change the band shapes under extreme temperature differences but for the conditions to be considered herein its variation with frequency is small and will be neglected.

III. DETERMINATION OF VIBRATIONAL MATRIX ELEMENTS

The fact that the rotational states equilibrate quickly to a Boltzmann distribution in equilibrium with the gas kinetic temperature at low values ranging from 300° K to 500° K is of considerable value in that it greatly reduces the overlap of the various bands. In order to make use of the experimental spectra it is first necessary to determine the proper rotational temperature T_R . For intense sources this is accomplished with high resolution spectra to separate the rotational lines as shown for the CO first overtone in Figure 4. At the rotational temperature depicted here (~ 385° K) there is almost no overlap of the high frequency tail of the 2-0 R branch ($J' \geq 9$). For spectra of lower radiance T_R is obtained at lower resolution by fitting the high frequency tail of the 2-0 R branch to a catalog of band shapes using the measured slit function and equation (10). The overlap at the maximum of the 2-0 R due to the 3-1 R tail was usually less than 2% for the rotational temperatures of these data (if the overlap is greater an iteration procedure is used). The derived temperature may be checked by subtracting the profile of the (2-0) P branch from the total band intensity and checking the resulting shape of the (3-1) R branch (see Figure 3). This has been done and it shows a reliance of about $\pm 15^\circ$ K for T_R .

Once the rotational temperature is established the vibrational bands are successively subtracted and the magnitude of each subtraction then gives the product

$$P(v', \Delta v) \cdot \exp \left\{ \left[(x_e - 1) v' + x_e v'^2 \right] \frac{hc \omega_e}{k T_V} \right\}. \quad (15)$$

Consequently, if one determines a vibrational temperature T_V by assuming a relative value between the first two vibrational transition probabilities the others are determined. The important point is that the matrix elements, $\left| \int \psi_{v'} M \psi_{v''} dr \right|$, are found empirically!

Observation of only the $\Delta v = 2$ sequence (first overtone) does not determine the value of $P(3-1)$ relative to $P(2-0)$; however, this is just the region where the linear dipole and Morse oscillator approximations leading to the expression, $\frac{(v'' + \Delta v)!}{v''! \Delta v!}$, are relatively good, so that the value $P(3-1) \sim 3$ vs $P(2-0)$ normalized to 1 is a good approximation, particularly for CO.

Since the approach, as described, depends on the vibrational states being in a Boltzmann distribution, pairs of data with different vibrational temperatures were used to ratio out the $P(v', \Delta v)$'s and thus Boltzmann distributions were confirmed by a quadratic fit in v . An illustration of data obtained for this purpose are shown in Figure 5. At a constant partial pressure of 300 mTorr of active nitrogen the vibrational temperature of CO was changed by varying the partial pressure of CO. Also, T_V can be controlled by the discharge power or varying the distance from the discharge to the point of mixing.¹⁹

Assuming a value of 2.95 for $P(3, \Delta v = 2)$ a preliminary best fit for the second overtone transition probabilities are shown in Figure 6. A theoretical spectrum with $T_R = 400^\circ \text{K}$ and $T_V = 3000^\circ \text{K}$ is compared with experimental data. These two curves are not normalized as shown; however, the agreement here and at other temperature is fairly good. The trend of doubling successive values is actually found to be a lower limit but is still markedly larger than the simple algebraic expression $\frac{(v'' + \Delta v)!}{v''! \Delta v!}$. For example for the 6-4 transition we find a value of 24 whereas the above approximation yields 15. Comparison of our experimental data with the most recent analytic work on CO¹⁵ is shown in Figure 7. It is apparent that values of the matrix elements obtained by Young and Eachus at higher v 's are too small since the analytic curve falls off too fast and does not exhibit the experimentally observed structure (maxima).

That the large magnitudes of the derived transition probabilities at high v 's is reasonable can be easily ascertained as follows. At a vibrational temperature of 3200°K , for example, the percentage of molecules $(N_v/N_{\text{total}} \times 100)$ in the level $v = 10$ is .0069% versus 9.1% in $v = 2$, a

factor of $N_{10}/N_2 \approx 1/1500$. Yet in Figure 5 for the spectrum at $T_{\text{vib}} = 3200^\circ \text{K}$ the peak at 2.58μ which corresponds primarily to the 10-8 R branch (overlapped most strongly by the 9-7 P branch) has almost half the magnitude of the 2-0 R branch at 2.33μ .

IV. DISCUSSION

The procedure as outlined here is easily applicable, of course, to the fundamental sequence ($\Delta v = 1$) and higher overtones that can be obtained experimentally. Carbon monoxide excited by active nitrogen is a very intense source and Figure 8 shows spectra of the first and second overtones obtained at low resolution ($\lambda_\alpha = 72 \text{ \AA}$) with a vibrational temperature greater than 5000°K . Empirical determination of the vibrational matrix elements for high v 's for $\Delta v = 1, 2$, and 3 will provide an excellent experimental check for the correct eigenfunctions as well as the dipole moment dependence on internuclear distance.

It is feasible to obtain these transition probabilities, perhaps with somewhat higher accuracy, by using much higher resolution to reduce the overlap. The values obtained at low resolution depend strongly on the rotational temperature and accurate knowledge of the rotational band shape. For example, the anharmonic vibration-rotation interaction term which can be important has not yet been carefully determined experimentally for high v and J values. High resolution to obtain the magnitude of the individual contributing rotational lines would overcome this problem. However, the use of low resolution techniques has greater signal/noise which permits one to obtain data over a wider range of conditions and study other molecules where the source radiance may be much lower.

In addition, one seldom has the opportunity to obtain data with high resolution on many phenomena of interest and the understanding of low resolution band profiles permits valuable interpretation. Examples of this are illustrated in Figures 9 and 10, spectra of a high altitude nuclear detonation. These spectra were obtained from a high flying aircraft with interferometer spectrometers.²⁰ NO, CO and NO^+ are easily identified both in the fundamental region of Figure 9 and in the overtone region of Figure 10. These are precisely the species one expects in high temperature air ($T > 2000^\circ \text{K}$) and is the first observation of the infrared spectrum of NO^+ . From knowledge of the integrated intensities one can obtain the relative concentrations of each and if the system were in chemical and kinetic equilibrium, the temperature of the gas can be determined provided the density is known.²¹

If the vibrational matrix elements are accurately known, however, the kinetic state of the gas can be determined directly from the band profile independent of chemical equilibrium, density or even vibrational-rotational equilibrium. It is interesting to note that it is the NO fundamental but the CO first overtone that occur in good atmospheric spectral 'windows' and allow reliable band shape analysis. It is apparent from Figure 10 that CO is in the 3000° K to 5000° K vibrational temperature range.

This direct experimental approach is not necessarily limited to diatomic molecules. For example, CO₂ and N₂O have been observed in vibraluminescence^{22,23} and highly excited vibrational modes are observed whereas the rotational temperature is typically 400° K. This permits the same type of analysis although the question of "temperature" may be a bit more complicated. It is also not necessary to have a Boltzmann distribution of vibrational states to determine the dipole moment expansion coefficients. If one obtains simultaneously the fundamental and overtone spectra the unknown population of the upper state can be ratioed out:

$$I_{nm} \nu_{nm}^4 / I_{nm'} \nu_{nm'}^4 = |R_{nm}|^2 / |R_{nm'}|^2 \quad (16)$$

However, this approach does not give the transition probabilities directly but in some cases can yield the dipole moment functional dependence on internuclear distance.²⁴

The authors would like to acknowledge the aid of John P. Kennealy for both theoretical and experimental assistance and wish to thank Michael L. Forman for his help in programming and compiling the theoretical spectra.

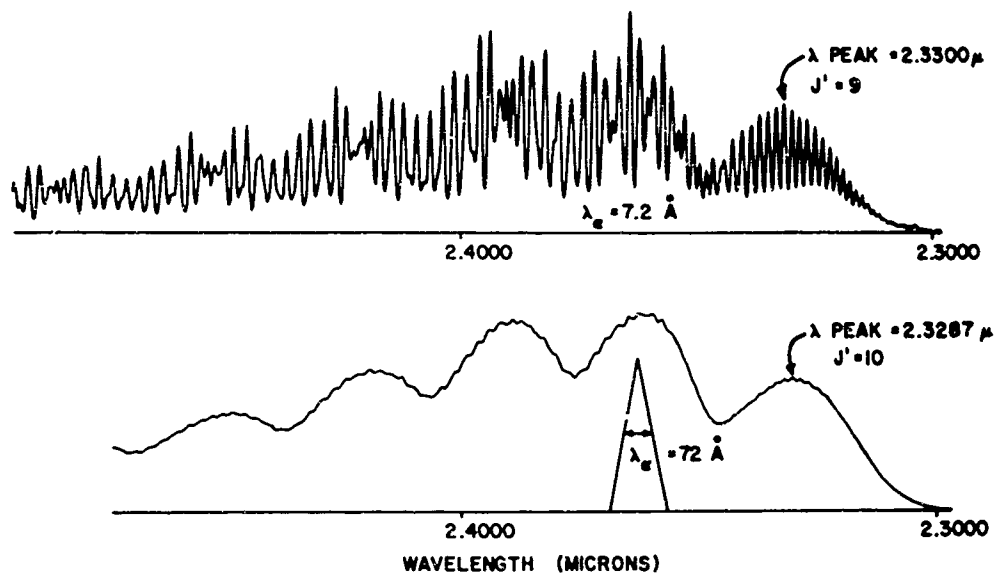


Figure 1: Spectra of the CO first overtone excited by vibrational exchange with N_2 . The effect on the band shape of two different slit widths is demonstrated.

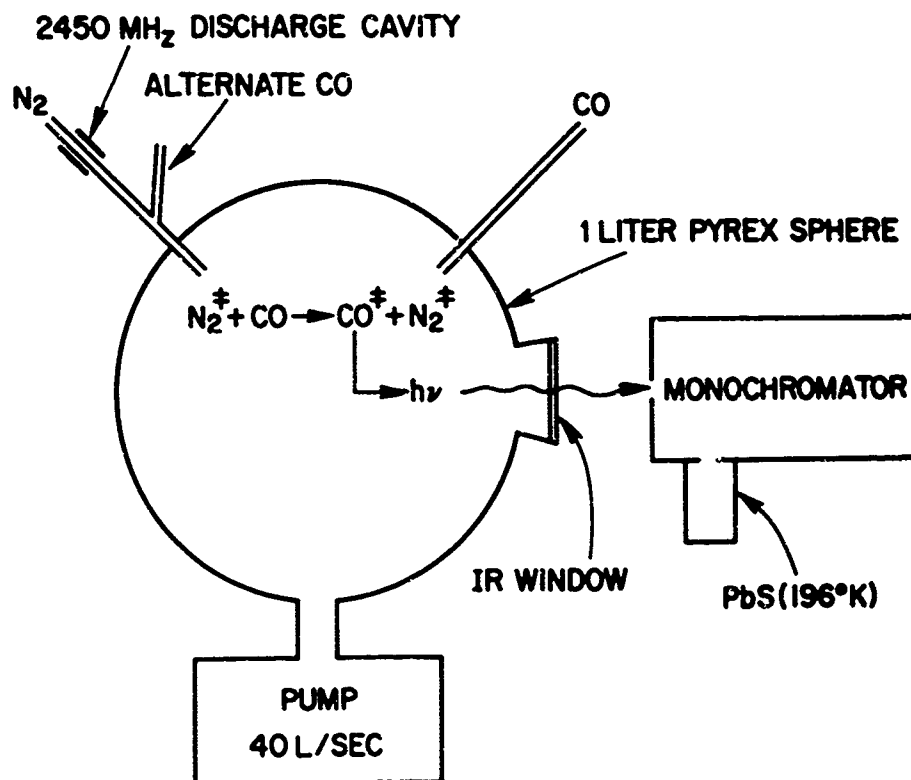


Figure 2: Schematic of the N_2 - CO vibrational system.

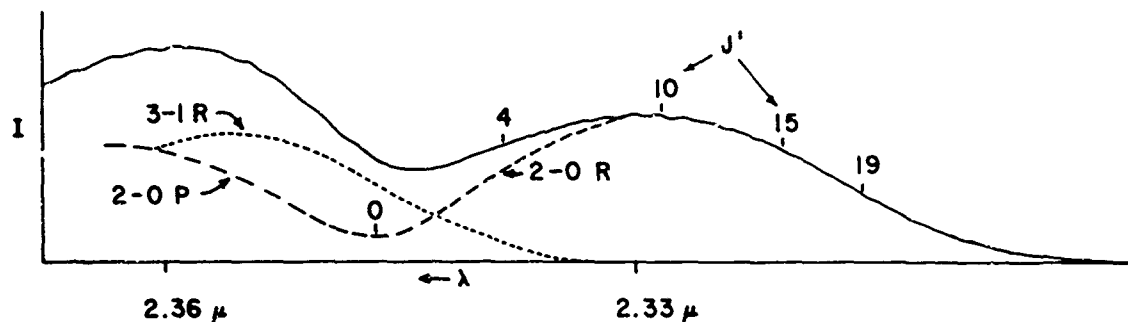


Figure 3: CO first overtone band profiles under low resolution with a rotational temperature of $\sim 385^\circ \text{K}$. The overtone spectrum can be written as

$$I(\lambda) = \frac{(\text{Const.})}{\lambda^4} \sum_{v'=2}^{\infty} I_{v'}(T_R, J') P(v', \Delta v) \exp \left\{ -\frac{[(x_e - 1)v' + x_e v'^2] h c \omega_e}{k T_V} \right\}$$

where $I_{v'}(T_R, J')$ is the profile of the v' -th band at a rotational temperature of T_R and $P(v', \Delta v)/\lambda^3$ is the transition probability and T_V is the vibrational temperature.

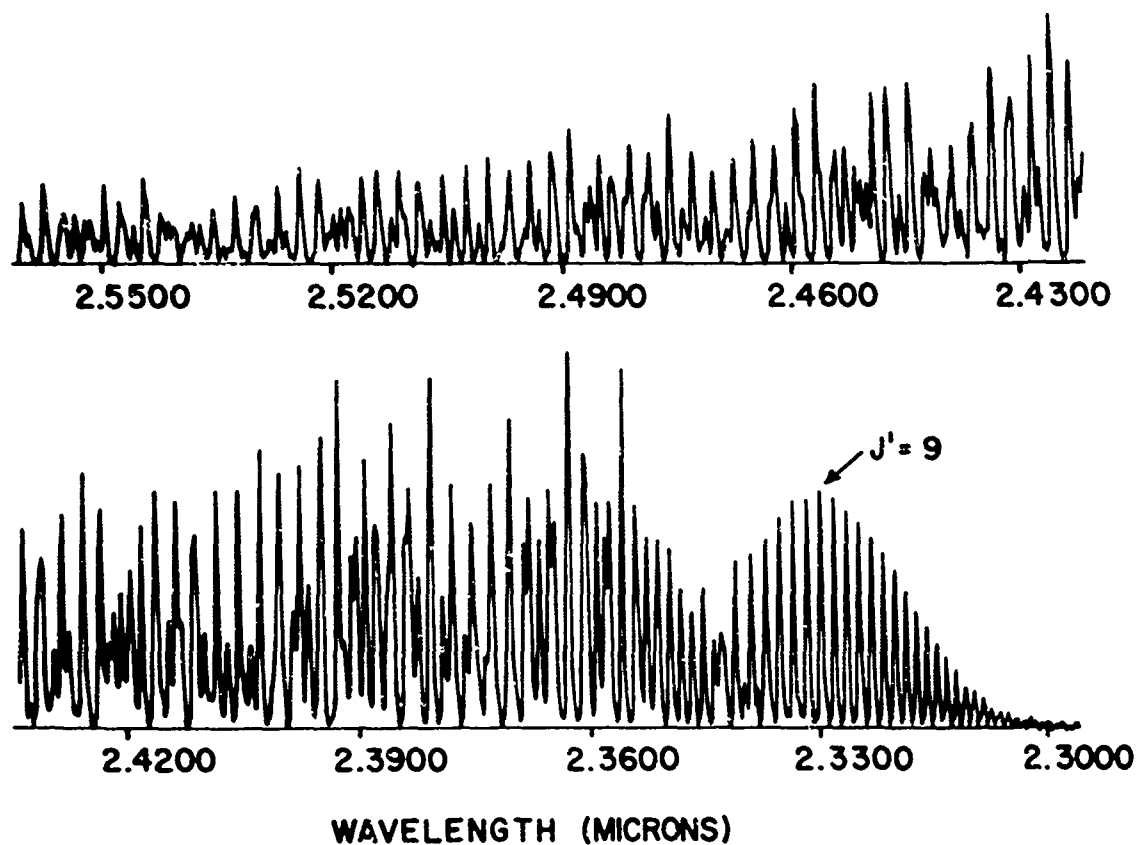


Figure 4: High resolution spectrum of the CO first overtone which shows the lack of overlap for $J' \geq 9$ of the 2-0 R branch. T_R is easily obtainable.

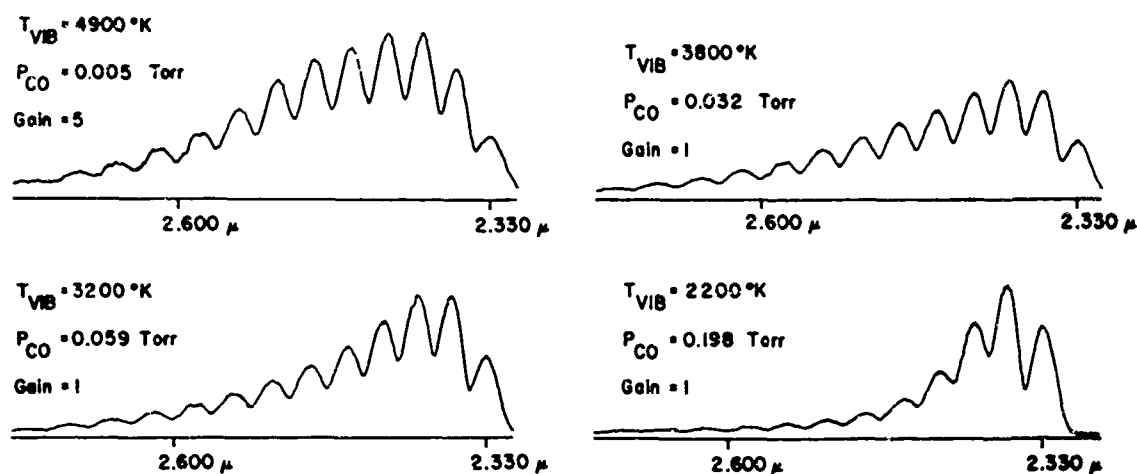


Figure 5: Spectra of the CO first overtone with various vibrational temperatures, obtained by varying the partial pressure of CO in active nitrogen.

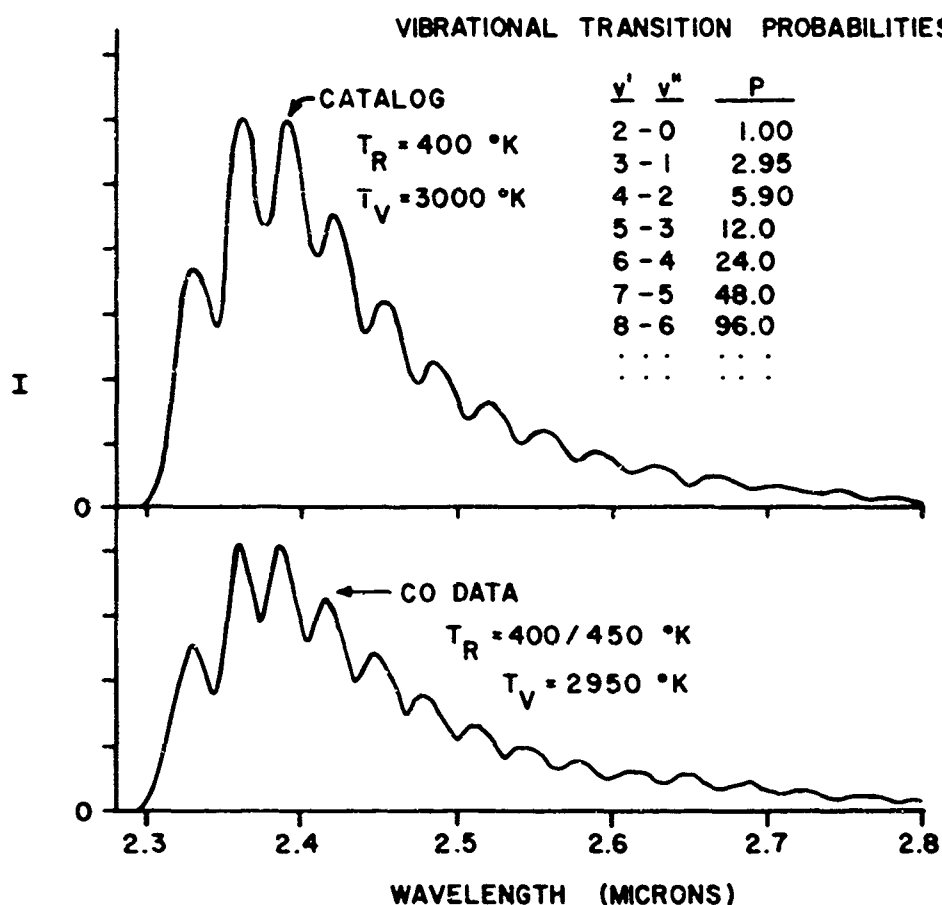


Figure 6: Comparison of a theoretical spectrum (upper curve) with experimental data. The P's are actually the square of the vibrational matrix elements. The curves are not normalized.

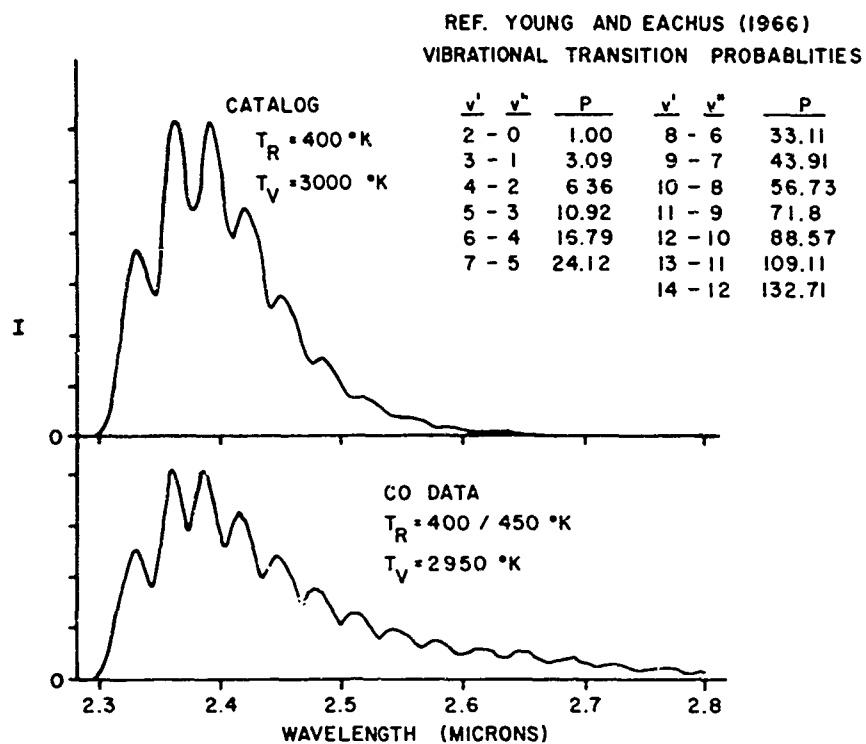


Figure 7: Comparison of the analytically predicted spectrum of Young and Eachus¹⁵ (upper curve) with experimental data.

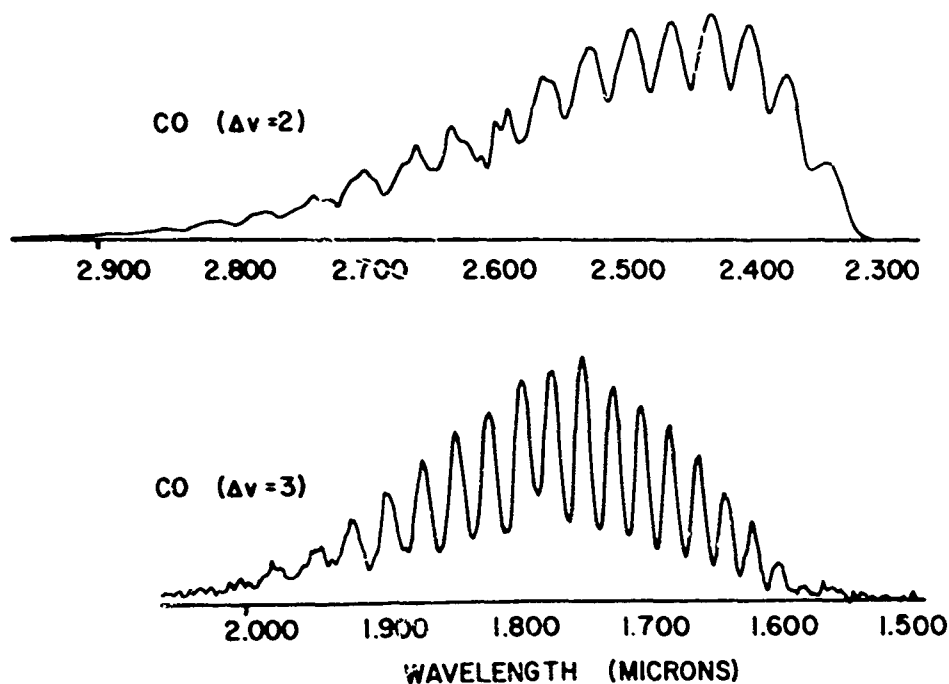


Figure 8: Spectra of the first and second overtone of CO excited by N_2 - CO vibrational luminescence. The poor appearance of the $\Delta v = 2$ sequence at 2.6μ and higher wavelengths is caused by H_2O and CO_2 absorption in the spectrometer.

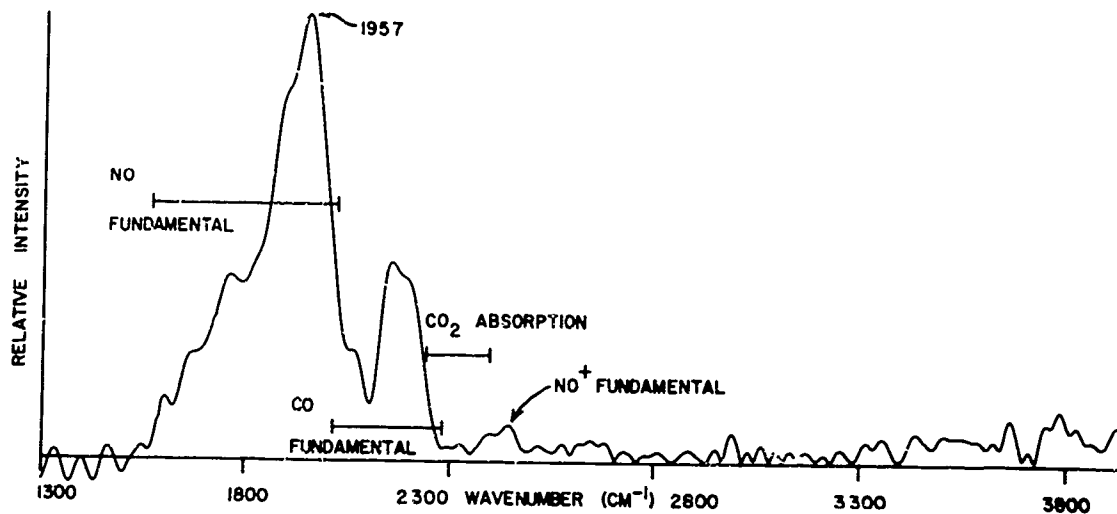


Figure 9: Emission spectrum of a high altitude nuclear detonation obtained by an interferometer spectrometer showing the fundamental bands of NO, CO and NO⁺.

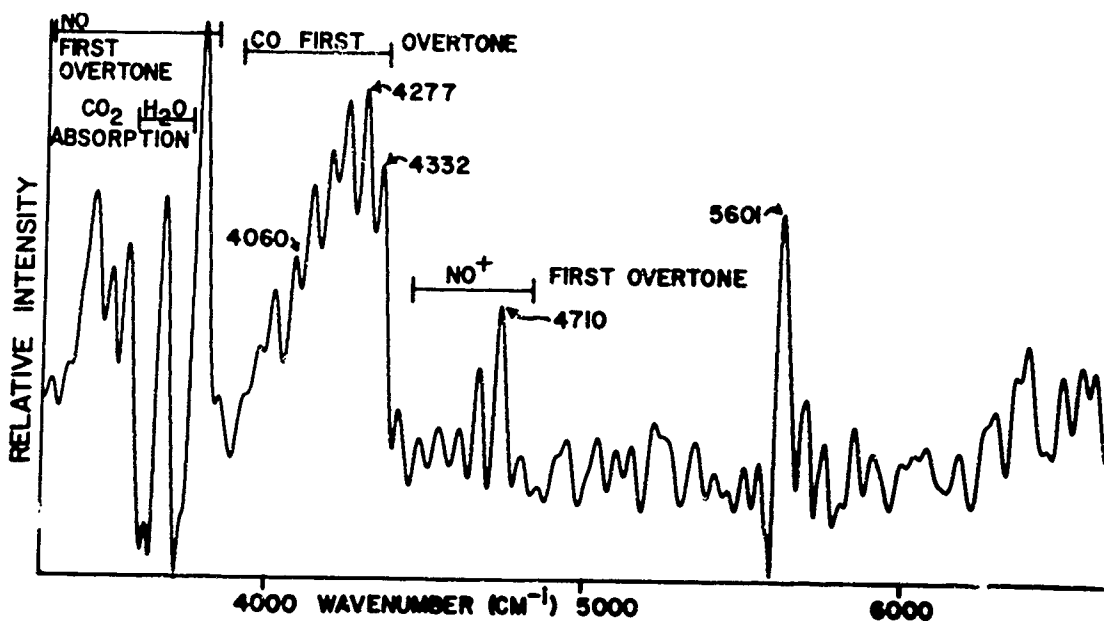


Figure 10: Emission spectrum of a high altitude nuclear detonation showing the first overtones of NO, CO and NO⁺. It is obvious from the profile of the CO spectrum that the gas is in the 3000 to 5000° K temperature range.

REFERENCES

1. S.S. Penner, "Quantitative Molecular Spectroscopy and Gas Emissivities", Addison-Wesley Publishing Company, Inc., Reading, Mass. (1959).
2. J.D. McKinley, D. Garvin, and M. J. Boudart, J. Chem. Phys. 23, 784 (1955).
3. J.K. Cashion and J. C. Polanyi, J. Chem. Phys. 29, 455 (1958).
4. F. Legay and N. Legay-Sommaire, C. R. Acad. Sci. 257, 2644 (1963).
5. G. Herzberg, "Spectra of Diatomic Molecules", D. Van Nostrand Company, Inc., Princeton, N. J. (1950).
6. J. W. Cooley, Math. of Computation, 15, 363 (1961).
7. R. N. Zari and J. K. Cashion, University of California Lawrence Radiation Laboratory Report UCRL-10881 (July 1963).
8. B. L. Crawford, Jr. and H. L. Dinsmore, J. Chem. Phys. 18, 983 (1950).
9. E. B. Wilson, Jr. and A. J. Wells, Jr., J. Chem. Phys. 14, 578 (1946).
10. S.S. Penner and D. Weber, J. Chem. Phys. 19, 807 (1951).
11. J. C. Breeze and C. C. Ferriso, J. Chem. Phys. 43, 3253 (1965).
12. J. L. Dunham, Phys. Rev. 35, 1347 (1930).
13. R. C. Herman and K. E. Shuler, J. Chem. Phys. 22, 481 (1954).
14. H. S. Heaps and G. Herzberg, Z. Physik 133, 48 (1952).
15. L. A. Young and W. J. Eachus, AVCO Everett Research Report No. 239, Everett, Mass. (Jan. 1966) - to be published in J. Chem. Phys.
16. R. C. Herman and R. F. Wallis, J. Chem. Phys. 23, 637 (1955).
17. E. K. Plyler, W. S. Benedict and S. Silverman, J. Chem. Phys. 20, 175 (1952).

- 7
18. B. Schurin and R. Ellis, J. Chem. Phys. to be published (1966).
 19. J. P. Kennealy, A. T. Stair, Jr. and M. H. Bruce, Paper presented at the Sixteenth Annual Meeting of the French Physical Chemistry Society (June 1966), to be published in Fr. J. de Chemie Physique (1966).
 20. A. T. Stair, Jr., J. P. Cahill, and M. H. Bruce, paper presented at the Fall 1965 meeting of the Infrared Information Symposium (IRIS); to be published in the Proceedings (1966).
 21. J. Hilsenrath and M. Klein, "Tables of Thermodynamic Properties of Air in Chemical Equilibrium Including Second Virial Corrections from 1500° K to 15,000° K", Arnold Engineering Development Center, Tenn. AEDC-TR-65-58 (1965).
 22. F. Legay and P. Barchewitz, Comptes Rendus, 256, 5305 (1963).
 23. F. Legay, Le Journal de Physique, 25, 999 (1964).
 24. A. F. Ferguson and D. Parkinson, Planet. Space Sci. 11, 149 (1963).

(U) EXPERIMENTAL & THEORETICAL f -VALUES FOR
 λ 3076 Zn I, λ 3261 Cd I AND λ 2537 Hg I

by

T.M. Bieniewski, T.K. Krueger and S.J. Czyzak

General Physics Laboratory of
Aerospace Research Laboratories
Wright-Patterson Air Force Base, Ohio



T. M. Bieniewski

BIOGRAPHY

Dr Thomas M. Bieniewski

Dr Thomas M. Bieniewski, research physicist in the General Physics Research Laboratory, Aerospace Research Laboratories, began his employment in November 1962.

Dr Bieniewski was born in Posen, Poland. He came to the United States in October 1939. After graduating from De LaSalle High School, Detroit, Michigan, he attended the University of Detroit. He received his B.S. Degree in math from the University of Detroit in 1958. He attended the California Institute of Technology and received his M.S. degree in Physics, June 1960. He completed his graduate school requirements at the California Institute of Technology immediately prior to his employment at ARL. He obtained his Ph.D. degree in Physics in 1965.

Since his arrival at ARL, Dr Bieniewski has been conducting research in atomic spectroscopy to measure atomic transition probabilities. He is presently engaged in building a high dispersion vacuum spectrograph to support his work.

Dr Bieniewski is married to the former Karen Hook who, prior to their marriage, had been employed in the Fluid Dynamics Facilities Research Laboratory, Aerospace Research Laboratories, Wright-Patterson Air Force Base, Ohio.



T. K. Krueger

BIOGRAPHY

MR. THOMAS K. KRUEGER

Mr. Thomas K. Krueger, research physicist in the General Physics Research Laboratory, Aerospace Research Laboratories, became associated with ARL in March, 1955. He has been with the Air Force in military and civilian capacities since September, 1953.

Mr. Krueger was born in La Crosse, Wisconsin. After graduating from high school, he attended the College of St. Thomas in St Paul on a four-year scholarship and received a B.S. degree in physics and a commission as a second lieutenant in the AF reserve in June, 1953. He was called to active duty by the AF in September, 1953, and assigned to AFIT, where he received his M.S. in Nuclear Engineering.

After completing the course at AFIT in March, 1955, Mr. Krueger was assigned to ARL where he worked with the 2-MeV Van de Graaff accelerator group. He designed radiation shielding around the accelerator target for easy access to the target, while maintaining personnel safety. He also helped develop a scintillation detection system that would record gamma rays with a high degree of resolution.

In 1956, he became one of the monitors of the contracts for the design of the shielding around the reactors to be used for propulsion in the nuclear powered aircraft. At the same time, he performed a series of classified calculations relating to the optimization of the reactor shields and the resultant radiation in the crew compartment.

Following this he began a program for calculating the neutron scattering cross-sections of various elements of possible use in the shielding of reactors, since many of these cross-sections could not be measured. The technique involved fitting the cross-sections where measurements could be made to a particular model, and then interpolating the model to energy regions where measurements could not be made. This same model was used in a series of investigations to explain the behavior of the neutron strength function, a quantity related to the cross-section, as a function of the mass of the scattering nucleus. In 1958, he was released from active duty by the USAF and remained with ARL in civilian status.

In 1961, he started working in his current area of research: investigation of the theoretical transition probabilities and collision cross-sections due to electron excitation for allowed and forbidden lines of atoms and ions with astrophysical interest. The results of these investigations are to be used to determine the abundances of elements in stars and nebulae, and to determine the electron density and temperature in these objects.



S. J. Czyzak

BIOGRAPHY

DR. STANLEY J. CZYZAK

Dr. Stanley J. Czyzak, Director of the General Physics Research Laboratory, Aerospace Research Laboratories, began his civilian employment at ARL in September, 1961. His combined military and civilian Air Force career has been continuous since September, 1941.

Dr. Czyzak graduated from West High School, Cleveland, Ohio, in 1932; then attended Fenn College, Cleveland, Ohio, where he attained a B.S. Degree in Chemical Engineering, 1935, and a B.S. Degree in Civil Engineering, 1936. During the years 1936 - 1939, he did part-time graduate work at John Carroll University, Cleveland, and attained a M.S. Degree in Chemistry in 1939. He also worked as a metallurgist and research engineer in industry.

He was awarded a Stephen H. Wilder Research Fellowship, 1946-48. He graduated from the University of Cincinnati with a D.Sc. in Physics and Mathematics in 1948. He then worked as a nuclear research physicist at Argonne National Laboratory, 1948-1949, and research physicist, Battelle Memorial Institute, July 1949-Aug 1950.

In September, 1950, Dr. Czyzak joined the staff at the University of Detroit, Michigan, as Assistant Professor of Physics. Recalled to active duty during the Korean War as a Lt Colonel, Dr. Czyzak was assigned as Chief of the Modern Physics Section, Aeronautical Research Laboratory, WPAFB, Ohio. He directed and carried out research in nuclear and solid state physics. A successful area of research accomplished during this period was the growing of Cadmium Sulfide and Zinc Sulfide crystals, which were used in the development of the solar battery. He also started the nuclear research program on the study of nuclear structure. He returned to the University of Detroit in 1954 as Associate Professor of Physics and Vice-Chairman of the Physics Department. In 1960, he was awarded a National Science Foundation Senior Postdoctoral Faculty Fellowship at the University of Michigan. In September, 1961, he began his present employment at the Aerospace Research Laboratories.

As Director of the General Physics Research Laboratory, Dr. Czyzak is responsible for the administration of the laboratory and the laboratory's research programs in astrophysics, nuclear physics, theoretical physics and optical physics.

In addition to his duties as Director, Dr. Czyzak conducts a research program including calculation of atomic wave functions, transition probabilities and collision crosssections for various atoms and ions of astrophysical interest. In collaboration with Professor L. H. Aller of UCLA, he performs astronomical observations on gaseous nebulae and certain hot stars at Mt. Wilson and Mt. Palomar Observatories. He is currently a Brigadier General in the USAF Reserve.

ABSTRACT

For the three atomic transitions, λ 3076 ZnI, λ 3261 CdI, and λ 2537 HgI, theoretical oscillator strengths were calculated using wave functions obtained by the Hartree-Fock Self-Consistent Field Method (HFSCF) with exchange. The oscillator strengths for the same three transitions were also measured experimentally by the method of total absorption. The importance of configuration interaction in the HFSCF calculated wave functions is inferred from the comparison between the theoretical and the experimental oscillator strengths.

I. Introduction

In the past, spectroscopy has concerned itself primarily with the analysis of atomic spectra and the subsequent assignment of atomic levels, but it is only within the last 10 years that certain parameters important to the analysis of atomic processes have been seriously investigated. This may be partly attributed to the great interest developed in plasmas as well as to the availability of large computers. Certainly these two items have been very instrumental in the resurgence of the experimental and theoretical investigations in atomic physics. This is not to imply that this area of physics was completely dominant until fairly recently, since astrophysicists have always had a strong interest in this area, especially in so far as oscillator strengths or f -values, transition probabilities and collision cross-sections are concerned, because these parameters are of utmost importance in the determination of the abundances of the elements in stars and nebulae as well as the temperatures and densities of free electrons. However, since the interest was confined mostly to astrophysicists, the effort was small, but significant research was carried out by several of them as for example Aller, Baker, Condon, Garstang, Menzel, Osterbrock, Pasternack, Seaton, and Shortley. Important contributions were made by them during the period of the 30's, 40's and early 50's. In experimental spectroscopy the effort was equally limited and the investigations were carried out by Fillipov, King, Kuhn, Messenger, Stockbarger, Soleillet, and Webb. From the late 50's to the present time the interest in atomic spectroscopy has risen sharply in both experimental and theoretical work. In this paper will be presented the results of an experimental and theoretical investigation of three atoms, namely Zn I, Cd I, and Hg I. All three of these involve f -values for transitions from an ns^2 to an $nsnp$ configuration.

II. Apparatus and Experimental Procedures

The oscillator strengths reported here were measured by the method of total absorption in which a metallic sample is sealed in an evacuated cell and then heated to produce a vapor-solid equilibrium. From a measurement of the temperature of the cell, the atomic density can be calculated using vapor pressure data¹ for the element. A continuum of radiation irradiates the cell, and the resulting absorption spectrum is photographed in a high-dispersion spectrograph. Standard techniques of photographic photometry are then employed to reduce the data from the plates to obtain the equivalent widths W_λ .

A convenient expression for the equivalent width W_λ can be obtained by considering the attenuation of the incident intensity I_0 ($\text{ergs cm}^{-2} \text{sec}^{-1}$) (sterad^{-1}) (cm^{-1}) as it passes through the absorbing vapor. Within the absorption line, the transmitted intensity will be I_λ . When expressed in terms of these quantities, the equivalent width W_λ becomes

$$W_{\lambda} = \int_0^{\infty} \frac{I_0 - I_{\lambda}}{I_0} d\lambda \quad (1)$$

From equation (1), the equivalent width is seen to be the area measured under the line contour divided by the continuum intensity near the line. Generally both quantities are readily accessible to measurement.

For a spectral line on the linear or lower Doppler part of the curve of growth, i. e. the relationship between W_{λ} and Nf , the oscillator strength f is related to the equivalent width W_{λ} by the relation²:

$$W_{\lambda} = \sqrt{\pi} \Delta\lambda_D \sum_{n=1}^{\infty} \frac{(-1)^{n-1} C^n}{n! \sqrt{n}} \quad (2)$$

where $\Delta\lambda_D = \frac{\lambda}{c} \sqrt{\frac{2kT}{M}}$ is the Doppler width in wavelength units.

The dimensionless parameter C is defined by the equation:

$$C = \left(\frac{\sqrt{\pi} e^2 \lambda^2}{mc^2 \Delta\lambda_D} \right) Nf\ell \quad (3)$$

where N is the density of atoms contributing to the line, f is the absolute oscillator strength of the transition, and ℓ is the length of the absorbing column of vapor. The quantity in parentheses in the absorption cross section per oscillator, while $Nf\ell$ is the number of equivalent classical oscillators per unit area normal to ℓ . Once W_{λ} and N are known, the oscillator strength f can be conveniently found from equations (2) and (3).

Zn I, Cd I:

In this investigation an absorbing column of cadmium or zinc vapor was obtained by inserting the metallic sample into a 2.5 cm diameter quartz cell with plane parallel windows approximately 4 cm apart. After being fused to an all-glass vacuum system, the cell was evacuated and at the same time baked in an electric oven to release adsorbed gases from the cell walls. Pressures obtained by this technique were of the order of 10^{-8} mm of Hg (as read by an ionization gauge). After evacuation, the cell was fused shut and then inserted into a muffle furnace to vaporize the metallic charge.

The core of the furnace consisted of two concentric alumina muffles wound with either nickel or molybdenum wire. The inner muffle was wound along its entire length and provided the main portion of the heat required to vaporize the metallic sample. On the other hand, the outer muffle was only wound one-third of the way from each end. By heating both ends of the outer muffle, the temperature gradient inside the inner muffle could be kept uniform over a distance 6.25 cm about the center. This arrangement also permitted regulating the temperature gradient at the center of the furnace independently of the current heating the inner muffle. Before an experiment, the absorption cell was inserted into the center of the furnace, inside the inner muffle. Two alumina disks with 1.6 cm diameter apertures were placed on either side of the cell, and two more such disks were used to cap the ends of the inner heating muffle. Fig. 1 shows the arrangement of furnace elements, furnace apertures and absorption cell relative to one another. Also shown in Fig. 1 is a typical arrangement of radiation shields used in the furnaces to prevent excessive heat losses. With the cell in position, the furnace was heated by passing current through the resistance heating wire. Power for the furnaces was taken either directly from a 3 KVA Sola constant voltage transformer or from a temperature regulator backed by a 220 volt Variac. In operation, the furnace could attain steady state temperatures as high as 1350°C with a temperature gradient across the cell of less than 1°C.

Of the measurements taken in this investigation, the temperature measurement was the most critical because of the steep exponential dependence of the vapor pressure of metals on temperature. All temperatures were measured with platinum, platinum + 10% rhodium thermocouples with calibration certified by the National Bureau of Standards or with chromel-alumel thermocouples calibrated against a certified thermocouple. With the certified platinum, platinum + 10% rhodium thermocouples an accuracy of 1°C was attained, while the calibrated chromel-alumel thermocouples gave an accuracy of about 2°C. Altogether three thermocouples were used. One measured the temperature at the center of the cell, and the other two thermocouples measured the temperatures at both ends of the cell. An ice bath provided the 0°C reference junction. The output of the thermocouples was read on a potentiometer capable of resolving 0.1 microvolt. A certified Weston Standard Cell provided the standardizing voltage for the potentiometer.

Fig. 2 gives the essential features of the optical system. All lenses shown are quartz-lithium fluoride achromats. The source of continuous radiation was either a 1.2 KVA high-pressure mercury arc lamp operated directly from a D.C. generator through a ballast resistor or a high-pressure xenon arc lamp. It can be seen from Fig. 2 that the furnace apertures allow only the light passing through the absorption cell to enter the spectrograph. The spectrographs used in these measurements were either a 6.6 meter Rowland mount instrument giving a dispersion of 1.252 Å/mm in the second order or a 2 meter Czerny-Turner mount instrument giving a dispersion of 0.855 Å/mm. In all experiments the band pass admitted into either spectrograph was limited by a suitable array of filters.

All the data for the experiments with cadmium and zinc were photographed on Ilford N. 50 half-tone plates. These plates have very fine grain, but only moderate speed. Typical exposures ranged from 8 seconds to 6 minutes. All the plates were developed in fresh D-19 developer for 4 minutes at 20°C. Standard techniques of photographic photometry were employed to calibrate the plates and reduce the lines to equivalent widths. Any procedure that varied from normal photometric techniques was carefully checked with test plates to insure its accuracy.

Hg I:

Because of the high vapor pressure of mercury at room temperature, a somewhat different experimental procedure was adopted to measure the equivalent width. A stainless steel cell with quartz windows and a long glass cold finger was prepared. After placing a droplet of mercury at the bottom of the cold finger, the cell was evacuated and sealed. The cold finger was then immersed in an ice bath at 0°C while the cell remained at room temperature. In this manner the vapor pressure in the cell was adjusted exactly to the value 1.85×10^{-4} mm Hg. The continuum radiation from an argon arc operating at atmospheric pressure was then passed through the cell to form the absorption signal. After passing through the cell, the radiation was dispersed in a 2 meter Czerny - Turner spectrograph, and the resulting absorption line was scanned with an EMI 9558 QB photomultiplier. The photomultiplier output, after amplification, was then transferred to a recorder, and the recorder tracings were planimeted to find the equivalent width.

III. Theoretical Considerations

In order to calculate the f-values, accurate atomic wave functions are a necessary prerequisite. Atomic wave functions used in present-day calculations are usually obtained by the Hartree-Fock Self Consistent Field Method (HFSCF) with exchange. The methods and procedures for these calculations have been thoroughly described in the literature. For the heavier atoms such as those used in this investigation the method of Froese³ and Mayers & Hirsh⁴ are the best; either of the methods gives good results. In these methods one solves the second order differential equation for the radial wave functions of the electrons under certain boundary conditions. The program for solving the Hartree-Fock equations was written in Fortran II for the IBM 7090 computer and the equation which the program solves is the following:

$$\frac{d^2 P_a}{dr^2} + \left[\frac{2}{r} Y_a(r) - \epsilon_{aa} - \frac{\lambda_a(\lambda_a + 1)}{r^2} \right] P_a(r) = X_a(r)$$

where

$$Y_a(r) = Z - \sum_{\beta} q_{\beta} Y_0(\beta\beta, r) + Y_0(aa, r) + \frac{1}{q_a} \sum_k B_{aak} Y_k(aa, r) + \frac{1}{q_a} \sum_{\substack{\beta \\ k > 0}} C_{\beta ak} Y_k(\beta\beta, r),$$

$$X_a(r) = - \frac{2}{q_a r} \sum_{\substack{\beta \neq a \\ k > 0}} B_{\beta ak} Y_k(\beta a, r) P_{\beta}(r) + \frac{1}{q_a} \sum_{\beta \neq a} \epsilon_{\beta a} P_{\beta}$$

and

$$Y_k(\beta a, r) = r \int_0^{\infty} U_k(rt) P_{\beta}(t) P_a(t) dt$$

with

$$U_k = r^k / t^{k+1} \quad r < t$$

$$= t^k / r^{k+1} \quad t < r$$

The equations are solved subject to the restrictions:

$$\int_0^{\infty} P_a^2(r) dr = 1 \quad \text{and} \quad \int_0^{\infty} P_a(r) P_{\beta}(r) dr = 0 \quad \text{if } \lambda_a = \lambda_{\beta}, a \neq \beta.$$

The aggregate of the two numbers representing the principal quantum number and the orbital angular momentum is denoted by a or β ; ϵ_{aa} = the one electron energy parameter; λ_a = the orbital angular momentum; Z is the atomic number; q_a = number^a of electrons in shell a ; and $\epsilon_{\beta a}$ = the off diagonal energy parameter. The quantities $B_{\beta\beta k}$, $C_{\beta ak}$ and $B_{\beta ak}$ are the coefficients of the Slater integrals in the expression for the energy, E , of the ion or atom, i. e.

$$E = \sum_a q_a I_a + \sum_a \frac{1}{2} q_a (q_a - 1) F_0(a, a) + \sum_{\beta \neq a} q_a q_\beta F_0(\beta, a) - \sum_{a, k} \frac{1}{2} B_{aak} F_k(a, a) - \sum_{\substack{\beta \neq a \\ k > 0}} B_{\beta ak} G_k(\beta, a) - \sum_{\substack{\beta \neq a \\ k > 0}} C_{\beta ak} F_k(\beta, a).$$

The respective wave functions of Zn I, Cd I and Hg I were calculated by the method of Mayers & Hirsh⁴ for the following configuration of electrons outside of the closed shells: 4s², 4s4p; 5s², 5s5p; and 6s², 6s6p. These are the configurations involved in the measured spectra.

With these wave functions the necessary parameter required for the determination of the f-values was calculated, i. e. the dipole length:

$$\sigma^2(nl, n'l') = \frac{1}{4l^2 - 1} \left[\int_0^\infty r P(nl; r) P(n'l', r) dr \right]^2$$

where $l_p = l$ for the above mentioned transitions. The f-values can be obtained from the expression

$$S(\beta J, \beta' J') = \left[\sum_{a a'} (\beta J | a J) \{ S(a J, a' J') \}^{1/2} (a' J' | \beta' J') \right]^2$$

where $S(\beta J, \beta' J')$ is the line strength in the intermediate coupling caused by the spin-orbit (ζ) interaction, $S(a J, a' J')$ is the line strength in LS coupling, and $(\beta J | a J)$ and $(a' J' | \beta' J')$ are the coefficients of the transformation matrix connecting the two coupling schemes. $S(a J, a' J')$ is given by

$$S(a J, a' J') = (+)^2 \zeta(\lambda) \zeta(\mu) J^2$$

where $\zeta(\lambda)$ and $\zeta(\mu)$ are the coefficients involved in the transition and depend on the particular line of the multiplet and particular multiplet of the transition array respectively. The f-value for absorption can be then obtained by employing the following relation

$$f(J, J') = \frac{3.336 \times 10^{-1}}{2J' + 1} \bar{\nu} S(\beta J, \beta' J')$$

where the absorption and emission f-values are related by

$$\bar{\omega}_{J'} f(J, J') = \bar{\omega}_J f(J', J)$$

with the $\bar{\omega}_{J'}$ and $\bar{\omega}_J$ representing the appropriate statistical weights for the levels involved.

The spin-orbit parameter ζ can be calculated from the atomic wave functions, but a somewhat better value for it may be obtained from the observed energy levels. Under the assumption that the spin-orbit interaction is the only one causing the splitting of the energy levels, it can be shown for ns np configurations that

$$\zeta = \frac{2}{3} [{}^3P_2 - {}^3P_0].$$

where 3P_2 and 3P_0 are the respective energy levels involved in the transition.

IV. Results and Discussion

(a) Theoretical

	Zn I	Cd I	Hg I
transition	$4s^2 {}^1S_0 - 4s4p^3 {}^3P_1$	$5s^2 {}^1S_0 - 5s5p^3 {}^3P_1$	$5s^2 {}^1S_0 - 6s6p^3 {}^3P_1$
$\zeta_{\text{obs}} (\text{cm}^{-1})$	386.	1142.	4265.
$\sigma^2 (a_0^2 e^2)$	14.67	3.09	3.24
S(L)	1	1	1
S(M)	6	6	6
$S(J, J') (a_0^2 e^2)$	5.39×10^{-3}	7.11×10^{-2}	8.23×10^{-1}
$\bar{\nu} (\text{ryd})$.296	.279	.359
$f_{\text{theor}}^{\text{abs}}$	5.32×10^{-4}	6.63×10^{-3}	9.86×10^{-2}

(b) Experimental

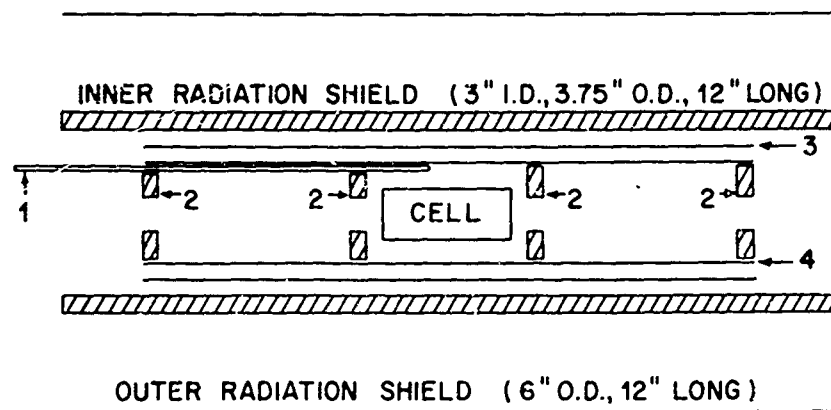
$\lambda (\text{\AA})$	3076.	3261.	2537.
$W_{\lambda} \times 10^{11} (\text{cm})$	7.80	4.24	5.18
$T(^{\circ}\text{K})$	642.5	475.8	273.2
$N(\text{atoms}/\text{cm}^3)$	3.89×10^{14}	7.93×10^{12}	6.53×10^{12}
$l (\text{cm})$	3.66	4.30	0.50
$f_{\text{abs}}^{\text{exp}}$	1.13×10^{-4}	1.94×10^{-3}	3.34×10^{-2}

In order to calculate the experimental f , one must consider the hyperfine structure of the spectral lines. The unresolved line recorded on the photographic plate contains all the components of the hyperfine structure pattern. If the separation between the components is greater than the Doppler width $\Delta\lambda_D$, then the observed equivalent width should be treated as the sum of the equivalent widths of each unresolved hyperfine component. For zinc and cadmium, the intensity distribution of the hyperfine structure components spans a wavelength interval less than one Doppler width. Therefore, the equivalent widths of the zinc and cadmium lines were treated as if there were no hyperfine splitting. (See references 5 & 6) For the mercury line, the hyperfine splitting separates the single line into seven distinct groups of components, each group being separated by a wavelength span greater than one Doppler width. (See reference 6) Therefore, the equivalent width in Table b was divided into seven equivalent widths according to the weight of each group. Each of these equivalent widths was then inserted into equation 3 to get C . Finally all seven values of C obtained in this manner were added together, and the resulting value of C was used in equation 4 to obtain f .

The theoretical calculations do not include configuration interaction. Had configuration interaction been included the theoretical f -values would have been approximately one-third the reported value. This would have agreed reasonably close to the experimental values. This estimate is based on the earlier work of Garstang⁷ and Steele & Treffitz⁸ who employed a semi-empirical method to take into account configuration interaction. However, the methods which they used are not applicable to the configurations reported here. At present theoretical calculations of atomic wave functions for heavy atoms have not as yet been developed to include configuration interaction that involve excited levels of this type, i. e. interactions between $nsnp$ and $nsn'p$ configurations. This problem is being investigated in order to improve the existing method for calculating atomic wave functions.

References

1. Hultgren, R., Orr, R. L., Anderson, P. D., & Kelley, K. K., "Selected Values of Thermodynamic Properties of Metals and Alloys" 1963, John Wiley & Sons, Inc., New York.
2. Unsold, A. "Physik der Sterneatmosphären" 1948, Springer, Berlin.
3. Froese, C. Can. J. of Physics 41, 1895, 1963.
4. Mayers, D. and Hirsh, A. "The Calculation of Atomic Wave Functions by Solution of the Hartree-Fock Equations" 1965 (ARL 65-62 Aerospace Research Laboratories, Wright-Patterson Air Force Base, Ohio).
5. Brix, P. and Steudel, A. Z. Physik, 128, 260 (1950)
6. Landolt-Bornstein, Zahlenwerte und Funktionen 1 No. 5 (1952), Berlin, Springer-Verlag, pp. 1-63.
7. Garstang, R. H. MNRAS 124, 321, 1962.
----- Ann. d'Astrophysique 25, 109, 1962.
8. Steele, R. and Treffitz, E. In Press 1966.



1. THERMOCOUPLE TUBE
2. FURNACE APERTURE
3. OUTER HEATING COIL (2" I.D. 10" LONG)
4. INNER HEATING COIL (1.75" I.D., 10" LONG)

FIGURE 1. SCHEMATIC VIEW OF FURNACE

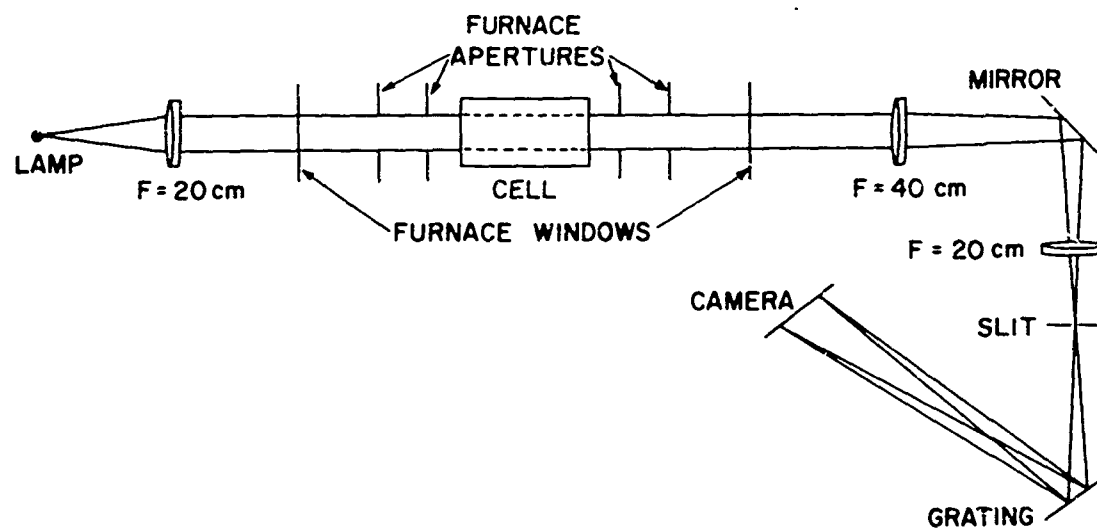


FIGURE 2. THE OPTICAL SYSTEM

STUDIES OF SURFACE LAYER TRANSPORT AND ITS CONTRIBUTIONS
TO THE PROPERTIES OF CERAMIC MATERIALS (U)

by

H. C. Graham, PhD.

and

N. M. Tallan, PhD.

Metallurgy and Ceramics Research Laboratory
Aerospace Research Laboratories
Office of Aerospace Research
Wright-Patterson Air Force Base, Ohio



Henry C. Graham

BIOGRAPHY

DR. HENRY C. GRAHAM

Dr. Henry C. Graham, Research Physicist of the Metallurgy and Ceramics Research Laboratory, Aerospace Research Laboratories, began his employment at ARL in September, 1960.

Dr. Graham attended high school in Mayville, New York, where he graduated Salutatorian. Following graduation he attended the New York State College of Ceramics at Alfred University, Alfred, New York, where he received his B.S. in Ceramic Engineering in 1956 and his M.S. in Ceramic Engineering in 1958. From September 1957 to March 1958, he was on active duty with the U.S. Army stationed at Ft Sill, Okla, and Ft Benning, Ga. During this period, he was trained as a Field Artillery officer with primary emphasis on the small unit commander's role. Dr. Graham remained active in Reserves through 1964 and completed the Associate Officers Field Artillery Course during this time. Upon release from active duty, he joined Pittsburgh Plate Glass Co. in their Basic and Applied Research Laboratory at Harmerville, Pa., where he conducted research on the processes involved in the controlled divitrification (crystallization) of glasses containing a nucleating agent.

Since joining the Air Force, he has been concerned with the defect structure of various metal oxides. Several unique measurement systems were set up which Dr. Graham used to measure various electrical properties of these oxides as a function of temperature, frequency and oxygen partial pressure. While at ARL, he has received his PhD. in Ceramic Engineering at Ohio State University, Columbus, Ohio. His thesis work was concerned with the particle size dependence of the electrical conductivity of sodium chloride and provided several pieces of corroborating data on items in the literature as well as new data which better explained some of the known properties of the material.



Norman M. Tallan

BIORGRAPHY

DR. NORMAN M. TALLAN

Dr. Norman M. Tallan is currently Supervisor of Ceramic Research in the Metallurgy and Ceramics Research Laboratory at the Aerospace Research Laboratories (ARL).

A native of Newark, N.J., Dr. Tallan received his PhD. degree in Ceramics at Alfred University in 1959. He received his M.S. in Ceramic Engineering in 1955 at Ohio State University and his B.S. in Ceramic Technology at Rutgers University in 1954.

Dr. Tallan joined ARL in June, 1959, as a research physicist. He was responsible for the initiation of a research program on the characterization of the point defect structure of non-metallic materials, the role of these defects in charge and mass transport properties, and the nature of the transport mechanisms involved.

In January, 1960, Dr. Tallan was named to his current position. He is responsible for the technical and administrative supervision of the overall in-house research program on ceramic materials and for the sponsored research program of the ceramics group. His research efforts have included thermodynamic studies of the concentrations of point defects and their variations with oxygen partial pressure and temperature in binary and ternary oxides, as well as experimental studies of defect structure dependent properties. Additional studies have included extensive work on dielectric relaxation effects, particularly those arising from dipolar rotations and from interfacial polarization in ionic solids, and studies of phase equilibria and microstructure in the zirconium-oxygen and several related systems.

STUDIES OF SURFACE LAYER TRANSPORT AND ITS CONTRIBUTIONS
TO THE PROPERTIES OF CERAMIC MATERIALS (U)

by

H. C. Graham, PhD.

and

N. M. Tallan, PhD.

ABSTRACT

A study is made of the particle size dependence of the conductivity for the normally slower moving chlorine ion in NaCl. It is shown that the chlorine ion conductivity can become more significant than sodium ion conductivity in ultra-fine grained materials. The enhancement is reciprocally dependent upon grain size indicating that the enhanced chlorine movement is in a subsurface region as proposed previously. The accepted Schottky energy is shown to be high by 0.4 eV, (1.77 instead of 2.12 eV). This difference is the direct result of assuming that the total intrinsic conductivity or diffusivity is sodium ion movement, whereas this study shows that the chlorine ion contributes significantly to this total intrinsic conductivity. The significance of the results is discussed with respect to being able to accurately predict and control essential fabrication processes and application properties of ceramic materials.

TABLE OF CONTENTS

	PAGE
I. Introduction	1
A. General	1
B. Ceramic Materials	1
C. Enhanced Diffusion	4
D. Objectives	8
II. Experimental Procedure	9
III. Experimental Results	20
A. Polycrystalline	20
B. Single Crystal	23
IV. Summary and Conclusions	25
V. References	28

I. INTRODUCTION

A. General

A striking feature of most of the major advances in materials science and technology in this century is that by and large they have come about through the application of phenomenological or mechanistic approaches to the problems at hand. This is characteristically true, for example, in the field of metallurgy. Studies of the mechanisms of diffusion, phase transformations, microstructural changes, and dislocation motion have led to the development of new alloys with vastly superior properties. This is perhaps even more evident in the relatively new field of semiconductor technology. The discovery and early development of the transistor is a classic example of the value of the phenomenological approach. There is no question of the key role played by mechanistic studies of diffusion, charge carrier formation and motion and charge compensation in elemental germanium. In fact, even the most recent advances in solid state device technology have evolved largely through this approach. Diffusion and oxidation studies in these materials have led to diffuse junction and passivation processes.

Unfortunately, the application of the phenomenological approach to the solution of problems in ceramic technology is still in its infancy. This is in large part due to the greater complexity of most phenomena in these materials in which the bonding is generally a mixture of ionic and covalent character and in which at least two, and frequently many more, species of ions are present. It is also due, at least in part, to the difficulty in characterizing these materials, so that meaningful and reproducible measurements of their properties can be made. Consequently a scarcity of basic knowledge about them exists. In a typical metal oxide, for example, one would find a bewildering number of different point defects, each in several possible different charge states, which could control its transport properties, and also great uncertainty about the nature of the transport mechanisms themselves.

B. Ceramic Materials

Yet it is in this realm, the study of the mechanisms by which electrical charges and the ions, or vacancies, themselves move through the crystal lattice, that the mechanistic approach can make truly significant contributions. It has long been recognized, for example, that many of the processes vital to the fabrication of ceramic bodies and many of the most important properties of the resultant ceramic structures are diffusion controlled. Several authors¹ have pointed out that the initial stage of sintering, the process by which the individual grains in a ceramic body become joined together during firing at high temperatures, is very often the result of diffusion. Similarly, it has been shown² that the elimination of porosity during

the later stages of densification and the growth of some grains at the expense of others during the later stages of the firing process are generally diffusion controlled. These processes, which ultimately determine the microstructure of the final ceramic piece, are crucial to its subsequent use, since the strength and mechanical properties of ceramic bodies vary tremendously with variations in microstructure. Similarly, creep of a ceramic body (its steady deformation under load at high temperatures), changes in composition and properties by departure from stoichiometry (in changing atmospheres at high temperatures), and the ability of a ceramic coating to protect a refractory metal from high temperature oxidation are all generally diffusion controlled.

A very significant feature of most diffusion controlled processes in ionic materials is that both positively and negatively charged species, ionic or electronic or some combination of the two, must move cooperatively. Since all of these species generally move at quite different rates, the overall process can only proceed at a rate determined by the slowest species which must move. For example, the initial stage of sintering can be looked upon as the joining together of two grains, initially spherical in shape, by the formation of a neck between them, as shown in Fig. 1(a). Material, in the case of metal oxide both metal ions and oxygen ions, must be transported from the grains to the growing neck. This transport may occur by diffusion through the volume or over the surface of the grains, by evaporation from the grains and condensation in the neck, or by plastic deformation. In the absence of large applied pressures, and in metal oxides where the vapor pressures are usually very low, the transport of material most often occurs by diffusion. Similarly, it has been shown³ that creep in dense ceramic bodies very often occurs by diffusion. When a ceramic body is subjected to a load at very high temperatures, as in Fig. 1(b), it can deform by the diffusion of material from regions of high stress to regions of lower stress.

In principle, therefore, to determine the diffusivity of the slower moving ion one can study the rate of initial neck growth, or alternatively the rate of initial shrinkage of a pressed pellet containing a multitude of grains, or one can study the rate of creep of a ceramic body. Conversely, if the diffusivities of the ions are known beforehand from regular diffusion measurements, one can predict the rate of such diffusion controlled processes from the known diffusivity of the slower moving species. In fact one might even anticipate the possibility of altering the defect structure of the material in order to increase or decrease the diffusivity of the slower moving species and thereby speed up or slow down the rate of any diffusion controlled process of interest. There have indeed been many studies in which excellent agreement has been obtained between diffusivities calculated from sintering or creep data and the diffusivities for the slower moving species measured

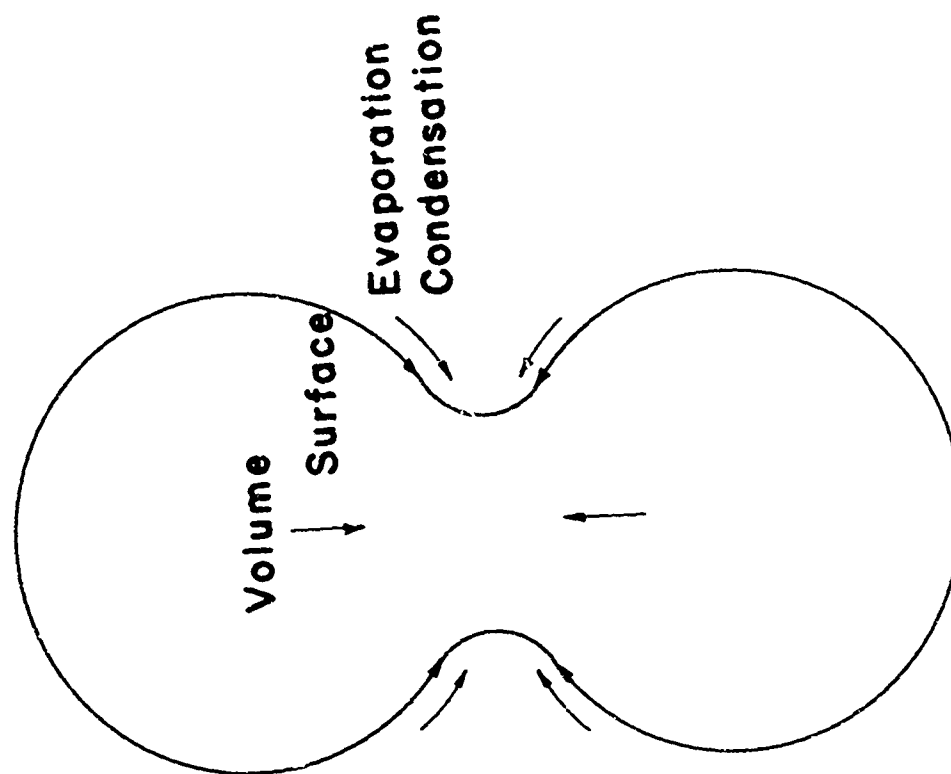


Fig. 1.(a) Necking of Spheres During Initial Sintering

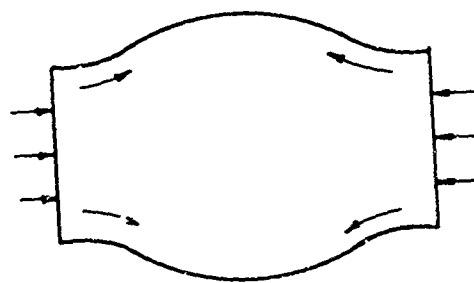


Fig. 1.(b) Diffusion of Material From High Stress to Low Stress Region

directly in diffusion experiments. Unfortunately, in the past several years there have also been reports of experiments in which the diffusivities calculated from sintering or creep data agree better with the diffusivities of the faster than the slower moving species. For example, Fig. 2 and 3, from the work of Palladino and Coble,⁴ show the agreement between diffusion coefficients calculated for creep and sintering in Al_2O_3 to be in very good agreement with directly measured values of the aluminum ion diffusion coefficient, yet direct diffusion measurements have shown the aluminum ion to be far faster moving than the oxygen ion. Such discrepancies in the literature have served to cast doubt upon the otherwise accepted models for these processes, the interpretation of the data, and in some cases even upon the data themselves.

C. Enhanced Diffusion

An apparent clue to the source of these discrepancies was introduced several years ago by Laurent and Bénard⁵. In the course of their diffusion studies on a series of alkali halides, they found that the diffusivity of the normally slower moving anion increased with decreasing particle size. Yet there was no apparent change in activation energy from that found even in the single crystal. The diffusivity of the normally faster moving species, the cation, was not affected at all by decreasing particle size. Their results for NaCl are shown in Fig. 4, as reproduced from their work⁵. It may be noted that if one extrapolated their results for NaCl to particle sizes much smaller than 50μ , the measured chlorine diffusivities might then be even greater than the measured sodium diffusivities. Clearly this reversal of the faster and slower moving species with decreasing particle size might account for the discrepancies noted above if the diffusion and sintering or creep measurements were made on specimens with widely differing particle size. In addition, if particle size does have so radical an effect on the transport properties and diffusion controlled processes in these materials, then an understanding of the mechanism of the enhanced diffusion of the slower moving specie with decreasing particle size is essential to further progress in this area.

Laurent and Bénard found, in autoradiographic studies of their specimens, that the anion movement was concentrated in the grain boundary regions. Real grain boundary diffusion, however, would be expected to require an activation energy considerably different from that required for bulk diffusion in a single crystal. Since they did not observe an activation energy different from that in the single crystal, Laurent and Bénard suggested that the anion movement was occurring in a surface layer surrounding each grain of sufficient thickness that the nature of each anion jump, from site to site in the lattice, is no different from that in the bulk of the inner grain. Therefore the activation energy for anion diffusion in the surface layer and in the bulk crystal would be the same. Yet for some as yet

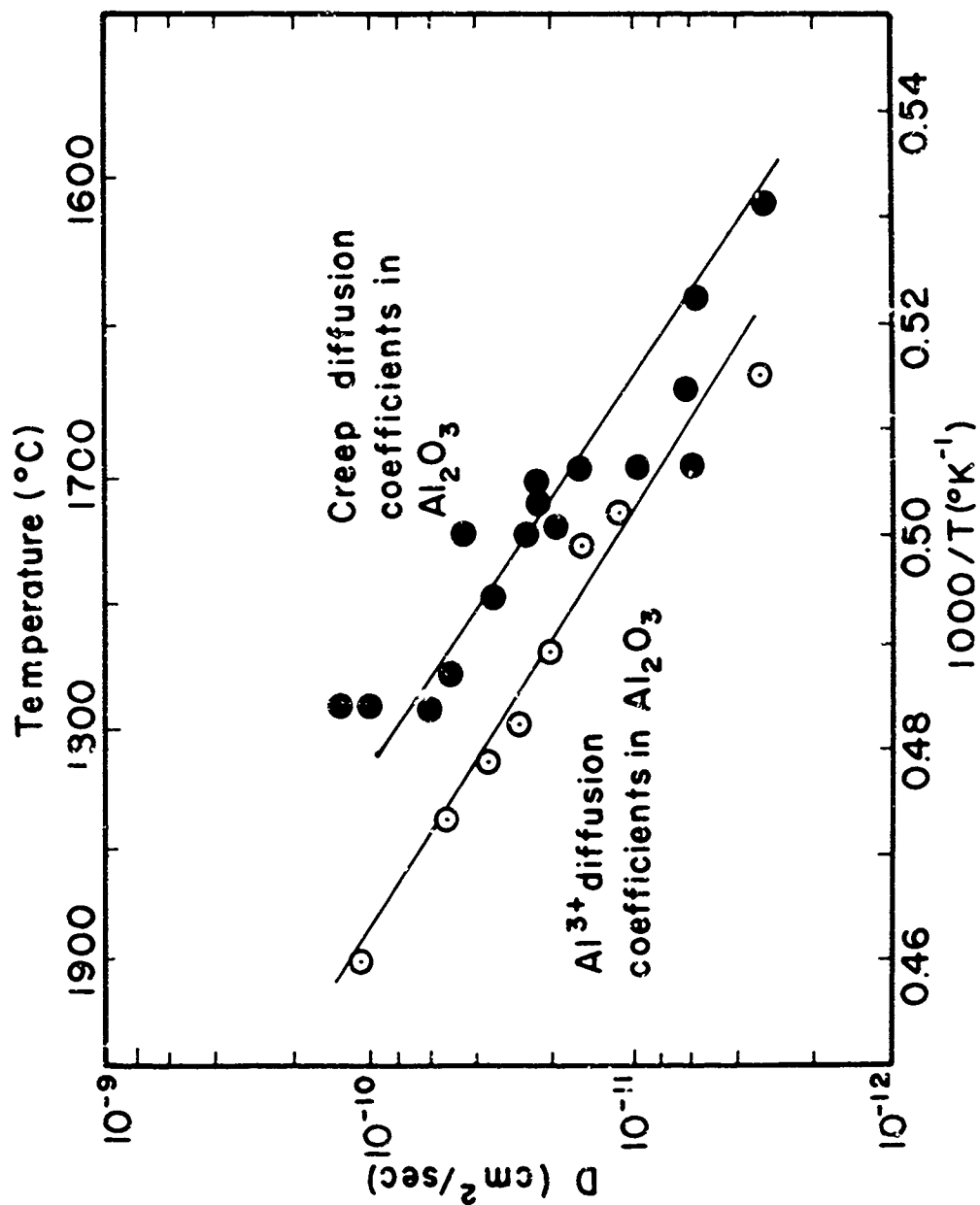


Fig. 2. Comparison of Directly Measured Diffusion Coefficients with Those Calculated from Creep Data on Al_2O_3 (after Paladino and Coble⁴)

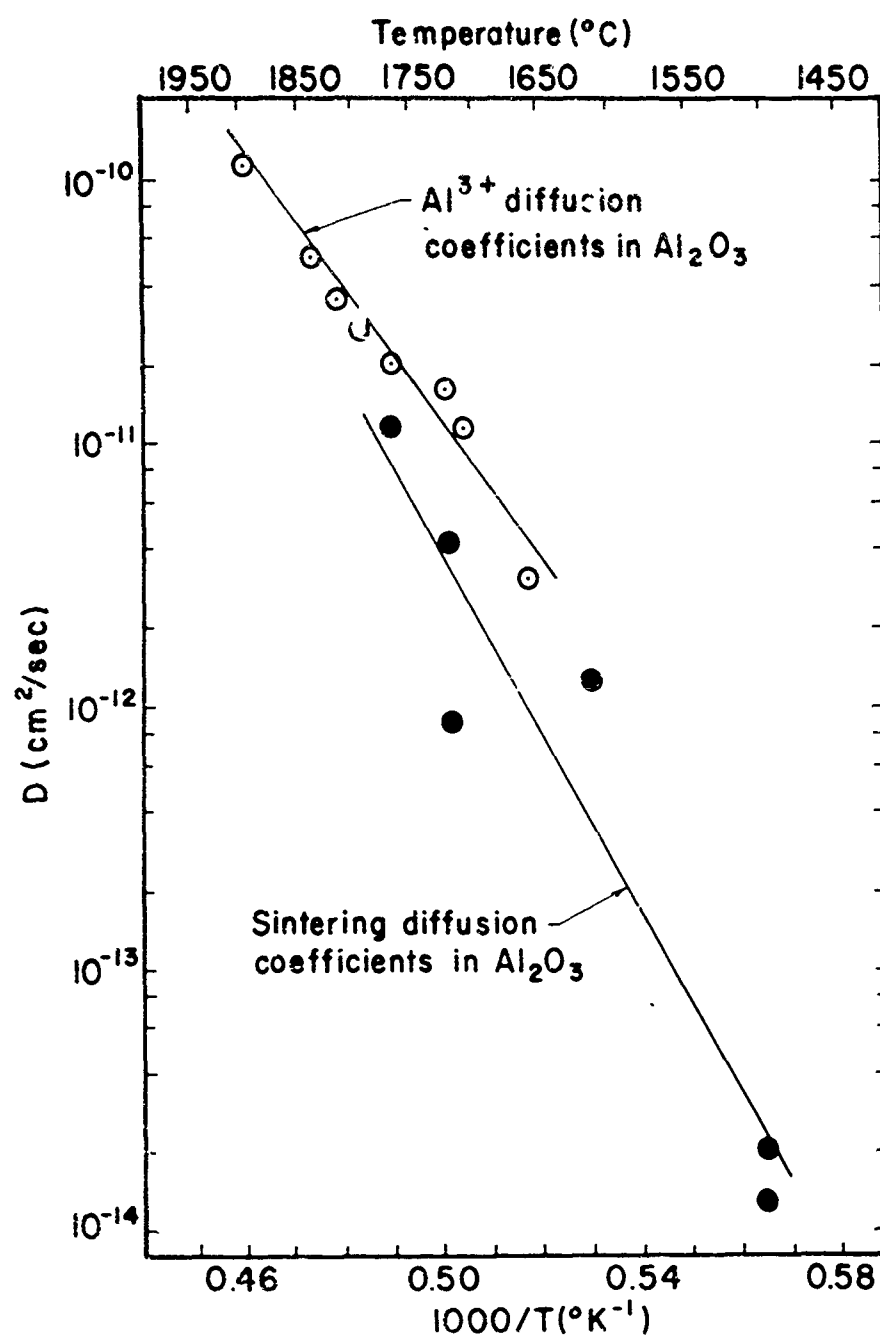


Fig. 3. Comparison of Aluminum Ion Self-Diffusion Coefficients with Diffusion Coefficients Calculated from Peck Growth Sintering Experiments (after Palumbo and Coble⁴)

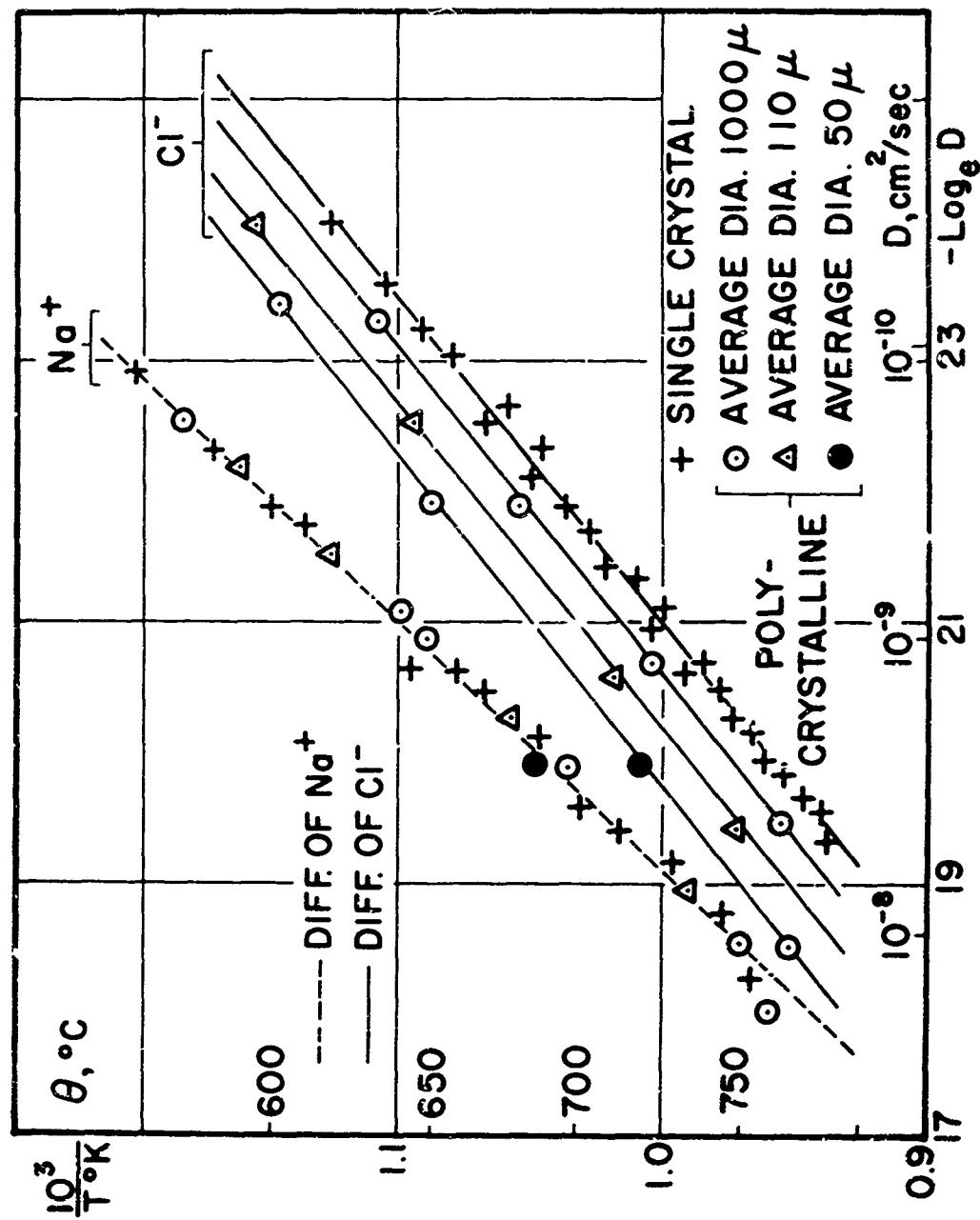


Fig. 4. Diffusivity versus Reciprocal Temperature for Na^+ and Cl^- in NaCl for Several Particle Sizes (after Laurent and Benard⁵)

undetermined reason, the number of anion jumps occurring in the surface layer is greater than the number occurring per unit volume in the interior of the grain or in a single crystal. Since, as shown in Fig. 5, the volume fraction of such surface layer material increases with decreasing particle size if its thickness remains essentially constant, one would expect the enhanced anion diffusivity in the surface layer to make a greater and greater contribution with decreasing particle size. On the basis of this model, with surface layer enhancement of the anion diffusion, one might expect to find cation motion fastest in single crystals or coarse grained materials but anion motion fastest in sufficiently fine grained polycrystalline specimens.

D. Objectives

Unfortunately, extensive diffusion measurements are extremely time consuming and in general it is very difficult to get enough data of sufficient precision to prove conclusively the detailed validity of such a model. In fact, since the appearance of the work of Laurent and Bénard, and despite its great importance and the many references to it in the literature, there has been little or no subsequent diffusion work to substantiate or repudiate it. On the other hand, it was felt that a laboratory well equipped to conduct electrical property studies could obtain the extensive data with the required precision much more readily. Furthermore, one of the materials extensively studied by Laurent and Bénard, NaCl, would lend itself ideally to an electrical conductivity study because it is universally accepted that the conductivity in this material is all ionic and that in single crystals, at least, it is essentially all due to sodium ion motion. Such a study would have the additional significant benefit of a verification of the model proposed by Laurent and Bénard through an independent type of measurement. As a result, an extensive study of the electrical conductivity of NaCl as a function of particle size was undertaken.

II. EXPERIMENTAL PROCEDURES

The basic experimental difficulty in the study of the electrical conductivity of NaCl as a function of particle size was to establish a means of measuring the chlorine contribution to the conductivity and then to follow the change in its contributions with a change in the average particle size. Since, as mentioned previously, the commonly accepted high temperature intrinsic charge transport in NaCl is by the sodium vacancy with no significant contribution from the chlorine ion, it would not be expected that conductivity measurements of single crystal samples would show a chlorine contribution. However, if the movement of the chlorine ion is indeed enhanced in the grain boundary region as proposed by Laurent and Bénard, then as the average particle size of a compact is reduced the contribution of

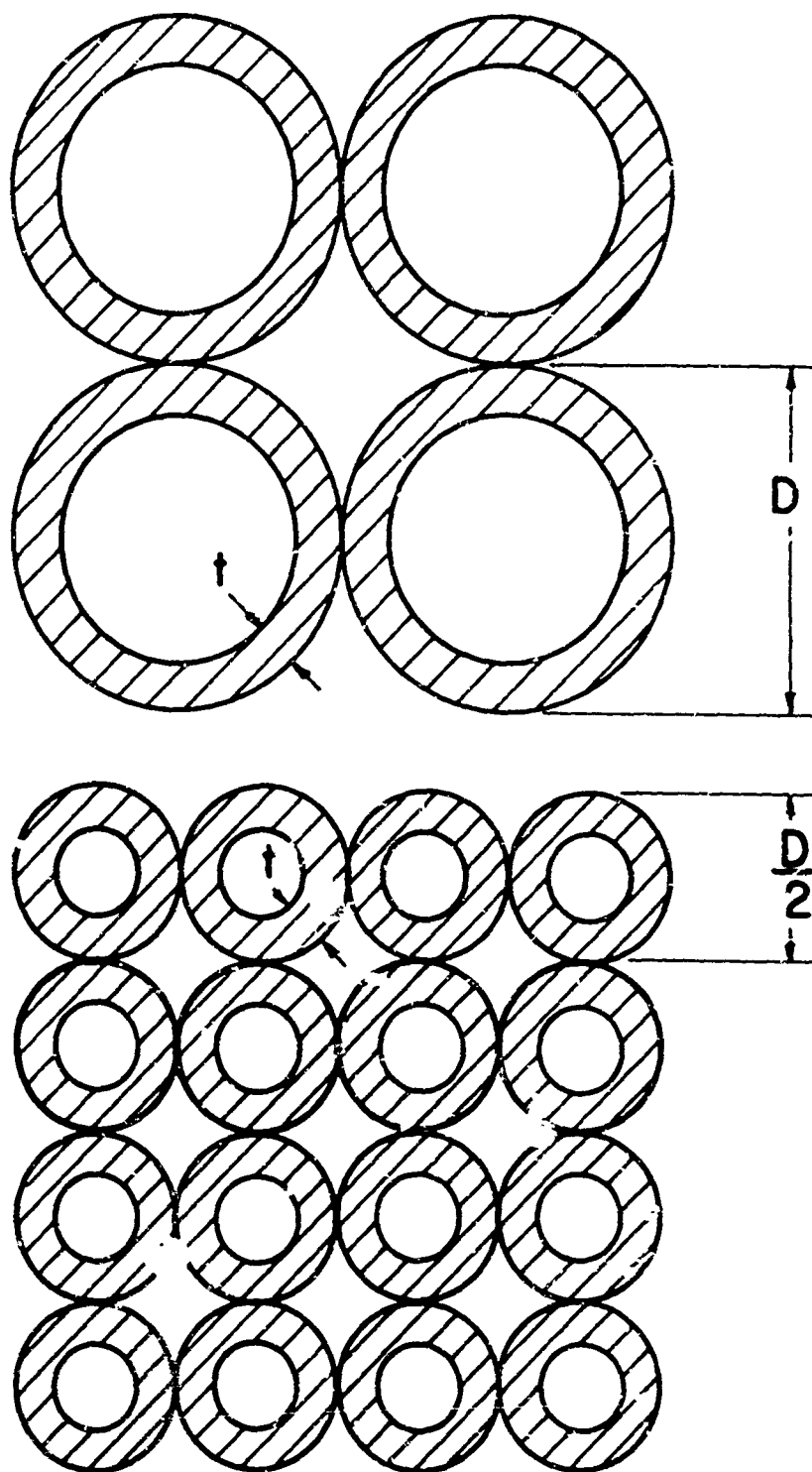


Fig. 5 Volume Fraction of Surface Layer Material versus Particle Size

the chlorine to the total conductivity should increase and be discernable. As also mentioned previously, it would be expected that the magnitude of the chlorine contribution would increase in direct proportion to the decrease in particle size and that the activation energy would remain constant. In addition, there should be little or no change in the magnitude of the sodium vacancy conductivity or in its activation energy.

One might also expect that at small enough particle sizes the enhanced movement of chlorine ions in the grain boundary regions will predominate, and in that case the conduction would no longer increase with further decrease in particle size.

The most promising approach to a measurement of this type, where a separation of two contributions to the total conductivity is required, is a polarization study. In this measurement technique the discriminating character of the metal electrodes, with respect to the type of charge carrier they will pass to the external circuit, is used to separate the contributions of the carriers. It has been known for some time that the transport of one type of charge carrier in a material may be blocked at an electrode while the other carrier or carriers may enter or leave the material freely at the electrodes⁶. This blocking is readily observable as a decrease in the current of the blocked carrier with time and the process is known as polarization.

Figs. 6 and 7 show schematically the circuits used to make polarization measurements at constant voltage and constant current⁷. The sample is represented by a parallel network consisting of resistances R_{NB} and R_B and capacitance C , where NB and B signify nonblocked and blocked respectively. R_B and C in series form an RC circuit whose time constant is determined by the magnitudes of R_B and C . In the sample, R_B would represent the true resistance to movement of the blocked ion, determined by its mobility, while the build up of charge at the electrode, tending to create a back emf, is analogous to the charging of C . Initially the total conductance of the sample is determined by the flow of current through both legs (the quantity through each being determined by the ratio of the resistances R_B and R_{NB}), but under steady state conditions the current flow of the blocked ion ceases since, in the equivalent circuit, the capacitor C is then fully charged. Therefore, the initial conductivity, σ_0 , is the sum of the conductivities of the two carriers and the steady state conductivity, σ_∞ , is the conductivity of the nonblocked carrier.

In the constant voltage mode (Fig. 6) the change in current passing through R_S is measured as a function of time. The diagram of the change in current as a function of time is for a sample which has three conduction mechanisms--two blocked and one non-blocked. The two blocked mechanisms are distinguished from one another by their different time constants. As shown, the first one seen would be a very fast mechanism such as a dipole

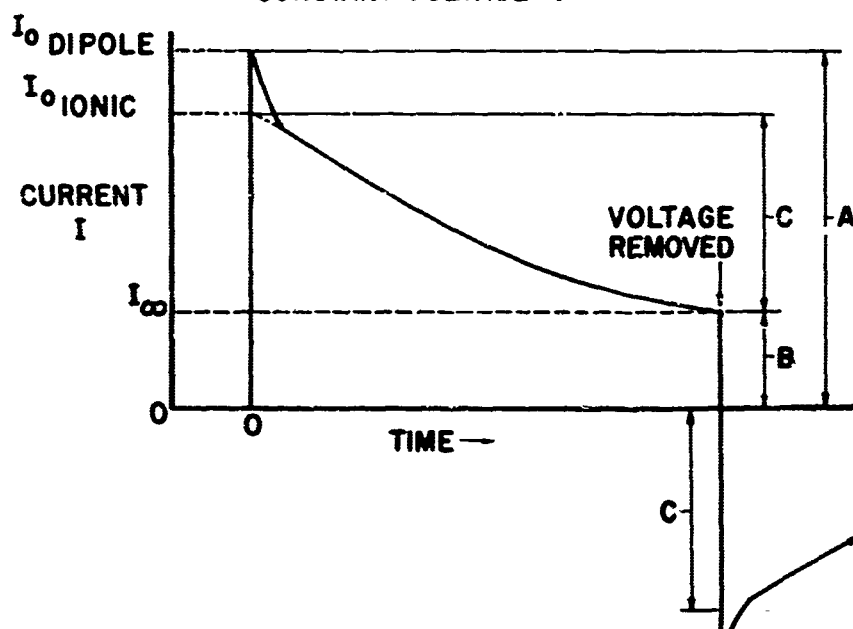
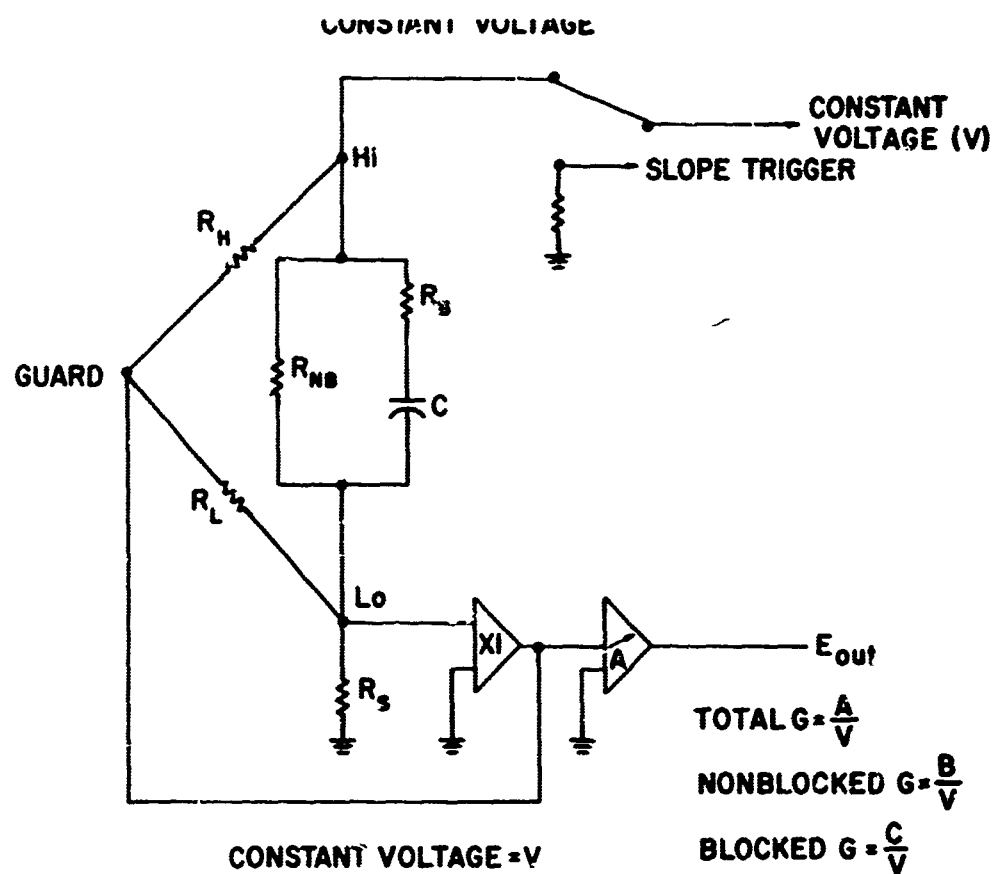


Fig. 6. Schematic of Polarization Circuit-Constant Voltage

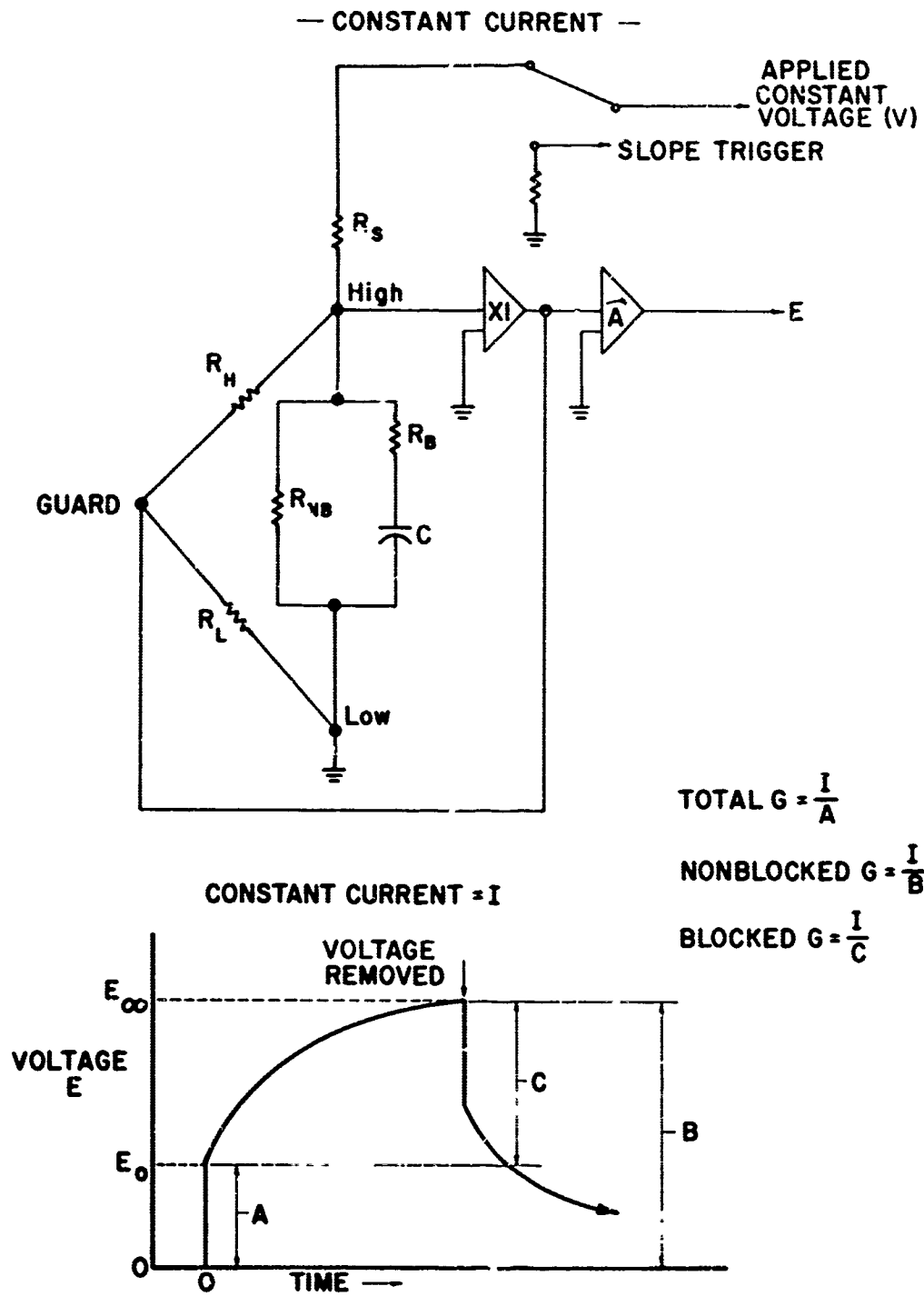


Fig. 7. Schematic of Polarization Circuit-Constant Current

rotation and the entire polarization of the dipole would be completed in a fraction of a second. The second polarization process would have a longer time constant and could be the build-up of charge carriers at an electrode or interface due to the movement of an ion to this blocking interface and not beyond it. The elimination of this particular ionic species from the conduction process with time means a decrease in the current passed through the material and hence a decrease in its conductivity with time. The third conduction mechanism involves the non-blocked charge carrier and leads to the steady state current flow, I_{∞} . In the case of NaCl, the sodium ion is a non-blocked carrier. Therefore, if the chlorine contribution is to be separated the chlorine ion will have to be the blocked carrier.

In the circuit operation the X1 amplifier maintains the low and guard points at the same potential. Since it has a high d. c. impedance (10^{10} ohms), it does not affect the current passing through R_S . Also, since R_L appears as an infinite resistance with the guard and low points at the same potential, the voltage drop measured across R_S will be a function only of the current passed through the sample.

Similar comments can be made for the constant current schematic and voltage vs. time plot shown in Fig. 7. Here, of course, the change in voltage across the sample is measured as a function of time for a constant current. The X1 amplifier maintains the high and the guard points at the same potential to again minimize the effect of surface currents.

The appropriate equations for each method are shown on the graphs and the transference numbers of the two carriers are calculated as follows:

$$t_{NB} = \frac{G_{NB}}{G_{TOTAL}} \quad \text{and} \quad t_B = \frac{G_{TOTAL} - G_{NB}}{G_{TOTAL}}$$

where the G's are conductances which can be converted to conductivities by inclusion of the geometry factor.

As mentioned, the time constant of the polarization process is in general a good indication of the nature of the carrier involved, i. e., a dipole rotation would be complete in a fraction of a second while a build up of ionic carriers at a surface or interface would be expected to take several minutes to several hours depending upon the material and the temperature.

Fig. 8 is a schematic representation of the sample and the circuit diagram of the sample, R_X , in an a. c. transformer bridge. The three-terminal guarding technique is used to eliminate stray impedance paths represented by R_H and R_L in the diagram. As with the polarization equipment, these impedances are eliminated so that the conductance measured is the conductance through the sample between the high and the low electrodes and not a surface conductance.

Fig. 9 shows the sample holder (itself shown in greater detail in Figs. 10 and 11) in place with a high temperature alumina tube separating it from the furnace (Fig. 12).

As indicated, the furnace is operated in a vacuum and the atmosphere in the sample chamber may be varied from 760 Torr to 10^{-5} Torr total pressure using various gas mixtures to control the oxygen partial pressure. The furnace sample holder combination has a temperature capability of 1800°C , since the equipment was designed for use with high temperature ceramic oxides. In the experimental work presented here, the highest temperature was limited to approximately 600°C since at temperatures greater than this vaporization of the sample tended to carry away the electrodes.

The electrodes used were Platinum Bright and they were matured at 500°C for 5 minutes in air after drying at 100°C in air.

The starting material was a very large single crystal. After cleaving several single crystal specimens from it, the remainder was mechanically ground and fractionated by dry sieving. The finest fraction was obtained by air milling a portion of the 75-150 fraction. The resultant fractions are given in Table I with the densities of the pressed samples. The polycrystalline samples were prepared by cold pressing the NaCl powder at 15,000 psi.

Table I

Sample	Measured particle size (μ)	Density	
		gm/cc	% theoretical
1	400 ± 200	2.121	97.9
2	75 - 150	2.117	97.7
3	44 - 74	2.103	97.1
4	Mostly 38	2.096	96.8
5	20 - 30	2.080	96.0
6	2 or less	2.072	95.7
single crystal	-	2.166	100.0

All samples were heated to about 500°C in a vacuum of 10^{-5} Torr when initially placed in the sample holder and prior to making any measurements. This was necessary to eliminate spurious data resulting from the

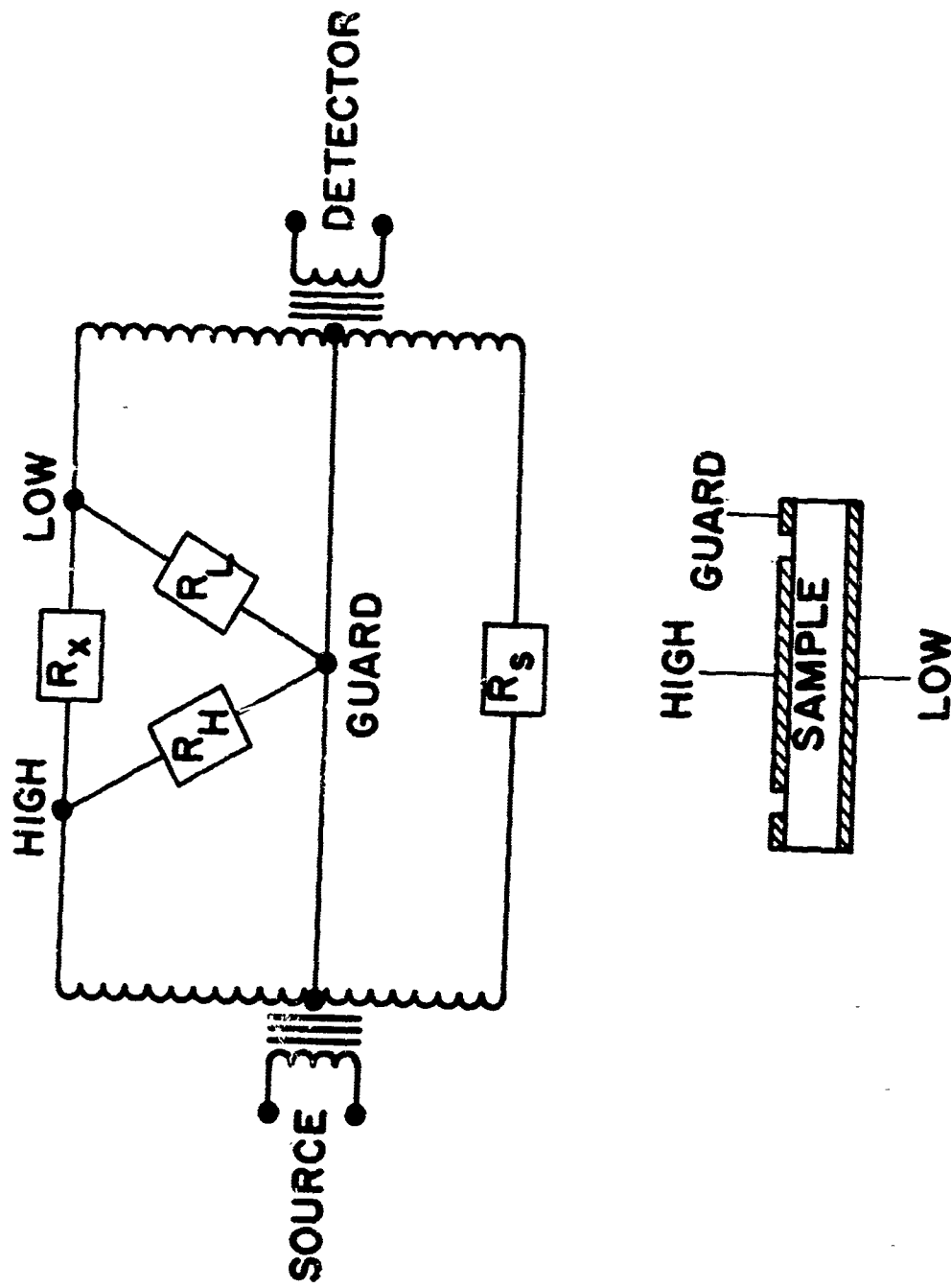


Fig. 8. Schematic of A.C. Circuit

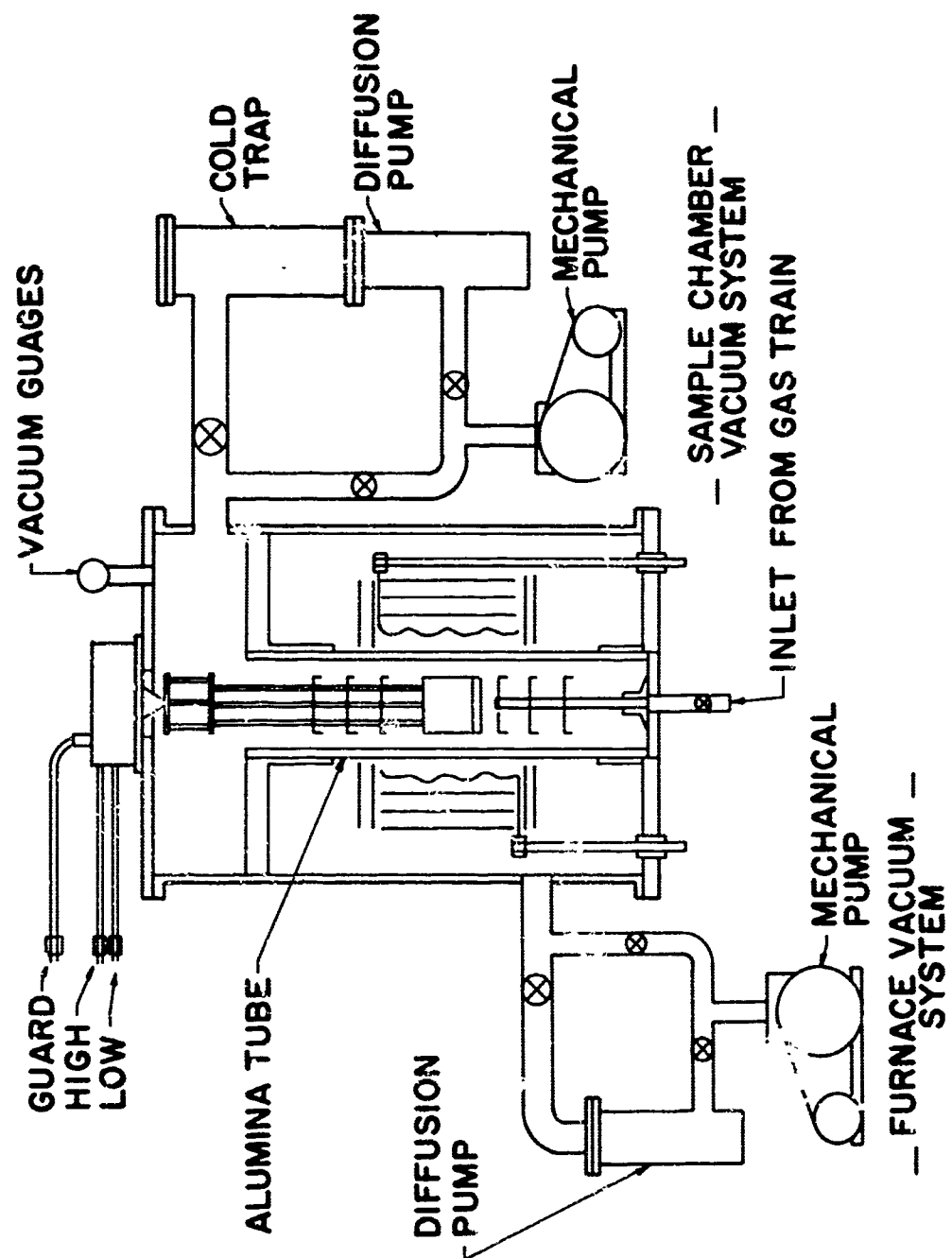


Fig. 9. Schematic of Environment Control Equipment



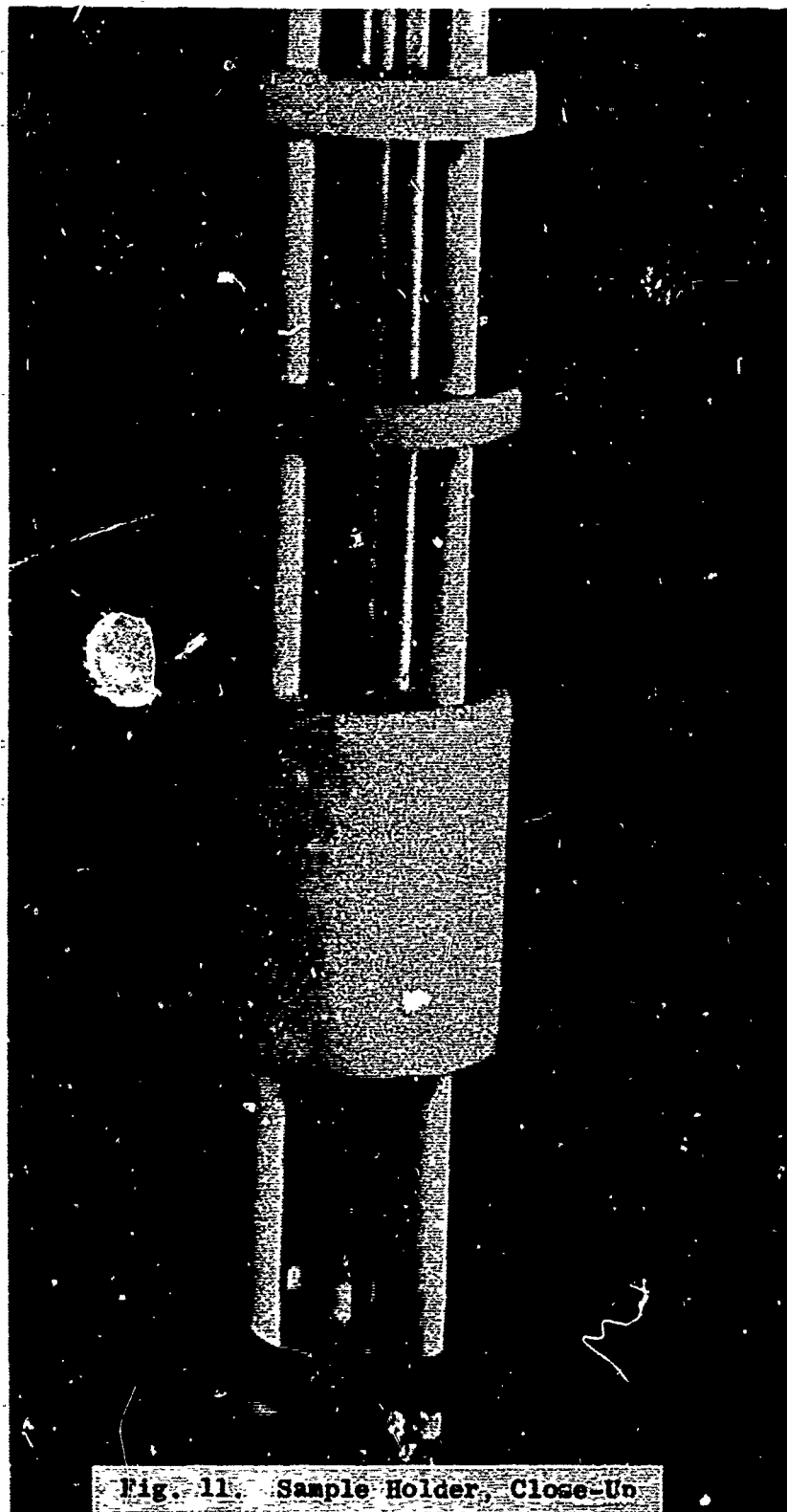
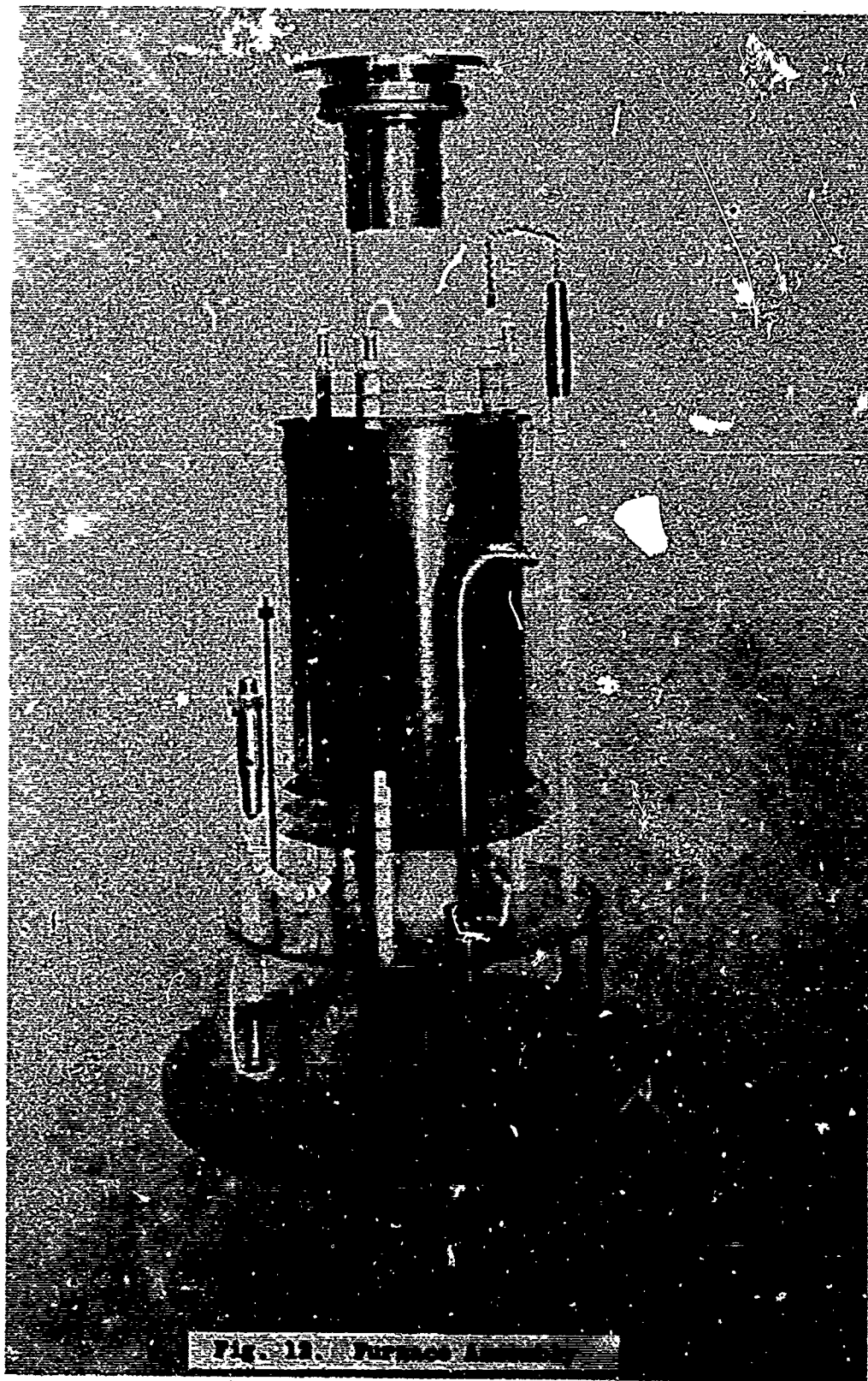


Fig. 11. Sample Holder, Close-Up



prior history of the samples. All measurements were made in a static vacuum at approximately 10^{-3} Torr, even though no dependence of the conductivities on the total pressure or the oxygen partial pressure was found.

III. EXPERIMENTAL RESULTS

A. Polycrystalline

The plot of conductivity vs. reciprocal temperature for each polycrystalline sample was qualitatively the same as that for sample 5, shown in Fig. 13. Each plot showed an initial conductivity, represented in Fig. 13 by the circles, and a steady state (non-blocked) conductivity represented by the triangles. The steady state conductivity curves all showed a high temperature intrinsic region and a lower temperature extrinsic region characterized by a lower slope. The high temperature intrinsic regions for all of these curves were in excellent agreement, as they should be in theory since this region is characteristic of the material and not the defects present in a particular specimen. If the high temperature intrinsic portions of all of the curves obtained are exactly superimposed, the plot shown in Fig. 14 is obtained.

The data for sample 1 were left off since they were the same as the data for sample 2. It is very clear that the total conductivity is increasing with decreasing particle size. There was a slight increase in the extrinsic steady state conductivity as will be shown. If it is assumed that the steady state conductivity is sodium vacancy conductivity and that the increase in the total conductivity is due to an increase in the chlorine ion conductivity the similarity to Laurent and Bénard's data (Fig. 4) is remarkable. Fig. 15 presents these data at 350°C plotted as a function of particle size. The scatter in the data points is due partially to some scatter in the σ_{∞} data for each sample. However, it is mainly the result of being unable to establish an effective particle size, since there was a large particle size distribution in each sample due to the agglomerating tendency of NaCl.

As indicated, the circles represent the steady state conductivity. It is quite well behaved, showing little particle size dependence. It may also be noted that the steady state values can be extrapolated to the single crystal value. This slight particle size dependence would probably not be detectable in a diffusivity experiment. The blocked contribution, $\sigma_0 - \sigma_{\infty}$, fits well on the line drawn using a reciprocal particle size dependence. This is the same dependence that Laurent and Bénard found for chlorine diffusivity⁵.

The upper portion of Fig. 15 shows the transference number for the enhanced conductivity, which is now assumed to be chlorine vacancy conductivity because of the correlation with the work of Laurent and Bénard. It is seen that even for the specimen with the smallest particle size the total conductivity still has a sodium vacancy contribution.

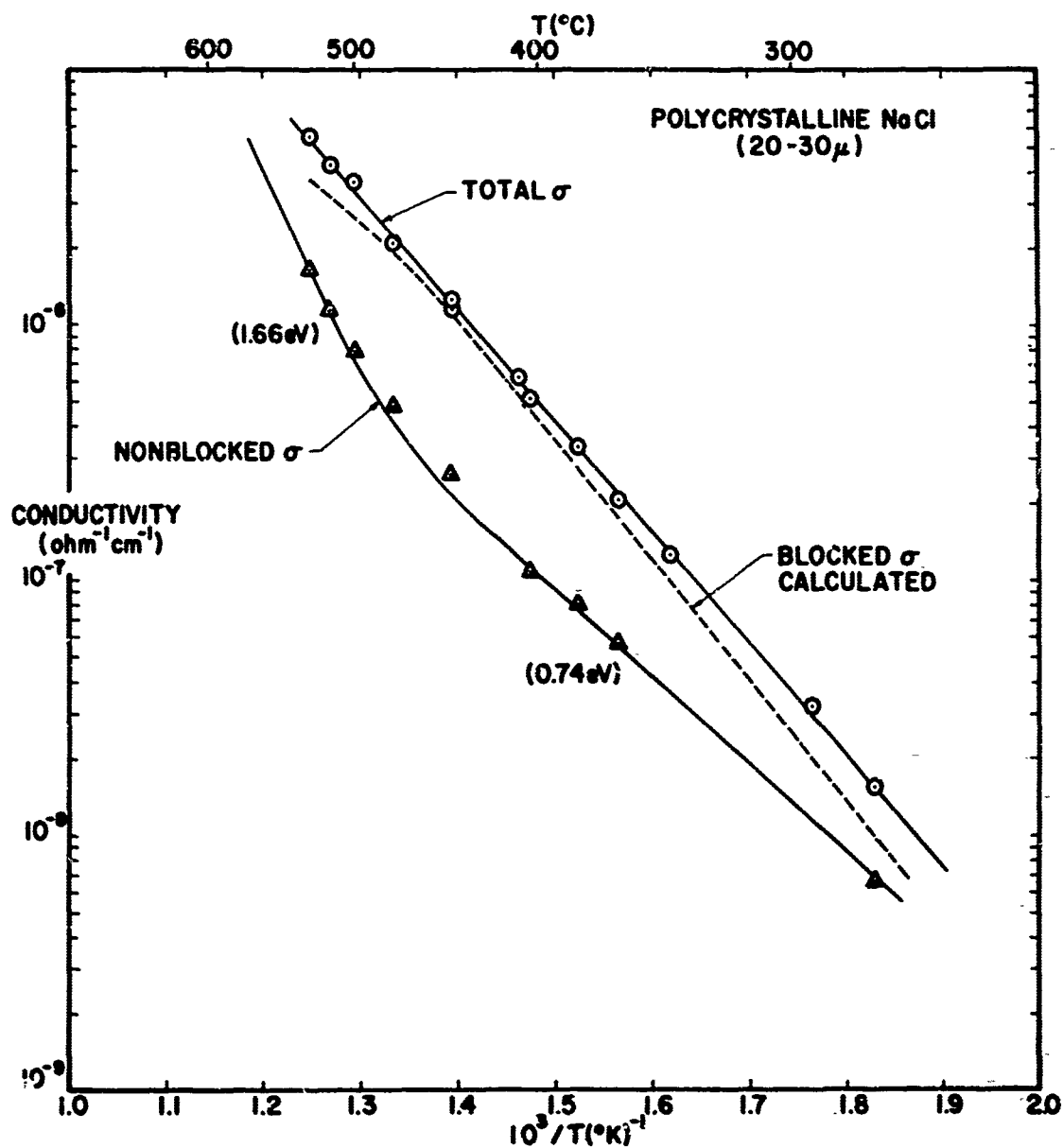


Fig. 13. Conductivity versus Reciprocal Temperature for Polycrystalline Sample Number 5

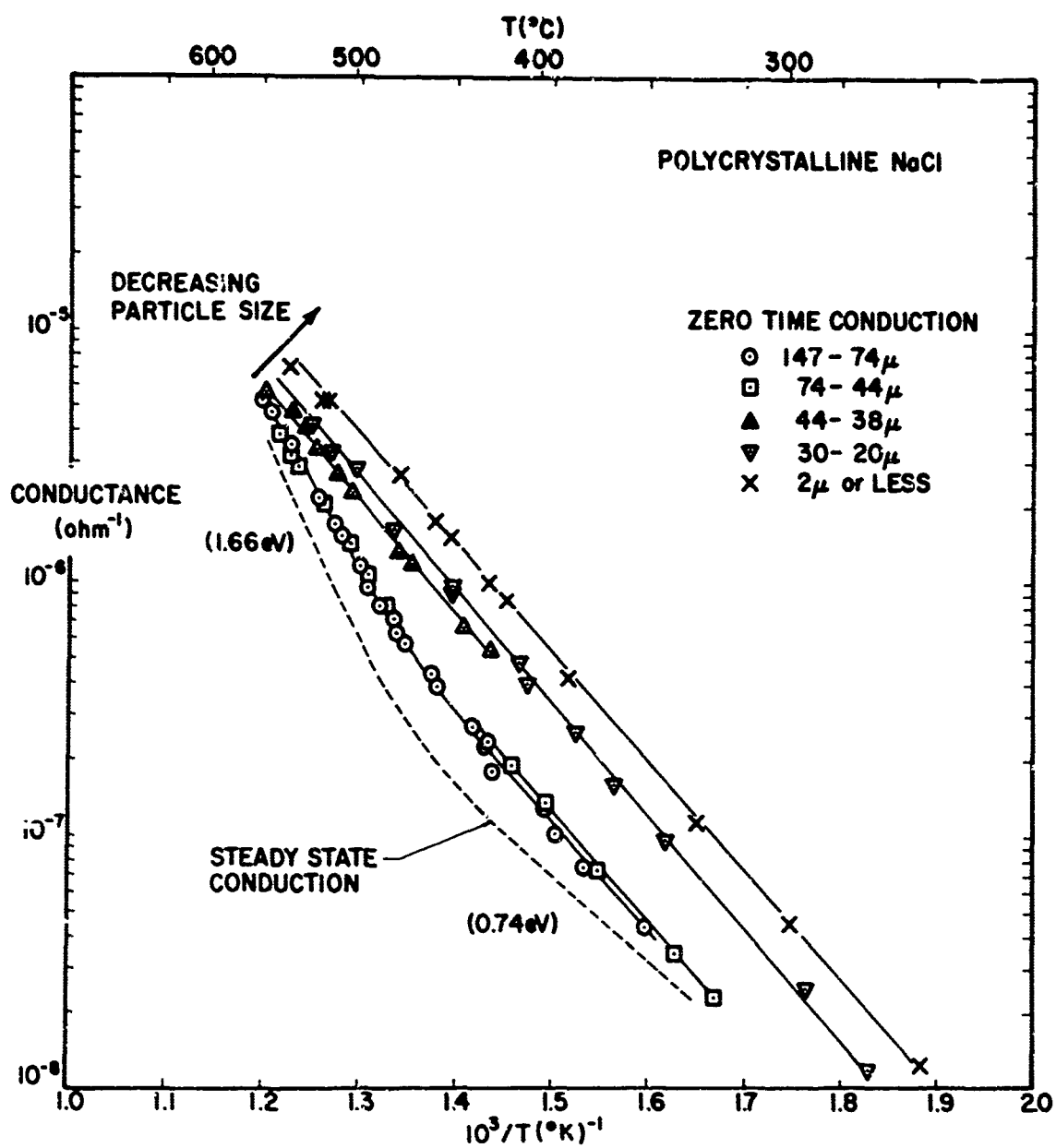


Fig. 14. Summary of Polycrystalline Data

Several other bits of information can be deduced from these data using a few qualified assumptions. First, since the total conductivity is still increasing even for the smallest particle size measured it may be assumed that the chlorine conductivity in the enhanced sub-surface region of the grain boundary is $\geq 10^{-7} \text{ ohm}^{-1} \text{ cm}^{-1}$ at 350°C . Second, since for equal contributions to the total conductivity the ratio of surface layer to bulk thickness is given by the ratio of bulk to surface layer conductivities, the thickness of the surface layer can be estimated to 0.1μ at 350°C . This is in good agreement with the layer thickness found in alumina by Johnson and coworkers⁸.

The activation energy calculated from all data for chlorine diffusion (dotted line Fig. 13) was $1.0 \pm 0.1 \text{ eV}$, which agrees well with literature values.^{9,10}

B. Single Crystal

The results for the single crystals completely support all conclusions reached from the polycrystalline results. In addition, there is extremely good evidence for the need to correct the literature values for the conductivity in the high temperature intrinsic region and the activation energy for defect formation calculated from it.

Fig. 16 presents the data for the as-received single crystal. The total conductivity curve agrees exactly with ^{the} accepted one¹¹, i. e., intrinsic energy 1.86 eV , extrinsic energy in the range $0.70\text{--}0.80 \text{ eV}$ and the break over point at about $6 \times 10^{-8} \text{ ohm}^{-1} \text{ cm}^{-1}$ and $1.4 \times 10^{-3} \text{ }^\circ \text{K}^{-1}$. However, in the intrinsic region the total conductivity is shown to be the sum of the conductivities of two ionic carriers.

The agreement of the energy from the steady state single crystal curve (1.66 eV) with that for the polycrystalline samples, coupled with the conclusion that σ_∞ is sodium vacancy conductivity for the polycrystalline samples, leaves little doubt that this is the true curve for intrinsic sodium vacancy conductivity and not the σ_0 curve.

Further evidence for this conclusion was obtained from a single crystal sample which had been doped with an excess of anion vacancies by the dissociation of F-centers introduced into the crystal by heating it in a sodium vapor atmosphere (Fig. 17). As can be seen, the overall effect was to reduce the extrinsic conductivity normally found at low temperatures. The fact that this new observable low temperature portion of the curve is the extension of the high temperature σ_∞ curve and not the σ_0 curve is strong evidence in favor of the high temperature steady state conductivity being sodium vacancy conduction.

Extending this conclusion to the calculation of the Schottky energy for the formation of anion and cation vacancies in NaCl leads to a much lower

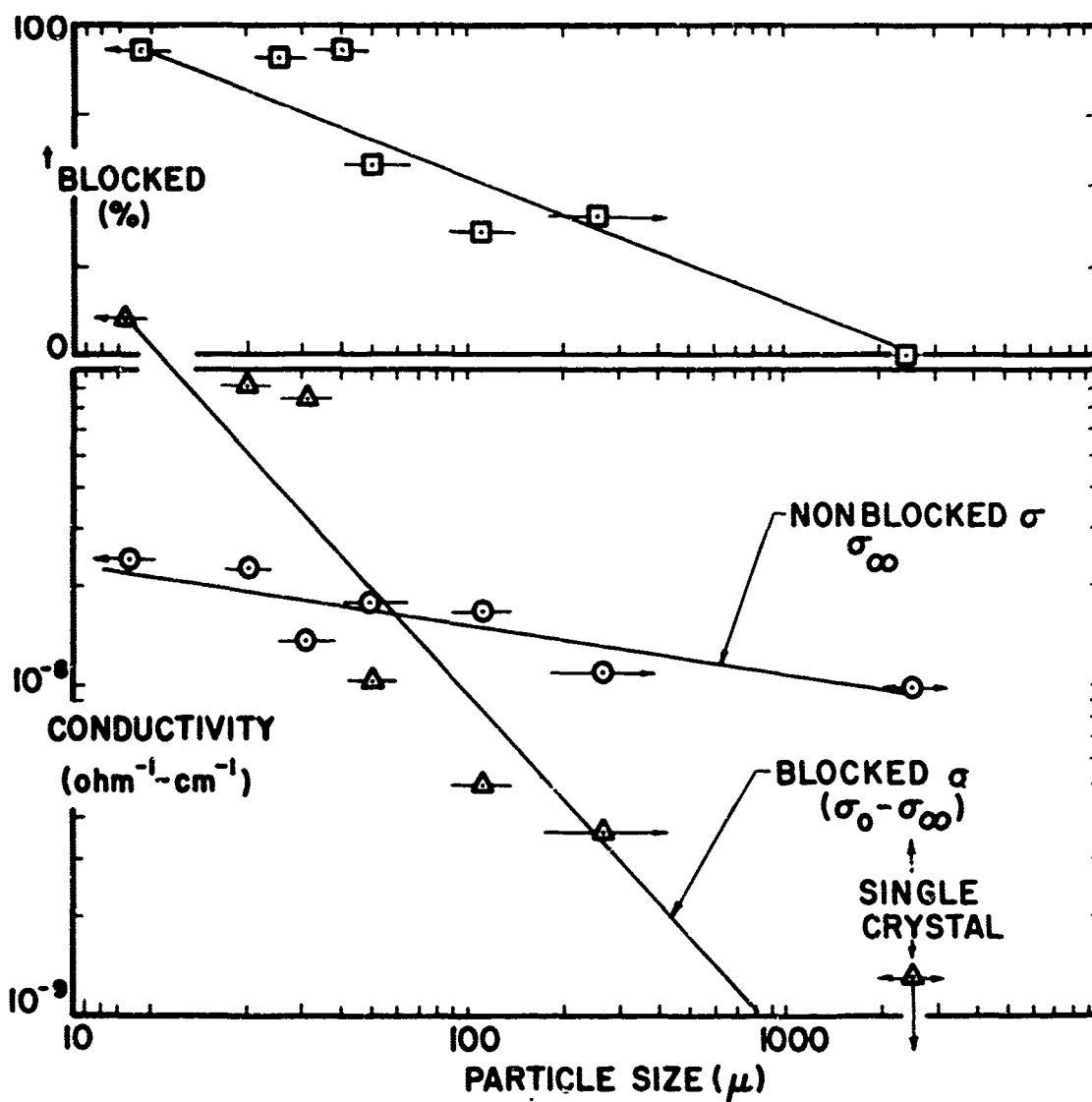


Fig. 15. Conductivity and Transference Number versus Particle Size at Approximately 350°C

new value. Since the intrinsic sodium vacancy activation energy is $1/2$ the Schottky energy plus the energy for movement and the extrinsic energy is simply the energy for movement, the newly calculated Schottky energy would be 1.72 eV [$2(1.66 - 0.80)$]. The previously accepted energy, based on 1.86 eV being the intrinsic sodium vacancy energy, is 2.12 eV¹².

Another interesting sidelight of the doped NaCl single crystal results is that this approach of additively coloring presents a quite attractive means of studying the intrinsic conduction of crystals, especially for those crystals normally having a small observable intrinsic conductivity range due to the early onset of the extrinsic mechanisms.

V. SUMMARY AND CONCLUSIONS

In summary, it may be said that the results completely support the earlier results of Laurent and Bénard for NaCl and in particular that:

1. Chlorine ion transport is enhanced in the subsurface region associated with grain boundaries.
2. The magnitude of the chlorine conductivity is reciprocally dependent upon particle size.
3. The energy for movement of the chlorine vacancy in the enhanced layer is the same as for movement in the bulk. (1.0 ± 0.1 eV).
4. Even for single crystal material the contribution of the chlorine ion is significant in the high temperature intrinsic range.
5. The accepted intrinsic energy for sodium vacancy transport (1.86 eV) is really the energy for a line which is the sum of two transport mechanisms, and the true value is closer to 1.66 eV. The Schottky energy then becomes 1.72 eV instead of 2.12 eV.
6. The movement of the sodium vacancy shows very little enhancement as the particle size is decreased.

Since there is now little doubt that the ion which is found to be the slower moving species in a single crystal study can make a major contribution to mass or charge transport in a polycrystalline ceramic material, and in fact that it can even become the faster moving species in ultra-fine grained ceramics, the mechanism of the enhanced movement in the sub-boundary layer must receive increased study. In fact, without such further clarification of this phenomenon, progress towards the goal of being able to accurately predict and control essential fabrication processes and applications of ceramic materials may be impossible.

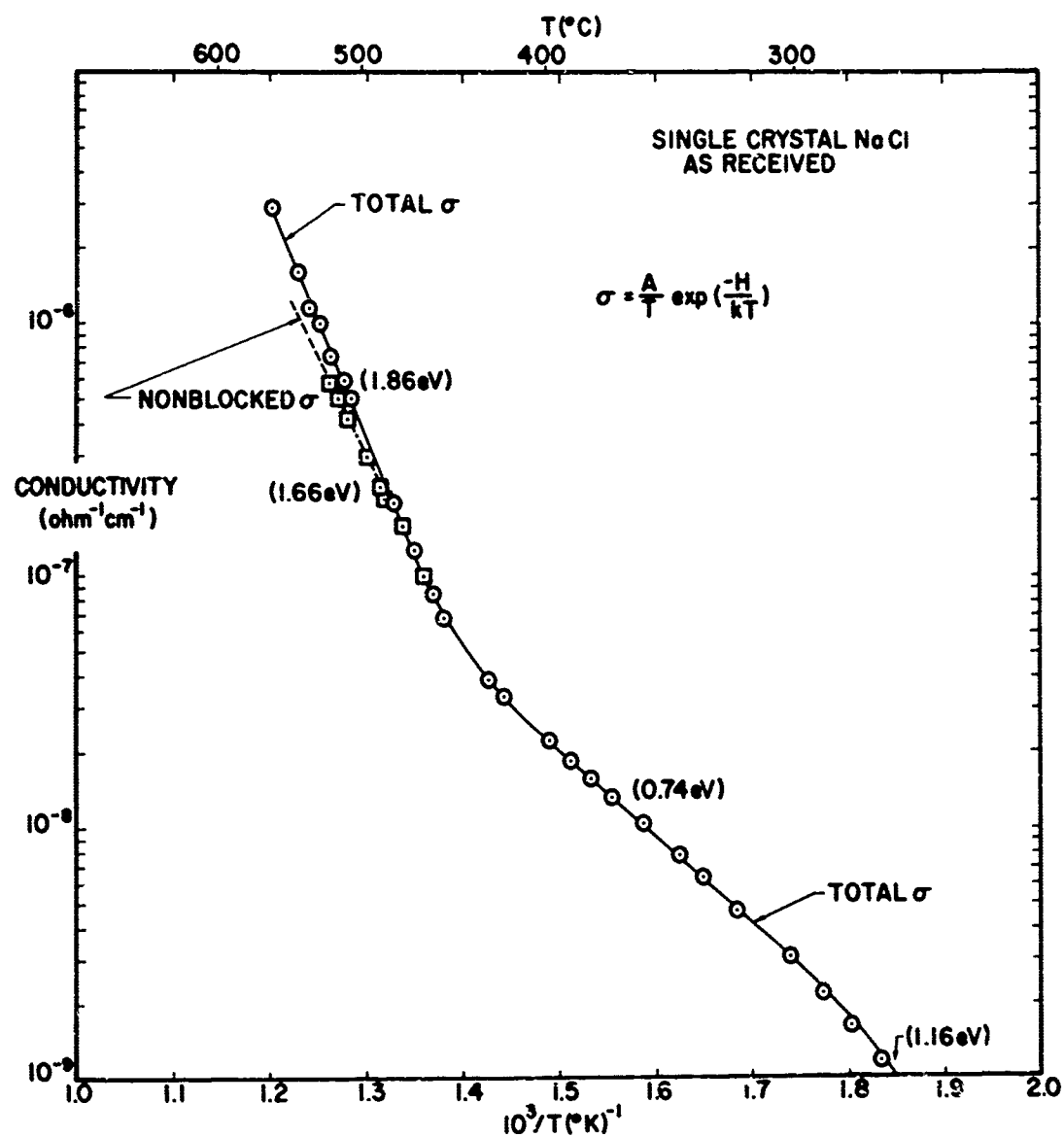


Fig. 16. Conductivity versus Reciprocal Temperature for
"As Received" Single Crystal

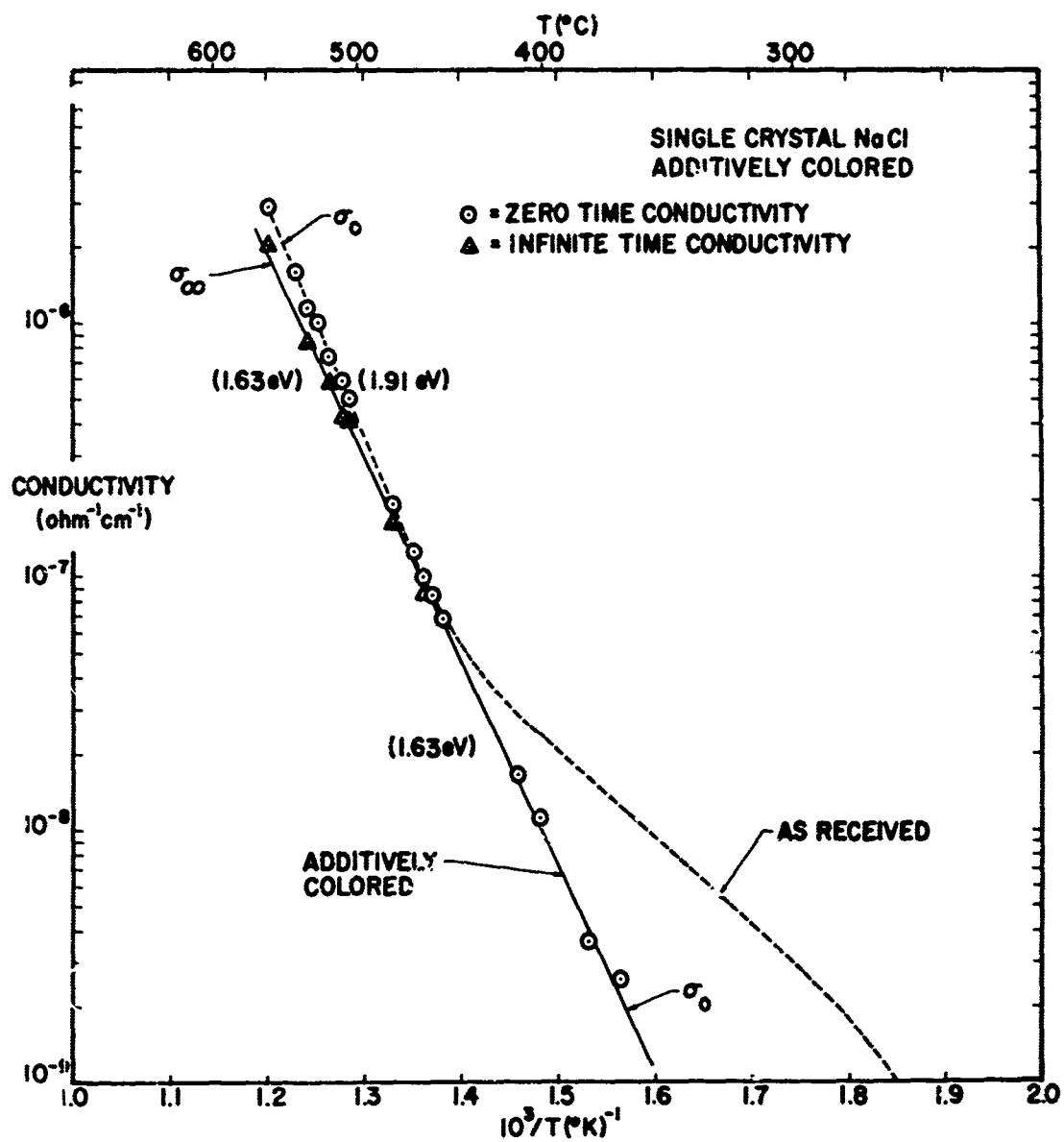


Fig. 17. Conductivity versus Reciprocal Temperature for Additivity Colored Single Crystal

REFERENCES

1. W. D. Kingery and M. Berg, "Study of Initial Stages of Sintering Solids by Viscous Flow, Evaporation-Condensation, and Self-Diffusion," *J. Appl. Phys.*, 26, 1205-12 (1955); R. L. Coble, "Initial Sintering of Alumina and Hematite," *J. Am. Ceram. So.*, 41, 55-62 (1958).
2. R. L. Coble, "Sintering Crystalline Solids: I, Intermediate and Final State Diffusion Models," *J. Appl. Phys.*, 32, 787-92 (1961).
3. Conyers Herring, "Diffusional Viscosity of a Polycrystalline Solid," *J. Appl. Phys.*, 21, 437-45 (1950).
4. A. E. Paladino and R. L. Coble, "Effect of Grain Boundaries on Diffusion-Controlled Processes in Aluminum Oxide," *J. Am. Ceram. Soc.*, 46, 133-136 (1963).
5. J. F. Laurent and J. Benard, "Autodiffusion Des Ions Dans Les Halogemures Alcalins Polycristallins," *J. Phys. Chem. Solids*, 7, 218-27 (1958).
6. J. Hokkinson, *Phil. Trans. Roy Soc. (London)* 166, 489 (1876); J. & P. Curie, *Am. Chem. Phys.*, 17, 385 (1888).
7. R. W. Vest, "Apparatus for Guarded Polarization Measurements," to be submitted to the *Rev. of Sci. Inst.*
8. D. L. Johnson and L. Barrier, Conference on Sintering and Related Phenomena at the University of Notre Dame, June 1965, paper C-4.
9. N. Laurance, "Self-Diffusion of the Chloride Ion in Sodium Chloride," *Phys. Rev.*, 120, 57-62 (1960).
10. L. W. Barr, J. A. Morrison, and P. A. Schroeder, "Anion Diffusion in Crystals of NaCl," *J. of Appl. Phys.*, 31, 624-31 (1965).
11. R. W. Dreyfus and A. S. Nowick, "Ionic Conductivity of Doped NaCl Crystals,"
12. R. W. Dreyfus and A. S. Nowick, "Energy and Entropy of Formation and Motion of Vacancies in NaCl and KCl Crystals," *J. Appl. Phys.*, Supplement to 33, 473-77 (1962).

(U) IMPULSE FACILITIES FOR SCRAMJET
RESEARCH AND DEVELOPMENT

by

Forrest B. Smith, Jr.

Propulsion Division, DCS/Research
Arnold Engineering Development Center
Arnold Air Force Station, Tennessee



Forrest B. Smith, Jr.

BIOGRAPHY

The author received his BS degree in Mechanical Engineering from Tennessee Technological University in June 1956. From June 1956 to October 1960, he was employed as a mechanical engineer by ARO, Inc., at the Arnold Engineering Development Center. Analysis of the performance characteristics of various propulsion systems to include turbojets and ramjets were the author's principal duties.

In October 1960, he was employed by the Air Force at Wright-Patterson AFB, Ohio. He worked in the Facilities Division of the Air Force Aero Propulsion Laboratory. In 1964, he joined the Air Force Staff as an Aerospace Engineer in the Propulsion Division, DCS/Research, Headquarters Arnold Engineering Development Center.

ABSTRACT

The complete simulation of hypersonic flows at specific environmental conditions of interest for SCRAMJET research and development is not possible with existing steady flow facilities. SCRAMJET test requirements dictate extreme weight flow and power requirements; hence, it becomes necessary to turn to a facility operating on an impulse basis to generate those conditions representative of high velocity free flight.

SCRAMJET testing requirements including component investigations as well as full system test requirements are discussed. Further, compatibility between components and cycle efficiency optimization experiments will require a facility capable of full flow duplication such that complete, nearly full-scale systems can be evaluated.

High reservoir temperature and pressure conditions (superior to steady flow facilities) can be achieved in the impulse facility; however, the increased capability is achieved at the expense of short run times. Also facility design problems are less severe in areas such as the nozzle throat, and the short duration high energy flow can be obtained more economically by a pulsed energy source.

Two general classes of impulse facilities which have been useful for SCRAMJET research and development are the reflected shock tunnel and the hotshot tunnel. A third impulse facility, the "chemical shot", which utilizes the chemical reactions of various propellant combinations in a constant volume reaction chamber as a means of producing high enthalpy and high pressure "simulated" air, has potential.

Results of analytical and experimental studies in the use of the reflected shock tunnel, research to ascertain the feasibility of using air as the test gas in the inductively driven hotshot tunnel, and finally the progress to date on the "chemical shot" idea are presented.

CONTENTS

	<u>Page</u>
I. INTRODUCTION.	1
II. SCRAMJET TEST REQUIREMENTS.	1
A. Requirements for Flight Duplication	1
B. Component Test.	2
1. Inlets	2
2. Combustors.	2
3. Expansion Nozzles	3
C. System	3
III. TEST CAPABILITIES OF IMPULSE FACILITIES	4
A. Shock Tunnel	4
1. Altitude Velocity Duplication.	5
2. Inlet Testing Capabilities	5
3. Combustor Environment Duplication.	5
4. Nozzle Non-Equilibrium Considerations.	6
5. Test Time Limitations.	6
6. Combustor Model Size Limitations	7
B. Hotshot Tunnel	7
1. Altitude Velocity Duplication.	8
2. Test Time Limitations.	9
C. The Chemical Shot Tunnel	9
1. Experimental Effort	10
2. Analytical Effort	10
3. Potential Payoff	11
IV. SUMMARY OF CONCLUSIONS	11
References	13

I. Introduction

With the advent of the Supersonic Combustion Ramjet (SCRAMJET) came the ground test facility requirement of duplicating and/or simulating typical flight environmental conditions corresponding to flight conditions within the airbreathing propulsion flight corridor (Fig. 1 and Ref. 1). Test facilities which have potential for satisfying SCRAMJET testing requirements fall into two general classifications, namely, steady flow facilities and impulse facilities. This paper is concerned with those research efforts directed toward the use of impulse-type test facilities for SCRAMJET component and systems tests. Impulse facilities which will be discussed in detail in the course of this paper include the tailored interface shock tunnel, the inductively driven hotshot tunnel, and a facility which will be alluded to as a "chemical shot tunnel", which utilizes the chemical reactions of various propellants in a constant volume reaction chamber as a means of producing high temperature and high pressure "simulated" air.

An analysis of SCRAMJET engine and component testing simulation requirements to include full duplication-type system testing, inlet Mach number-Reynolds number simulation testing, direct connect combustor testing, and the ability of an impulse facility to supply the environmental test needs will be discussed. Facility performance analysis, run times, test section size, and special facility limitations as they apply to current SCRAMJET requirements will be presented.

II. SCRAMJET Test Requirements

A. Requirements for Flight Duplication

Ideally, the experimental testing required for the development of the SCRAMJET components and systems should be done with full scale components in a flow environment duplicating that experienced during actual flight. In addition, facility run times should be of sufficient length to experimentally determine the heat flux and equilibrium temperature distribution on the SCRAMJET structure.

Examination of the flow environment experienced by a SCRAMJET flying in the airbreathing corridor shows that the test conditions are formidable. Total temperature, total pressure, input power requirements, and mass flow considerations in a hypersonic facility increase very rapidly with increasing flight speed and decreasing altitude. For example, at a velocity of 8,000 ft/sec and an altitude of 100,000 ft, the required total temperature is approximately 4800°R with a required total pressure of 2500 psia. Decreasing the altitude by a mere 13,000 ft to 87,000 ft, at the same velocity, results in approximately the same temperature requirements; however, the total pressure has been increased by a factor of 2 to 5000 psia.

Other parameters which should be considered when the duplication of flight conditions is required are power and mass flow per unit area. Stream power levels of the order of 10 to 20 Mw/ft² of stream area represent a typical airbreathing flight trajectory. For example, a hypersonic test facility incorporating a 6-ft-diam test section with full flow duplication at a flight velocity of 8000 ft/sec and an altitude of 87,000 ft would require approximately 400 lb of air per second at a stagnation temperature of 4750°R and a stagnation pressure of approximately 5000 psia. The stream power would be approximately 550 Mw, and if arc heated the power input assuming 50-percent efficiency would be in excess of 1000 Mw.

Considering the stagnation pressure and temperature requirements, power, and mass flow requirements, it does not appear practical to provide ground facilities large enough to test and evaluate large full-scale SCRAMJETS, particularly for continuous flow facilities. Hence, component and reduced scale testing together with data correction techniques will be the rule rather than the exception for large-scale SCRAMJET development.

B. Component Test

For component testing, full-flow duplication is not always required. The partial simulation required depends on the particular problem being investigated and sometimes on the type and capabilities of an available test facility. Some of the important primary parameters to be simulated for the different components are listed in Fig. 2. The parameters shown are those which are required for a meaningful test of the components or for comparing performance between different model configurations.

1. Inlets

The flow field behind a leading edge shock of an inlet and the shock shape are primarily dependent on free-stream Mach number, Reynolds number, ramp geometry, and leading edge geometry. Reynolds number-Mach number simulation on scaled models necessitates higher pressure and/or lower temperatures than those which will be experienced in actual flight. Differences in boundary layer between free-flight and scaled models can be most important in affecting transition and separation. Also, wall-to-stream temperature ratio is an additional parameter which should be simulated in inlet testing. Furthermore, the Reynolds number-Mach number simulation concept is subject to real gas correction throughout the flow field.

2. Combustors

The SCRAMJET combustor performance is a function of fuel injection and mixing, heat release by chemical reactions, heat losses to the walls, boundary-layer changes, shock wave interactions, and hence the analysis of such reactive flows is extremely complex.

It appears desirable, if not an absolute requirement, to impose several constraints upon SCRAMJET combustor testing. Air or near air gases should be used as the test gas, and the actual fuel should always be employed. The static temperature, static pressure, and velocity at the entrance to the combustor should be duplicated. As mentioned before, the mixing and reaction processes are intimately related, and quantitative effects on combustion efficiency requires testing with the aforementioned combustor entrance requirements. These combustor requirements are likewise summarized in Fig. 2.

3. Expansion Nozzles

The characteristics of the SCRAMJET expansion system are primarily affected by the following:

- a. Nozzle inlet Mach number
- b. Area expansion ratio
- c. Friction and heat losses
- d. Recombination losses

The gas leaving the combustor will be a nonhomogeneous mixture of dissociated combustion products. For recombination rate studies in the expansion process, the static temperature, static pressure, and gas composition should be fully simulated; and their time history through the test nozzle should be the same as that expected in the flight nozzle. Nozzle efficiency will be strongly dependent on the amount of recombination taking place in the nozzle and the prevention of freezing of the flow early in the expansion process. Friction, heat transfer, expansion losses must be determined. Recombination rates and hence nozzle efficiency will be strongly affected by nonuniform flow profiles, nonhomogeneous mixtures, and boundary conditions.

It seems very likely that testing with full-flow duplication in full-scale nozzles or nozzle segments will be required to completely access nozzle designs and their performance. The recombination rate study requirement for the exhaust nozzle is the main difference between exhaust nozzle and inlet testing requirements.

C. System

Because a system test must simultaneously satisfy the simulation parameters of the inlet, the combustor, and the nozzle components, it appears that nearly full-size models will ultimately be required. This occurs chiefly because the inlet requires duplication of R_{E1} and M_{E1} , whereas the static temperature, static pressure, and frequently, velocity must be duplicated to satisfy combustor requirements. As a result, true

static temperature, pressure altitude, and velocity must be matched. In addition, because the combined requirements fix the test section unit Reynolds number, the model must be full-scale if Reynolds number is also to be duplicated.

III. Test Capabilities of Impulse Facilities

As discussed previously, flight rating tests, materials, and structural integrity testing require long flow durations characteristic of steady flow facilities. Engine component development and component performance evaluations can be accomplished in short flow duration pulse facilities. The pulse facility, which has run times of the order of milliseconds, far exceeds the capability of steady flow facilities; however, the increased capability is achieved by a trade-off with available run time. The impulse facility, by virtue of its short flow times, circumvents many of the heat-transfer and material limitations of the steady flow facility and also allows the use of relatively simple, uncooled test hardware. The impulse facility with the inherent short duration flows has one attractive advantage in that the short duration of the flow has kept the nozzle throat temperature rise within tolerable limits even though the heat transfer to the nozzle throat may be very large. Projected total temperatures and total pressures have increased to the point where conduction-type cooling methods are no longer adequate even in the shock tunnel. The problem is even more severe in the case of the hotshot tunnel where the effective run time is possibly an order of magnitude greater than the shock tunnel. Therefore, it is concluded that various techniques for protecting the nozzle throat in an impulse facility represent an important limitation in future development of high performance impulse wind tunnels. The use of other throat materials, with ablating, refractory, or oxide coatings and more sophisticated cooling techniques to include transpiration cooling, needs to be extensively investigated on both an analytical and experimental basis.

A. Shock Tunnel

The ability of the shock tunnel to generate air flows at total temperatures and pressures representative of hypersonic flight has been well established. Very short duration (millisecond) testing time is the main difficulty associated with the shock tunnel; however, the "tailored-interface" technique has increased the available test time to a point where with the use of rapid response instrumentation techniques, accurate measurement of heat-transfer rates, pressures and forces can be made. The hypersonic shock tunnel in its present state of advancement is capable of duplicating re-entry flight conditions for various hypersonic vehicles over an important area of the re-entry corridor. However, duplication over the relatively high density range of interest for SCRAMJET cannot be obtained with present shock tunnels.

Operational capabilities of the Cornell Aeronautical Laboratory 96 in. hypersonic shock tunnel will be utilized for purposes of comparison in the course of this paper (Ref. 2).

1. Altitude - Velocity Duplication

The altitude velocity duplication capabilities of the CAL 96-in. existing operational shock tunnel together with the SCRAMJET flight corridor are shown in Fig. 3. As shown in the figure, it is apparent that full-flow duplication is possible for flight velocities of immediate interest within the referenced airbreathing flight corridor. However, many severe problems presently exist that prevent full exploitation of the tunnel capabilities. Limited test time, reservoir nonuniformities, nozzle throat heating, and interface burning are some of the problem areas that combine to limit the usefulness of the shock tunnel for SCRAMJET research and development.

2. Inlet Testing Capabilities

Outside of the altitude-velocity duplication envelope discussed in paragraph 1, simulation capabilities become of particular interest especially for inlet testing. If temperature is not being duplicated, a reasonably good coverage of the Reynolds numbers needed is possible, even taking into consideration the differences between model and full-scale. However, inadequacies readily exist at the higher Mach numbers and low altitudes.

Transition is difficult to predict and the analytical methods for predicting boundary-layer growth at high Mach numbers, especially for turbulent boundary layers, are not experimentally proven. Difficulty may be expected in achieving forced transition on inlet models in test at higher Mach numbers. If transition cannot be accomplished, then scale model contours must be corrected for boundary-layer growth consistent with wind tunnel conditions, and the performance adjusted to full-scale conditions by yet undetermined analytical methods.

Since turbulent boundary-layer profiles are necessary ahead of an isentropic compression surface of the inlet in order to avoid possible separation and if altitude-velocity duplication is necessary, such as for a system-type test, the need for facilities capable of accepting very large models is apparent.

3. Combustor Environment Duplication

Present shock tunnel thermodynamic capabilities for supersonic combustor component testing (direct connect) are shown in Fig. 4. These capabilities are shown as limits in terms of the CAL 96-in. tunnel to produce combustor entrance static pressure and temperature. Also shown are curves for reaction times as a function of static temperature and static pressure. The reaction time curves were derived from data presented in Ref. 3.

The facility limitation curves represent a maximum total pressure of 20,000 psia and an enthalpy level corresponding to a flight velocity of 8700 and 13,400 ft/sec as shown. The reaction lengths are

spotted on the curve at the intersection of the reaction time curves with the facility limitation curves. The length dimensions as shown are derived from the actual combustor velocity and not the free-stream velocity. Combustor inlet conditions which fall above the reaction time curve of 0.01 msec will result in a combustion process governed primarily by mixing, and the chemistry may be considered to be in equilibrium with the local state properties. In a mixing controlled process where the reaction kinetics are very fast, it should be possible to conduct meaningful and interpretable scale model SCRAMJET combustor tests.

Considering the reaction time line of 0.1 msec as a further limitation in order to make reaction lengths of the order of one foot or less, it is clearly evident that a free-stream velocity of approximately 8700 ft/sec, existing shock tunnel capabilities provide adequate coverage of combustor entrance conditions. However, for a free-stream velocity of 13,400 ft/sec, it can be seen that existing shock tunnel capabilities are generally marginal for duplicating both combustor pressure and temperature requirements.

4. Nozzle Nonequilibrium Considerations

At the high stagnation temperatures required for the simulation of high velocity flight, the test gas dissociates in the nozzle reservoir, and many of the dissociated particles generated do not recombine in the nozzle. One serious consequence of this dissociation is the formation of oxides such as nitric oxide which reduces the molecular oxygen content of the test air.

Based on the analysis in Ref. 4, it is concluded that residual concentrations of atomic species in the nozzle test section will not be of any particular consequence for that portion of the altitude-velocity map that can be duplicated in existing impulse facilities (12,000 to 13,000 ft/sec). As flow velocities increase (over 12,000 ft/sec), then nozzle flow nonequilibrium will assume increasing importance. As an example, the absolute pressure and temperature at the combustor entrance (inlet throat) may be substantially less for the nonequilibrium free-stream case than it would for the equilibrium case. This could be a very serious consequence in a system test because of combustor ignition and reaction time requirements.

5. Test Time Limitations

The duration of steady-state shock heated test gas (air) in the nozzle reservoir for the CAL 96-in. hydrogen driven shock tunnel is 2 to 3 msec at a shock Mach number of 8.0 (13,300 ft/sec) and 5 to 6 msec at a shock Mach number of 6 (8700 ft/sec). The test durations are terminated by either the arrival of the driver gas at the nozzle throat or the reflected head of the driver expansion.

Test time requirements for SCRAMJET component models or systems are dictated by a number of key factors. Some of the factors which have been investigated are as follows:

- a. The speed of the primary starting shock past a model
- b. Size of the model
- c. Sensor type and anticipated level of the measured variable
- d. Local-flow equilibrium time along a given model
- e. Test gas slug length

Although there is a lack of a definitive correlation of data, it can be concluded at this time that local equilibrium times to obtain steady flow have not been encountered that were greater than 5 msec except where separated flow on the model became incipient or established. Since a 1- to 2-msec duration of steady flow conditions is desirable to verify that the flow field is established, a test facility for SCRAMJET investigations should be capable of providing 7 to 8 msec of contamination free test time.

In light of the above discussion, it should be apparent that the steady-state test duration is marginal for conducting SCRAMJET tests in existing shock tunnels for the velocity range of 8700 to 13,300 ft/sec. Below 8700 ft/sec, where the majority of SCRAMJET tests have been conducted, the available test time is generally adequate for most test requirements. If model flow separation is encountered, the available test time even below 8700 ft/sec becomes marginal to inadequate.

6. Combustor Component Model Size Limitations

The maximum model entrance size for a direct connect combustor installation is dictated by the entrance thermodynamic conditions required and the maximum allowable throat size of the nozzle. Representative combustor entrance diameters corresponding to the capabilities of the CAL 96-in. hypersonic shock tunnel are such that large-scale combustor tests are impossible to perform under flight environmental duplication conditions, except perhaps at low total enthalpy levels and low static temperature levels.

B. Hotshot Tunnel

The AEDC hotshot Tunnel F has been chosen for discussion herein because it is believed the AEDC facility represents the highest performance hotshot facility currently available and operational. Of particular interest is the available inductive energy storage system rated at 10^8 joules; i.e., one million amperes at 20,000 V, a maximum test section diameter of 108 in., and an arc chamber slightly in excess of 1 cu ft. A more detailed description is included in Ref. 5.

The hotshot facility is different from the shock tunnel in several respects, and these differences are briefly discussed herein. Model size

limitations and nozzle nonequilibrium considerations for the hotshot tunnel are in general the same as discussed under shock tunnels and will not be discussed further.

The hotshot facility utilizes arc discharge in an arc chamber to raise the temperature and pressure of the continued test gas. Early investigations in the AEDC hotshot facilities used air as the test gas, but these experiences were unsuccessful because of (1) flow contamination of the test gas which resulted in large deviations of measurements, (2) inability to calculate arc-chamber enthalpy, and (3) the resulting depletion of oxygen caused by the formation of oxides and other contaminants. The thermo chemical effects were virtually eliminated by the use of nitrogen as the test gas instead of air. The use of nitrogen as the test gas was not considered detrimental to the validity of aerodynamic measurements since only small differences would exist when compared to air tests in the temperature range to 7200°R.

During the past few years, using nitrogen as the test gas at a temperature level to 7000°R, contamination levels, both chemical and mechanical (solid particles), have been reduced to the point at which the effects of contamination were no longer a problem. This vast change was brought about by the development of arc chamber design and means of arc initiation and termination. With this in mind and the advent of the SCRAMJET, a program was initiated to determine the feasibility of again using air as the test gas in hotshot Tunnel F.

Oxygen concentration as a function of reservoir temperature is presented in Fig. 5. The data show that the oxygen concentration is generally in the range of from 16 to 20 percent even at temperature levels to 7200°R. The total pressure profiles over the usable test section diameter are for all practical purposes identical to those obtained using nitrogen as the test gas under similar conditions for the three different throat configurations tested.

Gas sample analysis agreed with previous results, in that a dependence of oxygen content on contamination was indicated. Heat-transfer probes were utilized to monitor particle contamination. By relating the heat-transfer ratio based on measured quantities to the heat-transfer ratio based on calculated quantities, a measure of relative particle contamination levels can be made (Ref. 6). The heat-transfer ratio analysis indicated that the contamination levels were higher for the air runs than for runs utilizing nitrogen as the test gas; however, relative quantitative results are unavailable pending further experiments and analysis. Contamination levels (using air) might be further decreased with an optimum designed arc chamber baffle.

1. Altitude Velocity Duplication Envelope

The AEDC hotshot Tunnel F using air as the test gas is capable of duplicating flight up to a velocity of approximately 10,500

ft/sec. This capability is shown in Fig. 3. More specifically, the facility is capable of generating total temperature conditions in a range of 4800 to 7200°K and total pressure conditions in a range of 4000 to 20,000 psia.

2. Test Time Limitations

Run times for the hotshot tunnel are usually defined as the time from the establishment of steady flow in the nozzle until the decaying total pressure has decreased to an unacceptable percentage of the initial total pressure. Thus, the flow conditions in the test section are constantly changing during the useful run time. The useful run time will thus depend on the acceptable pressure variation of the initial pressure. A trade-off thus exists between test gas reservoir conditions, test section size, and useful run time for a fixed energy supply. Furthermore, an increase in arc chamber volume will reduce the unit energy level in the test gas and reduce the test gas reservoir conditions for a fixed energy supply. The useful run time of the Tunnel F facility is in the range of 50 msec and can be extended to 100 msec by accepting a further decay in reservoir conditions. Once again the run time is dependent on facility geometry. It should be recognized that the available run time thus described is of the order of ten times that available in the shock tunnel. In this regard, the hotshot tunnel could be very useful for probing slowly developing instabilities such as boundary-layer separation and other time dependent phenomenon for which shock tunnel test times are inadequate.

C. The "Chemical Shot"

The "chemical shot" tunnel is a hypervelocity test simulation facility which utilizes the constant-volume reactions of various propellants as a means of producing high enthalpy "simulation air."

The specific approach is the test simulation of high velocity airflow by the isentropic expansion of combustion and reaction products of a suitable fuel such as acetylene and nitrous oxide and/or nitric oxide. The primary criterion for simulation is that the mole fraction of oxygen in air be matched. This can be accomplished by the addition of nitrogen or oxygen to reduce or increase the oxygen concentration to 21 percent. Additionally with the use of helium or argon, the molecular weight of the simulated air can be also matched at 28.96. When these two matchings have been accomplished, it is found that the specific heat ratio of the gas mixture is very nearly the same as real cold air. Thus at a given set of flight conditions, the comparison of sonic velocities and flight Mach numbers is very good, as is the comparison between real and simulated air.

Depending upon the degree of diffusion expected in a SCRAMJET engine, the simulation inside the engine may also be suitable without further adjustment of the mixture composition. Analysis of SCRAMJET engines, such as presented in Ref. 7 has indicated that a velocity decrease

in the inlet of only about 1000 ft/sec is near optimum. Hence, this reflects very little diffusion temperature rise and in turn relatively little potential mismatching between the static properties of real and simulated air at the point of actual interest.

1. Experimental Effort

The experimental effort is concerned with evaluating the constant volume reactions of the exothermic decomposition of the oxides of nitrogen together with the additional heat release gained by burning acetylene in a constant volume chamber. The chamber will be sealed off by a burst diaphragm, similar to an arc heated hotshot chamber. Thus, the total heat release is absorbed as internal energy, and a very high pressure is created, from which the desired expansion occurs when the diaphragm breaks.

A design of the experimental test setup is shown in Fig 6. The combustion chamber maximum rated condition is 10,000 psia and about 8000°R. At a simulated air velocity of 12,500 ft/sec, the stagnation temperature of the product gases will equal the tolerable temperature limit. By proper adjustment of the test altitude, the stagnation pressure can also be held within tolerable limits. Furthermore at a temperature of 8000°R, the critical hardware problem is the melting of the nozzle throat. The forward nozzle throat is constructed by copper-infiltrated sintered tungsten. Analytical computations for the resultant time to melt the tungsten for a throat diameter of 0.50-in. is 120 msec. This time is probably marginal at the highest condition temperature and pressure because of the low anticipated pressure decay of 50 percent in 200 msec.

The nozzle geometry together with the 0.50-in. nozzle will permit testing at Mach numbers up to approximately 12.

2. Analytical Effort

Test gas composition as a function of simulated flight velocity is shown in Fig. 7. Nitrous oxide, nitric oxide, and acetylene are the reactants, and oxygen and nitrogen are used as diluents. The mole fraction of constituents in the product gas as a function of stagnation temperature and simulated flight velocity is presented. Mixtures of acetylene, nitrous oxide, and nitrogen can be used to obtain simulated flight velocities to 10,000 ft/sec. Velocities above 10,000 ft/sec can be obtained by substituting nitric oxide for some of the nitrous oxide. Gas velocities to 13,000 ft/sec can be achieved by using pure nitric oxide and acetylene. The gas properties of these mixtures remain quite similar to air over a major portion of the velocity regime. If desirable, the molecular weight can be compensated for by the addition of an inert gas such as helium or argon.

A computer program has been written which employs the following inputs: gross chemical composition, initial static temperature and pressure corresponding to a prescribed altitude ambient condition,

and internal energy increment. The energy increment may be an exothermic energy release, a heat release caused by combustion, or any combination thereof. The following outputs are provided: stagnation temperature and pressure, equilibrium chemical composition and density, and the velocity attainable by expanding the reservoir gases to ambient conditions.

For a given constant volume process calculation, the selection of a particular altitude and flight velocity will establish the combustion chamber loading pressure required for simulation of that particular point. The stagnation density will in turn be identical to the loading density of the combustion chamber before reaction.

3. Potential Payoff

The payoff of the "chemical shot" idea will be demonstrating the potential capability of constructing large-scale, long-run time test facilities powered by chemical propellants. The facility concept has a potential of providing total temperature conditions to 8000°R and total pressure conditions to perhaps 30,000 psia. A facility incorporating a 5-ft-dia combustion chamber and a Mach 10 facility nozzle with a 16-in. exit diameter would have a run time of approximately 8 sec (50-percent decay in total pressure). The maximum run time is governed by the combustion chamber size, nozzle throat size, and the nozzle throat heating problem. The cost of constructing such a facility utilizing chemical propellants for heating should be significantly cheaper than the cost of a comparable facility using other methods of heating; i.e., arc heater.

IV. Summary of Conclusions

The conclusions derived from this paper are summarized as follows:

1. Full flow duplication is possible for flight velocities to 13,000 ft/sec in currently existing shock tunnels. Available test time and nozzle throat heating combine to impose operational limits.
2. Large-scale models and therefore large-scale facilities are needed to provide inlet boundary-layer transition data at Mach numbers of current interest.
3. At velocities to 13,000 ft/sec, nozzle flow nonequilibrium does not present a problem in impulse facility testing. As flight velocities increase above 13,000 ft/sec, nonequilibrium considerations will assume increasing importance.
4. Conclusions on the nozzle and model starting time studies reveal that a minimum of 7 to 8 msec should be provided in order to obtain meaningful measurements. This is in contrast to the availability of only 2 to 3 msec in existing shock tunnels at a velocity of 13,300 ft/sec. Test times are generally adequate in the velocity range to 8700 ft/sec.

5. The complete SCRAMJET system test imposes the greatest demands on the facility with regard to performance, size, and test time. Complete similitude can only be attained with full-scale models.
6. Results of the feasibility of using air as the test gas in the AEDC hotshot Tunnel F may be summarized by stating that the use of air at reservoir temperatures to 7200°R did not result in significant oxygen depletion. Additional work is required in order to better define the contamination levels present.
7. The hotshot tunnel could be a very useful facility for probing slowly developing instabilities for which shock tunnel test times are inadequate. Test times in the range of 50 to 100 msec are possible in the AEDC hotshot Tunnel F, depending on facility geometry and defining an acceptable level of total pressure decay.
8. Analytical computations have revealed the potential capabilities of a high enthalpy test facility utilizing the exothermic reactions of oxides of nitrogen together with the added heat release obtained by burning acetylene in a constant volume reaction chamber as a method for heating. Total pressures to 30,000 psia can be generated and such a facility could have run times of the order of seconds.
9. Present facilities, both impulse type and certainly continuous flow, are limited in performance by nozzle throat heating limits.
10. Although not without problems, the hypersonic impulse facility which includes the shock tunnel, the hotshot tunnel, and the chemical shot facility can play an important role in airbreathing propulsion development.

REFERENCES

1. Zonars, D. "Building Hypersonic Vehicles from the Ground Up." Astronautics and Aeronautics, Vol. 3, No. 10, 1965, pp.54 through 58.
2. Cornell Aeronautical Laboratory "Description and Capabilities, Experimental Facilities Division, Hypersonic Shock Tunnel." Oct 1964.
3. Pergament, Harold S. "A Theoretical Analysis of Nonequilibrium Hydrogen-Air Reactions in Flow Systems" AIAA-ASME Hypersonic Ramjet Conference, Naval Ordnance Laboratory, April 23-25, 1963 (AIAA Paper 63-113).
4. Burke, A. F. and Wallace, J. E. "Aerothermodynamic Consequences of Nozzle Nonequilibrium." AEDC-TR-66-47, Feb 1966.
5. Lukasiewicz, J., Jackson, R., and Whitfield, Jack D. "Status of Development of Hotshot Tunnels at the AEDC." Paper presented at the AGARD Meeting on "High Temperature Aspects of Hypersonic Flow." Rhode-Saint-Genese, Belgium, April 3 - 6, 1962.
6. Griffith, B. J. and Clark, H. Lewis "Laminar Heat Transfer to Spherically Blunted Cones at Hypersonic Conditions" AIAA Journal, 2(3), 438-444 1964; Astronautics and Aeronautics, 2(3).
7. Stull, F. D. "Scramjet Combustion Prospects." Astronautics and Aeronautics 3(12) pp 45-52 (1965).

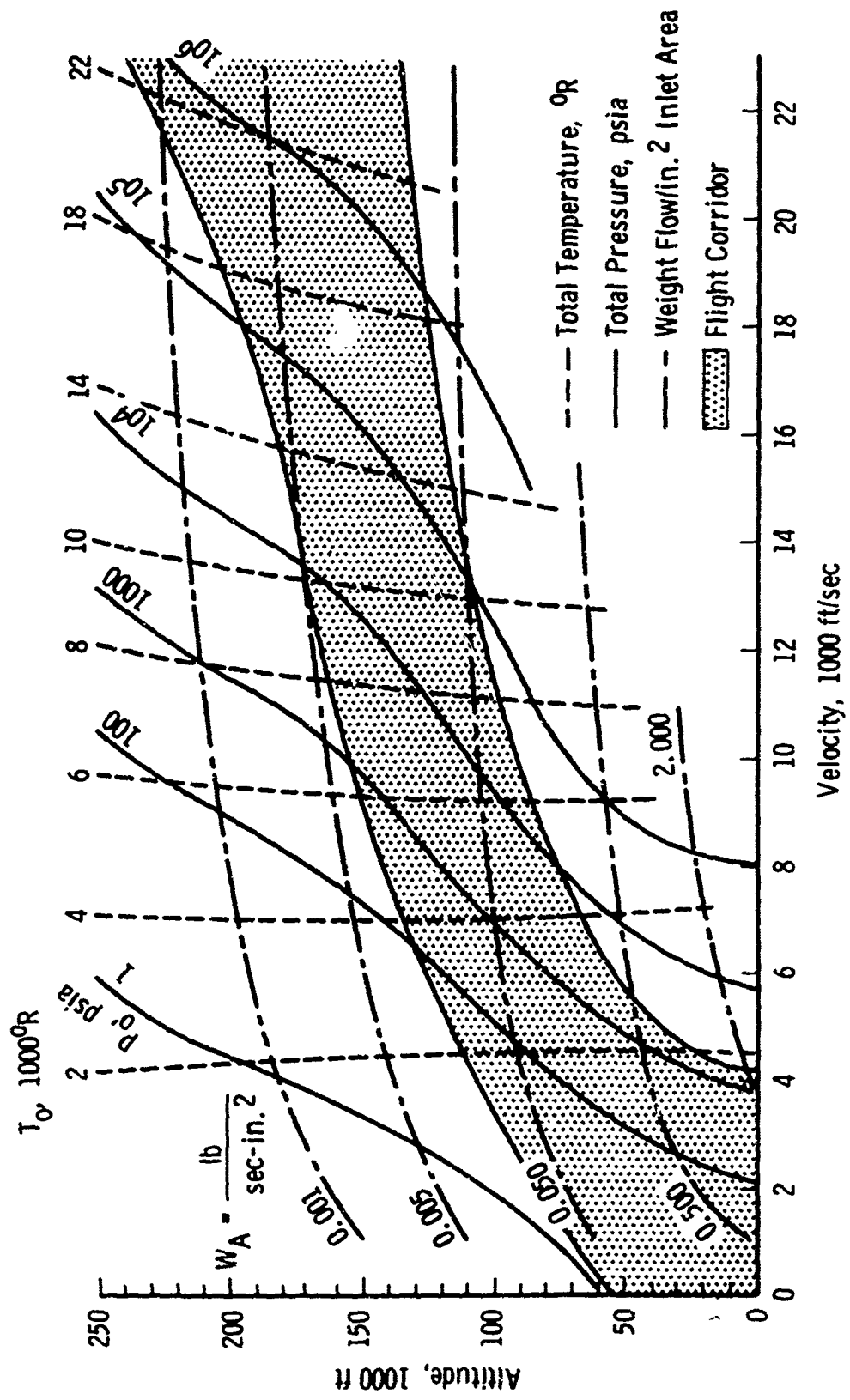
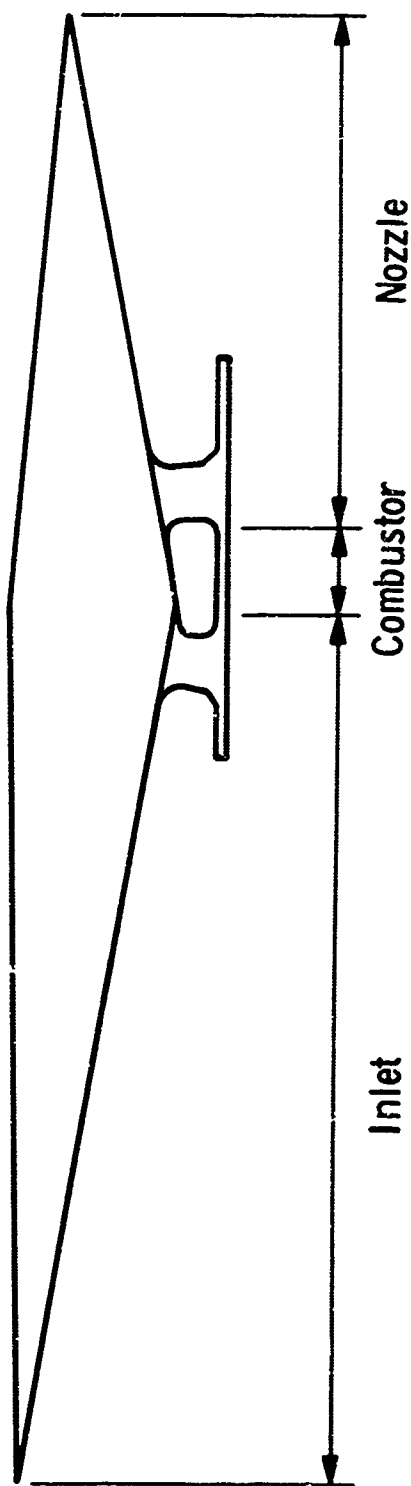


FIGURE 1 WIND TUNNEL RESERVOIR REQUIREMENTS FOR FLIGHT DUPLICATION



Primary Parameters for Significant Testing	Inlet	Combustors	Nozzles
	1. Mach Number 2. Reynolds Number 3. Wall to Stream Temperature Ratio 4. Gas Composition	1. Velocity 2. Static Temperature 3. Static Pressure 4. Gas Composition	1. Static Pressure 2. Static Temperature 3. Velocity 4. Gas Composition 5. Reynolds Number

FIGURE 2 SCRAMJET FACILITY TEST REQUIREMENTS

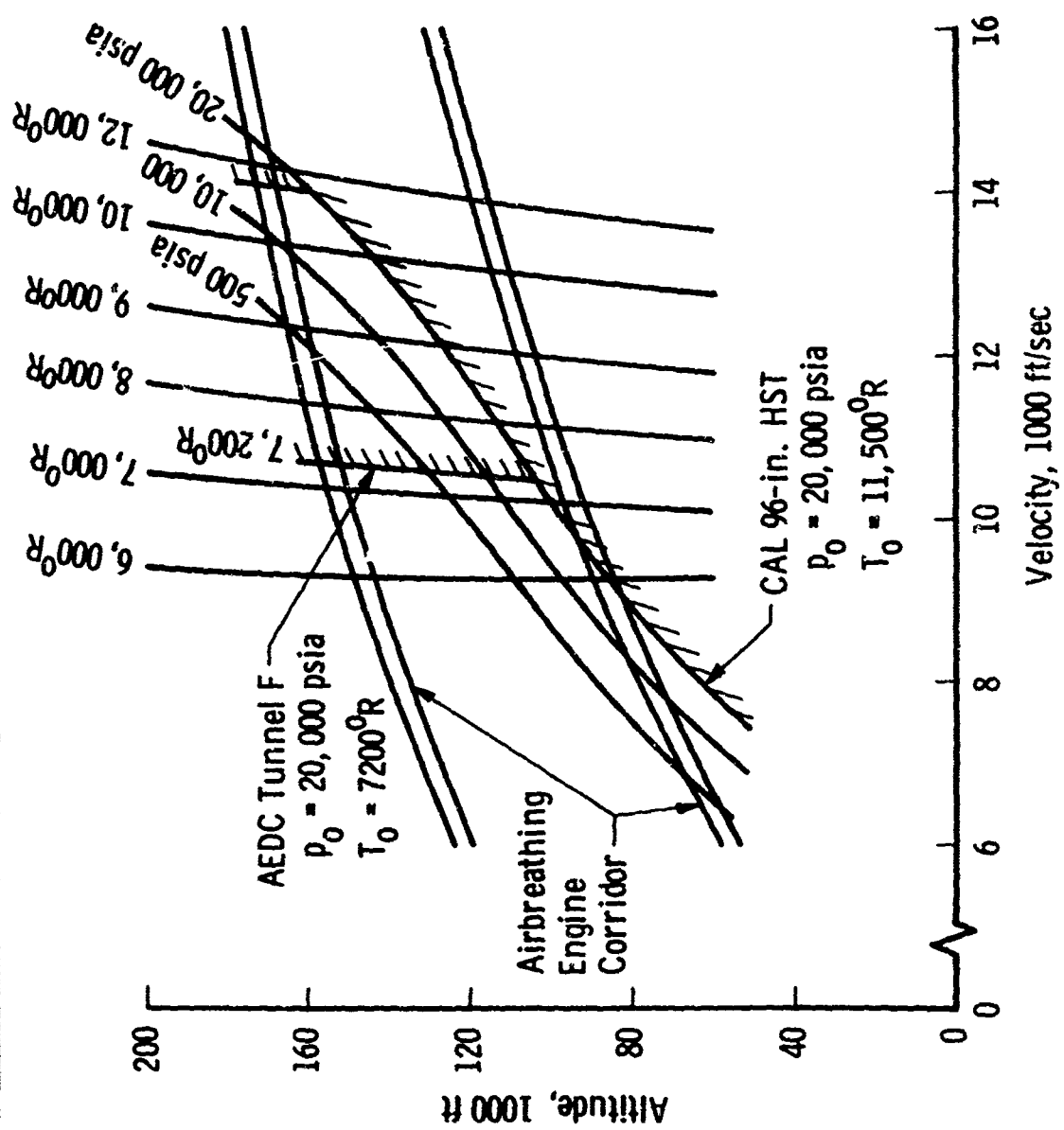


FIGURE 3 ALTITUDE VELOCITY DUPLICATION FOR THE CAL 96-IN. HYPERSONIC SHOCK TUNNEL AND THE AEDC TUNNEL F HOTSHOT TUNNEL

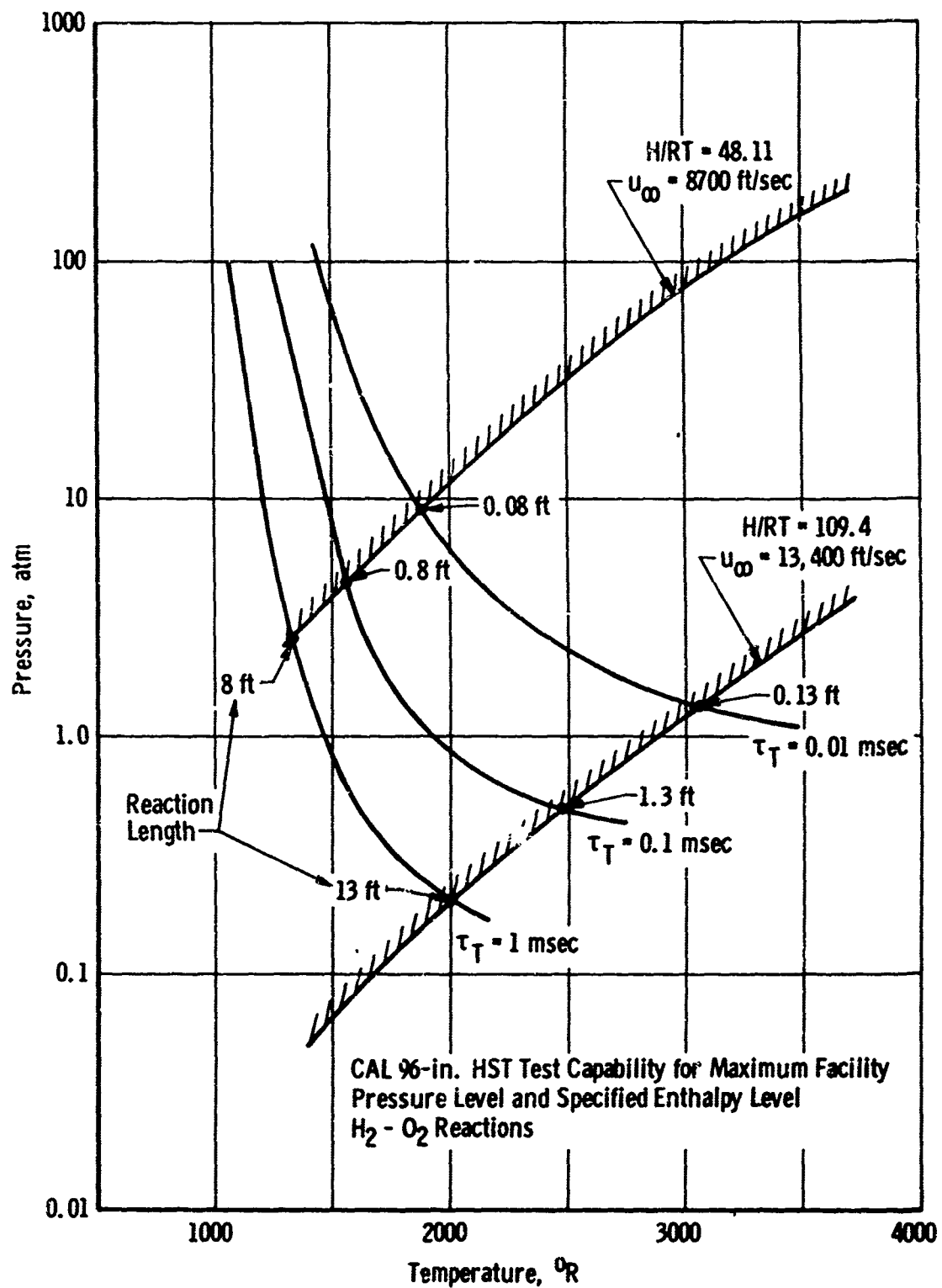


FIGURE 4 SCRAMJET COMBUSTOR INLET PRESSURE-INLET TEMPERATURE DUPLICATION CAPABILITIES FOR THE CAL 96-IN. HYPERSONIC SHOCK TUNNEL

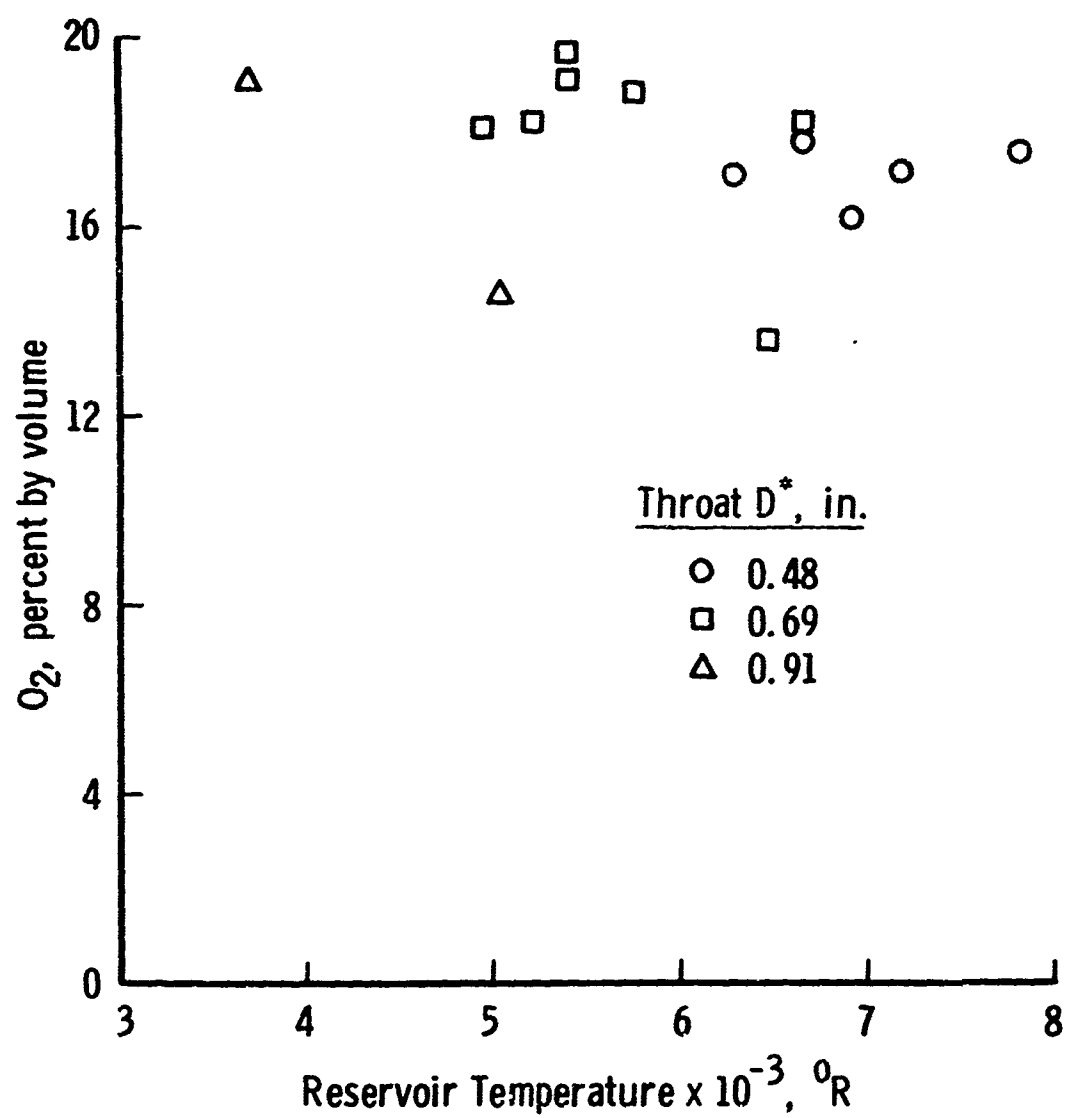


FIGURE 5 OXYGEN CONCENTRATION AS A FUNCTION OF RESERVOIR TEMPERATURE FOR AEDC HOTSHOT TUNNEL F

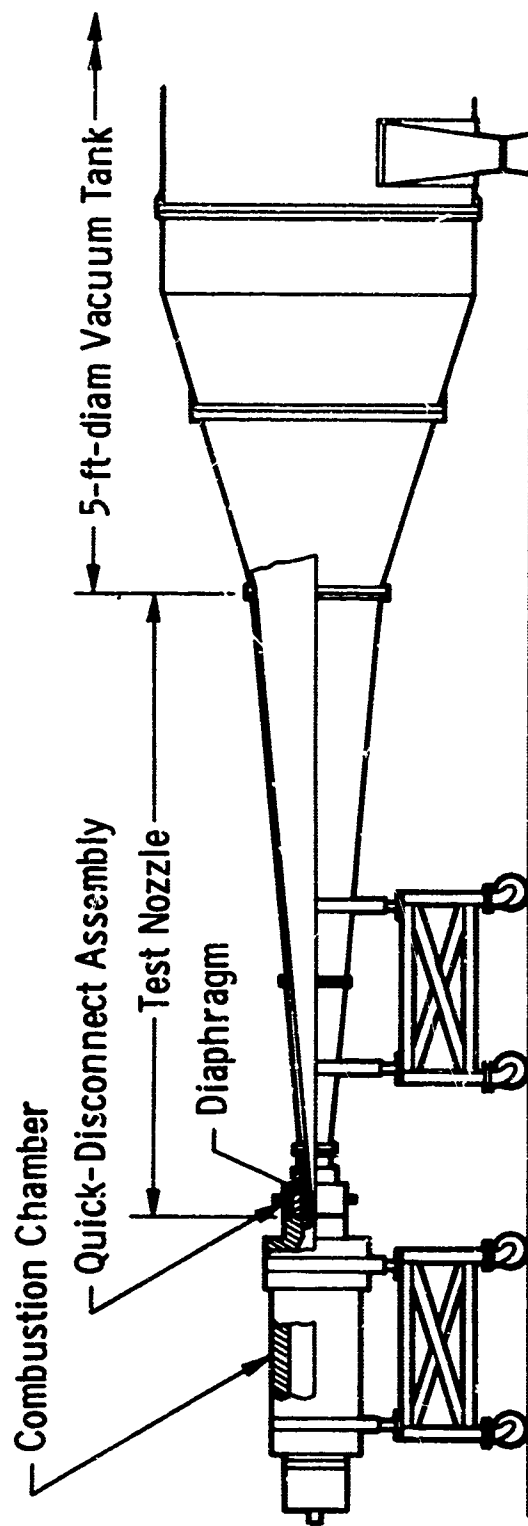


FIGURE 6 EXPERIMENTAL SETUP FOR "CHEMICAL SKOT TUNNEL" FACILITY

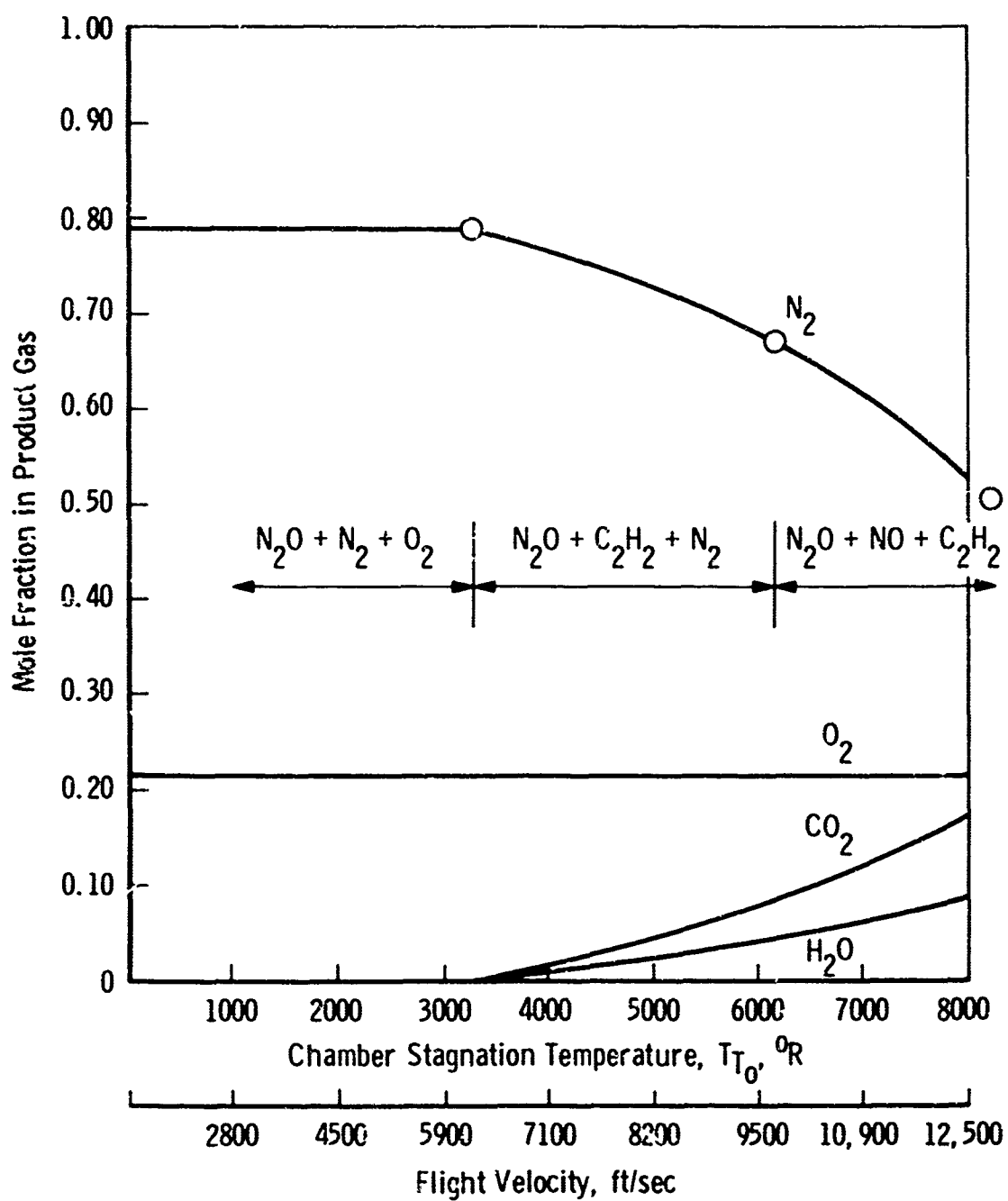


FIGURE 7 MOLE FRACTION OF CONSTITUENTS IN THE PRODUCT GAS AS A FUNCTION OF STAGNATION TEMPERATURE AND SIMULATED FLIGHT VELOCITY

**(U) SUPERSONIC COMBUSTION SIMULATION
FOR HIGH MACH NUMBER FLIGHT**

by
Robert G. Dunn
and
Emil J. Walk

**Fluid Dynamics Facilities Research Laboratory
Aerospace Research Laboratories
Wright-Patterson AFB, Ohio**



Robert G. Dunn

BIOGRAPHY

DR. ROBERT G. DUNN

Dr. Robert Garvin Dunn, Assistant Director of the Fluid Dynamics Facilities Research Laboratory, Aerospace Research Laboratories, and chief of the Facilities Research Branch, began his employment at ARL in January, 1951. His combined military and civilian Air Force career has been continuous since March, 1943.

Born in Lake Village, Arkansas, Dr. Dunn received his B.S. degree in chemical engineering at Louisiana State University in 1942. He received his M.S. degree in January, 1951, and his PhD degree in August, 1964, both at Ohio State University. During and after WWII, Dr. Dunn conducted low temperature tests on USAF aircraft engines at Fairbanks, Alaska, during the winters, and during the summers he commuted to Florida for similar experimental tests in the Air Force's Climatic Hangar. The test programs involved P-38 and B-17 through B-36, and turbojets, P-59 through F-84. Based on these investigations, Dr. Dunn perfected three specific systems for aircraft operation in extremely cold weather. The systems were: a priming system for rapid starting of reciprocating engines (resulted in an invention), a successful technique for the starting of turbojet engines with existing fuels, and a deicing system for turbojet engine fuel filters (resulted in two patents and general use in USAF military jet aircraft).

In January, 1951, he joined the Office of Air Research (now Office of Aerospace Research), where his duties were at first combustion and propulsion oriented. The major emphasis in this and succeeding positions gradually shifted to research and development on advanced facilities and techniques in the aeromechanics area.

Dr. Dunn assumed his present position in February, 1965. As Chief of the Facilities Research Branch, he is responsible for the planning and execution of a research program for the investigation of advanced facilities concepts in the aerosciences area. As Assistant Director of the Fluid Dynamics Facilities Research Laboratory, he assists in the management and technical direction of the research program on aerosciences facilities as well as the development and operation of major in-house facilities in this area.



Emil J. Walk

BIOGRAPHY

MR. EMIL J. WALK

Mr. Emil Johann Walk, Chief of the Hypersonic Facility Branch, Fluid Dynamics Facilities Research Laboratory, Aerospace Research Laboratories, began his employment in ARL in January, 1952. His combined civilian Air Force career has been continuous since May, 1946.

Born in Nuernberg, Bavaria, Germany, Mr. Walk graduated fourth in his class from the local high school and also served a four-year apprenticeship in tool making and design. He attended the Higher Technical Institute of State Bavaria where he graduated in the top ten of his class in mechanical engineering in 1928.

When he arrived at Wright Patterson AFB, in May, 1946, he worked as a member of an aerodynamics group on calculations and representatives of aerodynamic properties of air flow in wind tunnels, on air drying systems, and on specifications for the design of the AEDC supersonic wind tunnels. In the years 1950 and 1951, he was given the task to design the missing components for the project "Blowhard" and to initiate and follow through fabrication in the Experimental Engineering Shops of WADC. After the completion of this task, Mr. Walk transferred to the Aeronautical Research Laboratory as general engineer for research on and development of wind tunnel facilities. His position was converted to civil service on July 1, 1952. Since that time, his main endeavors have been the improvement of existing wind tunnel facilities and the development of more advanced methods to simulate or duplicate free flight conditions in ground test facilities.

Mr. Walk assumed his present position in February, 1965. As Chief of the Hypersonics Facilities Branch, he is responsible for the operation of the ARL hypersonic wind tunnels and other research facilities, the planning and design of new facilities or components, the development of electronics connected with the instrumentation and controls for these facilities, and the auxiliary utilities necessary for the experimental research.

ABSTRACT

Existing test facilities cannot provide the conditions necessary for adequate testing of complete hypersonic vehicle/engine configurations. A method of simulation is presented which makes possible the investigation of supersonic combustion for hypersonic flight under conditions essentially duplicating those of actual flight. The laboratory conditions necessary to simulate supersonic combustion occurring in vehicles moving with Mach numbers of 10 to 14 at altitudes of 100,000 to 200,000 feet are presented in the form of tables and graphs. All data are based on the assumption of 50% total pressure recovery in the inlet. The fuel considered is gaseous hydrogen. It is shown that several parameters occurring in flight can be duplicated in the laboratory. Methods for scaling experimental results to the flight conditions are discussed. It is concluded that separate investigation of Scramjet combustor problems, independent of hypersonic inlet studies, can yield highly significant results. It is further concluded that adequate supersonic combustion simulation under prolonged test conditions, in or near the region of flight Mach numbers 10 to 14, is not only possible but practical with facilities presently available and readily adaptable for this type of testing. It is feasible to duplicate all of the essential flight parameters in laboratory experiments, with combustor velocity and length used as scaling parameters to relate experimental results to the flight case.

CONTENTS

	<u>Page</u>
I. INTRODUCTION	1
II. SIMULATION OF SUPERSONIC COMBUSTION CONDITIONS	2
III. FLIGHT REGION CONSIDERED IN THIS STUDY	3
IV. FLIGHT CONDITIONS TO BE SIMULATED	4
A. External Conditions for the Flight Case	4
B. Internal Conditions for the Flight Case -- Air	4
C. Internal Conditions for the Flight Case -- Hydrogen	7
V. LABORATORY CONDITIONS REQUIRED FOR SIMULATION	9
A. Laboratory Test Conditions -- Air	9
B. Laboratory Test Conditions -- Hydrogen	10
C. Laboratory Test Conditions -- Hydrogen/Air Mixtures	11
VI. POTENTIALITIES FOR ADEQUATE SIMULATION IN GROUND TEST FACILITIES	12
VII. SCALING OF LABORATORY EXPERIMENTAL RESULTS TO FLIGHT CONDITIONS	16
VIII. CONCLUDING REMARKS	17
ACKNOWLEDGEMENTS	18
REFERENCES	19
TABLES	21
FIGURES	-

NOMENCLATURE

a	Speed of sound
A	Area
C_p	Molal heat capacity at constant pressure
h	Altitude
\dot{m}	Mass flow
m	Molecular weight
M	Mach number
p	Pressure ¹
R	Specific gas constant, $\frac{R}{m}$
\mathcal{R}	Universal gas constant
Re	Reynolds number per foot, $\frac{u\rho}{\mu}$
T	Temperature ¹
u	Velocity
α	Mass fraction
γ	Specific heat ratio
ϵ	Correction factor for real-gas expansion
ν	Dynamic viscosity
ρ	Density ¹

Subscripts

H_2	Hydrogen
t	Total conditions

- 1 Conditions in the ambient region (flight)
or air heater (laboratory)
- 2 Conditions in the inlet region (flight)
or stilling chamber (laboratory)
- 3 Conditions at combustor inlet (flight
and laboratory)
- 4 Conditions at combustor exit (flight and
laboratory)

Superscripts

- ()' (prime) Pertains to free-flight condition
(no prime) Pertains to laboratory test
condition
- * Pertains to conditions where the local
speed is equal to the local speed of sound

¹When used without the subscript t, the symbols p, T and ρ denote static conditions.

TABLES

- I External Flow-Stagnation Conditions
- II Combustor Entrance Conditions for the Flight Case (Air)
- III Combustor Entrance Conditions for the Laboratory Case (Air)

I. INTRODUCTION

It is generally recognized that supersonic combustion offers a strong potential as a propulsion mode for ramjet operation at hypersonic flight speeds -- resulting in the vehicles now referred to as Scramjets. It is also widely recognized that extensive studies in ground-test facilities are necessary if this new and promising technology is to advance rapidly. Existing test facilities are not capable of providing continuously the very high enthalpy test conditions required for complete duplication of the flight environment at the upper Mach numbers of interest. Continuous-type test facilities-- those providing seconds as opposed to milliseconds of test time -- are required for the investigation of a number of time-dependent aspects of supersonic combustion (such as the study of fuel-air mixing and combustion processes to achieve minimum combustion-zone length). In order to provide this type of facility within the present state-of-the-art, it is necessary to consider separate investigation of combustor and inlet problems and also to simulate rather than fully duplicate all parameters.

An investigation of this problem was undertaken in the Aerospace Research Laboratories in mid-1965. A study was initiated to determine the feasibility of utilizing the major components of one of ARL's hypersonic wind tunnels for supersonic combustion investigations. The specific project resulting in the development of an experimental facility for supersonic combustion studies in ARL is reported elsewhere (Ref. 1). However, a specific facility, with fixed geometry and other restrictions, is limited to a very narrow range of operation. For this reason, a separate investigation was initiated to define the laboratory conditions which would be required for the adequate simulation of supersonic combustion for high Mach number flight over a wide range of operation. It is this investigation which is described here. Fairly wide ranges of Mach number and altitude have been considered in order to provide flexibility in the choice of test conditions and comparison with free-flight.

The objectives of this paper are to define an adequate simulation treatment for the independent study of supersonic combustion and to establish the feasibility of such an approach.

The scope of this investigation encompasses examination of a number of flight conditions blanketing the flight corridor in the high Mach number region --

conditions prevailing at altitudes from 60,000 to 220,000 feet and Mach numbers 10 to 14. The laboratory combustor configuration envisioned is one in which the fuel and air streams move supersonically in the same direction, the fuel (hydrogen) being injected at the center of the air stream. The prolonged or continuous type of testing (seconds of test time) is assumed. The paper is concerned with direct investigation of the supersonic combustion problem independent of the hypersonic inlet problem, and particularly with the feasibility and desirability of taking such an approach. It is felt that the simulation treatment described will provide data directly applicable to the free-flight combustor problem. Key problems in the area of supersonic combustion for hypersonic flight are discussed in Reference 2.

The flight conditions considered in this paper may not correspond to any planned vehicle configuration or method of fuel injection, but the overall results of the approach described should lead to a better understanding of the phenomenon of supersonic combustion as applied to hypersonic flight.

II. SIMULATION OF SUPERSONIC COMBUSTION CONDITIONS

A type of simulation is considered in which the Mach number in the combustor is not an important parameter such as is the case in the usual aerodynamic investigation. In the supersonic combustion problem as applied to the Scramjet, the chemical composition of the flowing medium, the mixing of the streams of fuel and air, the chemical reactions taking place, and the reaction rates involved are the important factors to be considered. Investigation of the chemical aspects (composition, reactions, reaction rates) requires that the laboratory experiments be run under the same static pressure and temperature conditions as in the flight case, and also that the residence time in the combustor be the same. The flight parameters not duplicated in the laboratory will be the absolute velocities of the fuel and air streams; however, these velocities may be chosen such that the mixing time in the laboratory is nearly the same as that in flight. In summary, the primary parameters which require actual duplication in the study of supersonic combustion are the static temperature, static pressure, composition of the gases, residence time in the combustor,

and the velocity relationship between the mixing streams. These parameters can be duplicated in laboratory experiments without necessarily duplicating the absolute values of velocity of the two streams of fuel and air; the length of the combustor and the velocity then become scaling factors. This is the type of simulation considered in this paper.

Figure 1 illustrates the flow regions chosen for comparison of the free-flight and laboratory cases. Figure 1a is not intended to indicate a specific inlet configuration but is useful for discussion of the type of simulation under investigation. The airflow at Station 1 relative to the vehicle is hypersonic. The flow is decelerated through the inlet region to a lower but still supersonic Mach number at Station 3, the entrance to the combustor. Figure 1b illustrates a laboratory test configuration suitable for producing the desired flow conditions at Station 3 for the simulation of flight combustor characteristics. Station 2 represents here the laboratory air stagnation region. In the laboratory case the airflow is accelerated in a nozzle from Station 2 to Station 3 to obtain the desired combustor inlet conditions. At this point the fuel (gaseous hydrogen) is concentrically injected parallel to the airstream.

III. FLIGHT REGION CONSIDERED IN THIS STUDY

The flight conditions investigated in this study and to be simulated in the laboratory are those which would be experienced by vehicles in continuous flight at speeds in the neighborhood of Mach number 12.

In Figure 2 the points for which the flight conditions were calculated are indicated by small circles on the lines of constant free-flight Mach number. These points were chosen to blanket the continuous flight corridor in the range of Mach numbers 10 to 14.

The calculated results presented correspond to flight Mach numbers 10, 11, 12, 13 and 14 at geometric altitudes of 60,000 feet to 220,000 feet in intervals of 20,000 feet.

IV. FLIGHT CONDITIONS TO BE SIMULATED

A. External Conditions for the Flight Case

The only conditions external to the vehicle which were considered in the calculations for this investigation were the isentropic stagnation temperature, T_0 , and pressure, p_0 . Values of these parameters were needed for the calculation of the internal conditions for the flight case (air), discussed in the next section.

In order to calculate the flight stagnation conditions, a means to correct the ideal-gas flow data to real-gas data was required. The Sandia Corporation real-gas flow tables for dissociated air in equilibrium (Ref. 3) were used to calculate correction factors for the static-to-stagnation temperature ratios and pressure ratios. The data from this report were compared with ideal-gas flow ratios and the real-gas correction factors determined. The correction factors obtained were then plotted and cross-plotted to obtain a basis for reasonable interpolation and extrapolation. The isentropic stagnation temperatures and pressures for the chosen flight Mach numbers and altitudes are given in Table I and Figure 3.

B. Internal Conditions for the Flight Case -- Air

In the air intake of the vehicle the air experiences an increase in entropy while being decelerated through an oblique shock system to a lower Mach number. The geometry of the inlet determines the amount of the entropy increase and the corresponding drop in the stagnation pressure. In previous studies in which possible geometries of air inlets for hypersonic vehicles were discussed, it was found that a stagnation pressure reduction of 50% through the inlet can be reasonably expected in the flight Mach number range considered in this paper (Refs. 4, 5, 6). Therefore, the conditions at the combustor entrance were calculated with the assumption of 50% loss in stagnation pressure. The combustor entrance Mach numbers, Reynolds numbers, velocities and static conditions were determined for flight Mach numbers 10 to 14 at geometric altitudes of 60,000 to 220,000 feet and for static temperatures at the combustor entrance of 1400 to 2600°R in 200°R intervals. It was assumed throughout the calculations that the air remains in chemical equilibrium. For cases where values exceeded the ranges in pressures and temperatures

covered in the Sandia Corporation tables (Ref. 3), the curves of composition and thermodynamic properties of air given in Reference 7 were used as guidelines in the determination of real-gas correction factors. It is recognized that some of the extrapolations cannot be considered accurate and should be revised when data becomes available in the future. Since it is further recognized that chemical equilibrium may not exist in the inlet flow, the calculated data should be considered approximate, although sufficient, as a first step in the design of experimental test devices.

For the calculation of the combustor entrance conditions, a stagnation pressure was used which was one half of the flight stagnation pressure. This case was treated as if air at the reduced stagnation pressure were expanded isentropically through a convergent-divergent nozzle. In Table II and Figure 4 the velocity of the air entering the combustion chamber is presented as a function of altitude, flight Mach number and combustor entrance static temperature. Figure 5 is a plot of the combustor entrance static pressure and temperature versus altitude. These plotted results did not reveal any definite flight Mach number dependency within the range of flight Mach numbers considered (10 - 14). The relationship between the combustor entrance Mach number and the flight Mach number and altitude is depicted in Figures 6, 7, and 8. On the graph of Reynolds number as a function of static temperature at the combustor entrance (for various altitudes and flight Mach numbers) shown in Figure 9, several abrupt changes in slope may be noted. No attempt was made to fair the curves or, at this time, find physical reasons for the underlying behavior.

The procedures used to obtain the data discussed above were as follows:

- (1) The real static-to-stagnation temperature ratio is given by the assigned static temperature and the calculated flight stagnation temperature.

- (2) A correction factor, c , was taken from graphs based on data described in Section IV A for the appropriate values of T'_{t1} and $p'_{t3} = 0.5 p'_{t1}$.

- (3) The real-gas temperature ratio was divided by this correction factor to obtain the ideal-gas temperature ratio.

(4) The corresponding combustor entrance Mach number is

$$M'_3 = \left[5 \left(\frac{T'_{t1}}{T'_1} - 1 \right) \right]^{\frac{1}{2}}$$

which can also be obtained by interpolation from the tables of Reference 8.

(5) For this Mach number the ideal-gas static-to-stagnation pressure ratio is given by

$$\frac{p'_3}{p'_{t3}} = \left[1 + \frac{(M'_3)^2}{5} \right]^{-3.5}$$

which was converted to the real-gas pressure ratio by using a new correction factor which is again dependent on T'_{t1} and p'_{t3} .

(6) The static pressure p'_3 is then given by

$$p'_3 = \frac{p'_{t1}}{2} \left(\frac{p'_3}{p'_{t3}} \right)$$

(7) The local speed of sound a'_3 was taken from tables (Ref. 9) for values of T'_3 and p'_3 .

(8) The velocity is

$$u'_3 = M'_3 a'_3$$

(9) The dynamic viscosity μ was taken from Reference 9 for values of T'_3 .

(10) The density ρ'_3 was determined by the ideal-gas equation of state. Examination of typical compressibility factors indicated that this resulted in a maximum error of less than 0.2% in the region concerned.

(11) The Reynolds number per foot is given by

$$Re'_3 = \frac{\rho'_3 u'_3}{\mu'_3}$$

C. Internal Conditions for the Flight Case -- Hydrogen.

For comparison of laboratory test conditions with the corresponding flight conditions, calculations were made for an arbitrary set of static hydrogen conditions within the range of interest.

The hydrogen data were calculated for static temperatures $(T'_3)_{H_2}$ of 250, 500, 1000, 1500, 2000, 2500 and 3000°R. The velocities of the hydrogen were set at 0.5, 1.0 and 1.5 times the air velocities $(u'_3)_{air}$ given in Table II, which cover the entire range considered. The local velocity of sound is then given by

$$(a'_3)_{H_2} = \left[(\gamma'_3)_{H_2} R_{H_2} (T'_3)_{H_2} \right]^{1/2}$$

The specific heat ratio was taken from the tables of Reference 9 for moderate temperatures. For higher temperatures, up to 6000°R, the calculated molal heat capacity at constant pressure for hydrogen was taken from Reference 10 and converted to the specific heat ratio by

$$\gamma = \frac{C_p/R}{(C_p/R) - 1}$$

The effect of pressure on γ vanishes above 1000°R in the temperature range considered (Ref. 9), and, therefore, the values taken from Reference 10, which were calculated for one atmosphere, are assumed to be valid for any pressure at temperatures of 1000°R and higher.

With the assigned velocity and the local speed of sound, the Mach number is given. In this paper, only conditions such that the static pressures of the two streams (air and hydrogen) are equal, are considered. Hence, all pressures $(p'_3)_{air}$ from Table II are covered in these calculations. Since the specific heat ratio γ is in general the same for hydrogen and air, the flow tables of Reference 8 were used to obtain the static-to-stagnation temperature and pressure ratios. With these ratios and the Mach number obtained above, the approximate stagnation temperature $(T'_{t2})_{H_2}$ and pressure $(p'_{t2})_{H_2}$ can be obtained.

A specific heat ratio γ_{H_2} was determined for values of

$$\frac{(T'_{t2} + T'_3)_{H_2}}{2} \text{ and } \frac{(p'_{t2} + p'_3)_{H_2}}{2}$$

and the stagnation temperature and pressure calculated as follows:

$$(T'_{t2})_{H_2} = (T'_3)_{H_2} \left[\frac{\gamma_{H_2} - 1}{2} (M'_3)_{H_2}^2 + 1 \right]$$

and

$$(p'_{t2})_{H_2} = (p'_3)_{H_2} \left[\frac{\gamma_{H_2} - 1}{2} (M'_3)_{H_2}^2 + 1 \right]^{\frac{\gamma_{H_2}}{\gamma_{H_2} - 1}}$$

The calculated values of $(T'_{t2})_{H_2}$ and $(p'_{t2})_{H_2}$ were used to obtain new mean values between the stagnation and static conditions. For these new mean values a new specific heat ratio was determined and the calculations of $(T'_{t2})_{H_2}$ and $(p'_{t2})_{H_2}$ repeated. This iteration process was continued until the change in stagnation temperature and pressure approached zero.

The static density was calculated with the ideal-gas equation of state since the compressibility factor was so close to unity in the region considered, that the resulting error was negligible. The viscosity was obtained from Reference 9 and the Reynolds number calculated for the hydrogen flow at the combustor entrance.

In order to illustrate the effect of the hydrogen/air velocity ratio on the combustor entrance conditions for hydrogen, several graphs are presented in Figures 10 to 13. The specific flight conditions chosen for illustration are those corresponding to a flight Mach number of 12 at an altitude of 140,000 feet, where the velocity and static pressure of air at the combustor entrance were calculated to be 11,700 ft/sec and 2.05 psia, respectively. Figure 10 shows the variation of combustor entrance Mach number with static temperature. In the next

three figures are presented the static-to-stagnation pressure ratio, the stagnation temperature, and the Reynolds number, as a function of the static temperature. In all four figures, results are plotted for three velocity ratios, 0.5, 1.0 and 1.5.

V. Laboratory Conditions Required for Simulation

A. Laboratory Test Conditions -- Air

As mentioned earlier in this paper, for purposes of supersonic combustor simulation, the properties of the air which can be duplicated in present intermittent or continuous aerodynamic test facilities are the static temperature and static pressure at the combustor entrance. The range of data calculated was chosen with this in mind. By the choice of appropriate combustor entrance Mach numbers and stagnation conditions in the laboratory, the combustor entrance static conditions corresponding to those of a vehicle traveling at hypersonic speeds at altitudes between 100,000 and 200,000 feet can be duplicated. The total range treated is somewhat larger than can be attained with present ground test facilities in order (1) to give the calculated data, which are partially based on extrapolations of existing data, more accuracy and (2) to take account of further advancements in the state-of-the-art of testing methods.

For stagnation temperatures $T_{t1} = T_{t2} = T_{t3}$ of 2600°R to 4000°R, in intervals of 200°R, and static temperatures T_3 of 1000, 1500, 2000, 2200, 2400 and 2600°R, the Mach numbers M_3 were calculated. The real-gas effect on the value of M_3 was taken into account as before and the final M_3 was calculated by means of iteration. In Figure 14, the Mach numbers are plotted as a function of the static and stagnation temperatures.

With these calculated Mach numbers, the stagnation pressures p_{t2} and the inviscid area ratios A_3/A^* were calculated using the flow tables of Reference 7. To cover the range of the static pressures contained in Table II, the calculations were performed for static pressures p_3 of 0.01, 0.1, 1.0, 10, and 100 psia. The inviscid area ratios A_3/A^* are given in Figure 15 and the stagnation-to-static pressure ratios p_{t2}/p_3 in Figure 16, each as a function of T_3 and T_{t2} ; the absolute values of p_{t2} are illustrated in Figure 17.

In a manner similar to that described in Section IV A, the velocities u_3 and Reynolds numbers per foot Re_3 were calculated. The velocities and Reynolds numbers are presented in Figures 18 and 19, respectively, as a function of static and stagnation temperatures. The Reynolds numbers are plotted as the ratio Re_3/p_3 since the Reynolds number changes linearly with static pressure.

B. Laboratory Test Conditions -- Hydrogen

The laboratory test conditions chosen for hydrogen were tailored to fit the results obtained for air in the laboratory case. Calculations were made at several values of static pressure at the combustor entrance, these values being chosen to cover the same range of p_3 values as given for air in Section V A. The static temperatures $(T_3)_{H_2}$ chosen for the calculations are the same as assigned for the flight case in Section IV C. The velocities of the hydrogen at the combustor entrance, $(u_3)_{H_2}$, were selected to satisfy a specified relationship to the air velocity at this station. Caution must be exercised in the use of the results presented with respect to the static pressures $(p_3)_{H_2}$. Calculations were made for each $(p_3)_{H_2}$ value independent of $(p_3)_{air}$ values; however, it is noted that, in a given experiment, the condition

$$(p_3)_{H_2} = (p_3)_{air}$$

must be approximately satisfied to maintain supersonic flow conditions.

The computations for the combustor entrance conditions for hydrogen in the laboratory were carried out for the following p_3 , T_3 and u_3 values:

Static pressures $(p_3)_{H_2}$ of 0.01, 0.10, 1.0, 10 and 100 psia.

Static temperatures $(T_3)_{H_2}$ of 250, 500, 1000, 1500, 2000, 2500 and 3000°R.

Velocity ratios $\frac{(u_3)_{H_2}}{(u_3)_{air}}$ of 0.5, 1.0, 1.5 and 2.0 using the range of $(u_3)_{air}$ values from Table III.

As in Section IV C, the values for the specific heat ratios $(\gamma_3)_{H_2}$ were obtained from References 8 and 9 for all $(T_3)_{H_2}$ listed above. The same general procedure as indicated in

Section IV C was used to calculate Mach numbers, Reynolds numbers and stagnation pressures.

In order to illustrate, as in the flight case, the effect of hydrogen/air velocity ratio on the combustor entrance conditions for hydrogen, graphs are presented in Figures 20 to 24. The specific condition chosen for illustration is that of an air velocity of 6000 ft/sec. Figure 20 shows the variation of combustor entrance Mach number with static temperature. In the next four figures are presented the inviscid nozzle area ratio, the static-to-stagnation pressure ratio, the stagnation temperature, and the Reynolds-number-to-static-pressure ratio, as a function of the static temperature. In all five figures, results are plotted for four velocity ratios, 0.5, 1.0, 1.5 and 2.0.

It is pointed out that all of the data for hydrogen presented in this paper are based on an air velocity of 6000 ft/sec. A more general treatment of the hydrogen data, including graphs of all the calculated results, will be available in a forthcoming ARL technical report.

C. Laboratory Test Conditions -- Hydrogen-Air-Mixtures

The laboratory test conditions considered in this paper do not take into account the actual physical geometry of experimental apparatus. To apply the results to cases of specific physical geometries in the laboratory, the appropriate boundary layer may be computed, or determined from experimental data, and added to the dimensions indicated for the inviscid stream.

Cross-sectional areas of flow passages, mass flows of hydrogen, and gross mass fractions are based on inviscid flow conditions and an air mass flow of one pound per second. For mass flows other than those given, the cross-sectional areas of the inviscid streams can be scaled up or down in direct proportion to the mass flow rates.

The specific values of gross mass fraction chosen for this calculation are 0.005, 0.010, 0.015, 0.020 and 0.030. With the gross mass fraction defined as

$$(a_3)_{H_2} = \frac{\dot{m}_{H_2}}{\dot{m}_{H_2} + \dot{m}_{air}}$$

and the air mass flow fixed at one pound per second, the corresponding mass flows of hydrogen are

$$\dot{m}_{H_2} = \frac{(\alpha_3)_{H_2}}{1 - (\alpha_3)_{H_2}}$$

$(\alpha_3)_{H_2}$	0.005	0.010	0.015	0.020	0.030
$\dot{m}_{H_2} \frac{\text{lb mass}}{\text{sec}}$	0.005025	0.01010	0.01523	0.02041	0.03093

The nozzle exit area for hydrogen at the combustor entrance was calculated from the static density $(\rho_3)_{H_2}$, and the velocity $(u_3)_{H_2}$ obtained in Section V B, by the following relationship:

$$(A_3)_{H_2} = \frac{\dot{m}_{H_2}}{(\rho_3)_{H_2} (u_3)_{H_2}}$$

Similarly for air, the relationship for the nozzle exit area at the combustor entrance is

$$(A_3)_{\text{air}} = \frac{1}{(\rho_3)_{\text{air}} (u_3)_{\text{air}}}$$

The nozzle exit area for hydrogen is presented in Figure 25 as a function of the gross mass fraction $(\alpha_3)_{H_2}$, the static temperature of hydrogen and the hydrogen/air velocity ratio. The data shown in this figure corresponds to a specific condition where the air velocity is 6000 feet per second and the static pressure is 1 psia. Since $(A_3)_{H_2}$ is inversely proportional to $(p_3)_{H_2}$, the area for other static pressures, in the range of interest, is readily obtainable from this figure.

VI. Potentialities for Adequate Simulation in Ground Test Facilities

The choice of static conditions for the laboratory case was based on the present state-of-the-art of continuous hypersonic facilities. Zirconia air heaters are suitable to heat air to 4000°R and electric arc heaters exceed this temperature appreciably. Since serious problems still exist in the handling of oxidizing gas flows

at extreme temperatures, a value of 4000°R was chosen as maximum for the air stagnation temperature. Methods for obtaining stagnation pressures necessary for experimental supersonic combustion research do not present any problems up to 4000°R. The heating of the gaseous hydrogen can be accomplished with electrical resistance heaters using molybdenum as heating elements (Ref. 1). Molybdenum does not react with hydrogen at high temperature and has a high melting point (5200°R). The same material is suitable for the hydrogen injector nozzle; however, it must be protected on any surfaces which come in contact with high temperature air since molybdenum cannot be used in an oxidizing atmosphere. A newly developed coating permits the exposure of molybdenum to air at temperatures up to at least 4000°R.

It must be mentioned that there are economical factors in a practical facility design which impose other limitations on the simulation range obtainable. A fixed-geometry facility allows testing over only a very small range of combustor conditions; therefore, a number of replacement nozzles must be provided to widen the range of testing conditions.

Graphs have been presented in this paper showing the conditions to be expected at the combustor entrance in a typical hypersonic flight vehicle utilizing a supersonic combustion propulsion system. It is recognized that not all conditions within the ranges of these graphs can be simulated in any current-state-of-the-art facility. On the other hand, many conditions throughout the flight region chosen for this investigation can be simulated as described in this paper if the proper facility design choices are made.

We now consider a typical fixed-geometry design and the performance parameters to be expected. The design point considered for this example is a flight Mach number of 12 at an altitude of 120,000 feet. For a selected range of combustor entrance static temperatures

$$(T_3')_{\text{air}} = 1400 \text{ to } 2600^\circ\text{R}$$

the velocity and static pressure of air are shown in Figures 4 and 5, respectively, to be

$$(u_3')_{\text{air}} = 11,700 \text{ to } 10,800 \text{ ft/sec}$$

$$(p_3')_{\text{air}} = 1.8 \text{ to } 16 \text{ psia}$$

It is assumed that a facility is available to produce air at stagnation temperatures

$$(T_{t2})_{\text{air}} = 2600 \text{ to } 4000^\circ\text{R}$$

It is further assumed, for illustration purposes, that the air nozzle area ratio to be used is

$$\left(\frac{A_3}{A^*} \right)_{\text{air}} = 2.0$$

Figure 15 shows that, with such a facility, the combustor entrance static temperatures attainable are

$$(T_3)_{\text{air}} = 1400 \text{ to } 2250^\circ\text{R}$$

From Figures 14, 16 and 18, the Mach number, stagnation-to-static pressure ratio, and velocity are, respectively,

$$(M_3)_{\text{air}} = 3.3 \text{ to } 1$$

$$\left(\frac{p_{t2}}{p_3} \right)_{\text{air}} = 85 \text{ to } 2$$

$$(u_3)_{\text{air}} = 6100 \text{ to } 2200 \text{ ft/sec}$$

Selecting a combustor entrance static pressure of, for example,

$$(p_3)_{\text{air}} = 2 \text{ psia}$$

the required stagnation pressure of the air is found to be

$$(p_{t2})_{\text{air}} = 170 \text{ to } 4 \text{ psia}$$

In Figure 19 the corresponding Reynolds number is shown to be

$$(Re_3)_{\text{air}} = 1 \times 10^6 \text{ to } 1.7 \times 10^5$$

It is assumed that a heater is available for heating hydrogen up to 3000°R , that is,

$$(T_{t2})_{\text{H}_2} = 500 \text{ to } 3000^\circ\text{R}$$

Again for illustration purposes, it is assumed that the hydrogen nozzle area ratio to be used is

$$\left(\frac{A_3}{A^*}\right)_{H_2} = 1.015$$

For the specific case of

$$(u_3)_{air} = 6000 \text{ ft/sec and } \frac{(u_3)_{H_2}}{(u_3)_{air}} = 1.5$$

Figure 21 indicates that the combustor entrance static temperature for hydrogen is

$$(T_3)_{H_2} = 1800^\circ R$$

Figures 20, 22, and 23 show that the Mach number, static-to-stagnation pressure ratio and stagnation temperature, respectively, are

$$(M_3)_{H_2} = 1.15$$

$$\left(\frac{p_3}{p_{t2}}\right)_{H_2} = 0.44$$

$$(T_{t2})_{H_2} = 2240^\circ R$$

For a static pressure equal to that selected for the air

$$(p_3)_{H_2} = 2 \text{ psia}$$

the required stagnation pressure of the hydrogen is

$$(p_{t2})_{H_2} = 4.5 \text{ psia}$$

The corresponding Reynolds number is shown in Figure 24 to be

$$(Re_3)_{H_2} = 1.4 \times 10^5$$

As stated earlier, the most important parameters for simulation of supersonic combustion are the static temperature and pressure in the combustor. Duplication of the residence time in the combustor is essentially a matter of the proper combustor length. It is felt that duplication of these three parameters in the supersonic combustion process will provide a very adequate type of simulation in ground test facilities if the influence of stream velocity can be satisfactorily accounted for. In this simulation technique, for any given facility, there will be some degree of flexibility in the choice of air and fuel velocities; hence, it should be possible to choose an air/fuel velocity relationship which will provide a satisfactory simulation of the actual flight conditions. This is discussed in the next section.

VII. Scaling of Laboratory Experimental Results to Flight Conditions

In order that the results of laboratory experiments may find maximum application in the solution of flight problems related to supersonic combustion, scaling to the flight condition must be possible. In the type of simulation described in this paper, the key to adequacy of simulation and meaningful scaling lies in the choice of air and fuel velocities such that the mixing time in the laboratory is nearly the same as that in flight. Laboratory conditions may be chosen so that some desired relationship between the velocity of the fuel and the velocity of the air is the same as in flight; for example, this relationship may be the momentum ratio, velocity ratio, or velocity difference. It is readily apparent that the free-stream Reynolds number of the airflow must lie in the same range (i.e., laminar or turbulent) as for the flight case. The same is true for the hydrogen flow.

Under flight conditions expected for hypersonic vehicles the heterogeneous turbulent mixing process between two axisymmetric parallel streams is considered to be predominantly turbulent (Ref. 11). Since boundary layers, one in the air and one in the hydrogen fuel, will exist at the origin of mixing, the assumption can be made that one of these boundary layers is turbulent or that transition from laminar to turbulent flow occurs in

a negligibly short distance downstream. A discussion of both the laminar and turbulent mixing processes occurring in axisymmetric streams of air and hydrogen, in the presence of chemical reaction, is given in Reference 12.

It is noted that, in the cases considered here, the static pressure and temperature for a given stream (air or hydrogen) are the same in the laboratory and in flight; thus, the viscosity and density are also the same. Hence, the Reynolds number (per foot) is directly proportional to the velocity. In all of the laboratory cases described in this paper, the velocity of the air at the combustor entrance is much less (on the order of one half) than in the corresponding flight case. It follows that the Reynolds number of the airstream at the combustor entrance, in the laboratory cases, is reduced by the same amount (approximately one half) relative to the flight combustor Reynolds number. The same holds true for the hydrogen. Therefore, in using this simulation technique, care must be exercised to insure that the lower Reynolds number for the laboratory case (for either air or hydrogen) does not fall into the laminar flow region while the flow in the flight case is turbulent.

Let us consider further the example of a typical fixed-geometry design discussed in Section VI. It is assumed that laboratory conditions have been established such that the mixing process is the same as in the flight case. Hence, the air velocity and combustion-zone length are directly related and can be used for scaling to the flight conditions. Since the combustor velocity is lower in the laboratory case, then for the same residence time the laboratory combustor will be shorter than that in flight. The velocities in the earlier example are 11,700 ft/sec for the flight case and 6000 ft/sec for the laboratory case. The required flight combustor length for essentially complete combustion is, therefore, expected to be approximately $11,700/6000$ times the combustion-zone length determined in the laboratory.

VIII. Concluding Remarks

It is concluded that separate investigation of Scramjet combustor problems, independent of hypersonic inlet studies, can yield highly significant results. It is further concluded that adequate supersonic combustion

simulation under prolonged test conditions, in or near the region of flight Mach numbers 10 to 14, is not only possible but practical with facilities presently available and readily adaptable for this type of testing. This method of simulation will make possible the investigation of supersonic combustion for high Mach number flight under conditions essentially duplicating those of actual flight. Thus, it is feasible to duplicate all of the essential flight parameters in laboratory experiments, with combustor velocity and length used as scaling parameters to relate experimental results to the flight case.

The results of the calculations made in this investigation were quite extensive. It is contemplated that complete tables and graphs of the calculated data will be published in an ARL technical report.

As mentioned in the Introduction, an effort has been underway in the Aerospace Research Laboratories to develop an experimental facility for supersonic combustion studies. ARL's 30-inch hypersonic wind tunnel was modified to provide such a facility and is being used for experimental studies of supersonic combustion simulating flight conditions near Mach number 12 and 140,000 feet altitude.

ACKNOWLEDGEMENTS

We are indebted to Mr. D. G. Moore for valuable assistance in the preparation of tables and graphs and his critical review of computed results.

REFERENCES

1. Scaggs, N. E. and Dunn R. G., "Development of a Facility for Supersonic Combustion Simulation," presented at the AIAA Aerodynamics Testing Conference, Los Angeles, California, 21-23 September 1966.
2. Stull, F. D., "Scramjet Combustion Prospects," Astronautics and Aeronautics, 3, 48-52, December 1965.
3. Goin, K. L., "Mach Tables for Real Gas Equilibrium Flow of Air in Hypervelocity Test Facilities with Total Temperatures to 10,000°K," Sandia Corporation Monograph SCR-288, March 1961.
4. Ferri, A., "Possible Directions of Future Research in Air-Breathing Engines," presented at the Fourth AGARD Colloquium, Milan, Italy, 4-8 April 1960.
5. Ferri, A., "Review of Problems of Application of Supersonic Combustion," 7th Lanchester Memorial Lecture, Royal Aeronautical Society, London, England, 14 May 1964.
6. Ferri, A., "Supersonic Combustion Progress," Astronautics and Aeronautics, 2, 32-37, August 1964.
7. Moeckel, W. F. and Weston, K. E., "Composition and Thermodynamic Properties of Air in Chemical Equilibrium," NACA TN 4265, April 1958.
8. Ames Research Staff, "Equations, Tables, and Charts for Compressible Flow," NACA Report 1135, 1953.
9. Hilsenrath, J. et al, Tables of Thermodynamic and Transport Properties of Air, Argon, Carbon Dioxide, Carbon Monoxide, Hydrogen, Nitrogen, Oxygen and Steam, Pergamon Press, New York, 1960.
10. Wolfson, B. T. and Dunn, R. G., "Thermodynamic Properties of Selected Species Containing Carbon, Hydrogen, Oxygen, Helium and Argon," Aeronautical Research Laboratories, Report ARL 62-390, August 1962.

11. Ferri, A., Libby, P. A. and Zakkay, V., "Theoretical and Experimental Investigation of Supersonic Combustion," Aeronautical Research Laboratories, Report ARL 62-467, September 1962.
12. Ferri, A., Moretti, G. and Slutsky, S., "Mixing Processes in Supersonic Combustion," J. Soc. Indust. Appl. Math., 13, 229-258, March 1965.

TABLE I
EXTERNAL FLIGHT-STAGNATION CONDITIONS

Alt. kft	M _i	P _{ti} psia	T _{ti} °R
60	10	92740	6500
	11	210000	7560
	10	36700	6576
	11	101000	7670
	12	186000	8700
80	10	15400	6670
	11	35080	7750
	12	80800	8900
	13	167000	10000
	14	308000	11200
100	10	7018	6900
	11	16000	8000
	12	35675	9100
	13	80840	10400
	14	163600	11600
120	10	3350	7140
	11	7717	8230
	12	17360	9340
	13	37810	10830
	14	78620	12300
140	10	1635	7260
	11	3868	8320
	12	9062	9400
	13	20315	10900
	14	43390	12500
160	10	780	7100
	11	1930	8070
	12	4468	9200
	13	9800	10500
	14	20000	11900
180	10	329	6800
	11	824	7700
	12	1970	8670
	13	4406	9870
	14	8959	11100
200	10	130	6400
	11	312	7150
	12	731	8000
	13	1665	9000
	14	4218	10200
220	10	130	6400
	11	312	7150
	12	731	8000
	13	1665	9000
	14	4218	10200

TABLE II

COMBUSTOR ENTRANCE CONDITIONS FOR THE FLIGHT CASE (AIR)

Alt. kft	M _i	T _i °R	p _i psia	u _i ft/sec
60	10	1400	46.5	8816
		1600	74.15	8661
		1800	112.00	8506
		2000	161.92	8350
		2200	226.03	8195
	11	2400	306.50	8039
		2600	405.61	7884
		1400	48.48	9784
		1600	77.36	9642
		1800	116.83	9500
80	10	2000	168.94	9358
		2200	235.83	9215
		2400	319.78	9073
		2600	423.18	8931
	11	1400	15.70	8952
		1600	25.05	8794
		1800	37.83	8635
		2000	54.69	8476
		2200	76.35	8318
100	10	2400	103.53	8159
		2600	137.00	8001
	11	1400	18.68	10039
		1600	29.81	9894
		1800	45.02	9748
120	10	2000	65.09	9603
		2200	90.87	9458
		2400	123.22	9313
	11	2600	163.06	9167
	12	1400	5.61	11305
		1600	8.96	11168
		1800	13.53	11031
		2000	19.57	10893
		2200	27.31	10756
140	10	2400	37.03	10618
		2600	49.00	10481
	11	1400	16.31	10979
		1600	26.03	10842
		1800	39.32	10704
	12	2000	56.85	10567
		2200	79.36	10429
		2400	107.61	10292
		2600	142.40	10154
160	10	1400	5.79	9076
		1600	9.25	8918
		1800	13.96	8759
		2000	20.19	8601
	11	2200	28.18	8442
		2400	38.22	8283
		2600	50.57	8125
		1400	4.33	10311
		1600	6.90	10166
180	10	1800	10.43	10021
		2000	15.08	9876
		2200	21.05	9731
		2400	28.54	9586
	11	2600	37.77	9440
		1400	5.61	11305
		1600	8.96	11168
		1800	13.53	11031
		2000	19.57	10893
200	10	2200	27.31	10756
		2400	37.03	10618
		2600	49.00	10481
	11	1400	16.31	10979
		1600	26.03	10842
		1800	39.32	10704
		2000	56.85	10567
		2200	79.36	10429
		2400	107.61	10292
		2600	142.40	10154

TABLE II (CONT'D)

Alt. kft	M _i	T ₃ °R	p ₃ psia	u ₃ ft/sec
100	13	1400	5.92	12164
		1600	9.45	12032
		1800	14.28	11900
		2000	20.64	11768
		2200	28.82	11636
	14	2400	39.07	11504
		2500	51.74	11371
		1400	6.04	12848
		1600	9.65	12708
		1800	14.57	12569
120	10	2000	21.07	12440
		2200	29.41	12337
		2400	39.88	12197
		2600	52.77	12076
		1400	1.90	9513
	11	1600	3.03	9360
		1800	4.57	9207
		2000	6.61	9054
		2200	9.23	8900
		2400	12.52	8747
140	11	2600	16.57	8593
		1400	1.60	10679
		1600	2.56	10537
		1800	3.86	10395
		2000	5.58	10253
	12	2200	7.79	10110
		2400	10.57	9968
		2600	13.98	9826

Alt. kft	M _i	T ₃ °R	p ₃ psia	u ₃ ft/sec
120	12	1400	1.78	11671
		1600	2.86	11536
		1800	4.29	11401
		2000	6.19	11265
		2200	8.65	11130
	13	2400	11.73	10995
		2600	15.53	10860
		1400	1.83	12761
		1600	2.93	12632
		1800	4.42	12502
140	14	2000	6.39	12373
		2200	8.92	12243
		2400	12.10	12114
		2600	16.01	11984
		1400	2.10	13597
	15	1600	3.36	13471
		1800	5.07	13345
		2000	7.33	13219
		2200	10.23	13093
		2400	13.87	12967
160	16	2600	18.36	12841
		1400	0.62	9960
		1600	0.99	9811
		1800	1.49	9661
		2000	2.15	9512
	17	2200	3.01	9363
		2400	4.08	9213
		2600	5.40	9064

TABLE II (CONT'D)

Alt. kft	M _i	T ₃ °R	P ₃ psia	u ₃ ft/sec
140	11	1400	0.58	11115
		1600	0.93	10975
		1800	1.41	10835
		2000	2.03	10696
		2200	2.84	10556
	12	2400	3.85	10417
		2600	5.09	10277
		1400	0.59	12114
		1600	0.94	11980
		1800	1.42	11847
	13	2000	2.05	11713
		2200	2.86	11580
		2400	3.88	11446
		2600	5.14	11313
		1400	0.56	13428
	14	1600	0.89	13301
		1800	1.34	13173
		2000	1.94	13046
		2200	2.71	12918
		2400	3.86	12791
		2600	4.86	12663
		1400	0.56	14437
		1600	0.90	14313
		1800	1.36	14188
		2000	1.97	14064
		2200	2.75	13940
		2400	3.72	13816
		2600	4.93	13691

Alt. kft	M _i	T ₃ °R	P ₃ psia	u ₃ ft/sec
160	10	1400	0.23	10306
		1600	0.37	10160
		1800	0.56	10014
		2000	0.81	9868
		2200	1.13	9722
	11	2400	1.53	9576
		2600	2.02	9429
		1400	0.20	11461
		1600	0.32	11324
		1800	0.48	11187
	12	2000	0.69	11049
		2200	0.97	10912
		2400	1.31	10775
		2600	1.73	10638
		1400	0.22	12468
	13	1600	0.35	12336
		1800	0.53	12205
		2000	0.77	12073
		2200	1.07	11941
		2400	1.45	11810
		2600	1.92	11678
		1400	0.21	13755
		1600	0.33	13628
		1800	0.50	13502
		2000	0.72	13376
		2200	1.00	13249
		2400	1.36	13123
		2600	1.80	12996

TABLE II (CONT'D)

Alt. kft	M _i	T _j °P	p _j psia	u _j ft/sec
160	14	1400	0.20	14909
		1600	0.32	14785
		1800	0.48	14662
		2000	0.69	14539
		2200	0.97	14416
		2400	1.31	14293
		2600	1.73	14170
		1400	0.12	10174
		1600	0.20	10027
		1800	0.29	9879
180	10	2000	0.43	9732
		2200	0.60	9585
		2400	0.81	9438
		2600	1.07	9291
		1400	0.10	11451
		1600	0.17	11314
		1800	0.25	11178
		2000	0.36	11040
		2200	0.51	10902
		2400	0.69	10765
	12	2600	0.91	10628
		1400	0.10	12492
		1600	0.17	12361
		1800	0.25	12230
		2000	0.36	12098
		2200	0.50	11967
		2400	0.69	11835
		2600	0.91	11704

Alt. kft	M _i	T _j °R	p _j psia	u _j ft/sec
180	13	1400	0.10	13657
		1600	0.17	13531
		1800	0.24	13404
		2000	0.35	13277
		2200	0.49	13151
		2400	0.66	13024
		2600	0.88	12898
		1400	0.10	14708
		1600	0.15	14584
		1800	0.23	14461
200	10	2000	0.33	14338
		2200	0.46	14214
		2400	0.63	14091
		2600	0.83	13967
		1400	.07	9841
		1600	.11	9691
		1800	.16	9540
		2000	.23	9390
		2200	.33	9240
		2400	.44	9090
	11	2600	.59	8939
		1400	.06	11030
		1600	.10	10891
		1800	.15	10751
		2000	.22	10611
		2200	.31	10471
		2400	.41	10331
		2600	.55	10191

TABLE II (CONT'D)

Alt. kft	M ₁ '	T ₃ °R	P ₃ psi	u ₃ ft/sec
200	12	1400	.05	12170
		1600	.09	12037
		1800	.13	11905
		2000	.19	11772
	13	2200	.26	11639
		2400	.36	11506
		2600	.47	11373
		1400	.06	13247
	14	1600	.09	13118
		1800	.14	12991
		2000	.20	12863
		2200	.29	12735
220	12	2400	.39	12607
		2600	.51	12479
		1400	.05	14301
		1600	.09	14177
	13	1800	.13	14053
		2000	.19	13928
		2200	.26	13804
		2400	.35	13680
	14	2600	.47	13555
		1400	.04	9418
		1600	.06	9263
		1800	.10	9108
220	12	2000	.14	8953
		2200	.20	8798
		2400	.26	8644
		2600	.35	8489
	13	1400	.04	13617
		1600	.07	13491
		1800	.10	13364
		2000	.14	13238
	14	2200	.20	13111
		2400	.27	12985
		2600	.36	12858
		1400	.04	10335
	13	1600	.07	10190
		1800	.10	10044
		2000	.15	9899
		2200	.20	9753
	12	2400	.28	9608
		2600	.37	9462
		1400	.04	11435
		1600	.06	11297
	11	1800	.10	11160
		2000	.14	11023
		2200	.20	10886
		2400	.26	10749
	10	2600	.34	10612
		1400	.03	12591
		1600	.05	12461
		1800	.07	12330
	9	2000	.11	12200
		2200	.15	12096
		2400	.20	11939
		2600	.27	11808
	8	1400	.04	13617
		1600	.07	13491
		1800	.10	13364
		2000	.14	13238
	7	2200	.20	13111
		2400	.27	12985
		2600	.36	12858
		1400	.04	10335
	6	1600	.07	10190
		1800	.10	10044
		2000	.15	9899
		2200	.20	9753
	5	2400	.28	9608
		2600	.37	9462
		1400	.04	11435
		1600	.06	11297
	4	1800	.10	11160
		2000	.14	11023
		2200	.20	10886
		2400	.26	10749
	3	2600	.34	10612
		1400	.03	12591
		1600	.05	12461
		1800	.07	12330
	2	2000	.11	12200
		2200	.15	12096
		2400	.20	11939
		2600	.27	11808
	1	1400	.04	13617
		1600	.07	13491
		1800	.10	13364
		2000	.14	13238
	0	2200	.20	13111
		2400	.27	12985
		2600	.36	12858
		1400	.04	10335

TABLE III
COMBUSTOR ENTRANCE CONDITIONS FOR THE LABORATORY CASE (AIR)

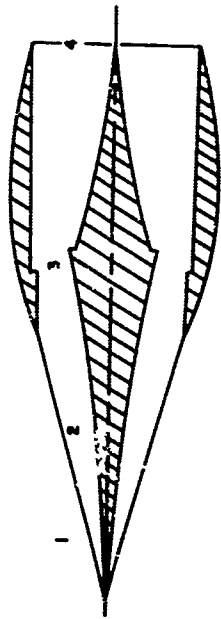
$P_3 = .01 + 100$ psia			$P_3 = .01$ psia		$P_3 = .1$ psia		$P_3 = 1$ psia		$P_3 = 10$ psia		$P_3 = 100$ psia		
T_3 °R	T_{t2} °R	M_3	u_3 ft/sec	Pt ₂ psia	Re ₃ 1/ft	Pt ₂ psia	Re ₃ 1/ft	Pt ₂ psia	Re ₃ 1/ft	Pt ₂ psia	Re ₃ 1/ft	Pt ₂ psia	Re ₃ 1/ft
1000	2600	3.12	4805	.4802	.673 ⁴	4.802	.673 ⁵	48.02	.673 ⁶	480.2	.673 ⁷	4802	.673 ⁸
	2800	3.23	4974	.5771	.697 ⁴	5.771	.697 ⁵	57.71	.697 ⁶	577.1	.697 ⁷	5771	.697 ⁸
	3000	3.41	5251	.7691	.736 ⁴	7.691	.736 ⁵	76.91	.736 ⁶	769.1	.736 ⁷	7691	.736 ⁸
	3200	3.58	5513	.9988	.772 ⁴	9.988	.772 ⁵	99.88	.772 ⁶	998.8	.772 ⁷	9988	.772 ⁸
	3400	3.75	5775	1.304	.809 ⁴	13.04	.809 ⁵	130.4	.809 ⁶	1304	.809 ⁷	13040	.809 ⁸
1500	3600	3.92	6037	1.684	.846 ⁴	16.84	.846 ⁵	168.4	.846 ⁶	1684	.846 ⁷	16840	.846 ⁸
	3800	4.07	6268	2.083	.878 ⁴	20.83	.878 ⁵	208.3	.878 ⁶	2083	.878 ⁷	20830	.878 ⁸
	4000	4.21	6483	2.533	.908 ⁴	25.33	.908 ⁵	253.3	.908 ⁶	2533	.908 ⁷	25330	.908 ⁸
	2600	2.08	3879	.0895	.280 ⁴	.8954	.280 ⁵	8.954	.280 ⁶	89.54	.280 ⁷	895.4	.280 ⁸
	2800	2.28	4252	.1243	.307 ⁴	1.243	.307 ⁵	12.43	.307 ⁶	124.3	.307 ⁷	1243	.307 ⁸
2000	3000	2.46	4588	.1664	.331 ⁴	1.664	.331 ⁵	16.64	.331 ⁶	166.4	.331 ⁷	1664	.331 ⁸
	3200	2.63	4905	.2224	.354 ⁴	2.224	.354 ⁵	22.24	.354 ⁶	222.4	.354 ⁷	2224	.354 ⁸
	3400	2.78	5185	.2846	.374 ⁴	2.846	.374 ⁵	28.46	.374 ⁶	284.6	.374 ⁷	2846	.374 ⁸
	3600	2.93	5464	.3653	.394 ⁴	3.653	.394 ⁵	36.53	.394 ⁶	365.3	.394 ⁷	3653	.394 ⁸
	3800	3.06	5707	.4514	.411 ⁴	4.514	.411 ⁵	45.14	.411 ⁶	451.4	.411 ⁷	4514	.411 ⁸
	4000	3.15	5875	.5220	.424 ⁴	5.220	.424 ⁵	52.20	.424 ⁶	522.0	.424 ⁷	5220	.424 ⁸
	2600	1.35	2882	.0289	.131 ⁴	.2894	.131 ⁵	2.894	.131 ⁶	28.94	.131 ⁷	289.4	.131 ⁸
	2800	1.58	3373	.0403	.153 ⁴	.4026	.153 ⁵	4.026	.153 ⁶	40.26	.153 ⁷	402.6	.153 ⁸
	3000	1.78	3800	.0533	.173 ⁴	.5329	.173 ⁵	5.329	.173 ⁶	53.29	.173 ⁷	532.9	.173 ⁸
	3200	1.94	4142	.0706	.188 ⁴	.7057	.188 ⁵	7.057	.188 ⁶	70.57	.188 ⁷	705.7	.188 ⁸
	3400	2.10	4484	.0914	.201 ⁴	.9141	.201 ⁵	9.141	.201 ⁶	91.41	.201 ⁷	914.1	.201 ⁸
	3600	2.27	4846	.1201	.220 ⁴	1.201	.220 ⁵	12.01	.220 ⁶	120.1	.220 ⁷	1201	.220 ⁸
	3800	2.38	5082	.1473	.235 ⁴	1.473	.235 ⁵	14.73	.235 ⁶	147.3	.235 ⁷	1473	.235 ⁸
4000		2.52	5380	.1845	.245 ⁴	1.845	.245 ⁵	18.45	.245 ⁶	184.5	.245 ⁷	1845	.245 ⁸

NOTE: To conserve space a group of digits followed by a numerical superscript n indicates that the decimal point should be moved n places to the right.
Example: .571⁶ = 571000

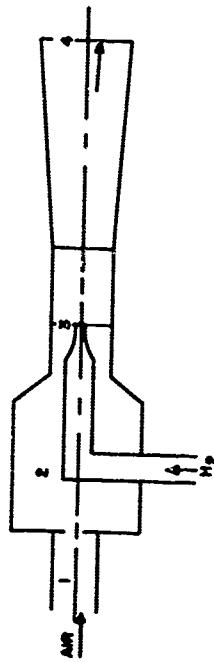
TABLE III (CONT'D)

$P_3 = .01 + 100 \text{ psia}$				$P_3 = .01 \text{ psia}$			$P_3 = .1 \text{ psia}$			$P_3 = 1 \text{ psia}$			$P_3 = 10 \text{ psia}$			$P_3 = 100 \text{ psia}$		
T_3 °R	T_{t2} °P	M_3	u_3 ft/sec	P_{t2} psia	Re_3 1/ft	P_{t2} psia	Re_3 1/ft	P_{t2} psia	Re_3 1/ft	P_{t2} psia	Re_3 1/ft	P_{t2} psia	Re_3 1/ft	P_{t2} psia	Re_3 1/ft			
2200	2600	1.06	2368	.0198	.925 ³	.1983	.925 ⁴	1.983	.925 ⁵	19.83	.925 ⁶	198.3	.925 ⁷					
	2800	1.31	2927	.0275	.114 ⁴	.2748	.114 ⁵	2.748	.114 ⁶	27.48	.114 ⁷	274.8	.114 ⁸					
	3000	1.52	3396	.0367	.133 ⁴	.3669	.133 ⁵	3.669	.133 ⁶	36.69	.133 ⁷	366.9	.133 ⁸					
	3200	1.71	3820	.0490	.149 ⁴	.4897	.149 ⁵	4.897	.149 ⁶	48.97	.149 ⁷	489.7	.149 ⁸					
	3400	1.86	4155	.0624	.162 ⁴	.6239	.162 ⁵	6.239	.162 ⁶	62.39	.162 ⁷	623.9	.162 ⁸					
	3600	2.02	4520	.0782	.175 ⁴	.7825	.175 ⁵	7.825	.175 ⁶	78.25	.175 ⁷	782.5	.175 ⁸					
2400	3800	2.16	4825	.1020	.189 ⁴	1.020	.189 ⁵	10.20	.189 ⁶	102.0	.189 ⁷	1020	.189 ⁸					
	4000	2.29	5116	.1267	.200 ⁴	1.267	.200 ⁵	12.67	.200 ⁶	126.7	.200 ⁷	1267	.200 ⁸					
	2600	0.72	1675	.0139	.571 ³	.1392	.571 ⁴	1.392	.571 ⁵	13.92	.571 ⁶	139.2	.571 ⁷					
	2800	1.03	2396	.0191	.817 ³	.1908	.817 ⁴	1.908	.817 ⁵	19.08	.817 ⁶	190.8	.817 ⁷					
	3000	1.26	2931	.0254	.100 ⁴	.2541	.100 ⁵	2.541	.100 ⁶	25.41	.100 ⁷	254.1	.100 ⁸					
	3200	1.46	3396	.0335	.116 ⁴	.3348	.116 ⁵	3.348	.116 ⁶	33.48	.116 ⁷	334.8	.116 ⁸					
2600	3400	1.65	3838	.0444	.131 ⁴	.4437	.131 ⁵	4.437	.131 ⁶	44.37	.131 ⁷	443.7	.131 ⁸					
	3600	1.81	4210	.0570	.144 ⁴	.5703	.144 ⁵	5.703	.144 ⁶	57.03	.144 ⁷	570.3	.144 ⁸					
	3800	1.96	4559	.0722	.155 ⁴	.7223	.155 ⁵	7.223	.155 ⁶	72.23	.155 ⁷	722.3	.155 ⁸					
	4000	2.11	4908	.0938	.167 ⁴	.9379	.167 ⁵	9.379	.167 ⁶	93.79	.167 ⁷	937.9	.167 ⁸					
	2600	0.00	0	.0100	0	1.000	0	1.000	0	10.00	0	100.0	0					
	2800	0.71	1715	.0138	.514 ³	.1379	.514 ⁴	1.379	.514 ⁵	13.79	.514 ⁶	137.9	.514 ⁷					
2800	3000	0.99	2391	.0183	.717 ³	.1834	.717 ⁴	1.834	.717 ⁵	18.34	.717 ⁶	183.4	.717 ⁷					
	3200	1.24	3164	.0248	.949 ³	.2480	.949 ⁴	2.480	.949 ⁵	24.80	.949 ⁶	248.0	.949 ⁷					
	3400	1.42	3429	.0317	.103 ⁴	.3166	.103 ⁵	3.166	.103 ⁶	31.66	.103 ⁷	316.6	.103 ⁸					
	3600	1.59	3840	.0405	.115 ⁴	.4054	.115 ⁵	4.054	.115 ⁶	40.54	.115 ⁷	405.4	.115 ⁸					
	3800	1.73	4178	.0504	.125 ⁴	.5044	.125 ⁵	5.044	.125 ⁶	50.44	.125 ⁷	504.4	.125 ⁸					
	4000	1.88	4540	.0637	.136 ⁴	.6370	.136 ⁵	6.370	.136 ⁶	63.70	.136 ⁷	637.0	.136 ⁸					

a. FLIGHT CASE



b. LABORATORY CASE



LEGEND

- 1 Ambient region (flight) or air heater (laboratory)
- 2 Inlet region (flight) or mixing chamber (laboratory)
- 3 Combustor inlet (flight and laboratory)
- 4 Combustor discharge (flight and laboratory)

Fig. 1. Typical Geometries for Flight and Laboratory Cases

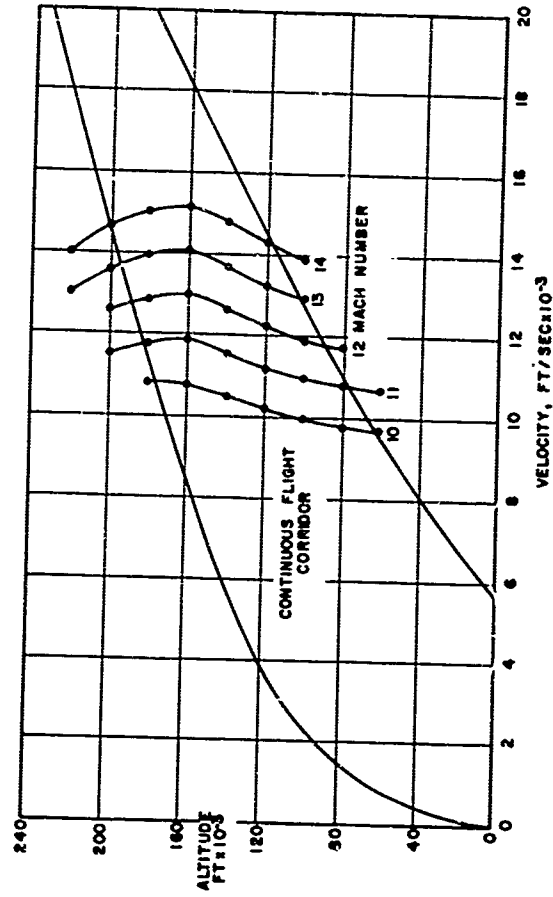


Fig. 2. Flight Regime Under Study for Simulation

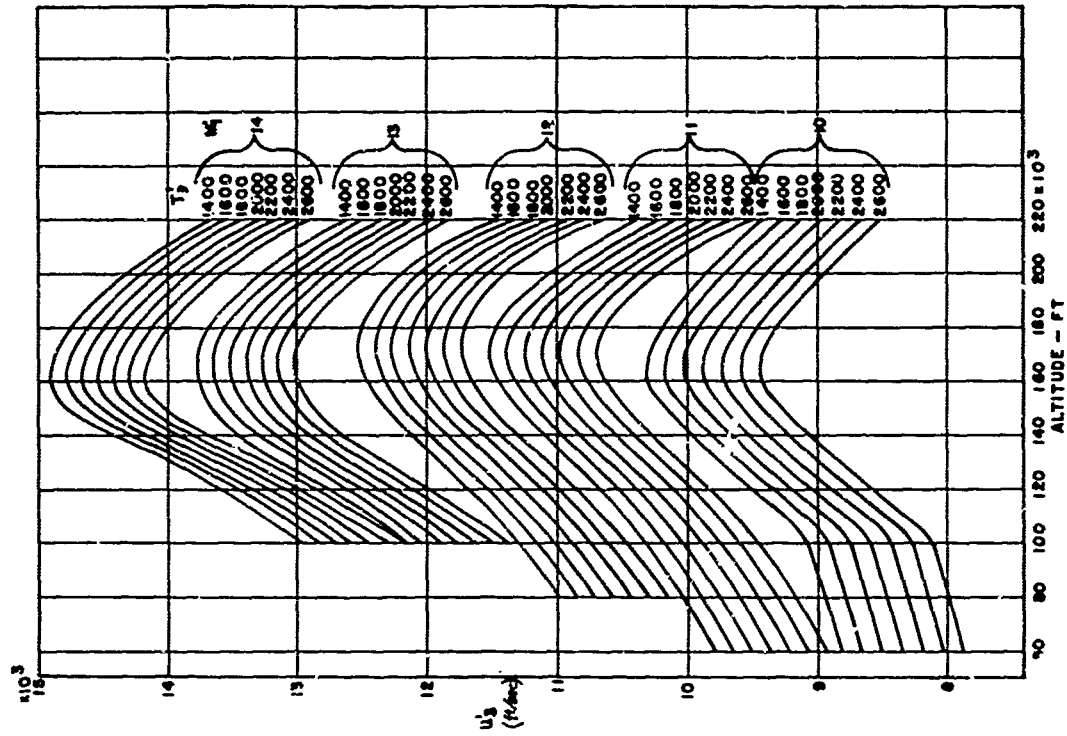


Fig. 4. Combustor Entrance Conditions for the Flight Case (Air) -- Velocity as a Function of Altitude, Flight Mach Number and Static Temperature

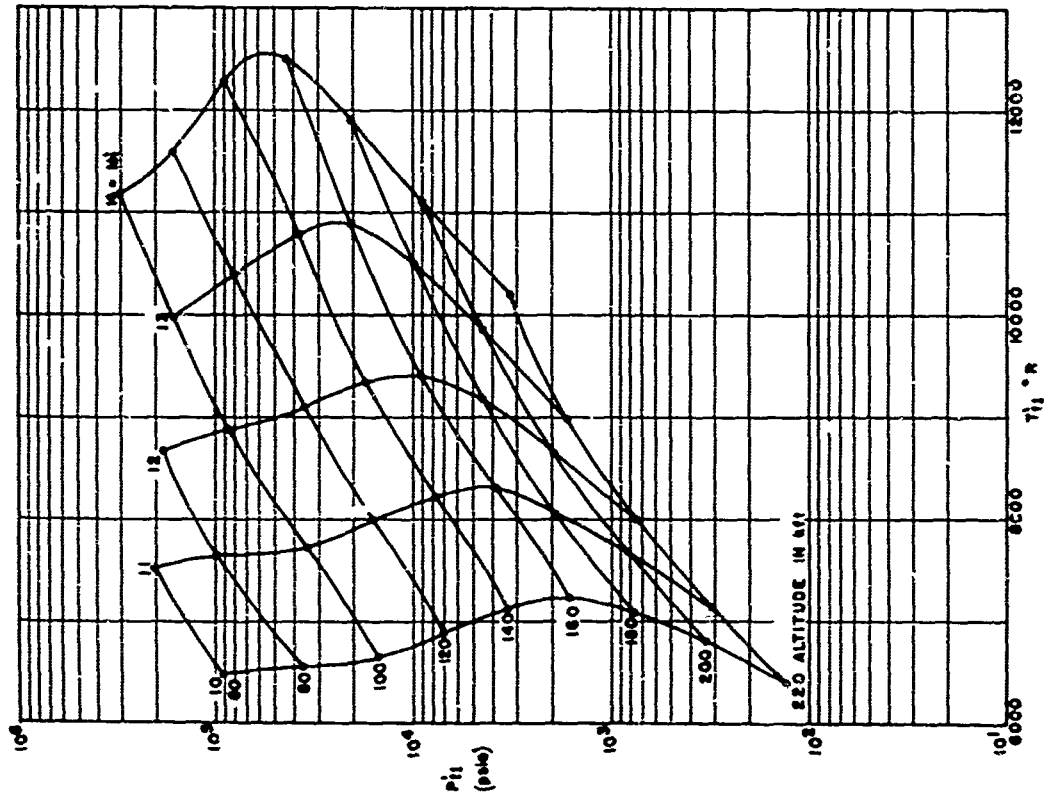


Fig. 3. External Conditions for the Flight Case -- Stagnation Pressure and Temperature as a Function of Altitude and Flight Mach Number

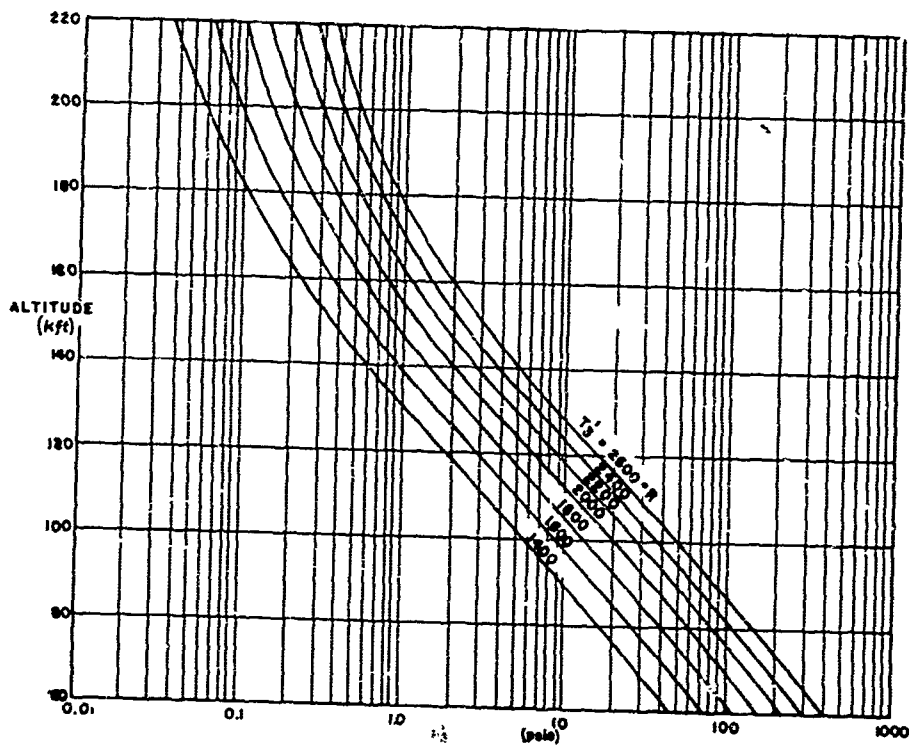


Fig. 5. Combustor Entrance Conditions for the Flight Case (Air) -- Static Pressure as a Function of Altitude and Static Temperature for Flight Mach Numbers 10 to 14.

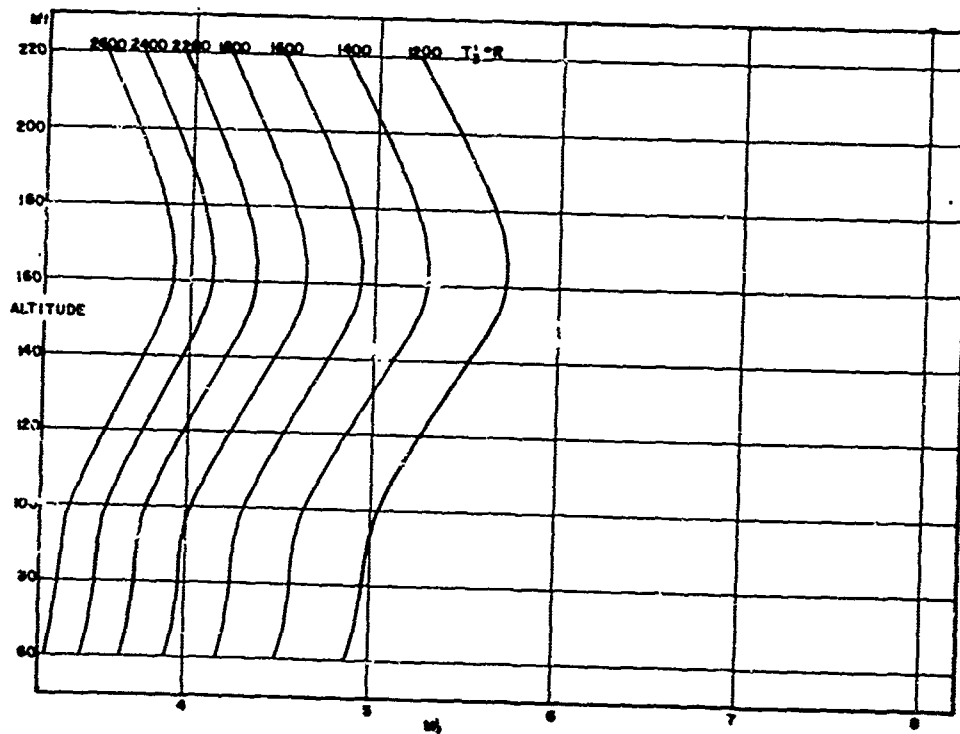


Fig. 6. Combustor Entrance Conditions for the Flight Case (Air) -- Combustor Mach Number as a Function of Altitude and Static Temperature for a Flight Mach Number of 10

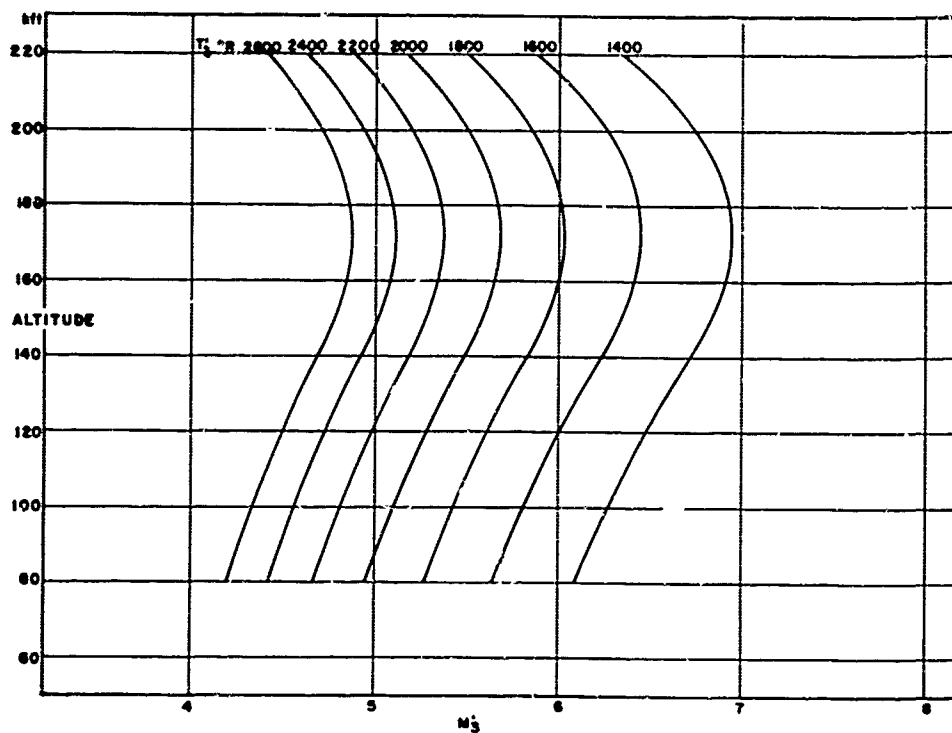


Fig. 7 Combustor Entrance Conditions for the Flight Case (Air) -- Combustor Mach Number as a Function of Altitude and Static Temperature for a Flight Mach Number of 12

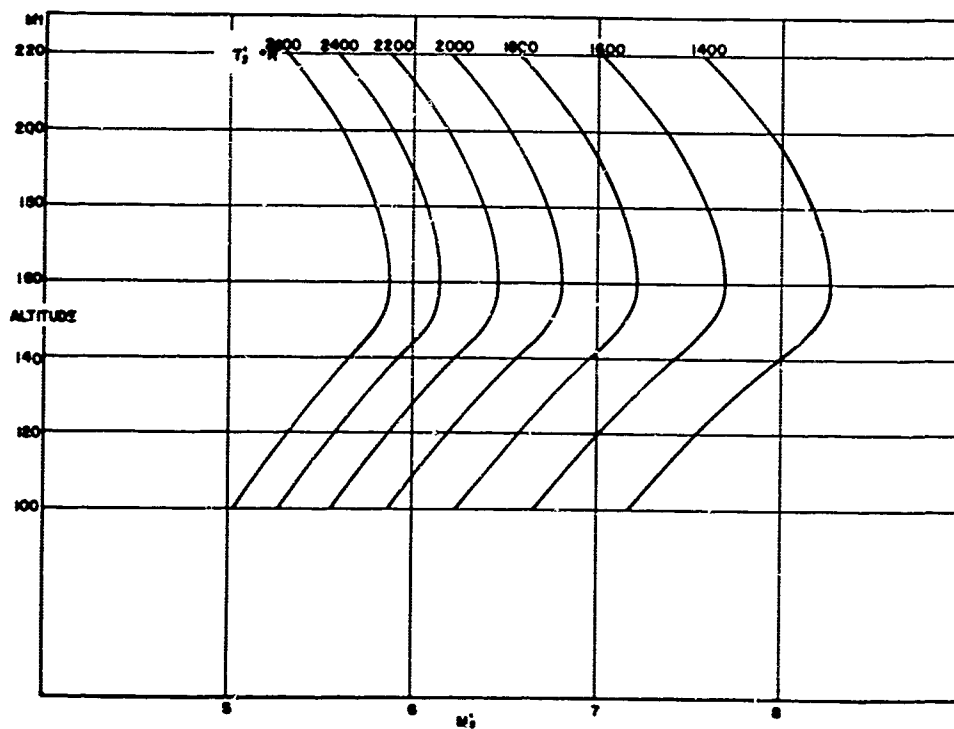


Fig. 8. Combustor Entrance Conditions for the Flight Case (Air) -- Combustor Mach Number as a Function of Altitude and Static Temperature for a Flight Mach Number of 14

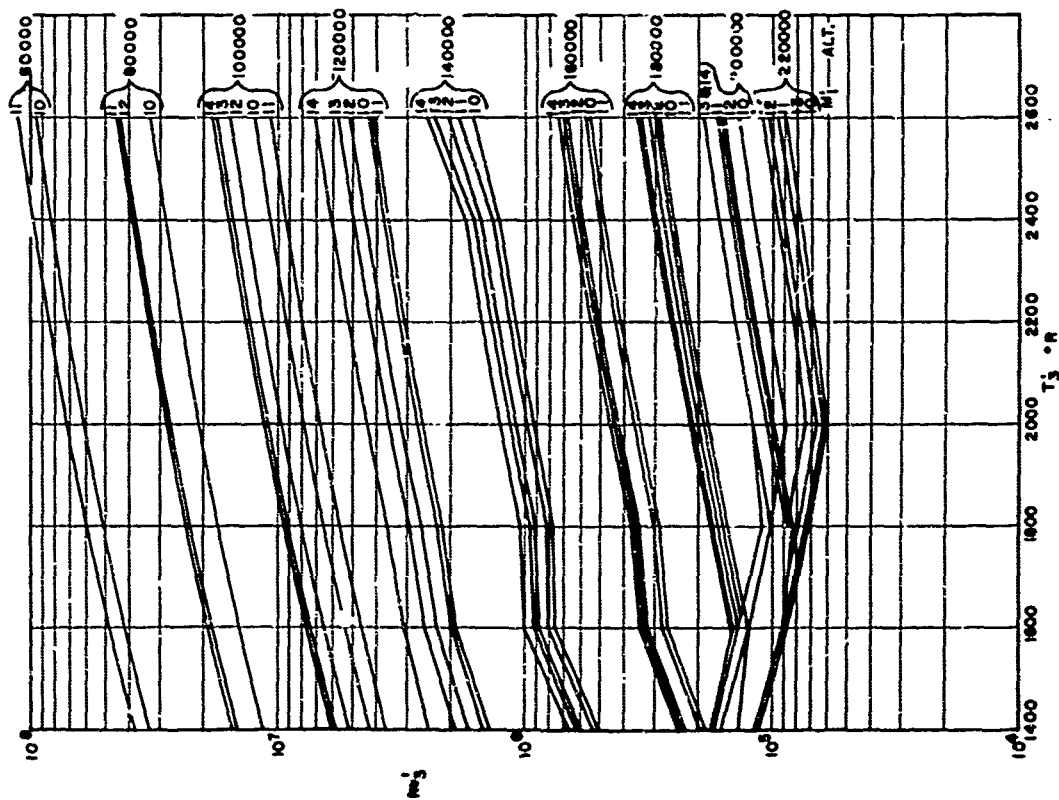


Fig. 9. Combustor Entrance Conditions for the Flight Case (Air) -- Reynolds Number per Foot as a Function of Static Temperature, Flight Mach Number and Altitude

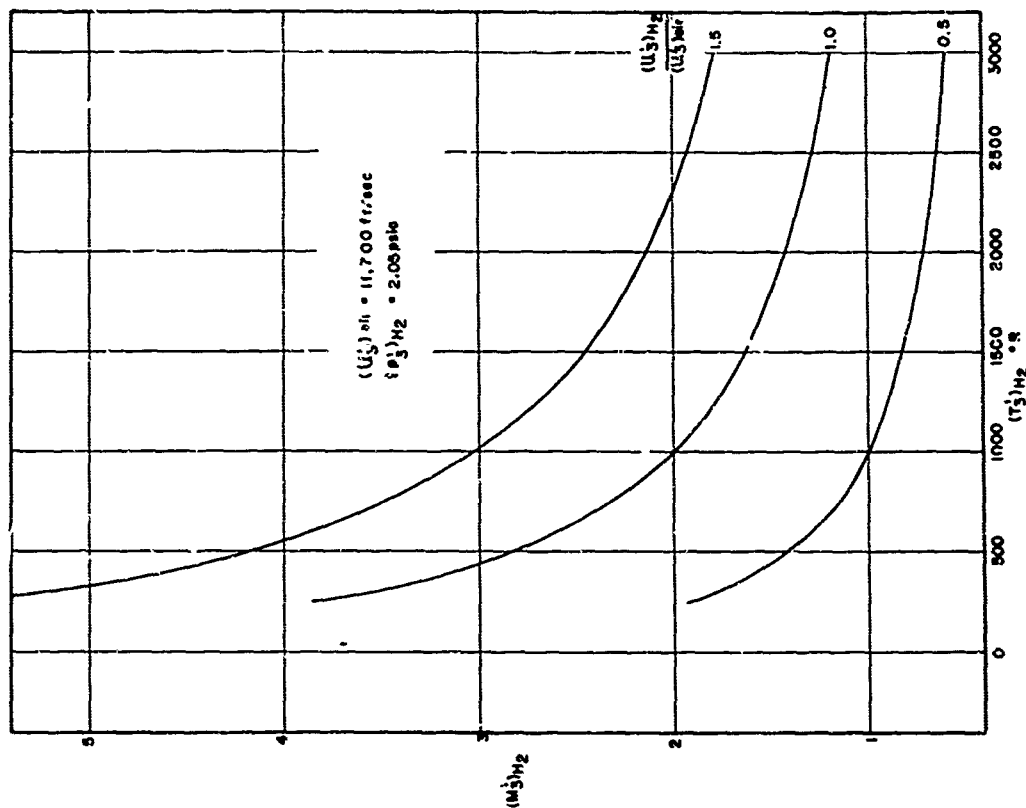


Fig. 10. Combustor Entrance Conditions for the Flight Case (Hydrogen) -- Mach Number as a Function of Static Temperature and Velocity Ratio

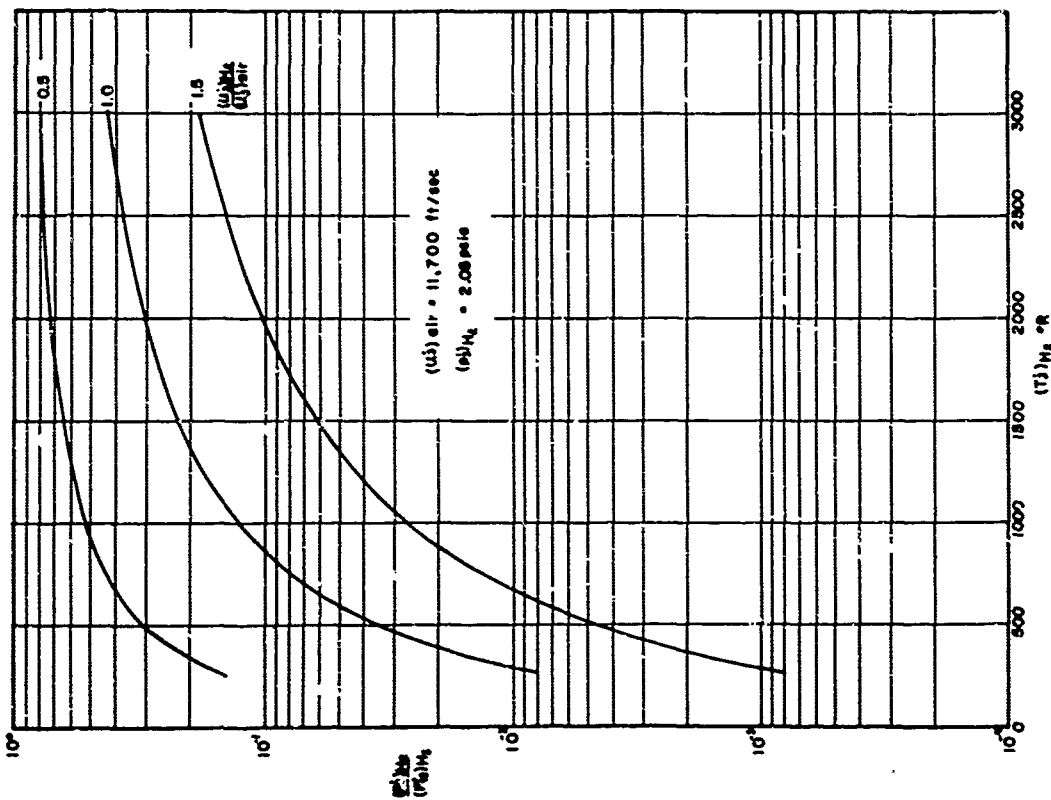


Fig. 11. Combustor Entrance Conditions for the Flight Case (Hydrogen) -- Static-to-Stagnation Pressure Ratio as a Function of Stagnation Temperature and Velocity Ratio

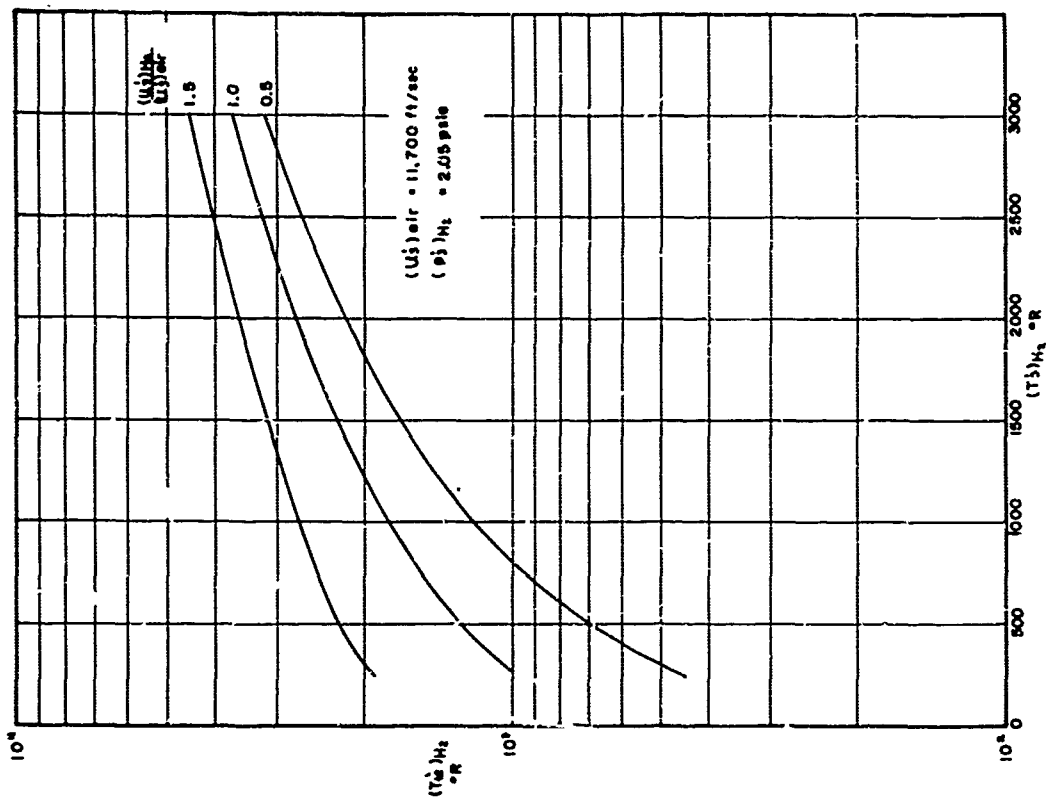


Fig. 12. Combustor Entrance Conditions for the Flight Case (Hydrogen) -- Stagnation Temperature as a Function of Static Temperature and Velocity Ratio

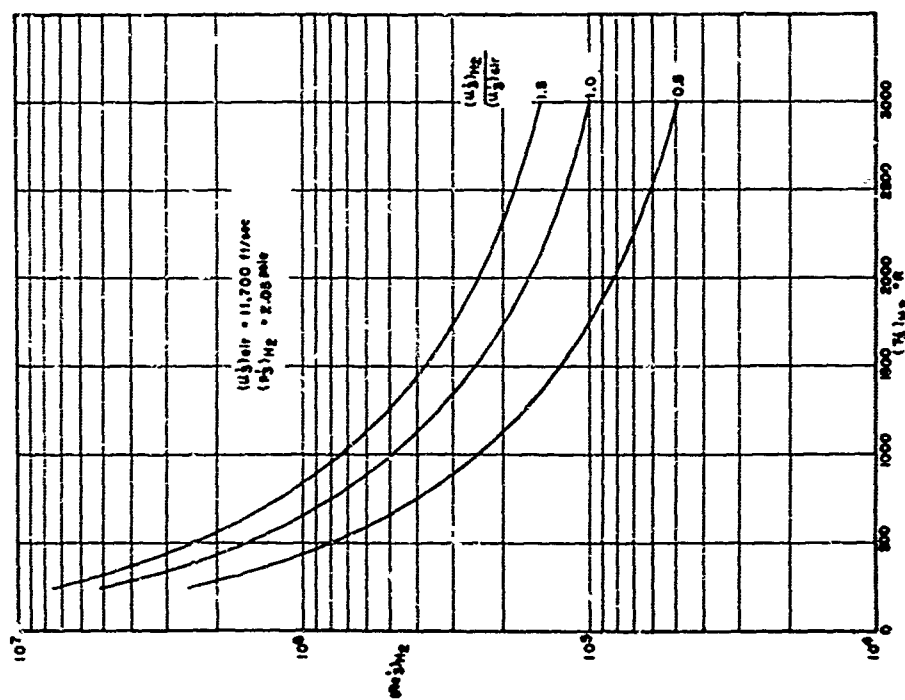


Fig. 13. Combustor Entrance Conditions for the Flight case (Hydrogen) -- Mach Number per Foot as a Function of Static Temperature and Velocity Ratio

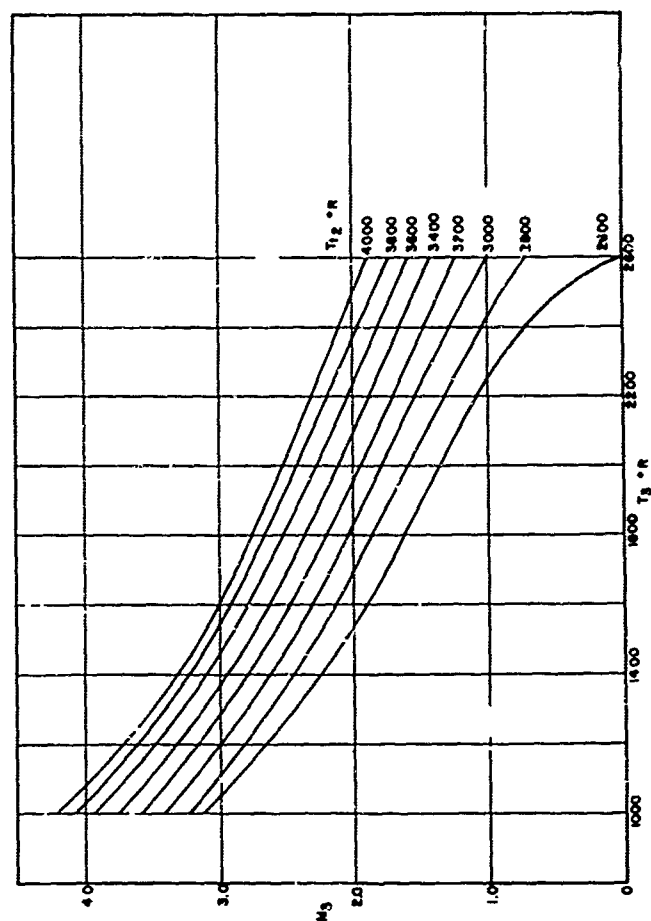


Fig. 14. Combustor Entrance Conditions for the Laboratory Case (Air) -- Mach Number as a Function of Static and Stagnation Temperature

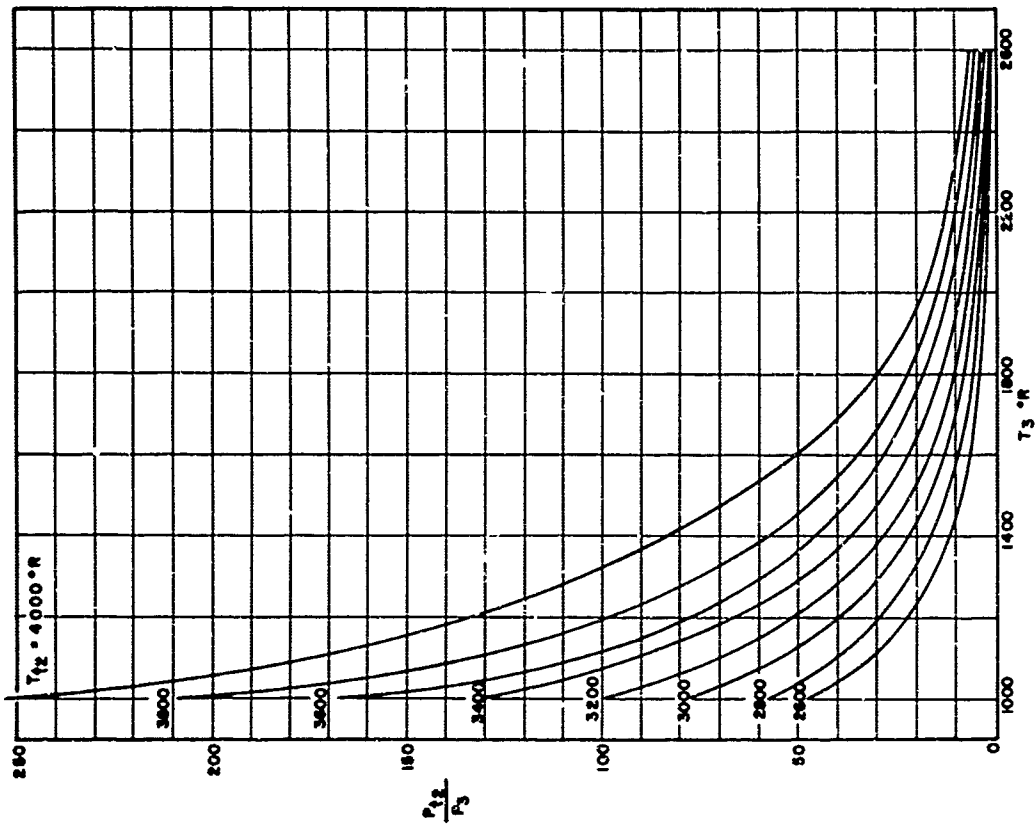


Fig. 16. Combustor Entrance Conditions for the Laboratory Case (Air) -- Ratio of Stagnation-to-Static Pressure as a Function of Stagnation Temperature

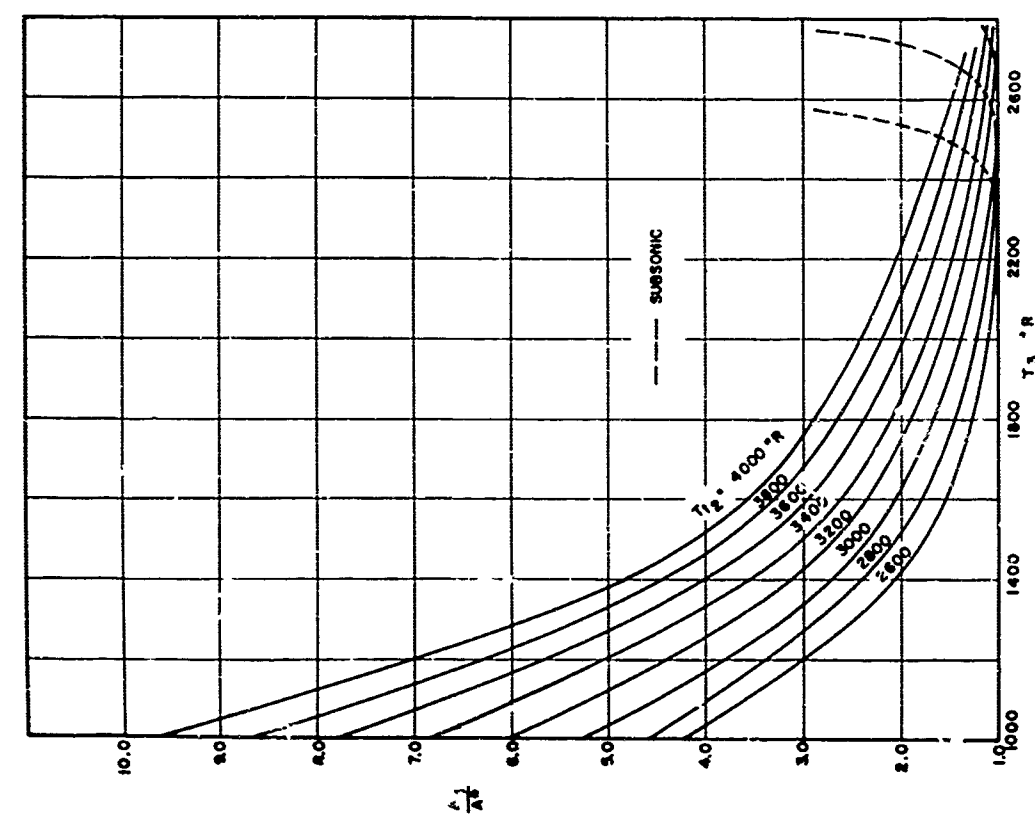


Fig. 15. Combustor Entrance Conditions for the Laboratory Case (Air) -- Nozzle Area Ratio as a Function of Stagnation Temperature

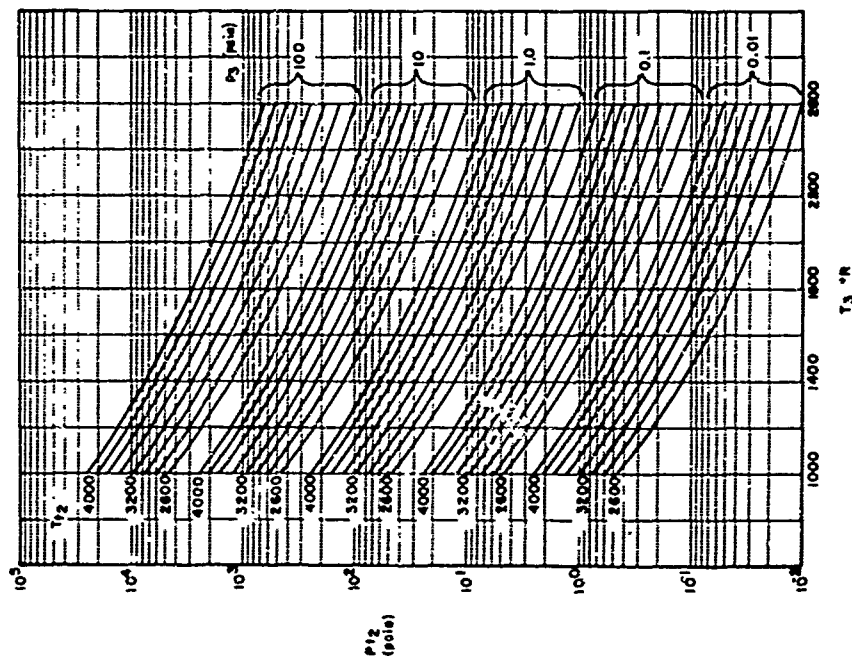


Fig. 17. Combustor Entrance Conditions for the Laboratory Case (Air) -- Stagnation Pressure as a Function of Static and Stagnation Temperature

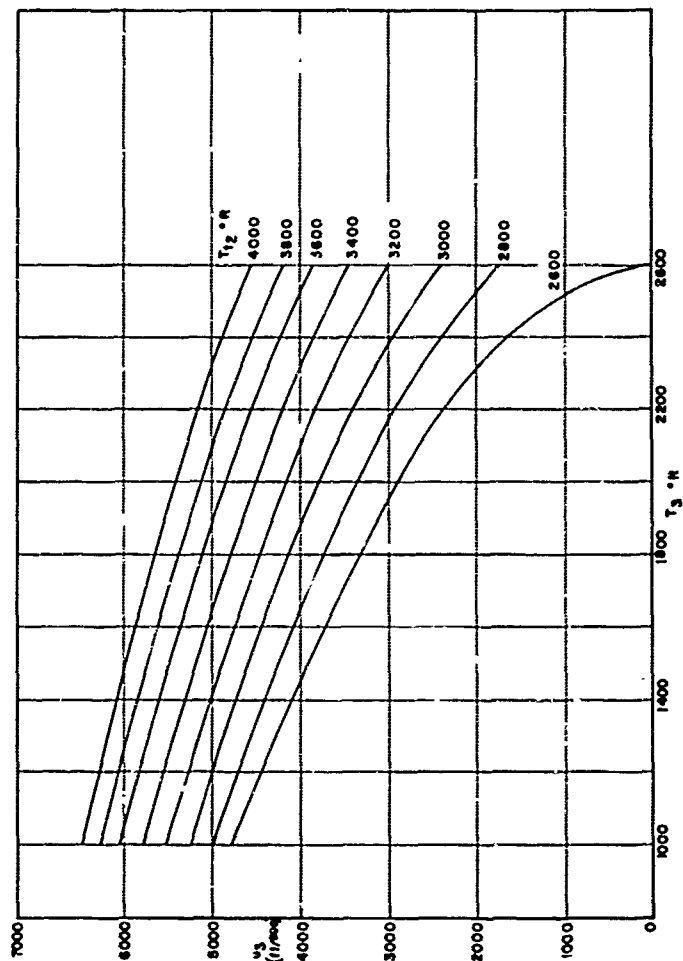


Fig. 18. Combustor Entrance Conditions for the Laboratory Case (Air) -- Velocity as a Function of Static and Stagnation Temperature

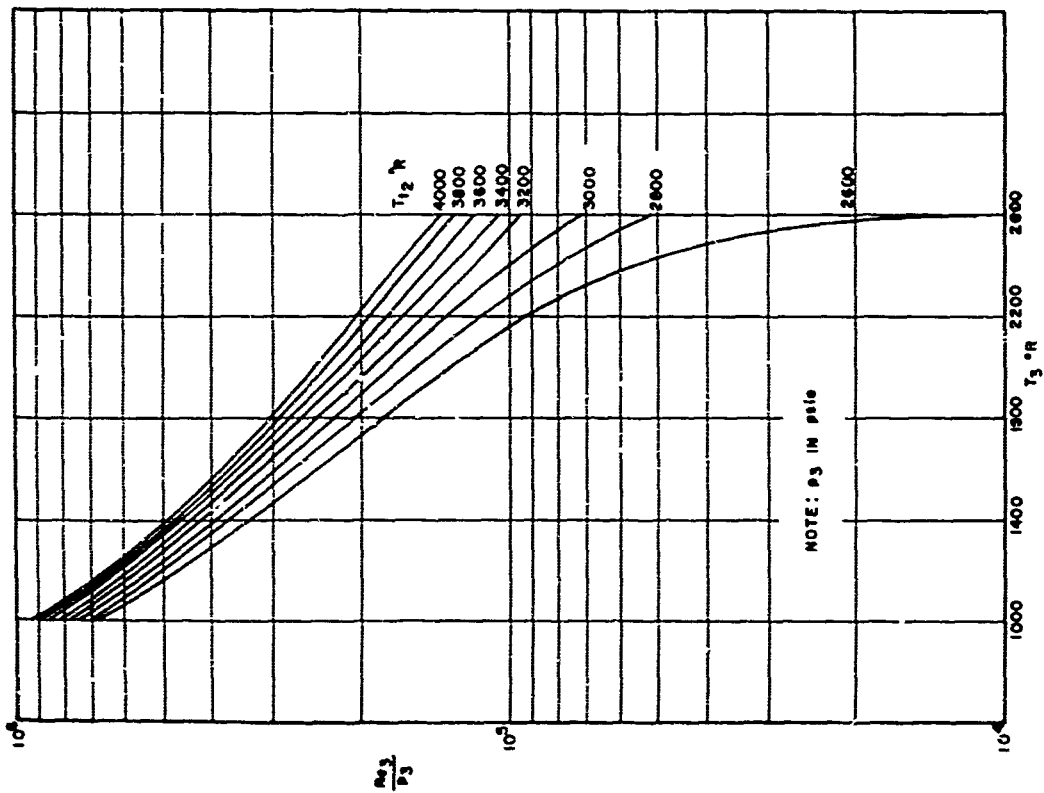


Fig. 19. Combustor Entrance Conditions for the Laboratory Case (Air) -- Ratio of Stagnation Pressure (per Foot) to Static Pressure as a Function of Static and Stagnation Temperature

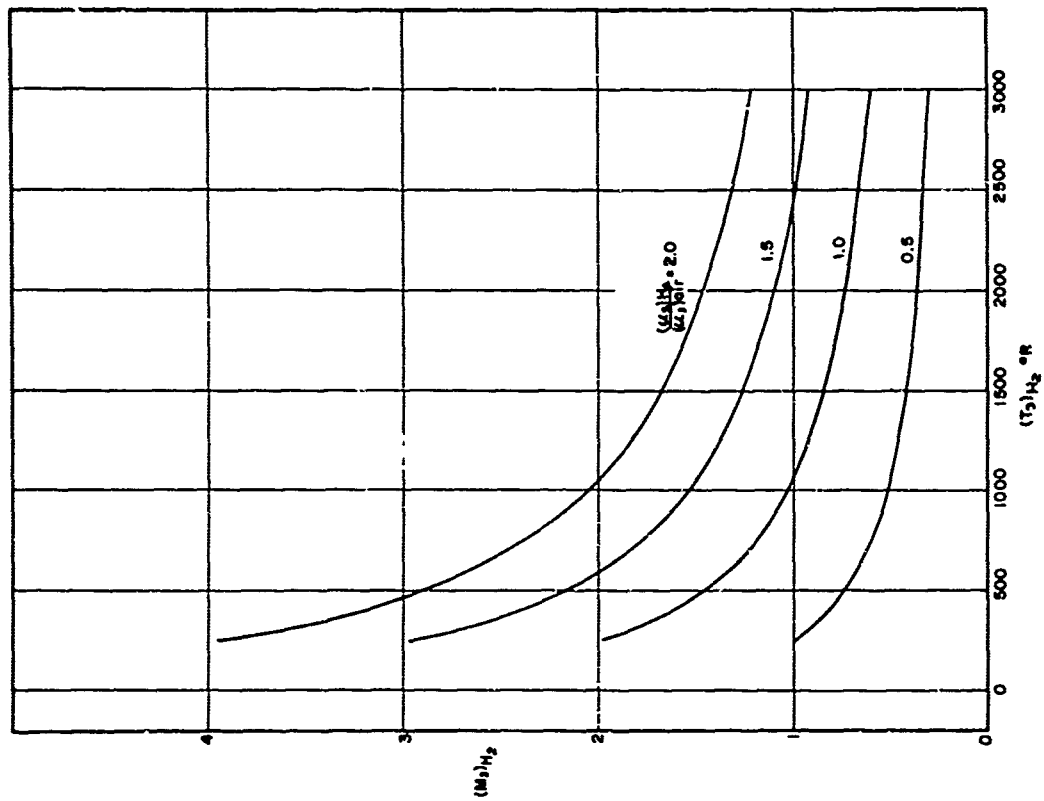


Fig. 20. Combustor Entrance Conditions for the Laboratory Case (Hydrogen) -- Mach Number as a Function of Static Temperature and Velocity Ratio (at an Air Velocity of 6000 Feet per Second)

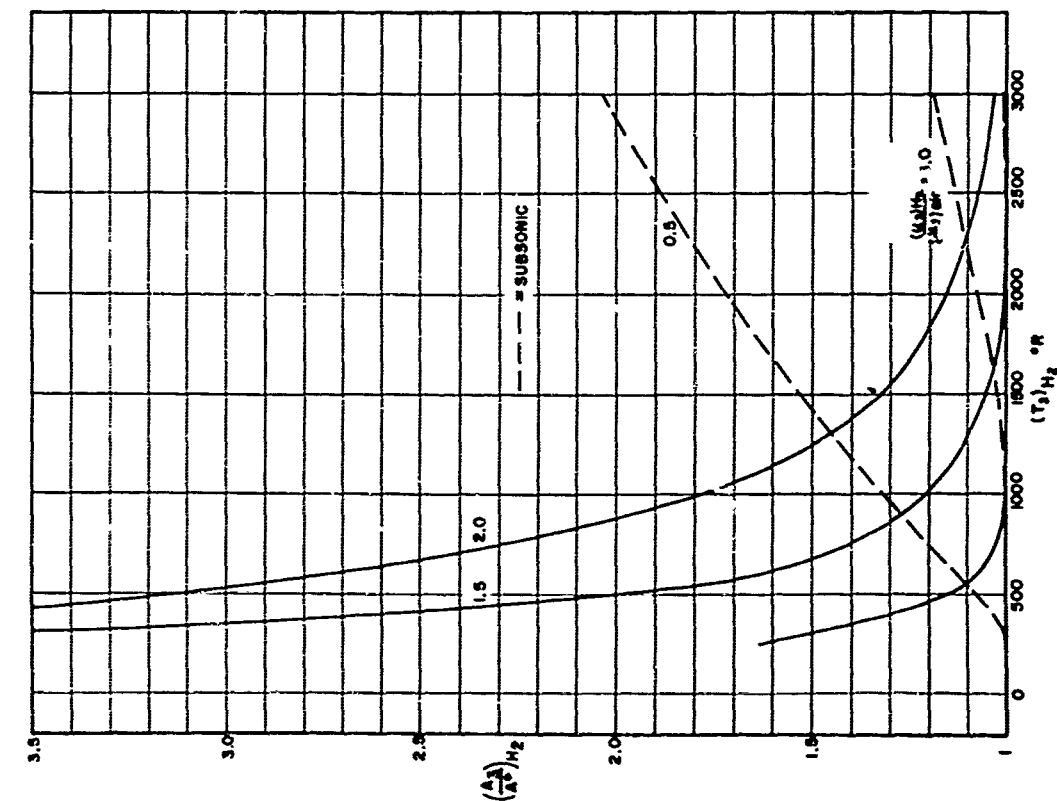


Fig. 21. Combustor Entrance Conditions for the Laboratory Case (Hydrogen) -- Nozzle Area Ratio as a Function of Static Temperature and Velocity Ratio (at an Air Velocity of 8000 Feet per Second)

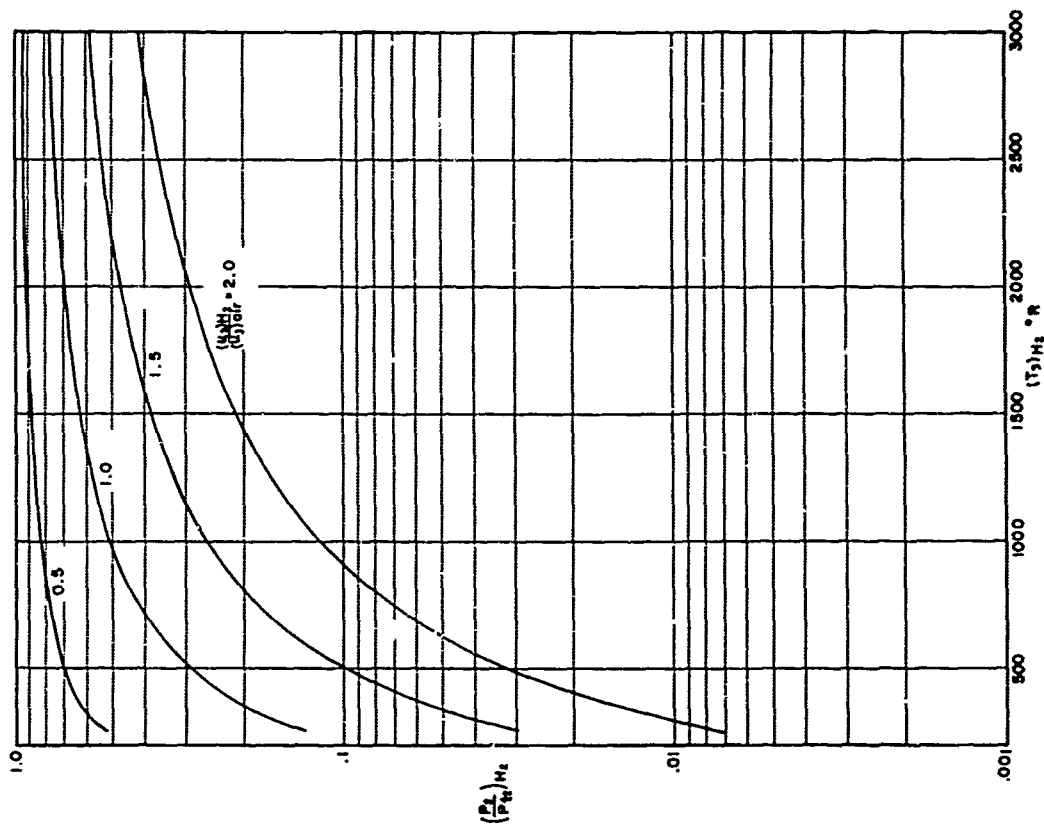


Fig. 22. Combustor Entrance Conditions for the Laboratory Case (Hydrogen) -- Ratio of Static-to-Stagnation Pressure as a Function of Static Temperature and Velocity Ratio (at an Air Velocity of 8000 Feet per Second)

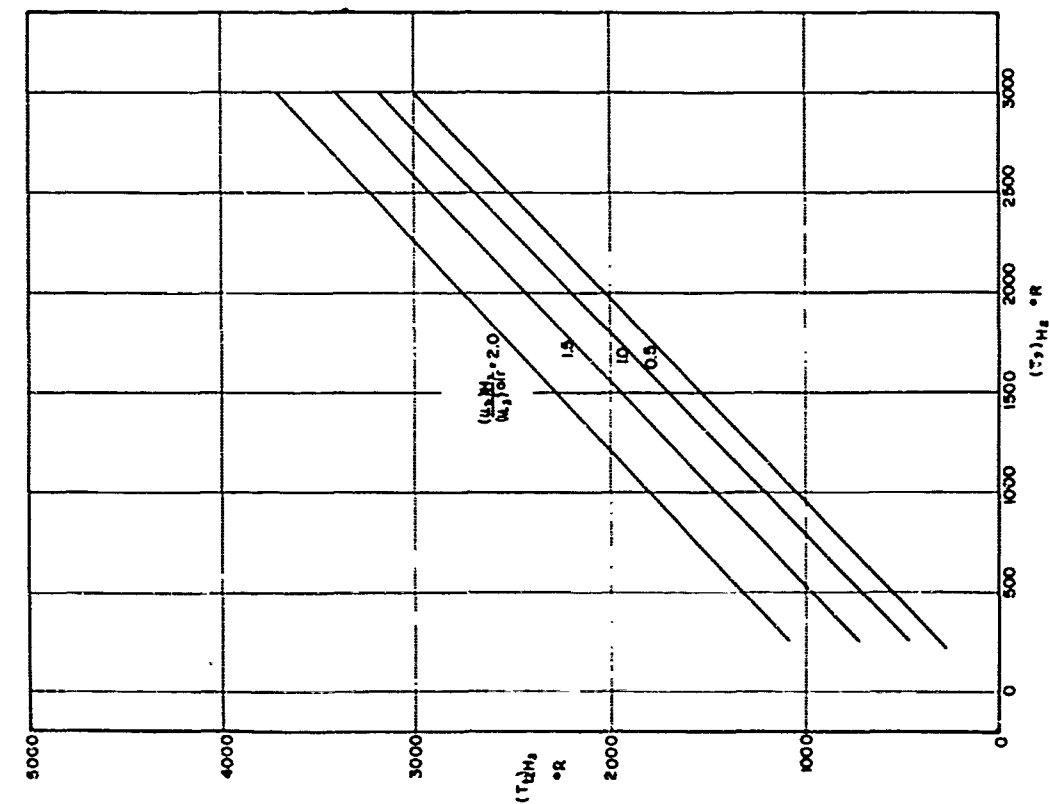


Fig. 23. Combustor Entrance Conditions for the Laboratory Case (Hydrogen) -- Stagnation Temperature as a Function of Static Temperature and Velocity Ratio (at an Air Velocity of 6000 Feet per Second)

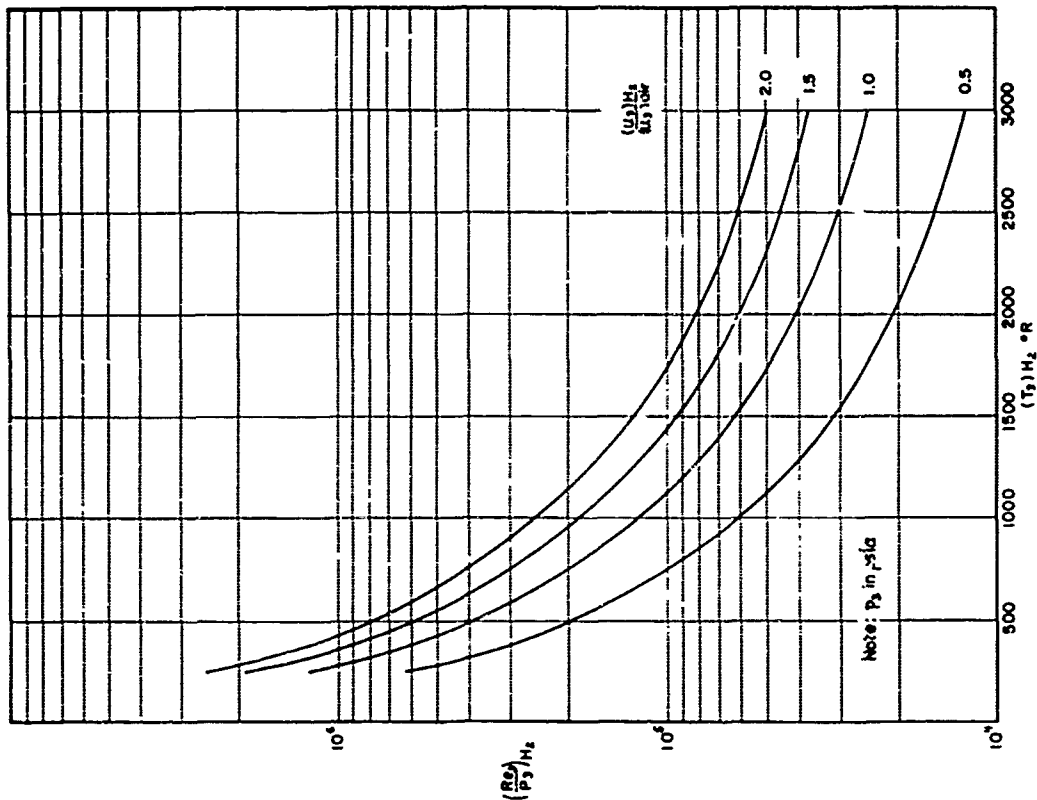


Fig. 24. Combustor Entrance Conditions for the Laboratory Case (Hydrogen) -- Ratio of Reynolds Number (per foot) to Static Pressure as a Function of Static Temperature and Velocity Ratio (at an Air Velocity of 6000 Feet per Second)

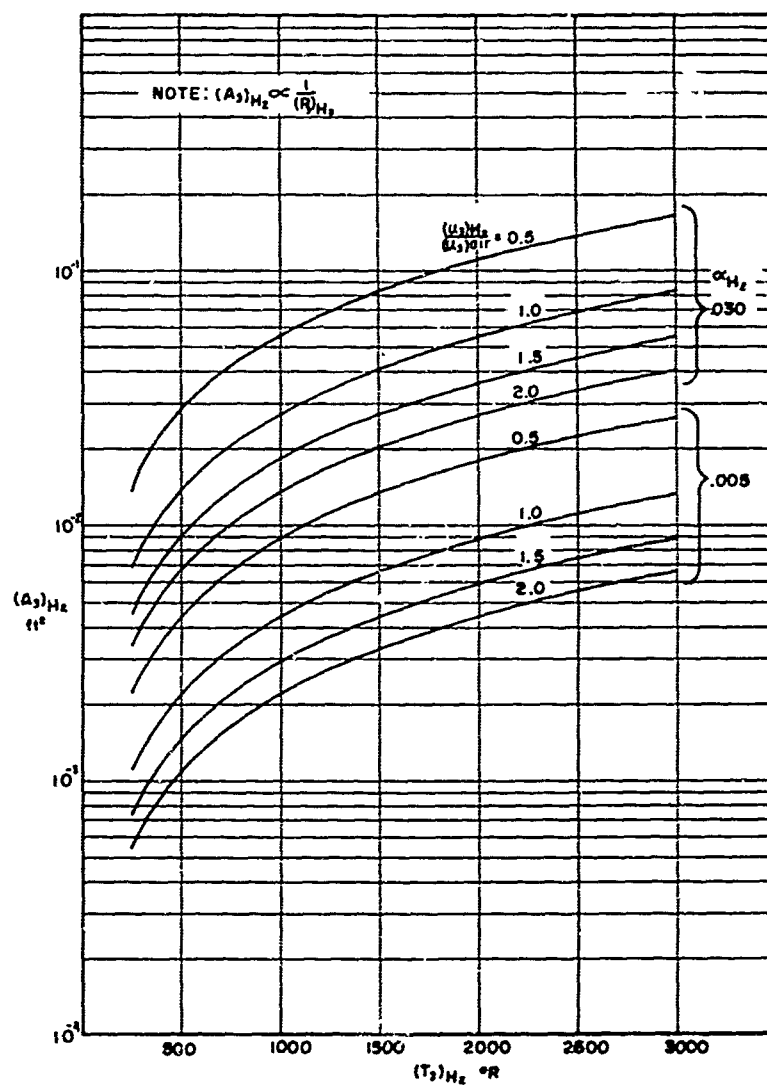


Fig. 25. Compressor Entrance Conditions for the Laboratory Case (Air/Hydrogen Mixture) -- Hydrogen Nozzle Exit Area as a Function of Static Temperature, Velocity Ratio and Mass Fraction (at an Air Velocity of 6000 Feet per Second and a Static Pressure of 1 psia)

HYDROCARBON FUELS FOR HYPERSONIC VEHICLES (U)

by

Herbert R. Lander, Jr.
Alan E. Zengel

Air Force Aero Propulsion Laboratory
Research and Technology Division
Wright-Patterson Air Force Base, Ohio



Herbert R. Lander, Jr.

BIOGRAPHY

Mr. Herbert R. Lander, Jr. is a Project Engineer in the Fuels, Lubrications, and Hazards Branch of the Air Force Aero Propulsion Laboratory. Associated with the Aero Propulsion Laboratory since 1961, he has been responsible for improving hydrocarbon fuel thermal stability, for the development of improved para-ortho hydrogen catalysts, and for research on endothermic hydrocarbon fuel concept.

Mr. Lander previously was employed by the Monsanto Research Corporation in Miamisburg, Ohio. He graduated from the University of Dayton in 1960 with a B. S. in Chemical Engineering. He presently is pursuing an advanced degree in chemical engineering in the graduate school at the Ohio State University.



Alan E. Zengel

BIOGRAPHY

Mr. Alan E. Zengel is a Project Engineer in the Fuels, Lubrications, and Hazards Branch of the Air Force Aero Propulsion Laboratory. Associated with the Aero Propulsion Laboratory since 1962, he has been responsible for the fuels research effort for the commercial supersonic transport, for the development of slurry fuels for low altitude ramjet-powered vehicles, and for in-house research on hydrocarbon fuel thermal stability.

Mr. Zengel previously was employed by the Monsanto Research Corporation in Miamisburg, Ohio. He graduated from the University of Illinois in 1958 with a B. S. in Chemical Engineering. He was awarded a Masters in Business Administration with a major in Industrial Management from Miami University in 1963, and presently is pursuing an advanced degree in chemical engineering in the graduate school at the Ohio State University. Mr. Zengel is a registered professional engineer in the state of Ohio.

HYDROCARBON FUELS FOR HYPERSONIC VEHICLES (U)

Herbert R. Lander, Jr.
Alan E. Zengel
Air Force Aero Propulsion Laboratory
Wright-Patterson Air Force Base, Ohio

ABSTRACT

Fuels for hypersonic vehicles must meet rigid requirements in order to serve the dual role as a coolant and as a combustion energy source. Hydrogen has received the major emphasis for this role because of its excellent cooling capability and combustion characteristics. The disadvantages with using hydrogen are its low boiling point and its low density; these disadvantages result in various handling and design problems.

The incentive of using fuels with greater density and better handling characteristics is important. Hydrocarbons have limited cooling capability; but additional heat sink capacity may be realized by allowing the hydrocarbon fuel to undergo a phase change, thus absorbing the latent heat of vaporization, and then allowing the gaseous fuel to react endothermically and to form combustible products. Endothermic reaction requires heat addition and the reaction products furnish additional cooling by absorbing sensible heat.

Endothermic reactions can be classified as either thermal or catalytic. Thermal reactions are simplest in application, but have the two disadvantages of low reaction rates at temperatures below 1200°F and of relatively low heats of reaction in comparison to catalytic reactions. For this reason, the catalytic endothermic reaction has received the more effort. Catalytic studies thus far have shown that the group of hydrocarbons with the greatest endothermic reactivity are the naphthenes. Laboratory investi-

gations have indicated that the methylcyclohexane (MCH)/platinum on alumina system has a total heat sink capacity of approximately 2000 British Thermal Units (BTU)/pound of fuel at 1340°F at a volumetric flow rate of 100 cubic feet/hour of fuel/cubic foot of catalyst and at a pressure of 10 atmospheres.

NOMENCLATURE

<u>Symbol</u>	<u>Definition</u>
r	rate of reaction
A'	constant in Arrhenius equation
E	energy of activation
R	gas constant
T	absolute temperature
A, R, A	symbols representing reactants and products of chemical reaction
K_A, K_R	equilibrium constants for adsorption and desorption of methylcyclohexane
K_m, K_h	equilibrium constants for adsorption and desorption of methylcyclohexane and hydrogen respectively
P_A, P_R	partial pressures of A and R
P_m, P_h	partial pressures of methylcyclohexane and hydrogen
j	symbol representing an active site
W	weight of catalyst
F	flow rate
X	conversion
π	total pressure
$\Delta P/P$	partial pressure decrease across fluid film divided by partial pressure in bulk stream
k_a	mass transfer coefficient
g_m	molar flow rate
G_m	molar flow rate
D	particle diameter
j_m	Colburn factor
ρ	gas density

μ	gas viscosity
k_e	effective thermal conductivity
k_c	thermal conductivity of gas
k_{td}	thermal conductivity of gas due to turbulent diffusion
k_r	thermal conductivity due to radiation
K_p	thermal conductivity of gas of solid particles

HYDROCARBON FUELS FOR HYPERSONIC VEHICLES (U)

Herbert R. Lander, Jr.
Alan E. Zengel
Air Force Aero Propulsion Laboratory
Wright-Patterson Air Force Base, Ohio

INTRODUCTION

Dissipating heat is the major problem of hypersonic flight. Aircraft traveling at high speeds are not able to reject heat to the surrounding air by convection since this air is heated by the passage of the vehicle. Heat will be radiated to space, but radiation cooling is limited to the portion of the engine and vehicle which views surrounding space. Heat generated in the engine and heat generated by the stagnation temperature of the surrounding air must be dissipated in order to keep material temperatures at tolerable levels.

The most logical heat sink aboard an aircraft is the fuel. The fuel in present supersonic aircraft flows through heat exchangers and thus cools engine oil and hydraulic fluids. The fuel in hypersonic vehicles would be required to cool the engine nozzle, the engine inlet, leading edges, and the combustion chamber.

Liquid hydrogen is the fuel that has received the most attention for hypersonic flight. This fuel has excellent cooling capabilities because of its low storage temperatures and because of its high specific heat in the gaseous state. However, penalties are associated with its use. First, liquid hydrogen is a cryogenic fluid that boils at -423°F under one atmosphere of pressure and, consequently, is difficult to handle and to store. Secondly, liquid hydrogen has a low density of 4.44 pounds/cubic foot at its boiling point and, therefore, requires large-volume aircraft tanks for storage. Fortunately, hydrogen has high energy release per pound of fuel, and the overall calculated performance of liquid hydrogen in hypersonic engines is so attractive that certainly air-breathing engines will be developed to operate with this fuel in the future. Fuels of greater density and better handling characteristics than hydrogen are desirable. Hydrocarbons exhibit these advantages, but the conventional use of hydrocarbon fuels is limited by the cooling capability.

Hydrocarbon fuels used in current aircraft can meet the cooling requirements for flight speeds to approximately Mach 3.5 as indicated for engine-cooling requirements in Figure 1.¹ At the higher temperatures associated with higher speeds, the present hydrocarbon fuels tend to degrade in the liquid state into polymeric gum materials that foul heat exchanger surfaces, plug orifices, and stick close tolerance parts. Thus, liquid hydrocarbons are limited to approximately 550°F , and their heat sink capability is curtailed seriously. Improved processing and elimination of dissolved oxygen would eliminate this problem. If this problem is solved, additional heat sink may be realized by allowing the hydrocarbon fuel to undergo a phase change and thereby absorbing the latent heat of vaporization. For example, an advanced hydrocarbon fuel may absorb 300 BTU/pound when heated from 60°F to 600°F . Then, an additional 80 BTU/pound may be obtained

by allowing vaporization to occur. This additional heat sink is not great and becomes even smaller as the pressure in the fuel system is increased. Figure 2 shows that 125 BTU of latent heat per pound of fuel is realized when vaporization occurs at 10 atmospheres, i.e., the path from A to B. Only 75 BTU/pound of latent heat is required for vaporization at a higher pressure such as 15 atmospheres, i.e., the path from C to D. Finally, if the pressure in the system is above the critical pressure, no distinction between the liquid and vapor states and no heat absorption due to vaporization can be realized. The exact operating pressures in hypersonic aircraft fuel systems are not known but these pressures apparently will be above 20 atmospheres. Consequently, the vaporization process will add little or no overall heat sink.

A hydrocarbon fuel vapor is not able to absorb as much heat as gaseous hydrogen. This fact can be illustrated simply by comparing the specific heats. Hydrogen has a specific heat of approximately 3.5 BTU/pound $^{\circ}\text{F}$, but hydrocarbon vapors have specific heats of only 0.3 BTU/pound $^{\circ}\text{F}$ at the same temperature. Hydrocarbon fuels seemingly are limited to below the Mach 3.5 speed because of the inability to provide the required cooling. However, a further step greatly increases the cooling capability: the hydrocarbons may react endothermically or, in other words, may undergo a chemical reaction that requires the addition of heat for completion.

ENDOTHERMIC FUEL POTENTIAL

A vast body of literature exists on the endothermic catalytic reactions of hydrocarbons such as the dehydrogenation of paraffins and naphthenes. These studies are concerned primarily with low conversions and low temperatures and are directed more toward obtaining a useful product than toward absorbing large amounts of energy.

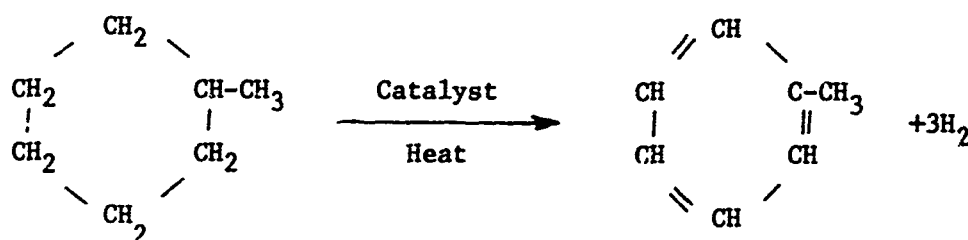
Latent and sensible heat obtainable from most hydrocarbons are approximately 1000 BTU/pound at 1340 $^{\circ}\text{F}$ with the possibility of an additional 800 to 1000 BTU/pound being available from a reaction with high conversions and high selectivities. Table I outlines the maximum cooling capability of various fuels including hydrogen.² This cooling capability is measured from 70 $^{\circ}\text{F}$ to 1340 $^{\circ}\text{F}$ at 10 atmospheres of pressure for the hydrocarbons. The type of endothermic reaction, the resulting product, and the equilibrium conversion based on thermodynamic considerations are noted if applicable.

The amount of heat-sink capacity aboard a particular aircraft will depend on the following factors:

1. Amount of space available for storage of the fuel
2. Amount of fuel to be carried to accomplish a certain mission.

These factors can be determined from the volumetric heat sink, e.g., thousands of BTU/cubic foot of fuel, and the available heat sink as a proportion of the heat of combustion.

N-octane looks the most attractive of hydrocarbons based on cooling capacity per unit mass; its endothermic heat of reaction of 1440 BTU/pound is obtained by the dehydrocyclization and dehydrogenation of the n-octane to styrene and hydrogen. However, this reaction is very complicated from a practical viewpoint and requires a catalyst to be bifunctional in order to cyclize the n-paraffin and to remove the hydrogen. Experimental data on the dehydrocyclization of n-octane over the standard chromia on alumina catalyst have given a heat of reaction of only 236 BTU/pound with selectivity of less than 10 per cent for styrene.³ The most promising hydrocarbon tested to-date is methylcyclohexane (MCH) with the chromia on alumina or platinum on alumina catalyst; the latter is the more active and selective. The chemical reaction strips three moles of hydrogen gas from one mole of methylcyclohexane to yield toluene. The chemical reaction is pictured as follows:



Thus the heat sink capabilities shown in Table I compared to the requirements in Figure 1 show that hydrocarbons undergoing endothermic reactions may be capable of meeting the cooling requirements for flight speeds to Mach 7. Experimental values approaching the theoretical values for the total heat sink from the dehydrogenation reaction over platinum on alumina have been obtained.³

The cooling capability based on volumetric considerations ranges from approximately 30,800 BTU/cubic foot for hydrogen to approximately 109,000 BTU/cubic foot for n-octane; MCH has a value of 94,000 BTU/cubic foot. Thus, the desirability of using endothermically reacting hydrocarbons in volume-limited applications of hypersonic vehicles is indicated clearly. The best hydrocarbons are practically equivalent to hydrogen on the basis of the fraction of the heat of combustion available as endothermic capacity.

Chemical Heat Sink Reactions

Endothermic reactions can be classified as either thermal or catalytic. Thermal reactions are the simplest in application, but have the two disadvantages of low reaction rates at temperatures below 1200°F and relatively low heat of reaction in comparison to catalytic reactions.

Figure 3 is a comparison of thermal and catalytic reaction types. The data in this chart are for the thermal cracking of cetane and the catalytic dehydrogenation of methylcyclohexane. The rate constant at 800°F for the catalytic reaction is approximately 1 second^{-1} ; the thermal reaction is considerably lower at $10^{-6} \text{ seconds}^{-1}$. The rate constants become equal at approximately 1300°F with a constant of approximately 5 seconds^{-1} . Figure 4 relates the comparison of heat sink versus conversion for the catalytic and thermal reactions of methylcyclohexane. The maximum attainable endothermic heat of reaction from the thermal reaction is approximately 300 BTU/pound of fuel at 60 per cent conversion; the higher conversions give less heat sink due to exothermic reactions between reactive products. The reaction heat sink from the catalytic dehydrogenation of methylcyclohexane is a linear function of conversion with a maximum heat sink of 900 BTU/pound of fuel.

The use of catalysts to promote chemical reactions has become an important part of industrial processing. The catalyst may serve either or both of two purposes: increase the rate of a chemical reaction or cause one of several possible reactions to occur selectively. Selectivity is the ability of a catalyst to increase the rate of one reaction by several magnitudes and thus to leave the rate of a competing reaction unchanged. Table II demonstrates that the selective dehydrogenation of methylcyclohexane to toluene and hydrogen increases the heat sink available from the reaction at the same reacting pressure and flow rate.³ The catalyst used in this comparison was a laboratory preparation of 1 per cent platinum supported on alumina. The thermal reaction with methylcyclohexane had a conversion of 62.4 per cent, a selectivity for toluene of only 2.7 per cent, and low heat of reaction of 160 BTU/pound of fuel. The catalytic reaction, although obtained at a lower temperature, gave a conversion of 98.6 per cent, a selectivity for toluene of 99.5 per cent, and a heat of reaction of 923 BTU/pound of fuel.³ A highly selective catalyst is required for high heat sink, for the cleanness of the reaction, and for relatively low reaction temperatures. Both the cleanness of reaction and the relatively low reaction temperatures are attractive from the standpoint of preventing coking and gum formation.

Catalytic Reactions

The advantages of the catalytic method of causing an endothermic reaction has stimulated the Air Force Aero Propulsion Laboratory to concentrate on developing a practical catalytic reactor-fuel combination. Recent research in this area indicates that the dehydrogenation of methylcyclohexane is a feasible endothermic reaction that can provide to 900 BTU/pound of fuel reaction-heat sink if conducted over a catalyst. Methylcyclohexane dehydrogenation is the current endothermic reaction receiving the most attention and will be discussed in detail to provide insight into the problems associated with this heat sink scheme.

A general relationship between catalyst and reactant has been developed. A postulate for the development of the rate equation is that a

gas-phase reaction actually occurs on the surface of a solid catalyst and involves the reaction of the molecules which are chemically adsorbed on the active centers of the surface. A catalyst would increase the rate of reaction through its ability to adsorb the reactants in such a form that the activation energy necessary for the reaction is reduced far below its value in the thermal reaction.

The energy changes during a catalytic reaction differ considerably from those of a thermal reaction. These energy changes for a controlling surface reaction are shown in Figure 5. The thermal reaction in Figure 5 must proceed by creating an activated specie with energy E_t . This activated specie then may proceed to the reaction product by going down the energy hump to the product gas, B. The difference between the energy of the reactants and the energy of the products is the thermodynamic value of the heat of reaction, ΔH . The catalytic reaction proceeds more rapidly because the energies of adsorption reduce the reaction energy required to complete the reaction. The catalytic type reaction in contrast to the thermal reaction proceeds by a series of steps. The first step, the adsorption of the reactant on the surface of the catalyst, requires an amount of energy given by E_a and has a heat of adsorption given by ΔH_a . After adsorption, the reactant molecule reacts on the surface. The energy required for this step is the difference between the maximum energy for the catalytic route and the energy of the adsorbed reactants and is given by E_c . This energy requirement is less than that for the thermal reaction because of the energy remaining from the adsorption step; thus, the reactants in the adsorbed state required less energy. The rate of reaction may be represented by an Arrhenius equation:

$$r = A' e^{-E/RT}. \quad (1)$$

The Arrhenius representation shows that the rate will be greater at the same temperature for reactions with lower energies of activation; thus, the catalyst increases the rate. However, only the rate is affected and the thermodynamic functions, such as heat of reaction and equilibrium, are not changed.

The catalytic conversion of a gas molecule in the main stream to a product in the main gas stream requires the reactant to be transferred to the gas-catalyst interface, to be adsorbed on the surface, and to be transformed to the desired products that subsequently are desorbed and returned to the flowing mainstream. The rate for each of these steps influences the distribution of concentrations in the system and has a role in the determination of the overall reaction rate.

A catalytic gas-phase reaction over a porous particle is assumed to consist of the following steps:

1. Diffusion of the reactant to the surface of the catalyst
2. Diffusion into the pores of the catalyst
3. Chemical adsorption of the reactant on the catalyst

4. Chemical reaction(s) on the catalyst surface
5. Chemical desorption of the products from the catalyst
6. Diffusion of products to the exterior of the catalyst
7. Diffusion from the surface to the main gas stream

Steps 1, 2, 6, and 7 are physical steps, the laws of diffusion rather than the laws of chemical reactions determine the rates. If any of these physical steps are rate-controlling, the catalyst is not being used to its fullest potential and the rates of these steps must be increased. If either Step 1 or 7 is rate-controlling, the reactant molecules cannot be supplied to the active catalyst surface or the product molecules cannot be removed fast enough to make maximum use of the catalyst activity. This problem results from the diffusion associated with the stagnant gas boundary around the catalyst pellet and can be overcome by increasing the velocity of the flowing gas through the catalyst bed and thus lowering the film resistance. If the gas velocity were sufficiently large to hold the film resistance to a minimum, the physical aspect may continue to limit the effectiveness of the catalyst; e.g., if Steps 2 and 6 are controlling. These steps include the internal diffusion processes that can be eliminated by reducing the size of the catalyst pellet. Thus, every fluid catalyst system needs a minimum velocity of the gas stream and a maximum catalyst pellet size to nullify the controlling effects of the physical steps.

The chemical steps include those of chemical adsorption and desorption and the surface reaction in the adsorbed state. These steps are illustrated by the following series of reactions:

reaction gas + active site \rightleftharpoons adsorbed reactant

adsorbed reactant \rightleftharpoons adsorbed product

adsorbed product \rightleftharpoons product gas + active site

Preliminary Reactor Design

A kinetic rate equation developed from the above reactive site theory would consist of the three chemical steps in series. For example, the methylcyclohexane reaction given above may be represented as:



However, the consecutive steps involved in this scheme for single site, surface reaction would be summarized as follows:

1. Reactant A reacts with active site j to produce the adsorbed specie A_j .

2. The surface reaction proceeds as:



S, one of the products, is desorbed and R remains in the adsorbed state.

3. R is desorbed,



and the active site becomes available for further reaction.

If a reaction on the surface is slow compared to the adsorption and desorption steps, the latter apparently are in equilibrium. Thus, equilibrium constants for the adsorption and desorption steps are:

$$K_A = \frac{A_j}{j P_A} \quad (5)$$

and

$$K_R = j \frac{P_R}{R_j}. \quad (6)$$

The rate equation from the Law of Mass Action is:

$$r = k A_j. \quad (7)$$

The term A_j is not measurable. Therefore, in order to express the rate in terms of partial pressures, equilibrium and rate constants, a substitution of the adsorption equilibrium expression in the rate equation yields:

$$r = k K_A P_A j. \quad (8)$$

To find an expression for j , the total number of active sites is assumed to be constant and is expressed as:

$$L = j + A_j + R_j. \quad (9)$$

L is the total number of active sites. Substituting equilibrium expressions into this equation results in:

$$L = j + K_A P_A j + j \frac{P_R}{K_R}. \quad (10)$$

Combining L and K, finding a solution for j, and making these changes in the rate equation yields the final rate expression:

$$r = \frac{k K_A P_A}{1 + K_A P_A + K'_R P_R} \quad \text{where } K'_R = \frac{1}{K_R} \quad (11)$$

Use of the Kinetic Equation

The kinetic rate expression, after the constants are obtained, can be used for the preliminary design of a reactor. The basic equation for a fixed-bed reactor with assumed plug flow is:

$$rdw = Fdx. \quad (12)$$

This basic equation is restated and an expression for r is known in terms of x:

$$W/F = \int \frac{xdx}{r} \quad (13)$$

The result may be integrated to express the weight of catalyst as a known flow rate. The rate expression for the dehydrogenation of methylcyclohexane over chromia-alumina catalyst has been examined and, for illustrative purposes, will be used to size a fixed-bed catalytic reactor.

The rate expression for the conversion of methylcyclohexane to toluene and hydrogen over a chromia-alumina catalyst is:⁴

$$r = \frac{k K_m P_m}{1 + K_m P_m + K_h P_h} \quad (14)$$

The relationship of k, K_m , and K_h with temperature also is known.³ Thus, this equation may be used to extrapolate to high temperatures and pressures and can provide the means to find the reaction rate at 800°F, 900°F, and 1000°F. The rate equation must be expressed in terms of X in order to generate W/F versus X curves. The partial pressure of MCH may be expressed as:

$$P_m = \frac{1 - x}{1 + 3x} \pi \quad (15)$$

The partial pressure of hydrogen may be expressed as:

$$P_h = \frac{3x}{1 + 3x} \pi \quad (16)$$

Substitution of these expressions into the rate equation and the subsequent substitution of the rate equation into the integral equation for a fixed-bed reactor yields the following equation:

$$W/F = \frac{1}{kK_m \pi} \int_0^x \frac{(1+3x) dx}{1-x} + \frac{1}{R} \int_0^x dx + \frac{3K_H}{kK_m} \int_0^x \frac{x dx}{1-x} \quad (17)$$

This equation may be integrated directly as:

$$W/F = \frac{1}{kK_m \pi} [3x - 4 \log(1-x)] + \frac{x}{k} + \frac{3K_H}{kK_m} [1-x - \log(1-x)] - \frac{3K_H}{kK_m} \quad (18)$$

A complete curve of W/F versus X results from finding the values of the constants at a given condition and choosing an X. Table III gives the W/F values for various values of X at 10, 20, and 30 atmospheres of pressure and at 800°F, 900°F, and 1000°F. These values are plotted in Figure 6.

The weight of the catalyst required for a desired conversion may be found with known W/F values by simply multiplying the W/F value by the flow rate. Also, the additional reaction heat sink available at a given conversion is determined by finding the relation between the conversion and endothermic heat of reaction at 25°C. The total heat of reaction is found by subtracting the heat of formation of MCH from the heat of formation of toluene. If X equals 1, this heat of reaction is 900 BTU/pound of MCH. If X equals 0.2, only 0.002 pound moles of the total 0.0102 pound moles basis have been converted; thus, the heat of reaction is 176 BTU/pound of MCH. A plot of heat of reaction versus conversion was shown in Figure 3.

The weight of catalyst required for a desired heat sink under the conditions of interest now can be found. Such weights at different flow rates and pressures at 1000°F are plotted in Figure 7. Similar plots are made for 900°F and 800°F in Figures 8 and 9.

The determination of film diffusion as a factor in the catalyst bed operation is illustrated. Flow rate at 10 pounds per second at 1000°F and 10 atmospheres would be the condition where film diffusion most likely would be a factor. Film diffusion can be neglected if the $\Delta P/P$ ratio at the entrance of the reactor is significantly less than 0.01. The first step is to find the rate at the entrance where $P_m = \pi$ and $P_h = 0$. Thus, the rate equation becomes:

$$r = \frac{kK_m \pi}{1+K_m \pi} = 0.412 \quad (19)$$

Also known is:

$$r = k_g a_m (P_m - P_{mi}) \quad (20)$$

P_{mi} is the partial pressure on the catalyst side of the film interface and $k_g a_m$ is the mass-transfer coefficient.

The value for $k_g a_m$ may be found from the Colburn j_m factor that is equal to:⁵

$$j_m = \frac{k_g a_m}{G_m} \left(\frac{\mu}{\rho d} \right)^{2/3} \quad (21)$$

A plot of j_m versus a modified Reynolds number based on the diameter of a particle is available. Based on this plot and the assumption that the catalyst was contained in a heat exchanger with 1500 tubes of one-inch diameter, a value of 2.5 was found for j_m .³ Solution of the j_m equation gave a value of 4.5×10^4 for $k_g a_m$. This value in turn yielded a $\Delta P/P$ of 1.6×10^{-5} . The $\Delta P/P$ ratio is significantly less than 0.01; thus, film diffusion apparently is not important at these high-flow-rate conditions.

The weight of the catalyst under all conditions chosen is found to be significantly above 1000 pounds, a reasonable upper limit for a catalyst weight aboard a 250,000-pound aircraft. The fact that a potentially heavy piece of equipment would be required to contain the catalyst has not been considered at this point; the objective of this example has been to show the feasibility of this reaction on the basis of catalyst weight alone.

The weight of the catalyst is very sensitive to temperature. The temperature required to give a significant heat sink without a great weight penalty must be determined. The weight of the catalyst is dependent upon the rate of the catalytic reaction which changes with temperature by the familiar Arrhenius rate law. Thus, a plot of catalyst weight versus the reciprocal of temperature yields a straight line to be extrapolated to a reasonable catalyst weight for our purpose of demonstrating feasibility. Such a plot for an additional 800 BTU/pound of MCH realized through reaction is shown in Figure 10 for flow rates of 20 and 10 pounds per second. The plot indicates that temperatures of 1390°F at the high flow rate and 1215°F at the low flow rate are required to lower the catalyst weight to 1000 pounds. Catalyst weight increases exponentially with increases in conversion as shown in Figures 7, 8, and 9. Thus, a first-generation, practical, endothermic heat sink system may take less than 100 per cent conversion.

The endothermic reaction heat sink scheme is feasible from a chemical engineering standpoint. In order to reduce a catalyst bed weight to 1000 pounds, the fuel-catalyst combination must operate above 1200°F, not an unreasonable temperature on a hypersonic vehicle. However, this fuel-catalyst combination was chosen because of the availability of complete kinetic data and is not the best solution. As mentioned above, a much more reactive catalyst is platinum on alumina. Unfortunately, a fully developed

kinetic-equation of the dehydrogenation of methylcyclohexane over platinum on alumina is not available; even preliminary calculations on the catalyst weight cannot be made. Table IV compares experimental results of the two catalysts with methylcyclohexane under comparable conditions and clearly shows that platinum on alumina is a vastly superior catalyst and that a given heat sink may be achieved by a lower weight catalytic reactor using platinum on alumina rather than with chromia on alumina.

Effects of Various Parameters

An equilibrium plot of the conversion of methylcyclohexane to toluene and hydrogen versus temperature at various pressures is illustrated in Figure 11. This plot shows that thermodynamics does not limit the conversion at the pressures of interest at approximately 1000°F. Methylcyclohexane reacts thermally to give cracked products, and the heat of reaction is relatively low due to concurrent exothermic reactions between these products. Based on this information and the available literature, emphasis has been placed on the catalytic dehydrogenation of methylcyclohexane over available catalysts. The resulting effort has included the kinetic study on the chromia system and investigations with the more active platinum system and has aimed more at demonstrating the possible heat sink potential without regard for reaction mechanism. Heat transfer effects seemed to be the limiting phenomena with the methylcyclohexane/platinum on alumina system. Heat transfer phenomena through packed beds have been studied experimentally and theoretically.⁶ A derived expression for the effective thermal conductivity in terms of the contributions for each mechanism responsible for the radial heat transfer is represented as:

$$k_e = k_c + k_{td} + k_r + k_p . \quad (22)$$

The total rate of flow per unit area, q , is defined by the following expression:

$$q = k_e \frac{dt}{dr} . \quad (23)$$

An increase in heat transfer can result from an increase in the effective thermal conductivity. The only way to increase the effective thermal conductivity is to increase the thermal conductivity of the packing materials if the system dimensions, the gas, and the flow rate are held constant. Table V demonstrates the effect of diluting the catalyst bed with 65 per cent by volume of inert copper shot for the methylcyclohexane/platinum on alumina system.³

Copper has a thermal conductivity approximately 150 times that of alumina and probably at least 40 times that of 1 per cent platinum on alumina. Copper at 212°F has a thermal conductivity of 218 BTU/(hour-foot-°F) as compared to 47 and 1.45 for platinum and alumina respectively.

The data on the catalytic conversion of MCH at essentially the same flow rates and the same furnace block temperatures, but with inert

copper shot replacing the catalyst in the second run and increasing the effective thermal conductivity are presented in Table V. The addition of the inert copper reduced the available catalyst, but greatly increased the effective thermal conductivity. The temperature dropped to 649°F in the undiluted catalyst bed, reaction possibly was equilibrium-limited, the conversion dropped to 60.4 per cent, and the selectivity for toluene was high at 99.4 per cent. When the bed was diluted with 13 milliliters of copper shot, the catalyst bed temperature dropped only to 838°F, the reaction was not equilibrium-limited, and the conversion was 97.2 per cent with 98.0 per cent selectivity for toluene. These data clearly indicate that the catalyst is extremely active, but that a radial heat transfer problem is associated with the poor thermal conductivity of the catalyst bed. Future investigations will attempt to eliminate the heat transfer problems of the reacting system. Possible avenues of investigation will be coated tubes; various reactor configurations including long, thin reactor beds; and catalysts with higher thermal conductivities. Another problem associated with the use of packed bed reactors is the pressure loss encountered in pumping the gas through the bed.

The effect of pressure on the dehydrogenation of methylcyclohexane over the platinum alumina catalyst at pressures of 10, 20, and 30 atmospheres and two different flow rates is shown in Figure 12.³ The reaction was sensitive over this range of pressure for liquid hourly space velocities (LHSV) of 50 to 150. Figure 12 can be summarized by stating that the conversion and heat of reaction declined with increasing pressure in spite of the increased contact produced by the high pressure. At the 50 LHSV and at 10, 20, and 30 atmospheres of pressure, the methylcyclohexane conversions of 93.3 per cent, 89.8 per cent, and 87.1 per cent were obtained respectively with heats of reaction of 877, 844, and 818 BTU/pound. At the 150 LHSV and at 10, 20, and 30 atmospheres of pressure, the methylcyclohexane conversions of 61.1 per cent, 58.6 per cent, and 51.6 per cent were obtained respectively with the corresponding heats of reaction of 574, 550, and 532 BTU/pound. The catalyst used in these runs was diluted with an equal volume of inert copper shot to eliminate some of the heat transfer problem associated with endothermic reactions in packed bed reactors. The selectivities for toluene in all of the reactions was greater than 98 per cent.

The mechanism explaining the effect of pressure on this reaction system is not understood at this time. The results may be due to equilibrium effects.

SUMMARY

Catalytic studies thus far have shown that the group of hydrocarbons with the greatest endothermic reactivity are the naphthenes. Laboratory investigations have indicated that the methylcyclohexane/platinum or alumina system has a heat sink of 2000 BTU/pound at 1340°F at an LHSV of 100.

Current efforts are aimed at scaling this fuel scheme to aircraft system simulators and analytically and experimentally determining the feasibility of applying this system to various hypersonic vehicles. Major emphasis will be placed on establishing the feasibility of supersonic combustion of catalytically converted fuels and on determining the methods for obtaining the most efficient cooling from reacting fuel.

REFERENCES

1. "Fuels for Advanced Air-Breathing Weapon Systems", Arthur V. Churchill, Capt. John A. Hager, and Alan E. Zengel, Society of Automotive Engineers Paper No. 650804, October, 1965
2. Vaporizing and Endothermic Fuels for Advanced Engine Application, Shell Development Company, Report No. APL-TDR-64-100, Part I, September, 1964.
3. Vaporizing and Endothermic Fuels for Advanced Engine Application, Shell Development Company, Report No. APL-TDR-64-100, Part II, June, 1965.
4. "Kinetics of Methylcyclohexane Dehydrogenation to Toluene on Chromia Alumina", Gordon Ray Youngquist, Ph.D. Thesis in Chemical Engineering, University of Illinois, 1962.
5. Chemical Engineers' Handbook, John H. Perry, Editor, Third Edition, McGraw-Hill Book Company, 1950.
6. "Heat Transfer in Packed Beds", W. B. Argo and J. M. Smith, Chemical Engineering Progress, 1953, Volume 49, No. 8.

TABLE I
ENDOTHERMIC CAPACITIES OF SOME FUELS

Fuel	Type Reaction*	Products	Equilibrium Conversion (Per cent)	Heat Absorbed (1340°F, 10 atmospheres)			
				BTU/pound			Per cent of ΔH_c
				Chemical	Physical	Total	
Methane	none	--	--	--	1460	1460	41.6
Propane	DH	C_3H_6, H_2	40	510	1240	1750	78.9
Propane	Cr	C_2H_4, CH_4	95	740	1240	1980	89.2
n-Hexane	DHC	C_6H_6, H_2	99	1250	1030	2280	94.3
n-Octane	DHC	C_8H_{12}, H_2	99	970	1030	2000	88
n-Octane	DHC-DH	C_8H_{10}, H_2	99	1440	1030	2470	109
MCH*	DH	C_7H_8, H_2	99	940	1016	1956	94.1
Prop. tet.*	DP	C_3H_6	99	630	945	1575	74.8
H ₂	none	--	--	--	6500	6500	30.8

* DH = dehydrogenation, Cr = cracking, DHC = dehydrocyclization, DP = depolymerization, MCH = methylcyclohexane, Prop. tet. = propylene tetramer.

TABLE IJ
EFFECT OF CATALYST SELECTIVITY ON REACTION HEAT SINK*

	Reaction	
	Thermal	Catalyst
Catalyst	---	Platinum on Alumina
MCH Conversion (Per cent by weight)	62.4	98.6
Bed Temperature (°F)	1300	842
Selectivity for Toluene (Per cent)	2.7	99.5
Heat of Reaction (BTU/pound)	160	923
Total Heat Sink (BTU/pound)	1280	1633

* Feed, Phillips "pure" grade methylcyclohexane (MCH); system pressure, 10 atmospheres; liquid hourly space velocity (LHSV): $20 \left(\frac{\text{volume of feed/hour}}{\text{volume of the reactor}} \right)$.

TABLE III
W/F VALUES FOR DIFFERENT DEGREES OF CONVERSION

Conversion	<u>1000°F</u>			<u>900°F</u>			<u>800°F</u>		
	10 atm.	20 atm.	30 atm.	10 atm.	20 atm.	30 atm.	10 atm.	20 atm.	30 atm.
.2	4.2	3.2	2.8	18.27	14.5	13.3	66.8	56.9	53.6
.4	9.1	5.9	5.4	40.1	32.0	29.3	155	133.6	126.4
.6	15.15	11.3	9.9	68.6	55.0	50.4	282	246	234.4
.8	24.0	17.7	15.6	112.8	94.4	87.1	507	448.6	429
.9	32.0	23.5	20.7	155.1	125.3	115.5	--	--	--
1.0	--	--	--	--	--	--	--	--	--

TABLE IV
METHYLCYCLOHEXANE DEHYDROGENATION

	Temperature (°F)	MCH Conversion (Per Cent)	Selectivity for Toluene (Per Cent)	Reaction Heat Sink
1 per cent Platinum on Alumina	1022	91.1	99.2	856
Chromia on Alumina	1022	22	75	200

TABLE V
EFFECT OF IMPROVED HEAT TRANSFER ON
METHYLCYCLOHEXANE DEHYDROGENATION

LHSV	Active Catalyst Volume (Milliliters)	Reaction Temperature (°F)		MCH Conversion (Per Cent)	Heat of Reaction
		Block	Catalyst		
53	20	1112	649	60.4	565
50	7*	1112	838	97.2	896

* Bed diluted with copper shot, 13 milliliters.

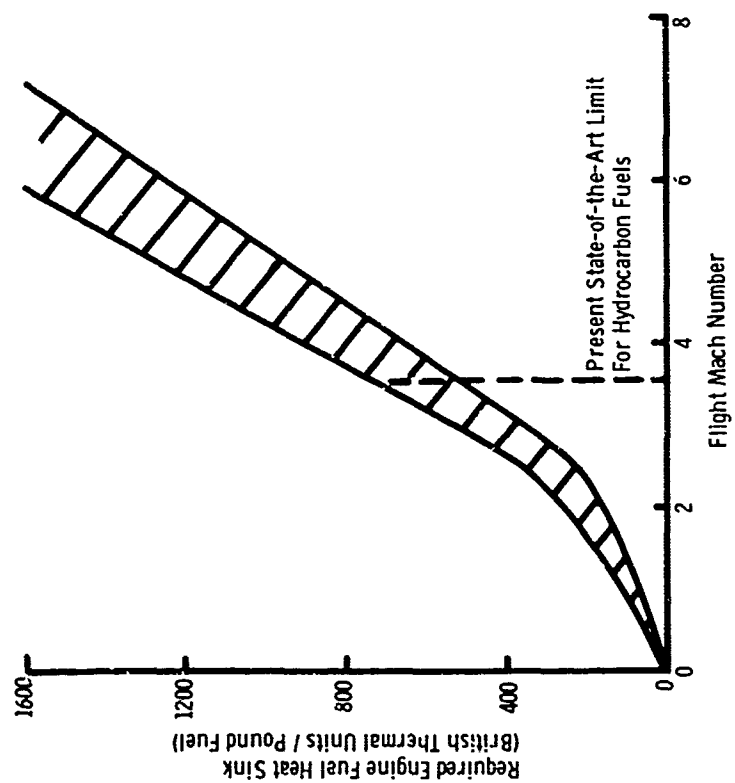


FIGURE 1 REQUIRED ENGINE FUEL HEAT SINK VERSUS FLIGHT MACH NUMBER

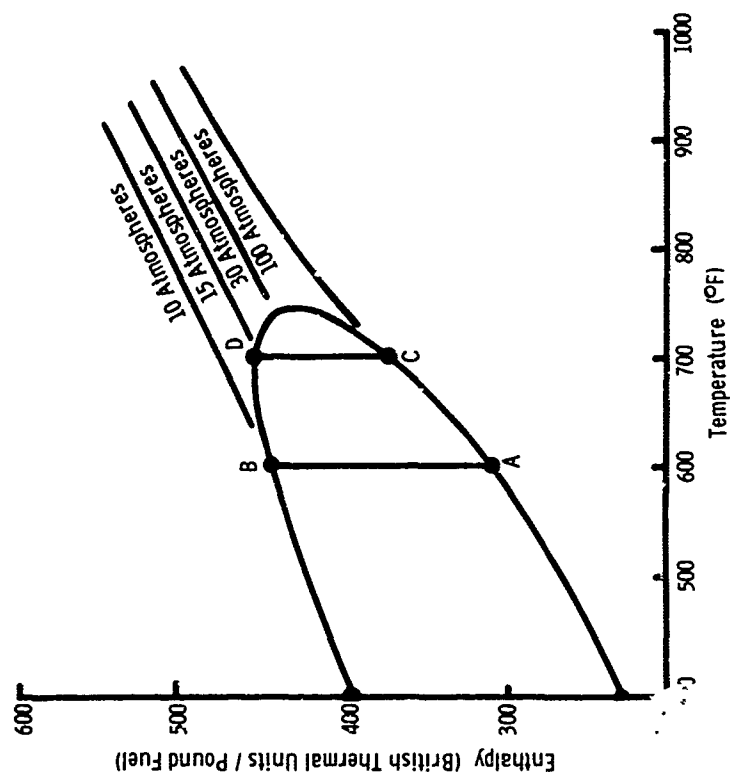


FIGURE 2 ENTHALPY VERSUS TEMPERATURE FOR AN ADVANCED HYDROCARBON FUEL

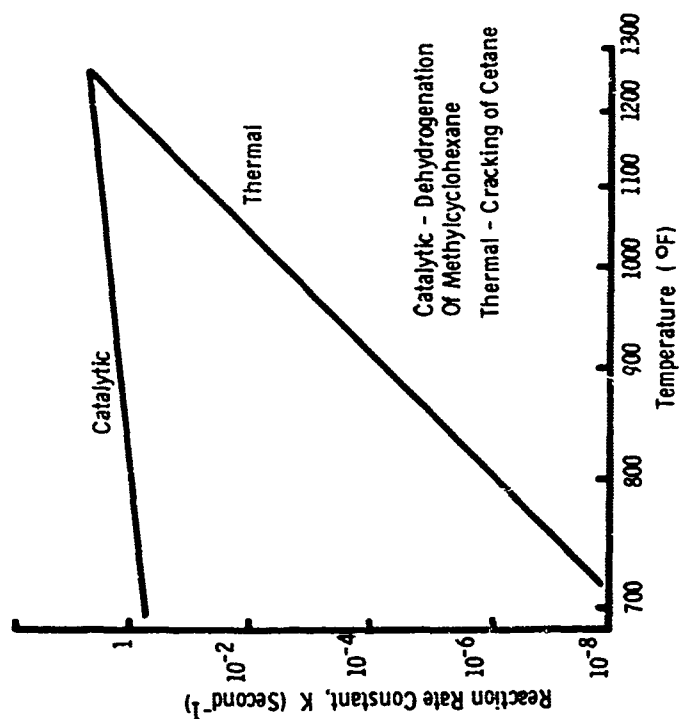


FIGURE 3 COMPARISON OF THE REACTION RATE CONSTANTS OF THERMAL AND CATALYTIC REACTORS

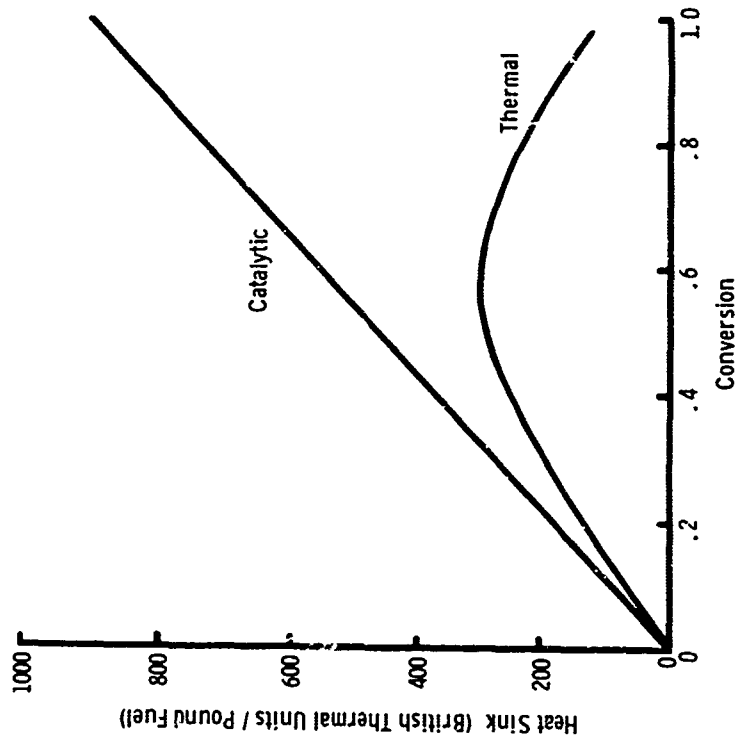


FIGURE 4 COMPARISON OF THE HEAT SINK OF THERMAL AND CATALYTIC REACTORS OF METHYLCYCLOHEXANE

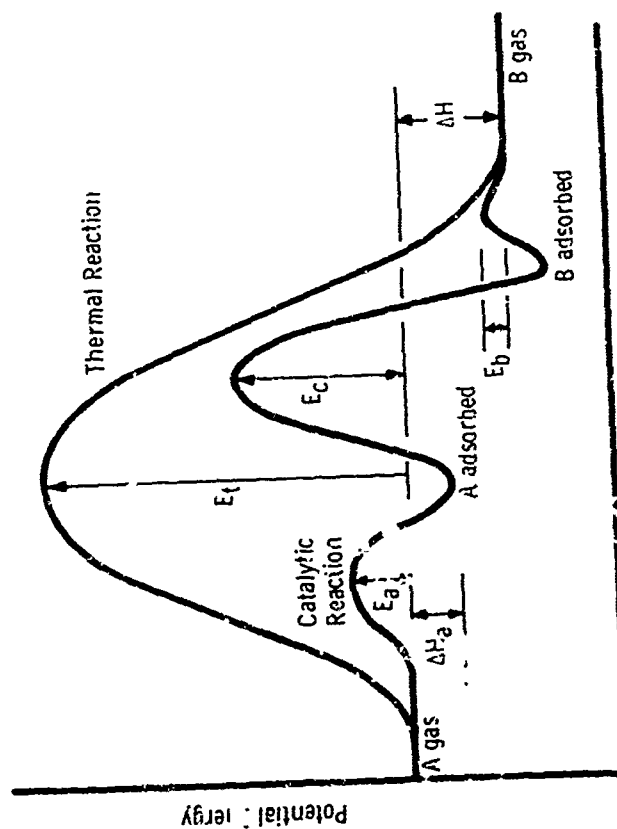


FIGURE 5 ENERGY CHANGES DURING REACTION

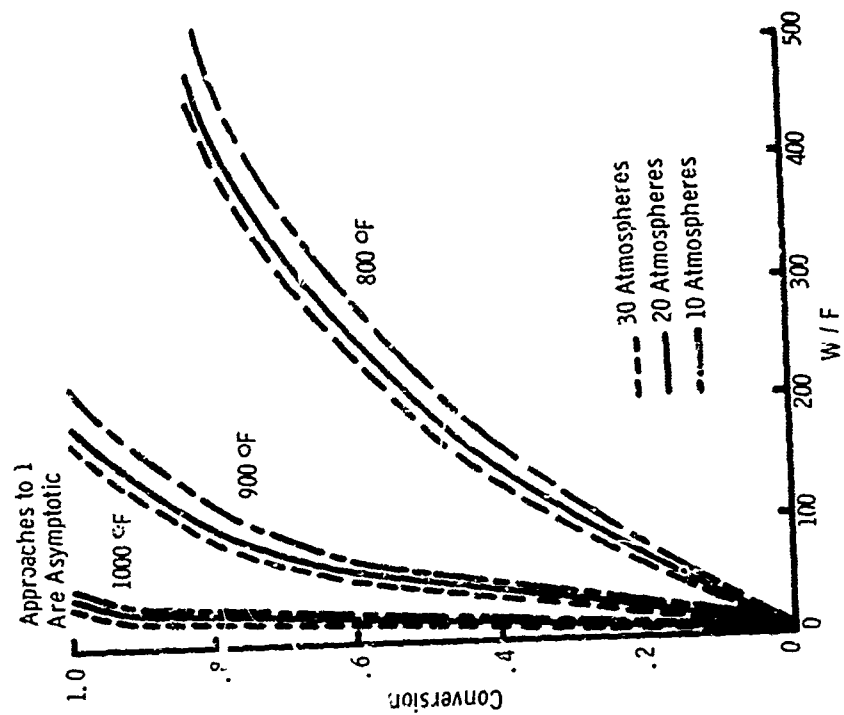


FIGURE 6 CONVERSION VERSUS W/F

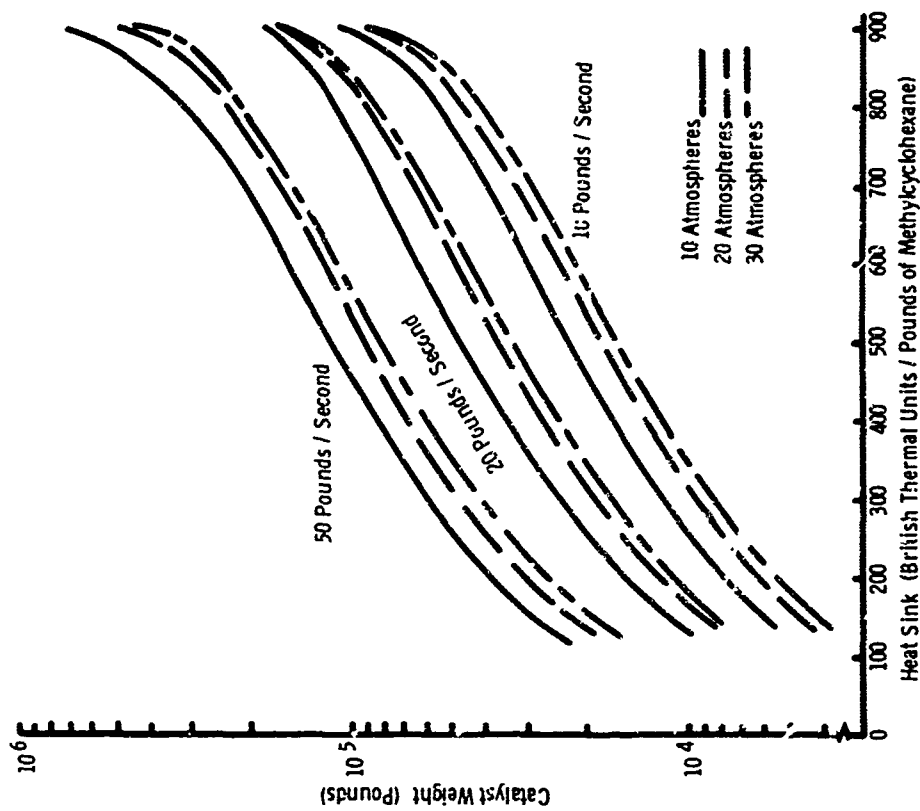


FIGURE 7 CATALYST WEIGHT VERSUS REACTION HEAT SINK AT 1000°F

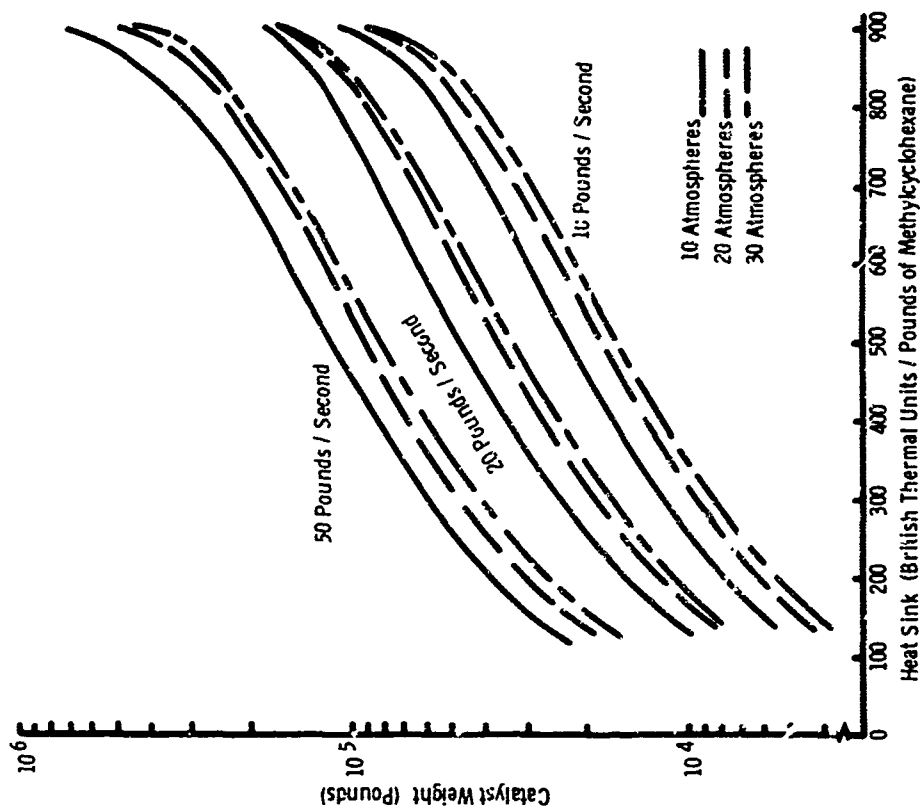


FIGURE 8 CATALYST WEIGHT VERSUS REACTION HEAT SINK AT 900°F

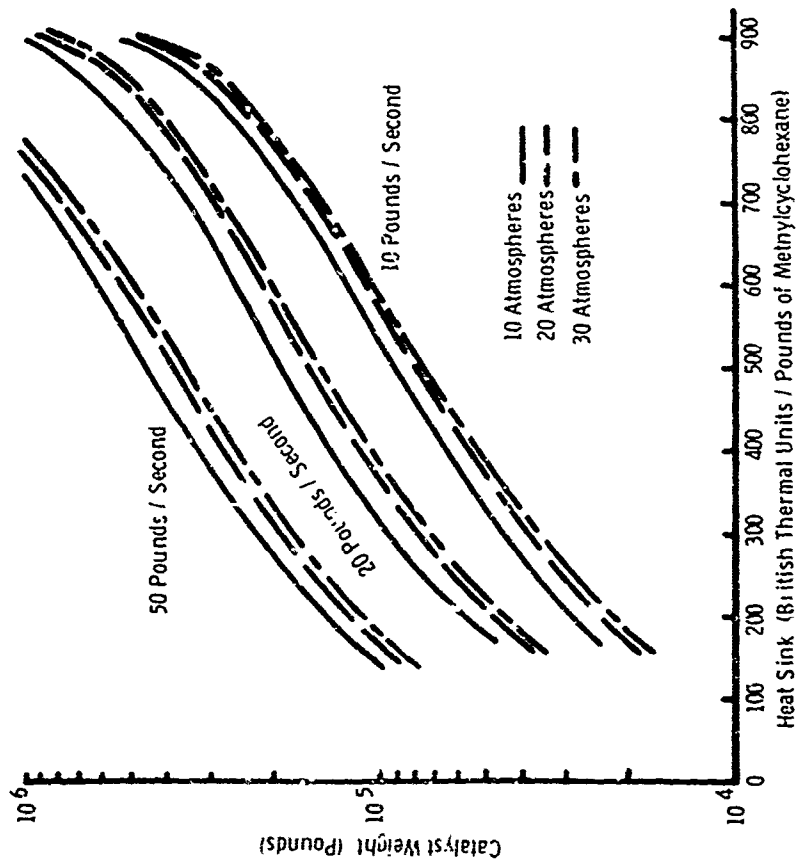


FIGURE 9 CATALYST WEIGHT VERSUS REACTION HEAT SINK AT 800°F

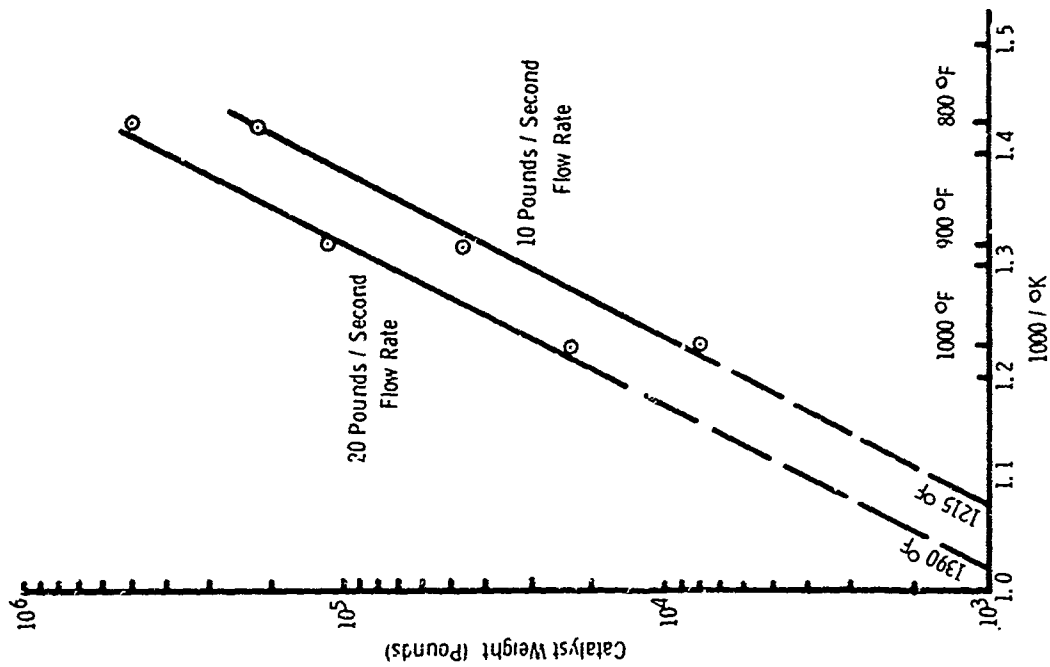


FIGURE 10 CATALYST WEIGHT VERSUS RECIPROCAL TEMPERATURE

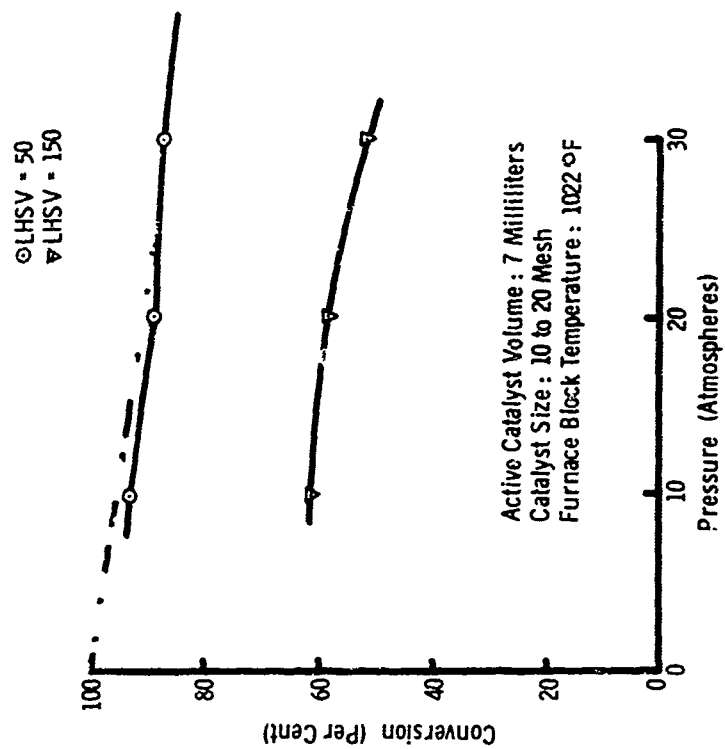


FIGURE 12 EFFECT OF PRESSURE ON THE CONVERSION OF METHYLCYCLOHEXANE OVER ONE PERCENT PLATINUM ON ALUMINA

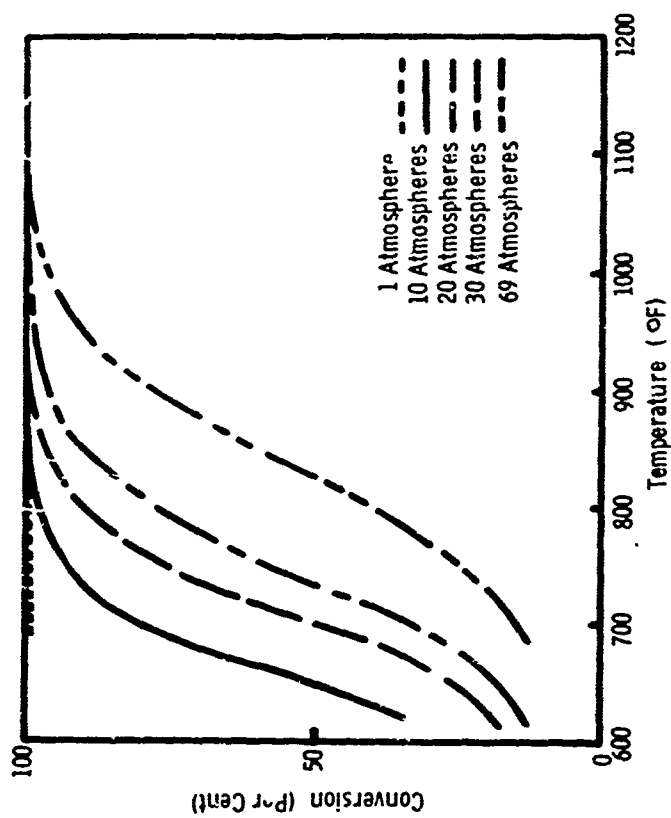


FIGURE 11 EQUILIBRIUM CONVERSION FOR THE SYSTEM METHYLCYCLOHEXANE-TOLUENE

(U) REAL TIME TEM-MODE ANALYSIS OF HE-NE LASERS

by

FERDINAND F. KUHN

DIRECTORATE OF GUIDANCE TEST
CENTRAL INERTIAL GUIDANCE TEST FACILITY
HOLLOMAN AIR FORCE BASE, NEW MEXICO



Ferdinand F. Kuhn

BIOGRAPHY

Ferdinand F. Kuhn, Chief of the Systems Analysis Branch of the AFMDC's Central Inertial Guidance Test Facility, began his missile career in January 1957 as a member of the Rocket Propulsion Team of the Directorate for Research and Development, Holloman AFB, New Mexico, and received his Ph.D. in Engineering from the University of New Mexico, Albuquerque, New Mexico, in 1966. Before joining the Guidance Test Facility in 1961, Dr. Kuhn was task engineer for the Liquid Propulsion Rocket Engines at the Holloman High Speed Test Track. He now directs the performance evaluation analysis of conventional and non-conventional guidance systems subjected to laboratory and rocket sled testing.

Dr. Kuhn was born in 1928 at Darmstadt, Germany and earned his MS in Engineering from the Darmstadt Institute of Technology in 1955. Prior to this time he performed undergraduate studies for one academic year at the Oklahoma State University, Stillwater, Oklahoma, as a result of a scholarship he won from the Institute of International Education. Dr. Kuhn's arrival at Holloman AFB in 1957 was part of Operation "Paper Clip".

REAL TIME TEM-MODE ANALYSIS OF HE-NE LASERS (U)

ABSTRACT

In connection with investigations of the Thermal Effects on He-Ne Gas Lasers, it was necessary to monitor and analyze the transverse electro-magnetic (TEM)-Modes of several Laser instruments.

The conventional methods of observing the TEM-Mode patterns such as direct photographs of the Laser beam or indirect visual observations of the Laser beam reflections from a screen were considered too time-consuming and dangerous, respectively.

This paper describes a unique device which was built by the author to circumvent these difficulties. It is referred to as "Automatic Laser Beam Detector and Real Time Transverse Electro-Magnetic Mode (TEM-MODE) Analyzer" and has the following novel features:

- a. It permits the optimal tuning of any continuous wave (CW) Laser without exposing the investigator to the dangers of looking directly at the Laser beam or its reflection. The beam can be analyzed in real time despite the wearing of safety goggles which filter out the particular Laser wavelength and hence render the beam invisible.
- b. It avoids possible ambiguities in distinguishing between various TEM-Modes by its ability to move by remote control the light sensing pinhole/photo-diode combination with respect to the center of the scanning motion of the Laser beam. The Laser beam can thus be analyzed from outside the radiation room.
- c. It allows the continuous observation of Laser power output changes as a result of TEM-Mode transitions from one mode to another.
- d. It permits the continuous observation and the tuning of a CW Laser for optimal "purity" in applications to the field of communication.

Several illustrative examples of actual results are presented.

REAL TIME TEM-MODE ANALYSIS OF HE-NE LASERS (U)

I. INTRODUCTION AND PURPOSE

High powered continuous wave gas Lasers have recently become an important tool in support of inertial guidance system testing at the Central Inertial Guidance Test Facility, CIGTF, (1) at Air Force Missile Development Center, Holloman Air Force Base, New Mexico. At present Lasers are used for possible application for determining rocket sled velocities (2) (3) as well as for the continuous monitoring of an inertial guidance platform during sled runs at Holloman high speed test track. (4)

During these developmental phases it was observed that the Laser power output varied considerably with ambient temperature. As a result of more stringent experiments at CIGTF with a Spectra Physics model 115 gas phase Laser (He-Ne) it was found that there exists a single maximum of the Laser power output with respect to the ambient temperature. (5) This was an unexpected phenomenon and, since no information could be found in the literature about the thermal behavior of gas Lasers, formed the basis for the author's Ph.D. dissertation. (6) This research was concerned with a thorough theoretical and experimental investigation of He-Ne Lasers and resulted in formulating a method for predicting their operational performance as a function of temperature. During the course of these investigations, it was necessary to monitor and analyze the transverse electro-magnetic (TEM)-Modes* of several Laser instruments. Specifically, the basic TEM₀₀-Mode, which is the preferred mode of operation had to be monitored while the Laser was subjected to various ambient temperatures. This was done in order to isolate Laser power output changes due to TEM-Mode changes from those due to strictly thermal effects on the Laser processes within the plasma.

With the increase in Laser power outputs, the dangers associated with tuning and experimenting, particularly with observing the TEM-Mode of the Laser beam with the unprotected eye, are becoming more apparent. According to Reference (12), there are numerous possibilities of biological damage due to Laser radiation.

* The transverse electro-magnetic (TEM)-Modes of Lasers and Masers are expertly described, both theoretically and experimentally, in References 7 through 11.

As to the conventional methods of observing the TEM-Mode patterns; the method of direct photographs of the Laser beam was considered too time-consuming, and the method of indirect visual observations of the Laser beam reflections from a screen was considered too dangerous for the above-mentioned investigations.

The author's applied research investigation concerning the thermal effects on the power output of He-Ne gas Lasers required, however, continuous and real time observations of the Laser's TEM-Mode. Because of the biomedical dangers associated with the conventional method of looking at the reflection of the Laser beam spots and because the wearing of safety goggles, which render the beam invisible, do not permit any real time observation of the beam, a device was built which allows the instantaneous analysis of the TEM-Mode in complete safety.

This device is referred to as "Automatic Laser Beam Detector and Instantaneous Transverse Electro-Magnetic Mode (TEM-Mode) Analyzer" and has the following novel features:

a. It permits the optimal tuning of any continuous wave (CW) Laser without exposing the investigator to the dangers of looking directly at the Laser beam or its reflection. The beam can be analyzed in real time despite the wearing of safety goggles which filter out the particular Laser wavelength and hence render the beam invisible.

b. It avoids possible ambiguities in distinguishing between various TEM-Modes by its ability to move by remote control the light sensing pinhole/photo-diode combination with respect to the center of the scanning motion of the Laser beam. The Laser beam can thus be analyzed from outside the radiation room.

c. It allows the continuous observation of Laser power output changes as a result of TEM-Mode transitions from one mode to another.

d. It permits the continuous observation and the tuning of a CW Laser for optimal "purity" in application to the field of communication.

The purpose of this paper is to present

(1) The basic definitions of transverse electro-magnetic (TEM) modes,

(2) a detailed description of the "Laser Beam Detector and TEM-Mode Analyzer" including the sequence of its operation,

(3) experimental and routine application of the TEM-Mode analyzer including experiments in verification of TEM-Mode theory, and

(4) proposed safe methods of Laser alignment.

II. TRANSVERSE ELECTRO-MAGNETIC (TEM) MODES

A gas Laser consists of an amplifying atomic medium occupying all or part of the volume of a resonator, such as a Fabry-Perot interferometer. The role of the resonator is to maintain an electro-magnetic field configuration, corresponding to a single or to multiple resonant modes, whose losses are replenished by the amplifying medium through induced emission of atoms in the upper of the two optically connected energy levels, (References 13 and 14). The atomic energy levels under consideration in this paper are the $3s_2$ and $2p_4$ levels for neon with the corresponding wavelength of 6328 Å, (Figure 1). The optical resonator for gas Lasers usually consists of a cylindrical plasma tube with two opposing reflectors at right angles to the cylindrical axis. The configuration of these reflectors can be (1) both plane parallel, (2) both curved, or (3) one plane and one curved.

The oscillation consists essentially of a standing wave generated by a plane wave bouncing back and forth between the two reflectors. A number of loss mechanisms can exist which attenuate the wave. The most important light losses are:

a. Transmission and absorption in the mirrors (reflectors).

b. Diffraction by the mirror apertures.

c. Absorption in the amplifying medium due to mechanisms other than the radiative absorption between the Laser levels.

d. Mode conversion due to imperfect mirrors.

The interferometer forms a multimode resonant cavity required to produce oscillation. For a high enough gain

the spontaneously emitted light will build up until the light losses are compensated by the gain of light energy. The frequency characteristics of gas Lasers are determined primarily by the cavity properties, such as cavity length and the shape of the mirrors.

A fundamental investigation on the oscillation modes and the corresponding losses of a Laser cavity of the Fabry-Perot type has been carried out by Fox and Li.⁽⁷⁾ The modes and the corresponding losses of the resonator were obtained as eigenfunctions and eigenvalues of an integral equation whose kernel depends on the shape of the end mirrors. These results show the existence of a whole series of transverse electro-magnetic modes possessing even and odd symmetry about the interferometer axis.

A normal mode consists of a electro-magnetic field distribution over the aperture of the interferometer which reproduces itself in successive transits between the mirrors. In traversing from one of the end plates of the Fabry-Perot system to the other, a wave will spread beyond the limits of the second plate and some energy will be lost by diffractive effects during transit; the field in the outer portion of the aperture is more greatly attenuated than the field at the center.

These field distributions and the resultant TEM-Modes are often characterized as:

- a. Axial modes; modes which have a symmetrical circular cross section of near Gaussian intensity distribution.
- b. Off-axial modes; modes which are anti-symmetric and may have several maxima in cross section.

Several of the more common TEM-Modes are presented in Figure 2. These beam apots clearly show the difference between axial and off-axial modes. Note that the TEM_{01}^* -Mode indicates the combination of two modes to form a composite circular-cymmetric mode, (References 7 and 10).

The characteristic electric field distribution "E" of some of these modes are illustrated in Figure 3. For all of these modes, the electric field is perpendicular to the direction of Laser beam propagation.

The modes of primary concern in this paper are the TEM_{00} -Mode and the TEM_{01}^* -Mode and the transitions between them. These modes could be most easily generated with the commercially available Laser instruments.

III. GENERAL DESCRIPTION OF THE AUTOMATIC LASER BEAM DETECTOR AND TEM-MODE ANALYZER

This device, built at the Guidance and Control Directorate, Holloman AFB, New Mexico, makes it possible to automatically search for and lock onto a Laser beam, and then to analyze the beam as to its TEM-Modes. The searching and analyzing operations are performed safely and remotely by use of a modified X-Y plotter and an oscilloscope, (Figures 4 and 5) thus eliminating the dangers associated with looking at the Laser beam either directly or at its reflection from a screen.

In the search mode, the device mechanically moves a photo-diode in a scanning fashion across a target area. The photo-diode is a light sensing element which is located behind a pinhole. After acquiring the Laser beam, which is indicated by the signal from the photo-diode, the search mode is terminated. The pinhole/photo-diode is now held fixed with respect to the Laser beam and the scan mode is initiated.

In the scan mode, an oscillating mirror moves the Laser beam across the now stationary pinhole/photo-diode (Figures 6, 7). The pinhole diameter (0.4mm) is one order of magnitude smaller than the Laser beam diameter, yet large enough to avoid diffraction. The TEM-Mode of the Laser oscillation can be observed in real time (instantaneously) by determining in real time the photon-density - or light intensity distribution of the Laser beam in a direction perpendicular to the Laser beam propagation. This is accomplished by feeding the output of the photo-diode into the Y-channel of an oscilloscope while the X-channel is triggered in synchronization with the oscillatory mirror motion (Figure 6). The resulting form of the electron beam on the oscilloscope is a direct representation of the TEM-Mode shape.

A remote control permits the movement of the pinhole/photo-diode over a small range in two dimensions; i.e., in the X and Y directions (Figure 8). Thus the pinhole can be precisely placed at the center of the scanning motion of the Laser beam. This is an important requirement to avoid ambiguities in the TEM-Mode analysis.

IV. DETAILED DESCRIPTION AND SEQUENCE OF OPERATION

IV.1 GENERAL

The entire set up of the device is shown in Figure 4.

The schematic of the device is presented in Figure 6.

IV.2 IMPLEMENTATION OF THE SEARCH MODE

A standard Moseley "autograph" X-Y recorder-plotter, Model 2D-2 (Figure 5) was modified so that a photo-diode would automatically sweep the entire surface of the plotter. The arrangement of the microswitches which perform the sweep, return, and stepping functions are shown in Figure 5. The pinhole and the light sensing element (photo-diode, LS 400) are mounted on the penholder of the X-Y plotter (Figure 5). A LEDEX switch controls the motion of the photo-diode in the Y direction by discrete steps, i.e., one step per sweep of the diode in the X-direction.

IV.3 IMPLEMENTATION OF THE REMOTE CONTROL

The remote controller contains the coarse and fine controls for the penholder of the plotter. These controls were obtained from the plotter and the wiring was accomplished per Operating and Maintenance Manual for the X-Y Plotter, Schematic Input and Servo-systems, Mod 2D-2, MD-9686. The remote controller is located close to the oscilloscope (Figure 8). It is used to start the search mode and to lock onto the Laser beam once the beam has been acquired. It permits the fine control of the photo-diode positioning in the X-Y plane. These features permit placing the pinhole into the geometric center of the scanning motion of the Laser beam. Note: The Y-axis coarse control is a ten-revolution potentiometer, 5K, actuated by the above mentioned LEDEX switch.

IV.4 IMPLEMENTATION OF THE SCANNING MOTION

The scanning motion of the Laser beam is generated by an oscillating mirror. The angle of oscillation is less than 1 degree. The frequency of oscillation is approximately 0.5 cycles per second. The mirror is mounted on a turntable which is made to oscillate by a lever action which in turn is actuated by an eccentric shaft mounted on the rotation disc of a phonograph (Figures 6 and 7).

IV.5 SYNCHRONIZATION OF THE SCANNING MOTION WITH THE X-CHANNEL OF THE OSCILLOSCOPE (FIGURE 7)

A microswitch mounted to the base of the phonograph (Figure 8) is actuated once during each revolution of the eccentric shaft, i.e., once per scan sweep of the Laser beam with respect to the photo-diode. The microswitch triggers the electron beam of a Tektronix Type RM

45A oscilloscope, thereby establishing the X-coordinate. The output of the photo-diode is fed into the Y-channel and deflects the triggered electron beam in proportion to the Laser light intensity received through the pinhole.

IV.6 CENTERING OF THE PINHOLE WITH RESPECT TO THE CENTER OF THE SCANNING MOTION

By decreasing the sweep rate of the electron beam, two or more Laser beam scanings across the pinhole can be observed on the scope (Figures 9 through 11). This permits the centering of the pinhole by observing the variations of the "dip in the camel's back" during the adjustments. If the pinhole is centered then this dip will return to the original level that the electron beam had at the time of its onset; compare oscilloscope traces on Figures 9 and 10. If the pinhole is not centered, the waveshape on the scope can be misinterpreted; for instance, a normal TEM₀₀-Mode may look like a TEM₀₁*-Mode, (Figure 11). By subsequently increasing the sweep rate, a single scanning of the Laser beam can be generated on the scope and the mode shape, and/or cavity tuning, can be observed and analyzed concurrently.

IV.7 SEQUENCE OF OPERATION OF THE AUTOMATIC LASER BEAM DETECTOR AND INSTANTANEOUS TEM-MODE ANALYZER. (Current configuration)

- a. Check to insure that all equipment is in the power off mode.
- b. Make the initial alignment of the target area (X-Y plotter) by means of a theodolite located at the target area. This assures that the Laser beam will "hit" the area once the Laser is turned on, (Section VI).
- c. Turn on the Laser and monitor the Laser power output by the power output meter, the instrument to the right of the scanning motion generator in Figure 4.
- d. Actuate the "main power" switch at the remote controller. This will supply 115 volts to the X-Y plotter. Then actuate the switches marked "Automatic/Man." and Start Sweep". This will initiate the automatic search mode.
- e. Set the oscilloscope to trigger the electron beam by its internal time base (Figure 4). Maintain this setting for the duration of the search mode.
- f. Look for a momentary rise and fall of the electron beam on the scope. This indicates that the Laser

beam has been acquired. (This process can be automated by use of a bell or a warning light.)

g. Terminate the search mode by putting the switch marked "Automatic/Man." into "Man." position. Under the current configuration of this invention this operation will cause the X plotter arm to return to the left hand side of the plotter.

h. Manually return the arm to the acquisition point by actuating the "X-axis" coarse control, i.e., the lower of the two control knobs until the electron beam deflection indicates the acquisition of the Laser beam.

i. Adjust both the "X-axis" and the "Y-axis" fine controls (the upper of the two control knobs) until the maximum deflection of the electron beam is obtained on the oscilloscope. This indicates that the pinhole/photo-diode is located approximately in the center of the Laser beam. Actuate the pushbuttons "up" and "down" if the "Y-axis" fine control does not provide enough range of adjustment.

j. Turn on the scanning motion generator (Figure 8). This operation establishes a center of motion of the Laser beam on the target area which will not necessarily coincide with the pinhole/photo-diode (Figures 9 and 10).

k. Position the pinhole/photo-diode in the center of motion. This is accomplished by simultaneously adjusting the "X-axis" fine control and observing the scope. During a complete scanning cycle the electron beam trace will rise and fall twice.

(1) If every other "fall" level (the lowest level the electron beam trace reaches after going through a maximum) during one scan cycle is not identical to the lowest level of the electron beam trace, the pinhole/photo-diode is not in the center of the Laser beam motion. Continue to actuate the "X-axis" fine control until the "fall" levels are identical. These "fall" levels correspond to the "dips in the camel's back".

(2) If the "fall" levels cannot be changed by actuating the "X-axis" fine control, a TEM₀₁*-Mode (Figure 11) is to be expected rather than a TEM₀₀-Mode.

1. Set the scope to be triggered by the external trigger switch (Figure 8). Depending on the sweep rate of the electron beam, a single trace of a single, double, or

triple scan is observed and may be photographed. From this trace the TEM-Mode is determined for the particular cavity tuning.

V. EXPERIMENTAL AND ROUTINE USE OF THE TEM-MODE ANALYZER

During the experimental phase of the research presented in Reference (6), the photon distribution in various TEM-Modes, particularly of the TEM₀₀ and TEM₀₁* pattern, have been determined using the device described above.

The mode pattern of three different commercial Laser instruments by Spectra-Physics were analyzed in the course of this study, i.e.,

a. He-Ne Laser, Model 115 (RF Excitation),
Figure 12.

b. He-Ne Laser, Model 131 (DC Excitation)
Figure 13,14.

c. He-Ne Laser, Model 116 (RF-DC Excitation),
Figure 15.

Figures 16 and 17 show the resulting oscilloscope traces for the transition from the TEM₀₁*-Mode to the TEM₀₀-Mode by mechanically tuning the cavity, (He-Ne Laser, Model 116). The intensity variations, for instance, between those of Figure 16 and those of Figure 17 could not be distinguished by the dangerous but conventional visual observation of the reflected image of the Laser beam.

V.1 EXAMINATION OF OSCILLOSCOPE TRACES

Examination of the oscilloscope traces presented in Figures 16 and 17 and in Figures to follow show a number of phenomena which warrant further explanation:

a. Most of these photos of oscilloscope traces contain a set of two oscilloscope traces, one of which represents a single scanning of the Laser beam across the pinhole. This is obtained at a particular sweep rate of the electron beam. The other trace represents a double scanning (back and forth) of the Laser beam across the pinhole. This is obtained by a lower sweep rate of the electron beam while the scanning motion frequency is kept constant. This latter trace serves as a check to assure that the pinhole is in the center of the scanning motion. A quadruple scanning, for instance, is added in Figure 18 which likewise allows a comparison between the TEM₀₀ and TEM₀₁* Modes.

b. The small ripples in some traces are caused by noise (room lights) introduced into the photo-diode. This is due to the fact that the Laser instrument had to be operated at a minimum power output for safety reasons.

c. The asymmetry of all traces with respect to the vertical axis is caused by the non-linear drive mechanism of the scanning motion generator; specifically, the point of contact between the eccentric shaft and the lever arm (Figure 6) varies, i.e., its distance with respect to the pivot point of the oscillating mirror is not constant during a complete scan cycle. Therefore, the fall time of the traces is shorter than the rise time which accounts for the asymmetric appearance of these traces.

d. The large noise ripples at the far right hand side of the double sweep traces are caused by the noise generated in actuating the X-channel trigger switch on the phonograph.

e. The ripples shown in Figure 18 result from variations of the RF excitation of the particular Laser instrument (Model 116) under test. The bottom trace of Figure 18 shows the mode pattern as a result of RF excitation superimposed on the DC excitation. The remaining traces show the effects of reducing the amount of RF excitation. This effect is demonstrated in more detail in Figure 19.

f. The difference in level of the "tops of the camel's back" of the TEM_{01}^* -Modes, is due to the fact that the horizontal axis of the scanning motion is not parallel to the X-axis of the field distribution (Figures 16 through 19). This is caused by the non-orthogonality of the axis of rotation of the oscillating mirror with respect to the electrical field axis of the Laser. Considering the specific purpose of this device, it was not deemed necessary to perfect it in this respect.

g. The scale in the vertical direction for these traces is relatively arbitrary for each individual oscilloscope trace, since the sensitivity of the scope was chosen so that the peak intensity in each TEM-Mode would cause full electron beam deflection. The horizontal scale, however, is the same for each pattern at a given sweep rate of the electron beam. It can be observed, therefore, that the lateral extent (Laser beam diameter) of the TEM_{00} -Mode increases during its transition up to and including the TEM_{01}^* -Mode. This indicates a verification of theory which predicts the trend as shown in Figures 16 and 17, i.e., that the extent of the mode increases with increase in order number.

V.2 TEM-MODE ANALYZER EXPERIMENTS IN VERIFICATION OF THEORY

Because of their particular importance in light of the TEM-Mode theory developed in References (7) through (11), the results of a number of special experiments with the TEM-Mode analyzer are presented in this section. These results verify the validity of the TEM-Mode analyzer.

a. One of the predictions of the theory presented by Boyd and Gordon (8) is that the diameter of the mode pattern is independent of the lateral extent of the cavity mirrors. Two different Laser instruments, i.e., the Model 115 and Model 131, were used for this verification experiment. The Model 115 Laser has an inner diameter (I.D.) of the plasma tube of 5mm while the Model 131 Laser has an I.D. of 2mm. The I. D. of the plasma tube definitely limits the upper bound of the Laser beam diameter. The vertical sensitivity of the oscilloscope was adjusted to obtain full electron beam reflection in the recording of the TEM₀₀-Mode of both instruments. As can be seen from Figure 20, the lateral extent of the spot size in the two cases is almost the same. Figure 20-A is one of the first photos taken with the TEM-Mode Analyzer as a result of experiments with the Model 115 Laser. Figure 20-B was taken from a series of observations of the Model 131 Laser, while it was located in the environmental chamber (Figure 14). Figure 21, pertaining to the Model 116 Laser, further substantiates this theory. The I. D. of the Model 116 instrument is 2.75mm.

b. The distribution of intensity in the TEM₀₀-Mode as a function of input power into the Laser instrument can be observed by comparing Figure 21, top trace with Figure 20-B, top trace. The difference in input (and output) power between the Model 116 and 131 (with almost identical I. D. of the plasma tube) is approximately one order of magnitude. As can be seen from the oscilloscope traces the lateral extent of the beam spot and, therefore, of the intensity distribution in the mode pattern, appears to be invariant with respect to output power of the Laser.

c. The analyzer was used to demonstrate the effects of the RF excitation on the Laser beam output, specifically, on the purity of the Laser beam. The purpose of the RF excitation is to suppress plasma noise and to increase the gain. Figure 19 shows these effects and the resultant quieting of the Laser beam.

From the preceding experiments it can be concluded that this device showed great improvements over other more conventional photographic methods (Figure 2) as far as both

resolution of the mode analysis and savings of time are concerned. An additional factor of consideration is the safety aspect of this apparatus, particularly in light of the continuous trend toward higher output power and the concern in medical circles about Laser radiation damage.

V.3 TEM-MODE ANALYZER USE TO DETERMINE MODE PATTERN CHANGES AS A FUNCTION OF TEMPERATURE

Figure 14 shows the overall set up of this test including the instrumentation for data recording and TEM-Mode analysis.

The alignment of the Laser with respect to the optical port of the chamber was checked with the TEM-Mode Analyzer. It was found that an angle of zero degree between the Laser beam propagation and the normal to the optical port resulted in minimum distortion of the TEM₀₀-Mode observed through the optical port, (Figure 22). In order to obtain good oscilloscope traces it was also necessary to turn on the circulation fans of the environmental chamber, (Figure 14). The effect of operating the chamber with and without fans on the oscilloscope traces can be seen in Figure 23-A.

From Figure 23-B and Figure 23-C, it is seen that the TEM₀₀-Mode did not change to any other Mode over the temperature range of these tests. Oscilloscope recordings at temperatures higher than 337.0°K could not be made due to lack of photographic film. The remaining noise, after the circulation fans were turned off, was due to the residual (Sunday) vibration in the environmental test laboratory. Note that the oscilloscope traces of Figure 22-C show a higher (workday) noise level.

VI. PROPOSED SAFE METHODS OF LASER ALIGNMENT

In order to align the Laser instrument initially with respect to a target area without having to observe the Laser beam directly, the following possible methods are proposed:

Alternative 1: Optical Flat

a. A position-adjustable optical flat is mounted on the Laser instrument such that the normal to the optical flat is approximately parallel to the line of Laser beam propagation.

b. An accurate alignment of the optical flat is made in the Laboratory.

(1) With the Laser turned on, the X-Y coordinates of the Laser beam on the target area are established. This can be done safely with the above described device since the voltages on the X-Y servo loops of the plotter are directly proportional to the X-Y coordinates of the penholder.

(2) The Laser is then turned off. The X-Y coordinates of the intersection of the normal to the optical flat and the target area can be established by means of the theodolite located at the target.

(3) The optical flat is subsequently adjusted to make its normal "hit" the target area at the proper distance "d" above the previously determined X-Y coordinates of the Laser beam where "d" corresponds to the distance of the normal to the optical flat from the center of the Laser beam propagation axis.

c. After alignment of the optical flat in the laboratory and with the Laser turned off, the target area for the Laser beam can be established by the theodolite over distances up to approximately 100 feet.

Alternative 2: Telescope

This approach is similar to the "Sighting in" of a telescope for a rifle.

A telescope is mounted on the Laser instrument. The accurate alignment of the scope is done in the laboratory in a fashion similar to the one outlined in Alternative 1 b. The crosshairs of the telescope are used to align the scope parallel to the line of Laser beam propagation by adjusting the scope until the intersection of the crosshairs coincides with the desired point of distance "d" above the X-Y coordinates of the Laser beam.

The advantage of this approach is the higher accuracy of the target alignment over larger distances depending on the focal length and resolution of the scope.

VII. REFERENCES

- (1) Wright, H. V., Major, USAF, "Central Inertial Guidance Test Facility Guide, Facilities and Capabilities", Technical Document Report, MDC-TDR-62-4 (1962)
- (2) Watkins, M. E., "Phase II Technical Summary Report and Final Report on Study of Laser Application to Velocity Measuring System", prepared for AFMDC, Holloman AFB, New Mexico, by Aircraft Armaments, Inc., Contract AF 29 (600)-4136 (1964)
- (3) Redifer, J. L., "Error Analysis of the Laser Ring-A-Round System", Defense Documentation Center, Number AD 453 157 (1964)
- (4) Olender, H. A., Captain, USAF, "An Investigation of a Laser/Interferometer Attitude Monitoring Device", Master of Science Thesis, AFIT, Wright-Patterson AFB, Ohio (1962)
- (5) Real, Jr., M. J., Major, USAF, "Laser Output Power Versus Environment Changes", Working Paper, AFMDC, Holloman AFB, New Mexico (1964)
- (6) Kuhn, F. F., "Thermal Effects on the Power Output of 6328 Å He-Ne Gas Lasers", A Dissertation submitted in partial fulfillment of the requirements for the degree of Doctor of Philosophy (Ph.D.), University of New Mexico, Albuquerque, New Mexico, June 1966
- (7) A. G. Fox, T. Li, "Resonant Modes in a Maser Interferometer", Bell System Techn J., 40 453 (1961)
- (8) G. D. Boyd, J. P. Gordon, "Confocal Multimode Resonator for Millimeter Through Optical Wavelength Masers", Bell System Techn J., 40 489 (1961)
- (9) G. D. Boyd, H. Kogelnik, "Generalized Confocal Resonator Theory", Bell System Techn J., 41 1347 (1962)
- (10) W. R. Rigrod, "Isolation of Axi-Symmetrical Optical Resonator Modes", Appl. Phys Letter, 2 51 (1963)

- (11) D. Rosenberger, "Oscillation Spectra in the He-Ne Gas Laser", NSTIC Translation No 1583 (from German) by Research and Development Services Department (Naval), Defense Documentation Center Number AD 464 775 (1965)
- (12) Laser Letter, Published by American Data Processing, Inc., 4th Floor, Book Bldg., Detroit, Michigan, Vol 2, 14 (1965)
- (13) A. Jariv, J. P. Gordon, "The Laser", Proc. IEEE, 51 1 (1963)
- (14) A. Einstein, "Zur Quantentheorie Der Strahlung", Phys. Zeitschrift, 18 121 (1917)

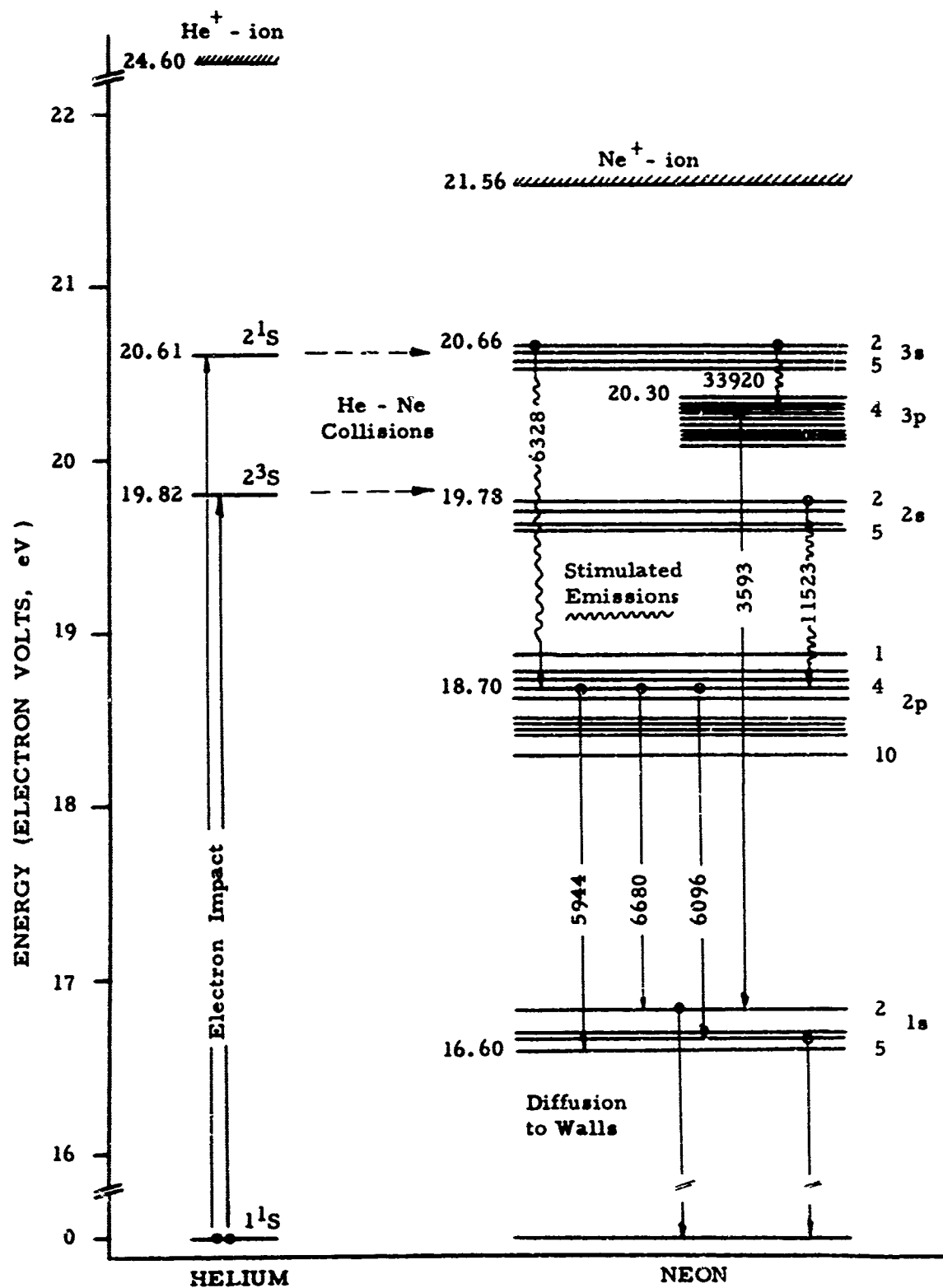


Figure 1. Energy-level Diagram for He and Ne

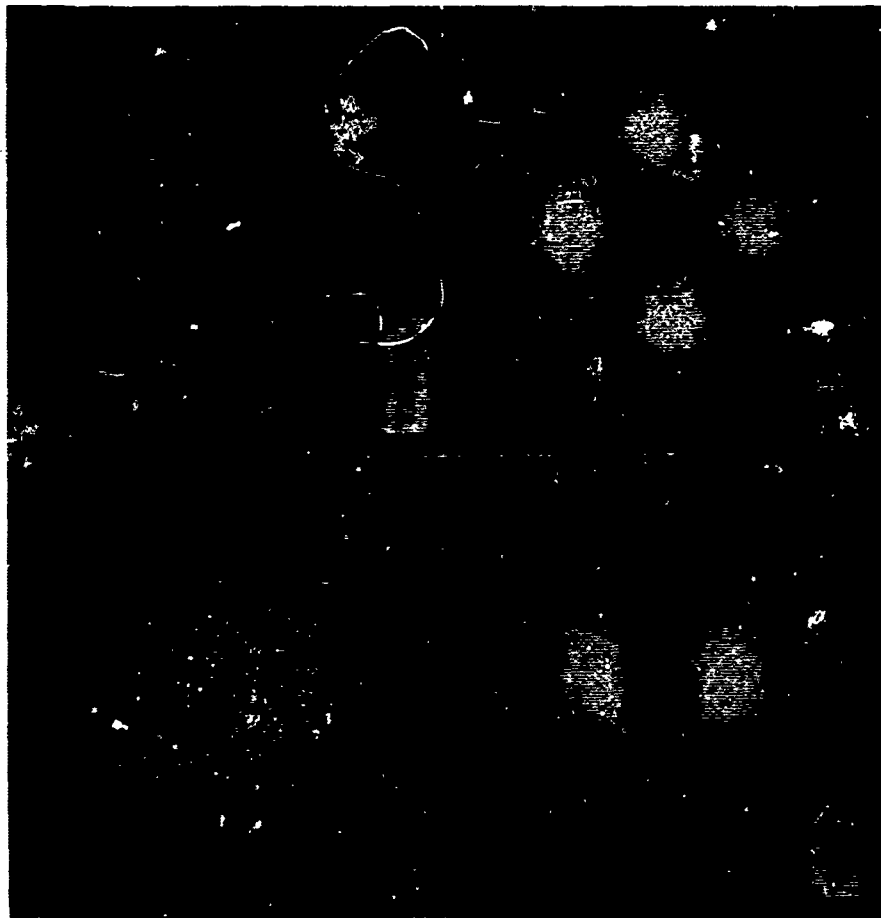


Figure 2. Beam spots as a function of field intensity) Distributions of various TEM-modes

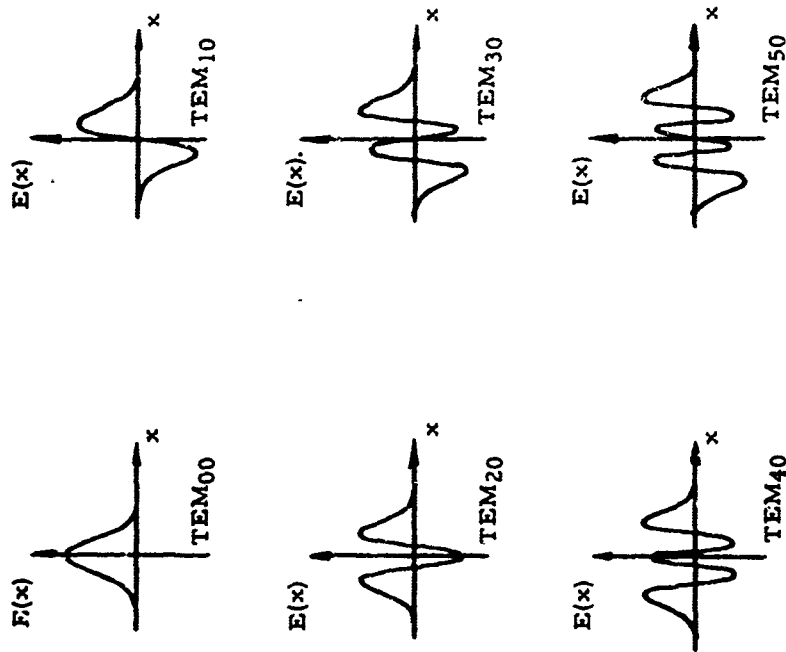


Figure 3. Field Distributions in Some Low Order TEM-Modes



Figure 4. Automatic Laser Beam Detector and Instantaneous TCM Mode Analyzer



Figure 5. Implementation of Automatic Laser Beam Searcher and Detector (Modified X-Y Plotter)

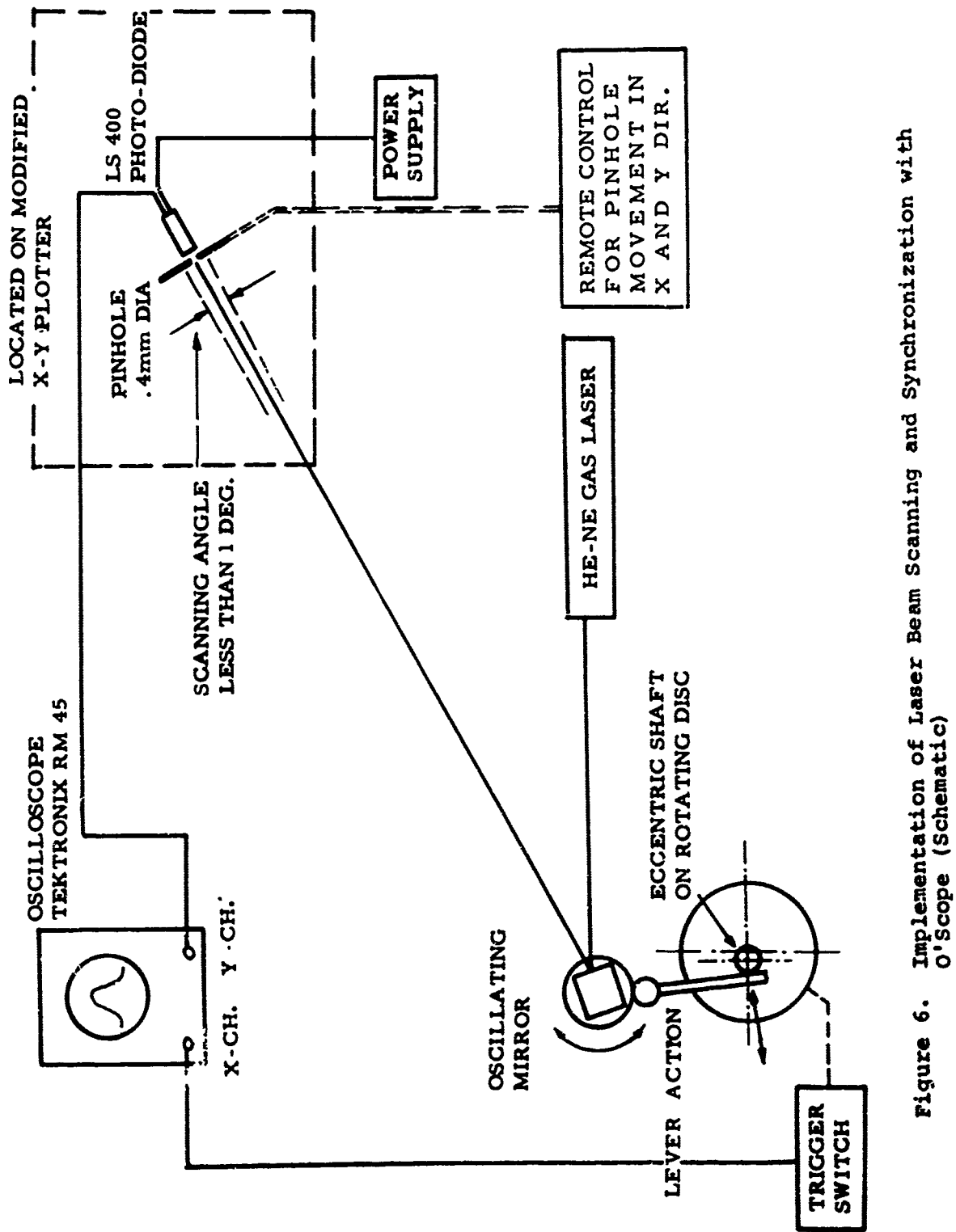


Figure 6. Implementation of Laser Beam Scanning and Synchronization with O'Scope (Schematic)

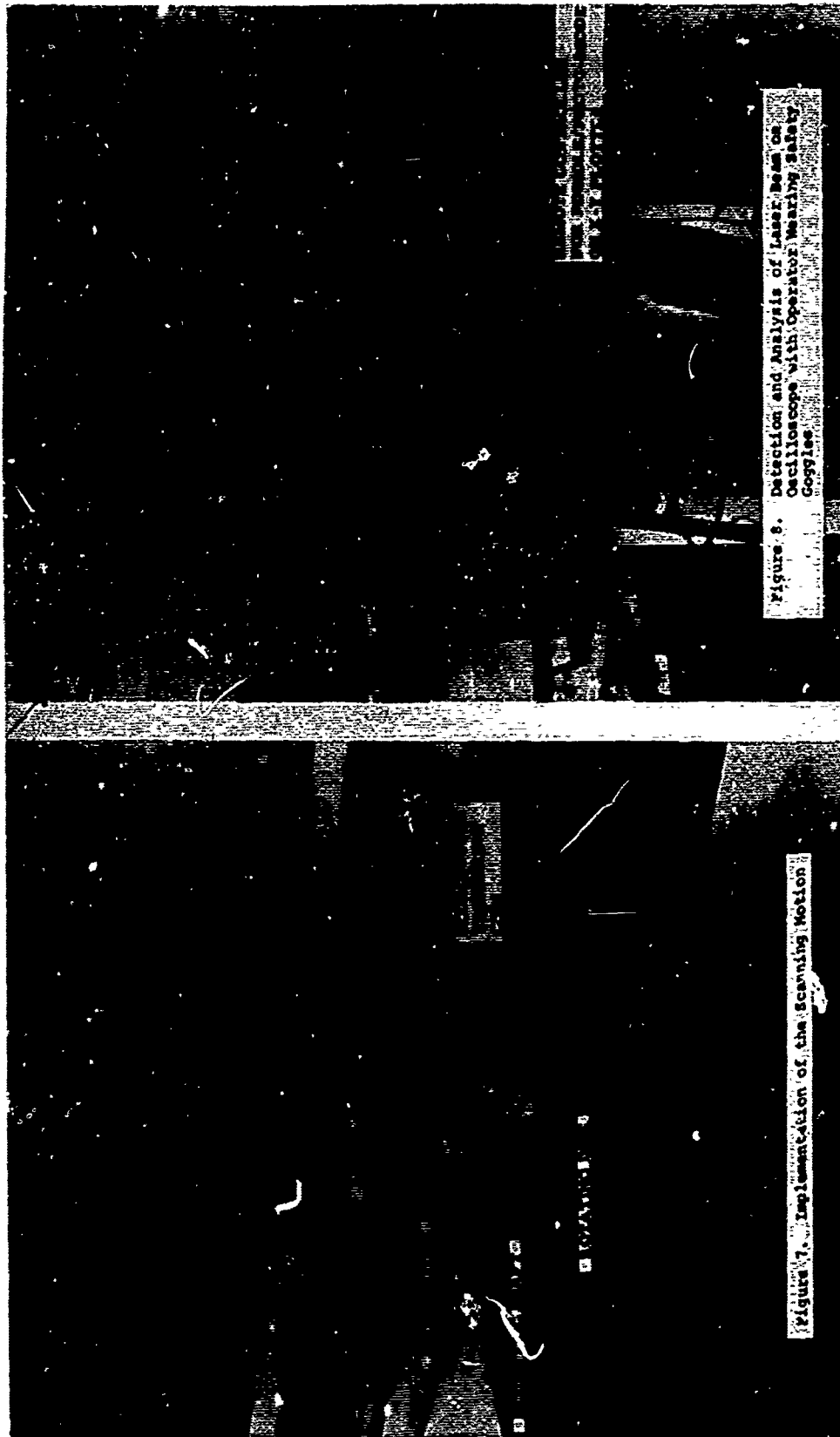


Figure 8. Detection and Analysis of Laser Beam on Oscilloscope with Operator Wearing Safety Goggles

Figure 7. Implementation of the Scanning Motion

1. The Commission of the European Communities (CEC) has been established by the Treaty of Rome, signed in 1957, and the Treaty of Amsterdam, signed in 1997.

2. The Commission is the executive body of the CEC, responsible for ensuring that the Treaty is applied correctly and for proposing and implementing the CEC's policies.

3. The Commission is composed of 20 members, who are appointed by the Council of Ministers for a five-year term.

4. The Commission is headed by the President of the Commission, who is elected by the Council of Ministers for a five-year term.

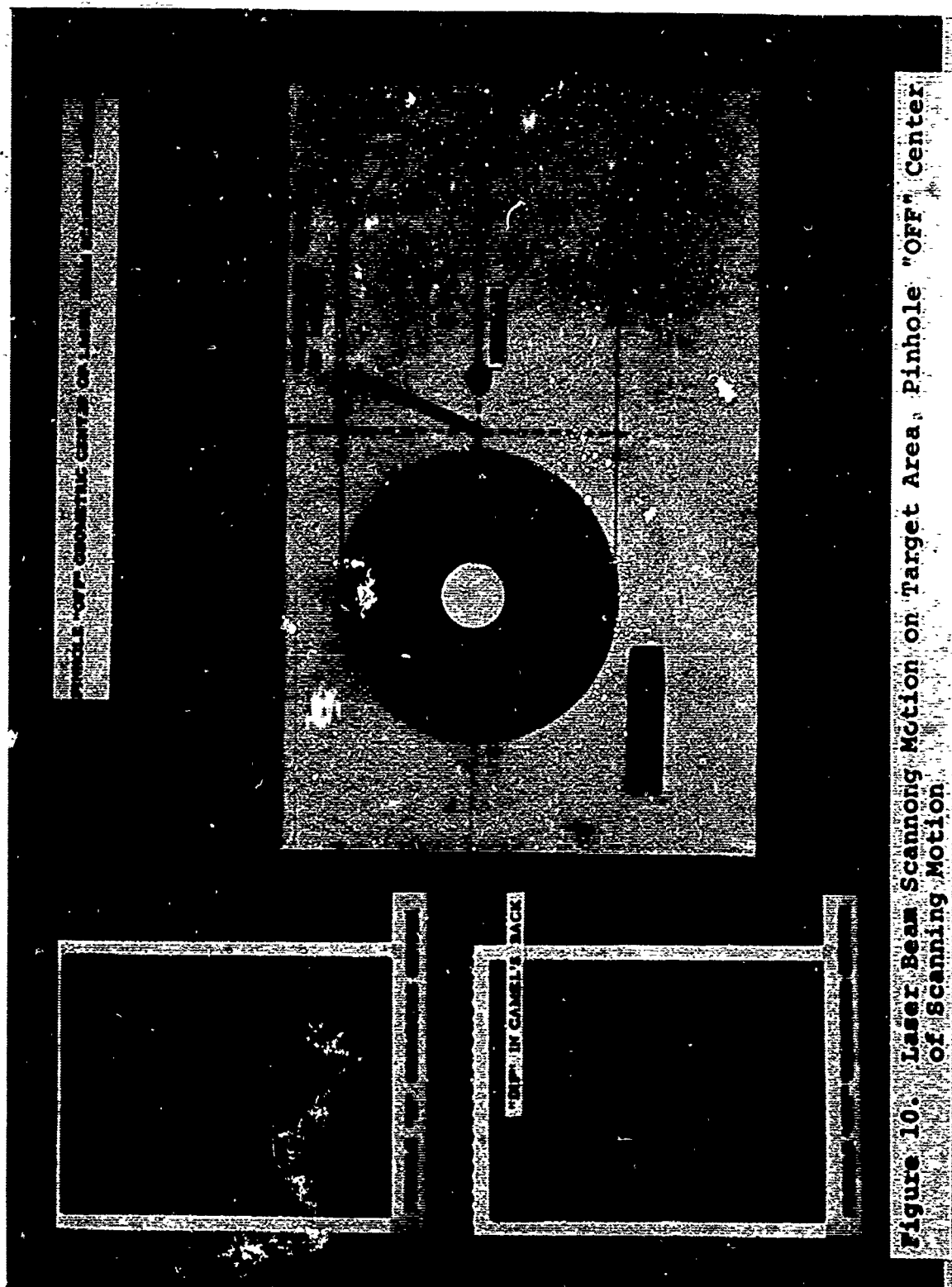


Figure 10. Laser Beam Scanning Motion on Target Area. Pinhole "OFF" Center of Scanning Motion.

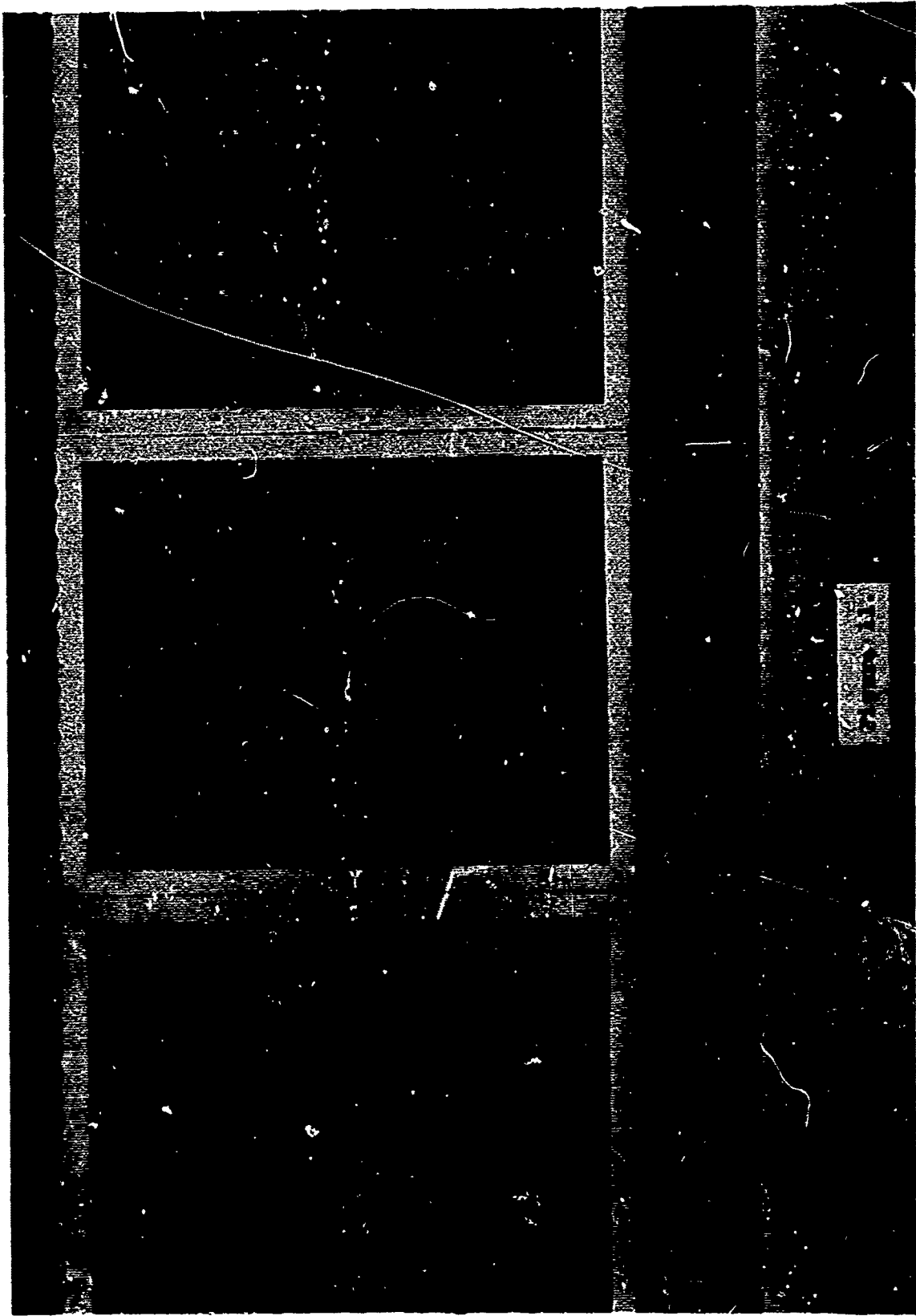




Figure 12. He-Ne Laser, Model 115, (RF Excitation)

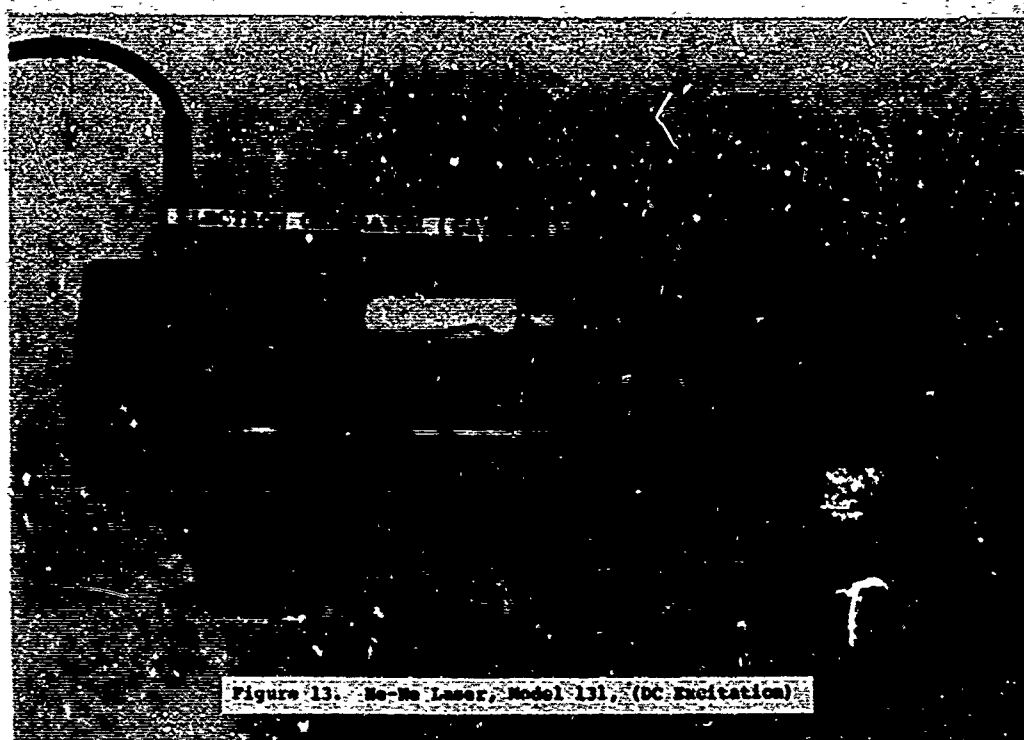


Figure 13. He-Ne Laser, Model 131, (DC Excitation)

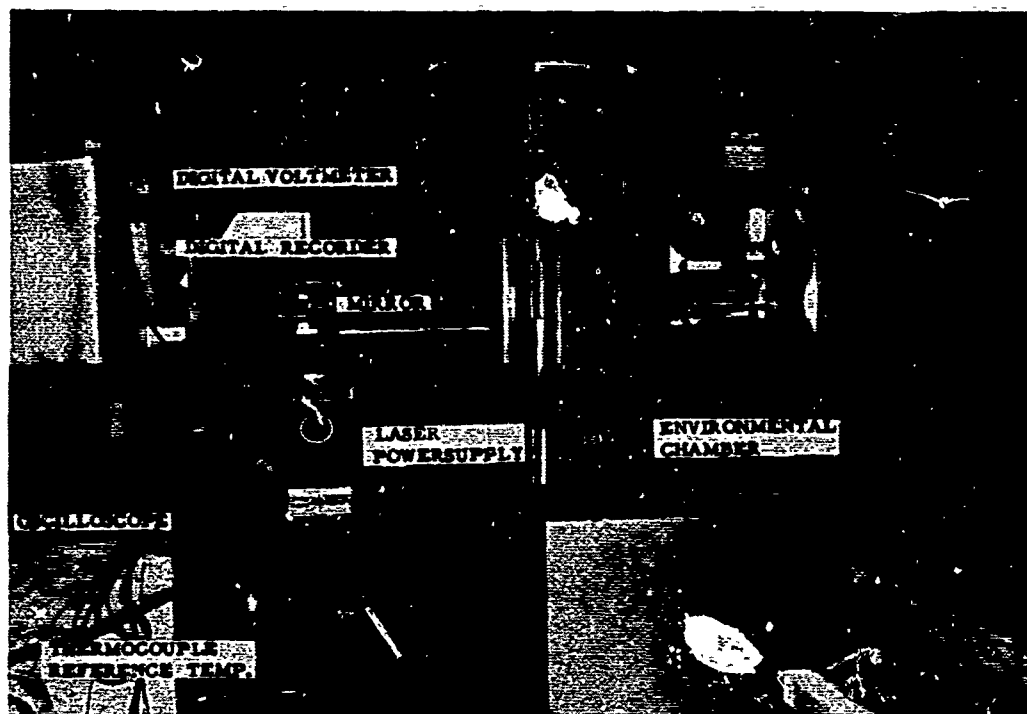


Figure 14. He-Ne Laser, Model 131, (DC Excitation), in Environmental Chamber

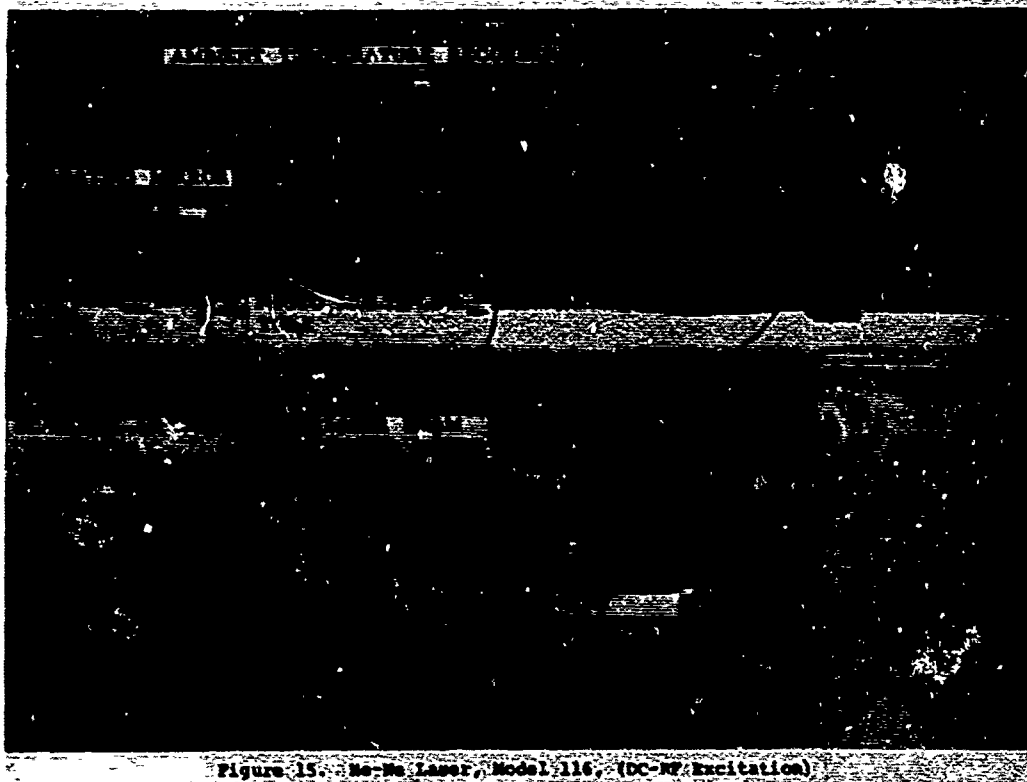


Figure 15. He-Ne Laser, Model 116, (DC-SP Excitation)

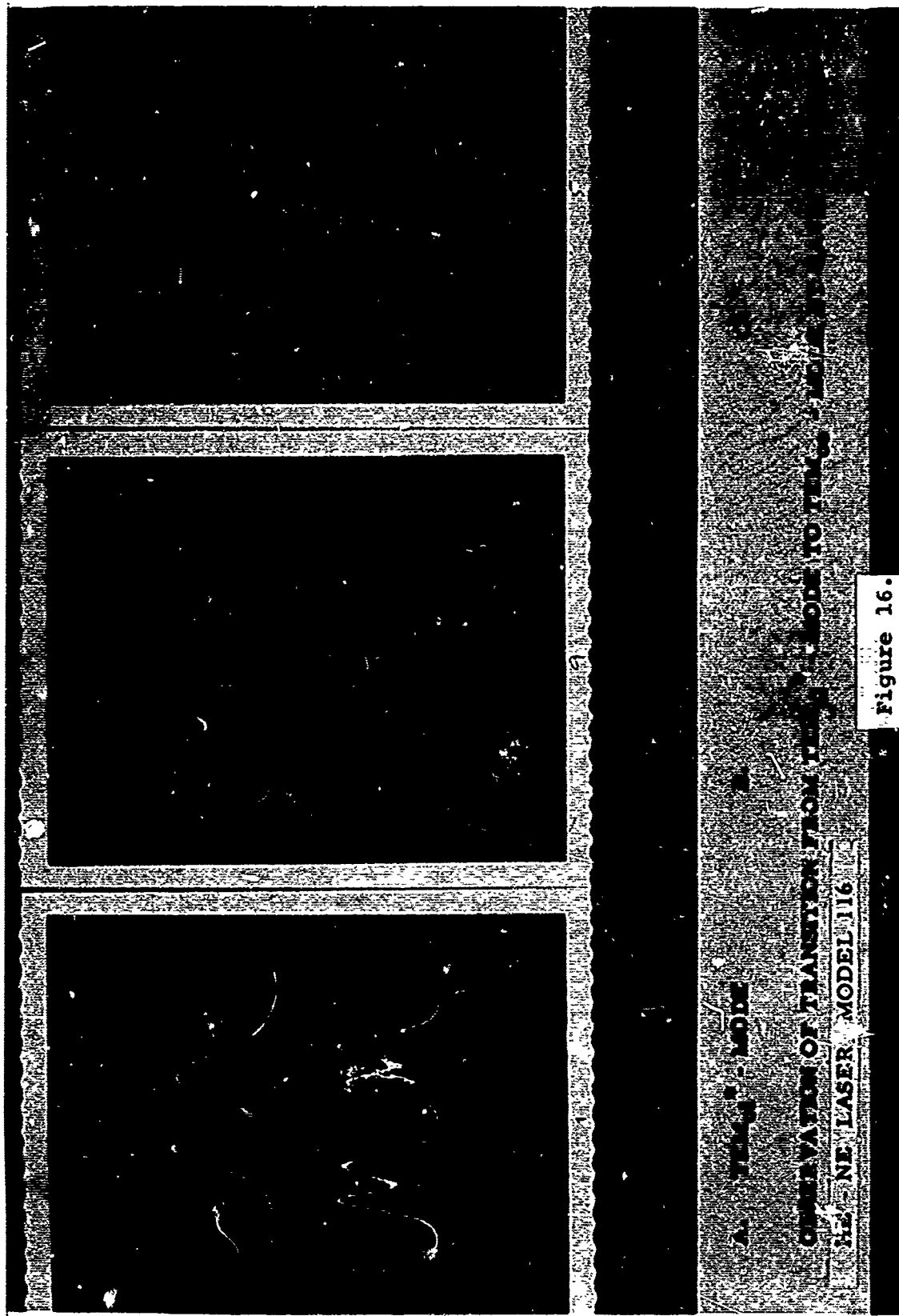
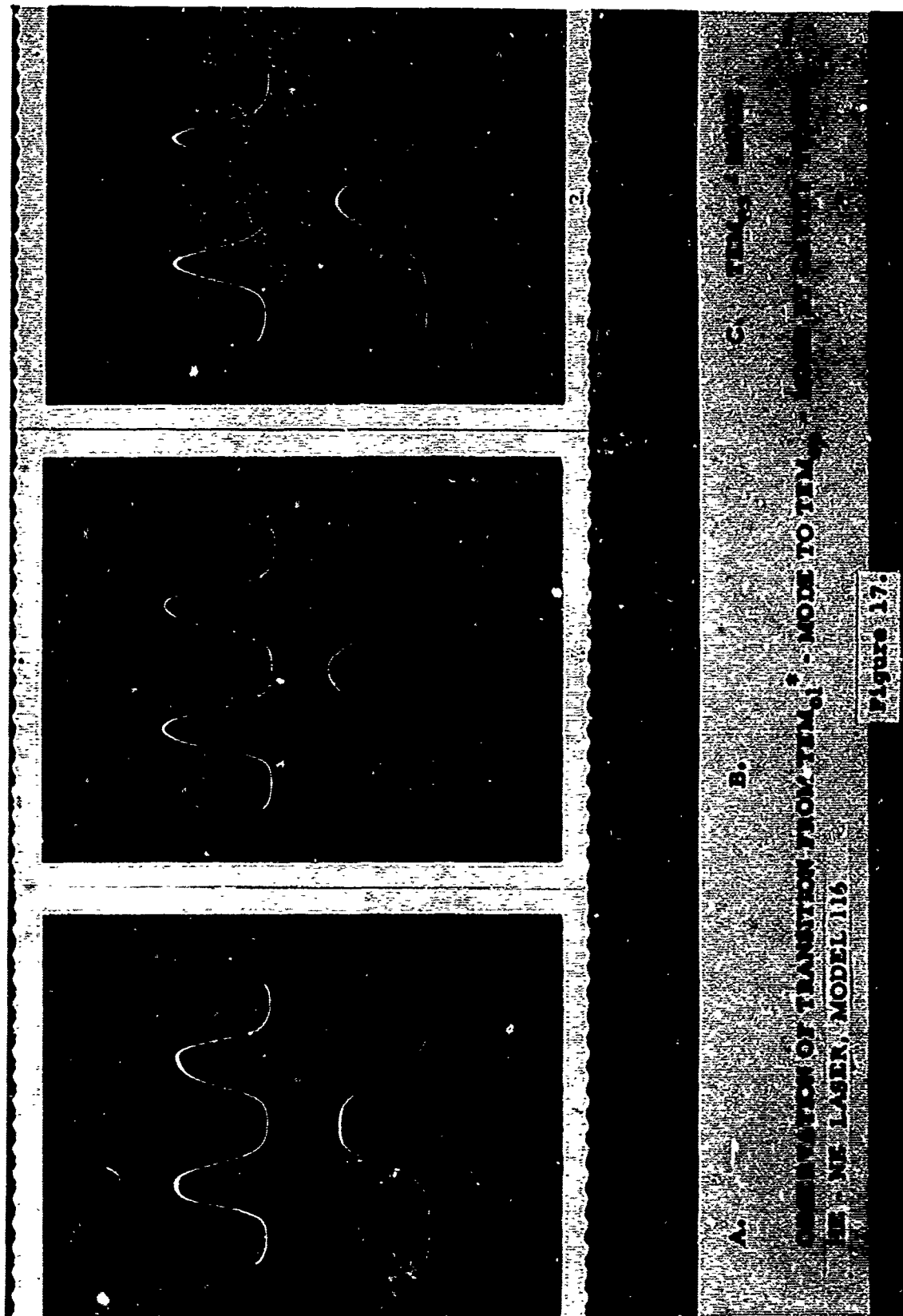
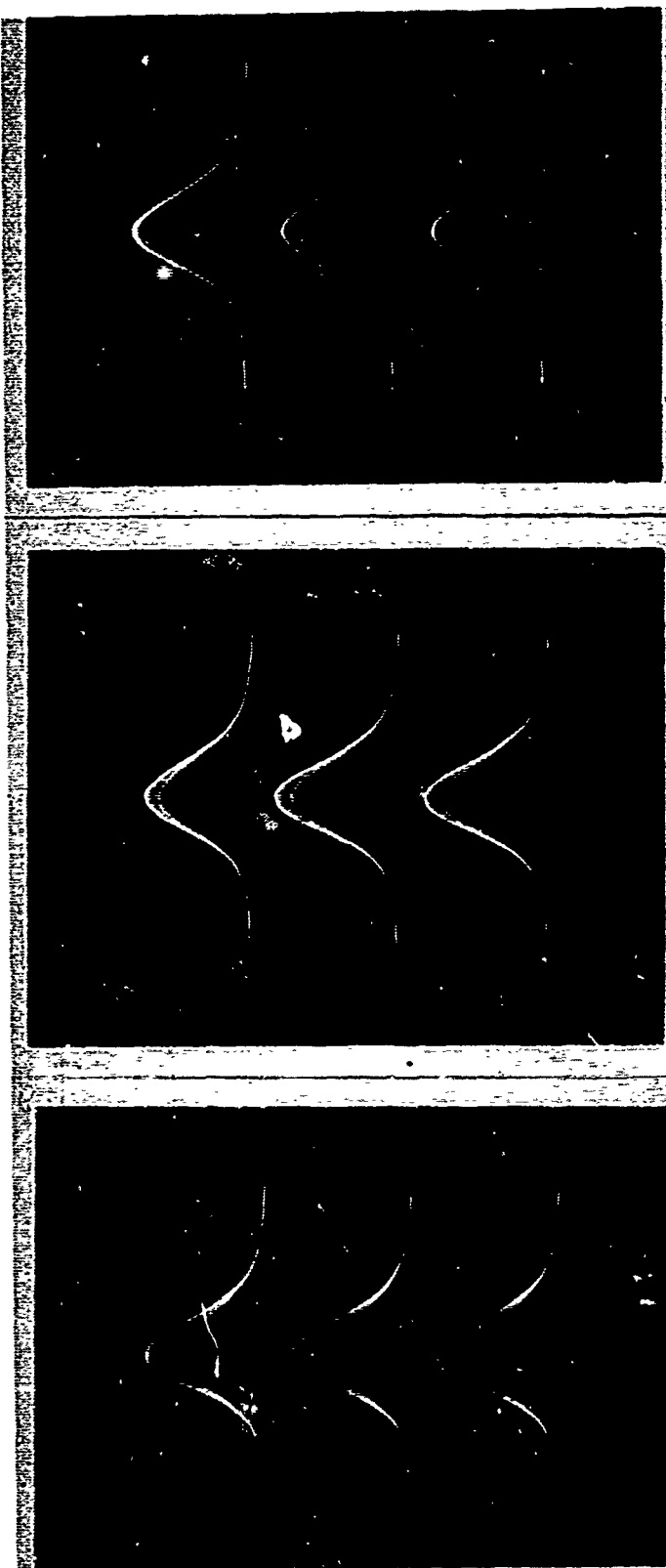


Figure 16.







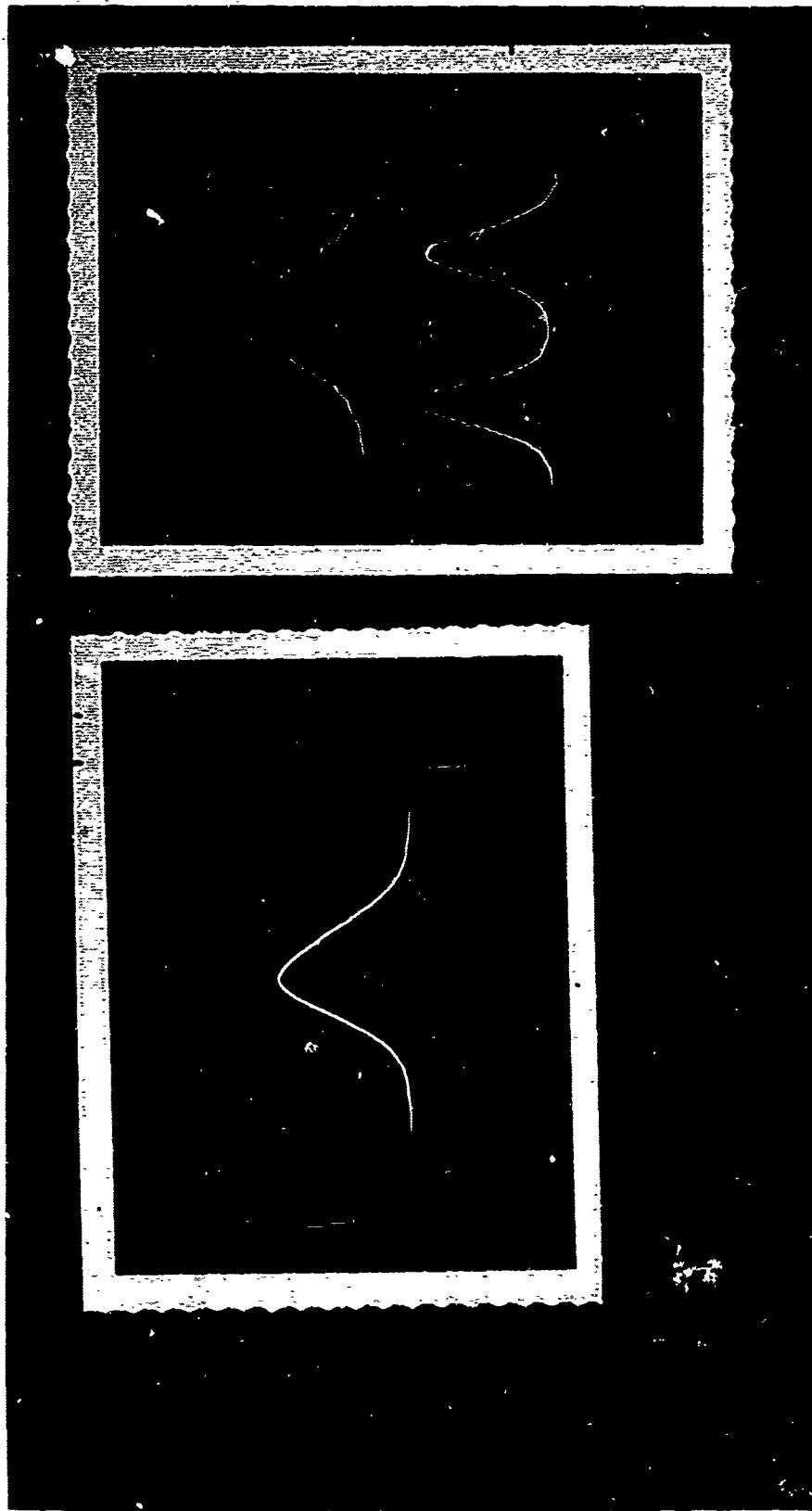
A. DC = 10 mA
RF = 0 mA

B. DC = 10 mA
RF = 50 mA

C. DC = 10 mA
RF = 65 mA

EFFECTS OF RF EXCITATION IN ADDITION TO THE DC EXCITATION ON THE TEM₀₀ - MODE
HE - NE LASER, MODEL 116 (DC - RF EXCITATION)

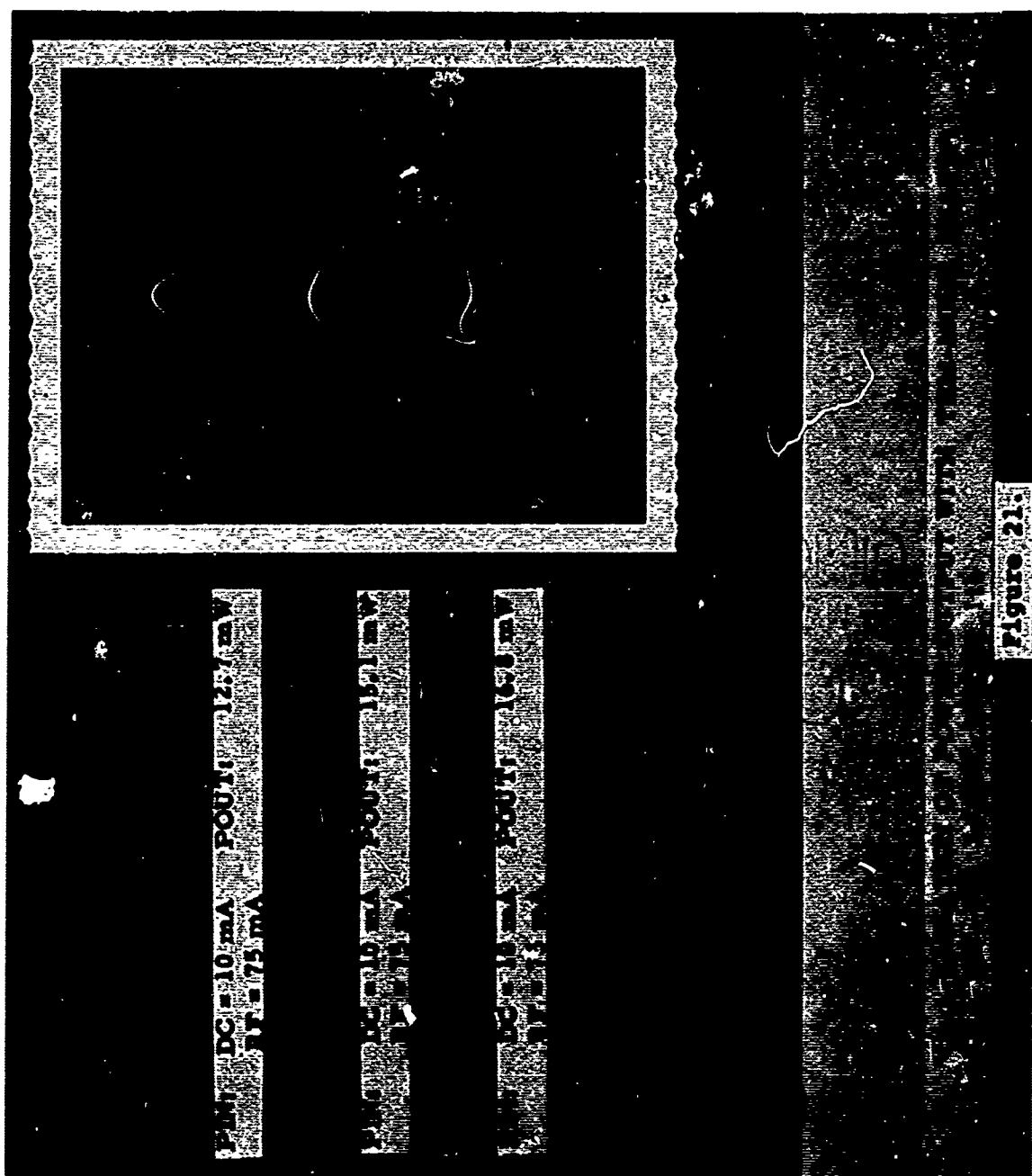
Figure 19:

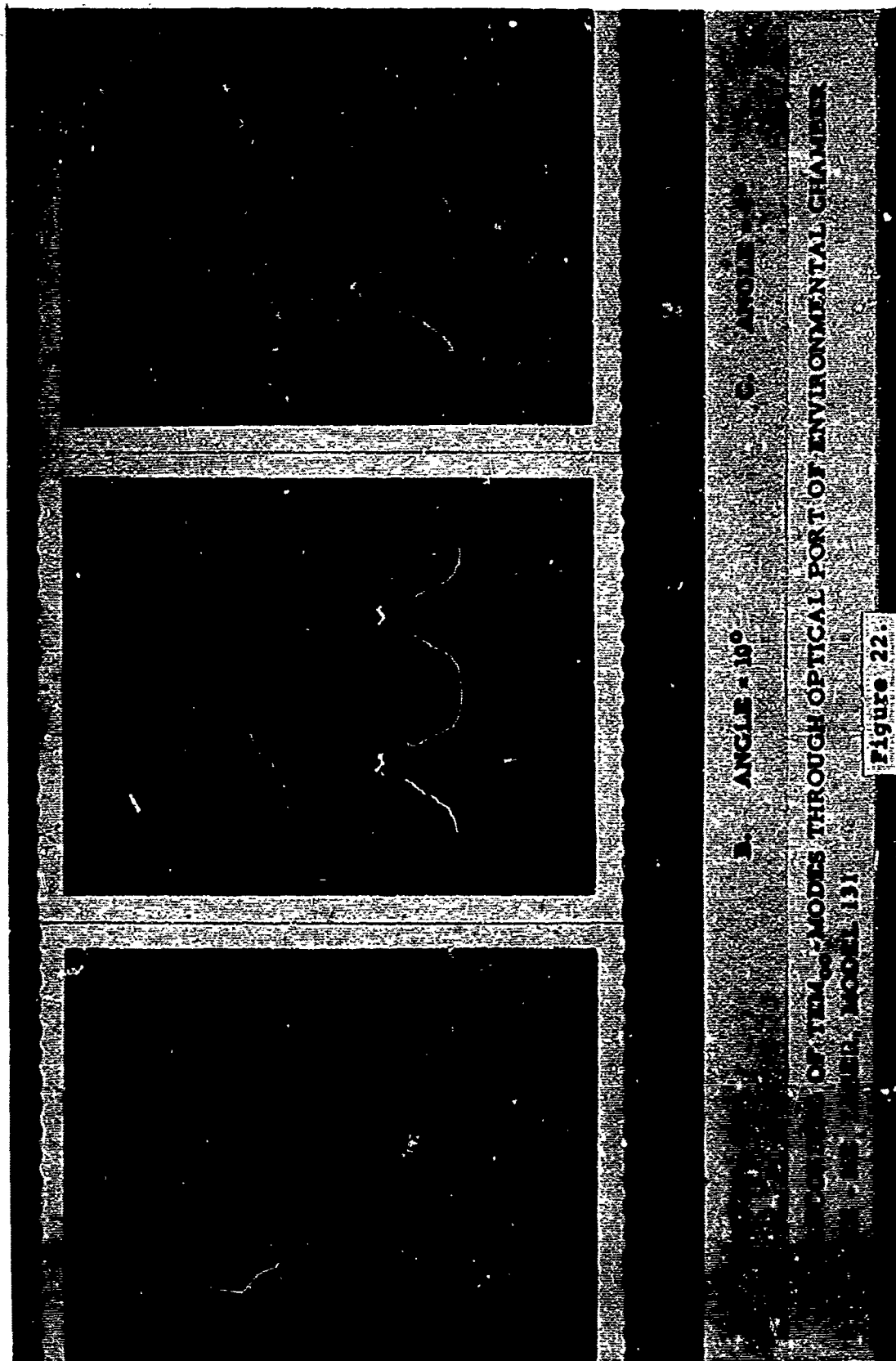


HE-NE LASERS A. MODEL 115, I.D. = 5mm B. MODEL 131, I.D. = 2mm

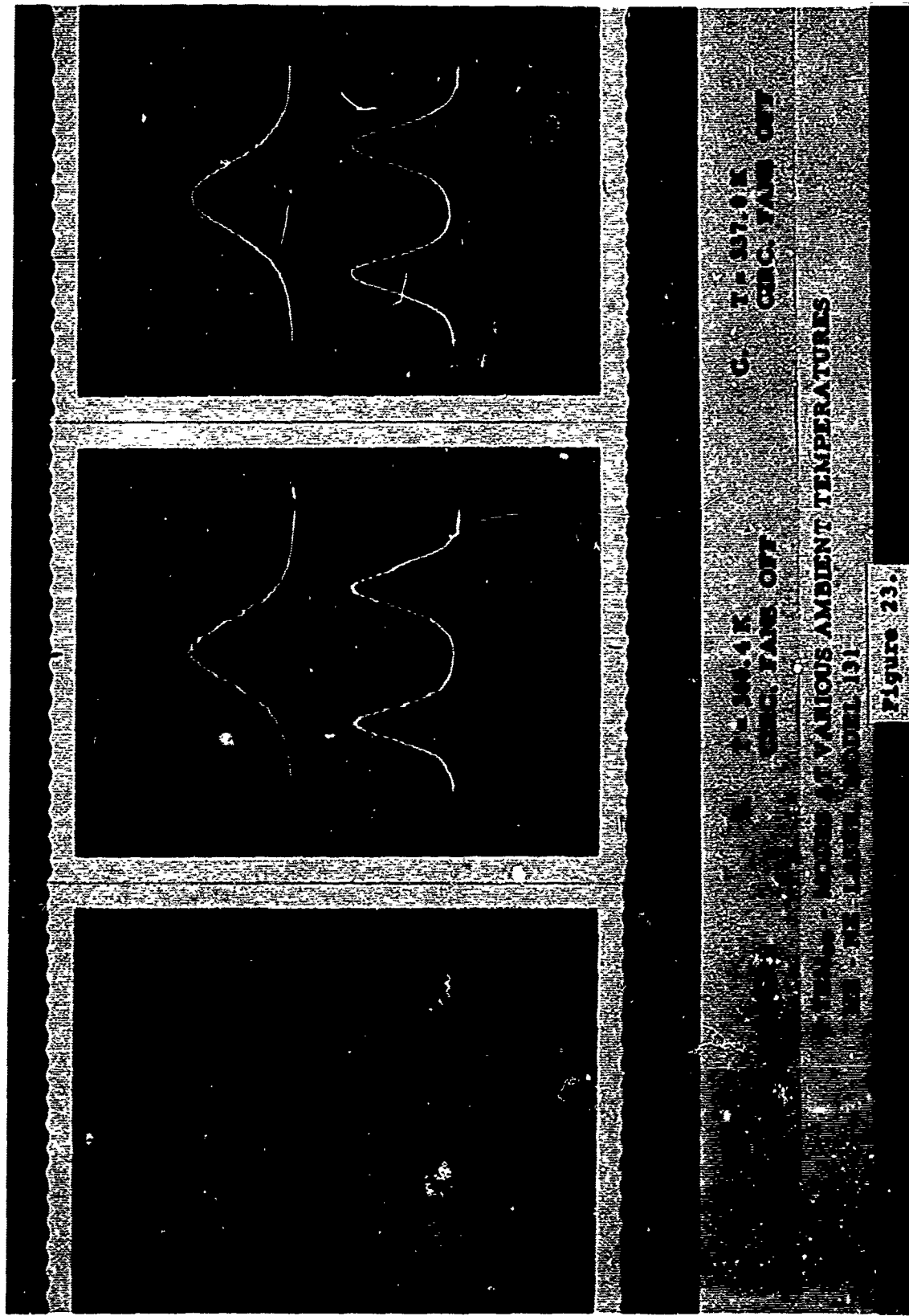
INFLUENCE OF EFFECTIVE CAVITY DIAMETER ON EXTENT OF TEM-MODES

Figure 20.





(1)



(U) LASING POTENTIAL OF II-VI COMPOUNDS

by

D. C. Reynolds

Aerospace Research Laboratories
Wright-Patterson AFB, Ohio



Donald C. Reynolds

BIOGRAPHY

Mr Donald C. Reynolds

Mr Donald C. Reynolds came to the Aerospace Research Laboratories in 1952 and was assigned as a research physicist for the Physics Research Branch. He held this position until 1956. At this time he advanced to the position of supervisory research physicist for the branch which he held until 1964. He was assigned as Chief of the Solid State Physics Research Laboratory in 1964 and presently holds the position of Director of the Solid State Physics Research Laboratory.

Mr Reynolds was born on July 28, 1920 in Sioux City, Iowa. He received his primary education from the Scotland High School, Scotland, South Dakota. In 1943 he received his B. S. degree in Physics from Morningside College and his M. S. degree in Physics from the University of Iowa in 1948. In addition he attended the Communications School while serving in the U. S. Army Air Corps.

Lasing Potential of II-VI Compounds

Abstract

Compounds prepared from elements of Group II and Group VI of the periodic table show great promise for laser operation at any wavelength between 7772\AA (CdTe) and 3200\AA (ZnS). Currently lasers operating at 4900\AA (CdS) and 6900\AA (CdSe) have been successfully produced. In addition compounds of the solid solutions CdS:Se have successfully demonstrated laser action allowing one to have lasers at any wavelength between 4900\AA and 6900\AA . The spectral region covered by II-VI compounds is the region in which the highest sensitivity has been achieved for detectors. This increases the potential for many practical applications.

Introduction

When electrons and holes recombine in a semiconductor there is a certain probability that light will be emitted. The energy released in the recombination process must occur either as light or as heat or a combination of both. In some semiconductors, of which germanium and silicon are prime examples, the recombination must proceed via a phonon process in order to conserve momentum. These materials are referred to as indirect band gap materials and in general are not suitable for lasers. The other type of semiconductor is called a direct band gap semiconductor and the recombination of hole-electron pairs can occur without phonon cooperation. All successful semiconductor lasers have been produced from the latter type of semiconductor.

The first successful semiconductor laser operation was obtained in a group of semiconductors called III-V Compounds. It is possible to choose a material in this group that will operate between approximately 0.65 and 8.5 microns.

There are at least two reasons why one would like to have a laser operating at shorter wavelengths. First, it would be easier to experiment with a laser operating in the visible region of the spectrum, as well as the desirability of having high intensity visible light sources. Second, detectors such as photomultiplier tubes are available for visible radiation and are by far the most sensitive detectors available. This same argument applied to lasers operating in the ultra violet region of the spectrum.

In considering laser applications, the use of lasers in communications systems offers many desirable features. In any operation of this type one must consider the losses in transmitting the radiation from the source to the detector. Atmospheric absorption in the visible and near ultra violet is variable and appreciably greater than in certain regions of the infra red. It might be concluded that for long range communication systems an infra red laser operating in a spectral region that is coincident with a transmission window in the atmosphere would be preferable. However, one cannot overlook the possibility of operating a system in the sensitive region of a high sensitive photomultiplier detector or light amplifying system.

It is known that II-VI Compounds are direct-band-gap semiconductors and as such offer the potential of operating at any specified wavelength between 3200\AA (ZnS) and $7,772\text{\AA}$ (CdTe), which covers the sensitive detector region. To date, laser operation has been demonstrated in CdS, CdSe and the solid solutions of CdS:Se. These two compounds and their

solid solutions permit operation at any specified wavelength between 4854Å (CdS) and 6792Å (CdSe).

Laser Consideration

In any source of coherent radiation it is necessary to achieve a population inversion. In the case of semiconducting materials it is necessary to raise the electrons from one energy state to a higher energy state relative to it. In semiconductors, this population inversion can be achieved by three different techniques:

1) Current Injection. This technique uses a P-N junction biased in the forward direction. Large numbers of electrons are injected from the N-region into the P-region, and recombination occurs close to the junction. An inverted population is obtained in this region and the recombination radiation propagates parallel to the junction. This type of pumping has been used in the GaAs junction-type lasers but has not been successfully employed in the II-VI Compounds.

2) Optical Pumping. In this case, one uses photons to obtain a population inversion by exciting electrons to higher energy states. The pump sources are flash lamps or arc lamps and, occasionally, other laser sources when such sources have the appropriate energy for exciting the electrons. The disadvantage of this type of pumping is that flash lamps put out a rather broad spectrum of radiation, whereas, the laser material has a rather narrow region of absorption. This results in an inefficient process. Laser sources provide efficient pump sources but the number of useable wavelengths is limited.

3) Electron Beam Pumping. In this technique, the laser sample cavity is bombarded with electrons having energies in the range from 10KV to a few hundred KV. The bombarding radiation excites electrons from valence to conduction band states in the semiconductor, giving rise to an inverted population. This type of pumping has been used successfully in several II-VI Compounds.

Once a population inversion has been achieved it is necessary to stimulate the recombination process in order to get coherent emission. A photon emitted by the stimulation from another photon is in phase with the first. The frequency of both photons is the same and they both travel in the same direction. The two photons will then have space, time and directional coherence. In order to obtain an avalanche process it is necessary to confine the photons to prevent their loss from the system and maintain them in the stimulating mode long enough to build up sufficient intensity to overcome bulk and surface losses in the material in order that both co-

herence and gain are achieved. This is accomplished by making resonant cavities of the material in question. In the case of the wurtzite type II-VI compounds the material is grown in a platelet form with the "c" axis in the plane of the plate. The preferred cleavage in these materials is in the direction of the "c" axis. Cavities are readily prepared by cleaving, which provides plane parallel faces normal to the face of the plate. The plates themselves also grow with plane parallel faces giving cavities as shown in Fig. 1.

Semiconductor Laser Materials

Semiconductor lasers were first reported in 1962, (1, 2, 3) the first being the GaAs injection laser. Since that time a family of lasers has been developed as shown in table I. These are all produced from III-V compounds and cover an appreciable portion of the spectrum from 0.65 μ to 8.5 μ . The short wavelength limit was obtained in GaAs:P alloys in which the direct band gap was retained.

II-VI compounds offer the greatest promise for covering the spectral region on the short wavelength side of 0.65 μ . Recently there have been rapid advances in the area of II-VI compound lasers. Basov and co-workers (4) have reported directionality, superlinearity and line narrowing of the photon emission from CdS crystals excited with an electron beam. Benoit, et al (5) have reported laser mode structure and directionality in the emission from CdS at 4.2°K and 20°K, using the same method of excitation. The first report of high efficiency laser action in CdS was by Hurwitz (6) at both 77°K and 4.2°K. He was also successful in pumping CdSe with an electron beam, where even higher efficiencies were achieved. Above the threshold, the Fabry-Perot structure of the laser line is observed as shown in Fig. 2. The Fabry-Perot mode spacing was calculated using the formula: $\Delta \lambda = \lambda_0^2 / 2l (n_0 - \lambda_0 \frac{dn}{d\lambda})$ where λ_0 is the photon wavelength, l is the cavity length, n_0 is the index of refraction, and $\frac{dn}{d\lambda}$ is the dispersion which is quite large in these materials. The calculated and experimentally measured mode spacings, along with the parameter values used in the calculations, are shown in Table 2.

The spontaneous and laser spectra of CdS are very similar to those of CdSe with the obvious exception of the difference in emission wavelength. The spontaneous line, centered at 6800Å for CdSe, corresponds to an emission line, which has been observed in photoluminescence experiments (7) and has been attributed to an exciton bound to an ionized acceptor. The spontaneous line in CdS at 4.2°K is the 4888Å line associated with an exciton bound to a neutral acceptor site. Some variation in wavelength is observed due to sample heating.

Hurwitz (8) has also employed electron beam excitation on platelet

type crystals of solid solutions of CdS:Se to produce laser oscillations at several wavelengths from red (6900\AA) to blue (4900\AA). Peak power outputs as high as 20 W/pulse and power efficiencies as high as 11% were obtained with these solid solutions. From the previous results on CdSe and CdS it is quite likely that the optical transitions in the solid solutions are associated with bound exciton complexes.

For lasers of the various CdS:Se compositions, measured values of threshold-beam-current-density and corresponding values of peak output power, as well as efficiencies, are given in Table 3. It is noted that the lowest efficiency and highest threshold occurs in pure CdS. It is also noted that some of the highest efficiencies and lowest thresholds occur near midrange of the solid solutions. It should further be pointed out that the width of all of the samples was 0.25 mm, while the beam diameter was 0.5 mm; consequently, the true efficiencies are at least 1.5 times higher than the values in Table 3.

From the experiments on II-VI compound lasers, several important conclusions may be drawn:

- 1) The population inversion is achieved through exciton states.
- 2) Hurwitz's work on electron-beam-injection is the first conclusive evidence that bound excitons are involved in laser emission from these materials.
- 3) High efficiency laser action is achieved in platelet type crystals and, in most cases, such crystals seem to be a practical necessity for electron-beam-induced laser action in these materials.
- 4) Some of the solid solution platelets (CdS:Se) have higher efficiencies than the pure compounds, an unexpected result.

The first three of these conclusions bear importantly on the present paper; in fact, they embody the main purpose of the paper.

Following the pioneering work of Thomas and Hopfield, much of the experimental work on bound exciton spectra in CdS, CdSe, and ZnO was done in the Solid State Laboratories of ARL by Reynolds, Litton and Collins;⁽⁹⁾ therefore, it is important to point out some of the connections between bound exciton transitions and laser emission in the II-VI compounds. The pioneering work on platelet-type crystal-growth in the II-VI compounds was done in the laboratories of ARL. Since the platelet type crystals have figures so importantly in the success of laser action in these materials, it is especially appropriate that the crystal-growing science which lead to the formation of these crystals be reviewed in the present

report. A further purpose of the paper is to propose an explanation (in terms of known lattice dynamics and other cooperative phenomena) for the unexpectedly high laser efficiencies in CdS:Se crystals of midrange concentrations.

Optical Transitions From II-VI Compounds

All of the low temperature spectra in II-VI compounds (transmission, reflection, emission) result from exciton transitions. The intrinsic exciton transitions occur on the long wavelength side of the intrinsic band gap by an energy equal to that of the binding energy of the exciton.

$$E_{h\nu} = E_{\text{gap}} - E_b$$

The energy diagram for such transitions is shown in Fig. 3. Here the energy is plotted as a function of the wave vector (K). On the long wavelength side of the intrinsic exciton transitions, a number of sharp line transitions are observed in several of the II-VI compounds. Several examples of these sharp line transitions are given in Table 4. These transitions result from bound exciton complexes. The model that is adopted for the bound exciton complex is that in which the complex is held together by forces analogous to those that exist in the hydrogen molecule or the hydrogen-molecule ion. Lampert⁽¹⁰⁾ was the first to consider the problem from the standpoint of bound aggregates of two or more charged particles in a non metallic solid. He described complexes analogous to H_2 , H_2^+ , and H^- . The first experimental observation of any of the above complexes was by Haynes⁽¹¹⁾ in silicon. Thomas and Hopfield⁽⁹⁾ have observed a number of the bound complexes and have identified them with several absorption and emission lines in CdS. In Fig. 4 one can show how it is possible to determine the type complex that is being observed from magnetic field data. From optical selection rules and group theoretic symmetry considerations, it can be shown that the g -value of the electron is isotropic, whereas the g -value of the hole has the form $g = g_{h11} \cos \Theta$, where Θ is the angle between the "c" axis of the crystal and the magnetic field direction. The symbols \ominus and \oplus refer to ionized donors and acceptors respectively, and $-$ and $+$ refer to electrons and holes. In the orientation $C \perp H$ it is seen from Fig. 4 that the transitions involving both the neutral donor and neutral acceptor complexes will split into doublets. At an arbitrary orientation the line splits into a quartet demonstrating the anisotropic hole g -value. If one considers the neutral donor complex in the orientation $C \perp H$ for the case of absorption, it is the electron in the lower state that splits. Thermalization of the electron spins results in the lower energy spin state becoming more densely populated. This results in the higher energy component of the magnetic-field-split doublet being more intense. In the neutral acceptor case it is the upper state that splits for the $C \perp H$ orientation. In this case, if emission is being observed

and the exciton lives long enough in the upper state for thermalization to occur, the lower energy spin state will become more densely populated. This will result in the lower-energy, magnetic-field-split doublet being the more intense. From these experiments the bound exciton complexes can be identified.

It was observed that the 4888\AA transition is the lasing transition in CdS. From the magnetic field data it is determined that this transition results from an exciton bound to a neutral acceptor site. In CdSe the lasing transition is the 6800\AA line. This transition has been associated with an exciton bound to an ionized acceptor.⁽⁷⁾ The assignment here is not as straight forward and may be questionable.

From these results one sees that the pertinent optical transitions giving rise to laser operation involve bound exciton complexes. Sharp line transitions in the solid solutions CdS:Se have not been observed. Consequently laser transitions in the solid solutions have not been correlated with specific bound exciton complexes however, it is quite likely that bound excitons are involved.

Since sharp line spectra are not observed in emission from ultraviolet excited platelets of CdS:Se solid solutions it appears that the structural quality of the solid solution plates is not as good as plates grown from the individual compounds. The question arises as to why the solid solutions have lower thresholds and higher efficiencies than the CdS platelets and some even higher than the CdSe platelets as is shown in Table 3.

Some insight into the problem might be gained from an oscillatory photoconductivity that has been observed in CdS crystals.⁽¹³⁾ This has been attributed to electrons in the conduction band whose lifetimes vary as a function of their energy. The lifetime of the conduction electron at certain energy values is smaller than at adjacent energy values whenever that energy coincides with the sum of the energy of the ground state exciton plus an integral multiple of a principal optical phonon energy. The shorter electron lifetimes are reflected as minima in the photoconductivity curve. The spacing of the minima show that the longitudinal optical phonons are the ones involved in the process.

The phonon spectrum of the solid solutions (CdS:Se) has been observed by infrared absorption and reflectivity.⁽¹⁴⁾ The infrared reflectivity spectrum for several solutions is shown in Fig. 5. The eigenfrequencies of both constituents are observed, with an intensity that roughly follows the relative concentration. This behavior is unexpected since it is generally assumed that these long-wavelength modes should involve a statistical average of the masses at the lattice sites and therefore should have a frequency which shifts smoothly as the concentration is varied. On the con-

trary, the behavior of the solid solutions is analogous to that of internal modes of molecular crystals. In such crystals, the vibration frequencies of groups of atoms inside a large molecule do not propagate outside and therefore remain unchanged in the solid solutions, where two different atomic masses may be substituted at the same place in the group.

The two phonon spectra may contribute to the increase in efficiency of the solid solutions for lasing. The electron beam pumping produces free hole-electron pairs. As in the case of the oscillatory photoconductivity, when the conduction electrons have an energy greater than the ground state exciton energy, by an amount equal to an integral multiple of a longitudinal optical phonon energy, they will lose their energy more rapidly and decay to the ground state exciton energy. Most excitons created and trapped in this way are in their ground states; as such, they represent the inverted population density necessary for laser action in the II-VI compounds. It is seen from Table 5 that if one considers five phonons in CdS, it is possible to scatter electrons into exciton states with energies, 0.19 eV above the ground state exciton. In the case of CdSe, there are seven phonons in this same energy region. In the case of the solid solutions, CdS:Se, there are twenty-four phonon combinations to cover the same energy region. The mechanism by which electrons lose energy in the conduction band by capturing phonons is shown in Fig. 6. The transition of the conduction electrons to the ground state exciton energy can occur either by cascading through single phonon processes or by direct capture of the multiple phonons necessary for the transition involved. Since the lasing transition in these materials involves a bound exciton, the inverted population must go through an exciton state. The additional phonon energies permit this process to proceed more rapidly and would thus reduce the probability for other recombination processes that might occur.

Growth of II-VI Crystals

The II-VI platelets investigated by Hurwitz were grown in our laboratory. Both bulk and platelet type crystals are grown from the vapor phase by substantially different techniques. The bulk crystals are grown at relatively high temperature (1200 - 1350°C) in a static system while the platelet type crystals are grown at lower temperatures (~ 900°C) in a gas flow.

Studies have shown that platelet type crystals have lower thresholds and higher efficiencies for laser action than do the bulk crystals. Such observations indicate a better crystalline quality in the platelet than in the bulk, and this is borne out by the crystal morphology.

In the growth of bulk crystals, some theories⁽¹⁵⁾ postulate the formation of a stable two dimensional nucleus on a crystal surface or edge for

the generation of new growth layers. Other theories postulate the generation of new layers with the aid of screw dislocations. Growth patterns on bulk CdS crystals show that both screw dislocations and edge nucleation occur. The influence of screw dislocations is shown in the growth pattern of Fig. 7. A well developed spiral with interlaced spirals is illustrated, the spiral occurring in the (0001) plane.

Growth of stepped crystal surfaces result from three processes: 1) a transport of molecules from the vapor to the surface; 2) diffusion of adsorbed molecules to the steps; and 3) diffusion of molecules along the edge of a step to a kink. The rate of advance of a straight step is

$$V = 2 (\sigma - 1) X_s \nu e^{-W/T}$$

where $(\sigma - 1)$ is the supersaturation, χ_s is the mean distance a molecule will wander over the surface of the crystal between the time it strikes and the time it evaporates, ν is an atomic-vibration-frequency-factor, and W is the evaporation energy. When the mean distance between kinks, χ_0 , is small, and the mean diffusion length of adsorbed molecules χ_s is large, $\chi_s \gg \chi_0$, the molecules will have a high probability of adhering to the step, if adsorbed near it, regardless of the orientation of the step. Therefore, the rate of advance of the step is independent of crystal orientation and rounded spirals result as shown in Fig. 7. If the rate of advance of a step is dependent on its orientation on the crystal face, a directional dependence of microscopic growth will be observed. The rate of advance of a step is a minimum when it lies parallel to a close packed direction. The kink-energy is highest for this orientation so the step has few kinks. If the relation $\chi_s \gg \chi_0$ is no longer true, directional growth results, the edge of the steps becomes straight and perpendicular to the slow growth direction. Examples of this type of growth pattern are shown in Figs. 8 and 9. Fig. 8 shows steps along the side of a pyramid. The step heights are large, $\sim 50,000\text{\AA}$. Smaller steps on the surface of the plateau are shown in Fig. 9. The pattern consists of a series of layers spreading out from a region at or near the crystal edge. The exact mechanism of generating the steps is not known, but Newkirk⁽¹⁶⁾ suggests that many screw dislocation sources may be present in a particular area of the crystal, each source generating a step too small to be seen by itself. Elbaum and Chalmers⁽¹⁷⁾ propose another mechanism for the generation of closed loops when the growth plane is parallel to the growth surface. Growth could take place by surface nucleation on the plateau, with layers being formed by edge growth on the edge of the critical nucleus. It is believed that the layers which are many atomic steps in height result from the coalescence of monatomic steps generated at or near the crystal edge. The slowing down of a monatomic step, caused by impurities or imperfections, would allow succeeding layers to catch up with it to form a polyatomic step.

Studies by Woods⁽¹⁸⁾ showed that the screw dislocation mechanism can operate when CdS crystals are condensed from vapor. However, the principal growth process at the higher supersaturations, where the major part of the growth occurs, appears to be two dimensional nucleation near the center of plateaus, leading to the formation of hexagonal terraced hills. No evidence was found to indicate that the closed hexagonal steps are generated from a pair of screw dislocations of opposite sign.

The mechanism for the platelet growth is quite different. Chikawa and Nakayama⁽¹⁹⁾ have shown that in the initial growth stage of platelets very thin needles, with an axis in a $\langle 10\bar{1}0 \rangle$ direction, grow outward from the walls of the silica growth tube at a rapid growth rate ($150\mu/\text{sec}$). When this growth stopped, the thickness increased on one side of the $\langle 0001 \rangle$ direction with a growth rate of $10\mu/\text{sec}$. The growth rate in the directions perpendicular to both the $\langle 0001 \rangle$ direction and the axis of a $(10\bar{1}0)$ whisker was less than $0.005\mu/\text{sec}$. They showed that the $(10\bar{1}0)$ needles contained two parallel dislocations, one of which has a Burgers vector $1/3 (2\bar{1}\bar{1}0)$ and the other of which is an edge dislocation with a Burgers vector (0001) . The dislocation structure of platelets in the growing stage is shown in Fig. 10. The dislocation with Burgers vector $1/3 (2\bar{1}\bar{1}0)$ is parallel to an edge along the $(10\bar{1}0)$ axis. A group of dislocation half-loops with Burgers vectors (0001) are near the growing edge of the platelet. Hirth and Frank⁽²⁰⁾ have shown that a dislocation with Burgers vector (0001) may slip out of a $(10\bar{1}0)$ whisker. Chikawa and Nakayama have shown theoretically that Burgers vector (0001) slips out of the $(10\bar{1}0)$ whisker toward the $\langle 0001 \rangle$ direction much more easily than toward the $\langle 000\bar{1} \rangle$ direction. When the dislocation slips out of the $(10\bar{1}0)$ whisker along the $\langle 0001 \rangle$ direction, dislocation half loops are formed which intersect the (0001) surface at many points where steps are formed. The closely spaced tips of the dislocation half-loops on the (0001) surface yield a smooth advancing surface. Since the half-loops have the tendency to become short by their lines tension,⁽²¹⁾ they stay near the surface of the platelet. Very low dislocation density of grown platelets is attributed to this tendency of the dislocation half-loops.

The dislocation with the Burgers vector $1/3 (2\bar{1}\bar{1}0)$ has a certain probability of slipping of the $(10\bar{1}0)$ whisker at one of the $(1\bar{2}10)$ surfaces. The probability is much smaller than that for the dislocation with Burgers vector (0001) . When this occurs, steps are formed dispersedly on the $(1\bar{2}10)$ surface and develop into hillocks. These hillocks cannot grow into long whiskers, however, because of the low supersaturation resulting from the geometrical position of the growing platelet with respect to the gas flow in the growing tube. The hillocks on the whiskers thus become striations on the platelet. This explanation is consistent with the observation that the striations are formed on one lateral surface of the platelet but not

on the other. Striations of this type are shown in Fig. 11.

From the growth mechanism it is observed that high structural quality crystals are inherently easier to achieve in platelet form than in bulk form. The platelets have elastic properties similar to whiskers and their optical properties are much more clearly defined than in bulk crystals.⁽⁹⁾ Etch studies on bulk CdS crystals show that relatively large dislocation concentrations may be present and may be rather inhomogeneously distributed throughout the crystal. A typical etch pattern is shown in Fig. 12 (a), (b) and (c). Fig. 12 (a) shows a pattern near the edge of the crystal whereas Fig. 12 (b) shows one that is approximately halfway between the edge and the center of the same crystal and in Fig. 12 (c) a pattern at the center of the crystal is shown. Near the edge of the crystal a large concentration of randomly distributed dislocations is observed. These are believed to result from stresses set up by more rapid cooling of the surface which would both create a large concentration of dislocations and provides a shorter time for rearrangement of the dislocation. The region shown in Fig. 12 (b) would tend to cool more slowly, resulting in smaller stresses, creating fewer dislocations, and allowing more time for rearrangement. Here, well-developed glide bands are observed. At the center of the crystal, the dislocation concentration is low.

The lessening of the structural quality of the crystal may be reflected in the lasing capabilities in several ways. The dislocations will tend to trap foreign impurities as well as point defects, providing extra recombination paths that will shorten the lifetime of free carriers as well as excitons. Scattering centers will be formed that will tend to scatter light out of the lasing mode. Absorption centers will be present that will take energy from the pump source without contributing to the laser, and these same centers will absorb emitted light from the laser.

These observations have been experimentally verified in that Hurwitz has not been successful in pumping II-VI bulk crystals. Basov and co-workers⁽⁵⁾ reported directionality, superlinearity and line narrowing in electron beam pumped bulk CdS but did not report cavity modes or far field patterns. At the same time Hurwitz⁽⁶⁾⁽⁸⁾ has been successful in pumping CdS, CdSe and CdS:Se platelets with an electron beam producing high efficiency lasers.

Conclusions

The initial experiments on the lasing properties of II-VI compounds show that they have considerable potential in the wavelength region from 3200Å (ZnS) to 7772Å (CdTe). This is a spectral region in which the most sensitive detectors are available, an important consideration in communication type applications. II-VI compounds offer the potential of a continuous coverage of the above spectral region by use of the appropriate

solid solutions.

The above experiments have shown that the platelet type crystals offer the highest efficiency lasers. This is undoubtedly due to the greater crystalline perfection in the platelets. With fewer dislocations there is also less tendency to trap foreign impurities. This leads to the conclusion that one must strive for greater crystalline perfection as well as a reduction in the foreign impurity content of bulk crystals.

The high efficiency and low threshold for lasing in some of the CdS:Se solid solutions may result from phonon scattering of conduction electrons to the ground state exciton. This could result from the greater number of phonon energies available in the solid solutions. It was observed that the highest threshold and lowest efficiency for lasing occurred in the CdS platelets. CdS has the fewest number of phonon energies available for any given energy range of the conduction electron above the ground state exciton energy. While this may be a factor in the lower CdS efficiency, there is also the possibility that the CdS platelets may be too perfect. In particular, the CdS platelets may be so perfect that too few defect states are available for capturing excitons. This possibility is currently being investigated.

In conclusion, we should also like to point out that this paper is the outgrowth of a most fruitful scientific collaboration between government and non-government laboratories, namely, ARL and Lincoln Labs. More importantly, it also represents a very useful "coupling" between pure and applied research. Without the platelet crystals supplied through the research work of ARL, the outstanding scientific achievement of Dr. Hurwitz would most likely not have been possible, and laser action in the II-VI semiconductors would still belong to the realm of the doubtful. By the same token, the laser work of Dr. Hurwitz has made possible the resolution of some puzzling questions regarding the physics of excitons and lattice dynamics in the mixed crystals.

Acknowledgment

I would like to express my sincere appreciation to C. W. Litton for a critical review of the manuscript in addition to his helpful suggestions.

References

1. R. N. Hall, et. al., Phys. Rev. Letters 9, 366 (1962).
2. M. I. Nathan, et. al., Appl. Phys. Letters, 1, 62 (1962).
3. T. M. Quist, et. al., Appl. Phys. Letters 1, 91 (1962).
4. N. G. Basov, et. al., Doklady Akad. Nauk. SSSR 155 783 (1964)
(English Translation: Soviet Physics - Doklady 9, 788 (1964).
5. C. Benoit a la Guillaume and J. M. Debever, Compt. Rend. 261,
5428 (1965).
6. C. E. Hurwitz, Appl. Phys. Letters 8, 121 (1966).
7. B. Wojtowicz - Natanson and T. Zakrgewski, Phys. Stat., Sol. 11,
873 (1965).
8. C. E. Hurwitz - To be published.
9. D. C. Reynolds, C. W. Litton and T. C. Collins, "Zeeman Effects
in the Edge Emission of CdSe," to be published; D. C. Reynolds and
C. W. Litton, Phys. Rev. 132, 1023 (1963); D. C. Reynolds, C. W.
Litton and T. C. Collins, Phys. Rev. 140, A1726 (1965).
10. M. A. Lampert, Phys. Rev. Letters 1, 450 (1958).
11. J. R. Haynes, Phys. Rev. Letters 4, 361 (1960).
12. D. G. Thomas and J. J. Hopfield, Phys. Rev. 128, 2135 (1962).
13. Y. S. Park and D. L. Langer, Phys. Rev. 132, 2450 (1963).
14. M. Balkanski, R. Beserman and J. M. Besson, to be published
(Solid State Communications).
15. M. Volmer and A. Weber, Z. Phys. Chem. 119, 277 (1925).
R. Becker and W. Dorin, Amm. Phys. Paris 24, 719 (1953).
16. J. B. Newkirk, Acta. Met. 4, 3 (1956).
17. C. Elbaum and B. Chalmers, Can. J. Phys. 33, 196 (1955).
18. J. Woods, British J. Appl. Phys. 10, 259 (1960); 11, 296 (1960).

19. J. Chikawa and T. Nakayama, J. Appl. Phys. 35, 2493 (1964).
20. J. P. Hirth and F. C. Frank, Phil. Mag. 3, 1110 (1958).
21. N. F. Mott, Nature 171, 234 (1953).

Table 1. Family of Lasers Produced From III-V Compounds.

Excitation	Semiconductor	Temperature	Wavelength (Microns)
P - N Junction	GaAs	Up to 300°K	0.85
	InP	Up to 300°K	0.9
	GaSb	77°K	1.6
	InAs	77°K	3.2
	InSb	77°K	5.3
	PbTe	12°K	6.5
	PbSe	12°K	8.5
	GaAs - P alloys	77°K	0.65 - 0.9
	InAs - P alloys	77°K	0.9 - 3.2 μ
	GaAs - InAs alloys	77°K	0.85 - 3.2 μ

Table 2. Calculation of Mode Spacing and Comparison with Experiment.

$\lambda(\mu)$	T(°K)	$\lambda_0(\text{\AA})$	n_0	$dn/d\lambda(\text{\AA}^{-1})$	$\Delta\lambda(\text{\AA})$	
					calc.	exp.
CdSe 230	4.2	6845	2.79	-5×10^{-4}	1.6	1.4
	77	6915	2.75	-5×10^{-4}	1.7	1.8
CdS 42	4.2	4910	2.88	-3.6×10^{-3}	1.4	1.4
	77	4950	2.85	-2.2×10^{-3}	2.1	2.1

Table 3. Threshold current density, peak output power, and maximum observed efficiency of CdS_xSe_{1-x} lasers at 4.2°K (upper figures) and 77°K (lower figures) using a 50 keV electron beam. Sample dimensions: 0.25 mm x 1.5 mm x 4 - 20 μ . Beam voltage: 50kV.

Mole % CdSe	Threshold Current Density (mA/cm ²)		Output Power (W)	Efficiency %
	0	100		
0	1000	10	0.7	0.7
	1200	5	0.4	0.4
11	80	10	7	7
	400	6	4	4
39	30	20	11	11
	80	8	9	9
55	40	11	9	9
	400	7	5	5
79	120	3	3	3
	600	1	2	2
82	100	5	4	4
	450	3	3	3
100	50	16	8	8
	200	14	7	7

Table 4. Some Bound Exciton Lines Observed in II-VI Compounds.

Material	Line	Wavelength λ
CdS	I ₁	4888.47
	I ₂	4867.17
	I ₃	4861.66
	(Zero Field Split)	4862.25
	I ₅	4869.14
	I ₆	5068.54
	(Zero Field Split)	5069.18
	I ₇	5084.81
	I ₁	3676.32
	I ₂	3680.63
ZnO	I ₃	3681.59
	I ₄	3687.12
	I ₅	3687.54
	I ₆	3688.40
	I ₇	3689.03
	I ₈	3689.26
	I ₉	3692.64
	I ₁₀	3695.50
	I ₁	6793.27
	I ₂	6794.61
CdSe	I ₃	6804.18
	I ₄	6805.85
	I ₅	6823.25
	I ₆	6827.43
	I ₇	6846.62
	(Zero Field Split)	6847.39
	I ₈	6355.14
	(Zero Field Split)	6857.35
	I ₉	6883.82

Table 5. Phonon Combinations Available in CdS, CdSe and CdS:Se Solid Solutions. These Cover the Energy Interval Between the Ground State Exciton Energy and 0.19 e. v. Above the Ground State Exciton Energy.

CdS	CdSe	CdS:Se
0.038 N	0.027 n	0.027 n
0.076 2N	0.054 2n	0.038 N
0.114 3N	0.081 3n	0.054 2n
0.152 4N	0.108 4n	0.065 n+N
0.190 5N	0.135 5n	0.076 2N
	0.162 6n	0.081 3n
	0.189 7n	0.092 2n+N
		0.103 n+2N
		0.108 4n
		0.114 3N
		0.119 3n+N
		0.130 2n+2N
		0.135 5n
		0.141 3N+n
		0.146 4n+N
		0.152 4N
		0.157 3n+2N
		0.161 6n
		0.166 3N+2n
		0.173 5n+N
		0.179 4N+n
		0.184 4n+2N
		0.189 7n
		0.190 5N

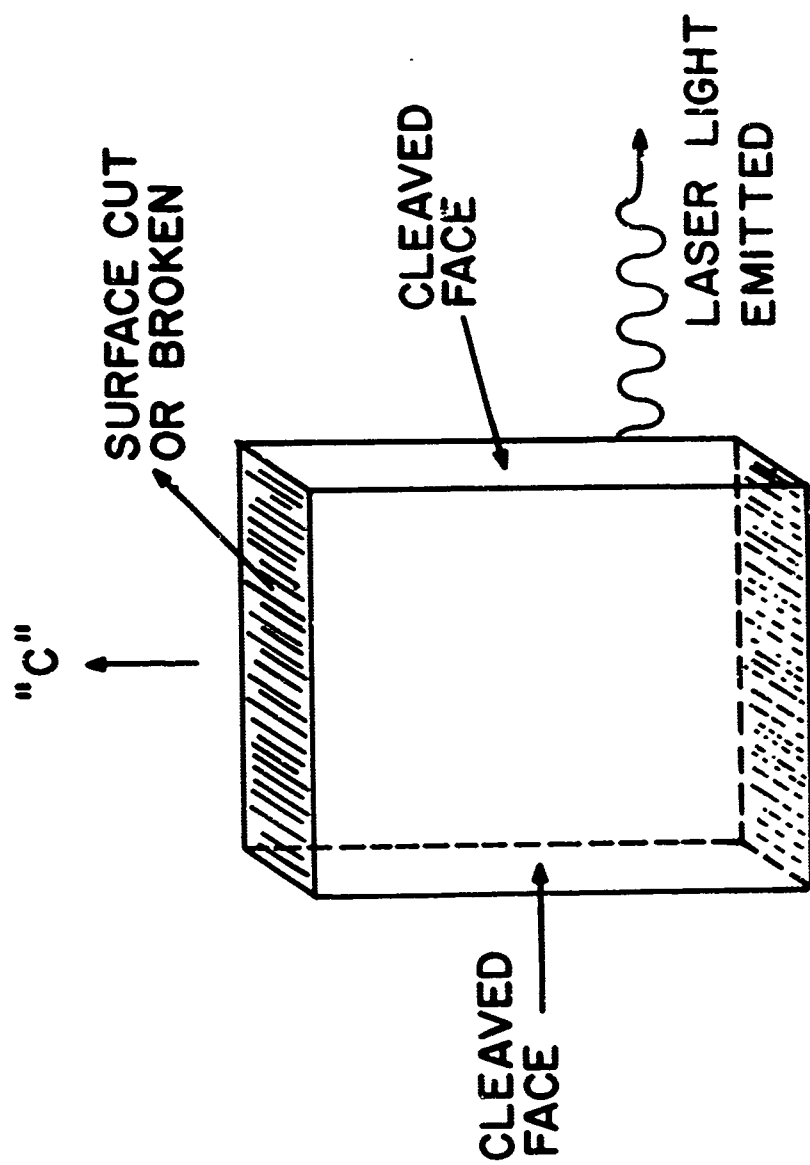


Fig. 1(a) Schematic of cavity cleaved from platelet

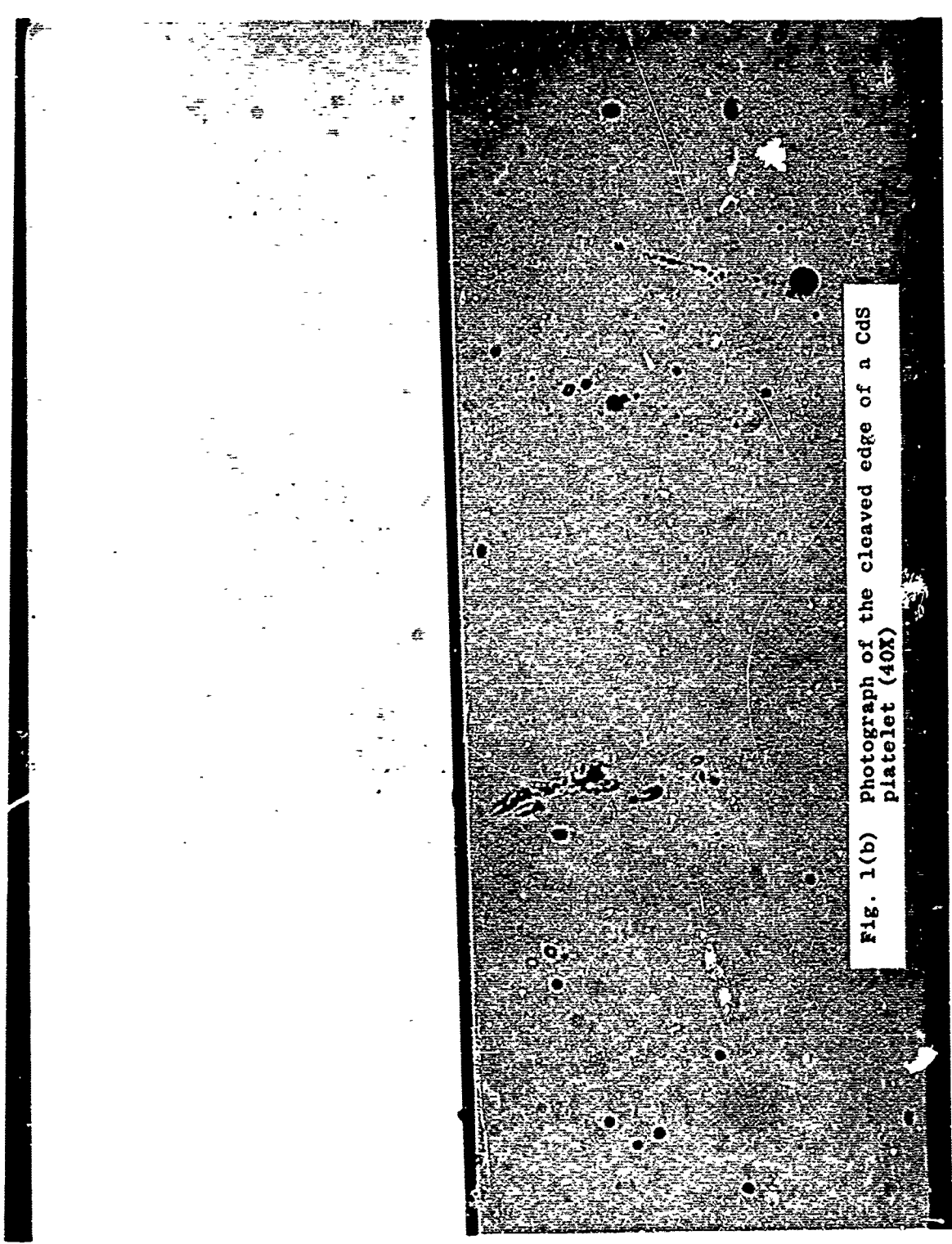
A high-magnification micrograph showing the edge of a CdS platelet. The surface is highly textured with numerous small, dark, circular features, likely pores or inclusions. The overall appearance is granular and somewhat irregular. A white rectangular label with black text is positioned in the lower right corner of the image.

Fig. 1(b) Photograph of the cleaved edge of a CdS
platelet (40X)

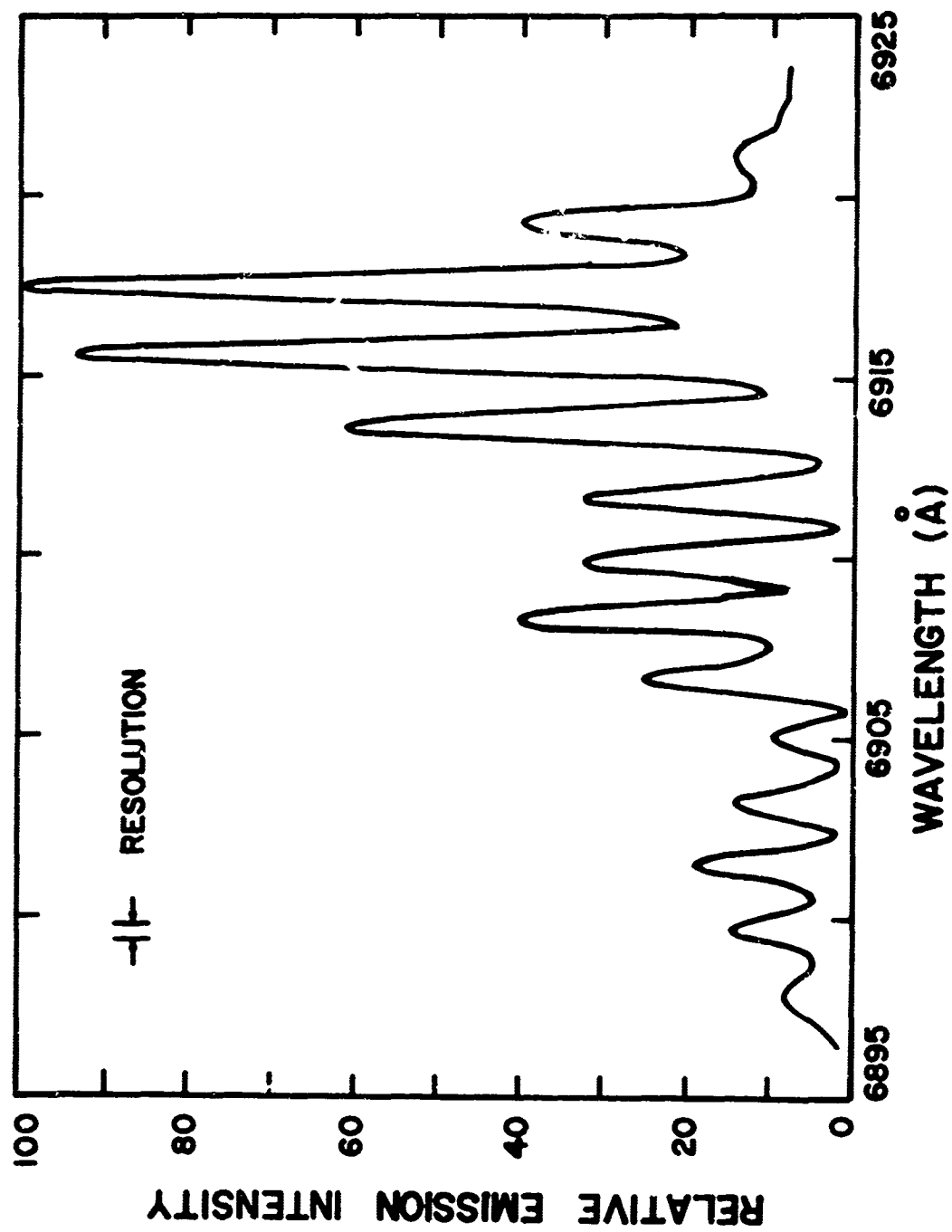


Fig. 2 Cavity modes for a CdSe laser at 77°K.

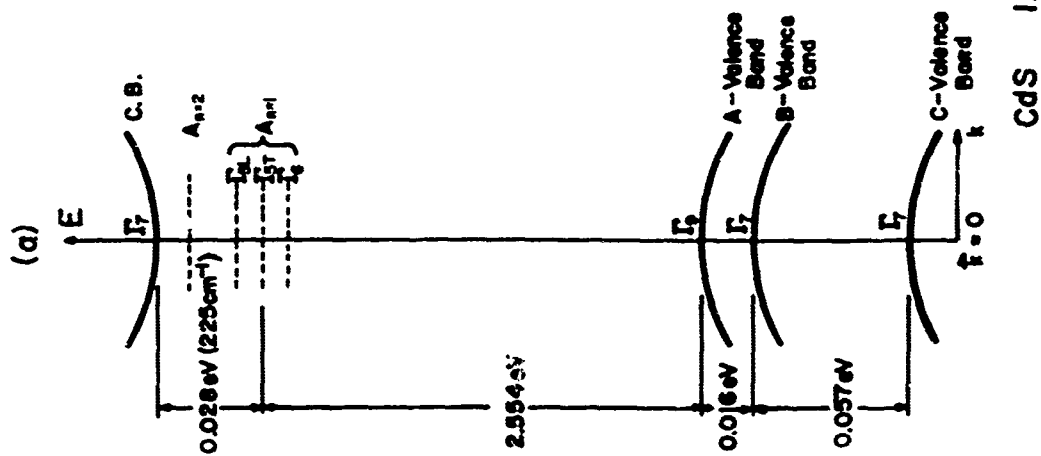
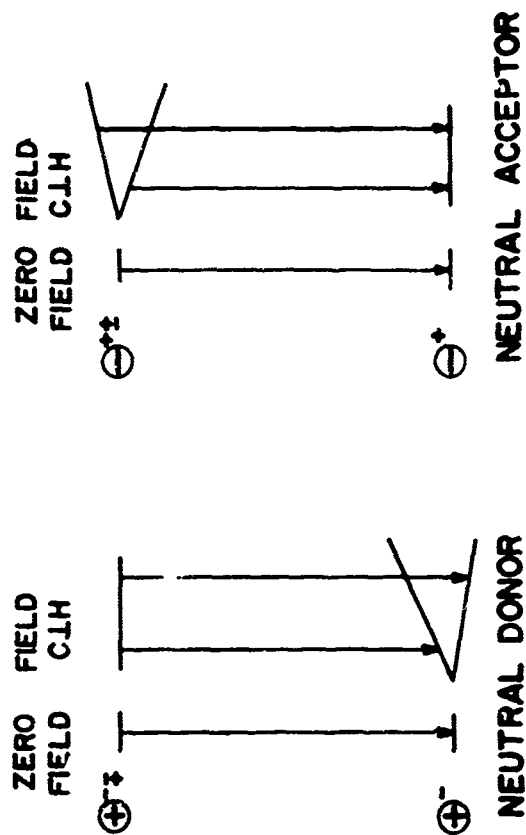


Fig. 3 Energy bands at $K = 0$ for CdS showing the ground state exciton energies Γ_5 , Γ_4 , Γ_3 and Γ_6 . The strong transition is the $\Gamma_5\Gamma_1$ transition.



$$g_n = g_{nH} \cos \theta$$

Fig. 4 Model for neutral donor and neutral acceptor bound exciton complexes.

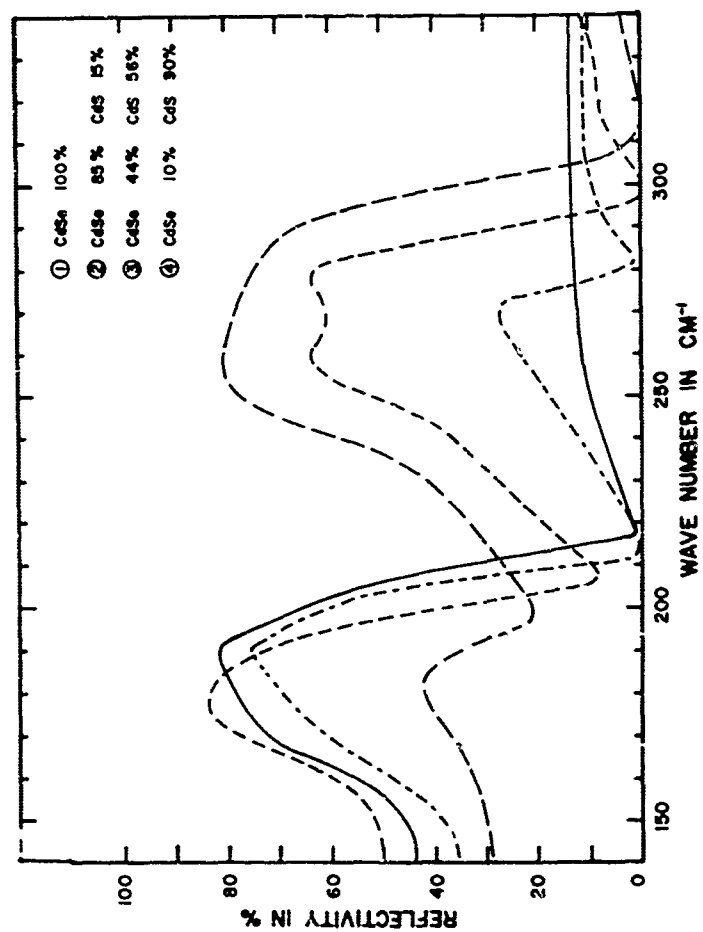


Fig. 5 The infrared reflectivity spectra of several solid solutions (CdS:Se).

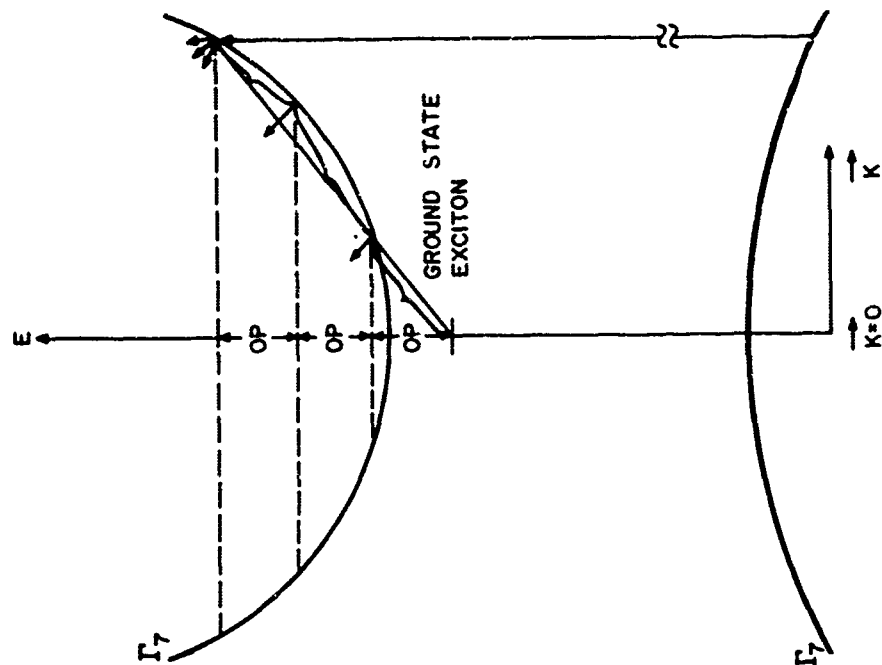


Fig. 6 Mechanism by which electrons lose energy in the conduction band by capturing phonons.

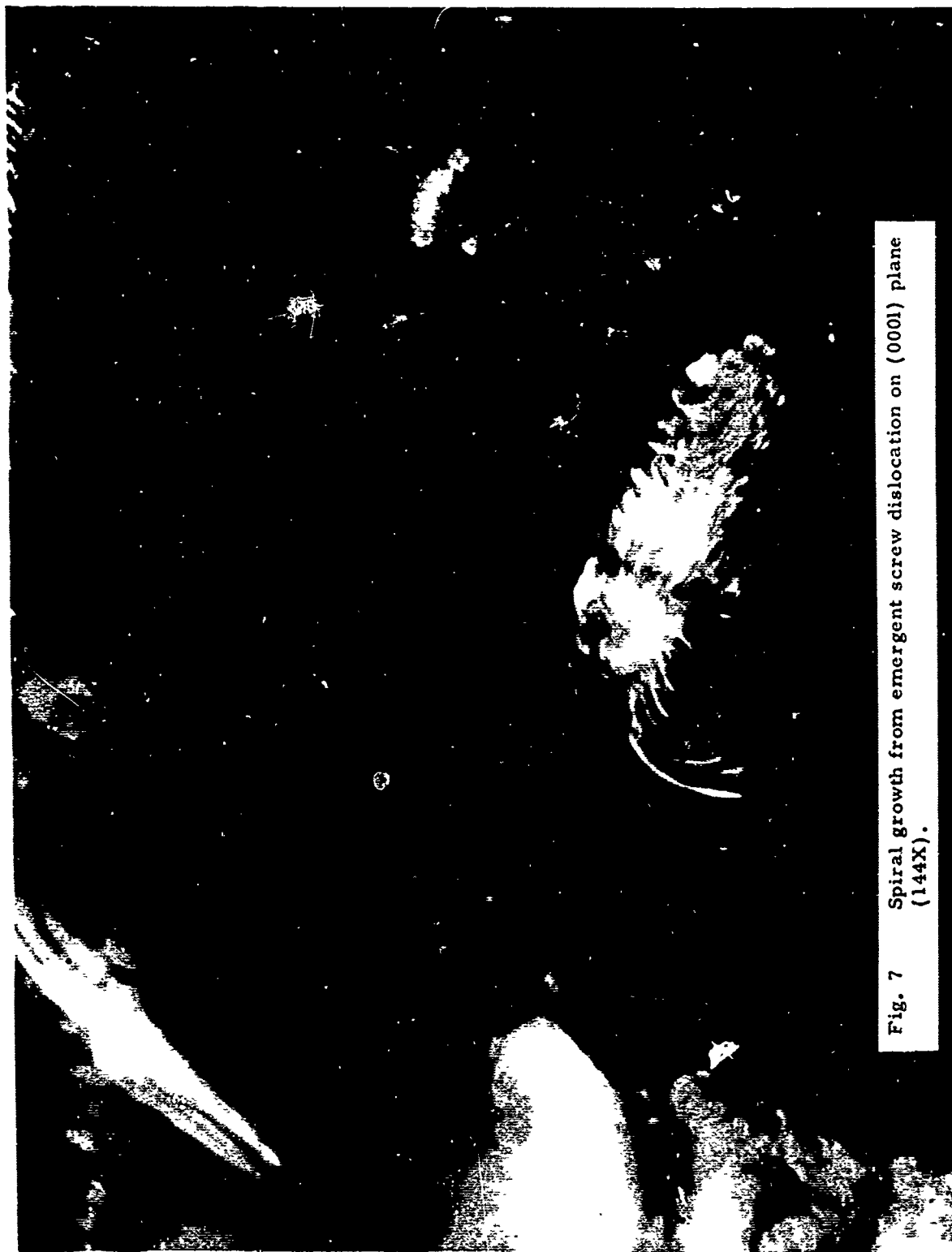


Fig. 7 Spiral growth from emergent screw dislocation on (0001) plane
(144X).

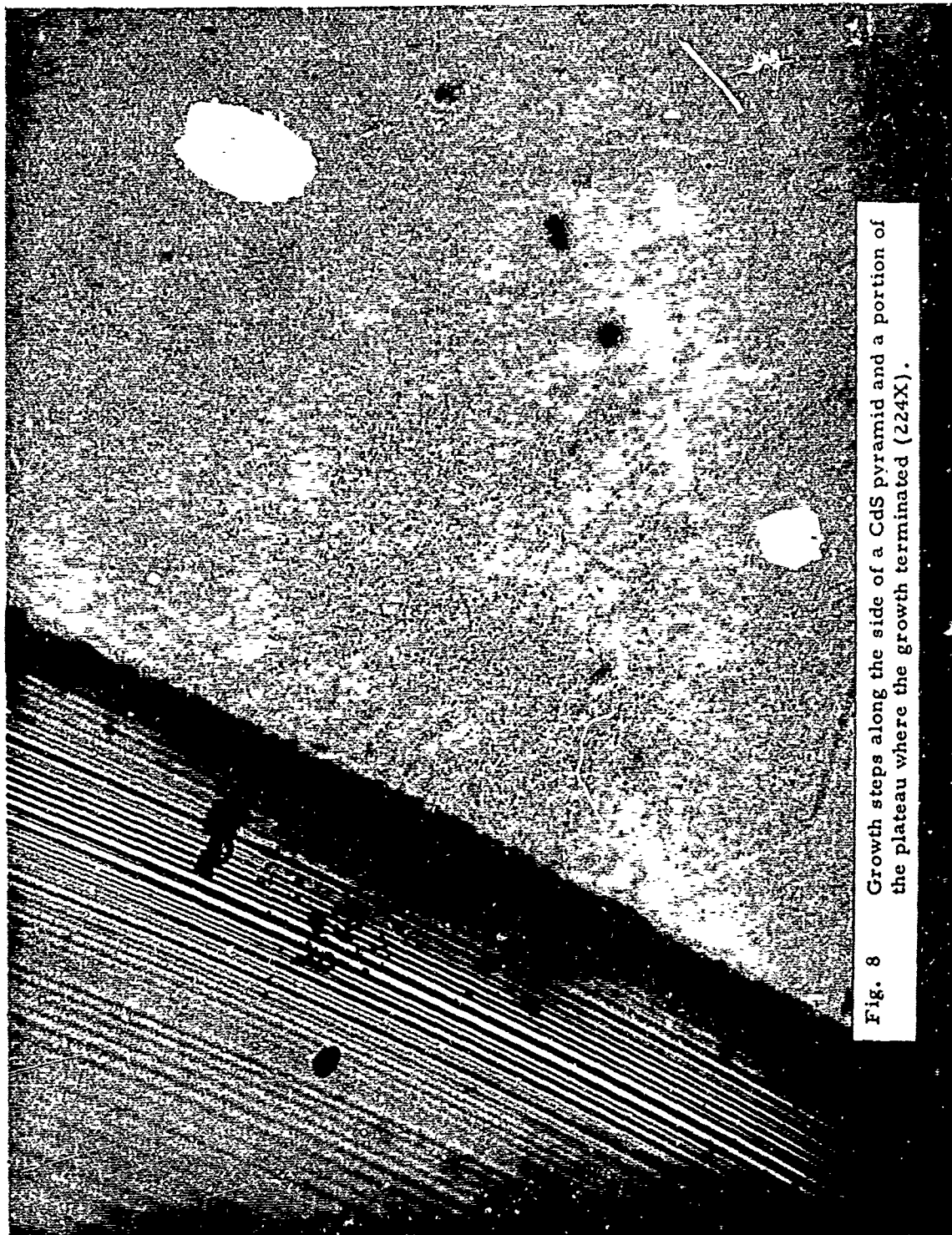


Fig. 8 Growth steps along the side of a CdS pyramid and a portion of the plateau where the growth terminated (224X).

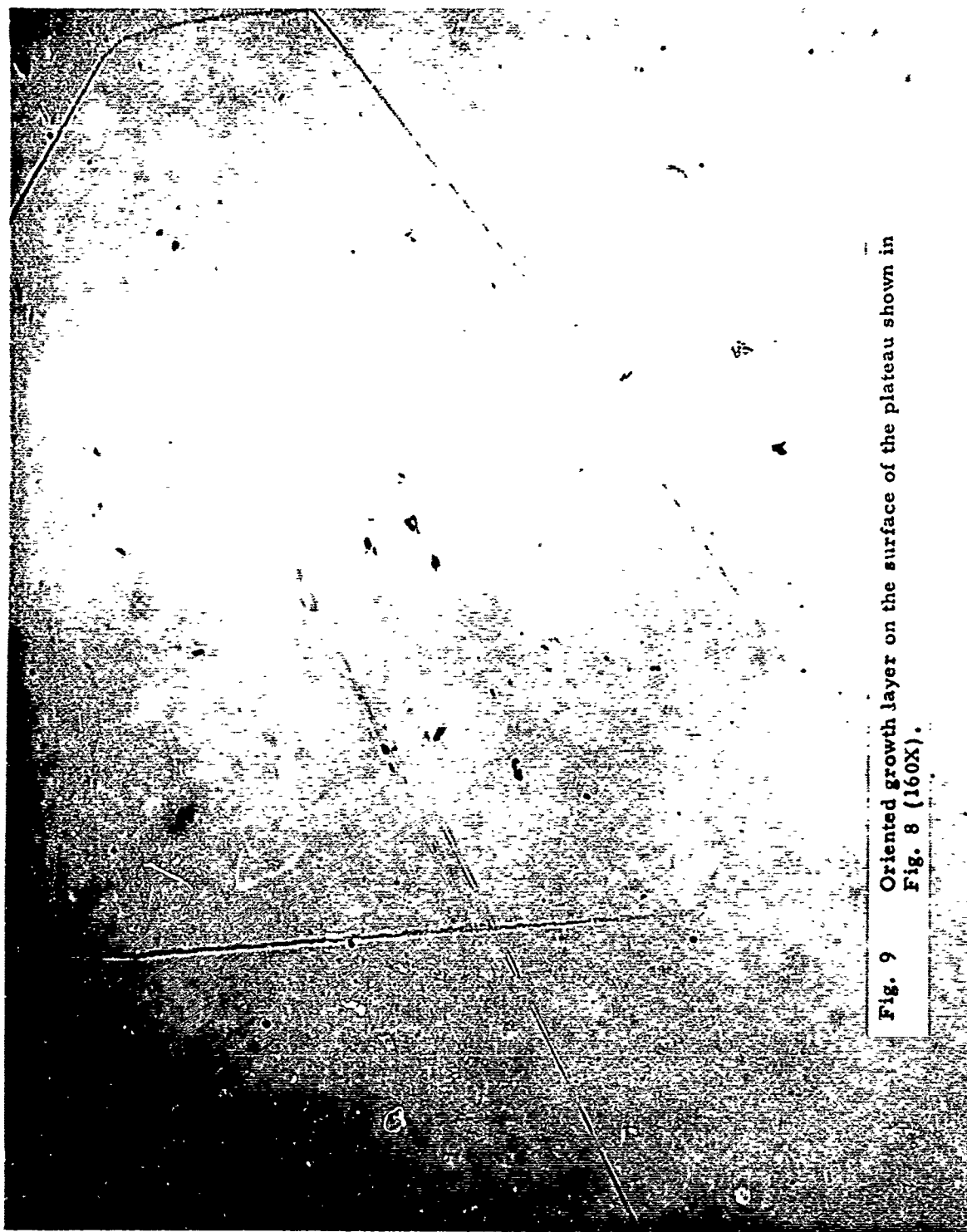


Fig. 9 Oriented growth layer on the surface of the plateau shown in Fig. 8 (160X).

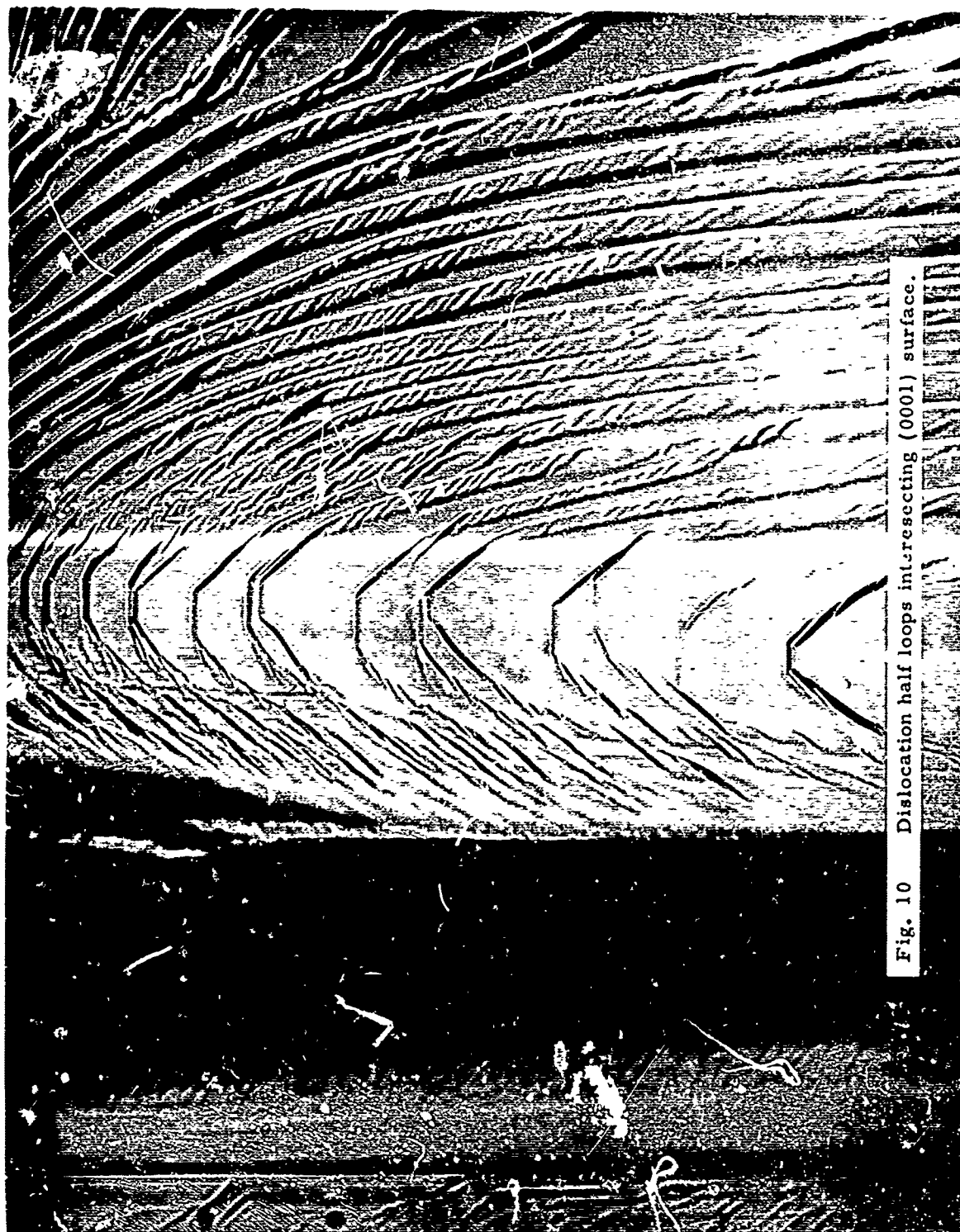


Fig. 10 Dislocation half loops intersecting (001) surface.

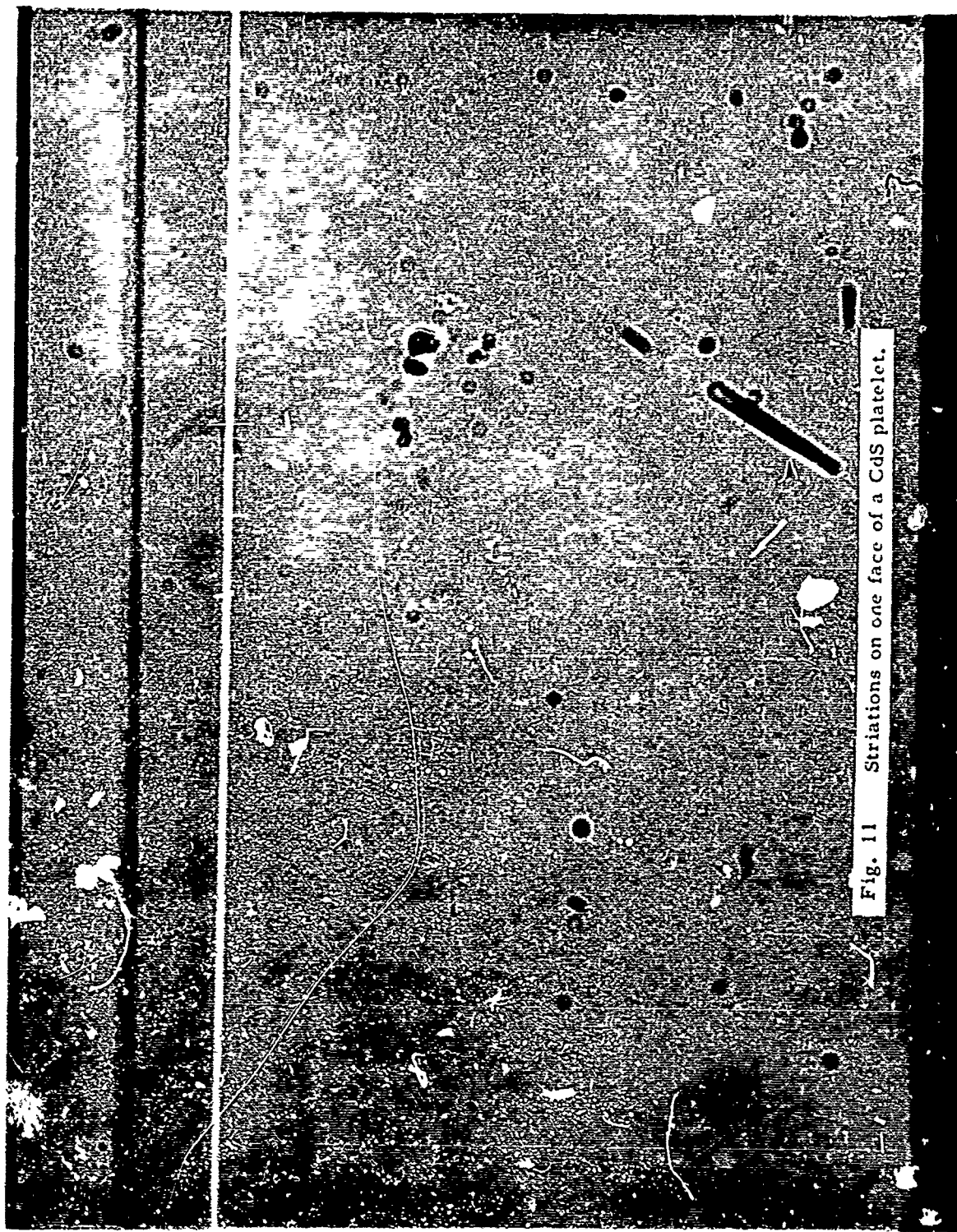


Fig. 11 Striations on one face of a CdS platelet.

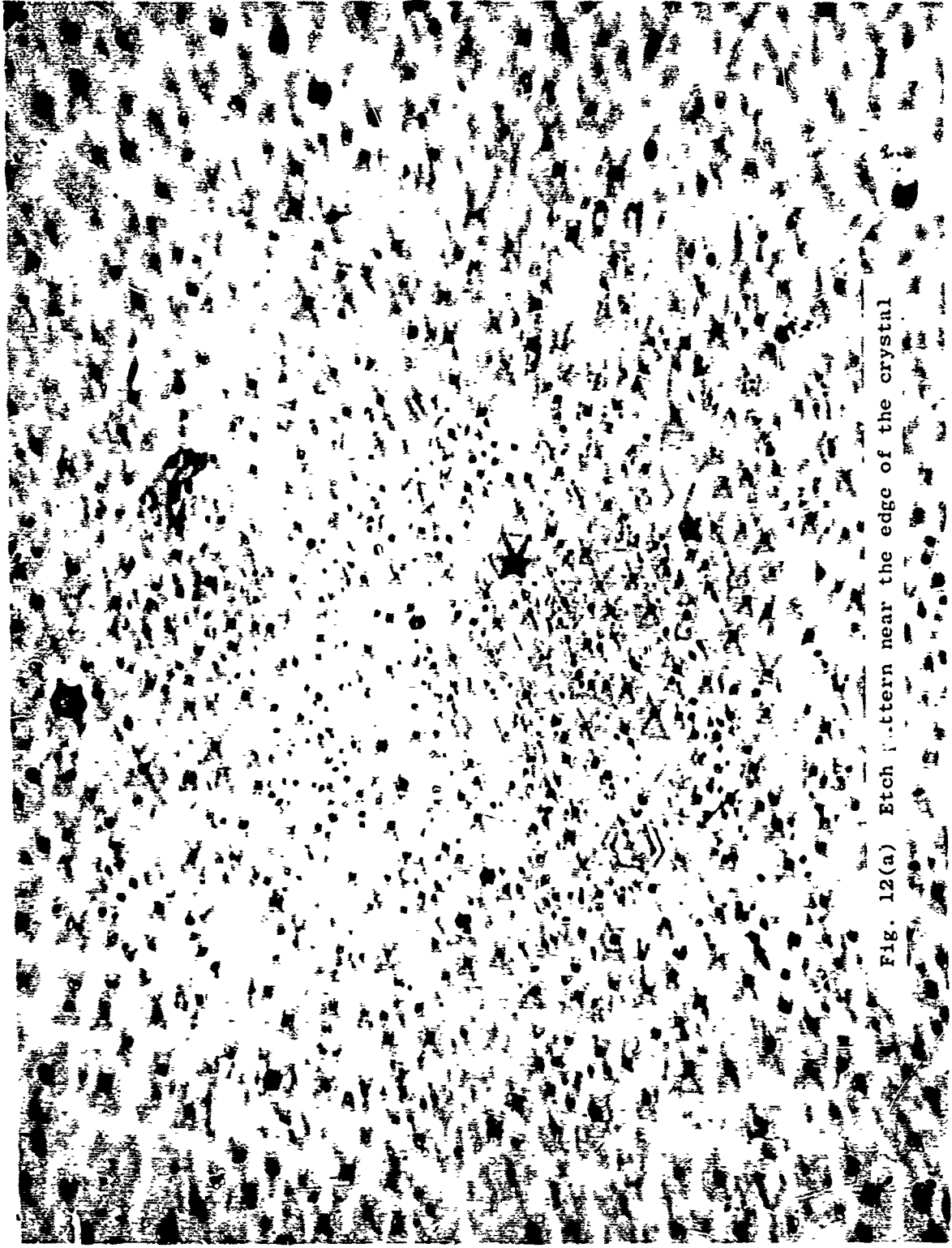


Fig. 12(a) Etch pattern near the edge of the crystal

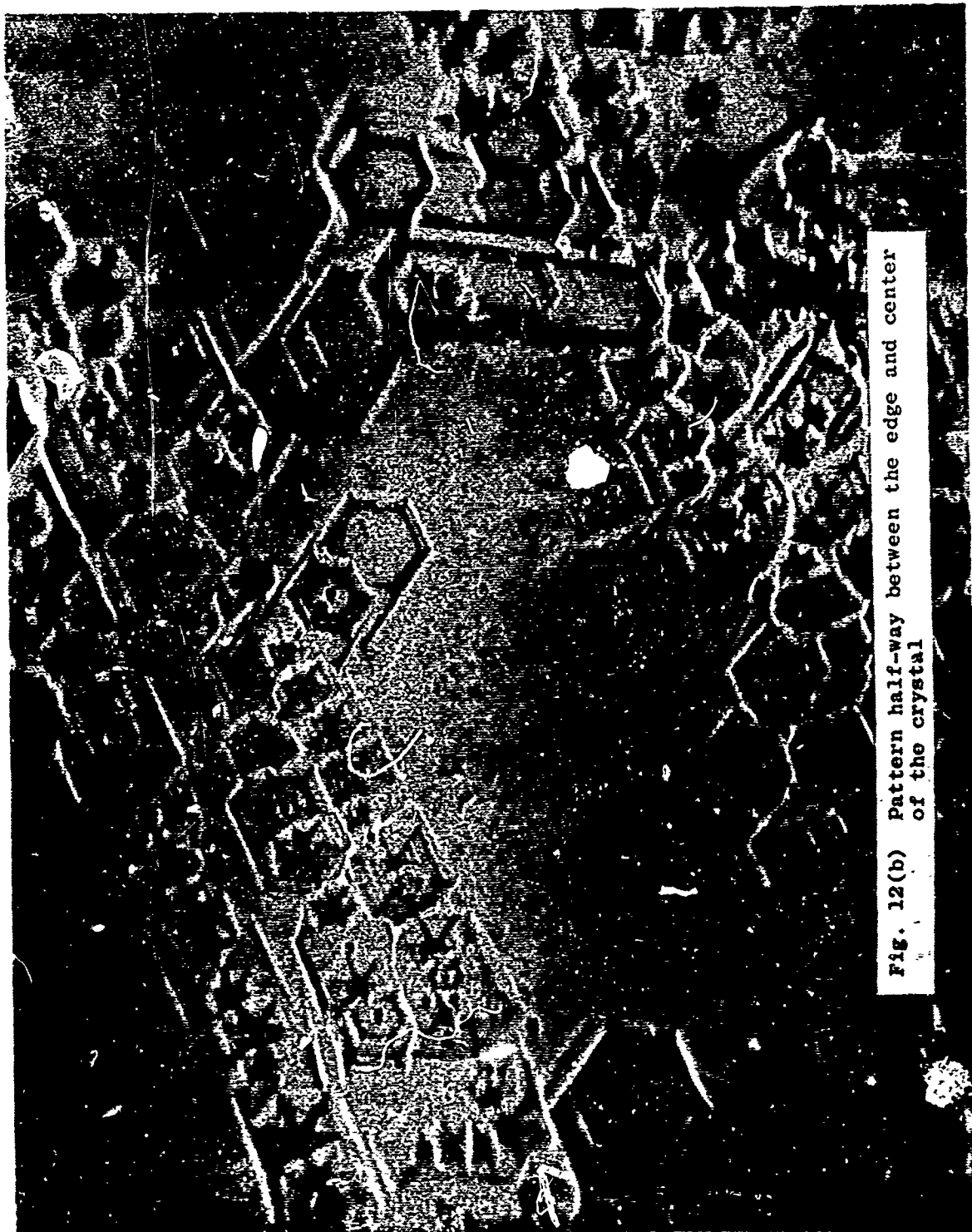


Fig. 12(b) Pattern half-way between the edge and center of the crystal

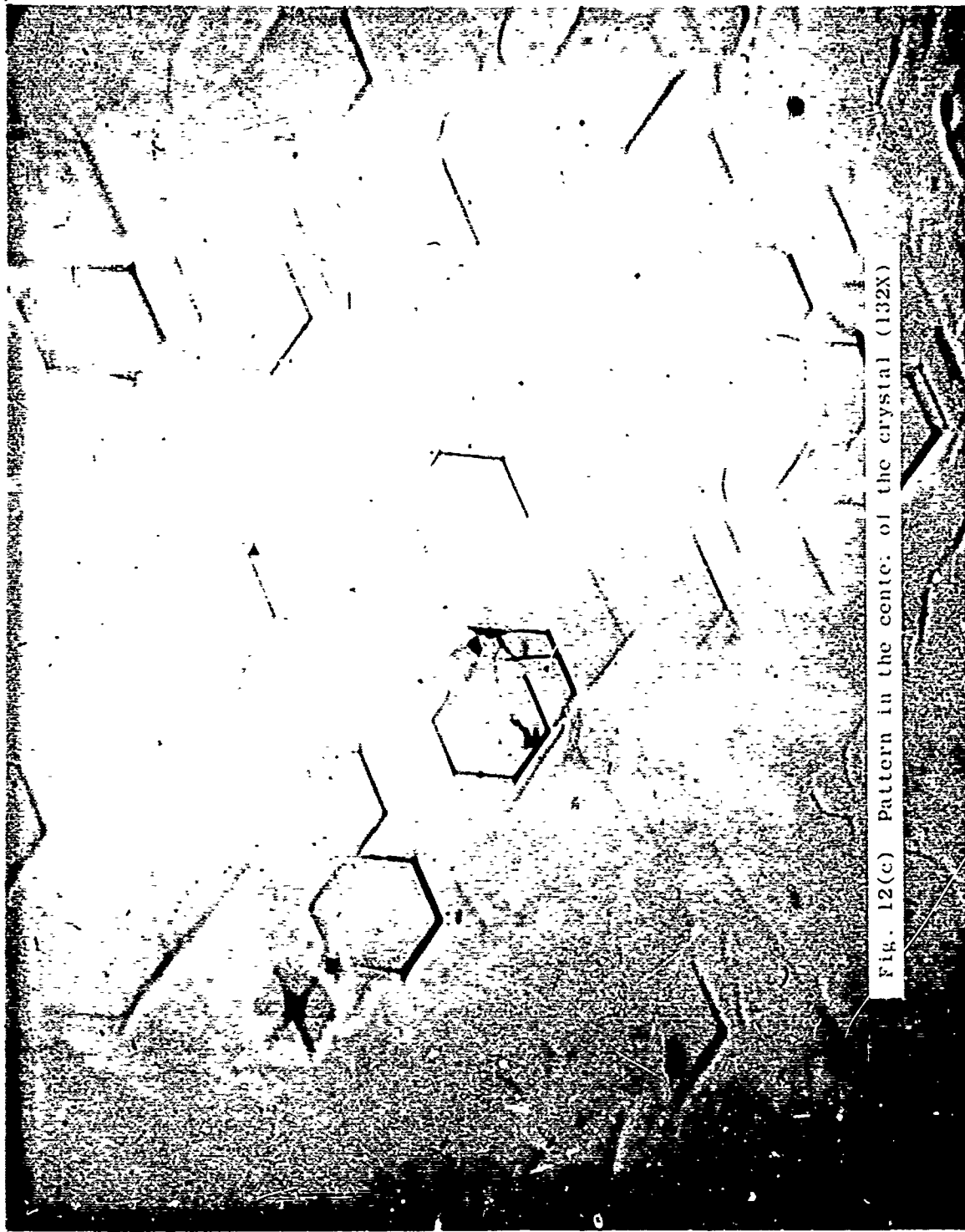


Fig. 12(c) Pattern in the center of the crystal (132X)

LASER BRIGHTNESS GAIN AND MODE CONTROL BY COMPENSATION
FOR THERMAL DISTORTION (U)

by

C. Martin Stickley

Air Force Cambridge Research Laboratories
Office of Aerospace Research
L. G. Hanscom Field, Mass.



C. Martin Stickley

BIOGRAPHY

Dr. C. Martin Stickley was born in Washington, D.C., on 30 October 1933. He received the BSEE from the University of Cincinnati in 1957, the MSEE from MIT in 1958, and the PhD from Northeastern University in 1964. He entered the Air Force in 1958 and was assigned to AFCRL. He was released from active duty in 1962 and has continued to work for AFCRL as a civilian employee since that time. He has been active in the laser field since its inception in 1960 and has published about 15 technical papers relating to this subject. Presently he is the acting chief of the Laser Physics Branch of the Optical Physics Laboratory at the Air Force Cambridge Research Laboratories.

ABSTRACT

Laser Brightness Gain and Mode Control by Compensation for Thermal Distortion (U)

by

C. Martin Stickley

Air Force Cambridge Research Laboratories

L. G. Hanscom Field
Bedford, Mass. 01730

In the limit of excellent optical quality of laser rods, the beam divergence will be determined by the optical distortion produced in the rod brought about by nonuniform absorption of pump light. For ruby lasers this has been shown to be approximately spherical and reproducible from firing-to-firing. Thus it should be possible to compensate for this by means of an external mirror having a curvature opposite to that induced in the rod, and by this technique reduce the beam divergence. The distortion produced in the rod is described in terms of a ray matrix of a thick lens whose focal length is a function of the input energy to the rod. A procedure is given for measuring this focal length to within $\pm 3\%$; it involves measuring the beat frequencies between transverse modes of a flat-mirror cavity containing the laser rod as an active element. After compensating an excellent optical quality rod with an external mirror a brightness gain of about 100 was achieved simultaneously with single transverse mode operation (TEM_{00}) at pump energies as high as 40% over threshold. This procedure for achieving single transverse mode operation is advantageous compared to other methods since (a) no extra elements are needed in the cavity; (b) the beam divergence is near the diffraction limit for the rod holder; and (c) the TEM_{00} mode is not only selected but enhanced in volume, thus increasing the power output in this mode and the mode stability of the laser.

Laser Brightness Gain and Mode Control by Compensation for Thermal Distortion (U)

by

C. Martin Stickley

Air Force Cambridge Research Laboratories
L. G. Hanscom Field
Bedford, Mass. 01730

I. INTRODUCTION

We report here a technique for achieving a brightness gain of the order of 100 simultaneously with single transverse mode operation (TEM_{00}) of a long pulse ruby laser at pump energies as high as 40% over threshold without the use of apertures.

The excited transverse modes of ruby lasers with attached mirrors are typically complex and of high order¹ and result in low brightness. Poor quality ones oscillate in filaments and have even lower brightness in the far field. The brightness can be increased somewhat by using external mirrors² since the mode diameter increases, the cavity Q increases, and mode divergence decreases as the cavity is lengthened. Somewhat lower order modes are excited in this manner since their larger cross sectional area, compared to the same transverse modes with mirrors on the end of the laser rod, more closely matches the area of the inverted region of the ruby rod. The match is still poor, however, and still results in modes being excited whose divergence is twenty or more times the plane wave diffraction limit of the end of the laser rod. In many ruby lasers this can be due to filamentary operation, but in the limit of good optical quality, (that is, freedom from internal path length variations parallel to the mirrors) the beam divergence should be determined by the approximately spherical optical distortion³⁻⁵ brought about by nonuniform absorption of pump light.⁶⁻¹¹ The distortion is such that the plane parallel ruby rod becomes a slightly positive or negative lens depending on the product of the rod radius and doping concentration. Only a small amount of this type of distortion^{1, 12} is necessary to cause the modes to be those of a curved mirror resonator,^{13, 14} with an accompanying reduction in brightness, rather than a plane parallel resonator.¹⁵ Since the pump induced distortion is reproducible it should be possible to compensate for this by means of an external mirror having a curvature opposite to that induced in the rod. Thus, sinusoidal (Fox and Li¹⁵) modes could be excited if the mirror was precisely matched to the internal curvature in the rod. The brightness (watts/cm²/steradian) in the far field should certainly be increased as a result of two factors: (a) the mode divergence will decrease, and (b) the mode intensity will increase since it will have a greater volume.

We note that this is a preferred way of achieving single transverse mode operation for the following reasons: 1. No extra elements are needed in the cavity. This is desirable since they not only degrade its optical quality but tend to become damaged at high power levels as a result of absorption of energy. 2. The desired TEM₀₀ mode is not only selected but enhanced in volume, thus increasing the power output in this mode and the mode stability of the laser. The volume enhancement is produced by the external mirror which is designed to precisely defocus the impinging wavefront to the same degree that it was focused after propagating through the laser rod (the terms "defocus" and "focus" should be interchanged if the laser medium behaves like a concave lens). Mode selecting with small apertures and small mirrors^{16, 17} only selects one mode out of numerous others and does not alter its volume. 3. A beam if generated whose divergence approaches that of the diffraction limit of the laser rod (the closeness to this is a measure of the degree of success of the compensation) without the use of a collimating lens or lenses. Siegman¹⁸ analyzed and experimentally investigated a scheme somewhat similar to the one we are reporting on in which a mirror with a large divergence was polished on one end of the laser rod (a principal advantage compared to the technique we have used) and a small mirror (less than the rod diameter) deposited on the remaining flat end of the rod so that the output beam could escape around it. This system requires collimation, however, and it is not certain that as bright a beam could be produced. His system was designed to have large diffraction losses (35% loss per traversal of the cavity) with the goal of achieving transverse mode selection, thus the threshold is high at room temperature. Although the system worked as he had predicted (in terms of higher threshold and near field distribution) no information was given as to its success as a mode selector or to what extent the brightness was increased. It should be remarked that the compensation technique being discussed in this paper could, in principle, be carried out directly on the rod as Siegman did, however, in order to achieve transverse mode selection with almost flat mirrors the deviation from perfect compensation, ^{1, 12} measured in terms of λ/Q where λ is the wavelength and Q a real number, must be such that $Q > N$. N is the Fresnel number of the resonator and is typically greater than 300 for ruby rods. Ruby rods having such optical perfection cannot be grown within the present state-of-the-art. Thus it is not practical to attempt such an experiment at this time.

In the following section we outline the theory of the compensation procedure. Section III discusses the method used for determination of the focal length of the rod. Sections IV and V contain experimental results and conclusions respectively, and Appendix A summarizes the procedure for determining the ray matrix representing the laser rod.

II. THEORY OF THE COMPENSATION PROCEDURE

The resonator we will analyze is shown in Fig. 1. For the purposes of this analysis the ruby rod can be represented as a thick lens having thickness t , refractive index n , a focal length f and end surface curvatures r_1 and r_2 all of which depend on the energy dissipation as a function of position in the rod. We desire to adjust the resonator to compensate for any distortion introduced in a wavefront after it propagates through the rod, so that the emitted beam will be as close as possible to a plane wavefront. For practical convenience we would like to accomplish all of the compensation with one mirror so that we can use one optical flat. Thus we set the radius of curvature of, say, mirror 2 equal to infinity. The design of mirror 1 can be arrived at by application of Kogelnick's theory¹⁹ of resonators with internal optical elements. A resonator is stable if

$$-1 \leq G_1 G_2 \leq +1 \quad 1.$$

where G_1 and G_2 are dimensionless parameters describing the design of the resonator. These G factors are given by Kogelnick¹⁹ as

$$G_1 = \frac{a_1}{a_2} \left\{ 1 - \frac{d_2}{f} - \frac{1}{R_2} \left(d_1 + d_2 - \frac{d_1 d_2}{f} \right) \right\} \quad 2.$$

and

$$G_2 = \frac{a_2}{a_1} \left\{ 1 - \frac{d_1}{f} - \frac{1}{R_2} \left(d_1 + d_2 - \frac{d_1 d_2}{f} \right) \right\} \quad 3.$$

where a_1 and a_2 are the radii of mirrors 1 and 2, and d_1 and d_2 are the distances from the principal planes of the thick lens to the corresponding mirrors (see Fig. 1). Since we have set $R_2 = \infty$, the condition we desire to satisfy, $G_1 G_2 = +1$, reduces to

$$\left\{ 1 - \frac{d_2}{f} - \frac{1}{R_1} \left(d_1 + d_2 - \frac{d_1 d_2}{f} \right) \right\} \cdot \left(1 - \frac{d_1}{f} \right) = 1 \quad 4.$$

For convenience we will set $d_1 = d_2 = d$ and will maintain this convention throughout the remainder of this article and the experiments, except

where noted. We can now solve for R_1 in terms of f and d . We obtain

$$R_1 = -(f - d) \quad 5.$$

If we had not set R_2 equal to infinity but instead let $R_1 = R_2 = R$ we would have obtained

$$R = -(2f - d) \quad 6.$$

It will be instructive at this point to explore further the thick lens model which we have assumed to represent the laser rod. The lens thickness (or the rod length) is designated by t and has refractive index n both of which are x and y dependent due to nonuniform absorption of pump light. We neglect the y dependence and thus assume the pump energy density in the rod to be radially symmetric (actually a practical necessity if good compensation is to be achieved) and the crystal to be isotropic. This latter assumption is not completely valid for ruby but we shall neglect this difference in this analysis. Since the departures of t and n from their values at $t(x=0) = t_0$ and $n(x=0) = n_0$ will always be small³ we can write

$$t(x) = t_0 + \frac{\partial t}{\partial T} (T(x) - T_0) \quad 7.$$

and

$$n(x) = n_0 + \frac{\partial n}{\partial T} (T(x) - T_0) \quad 8.$$

where $T(x)$ is the temperature profile in the laser rod, and $T(x=0) = T_0$. It is further assumed that $T(x)$ is parabolic and can be written

$$T(x) = T_0 (1 - 2x^2/g^2) \quad 9.$$

We will assume g^2 to be an adjustable parameter which is positive if the energy density (and thus the temperature) is greatest in the center of the rod. Substitution of equation 9 into equations 7 and 8 gives

$$t(x) = t_0 - \left(\frac{2T_0 x^2}{g^2} \right) \cdot \frac{\partial t}{\partial T} \quad 10.$$

and

$$n(x) = n_0 - \left(\frac{2T_0 x^2}{g^2} \right) \frac{\partial n}{\partial T} \quad 11.$$

This form of the variation of t and n with x is in excellent agreement with the form of the distortion for ruby rods with rough sides and can be used as a good approximation to its form in the central one-half region³ (where oscillation normally develops) of a ruby rod with polished sides. Therefore, this justifies our assumption for the form of the temperature distribution. We can express the variation in thickness of the rod in terms of radii of curvature r_1 and r_2 of its end surfaces. These radii r , which we will assume to be equal and positive as drawn in Fig. 1, are determined by

$$r = -2(d^2 t / dx^2)^{-1} \quad 12.$$

which is

$$r = + \frac{g^2}{2T_0} \cdot \left(\frac{\partial t}{\partial T} \right)^{-1} \quad 13.$$

The "2" is included in equation 12 in order to divide the distortion equally at each end of the rod. Furthermore, to bring our notation into agreement with that of Kogelnick¹⁹ we will designate

$$\frac{1}{b^2} = \frac{T_0}{n_0 g^2} \cdot \frac{\partial n}{\partial T} \quad 14.$$

so that equation 11 becomes

$$n(x) = n_0 (1 - 2x^2 / b^2) \quad 15.$$

The relationship between these parameters and the rod focal length f can be obtained by deriving the ray matrix for the rod using the notation and sign convention in Fig. 1. This is done in Appendix A. The result is given as equation A5 and is correct to terms of the order of $1/rb^2$. From ray matrix theory it is known²⁰ that

$$f = - \frac{1}{C} \quad 16.$$

and

$$h = \frac{D - 1}{C} \quad 17.$$

where C and D are those elements of the ray matrix and h is the distance from the vertex of the lens to the principal plane. Upon substitution from equation A5 into equations 16 and 17 we obtain

$$\frac{1}{f} = \left(1 - \frac{2t^2}{b^2}\right) (n-1) \left(\frac{2}{r}\right) + \frac{4tn}{b^2} - \frac{t(n-1)^2}{nr^2} \quad 18.$$

and

$$h = \left(\frac{2t^2}{b^2} + \frac{t(n-1)}{nr}\right) f \quad 19.$$

It will be shown at a later stage in this article that for the curvatures we are attempting to compensate, $2t^2/b^2 \ll 1$, and $t(n-1)^2/nr^2 \ll 2(n-1)/r$. Equation 18 then becomes

$$\frac{1}{f} = \frac{2(n-1)}{r} + \frac{4tn}{b^2} \quad 20.$$

As shown in equation 15 $1/b^2$ is indicative of the extent of the refractive index variation which exists in the rod. We can account for the passive or unpumped refractive index variation by writing

$$1/b^2 = 1/b_u^2 + 1/b_p^2 \quad 21.$$

where we define $1/b_p^2$ as that part of the index variation which exists when the rod is pumped and $1/b_u^2$ as the part describing the unpumped index variation. Within the present state-of-the-art of optical polishing it is not necessary to do this for the length variation with x, that is, we assume the ends to be flat and parallel. Upon substituting equation 21 into 20 we obtain

$$\frac{1}{f} = \frac{1}{f_p} + \frac{1}{f_u} \quad 22.$$

where

$$\frac{1}{f_p} = \frac{2(n-1)}{r} + \frac{4tn}{b^2} \quad 23.$$

and

$$\frac{1}{f_u} = \frac{4tn}{b_u^2} \quad 24.$$

The components of $1/f$ should be related through the thermal properties of the laser rod. ^P Such a relation is obtained by combining equations 13 and 14

$$\frac{r}{b^2} = \frac{\partial n / \partial T}{2n_0 \partial t / \partial T} = \frac{\alpha_n}{2n_0 t \alpha_t} \quad 25.$$

where we have set the left hand side of equation 14 equal to $1/b^2$ in agreement with our change in notation. Factoring a $2/r$ out of ^P both terms in equation 23 and substituting equation 25, we have the result

$$\frac{1}{f_p} = \frac{2}{r} \left(n-1 + \frac{\alpha_n}{\alpha_t} \right) \quad 26.$$

is serves to illustrate the relative importance which the thermal expansion and refractive index changes have on determining the rod focal length. If $\alpha_n \ll \alpha_t$, the distortion in the rod is due principally to thermal expansion, ⁿ and if $\alpha_n \gg \alpha_t$, it is due to refractive index changes.

Returning to equation 19, if one factors a $t/2n$ out of the bracketed expression, the remaining terms in it are equal to $1/f$ (see equation 20) thus cancelling the f in equation 19. It then reduces to

$$h = \frac{t}{2n} \quad 27.$$

which is shown in Fig 1. Note that within the approximations involved it is independent of length and index changes.

III. MEASUREMENT OF THE ROD FOCAL LENGTH

As it was mentioned early in Part II, if d is chosen we must know f before R_1 can be determined. f can be measured through proper interpretation of distortion photographs,³⁻⁵ but a considerably more accurate method is through measurement of the transverse mode beat frequency¹ of a cavity containing the rod to be compensated and which is being pumped under approximately the same pumping conditions which will be used for the compensation. The accuracy for these two methods is $\pm 3\%$ for the latter one compared to, say, $\pm 20\%$ for the former one for slight curvatures.

The resonant frequencies ν for a cavity of this type are given by¹⁹

$$\nu = \frac{cq}{2L} + \frac{c}{2\pi L} (m+n+1) \cos^{-1} \sqrt{G_1 G_2} \quad 28$$

where q is the longitudinal mode number, m and n the transverse mode numbers, c is the speed of light in vacuum, L (shown in Fig. 1) the optical length of the cavity, and G_1 and G_2 are as defined in equations 2 and 3. The difference frequency $\Delta\nu$ between transverse modes ($\Delta q = 0$, $\Delta(m+n) = 1$) can be written from equation 28 as

$$\Delta\nu = \frac{c}{2\pi L} \cos^{-1} \sqrt{G_1 G_2} \quad 29.$$

The greatest accuracy is achieved in this measurement if flat mirrors are used ($R_1 = R_2 = \infty$).

Equation 29 can therefore be written as

$$\Delta\nu = \frac{c}{2\pi L} \cos^{-1} \left(1 - \frac{d}{f}\right) \quad 30.$$

Solving for f we obtain

$$f = \frac{d}{1 - \cos \left(\frac{2L\pi\Delta\nu}{c} \right)} \quad 31.$$

This compensation procedure was carried out on a rod whose path length variations are illustrated in Fig. 2; the difference in path length between a bright and a dark fringe is $\lambda/4$. We estimate that this rod has

refractive index variations no greater than $\lambda/10$ in the central one-half region where laser action occurs; also, it has a path length maximum in the center. The rod was cut from a slow grown, standard orientation Linde boule (circa 1961) so that the rod axis was parallel to the boule axis. It is 4.74 mm in diameter and 3.81 cm long and its lateral surface is polished. When examined through crossed polaroids it shows no evidence of strain or deviations in the c axis.

It was mounted in a laser head containing a helical FX 60 flash-lamp (2.8 cm inside diameter and 7.5 cm long) which was wrapped with heavy, polished metal foil. The rod was held with holders designed to minimize hot air seepage into the optical path; the flat end surfaces of the rod were antireflection coated with one layer of magnesium fluoride and were aligned parallel to and midway between two external, flat, multiple-layer dielectric coated mirrors with reflectivities of 96% and 85%. The rear surfaces of both mirrors were cut at an angle of 30 minutes to the primary surface. Threshold was 1058 Joules at 74°C using a 1.8 millisecc long, flat pump pulse.

The transverse mode beat frequencies were measured with a TRW Products image converter camera using streak photography in the far field of the beam. The details of this measurement are well summarized in reference 1 and will not be repeated here. The left hand portion of Fig. 3 shows three streak photographs each having a duration of approximately 50 nanosec.; the right hand side represents the interpretation of each one. Since the optical length of the mirror separation was 52.9 cm, one would expect the beat frequency between modes differing by a q of unity to be 284 MHz. The modes beating in Fig. 3a have difference frequency of the order of 570 MHz which is close to 2×284 MHz. This fact in combination with the uniformity in cross section of the beat leads us to the conclusion that a $\text{TEM}_{0,0,q}$ mode is beating with a $\text{TEM}_{0,0,q+2}$ mode; this conclusion is illustrated by the heavy lines marked as shown on the right hand side of Fig. 3a. In Fig. 3b the frequency is approximately 540 MHz (the exact determination of these frequencies, and therefore the difference frequency $\Delta\nu$ which we are seeking, was limited to about $\pm 2.5\%$ by the uncertainty in the calibration of the streak rate; this could be improved if necessary to $\pm 1\%$ or less). Also the phase of the beat alternates spatially from side-to-side with time which is characteristic of a $\text{TEM}_{0,0}$ mode beating with a $\text{TEM}_{0,1}$ mode. These two items of information leads us to the designation shown on the right hand side of Fig. 3b. Without going further we could conclude that $\Delta\nu = 30$ MHz, however, we have included Fig. 3c to strengthen our deduction. Here the beat between a $\text{TEM}_{0,0}$ mode and a $\text{TEM}_{0,1}$ mode has a frequency of about 600 MHz, and furthermore, one period of a beat is distinguishable at about 30 MHz.

Additional consideration of the phases of these beats leads us to the designation shown on the right hand side of Fig. 3c. (If three modes are present one would expect to see three beats; the third or between $TEM_{0,1,q}$ and $TEM_{0,1,q+2}$ might not be observable if these modes were weak relative to $TEM_{0,0,q}$.) Thus this supports our conclusions drawn from Figs. 3a and 3b.

Having obtained ΔV we now compute f from equation 31 to be 445 cm. Since $d = 24$ cm, $R = 421$ cm.

As a check on the value we have obtained for f , we can compare it with a distortion photograph made using a Twyman-Green interferometer of a rod having comparable geometry. The number of fringes F between two points of a Twyman-Green photograph is

$$F = \frac{2}{\lambda} \cdot (t \Delta n + (n-1) \Delta t) \quad 32.$$

$F = 1$ between either two bright fringes or two dark fringes. Δn and Δt are the refractive index and length variations between the two points. If we designate the two points as $x = 0$ and $x = a/2$, then $\Delta n = n(a/2) - n_0$ and $\Delta t = t(a/2) - t_0$. From the definitions of $t(x)$, $n(x)$ and r/b^2 we can write equation 32 as

$$F = \frac{2}{\lambda} \left[t \left(-\frac{a^2}{4rt} \frac{\alpha_n}{\alpha_t} \right) + (n-1) \left(-\frac{a^2}{4r} \right) \right] \quad 33.$$

$$= -\frac{2}{\lambda} \left(\frac{a^2}{8f} \right) \quad 34.$$

For $\lambda = .6943 \times 10^{-4}$ cm, $a = 0.237$ cm, and $f = 445$ cm, we obtain $F = -0.455$. To compare this fringe change with Fig. 1Ac of reference 3 we should divide by 1.4 to account for differences in rod length and pumping rates. If this is done it is found that the agreement is good, for it falls within the range of uncertainty of the measured value of F from the distortion photographs.

Knowing f we can also check our previous assumptions that $2t^2/b^2 \ll 1$ and $t(n-1)^2/nr^2 \ll 2(n-1)/r$. From equation 23 we can compute $r \approx 6f = 26.7$ meters. Since $r/b^2 = \alpha_n / 2nt \alpha_t$, we find that $1/b^2 \approx 1/15,700$ cm⁻², thus the validity of neglecting $2t^2/b^2$ compared to unity is excellent. Similarly, the other approximation becomes $.5 \times 10^{-6} \ll .6 \times 10^{-3}$ which is obviously acceptable.

IV. EXPERIMENTAL RESULTS

A convex mirror was made having a curvature of 4.21 meters, and to it was applied a 98% reflectance multiple layer dielectric coating. The laser was first operated with the two flats and the data shown in Fig. 4a, b, and c were recorded. The 96% flat mirror was immediately replaced with the 98%, 4.21 meter convex mirror and the data in Fig. 4d, e, and f were obtained. The results are summarized in Table I.

Table I: Experimental Results

	Threshold	Beam Divergence*	Peak Power*	Brightness
Before Compensation	1.00	1.7 millirad	1	1
After Compensation	1.03	0.4 millirad	5.5	99

*Average values taken from Fig. 4

Major features of Fig. 4 show that the laser oscillated at all times in the $TEM_{0,0}$ mode; it had a beam divergence of a factor of four less than the divergence for uncompensated operation. This, in conjunction with the fact that the average spike height increases by a factor of 5.5, results in a brightness enhancement of $5.5 \times (4.25)^2 \approx 99$. No measurements of the energy output were made but it appears from the spiking photographs that this did not change. Fig. 5 illustrates compensated laser operation at 60% over threshold; it is at this point that other structure in the far field pattern becomes noticeable, however the divergence of the principal lobe remains at about 0.4 millirad. It was unexpected that the compensated laser would operate in such a stable manner (that is, there appears to be no transverse mode hopping) for it is known³⁻⁵ that the rod focal length is becoming shorter continuously with time. One might think, then, that the unpumped refractive index variations are more severe than the pumped ones and that we are simply compensating for the passive distortion. This would account for the extreme transverse mode stability. That is not the case, however, as is shown by the following calculation. The unpumped path length variation between the points $x = 0$ and $x = a/2$ can be expressed, using equation 15, as

$$[n(a/2) - n_0] t = -2n_0 t (a/2)^2 / b_u^2 \quad 35.$$

As we have already mentioned in Part III, the refractive index variation of the rod we are using is $\lambda/10$ as can be seen in Fig. 2. Equating this to the left hand side of equation 35, solving for b_u^2 and substituting the values for the rod's length and diameter, we find $f_u = 11.0$ meters, a factor of 2.4 larger than the total focal length f . This is strong evidence, then, that the mode stability is not due to compensation for an unpumped focal length which is shorter than that due to pumping.

Insight into what we believe to be the true reason for the mode stability can be obtained by considering the degree of compensation that was achieved. From the hundreds of compensated far field patterns which were observed, a $TEM_{0,1}$ mode was seen one time. From a measurement of the separation of its peaks one can compute¹³ the spot radius w_0 at the flat mirror from

$$\frac{s}{2(FL)} = \frac{\lambda}{w_0 \pi \sqrt{2}}$$

where s = the separation between the $TEM_{0,1}$ mode maxima, and (FL) is the focal length of the lens. For the compensated laser we obtained $2w_0 = 1.52$ mm, the beam diameter of the $TEM_{0,1}$ mode. If the compensation had been perfect we would have calculated a beam diameter equal to the rod holder aperture size, which is 3.8 mm, a factor of 2.5 too large. Thus, because the compensation was not perfect the mode instabilities which would have been associated with it were not observed. We note from this that some "detuning" from perfect compensation is, therefore, desirable if mode hopping is to be prevented. Other aspects of the design which undoubtedly contributed to its stability are: (a) the energy distribution in the center of a rod having this diameter and concentration ($0.04\% Cr^{+3}$) is quite flat¹⁰ thus the changes which would occur as a function of time were small; and (b) the Fresnel number of the resonator was $N \approx a^2/L\lambda = 3.9$ (where $2a$, in this case, is the aperture size of the rod holder) and for a $G_1 = 1.06$ and $G_2 = .94$ (see Table II) after compensation, Siegman's^{18,21} Fig. 7 (reproduced here in Fig. 6) gives an average diffraction loss per pass as 7% for the $TEM_{0,0}$ mode. What this loss is for the $TEM_{0,1}$ mode is not known exactly, but a first approximation to it can be made with the help of Fig. 8 of Fox and Li¹⁵ which gives the diffraction loss per pass for the lowest two modes for plane circular reflectors. The essence of the approximation is to say that the diffraction losses don't change for a combined decrease in the G value and Fresnel number. Since the 7% loss per pass point for the

TEM_{0,0} mode occurs at N = 2 for G = 1 we approximate from their figure that the loss per pass for the TEM_{0,1} mode is 17%. When the other losses per pass are included (due to transmission, scattering and excited state absorption²²) the net loss per pass becomes approximately 34% for the TEM_{0,0} mode and 44% for the TEM_{0,1} mode; higher order modes would have correspondingly higher losses. In summary, this design of the compensated laser is such that effective mode selection and stability can occur based on meaningful differences in diffraction losses; if a higher diffraction loss operating point is used threshold begins to increase considerably¹⁸ with, perhaps, no further gain in mode selectivity via diffraction loss. Thus TEM_{0,0} mode diffraction losses of about 10% may be near an optimum operating point for ruby lasers. It should also be added that the large increase observed in spike amplitude (see Table I) could be due to additional quenching of the already below threshold modes² by further increasing their diffraction losses; the population inversion would be driven further below threshold at the end of the spike.

To illustrate, however, that things are never completely understood we refer to Fig. 7. It shows that the delay time to threshold as well as the spike amplitude for movement of mirror 1 about the point L = 52.9 cm (or the point d₁ = d₂ = d) by plus and minus 1 cm. The delay to threshold does not change but the spike amplitude decreases by about a factor of two or more. One might think this behavior could be due to the sensitivity of the laser having the compensating mirror in exactly the correct position; this does not appear to be so however as can be seen from Table II.

Table II: Summary of Changes in G Values

	Before Compensation	After Compensation	After with d ₁ = d-1cm	After with d ₁ = d+1cm
G ₁	.9456 ± .0034*	1.0574	1.0551	1.0596
G ₂	.9456 ± .0034*	.9456	.9479	.9434
G ₁ G ₂	.894	.9998	1.0001	.9996

*This uncertainty is due to the uncertainty in ΔV(= +3%) and is representative of the uncertainties of the other values quoted in the Table.

Due to the uncertainty in ΔV , the absolute values are not known as well as they are indicated there. However, the changes are significant and they appear to be too small to be meaningful. The only possibility we can see for explaining this is that the operating point at $d_1 = d_2 = d$ happens to be at a minimum of the periodic variation in diffraction loss predicted by Fox and Li²¹ (see Fig. 6). A slight variation about that point could change the loss significantly of the higher order modes but might not for the TEM_{0,0} mode.

V. CONCLUSIONS

We have presented a theory of and outlined a procedure for precise compensation of laser cavities for the distortions in the laser material arising from nonuniform absorption of pump energy. We have carried out this procedure on an admittedly small sample of ruby but we feel that the high degree of success attained indicates the future potential of this technique for increasing the brightness of lasers by at least two orders of magnitude. Greater increases than this may be achieved by carrying out the compensation procedure carefully with laser rods of superior passive optical quality. Furthermore, this procedure is an excellent one for mode control for: (a) no extra energy absorbing elements are used in the cavity; (b) the mode volume is increased thus increasing the power in the mode and its stability, and (c) the beam divergence can be made to approach the plane wave diffraction limit of the laser system without the use of extra lenses. We also note that laser rods with polished lateral surfaces are the better type to use for long pulse operation since the curvature can be made to change very little in the central region of the rod in comparison with rods having rough sides. Conversely, rods with rough sides are the better type to compensate for Q-switching since the curvature can be quite uniform across the whole rod and not change during the time duration of the Q-switched pulse. Finally, this work emphasizes the advantages to be gained by using laser materials having excellent optical quality.

VI. ACKNOWLEDGEMENT

The writer wishes to acknowledge the assistance given by R. L. Townsend, Jr., in the early phases of this work, and the help of H. Miller in carrying out the compensation experiments.

APPENDIX A: Derivation of the Ray Matrix of a Ruby Rod

The usefulness of ray matrices to describe the propagation of the TEM₀₀ mode in optical systems has been pointed by several authors^{19,23,24}. Since we are interested in generating only that mode in the resonator of Fig. 1, we will apply these techniques to our problem. We use the conventions that: (a) light propagates from left to right (the + z direction); (b) x is positive above the z axis and negative below it; (c) angles are positive if the slope of the ray intersecting the side of surface of interest is positive; (d) radii of curvature are positive as shown; and (e) a different index will be used to designate each side of every surface a ray encounters; the numbering of these sides will be in the order in which light is passing through them. In accordance with these conventions there are four sides to be dealt with; thus, we have designated the position and slope of the input and output rays as x_1, θ_1 , and x_4, θ_4 , respectively. Abbe's Law of Sines describes the refraction at the ends of the rod. Thus we can write

$$\begin{bmatrix} x_2 \\ \theta_2 \end{bmatrix} = \begin{bmatrix} 1 & 0 \\ -\left(\frac{n-1}{r_1}\right) & \frac{1}{n} \end{bmatrix} \begin{bmatrix} x_1 \\ \theta_1 \end{bmatrix} \quad A1$$

and

$$\begin{bmatrix} x_4 \\ \theta_4 \end{bmatrix} = \begin{bmatrix} 1 & 0 \\ -\left(\frac{n-1}{r_2}\right) & n \end{bmatrix} \begin{bmatrix} x_3 \\ \theta_3 \end{bmatrix} \quad A2$$

The translation matrix for a medium in which the refractive index changes with x as in equation 15 is given by Kogelnick as

$$\begin{bmatrix} x_3 \\ \theta_3 \end{bmatrix} = \begin{bmatrix} \cos \frac{2t}{b} & \frac{b}{2} \sin \frac{2t}{b} \\ -\frac{2}{b} \sin \frac{2t}{b} & \cos \frac{2t}{b} \end{bmatrix} \begin{bmatrix} x_2 \\ \theta_2 \end{bmatrix} \quad A3$$

We will assume that $2t \ll b$ thus permitting us to write A3 as

$$\begin{bmatrix} x_3 \\ \theta_3 \end{bmatrix} = \begin{bmatrix} 1 - \frac{2t^2}{b^2} & t \\ \frac{-4t}{b^2} & 1 - \frac{2t^2}{b^2} \end{bmatrix} \begin{bmatrix} x_2 \\ \theta_2 \end{bmatrix} \quad A4$$

If A1, A2, and A4 are now combined, we will have

$$\begin{bmatrix} x_4 \\ \theta_4 \end{bmatrix} = \begin{bmatrix} A & B \\ C & D \end{bmatrix} \begin{bmatrix} x_1 \\ \theta_1 \end{bmatrix} \quad A5$$

where

$$A = 1 - \frac{2t^2}{b^2} - \frac{t(n-1)}{nr_1}$$

$$B = t/n$$

$$C = \frac{t(n-1)^2}{nr_1 r_2} - \left(1 - \frac{2t^2}{b^2}\right)(n-1) \left(\frac{1}{r_2} + \frac{1}{r_1}\right) - \frac{4tn}{b^2}$$

$$D = 1 - \frac{2t^2}{b^2} - \frac{t(n-1)}{nr_2}$$

References

1. C. M. Stickley, "A Study of Transverse Modes of Ruby Lasers Using Beat Frequency Detection and Fast Photography", *Applied Optics*, vol. 3, pp 967 - 979, August 1964.
2. J. I. Masters and J. H. Ward, "Laser Q-Spoiling Effects Using a Remote Reflector", *Proc. I. E. E. E.*, vol. 51, pp 221 - 223, January 1963.
3. R. L. Townsend, C. M. Stickley, and A. D. Maio, "Thermal Effects in Optically Pumped Laser Rods", *Applied Physics Letters* vol. 7, pp 94 - 96, August 15, 1965.
4. H. Welling, C. J. Bickart, and H. G. Andersen, "Change in Optical Path Length in Laser Rods Within the Pumping Period", *I. E. E. E. Jour. Quan. Elec.*, vol. QE-1, pp 223 - 224; August 1965.
5. H. Welling and C. J. Bickart, "Spatial and Temporal Variation of the Optical Path Length in Flash Pumped Laser Rods", *Jour. of the Op. Soc. of Amer.* vol. 56, May 1966 (to be published).
6. G. E. Devlin, J. McKenna, A. D. May, and A. L. Schawlow, "Composite Optical Rod Masers", *Applied Optics*, vol. 1, pp 11 - 15, January 1962.
7. J. McKenna, "The Focusing of Light by a Dielectric Rod", *Applied Optics*, vol. 2, pp 303 - 310, March 1963.
8. W. R. Sooy and M. L. Stitch, "Energy Distribution in a Polished Cylinder of Laser Material", *Jour. Appl. Phys.*, vol. 34, pp 1719 - 1723, June 1963.
9. H. C. Cooke, J. McKenna, and J. G. Skinner, "Distribution of Absorbed Power in a Side-Pumped Ruby Rod", *Applied Optics*, vol. 3, pp 957 - 961, August 1964.
10. J. G. Skinner, "Pumping Energy Distribution in Ruby Rods", *Applied Optics*, vol. 3, pp 963 - 965, August 1964.

11. G. Lampis, C. A. Sacchi, and O. Svelto, "Pump Energy Absorption in a Ruby Rod", *Applied Optics*, vol. 3, pp 1467 - 1470, December 1964.
12. S. R. Barone, "Perturbed Fabry-Perot Resonators", AFCRL 65-173; Scientific Report No. 2 on Contract AF19(628)-8817, January 1965.
13. G. D. Boyd and J. P. Gordon, "Confocal Multimode Resonator for Millimeter Through Optical Wavelength Masers", *Bell Sys. Tech. Jour.*, vol. 40, pp 489 - 508, March 1961.
14. G. D. Boyd and H. Kogelnick, "Generalized Confocal Resonator Theory", *Bell Sys. Tech. Jour.*, vol. 41, pp 1347 - 1369, July 1962.
15. A. G. Fox and T. Li, "Resonant Modes in a Maser Interferometer", *Bell Sys. Tech. Jour.*, vol. 40, pp 453 - 488, March 1961.
16. V. Evtuhov and J. K. Neeland, "Study of the Output Spectra of Ruby Lasers", *I. E. E. E. Jour. of Quan. Elec.*, vol. QE-1, pp 7 - 12, April 1965; also V. Evtuhov and J. K. Neeland, "Mode Control in a Ruby Laser", 21st Annual Conference on Electron Device Research, June 1963 (unpublished).
17. A. E. Siegman, R. J. Morris, and R. Wilson, "Ruby Laser Mode Control with Small Mirrors", 21st Annual Conference on Electron Device Research, June 1963 (unpublished).
18. A. E. Siegman, "Unstable Optical Resonators for Laser Applications", *Proc. I. E. E. E.*, vol. 53, pp 277 - 287, March 1965.
19. A. Kogelnick, "Imaging of Optical Modes - Resonators with Internal Lenses", *Bell Sys. Tech. Jour.*, vol. 44, pp 455 - 494, March 1965.
20. E. L. O'Neill, Introduction to Statistical Optics, Addison-Wesley Publishing Co., Inc., Reading, Massachusetts, 1963, pp 38 - 39.
21. A. G. Fox and T. Li, "Modes in a Maser Interferometer with Curved and Tilted Mirrors", *Proc. I. E. E. E.*, vol. 51, pp 80 - 89, January 1963.

22. Y. C. Kiang, J. Stephany and F. C. Unterleitner, "Visible Spectrum Absorption Cross Section of Cr^{3+} in the ^2E State of Pink Ruby", I. E. E. E. Jour. Quan. Elec., vol. QE-1, pp 295 - 298, October 1965.
23. M. Bertolotti, "Matrix Representation of Geometrical Properties of Laser Cavities", Nuovo Cimento, vol. 32, pp 1242 - 1257, June 1964.
24. W. Kahn, "Unstable Optical Resonators", Applied Optics, vol. 5, pp 407 - 413, March 1966.

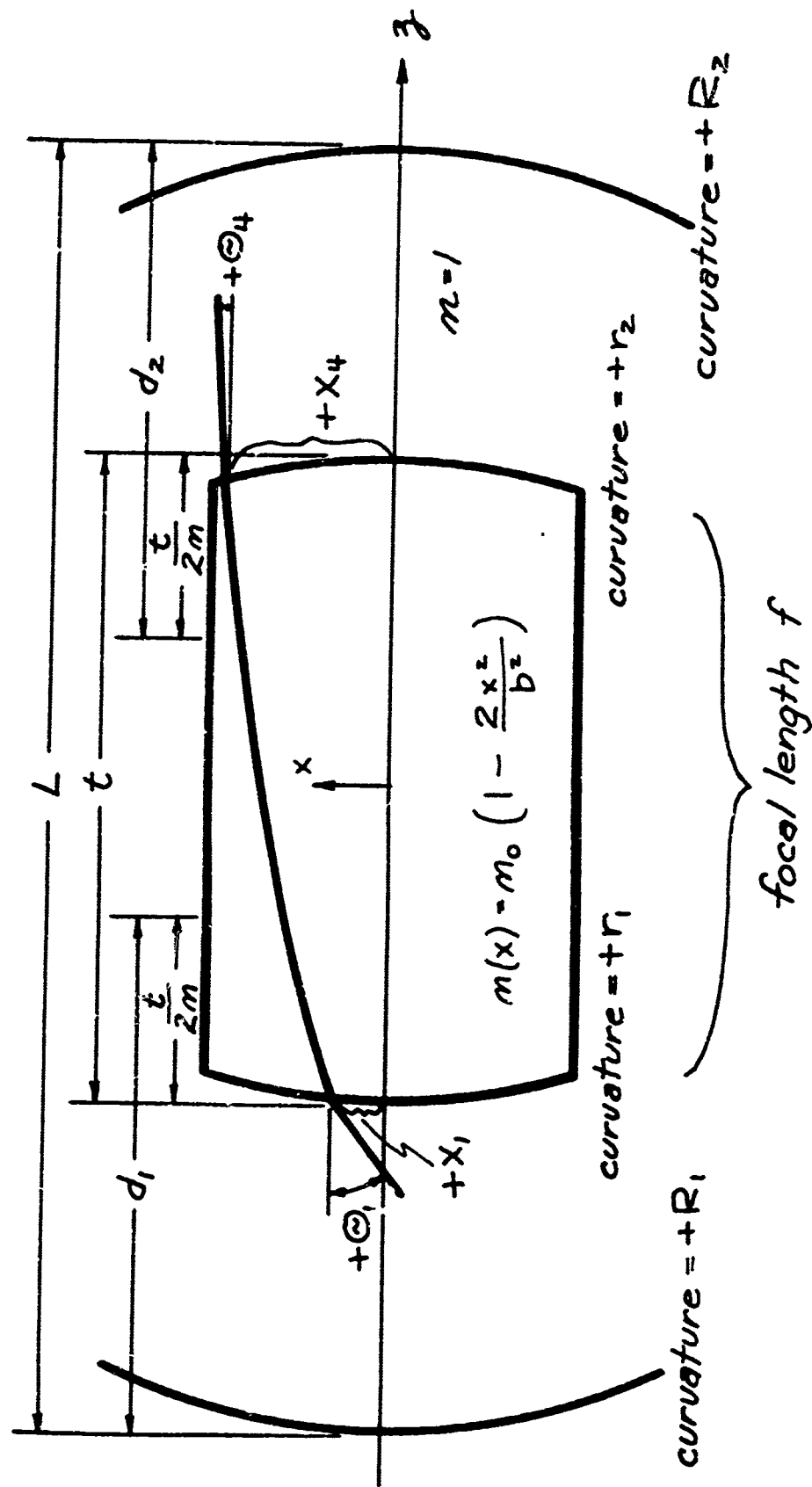


FIGURE 1 DIAGRAM OF THE RESONATOR TO BE ANALYZED. ALL CURVATURES, ANGLES, AND X POSITIONS ARE POSITIVE AS SHOWN.

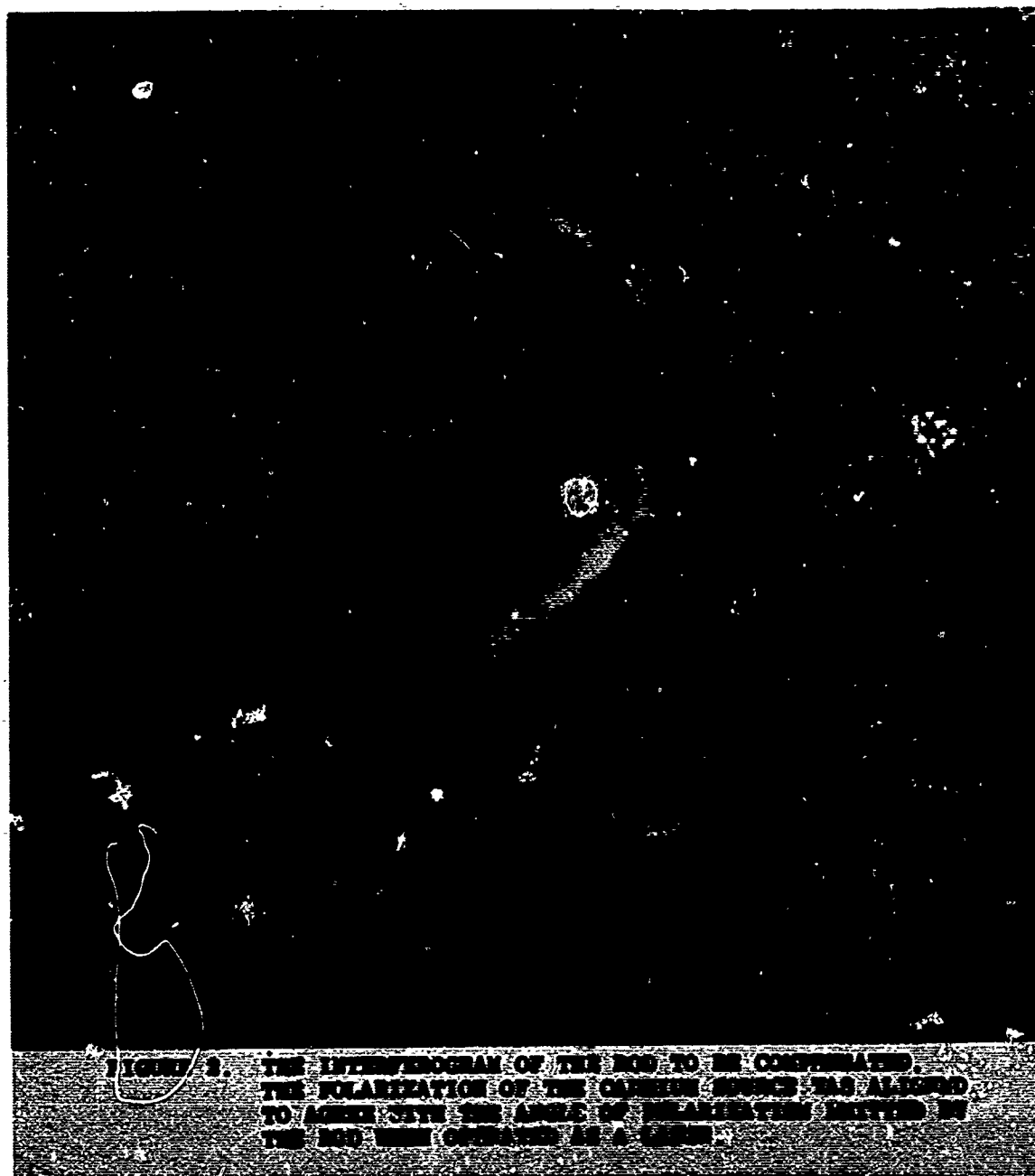


FIGURE 2. THE INTERFEROGRAM OF THE RGD TO BE COMPENSATED. THE POLARIZATION OF THE CANNON BEAM WAS ADJUSTED TO AGREE WITH THE ANGLE OF POLARIZATION INDICED BY THE RGD WHEN OBSERVED AT 45 DEGREES.

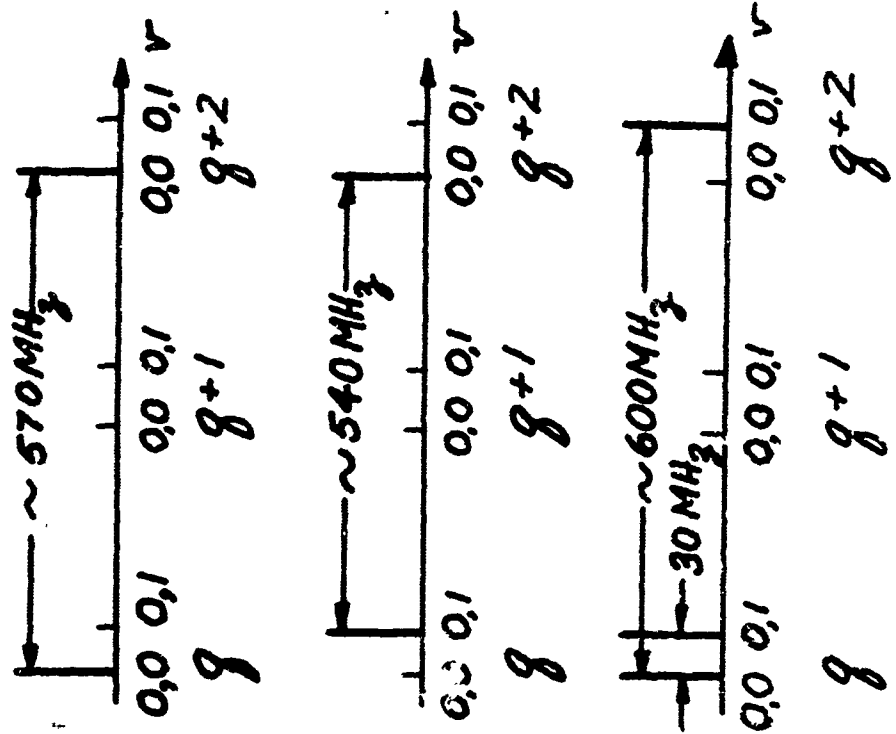
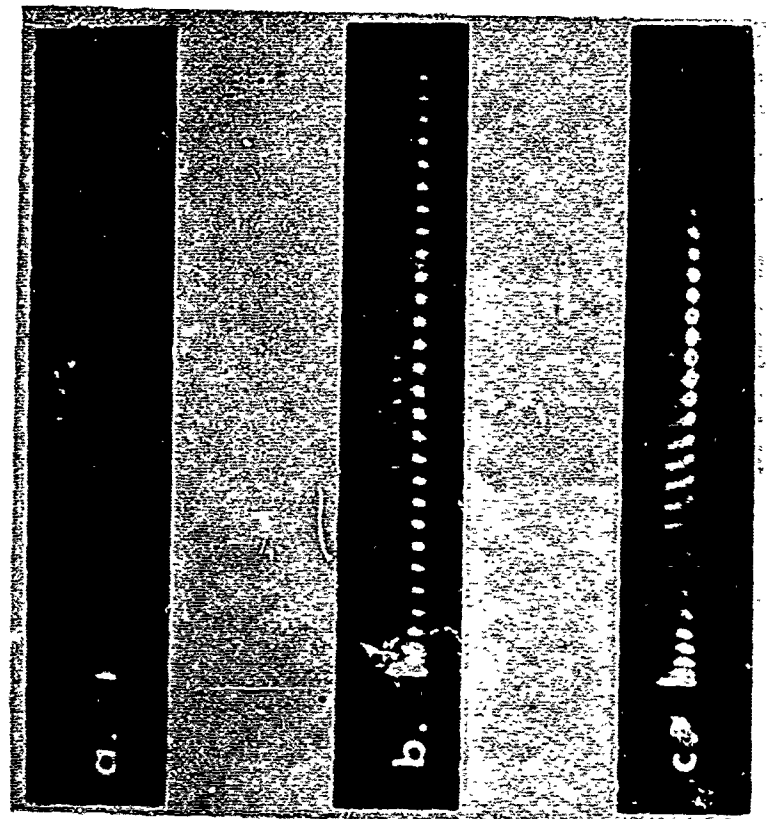


FIGURE 3 STREAK PHOTOGRAPHS OF BEAT FREQUENCIES AND THEIR INTERPRETATION. THE STREAK LENGTH IS APPROXIMATELY 50 NANOSEC. THE HEAVY LINES ON THE RIGHT HAND SIDE INDICATE THE MODES WHICH ARE BEATING.

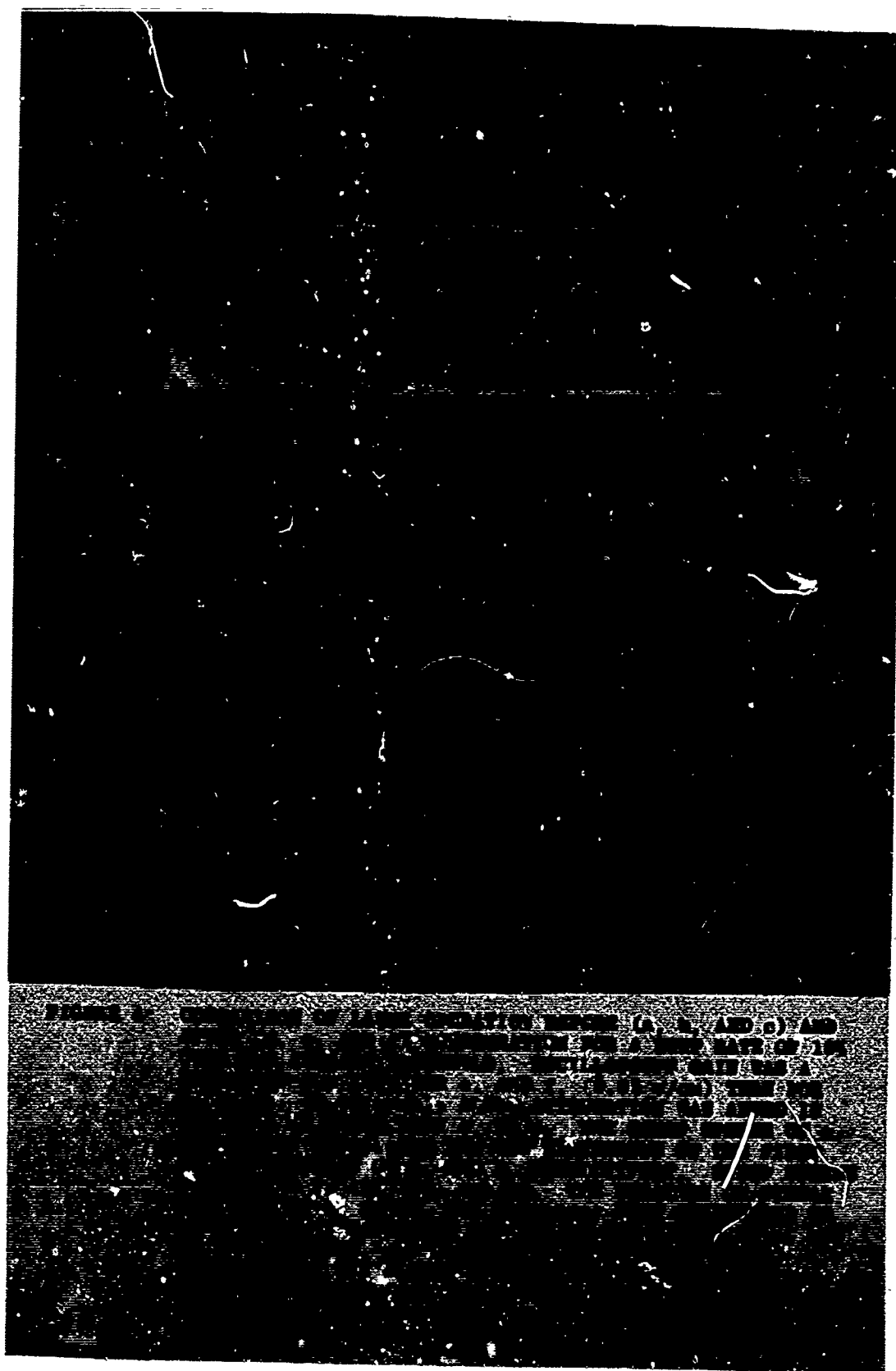


FIGURE 1. TRANSMISSION OF LIGHT THROUGH MIXTURE (A, B, AND C) AND
THEIR REFRACTION INDICES FOR A WAVELENGTH OF 100
MICRONS. THE MIXTURES WERE PREPARED BY A
METHOD DESCRIBED IN THE LITERATURE. THE
REFRACTION INDICES WERE MEASURED BY A
METHOD DESCRIBED IN THE LITERATURE.

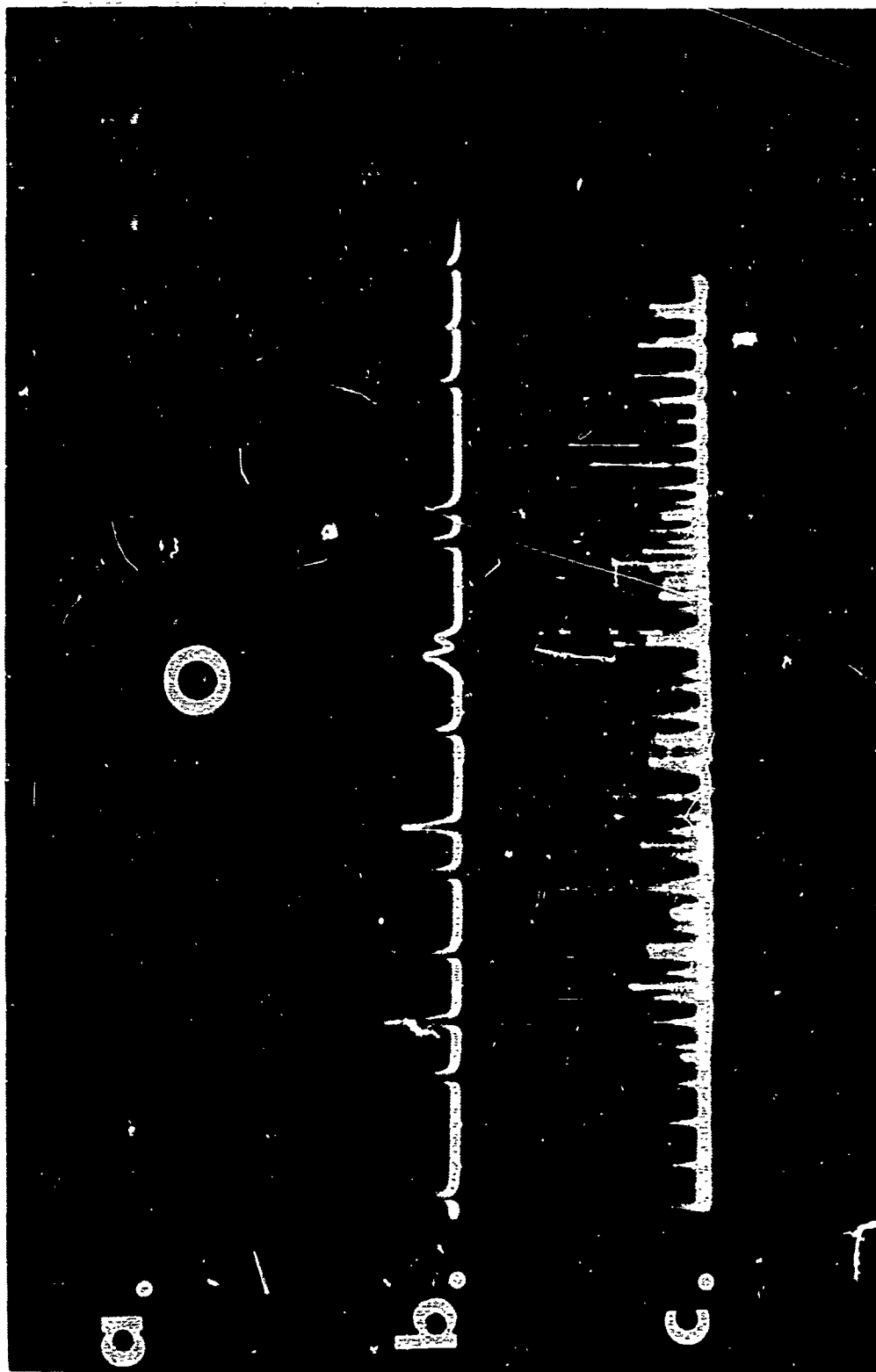


FIGURE 5 OPERATION OF THE COMPENSATED LASER WHEN PUMPED AT 60% OVE THRESHOLD. (A) 200 μ SEC STREAK PHOTOGRAPH OF THE FAR FIELD OF THE SPIKING IN (B); (B) EXPANSION OF THE SPIKING BETWEEN THE 2ND AND 4TH CENTIMETER OF (C); SWEEP SPEED IS 20 μ sec/cm (C) TOTAL SPIKING BEHAVIOR; SWEEP SPEED IS 100 μ sec/cm; DEFLECTION SENSITIVITY 0.1 v/cm FOR BOTH (B) AND (C).

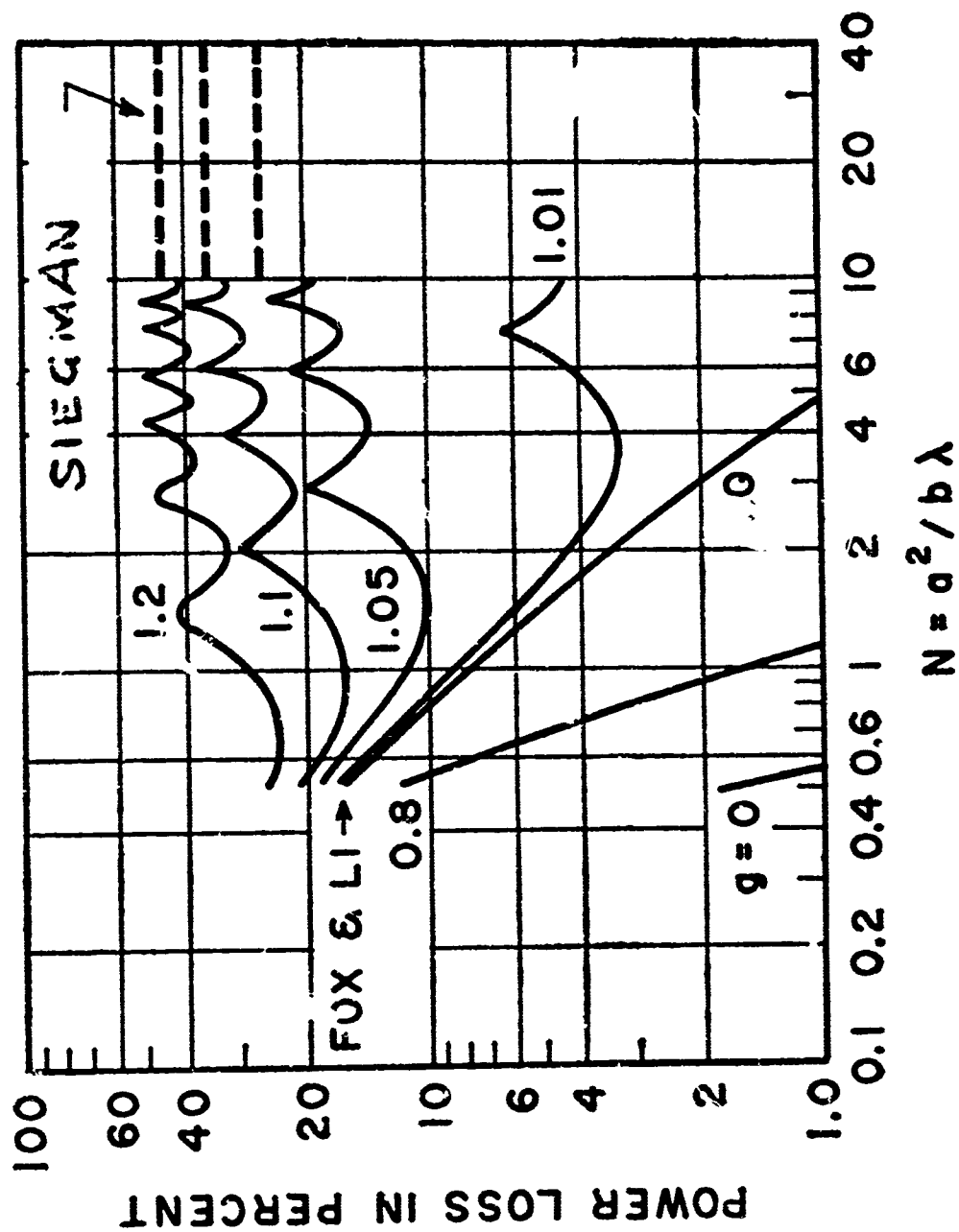


FIGURE 6 LOSS PER BOUNCE VS. MIRROR SIZE OR FRESNEL NUMBER N FOR VARIOUS STABLE AND UNSTABLE RESONATORS. THE SOLID CURVES WERE OBTAINED BY FOX AND LI USING AN ITERATIVE NUMERICAL APPROACH. THE DASHED LINES ARE THE RESULTS OF SIEGMAN'S ANALYSIS FOR THE SAME UNSTABLE G VALUES.

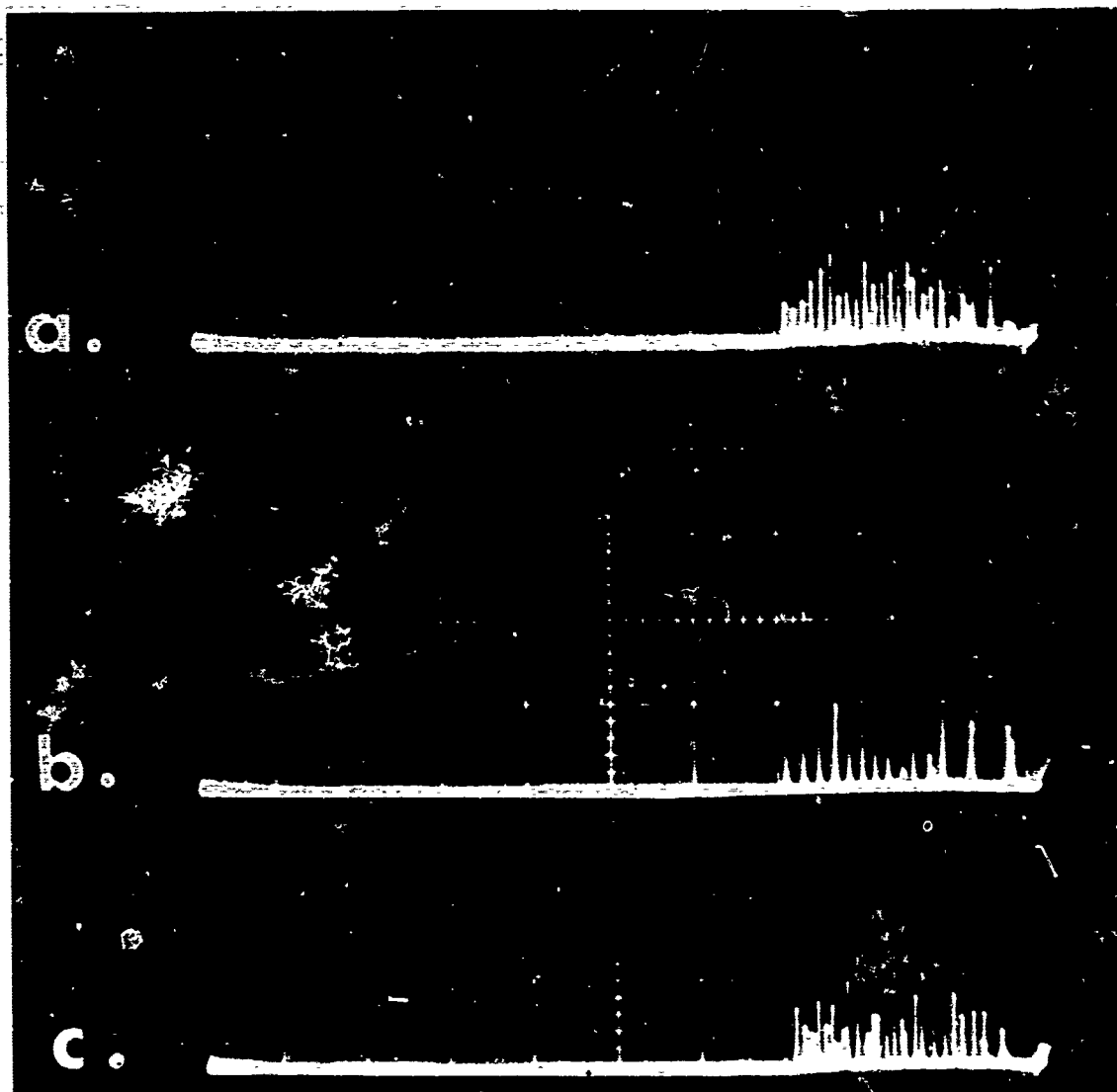


FIGURE 7 SPIKING BEHAVIOR OF THE COMPENSATED LASER VS. MOVEMENT OF THE COMPENSATING MIRROR. ALL SWEEP SPEEDS ARE 200₁ sec/cm AND ARE TRIGGERED BY THE RISE OF THE PUMP LIGHT. (A) MIRROR SPACING = 49.0 cm (NOT INCLUDING EXTRA OPTICAL PATH LENGTH DUE TO REFRACTIVE INDEX OF THE RUBY ROD; (B) MIRROR SPACING = 50.0 cm, THE DESIGNED POSITION FOR THE MIRROR. THE SPIKING OUTPUT HAPPENED TO BE GREATEST AT THIS POSITION; AND (C) MIRROR SPACING = 51.0 cm. DEFLECTION SENSITIVITY 0.05 v/cm FOR ALL THREE TRACES.

**LABORATORY INVESTIGATIONS OF PLASMA INTERACTIONS
WITH A DIPOLE MAGNETIC FIELD (U)**

by

Morton A. Levine and Allen G. Rubin

**Air Force Cambridge Research Laboratories
Office of Aerospace Research
L. G. Hanscom Field, Mass.**



Morton A. Levine

BIOGRAPHY

Morton A. Levine was born in Boston, Mass. on May 5, 1922. He attended public schools in Watertown, Mass. He holds a B.S. from the University of Mass. in physics in 1947, M.S. in physics from Tufts University in 1951, and is at present a part time Ph.D. candidate at Northeastern University. Mr. Levine has done graduate work at Boston University and Mass. Inst. of Tech.. His Master's Thesis was entitled "Energy Distribution of Extensive Air Showers". As a member of the armed forces, Mr. Levine was assigned to Los Alamos where he continued as a civilian staff member until 1946. From 1950 through 1954 Mr. Levine was a research associate at Tufts University where he published a series of papers on the pinch effect and other plasma phenomena. He joined the Air Force in 1955. Mr. Levine is presently Chief of the Plasma Astrophysics Branch, Space Physics Laboratory of AFCEI.



Allen G. Rubin

BIOGRAPHY

Allen G. Rubin was born in Lewiston, Maine on July 4, 1930. He attended public schools in Auburn, Maine, and Boston University, where he received a Ph. D. in 1957. In 1957 and 1958 he was a research physicist studying nuclear reactions at the Electronuclear Division of Oak Ridge National Laboratory. From 1959 to 1963 he performed research on the acceleration of electrons in plasmas at the Williamson Development Co., West Concord, Mass.. From 1963 to the present time as a physicist at AFCRL, he has been engaged in laboratory experiments of plasma interaction with magnetic fields.

**Laboratory Investigations of Plasma Interactions
with a Dipole Magnetic Field (U)**

Morton A. Levine and Allen G. Rubin

Air Force Cambridge Research Laboratories, Bedford, Mass.

Abstract

Bow shock formation and plasma trapping are alternative processes observed when a plasma streams into a magnetic dipole field. It is found that the breadth of the incoming plasma beam determines which process results.

INTRODUCTION

The interaction of the solar wind with the earth's magnetic field has been postulated to give rise to a collisionless bow shock. Recent satellite measurements have confirmed some of the gross features of the bow shock, however, neither the theory nor the space measurements have been able to shed much light on anything but the grossest aspects of the problem. Laboratory modeling experiments are now proving important to the understanding of missing details of the picture. This paper discusses one such experiment in which the collisionless shock is established and some of the conditions necessary to its formation are probed.

Satellite data now establishes the solar wind to consist of a plasma with a quiet sun density of 2-7 particles per cm^3 , a streaming velocity of from 250 to 750 km/sec, and an almost negligible internal temperature. Still, despite its low density and low temperature the electrical conductivity of the solar wind is effectively infinite because of the large distance factor for any interaction; and again, because of the large distances and areas over which the solar wind exerts pressure on the earth's magnetosphere and despite its low density, this interaction creates a variety of geophysical effects, some known and some suspected. Among the known effects are magnetic storms and the generation of under 40 kc. noise; among the suspected effects are the generation of mhd waves to heat the ionosphere and the injection of particles into the Van Allen belt. These are problems of operational importance to the Air Force and these are effects tied to the details of the solar wind interaction.

The study of the solar wind magnetosphere interaction in the laboratory has a long history starting with Birkeland¹ in 1896. However all of the early work involved the investigation of charged particle trajectories in a terella, or model earth field, and contribute only indirectly to the problems of cooperative phenomena that occur and dominate motions when both positive ions and electrons are present. The necessity of positive ions for charge neutrality was pointed out in 1919 by Lindemann², but the problems of wave interactions and turbulence mechanisms were not appreciated until the 1950's. This was at the time that a serious attempt to contain a plasma in a magnetic field was beginning as a part of the search for fusion power. The work of Bruch in 1931³ and of Malmfors in 1946⁴ are of interest mainly in their demonstrations of the Stormer orbits and are not of direct importance for the case of plasma interaction with the magnetosphere.

The modern experiments were started as a result of the development of wider interest in the problem and as a result of the development of new plasma sources. The earliest of these experiments, performed in 1962 by Bostick⁵, employed a copper plasma from a button gun. The magnetic field was provided by a current loop. Bostick's results, shown in Fig. 1, begin to show the outlines of a magnetosphere and indicate the possibility of trapping a plasma within the magnetosphere. However

because of the limitations of the plasma source, that is, low densities and large ion Larmor radii, a diffuse boundary results and details are difficult to scale to the real event. In fact, in 1962 and 1964 Osborne, Bachynsky and Gore⁶ repeated the experiment using a coaxial gun which produced a barium plasma and which also allowed them to vary the velocity and density of the plasma from the gun. They showed that at high velocity they were able to produce a standoff condition in which the plasma did not penetrate the magnetic field, but they also showed that at reduced densities and velocities the plasma did penetrate the magnetosphere and was trapped. This is illustrated in Fig. 2 taken from their paper. Finally, in 1964 Cladis et al.⁷, using a hydrogen plasma from a coaxial gun were able to produce a magnetospheric plasma cavity whose form checks with the theory of Beard⁸. The results of their experiment is shown in Fig. 3. The same general shape was found also by Kawashima⁹, as shown in Fig. 4.

The experiments cited go a long way toward establishing the validity of the theory of the shape of the magnetospheric surface, as determined by the plasma interaction. Unfortunately the shape theory is insensitive to the interaction, because the shape is determined primarily by the momentum balance condition.

There exists at this time a certain ambivalence in the theoretical approach to the bow shock. It can be shown that it may be possible to deflect the plasma around the magnetosphere by reshaping of the magnetic field lines (Piddington)¹⁰. On the other hand there may be a shock wave, and in that case it will probably involve turbulence of some sort. At this time the most widely accepted theory is that there is a shock near the boundary with some sort of turbulent field between the shock and the magnetosphere. This picture is reinforced by satellite measurements, particularly those of Ness¹¹.

To construct a simple picture of the interaction as the plasma enters the earth's magnetic field, the particle paths are bent, electrons in one direction, ions in the opposite direction, giving rise to a charge separation electric field \vec{E} . If the plasma is extensive enough this electric field is shorted and instead a current flows in the plasma. If the plasma conductivity is high enough, that is, if the magnetic Reynolds number is large enough the magnetic field is totally excluded and a sharp boundary and shock might form. On the other hand, if the plasma beam were limited in size, then the electric field would not be shorted. In this case the electric field is just sufficient to allow the plasma to penetrate the field with a velocity \vec{v}

$$\vec{E} = \vec{v} \times \vec{B} .$$

It is not possible to set a sharp defining criterion for penetration, however, by limiting the size of the beam it might be possible to approach the shock conditions gradually.

It might even be possible to pass from a condition of stable injection and flow into the field to the sharp boundary turbulent picture with the plasma flowing around the dipole field. This experiment would then serve two purposes; it would show how it would be possible for a narrow high energy beam of particles to penetrate the magnetic field and be trapped in a Van Allen belt. It would also show as a limiting process how a sharp plasma boundary and shock could form.

In order to perform a meaningful experiment it is important to satisfy certain scaling conditions. An important scaling condition is that the conductivity be sufficiently high so that the magnetic Reynolds number is greater than one, even for interaction lengths of the size of the electron gyro-radius. This will assure that the separation between the plasma and magnetic field will be independent of conductivity. In addition, the ion mean free path must be sufficiently long that a hard collision does not occur during one cyclotron period, or $\omega \tau > 1$. Such a plasma is sufficiently collisionless for this experiment. Additional requirements are that the ion Larmor radius be small compared to the equipment size, say of the order of 1 cm, and that a pressure balance exist between the plasma and magnetic field. From the pressure balance condition,

$$\frac{B^2}{2\mu} = N m v^2$$

and

$$N = \frac{B^2}{2\mu m v^2} .$$

From the ion Larmor radius condition,

$$r_L = 10^{-2} \text{ m} = \frac{mv}{eB}$$

or

$$\frac{B^2}{v^2} = \frac{m^2}{e^2 r_L^2}$$

so that

$$N > \frac{m}{2\mu e^2 r_L^2}$$

where m is the ion mass. Thus the density requires is $5 \times 10^{13}/\text{cm}^3$ for a hydrogen plasma. Using a $\langle \sigma v \rangle = 7.8 \times 10^{-8} \text{ cm}^3/\text{sec}$, the collisionless requirement leads to a velocity of $3 \times 10^6 \text{ cm/sec}$.

EXPERIMENTAL

The experimental arrangement is shown in Fig. 5. A hydrogen plasma is generated in a coaxial gun 60 cm. long and with a 5 cm. outer diameter and 1.5 cm. inner diameter. A fast-acting valve provides a burst of hydrogen between the coaxial electrodes. The energy for the gun is supplied by a 48 microfarad capacitor bank charged to 10 kV. The dipole field is generated by a 6 cm. diameter coil with a dipole moment of 212 amp-m^2 , and with a period of 400 microseconds. The vacuum chamber is a stainless steel cylinder 130 cm. long and 30 cm. in diameter. Normally a vacuum of 10^{-6} Torr was maintained in the chamber.

A screen of molybdenum mesh was placed in the muzzle of the gun to remove magnetic fields from the flowing plasma developed in the gun. The plasma was extensively measured using probes and streak photography. The plasma was found to have the following characteristics; it consisted of an almost square pulse of particle of $3 \times 10^{13} \text{ ptcls/cm}^3$ with a velocity of $2.4 \times 10^6 \text{ cm/sec}$, lasting 20 microseconds. All significant measurements were taken in the first 15 microseconds.

The width of the plasma beam was varied by inserting a series of stainless steel aperture limiters in front of the gun. A Beckman and Whitley image converter camera was employed to take photographs of the interaction with a one microsecond exposure time.

In the absence of the screen at the gun muzzle, a trapped magnetic field of about 100 gauss was measured in the plasma, which is reduced to about 1 gauss with the screen in place.

Figure 6 shows the configuration which results when the full beam width is employed. A sharp standing shock is seen. The plasma is incident from the left, and the position of the front of the magnetosphere is indicated by the dotted line. No plasma is visible inside the dipole field. The shock is a rather thin structure, about a centimeter thick, which is close to the ion Larmor radius.

Probe measurements were also made of the electric field in the $\vec{v} \times \vec{B}$ direction. In addition to a small steady electric field, a larger fluctuating electric field is observed at the boundary between the plasma and magnetic field of the order of 14 volts/cm.

Figure 7 is an image converter photograph taken with a 10 cm. diameter aperture limiter in the beam. A shock still forms in this case, but is more diffuse near the center.

Figure 8 shows the effect of narrowing the beam further with a 5 cm. diameter aperture limiter. In this case a shock no longer forms. The plasma penetrates into the dipole field and becomes trapped. It is clear that a beam considerably wider than the dipole is necessary for the formation of a sharp standing shock. The electric field was also measured in this case. A steady electric field of average magnitude $\vec{v} \times \vec{B}$ was measured, but in addition a larger fluctuating field of magnitude 10 volts/cm. is also present in this case.

CONCLUSIONS

As predicted by theory it was found that a narrow plasma beam does penetrate the magnetic field with the expected average electric field. However the unexpected result was that even in this case instabilities seem to be present, as revealed by large electric field fluctuations. Thus it is concluded that instabilities can develop in the case of a gradual deceleration and even without a sharp plasma boundary. This may be related to the predictions of two stream instabilities as discussed by Bernstein, Fredricks and Scarf.¹²

Finally, it was found that a flowing plasma without internal magnetic field will establish a sharp standing off shock. The width of the shock is of the order of the ion Larmor radius and turbulent interactions play an important part in its formation. It must then be concluded that under conditions which scale properly a shock can be seen, and under these conditions plasma is not observed to penetrate the magnetosphere.

REFERENCES

1. K. Birkeland, Arch. Sci. Phys., 1, 497 (1896).
2. F. A. Lindemann, Phil. Mag., 38, 669 (1919).
3. E. Bruche, Terr. Mag. and Atmos. Elec., 36, 41 (1931).
4. K. G. Malmfors, Ark. Mat. Astr. Fys., 34B, No. 1 (1946).
5. W. H. Bostick, H. Byfield and M. Brettschneider, J. Geophys. Res. 68, 5315 (1963).
6. F. J. F. Osborne, I. P. Schkarofsky and J. V. Gore, J. Geophys. Res. 69, 4441 (1964).
7. J. B. Cladis, T. D. Miller and J. R. Baskett, J. Geophys. Res. 69, 2257 (1964).
8. G. D. Mead and D. B. Beard, J. Geophys. Res. 69, 1169 (1964).
9. N. Kawashima, J. Phys. Soc. (Japan), 19, 227 (1963).
10. J. H. Piddington, Space Sci. Rev., 3, 724 (1964).
11. N. F. Ness, C. S. Searce and J. B. Seek, J. Geophys. Res. 69, 3531 (1964).
12. W. Bernstein, R. W. Fredricks and F. L. Scarf, J. Geophys. Res. 69, 1201 (1964).

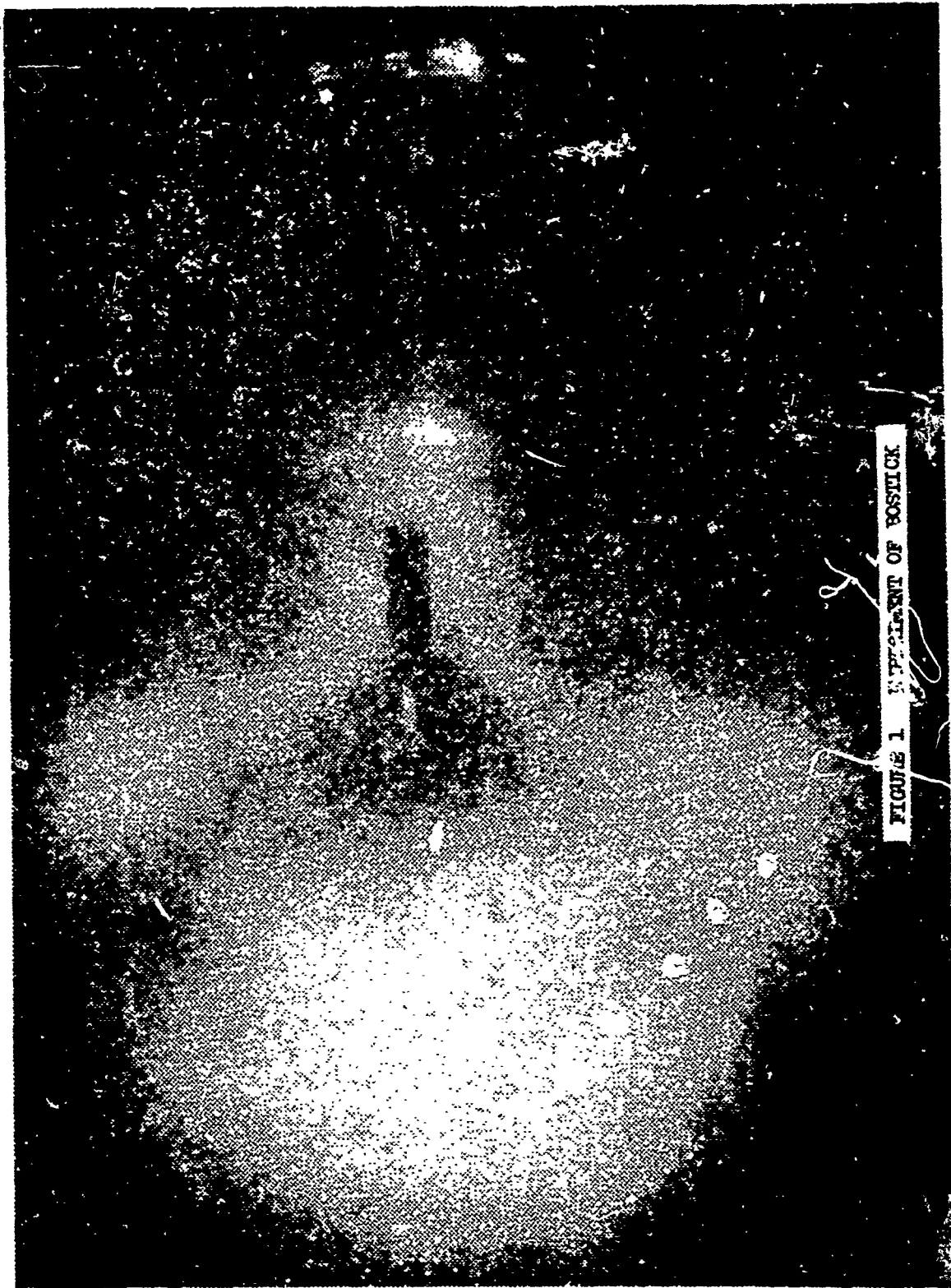


FIGURE 1 IMPACT OF POSTICK

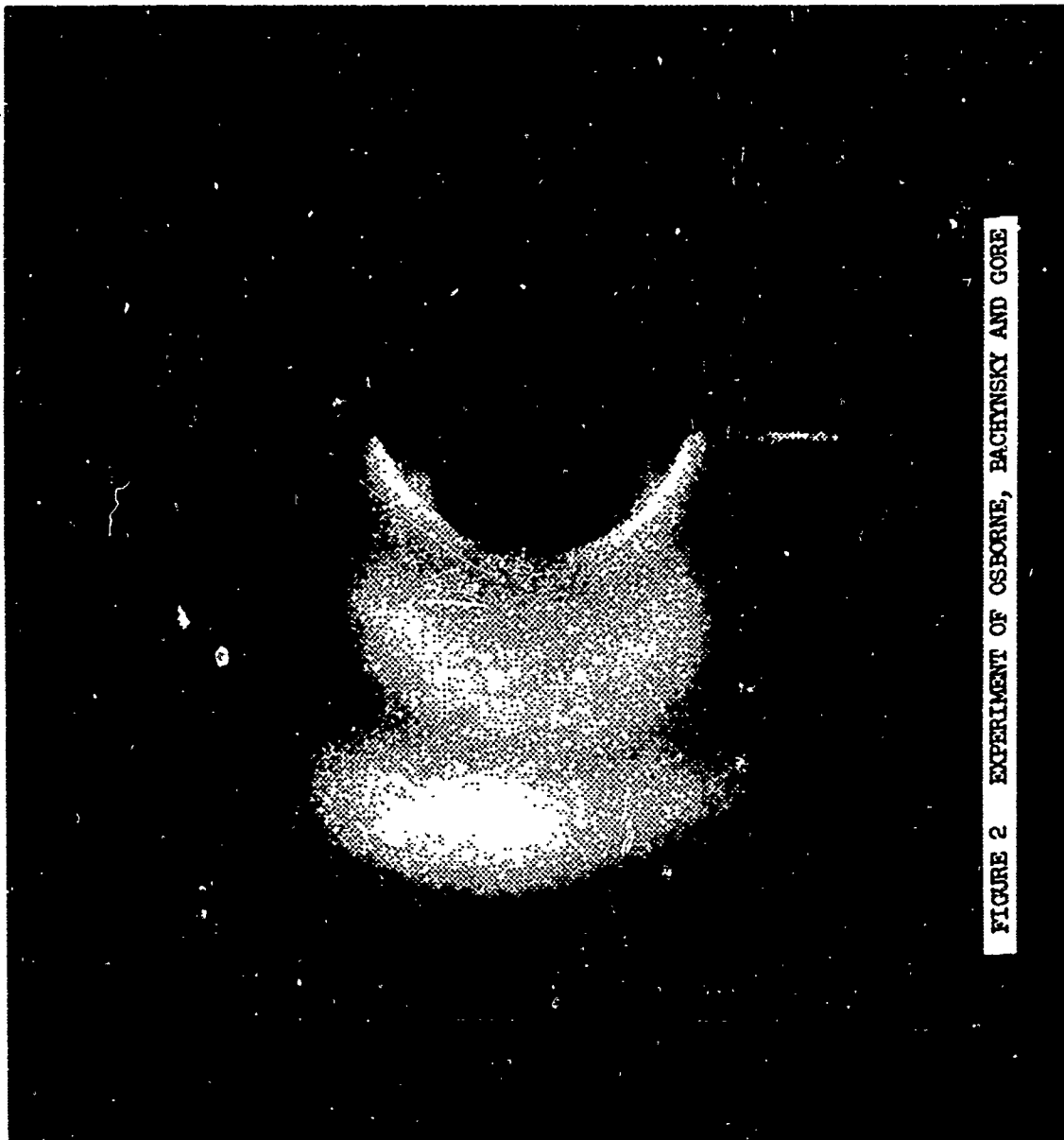


FIGURE 2 EXPERIMENT OF OSBORNE, BACHINSKY AND GORE

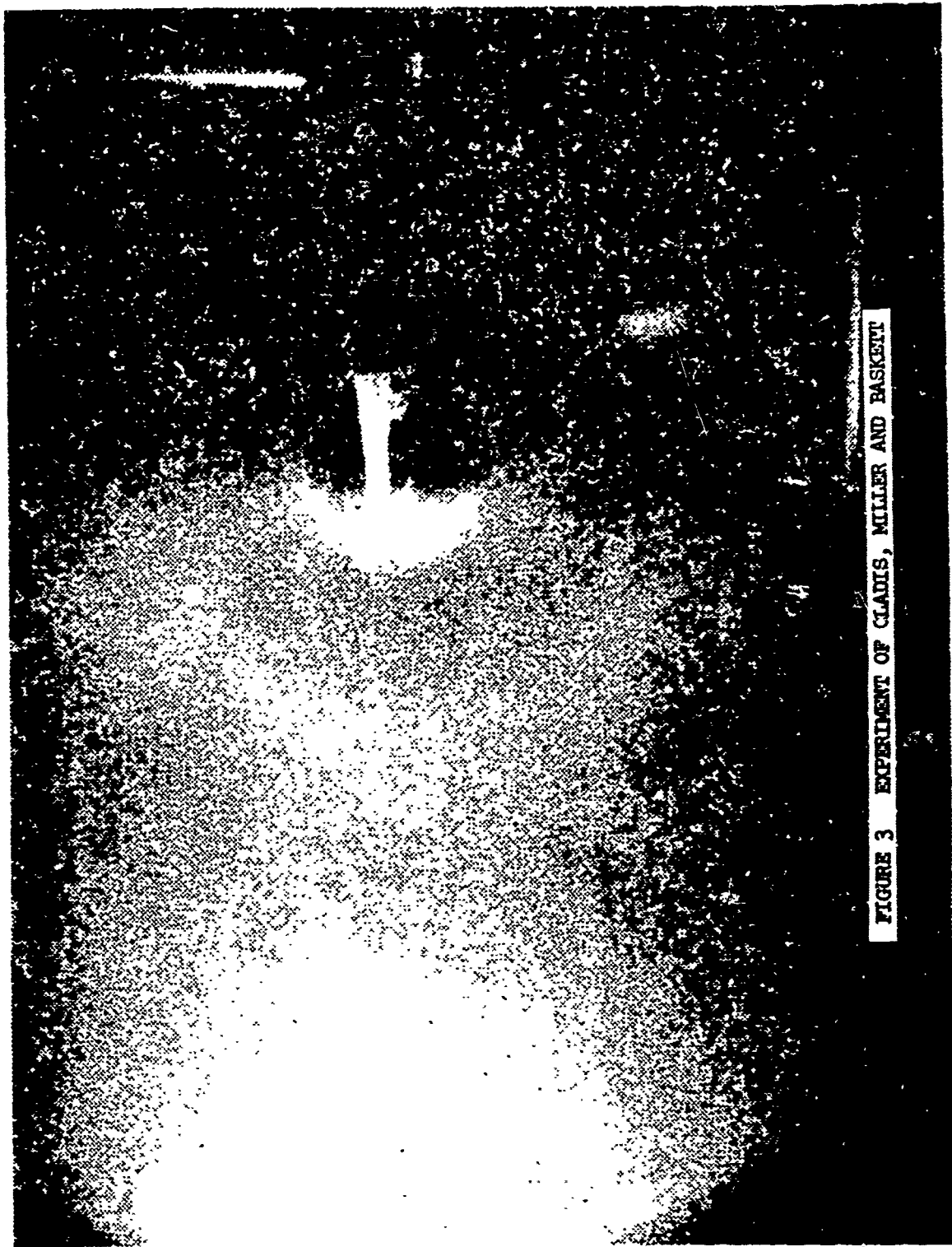


FIGURE 3 EXPERIMENT OF CLADIS, MILLER AND BASKETT

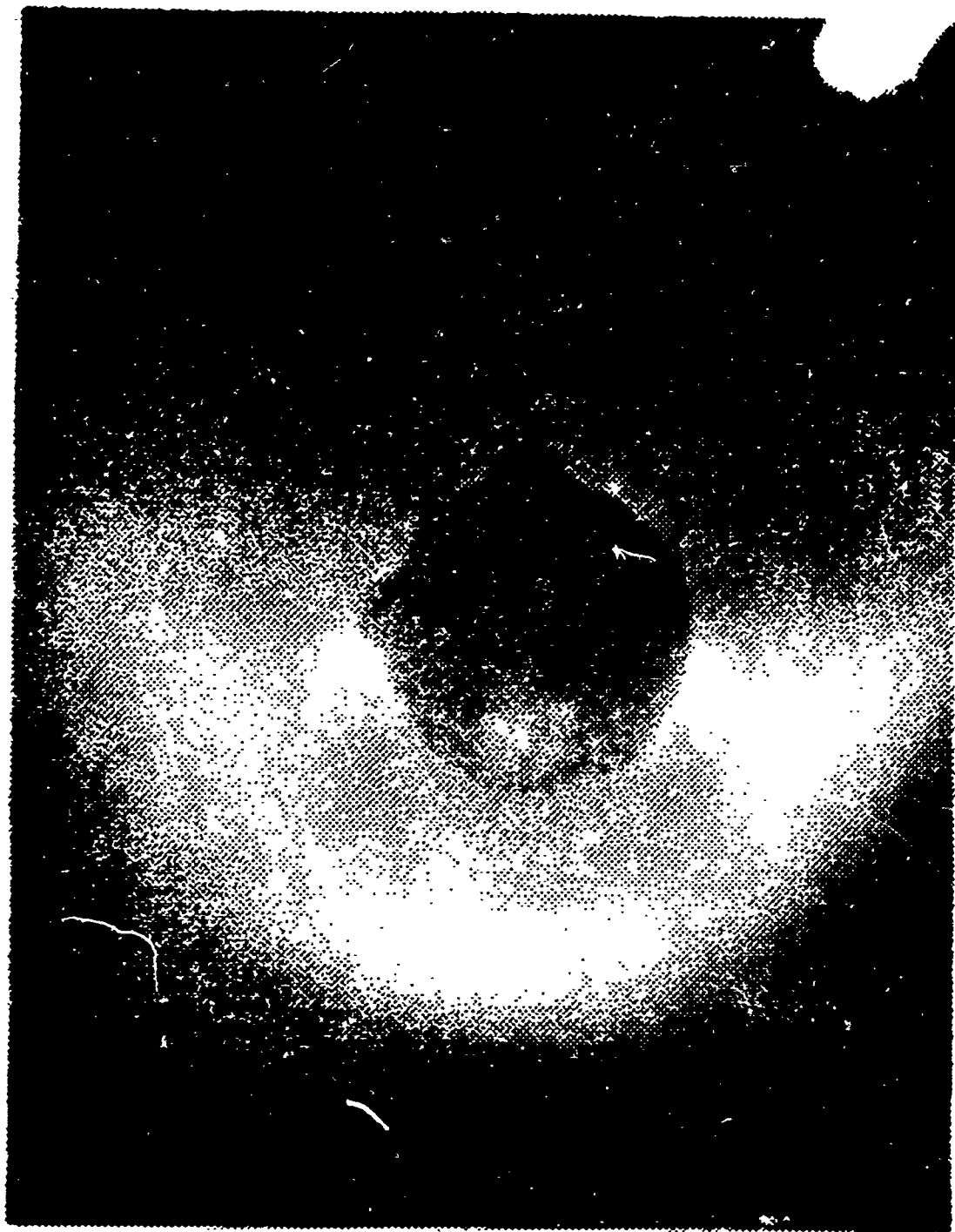


FIGURE 4 EXPERIMENT OF KAWASHIMA

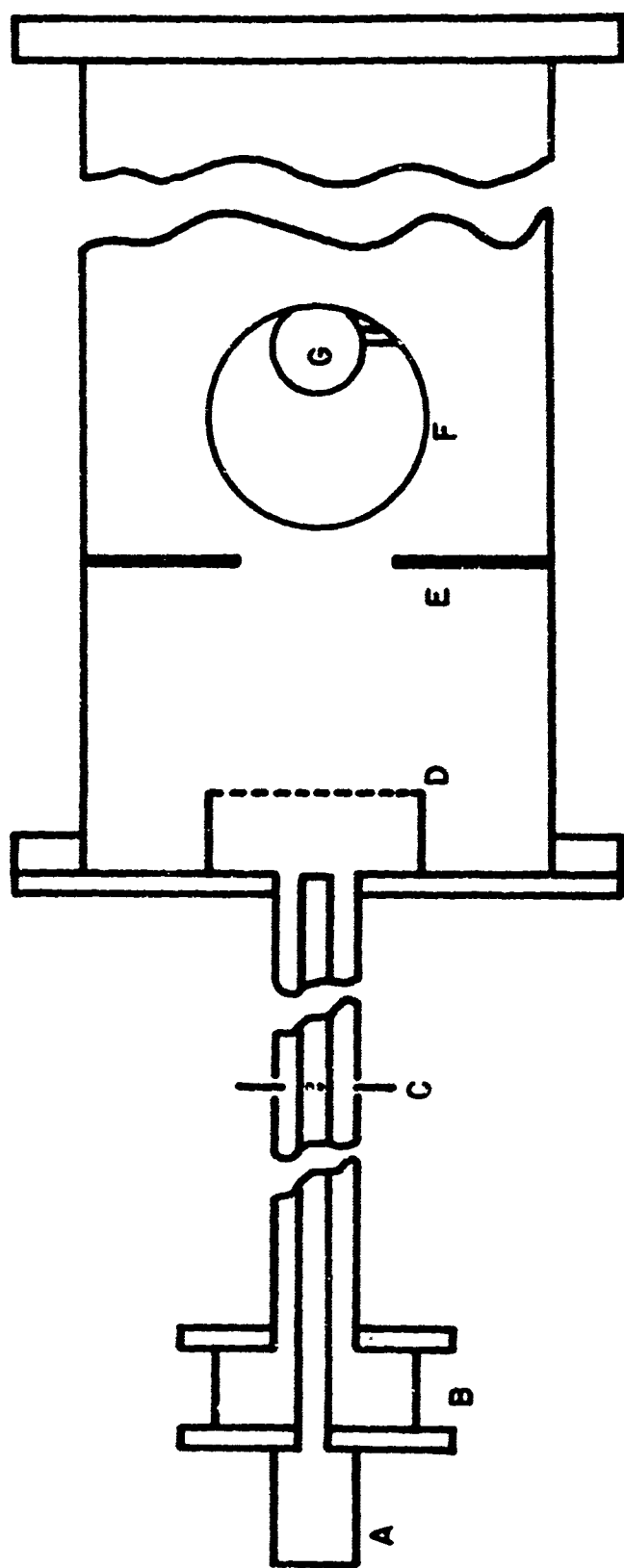


FIGURE 5 EXPERIMENTAL ARRANGEMENT

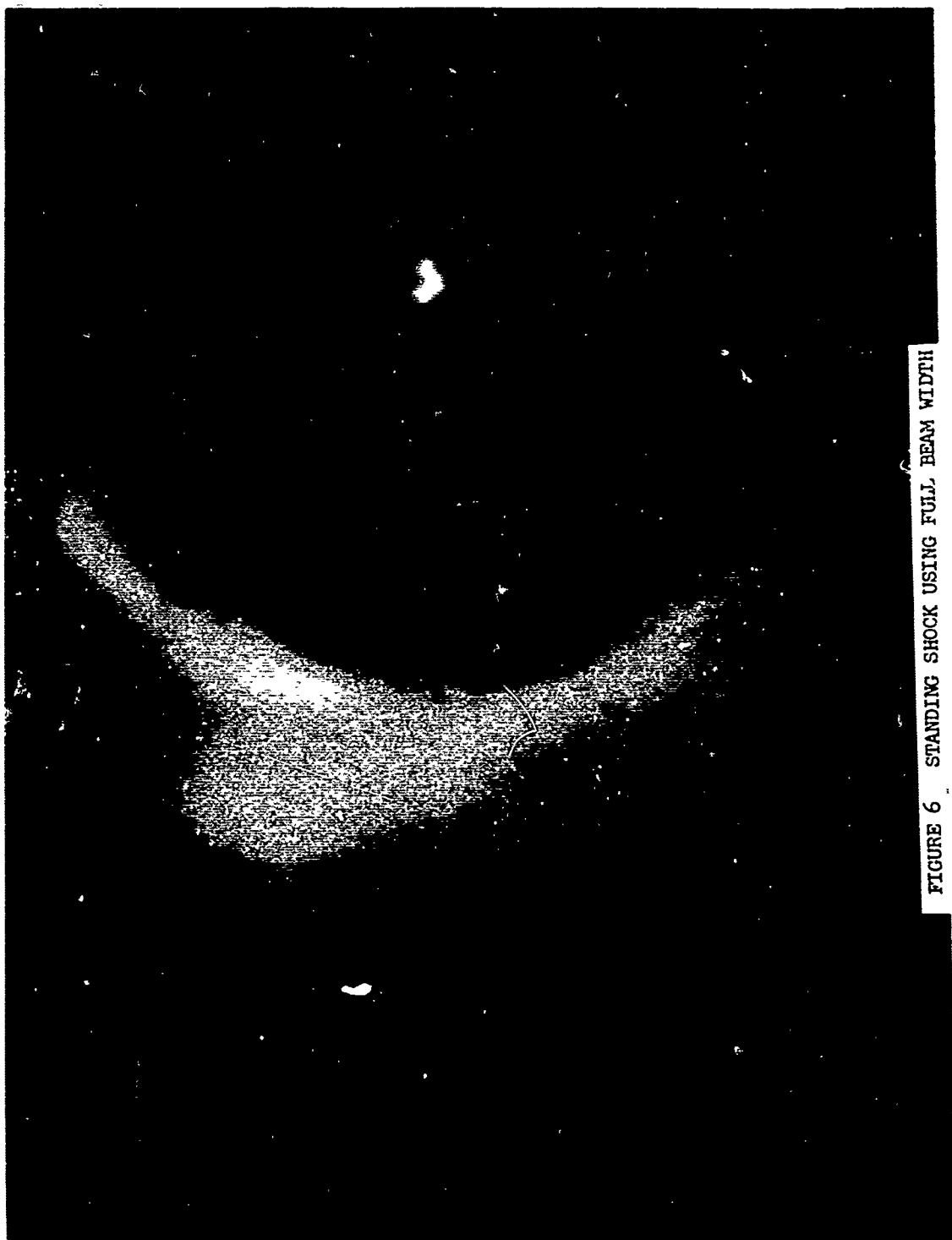


FIGURE 6 STANDING SHOCK USING FULL BEAM WIDTH

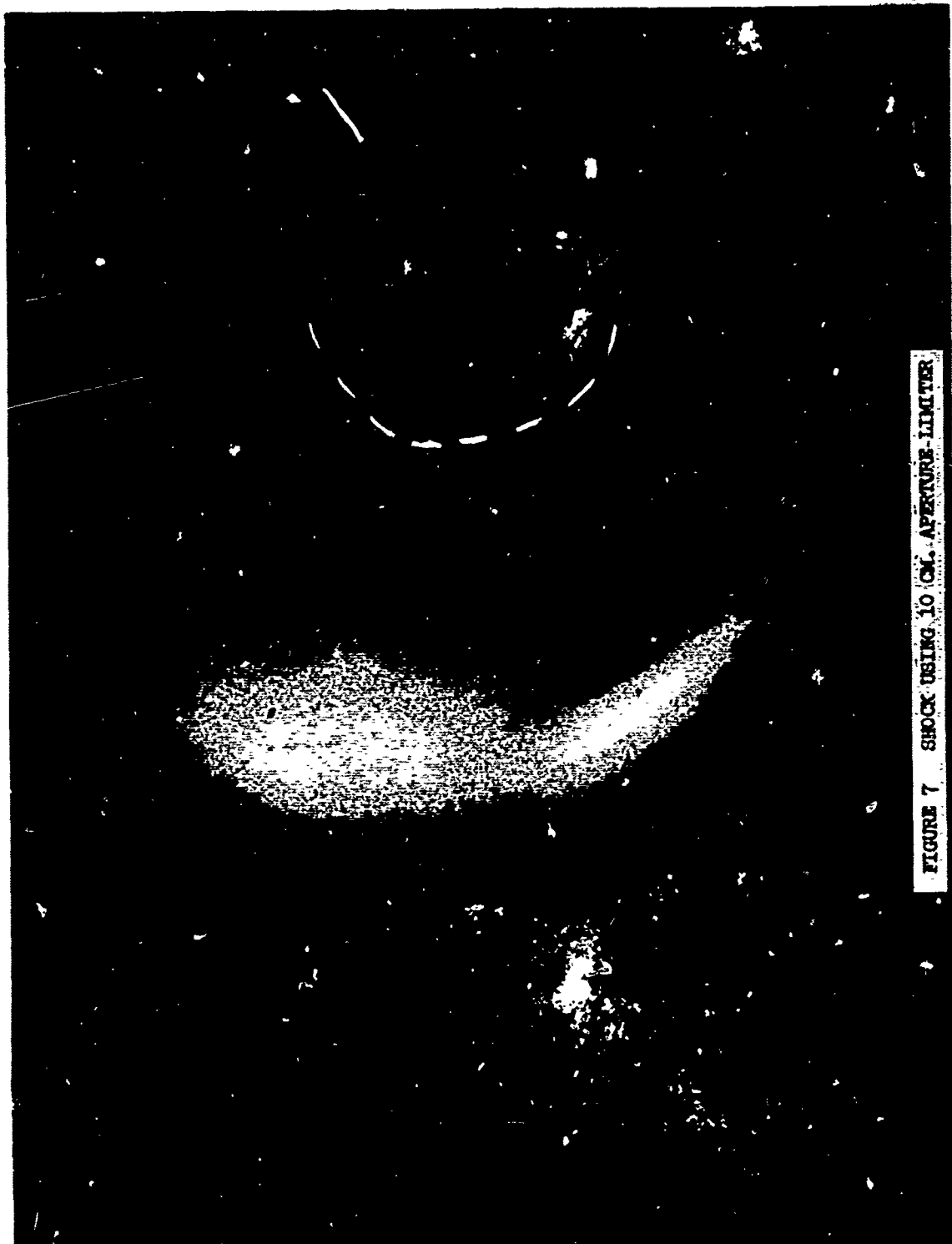


FIGURE 7 SHOCK USING 10 CM. APERTURE-LIMITER

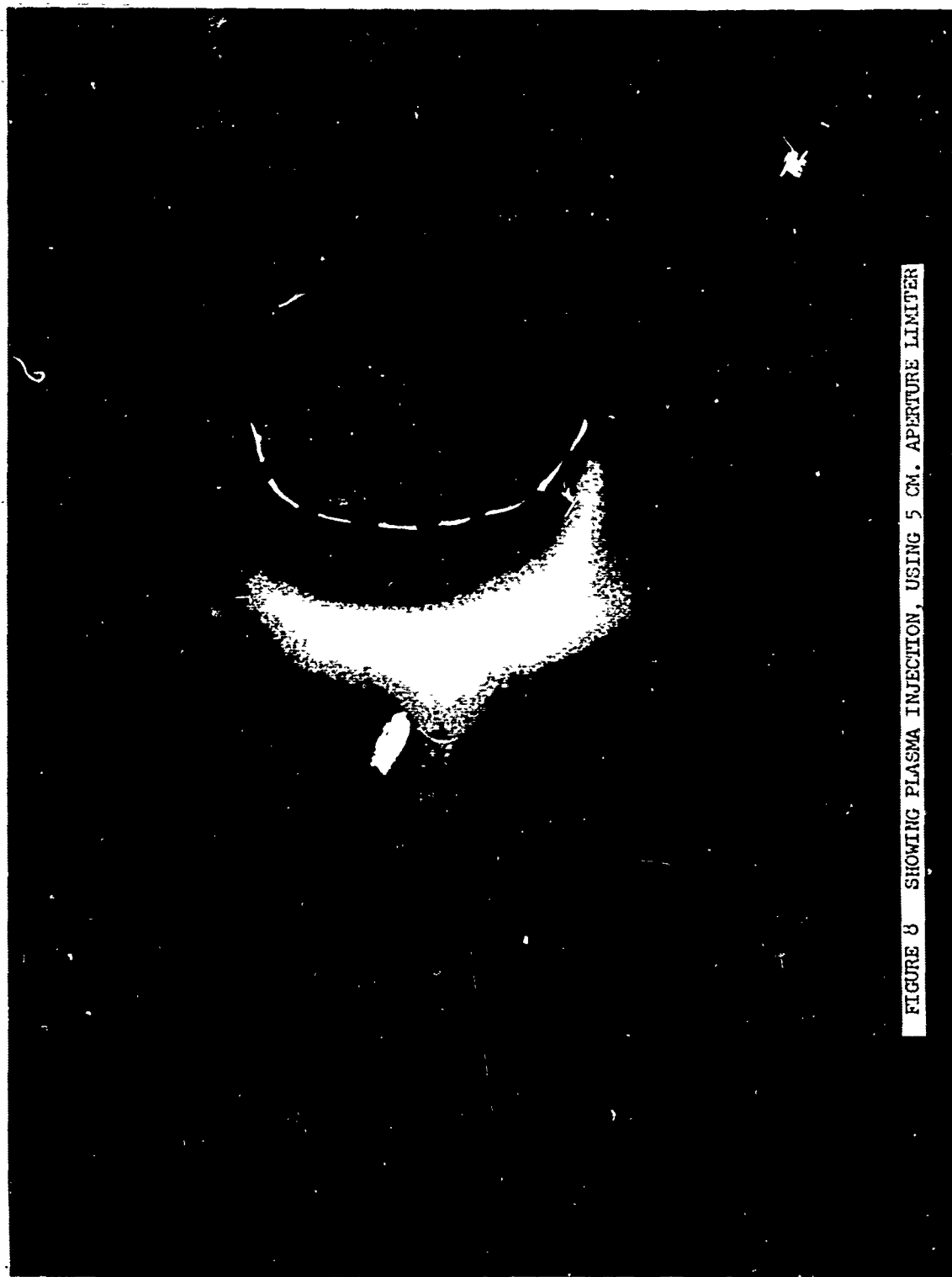


FIGURE 3 SHOWING PLASMA INJECTION, USING 5 CM. APERTURE LIMITER

RAPID REMOTE SENSING BY SPECTRUM MATCHING TECHNIQUE
PART 2. APPLICATION IN THE LABORATORY AND IN LUNAR OBSERVATIONS (U)

by

Graham R. Hunt, John W. Salisbury and John W. Reed

Air Force Cambridge Research Laboratories
Office of Aerospace Research
L. G. Hanscom Field, Mass.



Graham R. Hunt

Biography

Name

Graham R. Hunt, Born 2 December 1930, Australia

Education

B.Sc. (Hons), Physical Chemistry, 1952, Sydney University, Sydney, Australia

M.Sc., Physical Chemistry (Spectroscopy), 1954, Sydney University, Sydney, Australia

Ph.D., Physical Chemistry (Spectroscopy), 1958, Sydney University, Sydney, Australia

Experience

Dr. Hunt joined the Lunar-Planetary Research Branch of AFCRL in September 1963. Prior to this he was employed by Massachusetts Institute of Technology in the Spectroscopy Department. There he designed and modified a far-infrared spectrometer for use in a vacuum, and used it to study solid state spectra. He also worked on the numerous spectroscopic instruments available at MIT including the large echelle spectrograph to study the visible and near ultraviolet systems of NO_2 . He designed and built a 3 meter Ebert high resolution infrared spectrometer at the Chemistry Department of Tufts University from 1960 to 1962.

His main interests since joining the group have been to apply spectroscopic techniques to the study of the moon and planets, including the effects of radiation damage on the infrared spectra of silicates.



John W. Salisbury

Biography

Name

John W. Salisbury (AFCRL), Born 6 February 1933, Palm Beach, Fla.

Education

B.A., Geology, 1955, Amherst College, Amherst, Massachusetts

M.S., Geology, 1957, Yale University, New Haven, Connecticut

Ph.D., Geology, 1959, Yale University, New Haven, Connecticut

Experience

Dr. Salisbury has been engaged in lunar and planetary research at the Air Force Cambridge Research Laboratories since 1959. For the past four years he has been Chief of the Lunar-Planetary Research Branch, and as such has had full technical responsibility for determining the research objectives of the AFCRL lunar and planetary research program, and for devising and developing novel observational and experimental techniques and original theoretical approaches necessary for the accomplishment of these research objectives.

In his work, Dr. Salisbury has developed original theoretical concepts of the origin of lunar structures, the nature and probable location of lunar natural resources, the nature of lunar surface materials, and the location of a lunar base. Programs of balloon and rocket-borne spectroscopy designed to determine the compositions of the lunar surface materials and planetary atmospheres are currently in progress under his direction. Dr. Salisbury planned and directs the program of environmental studies under which a lunar simulation chamber has been used to study the properties of probable lunar materials in a simulated lunar environment. He participated as chief investigator in the experiments that demonstrated high vacuum adhesion of silicate powders.

John W. Reed's photograph is not included because he was transferred to permanent flying status prior to submission of the paper.

Biography

Name

John W. Reed, Captain 60689A (AFCRL)

Education

B.S., Physics, 1954, University of Missouri, Columbia, Missouri

Graduate Study, Physics, 1954-55, University of Missouri, Columbia, Missouri

USAF Pilot School, 1955-56, Webb AFB, Texas

Graduate Study, Astronomy, 1963-65, University of Arizona, Tucson, Arizona

Experience

Captain Reed joined the Lunar-Planetary Research Branch of AFCRL in April 1965. From 1958 to 1963 he was engaged in thermal radiation studies of nuclear detonations at AFCRL and served as Project Officer for participation in field exercises and aircraft modification. His graduate studies in astronomy included work in 26" telescope installation and alignment, photoelectric photometry, stellar spectroscopy on 36" equipment, and calibration studies on astronomical films.

Rapid Remote Sensing by Spectrum Matching Technique
Part 2. Application in the Laboratory and in Lunar Observations

by

Graham R. Hunt, John W. Salisbury and John W. Reed

ABSTRACT

A spectrum matching technique has been developed for rapid remote sensing of mid-infrared molecular vibration emission spectra of lunar and planetary surfaces. It is primarily useful when the remote sensing must be carried out in the presence of a variable intervening attenuator, which puts a premium on rapidity of measurement. A major advantage is achieved over conventional spectroscopic techniques when compositional differences and/or general compositional trends, rather than absolute composition, are the parameters to be measured. Laboratory tests of this technique with a simple spectrum matching instrument and with a more sophisticated x-y scanning instrument have demonstrated its feasibility. Use of the simple instrument on lunar targets has delineated very small, but consistent differences between different areas on the lunar surface. Among other things, these data indicate that the lunar surface materials possess a rough surface on a micron scale.

Rapid Remote Sensing by Spectrum Matching Technique
Part 2. Application in the Laboratory and in Lunar Observations

by

Graham R. Hunt, John W. Salisbury and John W. Reed

INTRODUCTION

A complete description and discussion of the general principles of the spectrum matching technique were presented in Part 1 of this paper (Hunt, 1966), and will be briefly reviewed here. The major purposes of the present paper are to present a limited laboratory demonstration of the technique and the results of some preliminary ground-based observations of the lunar surface.

The concept of spectral matching is simple and, in its present application, is based on the relationship (stated by Kirchhoff's law), which exists between the infrared emission spectrum and the reflection spectrum of solids. The function of the technique is to obtain characterizing compositional information about a remote inorganic surface, and this is achieved by collecting the infrared emission over a specified wavelength interval from a given surface and reflecting it in turn from a series of specified reflecting surfaces, or reststrahlen plates, of known composition, until a spectrum match is reached. A spectrum match is usually recognized between a given emitting surface and a particular reststrahlen plate when the value of the normalized integrated signal reaches a minimum. This is illustrated for a hypothetical case in Figure 1. Here it can be seen that the area under curve ER2, generated by reflecting emission E from reststrahlen R2 is smaller than under ER1 or ER3, and so this represents a spectrum match between E and R2. One may therefore say that the composition of the target whose emission is given by E is more like the composition of the reststrahlen plate whose reflection spectrum is given by R2 than either of the other two reststrahlen materials.

The maximum information available, in a remote sensing situation, concerning the composition of a given surface, is contained in a complete high resolution infrared spectrum, independently of whether the spectrum is available as absorption, emission or reflection.

In a real situation, such as in making ground-based observations of extraterrestrial objects, many factors militate against the acquisition of an ideal spectrum, but it is under such conditions, namely, when a remote, energy limited, emitting surface is to be observed through a relatively rapidly changing attenuator and/or from a moving observation point, that the advantages of extremely rapid data acquisition afforded by the spectrum matching technique are best utilized. The method is only limited by the quality and quantity of spectral information contained in the emission from the target, by the degree to which this information is available after

attenuation, the signal to noise available from the detection system, and by the appropriateness of selection of the reststrahlen plates with which the data are to be matched.

In the past, infrared observation of the lunar surface led to the quite general assumption by most authors (eg. Pettit and Nicholson, 1930; Pettit, 1940) that the moon emits as a black or grey body. However, more recent studies based both on laboratory measurements and on direct observations of the moon, indicate that this is not necessarily the case (eg. Burns and Lyon, 1962; Hunt and Salisbury, 1964; Murcray, 1965), although the deviation from black, or grey body emission does not appear to be large. The spectrum matching technique has been applied here in an attempt to determine the degree of compositional homogeneity of the lunar surface.

DESCRIPTION OF THE INSTRUMENTS

A diagram of the first simple spectrum matching instrument, constructed from components available in our laboratory in March 1965, is shown in Figure 2. This will be referred to henceforth as Instrument 1.

The instrument was constructed to accept an $f/15$ beam, which was focussed at a $\frac{1}{4}$ inch diameter aperture stop, A.S., immediately in front of which is located a 13 c.p.s. single bladed chopper, C. This insures that only the energy entering through the aperture is modulated, so that any emission from the transmission and reflecting filters, optics, and the inside of the instrument will not be incorporated in the detector output as meaningful signal. A 5 micron cut-on filter, F, is placed immediately after the chopper to restrict the wavelength range. The diverging $f/15$ beam may follow one of two equivalent paths, depending upon the location of the two position IN-OUT plane mirror M1. The beam is then converted to an $f/4.5$ beam by either one of the two torroidal mirrors M2 and M2', being refocussed between either of the pairs of reststrahlen plates R1 and R2, or R1' and R2'. Reflection from two surfaces of the same reststrahlen material was used to provide higher spectral purity. After reflection, the diverging beam is collected by torroidal mirrors M3 or M3' and focussed on the detecting elements of the Golay cells G or G'. After preamplification, the output from the Golay cells passes through a switch so that at any one time the output from either one of the Golays can pass through the common amplifier A to recorder T. The instrument was extensively baffled.

The second instrument, henceforth called Instrument 2, is described in detail elsewhere (Rehberg, et al., 1966). It is basically a Barnes Engineering Company Infrared Camera modified to scan an x-y raster in the focal plane of a telescope, and utilizes a liquid helium cooled, copper-doped germanium detector, the output of which is displayed on Polaroid PN55 film, as well as on an oscilloscope. Some laboratory data from this instrument, utilizing the spectral matching technique, is presented here to provide a clear visual demonstration of the method. Again, the spectral range of observation was limited by a 5 micron cut-on filter, inserted after the

chopper and immediately before the detector, and also by the spectral response of the detector. The spectral response of the filter and detector are shown in Figure 3.

LABORATORY EXPERIMENTAL PROCEDURE AND RESULTS

a. Instrument 1, Procedure. Polished plates of olivine and quartz were the only reststrahlen materials used, and the samples of quartz, albite and olivine listed in Figures 4 and 5 were examined with this instrument in the laboratory. These samples were placed in $\frac{1}{2}$ " holes in an aluminum disc. The disc was pivoted at its center on a precision hot plate such that it could be easily rotated to allow any one of the samples to be brought reproducibly, to the inspection position. The hot plate could be adjusted to provide a range of examining temperatures. Part of the energy emitted from the sample under inspection was allowed to pass through a $\frac{3}{8}$ " hole in a water cooled copper plate (which shielded the instrument completely from all other emission emanating from the heated sample fixture) and was then focussed on the entrance aperture of the spectral matcher.

The initial experiment in the laboratory was to replace the reststrahlen plates with plane mirrors and inspect the emission from each sample. This provided information on the relative radiance of the samples, and, because the samples are essentially in the same thermal environment, (although one does not expect their temperatures to be exactly the same because of the difference in particle size and because of the manner of heating) an indication of the amount of spectral information available is also provided.

This sample of coarse quartz consisting of particles lying in the size range 0.59 to 1.55 mm was arbitrarily selected as a primary reference, or "setting point". The procedure, when reststrahlen plates of olivine and quartz were used instead of mirrors, was to record the value of the signal received after the emission from each sample had been reflected from the quartz reststrahlen. The emission from the primary reference sample was then reflected from the olivine reststrahlen, and the magnitude of this signal was adjusted by altering the amplifier gain such that the signal value was exactly the same as the value of the signal recorded when the emission had been reflected from the quartz reststrahlen. A signal value was then recorded at this gain setting for each of the other samples. In this way, the instrument was used to normalize the signals recorded by reflection of the sample emitted energy from the olivine and quartz reststrahlens. This procedure was repeated for various gain settings on the instrument, and for different temperatures of the same sample, to provide data which would allow the instrument functions to be evaluated.

Instrument 1, Results. An example of the results obtained using the above procedure is shown in Figure 4 where the signal levels (after normalization) obtained on the recorder are plotted. The central set of signals were obtained by reflecting the emission from each sample from a plane

mirror, and so indicate the relative radiance of the samples. Differences in radiance, and the effect of the instrument function will be discussed later. The other two sets of signals were obtained using olivine and quartz reststrahlen plates, the signals from each reststrahlen plate being balanced at a recorder reading of 60 for sample 2. The signal received when the emission from a target is reflected from a quartz reststrahlen plate will be called the "quartz signal" and from an olivine reststrahlen plate, the "olivine signal".

In Figure 5 is plotted the difference between the magnitude of the olivine and quartz signals from each of the samples shown in Figure 4. As can be readily seen from these differences, or olivine minus quartz values, the magnitude of this difference arranges the samples in order from polished quartz to fine quartz, to fine olivine to polished olivine. The most definitive information (at the two limits) for the olivine minus quartz values is available from polished samples of the two minerals of the same composition as that of the reststrahlen plates--ie. for minerals having at the same time a maximum of spectral contrast and an exact spectrum match. For albite, there is also a corresponding gradation of the olivine minus quartz value from the polished sample to a sample of very fine particle size. The difference signals for all samples of very fine particle size are grouped together. This is to be expected, because the more finely ground a particular sample, the less spectral contrast is available in its emission spectrum, and the more nearly it resembles a black or grey body.

b. Instrument 2, Procedures. Four 1" x 1" x $\frac{1}{4}$ " polished samples of quartz, olivine, tremolite and albite were examined with the x-y scanning instrument. The surface examined was heated with radiant energy from a pair of heat lamps so that the temperature of the samples was maintained at about 45°C. The emission from these samples was focussed in the focal plane of the x-y scanning instrument, and five of the six pictures shown in plate 1 were produced by reflecting the emission from each of the samples, after passing through a P.E. 5 micron cut-on filter, in turn first from a plane mirror and then from reststrahlen plates of quartz, olivine, albite and tremolite. The emission was chopped at 100 cps against the emission from a black body at 27°C.

Instrument 2, Results. The results are displayed in pictorial form in plate 1.

Picture 1A is a photograph in the visible of the samples tested, with the sampled area outlined. The samples were resting on a sheet of aluminum foil, which is visible through the transparent quartz. The upper surfaces of the other samples are seen. In all cases, the infrared radiation sampled was emitted from the upper surfaces.

The remaining 5 pictures were produced with Instrument 2, and are composed of a raster of instantaneous processed signals (in the sense that they are the collected radiance from a small surface area which has been reflected from either a mirror or a reststrahlen plate) received from the targets

chopped against the emission from a black body source. Picture 1B was generated by reflecting the target radiance from a plane mirror and so is essentially a true relative radiance picture, presenting information corresponding to that shown in the middle line of Figure 4. In pictures 1C, 1D, 1E and 1F the emissions from the samples were processed by reflection from reststrahlen plates of quartz, olivine, albite and tremolite respectively.

Because, in the ideal case, a spectrum match is indicated for that sample whose signal magnitude is minimized, no difficulty is experienced in identifying the bottom sample in picture 1A as being the most quartz-like of the four samples pictured in 1C. It is obvious from a consideration of figures 1C through 1F that the information obtainable from some reststrahlen plates (such as quartz, tremolite and olivine) is more clearly definitive than from others (such as albite), even though a perfect spectral match for one sample has been achieved in each case. The albite case (1E) has been included to illustrate the effects produced by using a poor reststrahlen material.

Discussion of Laboratory Results

It is emphasized that spectrum matching is a technique of comparisons, involving comparisons of the relative magnitudes of the signals obtained when the emission of one target is reflected from a series of different reststrahlen materials, and/or when the emissions from a series of targets are reflected from one reststrahlen material. It is much easier to detect compositional differences among a series of targets, and the general nature of such differences (ie. acidic or basic rocks) than it is to specifically identify the composition of a given target. The latter involves all the problems of identification encountered in conventional spectroscopy.

It is now necessary to consider the functions of the various parameters in the expression which defines the magnitude of the signal recorded. This is given by

$$S(t) = \int_{\lambda_1}^{\lambda_2} [N_{bb}(\lambda, T) \{1 - R_s(\lambda) P_s(\lambda)\} A(\lambda, t) K(\lambda) R_R(\lambda)] d\lambda$$

where $S(t)$ is the integrated energy signal recorded at time t ; λ_1, λ_2 define the limits of the wavelength interval over which the integration is performed; $N_{bb}(\lambda, T)$ is the black body emission at temperature T ; $R_s(\lambda)$ is the reflectivity of the target material; $P_s(\lambda)$ is a function included to account for the nonideal surface condition; $A(\lambda, t)$ is the attenuation function; and $K(\lambda)$ is a general instrument function, and $R_R(\lambda)$ is the reflectance of a particular reststrahlen plate used.

The elements of this expression may be considered in terms of their dependence on the target, and the instrument.

Target: The expression $N_{bb}(\lambda, T) \{1 - R_s(\lambda) P_s(\lambda)\}$ defines the radiance of the sampled area on the target. The total energy emitted in a specified wavelength interval is equal to the emission of a black body at the same temperature modified by $R_s(\lambda) P_s(\lambda)$. For a series of samples of the same composition and temperature the radiance term is to be modified by the value of $P_s(\lambda)$ which is 1 for a target polished surface, and approaches zero as the surface becomes increasingly rough on a micron scale.

The relative radiances of 12 samples examined with Instrument 1, and four with Instrument 2 may be obtained from Figure 4 and Picture 1B respectively.

Instrument: The instrument function is expressed by $K(\lambda) R_R(\lambda)$. The constant value which can be assigned to $K(\lambda)$ for a given instrument is determined by the spectral dependence of the reflection losses due to all the optics encountered; by the transmission filters used to limit the wavelength range; by the spectral response of the detector; and also by the behavior of the entire detector-amplification and recording systems. Any or all of these contributing factors may be altered, in which case a new value for $K(\lambda)$ must be determined.

The other term to be considered in the instrument function is $R_R(\lambda)$, the reflectance of the reststrahlen plate (inclusion of which provides the point at which the spectrum matching technique differs from conventional radiometry). The following comments apply where the spectral information from the target corresponds either completely, or in part, to the spectral range where $R_R(\lambda)$ is not zero.

a. The use of a single plane mirror as a reststrahlen plate is pure radiometry over the limited wavelength interval specified by λ_1 and λ_2 and so provides information on the relative radiance of the samples.

b. The use of a plane mirror and reststrahlen plate in turn will tell whether or not the target is a black body--ie. whether or not the product of $R_s(\lambda) P_s(\lambda)$ equals zero. If a target is indeed a black body, assuming that the signal from the reststrahlen is normalized for its reflectivity, the signal level will be identical for both mirror and reststrahlen plate. For targets whose emission contains spectral information, the reststrahlen signal must be smaller than that from a black body at the same temperature. The combination of a mirror and single reststrahlen plate technique used on different targets will tell whether or not the product of $R_s(\lambda) P_s(\lambda)$ is different for the two samples. Thus, differences between two targets could be detected, which would be due to either composition, or grain size, or a combination of the two, but it is not possible to yet differentiate between these possibilities.

c. The use of two reststrahlen plates without a mirror may allow one to identify a difference obtained between two targets as being due to either a compositional difference, $R_s(\lambda)$, or a particle size (spectral contrast) difference, $P_s(\lambda)$. Whether or not this is possible to distinguish between

these possibilities with two reststrahlen plates alone depends upon whether the spectra of the two targets are sufficiently different from each other, and whether or not each of the two reststrahlen plates selected is spectrally similar to each of the two targets. Better information is obtained with a combination of a mirror and two reststrahlens.

An illustration of these points is available from a consideration of Figure 5. Here the values of the difference between the magnitudes of the olivine and quartz reststrahlen signals are plotted for the samples we have used.

The range of values for these signal differences, obtained for olivine and quartz reststrahlen plates, using a black body target as one limit and a polished quartz target as the other, will be referred to as the "quartz range". The range of olivine minus quartz signals obtained for a black body and a polished olivine target will be referred to as the "olivine range".

The following statements can be made about reststrahlen difference signals obtained from various targets.

1. If the olivine minus quartz value lies in the quartz range, the target is "quartz-like"; if in the olivine range, the target is "olivine-like";
2. if two targets are considered, and one lies in the quartz range and the other in the olivine range, one can say definitely that the two targets are compositionally different;
3. if the values from two targets both lie in the quartz range, or both in the olivine range, no matter how far separated they may be, one can only say that there is a difference either in composition, or in spectral contrast, or in both. With only two reststrahlen plates, it is not possible to proceed further.

This point is obvious from a consideration of Figure 5, where the entire range of olivine minus quartz values obtained from a series of albite samples, ranging from a polished sample to a finely divided sample lie within a small part of the quartz range. Any olivine minus quartz value obtained from an unknown target which lies in the range common to both quartz and albite could result from a sample of albite, or a considerably finer grained sample of quartz, or from some other material not yet considered. It should be pointed out that, for a whole range of samples of quartz of different particle size, the olivine minus quartz value will always lie in the quartz range, and that at every point one has achieved a perfect spectrum match.

To obtain more information, one must proceed to a third reststrahlen plate, chosen on the basis of the range in which the initial signals lay. If we consider two olivine minus quartz values which lie in the range common to quartz and albite, something other than quartz, yet a quartz-like material should be used. If we selected albite, then the quartz minus albite difference would lead to new arrangement of the difference values for the two sample. If one sample had been quartz, and the other albite, then the two quartz minus albite values would now lie on different sides of the B.B. value, indicating a definite compositional difference.

In the above discussion, it has been assumed that, when dealing with two or more targets, they were at the same temperature. The effects of temperature differences will be discussed more fully in the next section dealing with the lunar data.

The photographs shown in Plate I may now be discussed in reference to the reflection spectra of the reststrahlen materials shown in Figure 6 which are related by Kirchhoff's law ($E = 1 - R$) to the emission spectra of the sample materials of Plate I. Each of the 4 lower pictures is composed of a series of signals received when the emission from each element of the target is reflected from one of the reststrahlen materials. These signals are, however, not normalized, so that the relative degree of darkening in a particular picture is not always a direct indication of how near a spectrum match has been achieved.

For pictures IC, IE and IF, the darkest segment does indeed indicate a true spectrum match--ie. the sample material is indeed the same as the reststrahlen material, but in Figure IE, both the quartz and tremolite samples give lower signals than the albite sample when reflected from an albite reststrahlen. The albite reststrahlen plate was included as typical of a fairly poor reststrahlen material relative to, and in the presence of, the other three materials used. The merit of any material for a reststrahlen plate can be judged from its reflection spectrum. Albite is a poor reststrahlen material because its maximum reflectance is low, while over a large spectral interval its relative reflectance is high. Used with sample materials whose reflectance is high, such materials can make a large contribution to the signal obtained even though this is made over a small part of the spectral range. In the presence of quartz, whose spectrum almost completely overlaps that of albite, and even for tremolite, the amount of overlap and the reflectance values are sufficiently great to give the apparently anomalous information shown in ID.

First Lunar Application of the Technique

Spectrum matching observations of the lunar surface using the Perkins 69" telescope at Lowell Observatory in Flagstaff, Arizona were made during the April full moon period in 1965. Instrument I was used for these observations using dual reststrahlen plates, two of quartz and two of olivine. Using a 6.5 millimeter diameter aperture in the focal plane of the telescope, a circular spot approximately 70 km in diameter on the lunar surface was sampled.

The observational procedure was to select some feature on the moon, record the signal obtained by reflecting its emission from the quartz reststrahlen plates, track across the moon to Copernicus, which was always used as the "match point", and record the signal produced by reflecting its emission from quartz. The olivine reststrahlen was then inserted and the signal received from Copernicus was amplified so that it exactly matched the previous signal from Copernicus obtained with the quartz reststrahlen,

so as to normalize the two observations. The original feature was then reacquired by tracking the telescope across the moon and the signal from the feature was recorded after reflection from the olivine reststrahlen plate.

An example of the way in which the data was collected is shown in Figure 7, which also serves to illustrate exactly what has been plotted in Figure 8. The x-axis in Figure 8 records the difference in signal level for Copernicus and the target area when their emission was reflected from the quartz reststrahlens. This "quartz spread" value indicates the radiance difference and, if $R_s(\lambda)/R_q(\lambda)$ is small, the difference in temperature. Ignoring for the moment temperature effects, the "olivine minus quartz" reststrahlen signal values are indicative of a difference in composition and/or particle size of the feature relative to Copernicus, as shown by the difference in response of the two reststrahlen materials to the emitted radiation.

In Figure 8 are contained the results of observations made on the nights of April 13, 14, and 15, 1965. Plate 2 shows the location of each area studied.

The curves shown in Figure 8 were obtained using Copernicus as a reference point and have already had effects due to the instrument function removed by adjusting all readings to a common Copernicus match point of 60 on the recorder paper.

Figure 8 shows the continuous curves drawn through sets of data points obtained from the moon, and each set of points for a particular feature is enclosed in a box. The curves are of the shape shown because of the changing temperature of the features relative to Copernicus (our reference point), which is also changing in temperature due to movement of the subsolar point across the lunar disc during the lunar day. The effect of these temperature changes on the olivine minus quartz values is due to the shift of the peak of the black body curve to longer wavelengths at lower temperatures, which alters the magnitude of the signal from one reststrahlen material relative to the other.

Because of this temperature effect, a difference in the olivine minus quartz values for features separated along the x-axis are not in themselves meaningful. However, direct comparisons can be made between features in the same position of the x-axis. From Figure 8 it appears, for example, that there are significant olivine minus quartz differences between Mare Tranquillitatis and Mare Serenitatis, indicating either a difference in composition and/or spectral contrast. Unfortunately, insufficient clear nights were available during the late winter of 1965 to obtain a complete range of quartz spread (temperature) values for each area. Thus, direct comparisons are, in many cases, impossible. A lunar calibration curve was constructed by assuming that the central highlands are homogeneous in composition and particle size (at least with our spatial resolution) and by then examining different areas within the Central Highlands at progressively higher latitudes (and hence lower temperatures). The curve in the central block of Figure 8 was constructed in this way, and its consistency with

laboratory calibration curves suggests that it is the result of a valid assumption. Nevertheless, in interpreting the data presented in Figure 8, it must be borne in mind that data points separated along the x-axis must be compared with caution.

The differences recorded in Figure 8 lead to the following conclusions:

1. Features whose olivine minus quartz values lie along any one curve have approximately the same value for
2. The $R_S(\lambda)$ $P_S(\lambda)$ values for features which lie on different curves are different, but it is not possible to say whether these are compositional differences or particle size (spectral contrast) differences with the use of just two reststrahlen materials.
3. These differences are very small for the features we have so far examined on the moon in this way, indicating a general condition of low spectral content for lunar surface materials. This, in turn, indicates a rough surface for these materials on a micron scale.

Summary

A spectrum matching technique has been developed for rapid remote sensing of mid-infrared molecular vibration emission spectra of lunar and planetary surfaces. It is primarily useful when the remote sensing must be carried out in the presence of a variable intervening attenuator, which puts a premium on rapidity of measurement. A major advantage is achieved over conventional spectroscopic techniques when compositional differences and/or general compositional trends, rather than absolute composition, are the parameters to be measured. Laboratory tests of this technique with a simple spectrum matching instrument and with a more sophisticated x-y scanning instrument have demonstrated its feasibility. Use of the simple instrument on lunar targets has delineated very small, but consistent differences between different areas on the lunar surface. Among other things, these data indicate that the lunar surface materials possess a rough surface on a micron scale.

References

- Burns, E.A., and Lyon, R.J.P., 1962, "Errors in the Measurement of the Temperature of the Moon", Nature, V. 196, 463.
- Hunt, G.R., 1966, "Rapid Remote Sensing by "Spectral Matching" Technique. Part I: Description and Discussion of Method", Journal of Geophysical Research, October 1965.
- Hunt, G.R., and Salisbury, J.W., 1964, "Lunar Surface Features" Mid Infrared Spectral Observations", Science, V. 146, 641.
- Murci, F.H., 1965, "The Spectral Dependence of Lunar Emissivity", Journal of Geophysical Research, V. 70, 4959.
- Pettit, E. and Nicholson, S.B., 1930, "Lunar Radiation and Temperature", Astrophysical Journal, V. 71, 102.
- Pettit, E., 1940, "Radiation Measurements of the Eclipsed Moon", Astrophysical Journal, V. 91, 408.
- Rehnberg, J., et al., 1966, An Infrared Camera for astronomical and lunar observations: (in preparation).

ACKNOWLEDGEMENT

We wish to thank Dr. J. Hall, Lowell Observatory and Ohio-Wesleyan University for the use of the 69" Perkin's Telescope, and Professor C.H. Perry for recording the reflection spectra of the mineral samples.

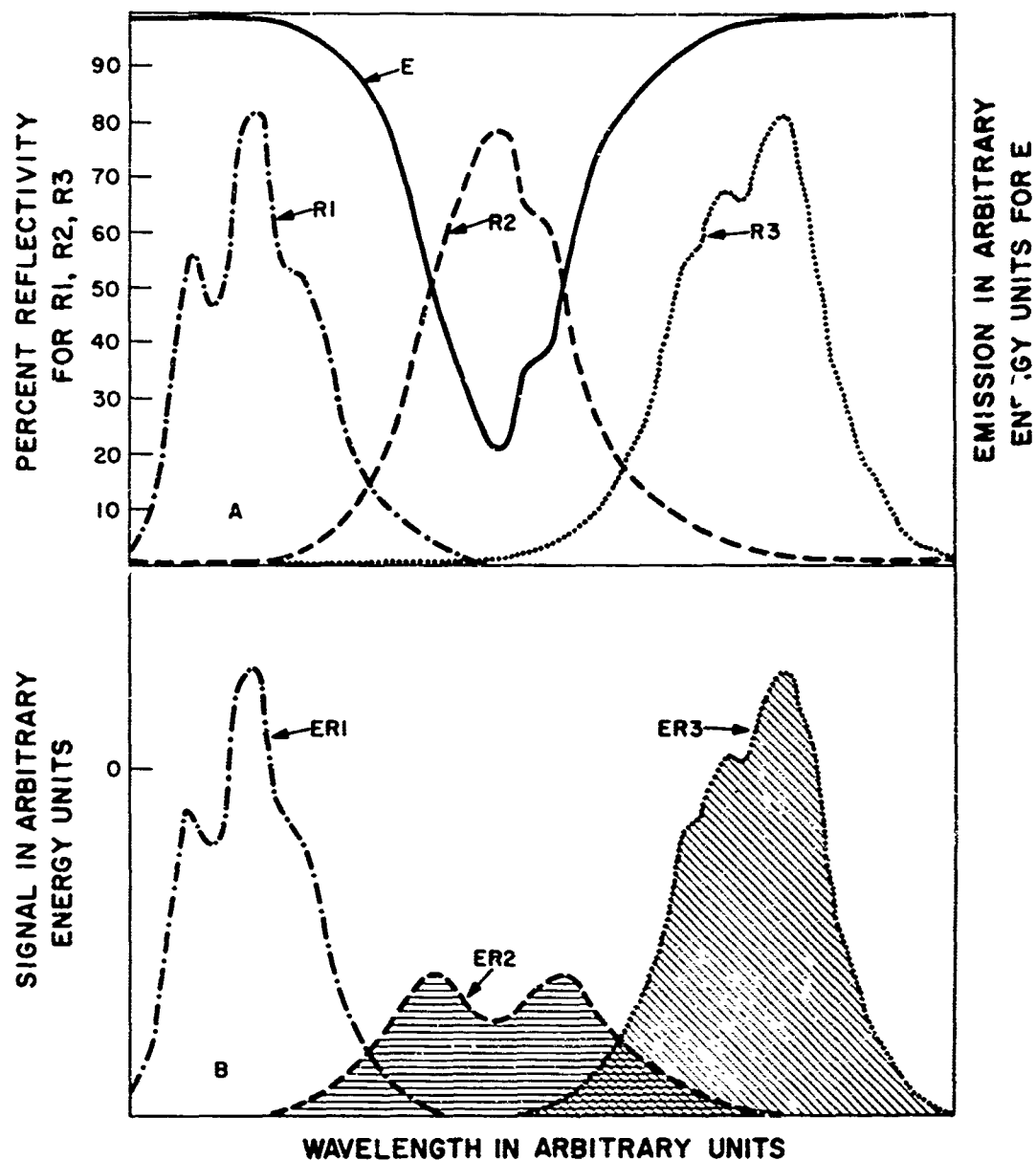


Figure 1. A. Specular reflection curves for three hypothetical reststrahlen materials (R1, R2, and R3), and one emission spectrum (E).
 B. Energy curves obtained when the emission (E) is reflected in turn from each of the reststrahlen materials.

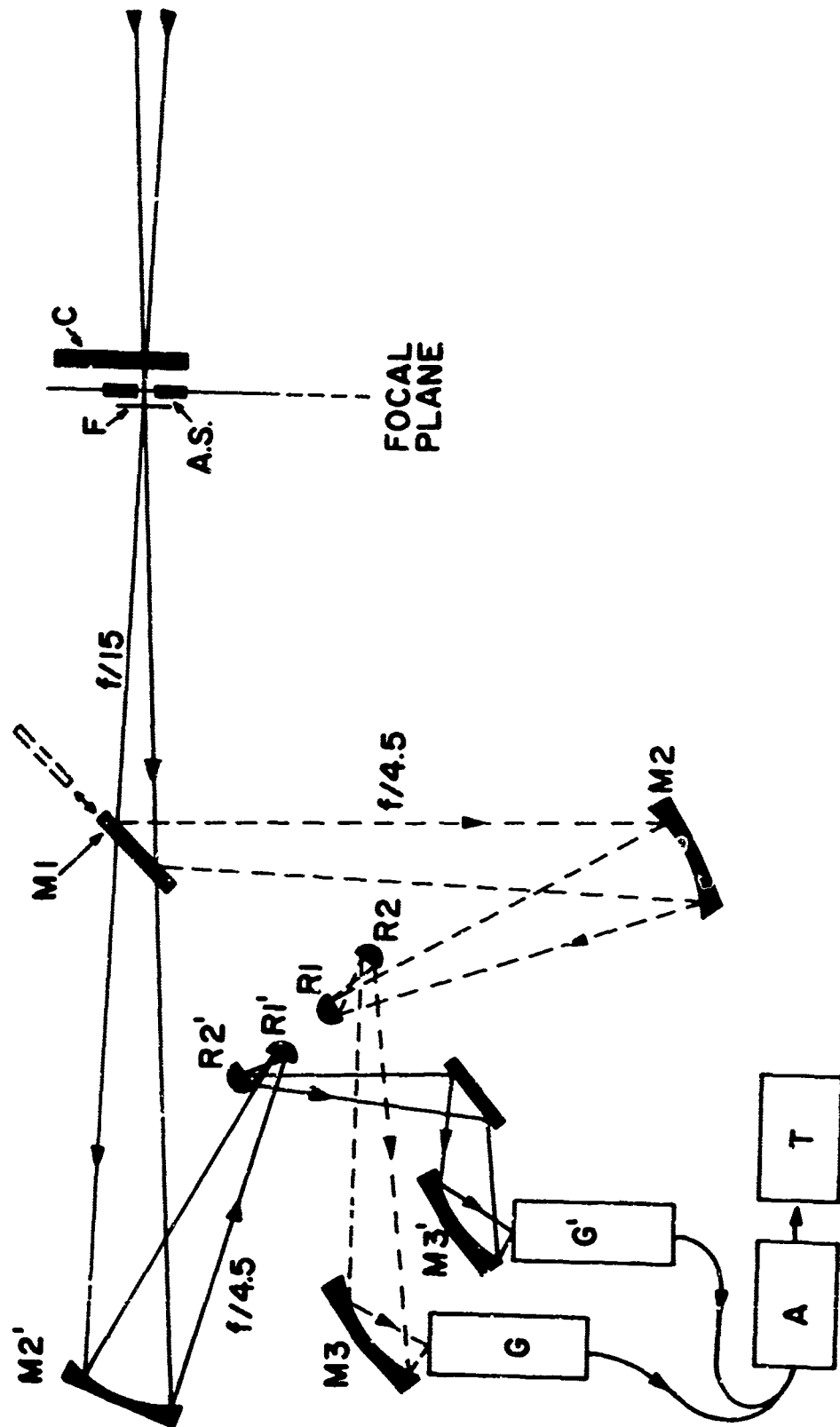
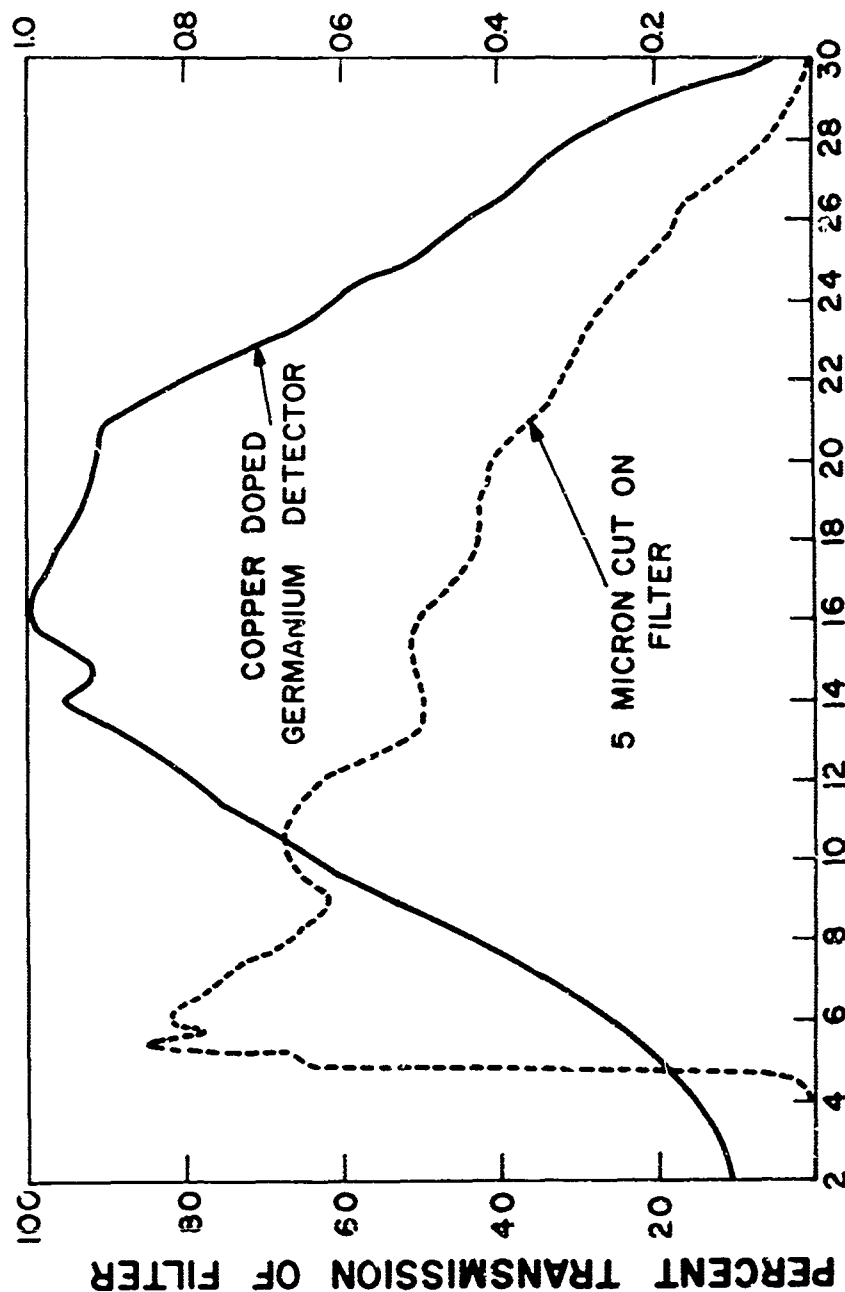


Figure 2. Optical block diagram of spectrum matching instrument 1, as used in the laboratory and on the 69" Perkins Telescope.

RELATIVE SPECTRAL RESPONSE OF DETECTOR



WAVELENGTHS IN MICRONS

Figure 3. Percent transmission spectrum of a 5 micron cut-on filter, and the relative spectral response of the liquid helium, cooled, copper-doped germanium detector.

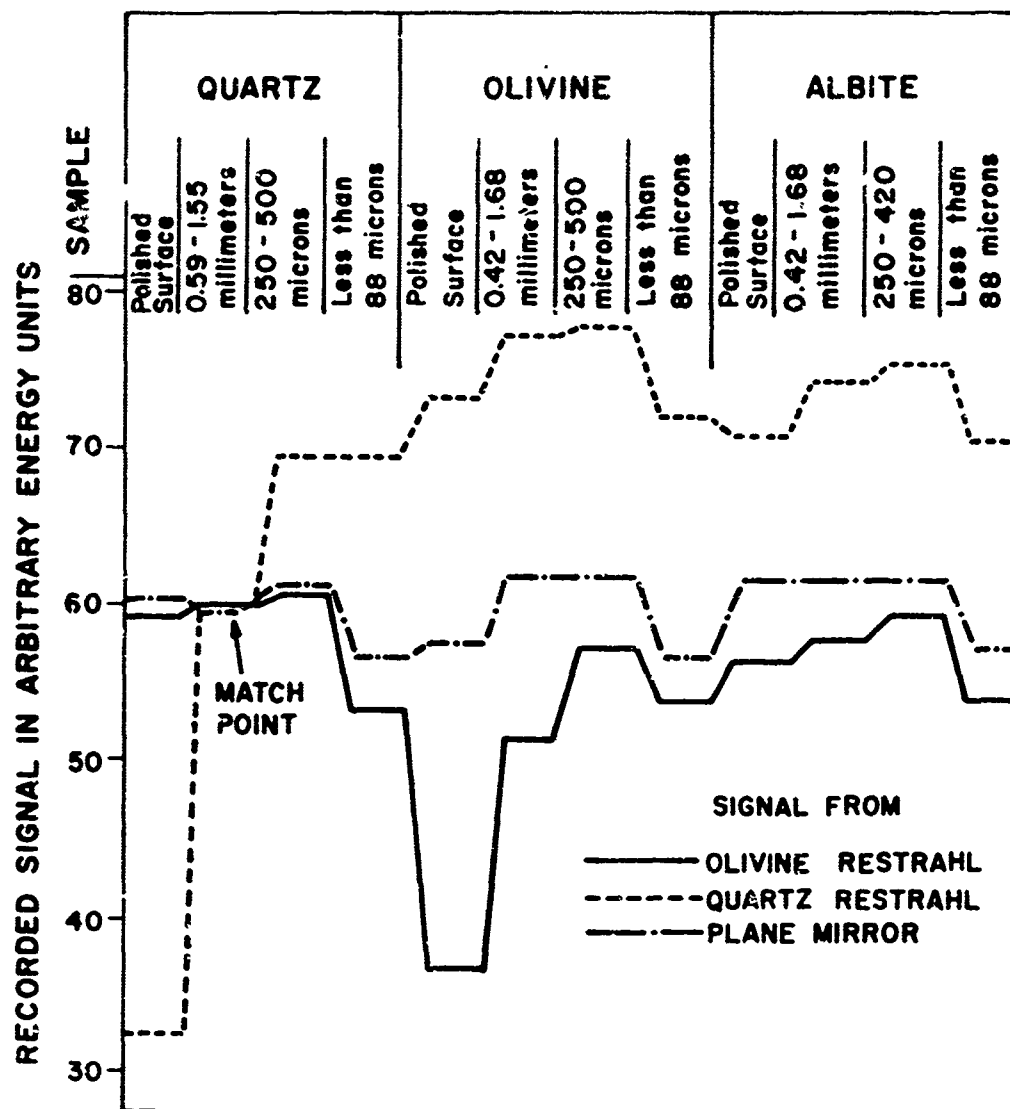


Figure 4. Normalized signal level, in arbitrary energy units, relative to the indicated match point, obtained when the emission from the sample specified at the top of the figure is reflected in turn from the polished surface of a sample of olivine, quartz, and a plane aluminized mirror. The signals obtained for the emission of each of the samples reflected from a particular reststrahlen material are joined with lines.

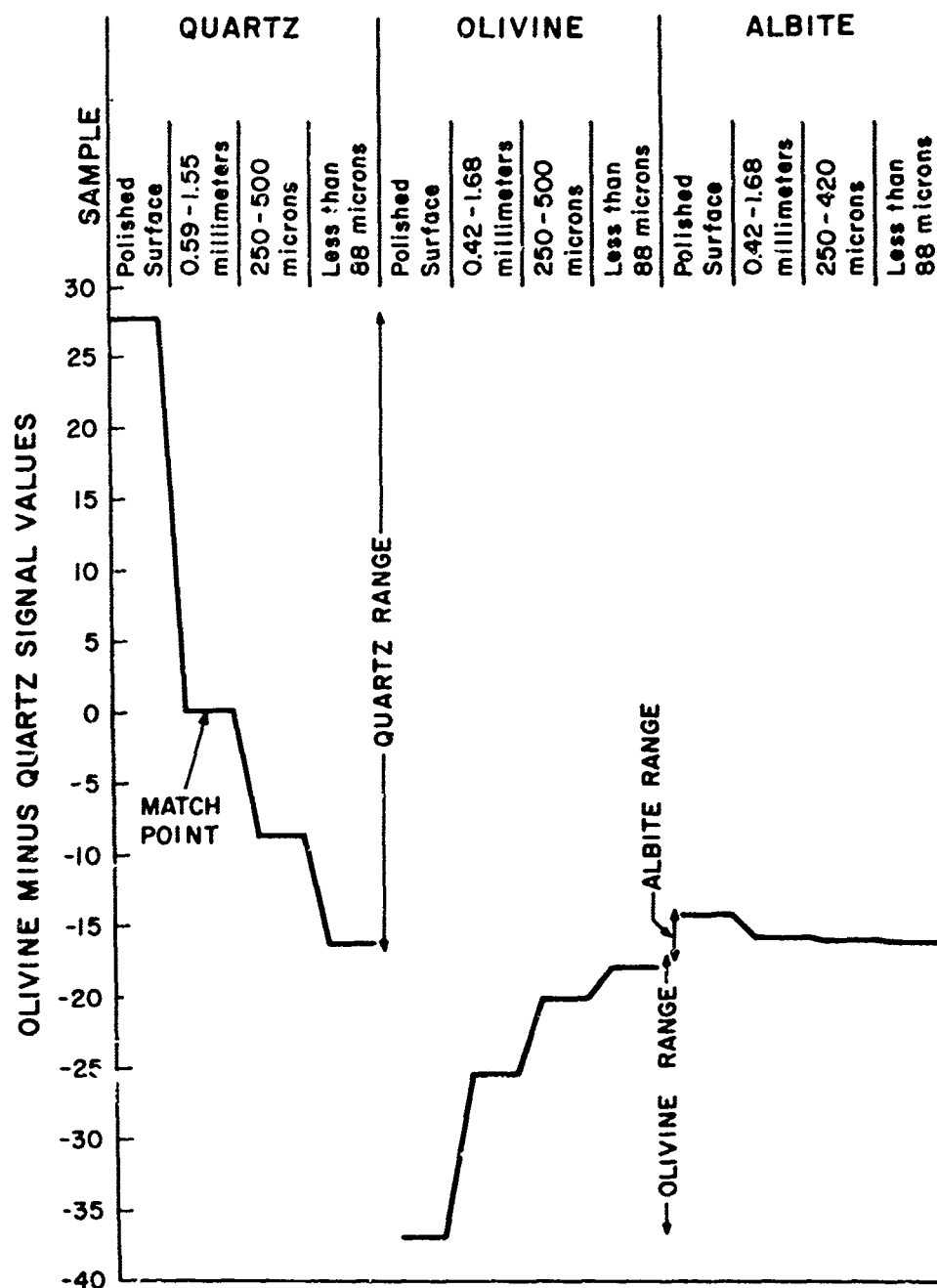


Figure 5. Normalized signal levels in arbitrary energy units, relative to the indicated match point, obtained when the emission from the quartz samples are reflected from a quartz reststrahlen plate (quartz range), the olivine samples from an olivine reststrahlen (olivine range), and the albite samples from an albite reststrahlen (albite range).

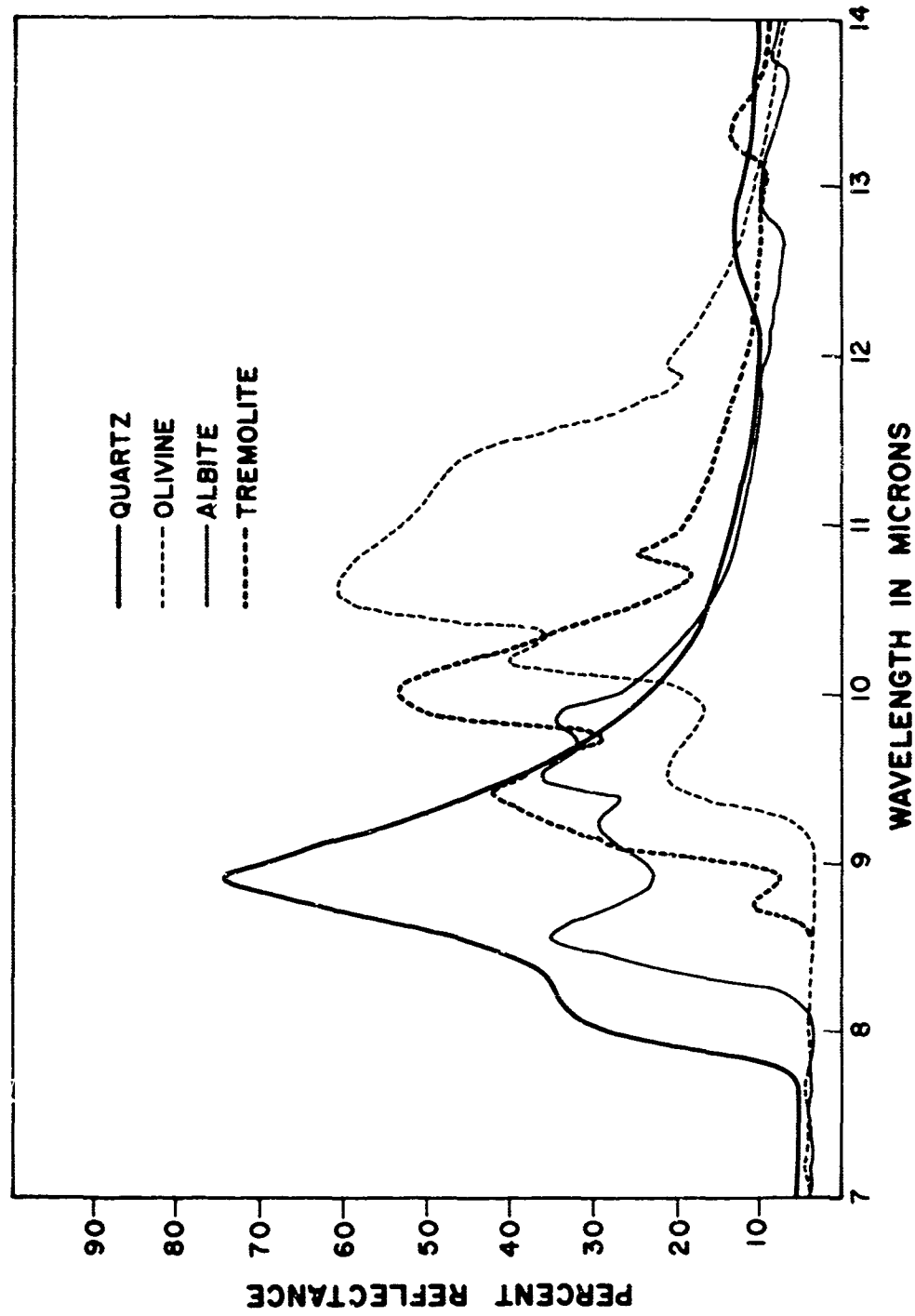


Figure 6. Percent specular reflectance curves for polished samples of quartz, olivine, albite and tremolite, recorded on a Perkin Elmer 521 spectrophotometer.

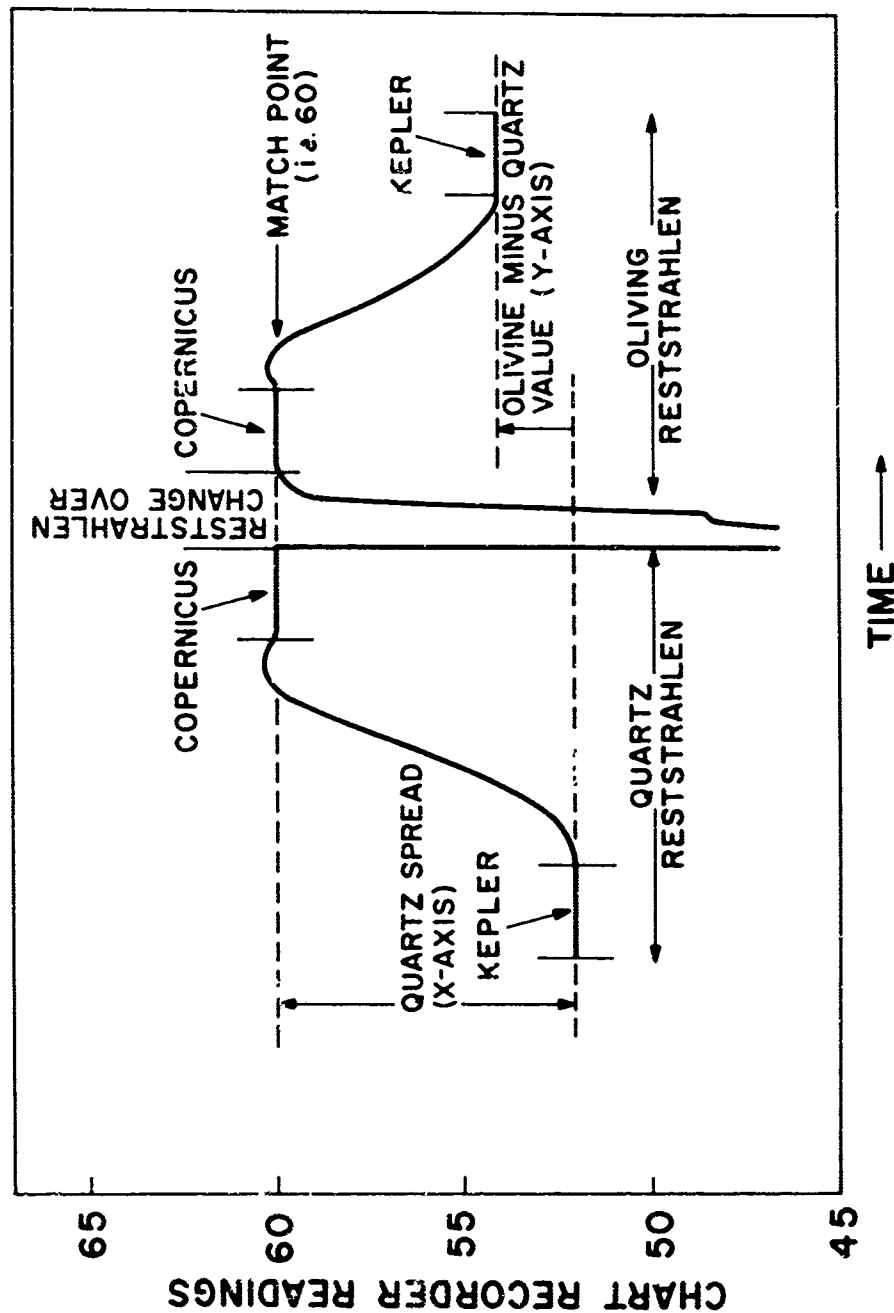


Figure 7. Illustration of the manner in which lunar measurements were obtained. With the quartz reststrahlen in, the signal from the feature Kepler was recorded. Copernicus was then located and a signal recorded in the same way. The quartz plate was then replaced by an olivine plate and the amplifier adjusted so that the reading obtained from Copernicus was of the same magnitude for both quartz and olivine reststrahlen plates. The original feature was then reacquired and another signal, from olivine, recorded. Data obtained for features in this way are plotted in Figure 8.

AFCRL

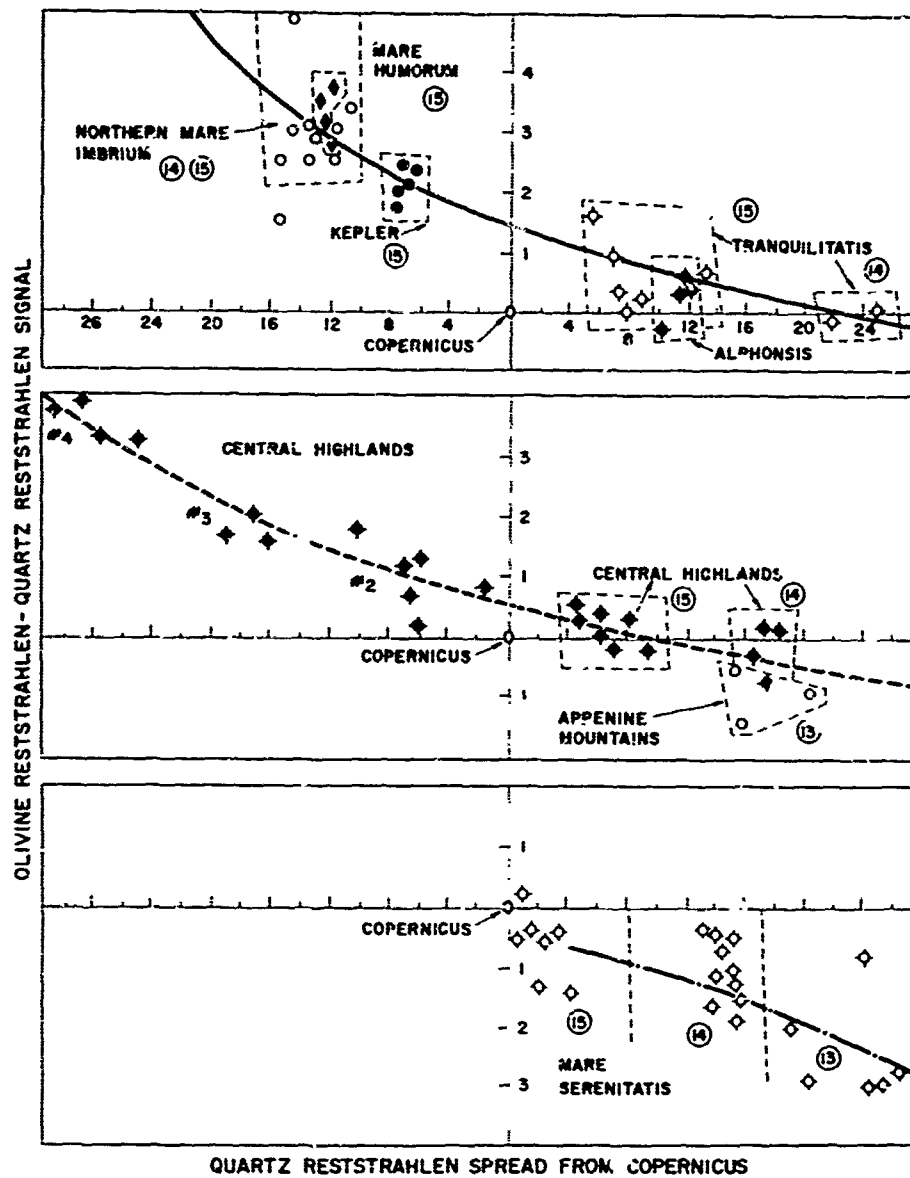
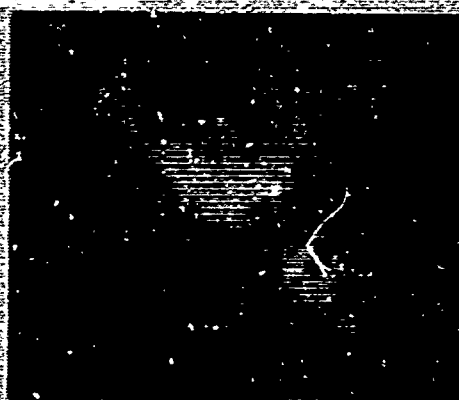


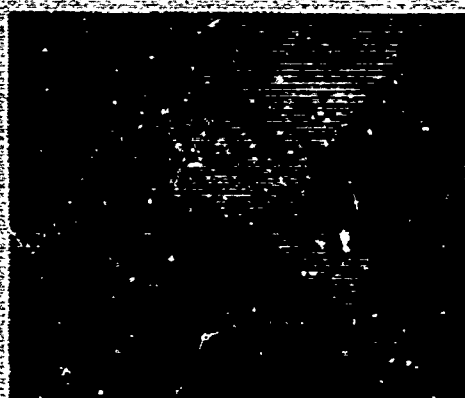
Figure 8. Data obtained from various features on the moon are plotted in terms of the difference in signal level for the quartz reststrahlen between the feature and Copernicus (x-axis) and in terms of the difference in signal level between the quartz and olivine reststrahlens for each feature (y-axis). The curves are drawn in each block to indicate the trend of the data. In the central block all measurements were made in the Central Highlands, those on the left from different areas, those on the right from the same area. The numbers indicate the date in March, 1965 on which each group of data prints were acquired.



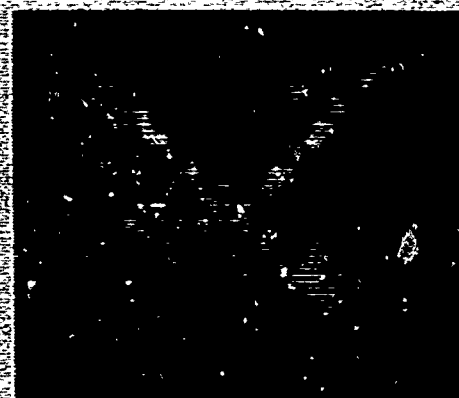
A VISIBLE PHOTOGRAPH



B RADIANCE



C QUARTZ RESTSTRAHLEN



D OLIVINE RESTSTRAHLEN



E ALBITE RESTSTRAHLEN



F TREMOLITE RESTSTRAHLEN

FIGURE 1. Illustration of the feasibility of the spectrum matching technique. The visible and infrared images of quartz, olivine, albite and tremolite shown in photograph A, are scanned with an infrared image device to produce pictures B, C, D, E, and F. Pictures B was produced after the infrared emission of the sample was reflected from a mirror, while pictures C, D, E, and F were produced using the indicated reststrahlen plates in place of the mirror.

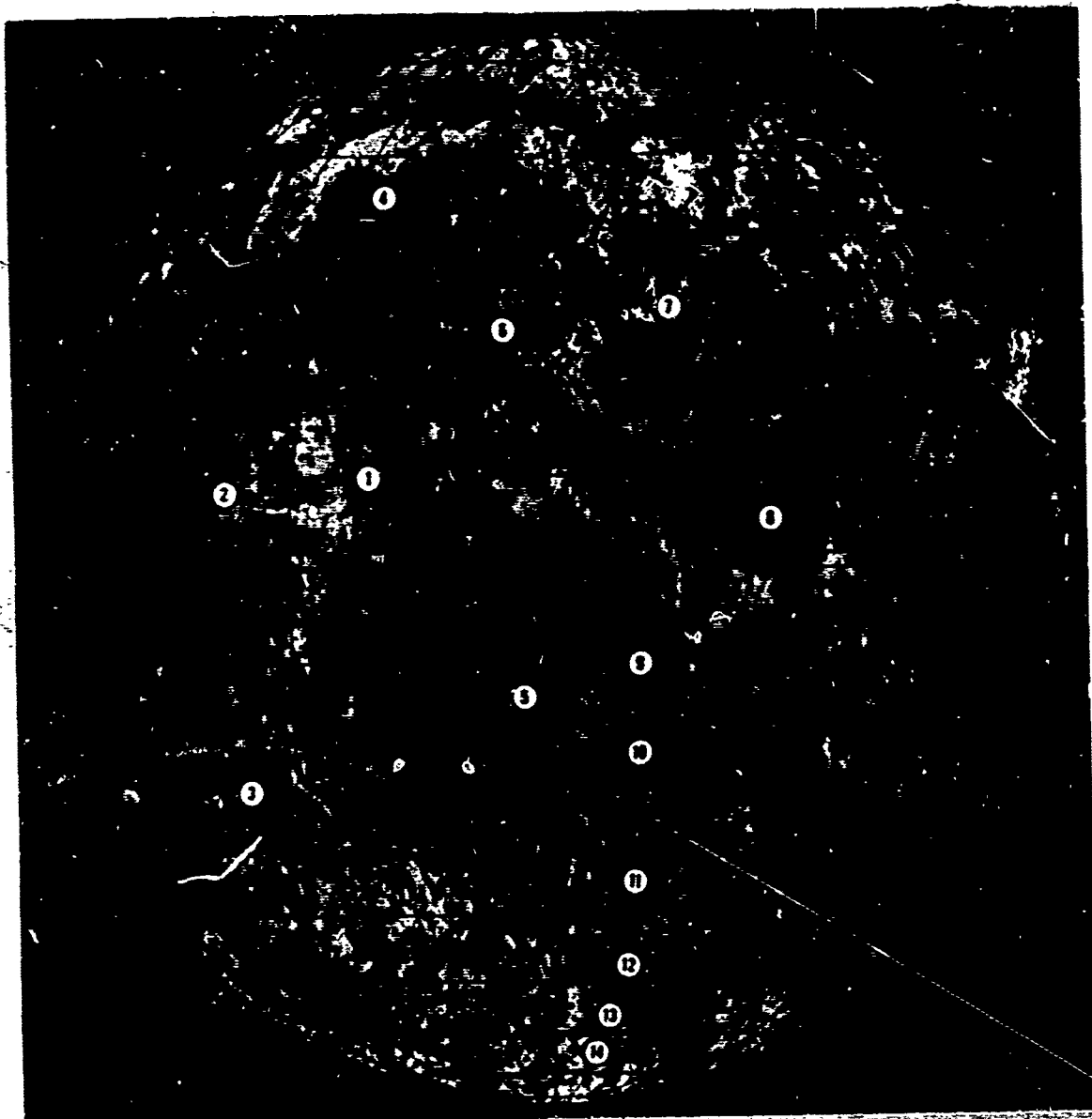


Plate 2. Location and sample size of lunar surface areas studied in the manner illustrated in Figure 7, with results as shown in Figure 8. The numbered areas are: (1) Copernicus, (2) Kepler, (3) Mare Humorum, (4) northern Mare Imbrium, (5) Alphonsus, (6) Apennine Mountains, (7) Mare Serenitatis, (8) Mare Tranquillitatis, and (9), (10), (11), (12), (13), and (14) are referred to generally as the Central Highlands. The Central Highlands data points on Figure 8 are from location (9).

ENVIRONMENTAL SYSTEM DEVELOPMENT FOR
RAPID DECOMPRESSION OF CHIMPANZEES
TO PRESSURES LESS THAN TWO TORR (U)

by

TOMMY L. DOBSON, BSME

Mechanical Section
Environmental Test Branch
Laboratory Test Division
Central Inertial Guidance Test Facility
Air Force Missile Development Center
Holloman Air Force Base, New Mexico



Tommy L. Debson

BIOGRAPHY OF MR. TOMMY L. DOBSON

Mr. Dobson was born in Fresno, California on April 24, 1935. He attended school in the Fresno City school system and graduated from Roosevelt High School in June 1953. He attended Fresno State College from 1953 to 1957 where he majored in Mechanical Engineering. At the end of his senior year, he was drafted into the U. S. Army. He spent two years at White Sands Missile Range. While at WSMR, Mr. Dobson worked as a mechanical engineer on the Redstone Missle Evaluation Project. In March 1960, he returned to Fresno State College and completed a two unit course required for graduation. Mr. Dobson was awarded a B. S. degree in mechanical engineering by Fresno State College in June 1960. He has been working in the Environmental Test Laboratory at Holloman AFB, New Mexico since his graduation. While at Holloman, Mr. Dobson has continued his studies at the Holloman Graduate Center, a branch of the University of New Mexico. At present, Mr. Dobson is a senior environmental engineer in the Environmental Test Branch. He was the project officer for the development of the rapid decompression system, and is now in charge of all testing in the decompression facility.

The animals used in this study were handled in accordance with the "Principles of Laboratory Animal Care" established by the National Society for Medical Research.

ABSTRACT

The Environmental Test Branch at Holloman Air Force Base has been performing a series of rapid decompression tests in support of the 6571st Aeromedical Research Laboratory and the NASA Manned Spacecraft Center. Eighteen tests have been performed, in which chimpanzees were decompressed from 179 torr (35,000 feet) to less than two torr (135,000 feet) in one second using a 100 percent oxygen atmosphere. This research is being performed so that mission rules, safety procedures, and necessary engineering designs may be incorporated into manned spacecraft to assure maximum chances of mission success for astronauts.

The Rapid Decompression System was designed and constructed as an "in-house" project. Existing chambers, equipment, and instrumentation were used as much as possible. A 40-cubic foot chamber and its life support system was connected to two chambers having a total volume over 4000 cubic feet. Instrumentation and equipment are provided to measure and control relative humidity, temperature, pressure, and gas composition. New test methods and safety procedures were developed. Several problems were encountered in the development of this unique test capability, and these problems and their solutions are described. Future test requirements will include decompression pressures below one torr and helium-oxygen atmosphere.

A short description of the results of the present test program is included. In presenting the paper, a short film showing the actual decompression of a chimpanzee will be shown.

TABLE OF CONTENTS

	<u>Page</u>
I. INTRODUCTION	1
II. SYSTEM AND TEST DESCRIPTION	1
III. SYSTEM COMPONENTS	2
A. Closed Environmental Assembly	2
B. Large Chamber Assembly	4
C. Decompression Valve	4
IV. SYSTEM CONFIGURATION PROBLEMS	5
V. FUTURE PLANS	7
VI. CONCLUSION	7

LIST OF ILLUSTRATIONS

FIGURE

- 1 Rapid Decompression System Diagram
- 2 Photograph: Chimpanzee in Closed Environmental Chamber
- 3 Photograph: 8' X 60' Vacuum Chamber

ENVIRONMENTAL SYSTEM DEVELOPMENT FOR
RAPID DECOMPRESSION OF CHIMPANZEES
TO PRESSURES LESS THAN TWO TORR (U)

I. INTRODUCTION

Research is being performed at Holloman AFB, New Mexico, so that mission rules, safety procedures, and necessary engineering designs may be incorporated into manned spacecraft to increase astronaut safety and assure maximum chances of mission success. It has become very desirable to investigate physiological and psychological results of rapid decompression to a near vacuum. In line with this, the 6571st Aeromedical Research Laboratory and NASA Manned Spacecraft Center have levied very stringent requirements on the Environmental Test Branch to simulate the necessary environments. To fulfill these requirements, a rapid decompression system had to be developed. Such a system was developed as an in-house project by the environmental test laboratory using existing chambers, equipment, and instrumentation as much as possible.

II. SYSTEM AND TEST DESCRIPTION

A rapid decompression system consists of three basic components; a small chamber in which the testing is performed (Figure 2), a large chamber (which is initially at a high vacuum, Figure 3) into which the gas from the small chamber is exhausted during decompression, and a valve to separate the chambers as shown in Figure 1 and Figure 2. The components chosen for our system were a closed environmental assembly for primates, a 40-cubic foot chamber and its life support system with a 16-inch, double-ported, balanced, rapid decompression valve; and two large chambers having a total volume of more than 4,000 cubic feet. To date, eighteen tests have been performed in the

rapid decompression system, during which chimpanzees have been decompressed from 179 torr (mm Hg), or 35,000 feet simulated altitude using a 100 percent oxygen atmosphere, to less than two torr (135,000 feet) in one second.

The chimpanzee is placed in the small chamber, and the chamber is purged to 100 percent oxygen. (See Figure 2) After a three hour denitrogenation period, the chamber pressure is reduced to 179 torr. After another half hour, the chamber is decompressed by opening the decompression valve to the large evacuated (0.14 torr) chambers. The valve is closed at the end of the decompression period, and the small chamber is repressurized to 179 torr in 30 seconds with oxygen. Decompression periods have been varied from 5 to 210 seconds. Instrumentation and equipment are provided to control, measure, and record temperature, pressure, gas composition, and relative humidity.

The results of the first nine tests were reported in NASA Contractor Report CR329, November 1965, "The Effect On The Chimpanzee Of Rapid Decompression To A Near Vacuum". Performance by all animals reached a baseline level within a four hour post-decompression period. All subjects survived in good health and no lasting effects or damage was detected.

In addition to the decompression tests with chimpanzees, more than 30 tests have been made with other biological specimens.

III. SYSTEM COMPONENTS

A. Closed Environmental Assembly

The closed environmental assembly for primates was manufactured by General Electric Company, Missile and Space Vehicle Department, Philadelphia, Pennsylvania. The assembly consists of four mobile sub-assemblies. The first sub-assembly is the chamber. Its internal dimensions are 30 inches deep, 48 inches high, and 48 inches wide, giving a volume of 40 cubic feet. All wall surfaces are fully water-jacketed to control wall temperature. A 7.5 by 8.5-inch

plexiglass window is provided in the wall over the pneumatic control panel for viewing the subject. One wall of the chamber is hinged to provide free access to the chamber. Two 50-pin connectors and twelve 1/4 inch tubing penetrations are provided on the chamber top for instrumentation. The pneumatic control console contains an absolute pressure gauge, a demand type precision oxygen regulator, oxygen supply valves, breath-down valve, bleed valve, vent valve, and purge valve.

The second sub-assembly is the life-support system. It provides a life supporting environment in the chamber proper. The chamber atmosphere is circulated through the system at about 10 cfm by a vaneaxial fan. After the "stale air" is removed from the chamber, a 500 cc per minute sample is circulated through an infrared type CO₂ analyzer. The remainder of the "air" is then passed through a CO₂ absorber which maintains a CO₂ partial pressure below 2 torr. After the gas is passed through one of two refrigerated dehumidifiers, a 300 cc per minute sample is circulated through an O₂ analyzer which operates on the para-magnetic principle. The cold "air" then passes through a heater-humidifier where the gas is reheated and a controlled amount of moisture is readmitted into the air stream before re-entering the chamber.

The third sub-assembly is the wall temperature control sub-system. It has the capability of heating or cooling the chamber walls by circulating a water-ethylene glycol mixture through them. The system consists of two insulated, 40-gallon tanks connected by three-way manual valves to an electrically-driven centrifugal pump. The hot tank is heated by thermostatically-controlled immersion heater coils, and the cold tank is cooled by refrigeration coils connected to a 1/3 hp hermetic refrigeration unit.

The final sub-assembly is the electrical control console. It displays the internal chamber environmental parameters and provides a means for controlling them. Indicator lights are provided to indicate operations of various components within the system. The CO₂ analyzer display panel and the O₂ analyzer indicator-recorder are also in this assembly.

Several modifications were made on the closed environmental assembly. A 12 by 22-inch plexiglass window was put in the chamber door to facilitate 16 mm moving picture, closed circuit television, and still photo coverage during the tests. The top of the chamber was modified to fit the 16 by 20-inch flanged opening on the decompression valve. Two isolation valves were installed between the chamber and life-support system to reduce the volume decompressed and to protect the life-support system during decompression. Three 37-pin Deutsch connectors were installed in the chamber to give more penetrations and to simplify changing the set-up between tests. For example, completely different instrumentation is used for other specimens than for chimpanzees.

B. Large Chamber Assembly

The small chamber is decompressed into two large altitude chambers. One chamber was manufactured by Midwest Tank and Manufacturing Company, Indianapolis, Indiana. Its internal dimensions are 8 feet diameter by 60 feet long. This chamber is connected by a 12-inch pipe to a chamber manufactured by COOK Electric Company, Nucledyne Division, Chicago, Illinois. The Cook Chamber's effective internal dimensions are 10 feet by 10 feet by 15 feet deep. These two chambers can be evacuated to 0.14 torr by three 850 cfm Beach-Russ rotary piston vacuum pumps.

C. Decompression Valve

The 16-inch, double-ported, balanced, rapid decompression valve is the same valve used for explosive decompression tests in

altitude indoctrination chambers for pilot training. These chambers are described in Air Force Tech Orders, 43D8 series. It is a pneumatically operated valve with a mechanical locking device so that it cannot be opened by mistake or by air pressure failure.

IV. SYSTEM CONFIGURATION PROBLEMS

Several problem areas were encountered during the system check-out period. One of the most serious was maintaining high oxygen concentration. After purging the system for three hours and having an oxygen concentration over 99 percent, the system pressure was reduced to 179 torr. The oxygen concentration would drop as low as 70 percent at this time. The cause was the chimpanzee couch. It was such a close fit in the chamber that about 1/3 of the chamber was not being purged. The purging lines were modified so that oxygen was piped to any closed areas as well as the top and bottom of the chamber. Closed areas in the life-support system also must be purged.

Another problem area was reaching and maintaining pressures below two torr after decompression. Most of the tests require drinking water in the chamber, and all tests require a container for body waste. Water ebullition and other outgassing resulted in an increasing pressure following decompression. A small finned refrigeration coil was obtained from Salvage and placed in the 60-foot tank over the pipe opening to the decompression valve. After the large chambers are evacuated, but before decompression, the coil is filled with liquid nitrogen. Without the LN_2 coil, pressures increased as much as 3 torr during the decompression period, but with the LN_2 coil, pressure increases are less than 0.2 torr.

Measuring the environmental conditions during and immediately following decompression was another problem area. Gas composition and relative humidity are not measured during decompression, but

temperature and pressure are measured. A small (gauge no. 30) Type T thermocouple, recording on a Brown Electronik 15 recorder, is used for temperature measurements. Pressure recordings are made using capacitance and strain gauge type sensors with Electronik 15 recorders. These give excellent profile recordings, but, because of the large scale, do not give dependable low pressure readings. Therefore, a liquid nitrogen cold-trapped McLeod gauge is used. Besides temperature and chamber pressure, several other environmental conditions are recorded during the remainder of the test. Chamber wall temperature, relative humidity, percent carbon dioxide, oxygen partial pressure, and 60-foot tank pressure are recorded on Brown Electronik recorders.

Safety is always a paramount factor in test work. Many of the system features and operating procedures are the result of safety considerations. Ground Safety and the Fire Department make frequent inspections of the laboratory. The Fire Department is notified before each test that a 100 percent oxygen test is being run. In case of any emergency, they will know what hazards exist and what equipment will be needed. The animal's safety must also be considered. An emergency power supply is operating in standby during critical portions of the test.

Working with oxygen is always a hazard. Vacuum pumps require special types of oil when pumping oxygen. Cellulube 220 is used in the small pumps on the closed environmental system. We have used this oil for the last six years, during several thousand hours of testing, with no problem. Tricresyl Phosphate (TCP) is recommended for use in the large pumps on the large chambers. Because TCP is poisonous, can be absorbed through the skin, and is very corrosive, we do not feel that it is worth the hazards to convert our large pumps. Therefore, 15 seconds before decompression, the large pumps are valved off and are not placed back into the system until the chambers are purged with air.

V. FUTURE PLANS

Decompressions of longer durations are being planned. Since under space conditions pressures are much lower than 2 torr, a good area for research would be rapid decompressions to pressures lower than 2 torr. By adding a system of sealed tanks in the small chamber to reduce its effective volume, decompressions to lower pressures can be performed. The United States is now using a helium-oxygen atmosphere in the high pressure test areas such as Sealab II. Russia uses nitrogen-oxygen in their manned spacecraft. By adding a few valves and the necessary gas analyzers, the rapid decompression system could be used for multi-gas atmosphere testing. Other future test areas could include the decompression of more than one animal or more than one decompression. By using pulse x-ray techniques, research could also be performed to determine the effect of rapid decompression on the major body organs

VI. CONCLUSION

The Environmental Test Branch has developed a rapid decompression system capable of decompressions from 179 torr to less than two torr in one second. They were given the problem of developing such a test capability, and they solved the problem by using a systems engineering approach. They succeeded in making a reliable, safe, and versatile system. Through an in-house effort, they used components on hand to give the Air Force a unique testing capability.

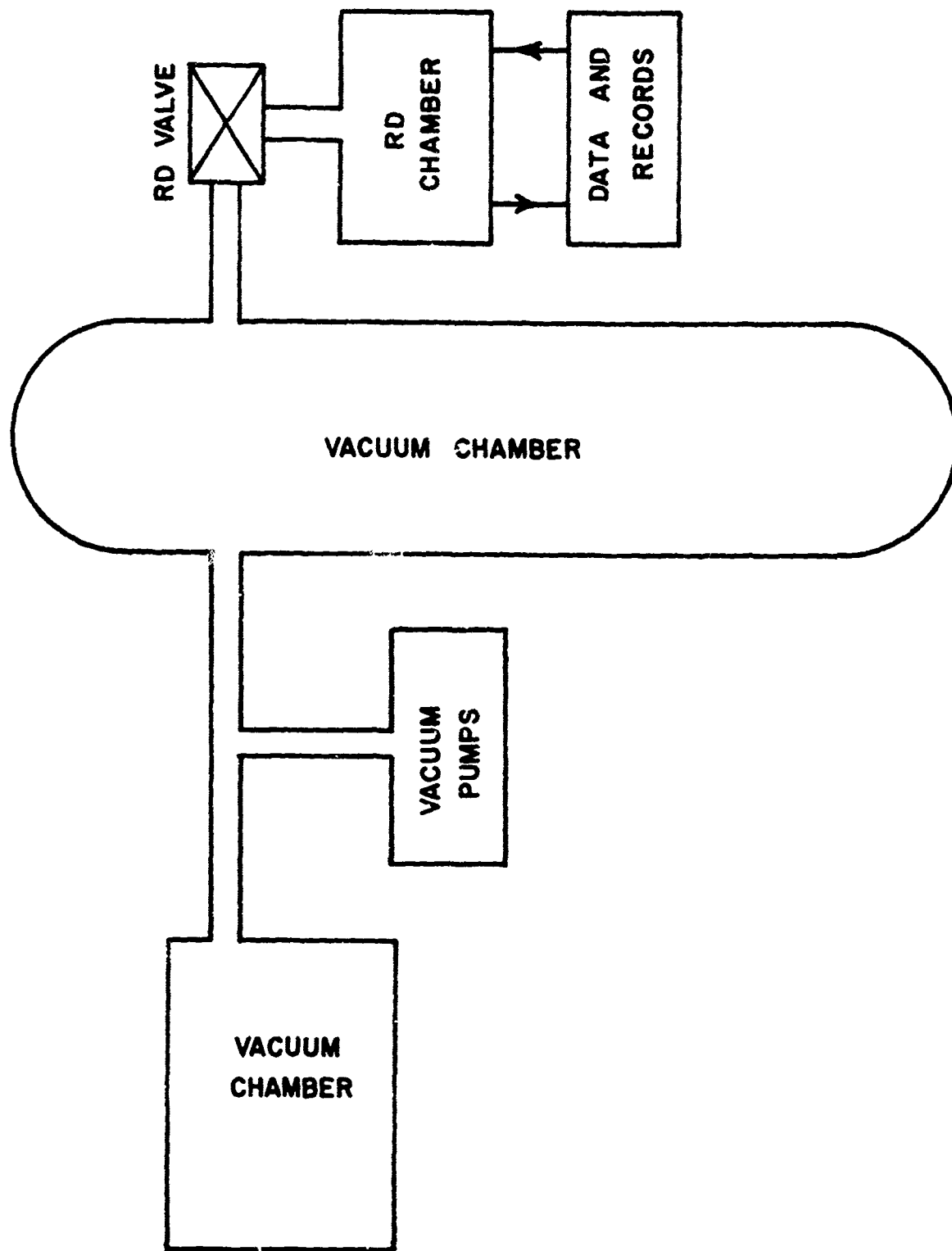


FIGURE 1 - RAPID DECOMPRESSION SYSTEM DIAGRAM



FIGURE 2 CHIMPANZEE AND-CLOSED ENVIRONMENTAL CHAMBER SYSTEM

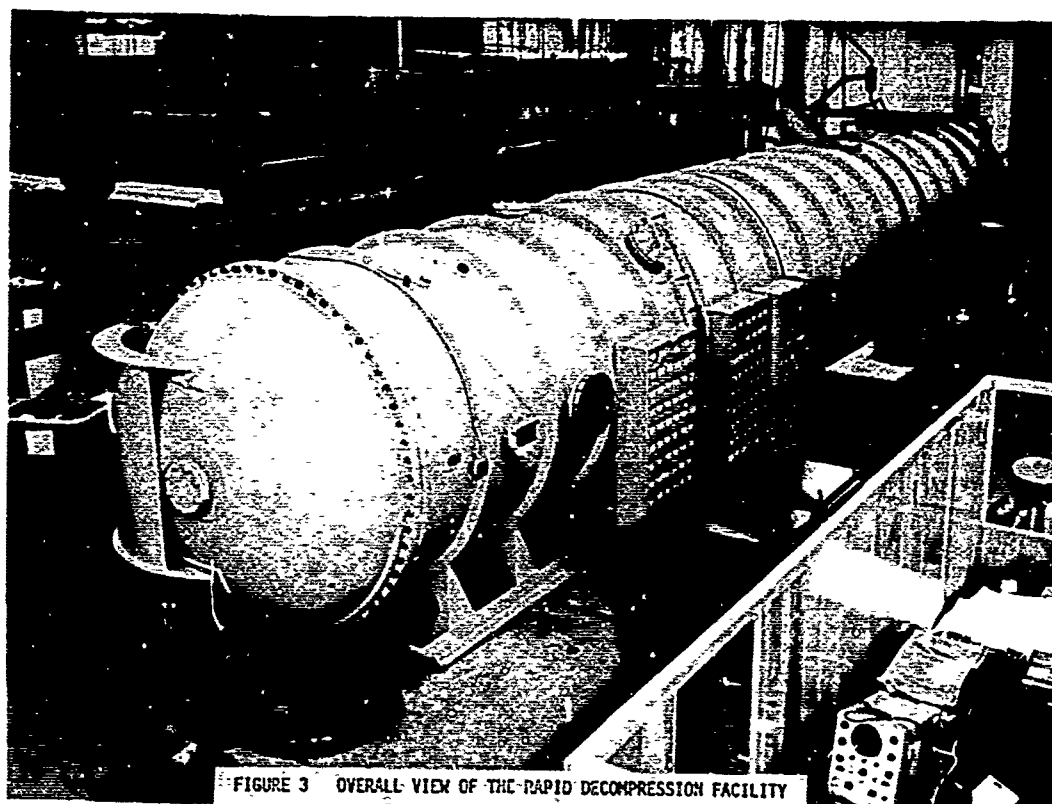


FIGURE 3 OVERALL VIEW OF THE RAPID DECOMPRESSION FACILITY

(U) FILAMENT WOUND AIRCRAFT TIRES

Theodore J. Reinhart, Jr.

**Materials Applications Division
Air Force Materials Laboratory
Wright-Patterson AFB, Ohio**



Theodore J. Reinhart, Jr.

Biographical Sketch

of

Theodore J. Reinhart, Jr.

Received his Degree in Chemical Engineering from Case Institute of Technology in 1955. He joined the B. F. Goodrich Tire Company in 1955, where he worked in the tire development department on the development of improved rubber compounds and adhesive formulations. In 1958 he transferred to the Defense Products Division of the B. F. Goodrich Company, where he worked in the area of filament wound motor cases, high pressure and exit cones and heat resistant adhesives.

In 1960, Mr. Reinhart moved to the Applications Division of the Air Force Materials Laboratory, where he has specialized in the areas of filament winding, adhesive materials and structural applications of composite materials. He is presently Technical Manager for Specialty Materials in the Applications Division of the Air Force Materials Laboratory.

Mr. Reinhart is a member of the Society of Plastics Engineers, The Society of Aerospace Materials and Process Engineers and the Alpha Chi Sigma (Professional Fraternity). He has published over 20 papers in the area of plastics and adhesives, has given numerous presentations at National meetings over the past five years. He has been awarded four patents to date, and has several more pending allowance.

ABSTRACT

This paper discusses a new concept or invention, the filament wound, toroidal, aircraft tires. The disadvantages of present tire designs and the requirements for improved tires are shown. The advantages and potential of the new design are discussed. The results of a program to exploit the filament wound tire are given.

The approach taken has been to design a filament wound tire of the same size as a current tire in Air Force use and which uses a standard aircraft wheel. The prototype tires are burst tested and subjected to the qualification, dynamometer tests of the military tire specification. Results to date have shown that tires of greater strength to weight can be produced. However, air entrapment has been a problem. It can be solved by certain changes in the filament winding process and the uses of pre-impregnated tapes.

Discussions are presented on the uses of advanced tire materials, the other applications for this tire design. It is concluded that optimization of the new tire design and of the fabrication techniques will result in tires capable of very high load operation, better capability for Limited War operations, reductions in weight, and more reliability when compared to conventional tires.

This tire configuration invented by the author has great potential for the production of aircraft and other vehicular tires that have at least the following advantages when compared to conventional tires: (1) Filament wound tires are stronger at equal weight, (2) they are capable of operating at higher deflections, (3) the fabrication process lends itself to complete automation,

(4) reinforcements are utilized to their fullest potential, (3) enables the effective usage of high strength reinforcements such as glass or steel filaments in conjunction with many specialty elastomers that cannot be utilized in conventional tires. Prototype tires have been tested both statically and dynamically. The results to date have been very encouraging. Certain quality limiting problems have been defined and steps are being taken to solve them. Carcass hydroburst tests have shown the filament wound carcass to be about 15% stronger than the conventional tire.

The contractual program has successfully demonstrated the feasibility of this tire concept.

The paper discusses the advantages, problem areas and future potential of continuous cross section tires as compared to conventional tires. Presented are discussions concerning the use of advanced tire materials and spin-off applications. It is concluded that the perfection of this tire configuration and its associated manufacturing technology will result in tires capable of sustained very high load operation, reductions in weight and increased reliability when compared to present day conventional tires.

I. INTRODUCTION

Conventional tires, i.e., those that have their reinforcing filaments or cords anchored around one or more bead bundles, as shown in Figure 1 have been under more or less intensive development for about 50 years. As can be expected, conventional tires have been developed to the state where they are a remarkably efficient and reliable structure. An example of the state-of-the-art is shown in Figure 7A(top). This is a cross section of a B-58 tire. This tire perhaps more so than any other aircraft tire manufactured to date represents the high point in tire design, superb craftsmanship and structural efficiency of which the tire industry is presently capable of providing.

One might ask if all this is true what is the need for another tire design regardless of how new or novel it is? One answer is that nothing is perfect. The present tire design, like all things, has certain problems. But, in addition to this somewhat obvious answer one could also say that, with the present tire design, past attempts to use materials with better properties have not resulted in any appreciable pay off. In addition, certain systems requirements increase the urgency to secure certain features which cannot be secured to any appreciable degree with the present tire.

This paper will discuss the reasoning that leads to the development of the filament wound, continuous cross section tire, explain the basic tire design and fabrication procedures, describe the advantages and unique features of this novel tire, and finally will discuss the progress and problem areas in the exploratory development work performed to date and potential advanced applications and spin-off that the development of this concept may make practicable.

II. CONVENTIONAL TIRE

Fabrication Technique

To best understand the later discussion of the disadvantages of the current tire design one should be familiar to some degree with the fabrication technique. The following is a description of the process.

The fabrication of conventional tires is a hand lay up operation in which the quality of the product is a direct function of the skill and reliability of the tire building personnel. Through the years much has been done through time and motion study techniques to bring all of the materials of construction within convenient reach of the tire builder, however, only he is responsible for the proper assembly of the tire components. Present day, conventional tires are fabricated on collapsible, cylindrical building drums. The carcass plies of rubber coated nylon cords are applied to the building drum and stitched and rolled together to eliminate all trapped air. The steel wire bead hoops are positioned at each end

of the cylinder and a short length of the previously applied carcass plies is turned up around the bead to lock it in place. The slab of tread and sidewall rubber is then positioned circumferentially around the mid-point of the cylinder. The assembly is once more rolled down to insure elimination of trapped air. At this point the building drum is collapsed and the cylindrical, (green) uncured tire is removed from the drum. This uncured rubber cylinder looks like a hollow beer barrel at this point and in no way resembles what it will look like after cure; namely a tire.

The process of transforming this hollow rubber barrel into the familiar tire shape is called "lifting". This process involves the insertion of the lifting pressure bag into the rubber cylinder ~~now~~ as above, insertion of the rubber barrel into the lifting fixture, expansion of the lifting bag by air pressure and compressing the beads together to form the familiar tire shape. Before the tire is inserted into the curing mold the pressure bag is removed. Thus the terminology has developed of the bagging and debagging operations. This so called lifting process is accomplished automatically and subjects the uncured tire to severe deformation and shear. This step also requires that the rubber compounds used have very good building tack in order that the tire hold together instead of simply coming apart at the seams. In many tire operations the lifting pressure bag is used as the curing bladder to contain the steam during curing of the tire. After this procedure the tire is then inserted into the split curing mold, the clam shell curing press is closed and the internal and external heat and pressure are applied. After curing only minor trimming of vent plugs and final inspection are necessary prior to tire usage.

III. CONVENTIONAL TIRE

Disadvantages

In several analyses of the materials requirements of advanced and conventional aircraft systems the need for improved tires was indicated. One of the specific improvements desired was increased flotation or contact area. Another desired feature was improved abrasion and cut resistance, a particularly important need for Limited War operations. Ways of achieving this latter goal involved the use of wire and other reinforcements which are heavy and increase the tire weight considerably. With the conventional tire one can only go so far in securing increased flotation simply because you can't allow large deflections without pulling the beads off of the wheel rims.

In the present tire all loads are transferred in a shear mode by the reinforcing cords to the steel wire bead bundles and thence to the wheel. It would be far more preferable that the loads be in a tension mode since the reinforcements are far stronger in this mode. As performance requirements of aircraft increase, as they

always do, the designer can deal with this in several ways. He can provide more and more bead bundles. This results in large or thick bead sections as can be seen in Figure 7A on the B-58 tire. This results in a massive build up of cord and rubber which prevents uniform sidewall deflections. This necessitates the use of filler stocks. The large bead section acts as heat sink under stress and temperature builds up in these areas. The thick bead sections act as hinge points and the resultant rocking or flexing about this hinge point imparts severe flexural fatigue conditions. As a consequence heat build up in the thick bead areas results in failure at the beads. This is one very common failure point in a tire. One can readily see that with the present tire very good adhesion at high temperatures under severe flexing is required. Success in achieving this adhesion with advanced materials has been poor.

The alternative to meeting increased loads and stresses with larger bead areas is to increase the number of tires. Some aircraft have as much as 28 tires. While this is a solution, it is not the most desirable one.

Present tires are made manually. The quality of the ply lay ups is dependant strictly on the skill of a man. There is no possible way to control orientation and to uniformly tension the cord reinforcements in the present ply lay up procedure. As a consequence the reinforcements are not being used to their maximum capability. Less than optimum results of using high strength filaments such as steel and glass are secured. With glass filaments to achieve success one must be able to uniformly tension the filaments during tire fabrication. This is not possible in the conventional aircraft tire. Because the present process involves a lot of manual labor tire fabrication time is very long. Ten hours is a typical fabrication time for an aircraft tire.

IV. CONTINUOUS CROSS SECTION TIRES

The disadvantages cited above inspired the thinking which resulted in the concept of the continuous cross section tire (toroidal tire). Figure 2 illustrates this design. There are certain features of this design and of the fabrication process that indicate that the disadvantages of the present tire can be overcome to a great degree.

V. FABRICATION AND DESIGN FEATURES

This design involves the adaption of filament winding techniques and their inherent reliability and reproducibility, to the problems involved in tire fabrication. Figure 2 shows the continuous rubber impregnated reinforcing cords (32 or 34) being wound onto a rubber lined (18) form or air cell (12). Item (16) is the internally contained bead retaining ring. By utilizing the filament winding process we can virtually automate carcass fabrication, eliminate the

manually performed forming and bagging steps, because the tire is fabricated in its final cured shape. We have essentially precision placed and uniformly pre-tensioned reinforcements which is very critical to the effective use of fiberglass or steel cord. This allows all of the cords to work together and share the loads. In other words the cords will be used efficiently. One could forecast that carcass production could be achieved in minutes rather than in many hours as is now the case. Thus eliminated are the thick beads and ply turn up areas which were previously noted as disadvantages of the conventional design and replaced them with an internally contained bead ring and continuous (uncut) reinforcing plies. In addition, this design eliminates the inflation transfer of loads by a shear mode to the wheel.

As can be seen almost all of the problem areas that were discussed for the conventional design have been eliminated. We have a configuration in which the reinforcements are continuous, carry inflation and vehicle braking loads in tension to the wheel and bead, has a cross section which is thin and nearly uniform in thickness and thus provides for uniform side wall deflection. The ability to provide increased contact areas is greatly increased because the tire can be deflected without danger of coming off of the wheel.

VI. MATERIALS

In the area of materials usage this concept allows the compounder to formulate his elastomers for performance rather than to be inhibited by the building tack and handling requirements as is presently the case. Many elastomeric compounds heretofore eliminated from tire construction may now be utilized. Elastomers in the form of emulsions and dispersions can be considered. Since we have eliminated ply turn ups and can control tensions we can now make use of the very strong and stiff reinforcements such as high strength glass and steel filaments. The advantages can be summarized. The thin, uniform cross section should eliminate bead heat build up failures and provide for uniform deflection in the entire side wall. Since this concept eliminated the rim seal the tire should have extreme deflection capabilities without loss of pressure. Also since the reinforcement is continuous, and uniformly tensioned the filament wound tire carcass should be much stronger than its conventional counterpart.

Considering these postulated advantages the Air Force Materials Laboratory embarked upon a contractual R & D feasibility study to demonstrate this tire design concept.

VII. EXPLORATORY APPLICATIONS PROGRAM

As a result of competitive bidding the Aerojet-General Tire Corp. was awarded a contractual program, the objective of which was

to demonstrate the feasibility, practicability and performance of this novel tire design concept. The program involved the design, fabrication and dynamometer test of 30x7.7 type VII (extra high pressure) 12 ply rated aircraft tire prototypes. In addition, the tire was to be mounted to a conventional aircraft wheel and was to be cured in conventional tire equipment. These compromises were made in an attempt to stay within rather limited funding and to provide rapid concept evaluation. Also as will be discussed the program was beset by a series of prototype quality limiting problems, all which could not possibly have been foreseen.

The design and fabrication concepts proposed for this exploratory work differed only in minor details from those set forth in the author's patent. Figure 3 shows the basic tire components; the filament wound carcass; the fiberglass bead ring; the air passage; the soluble plaster winding form; and the air retaining liner. Figure 4 shows the conventional and the filament wound inflated profiles side by side.

Figure 5 depicts a cross section of the filament wound prototype mounted on a conventional tubeless aircraft rim. This figure shows the inflation air passage, the fusable safety plug and the relation of the tire bead ring to the wheel flange. Figure 6 is a process flow sheet for the fabrication of the prototypes.

The soluble plaster winding form is fabricated using the sweep template fixture as shown in Figure 7. The completed mandrel ready for insertion of the fiberglass/epoxy bead ring is shown in Figure 8. The fiberglass/epoxy bead rings are filament wound onto the cylindrical mandrel as shown in Figure 9, cured in a hot air oven and then machined to final configuration. The mandrel and bead ring assembly are then covered with two layers of butyl rubber which form the air retaining liner. Two air passages and valve bodies are then installed 180° apart in the inner or rim side of the tire.

The rubber covered mandrel is then installed in the winding machine and wound with a pre-treated nylon 840/2 aircraft tire cord. Instead of winding with a rubber impregnated cord funding and time limitations dictated that we fabricate prototypes using bare cords and covering alternate layers of cord with sheet rubber material. A serious problem of air entrapment within the carcass was immediately recognized and continued to be a serious problem throughout the program.

Figure 10 shows the rubber covered mandrel mounted in the contractor furnished winding machine. The cord pattern normally 29 ends per inch has been widened for easy visibility. After the proper number of cord plies have been applied the carcass is ready for tread and sidewall rubber application. The cord pattern shown in Figure 10 is identical to that in the conventional design tire. This was done to allow us to utilize the off-the-shelf 30x7.7 tire as a control.

The winding completed, the tire, Figure 11, is mounted on a conventional tire building drum. Figure 12 shows the tire builder applying the flat tread slab to the tire carcass. This was another troublesome step. The tread slab, being intended for a conventional tire is flat. It is also quite thick and tough and would not readily conform to the shape of the filament wound tire. Figure 13 shows the excess rubber being trimmed. This step also allowed the entrapment of air within the carcass. After completion of the tire carcass building process the plaster mandrel is then dissolved out (Figure 14). This is accomplished using warm, dilute acetic acid. This step presently takes about one hour.

Figure 15 shows the tire, which has been leak checked with a halogen sniffer or detector, ready to be installed in the curing press. The prototypes were cured in a conventional 30x7.7 production mold, Figure 16. Pressure on the inner circumference of the tire (rim side) was obtained by the use of an internal curing ring, which is not shown in Figure 16. Figure 17 shows prototype #4 immediately after its extraction from the mold. The blisters which were quite a disheartening sight were subsequently repaired and the tire was dynamometer tested. Figure 18 shows tire #7 which looked perfect but would not hold air when mounted on the test wheel. Subsequently it was found that the bead ring was broken due to improper mold clearances. At least the trapped air problem was not evident here. Figure 19 shows a close up view of the wheel (rim) surface of the tire and the built in air passage.

Figure 20 shows prototype #8 after about 20-200 mph landings. The noise level on subsequent landing gradually increased until chunks of the tread flew off on the 26th landing. Small air voids between the tread and the carcass were responsible. Figure 20A shows a cross section of a filament wound prototype which shows entrapped air causing a relatively large blister and some smaller blisters in the outer carcass area under the tread. Trapped air will continue to be a problem until our fabrication procedure is upgraded to use a rubber pre-impregnated or precoated reinforcement. Figure 21 shows the typical high speed landing failure. It is planned to recap these tires for future testing where tread retention is not a serious problem. Figures 22 and 23 are X-ray photographs of voids and trapped air between the tread and the carcass of tire #4.

The tires were cured normally using 250 psig internal steam. In an attempt to reduce the trapped air in the carcass tire #10 was cured at 400 psig internal steam. However, the valve blew out after 40 minutes due to creep of the adhesive bond holding the valve in place caused by the higher stresses. The carcass of this tire was well formed with no evidence of trapped air in the carcass or under the tread.

Included in the testing program was the development of static load deflection curves for various tire inflation pressures.

Figure 23 shows that the load deflection curves of the conventional control and the filament wound prototype are essentially identical.

Tire carcass strength is determined by a wheel mounted hydro-burst test. The control tire burst at 720 psig. The production average is 650 psig. The two filament wound prototypes burst at 800 psig and 790 psig giving good "x" type breaks in the crown area. Carcass strength is a requirement for good dynamometer performance but alone it is not a guarantee of good performance. The prototypes qualify at least as to their strength.

Figure 24 shows the history of the prototypes involved in the contractual feasibility study.

Figure 25 compares the conventional control and the filament wound prototype dimensions with the static specification requirements. The only really serious discrepancy is in the balance category. No attempt was made to obtain specification balance in the prototypes. No serious problems would be anticipated in securing adequate balance.

All in all considering the level of effort and the compromises involved due to the adaption of conventional equipment and processes to this not so conventional tire the feasibility demonstration must be considered quite successful. Tire #12 survived 38 low speed high energy absorption landings before a leak in the liner developed and the testing was concluded.

Once the processing problems have been overcome and good quality prototypes become available we will be able to do extensive dynamometer testing. This work may uncover other weak spots that are not now foreseen; but the full potential of the new design will be conclusively demonstrated.

VIII. POTENTIAL PAYOFF OF THIS NEW TIRE DESIGN

Large Size Tires

It is anticipated that the filament wound tire, when fabricated in the C-5A size (49" x 17") will show about 20% weight savings over the conventional tire without loss of performance. In addition these tires may be operated at very low pressures without danger of coming off of the wheel, because they do not depend on internal pressure to remain on the wheel. This capability could be very valuable to Limited War support operations, where it is required that large aircraft have the capability to land on relatively soft runways with minimum danger of tire failure. The tire can be made to fit standard wheels so that no retrofit will be required. Also considering that reinforcements such as glass and steel filaments, which are much stronger than nylon, could be effectively utilized, greater weight savings over nylon are potentially available.

Heat Resistance

Attempts to fabricate tires of increased heat resistance to date have merely involved the use of improved elastomers and reinforcements in the conventional design. As previously discussed the conventional design seriously penalizes the presently available, heat resistant elastomers and reinforcements. This new concept is tailor made to effectively utilize the heat resistant elastomers such as resin cured butyl, the silicones or the vitons, and the heat resistant reinforcements such as steel cord or glass or carbon filaments. It is anticipated that advanced manned aircraft will require tires that are more heat resistant than the nylon/natural rubber tires that are now on the B-70. Tires fabricated from the above materials could withstand temperatures of from 400°F to 500°F for relatively long periods of time.

Spin-Off Applications

The tire design concept as outlined should have many military applications other than for aircraft. It should make possible a high speed, all terrain vehicle which would be capable of varying its tire pressure almost to zero without loss of the tire from the wheel thus providing a good "get home" capability. Also truck and other heavy duty tires for Limited War applications could be fabricated using extreme cut and abrasion resistant elastomers, in radial ply constructions.

IX. SUMMARY

This paper has reviewed the circumstances and thinking that lead to the invention of the continuous cross section, filament wound tire. The advantages and potential of this novel design and tire configuration as compared to conventional tires have been discussed. Figure 27 is a brief review of the conventional tire problem areas that we think we have solved. Figures 28 and 29 review the performance and materials utilization advantages that will accrue through the perfection of this design. In addition to all of these advantages this concept lends itself to completely automated fabrication. The carcass will be completely formed in the filament winding machine as shown in Figure 30. Recently the AMF Co. has introduced a new machine tire recapping process called "ORBITREAD". This machine can be programmed to automatically apply the tread and sidewall stock to the filament wound tire. Figure 31 shows a rough concept of how this operation might look. The "ORBITREAD" process will be evaluated in our FY67 contractual effort. The incorporation of this step will result in a truly automated process which could eventually result in better quality and lower cost tires.

It should be noted that the author has received Patent #3,171,462 for the invention of this tire.

REFERENCES

1. WADD-TN-60-195
2. RTD-TR-63-7013
3. AFML-TR-66-154
4. Private conversations with many industry and government tire experts

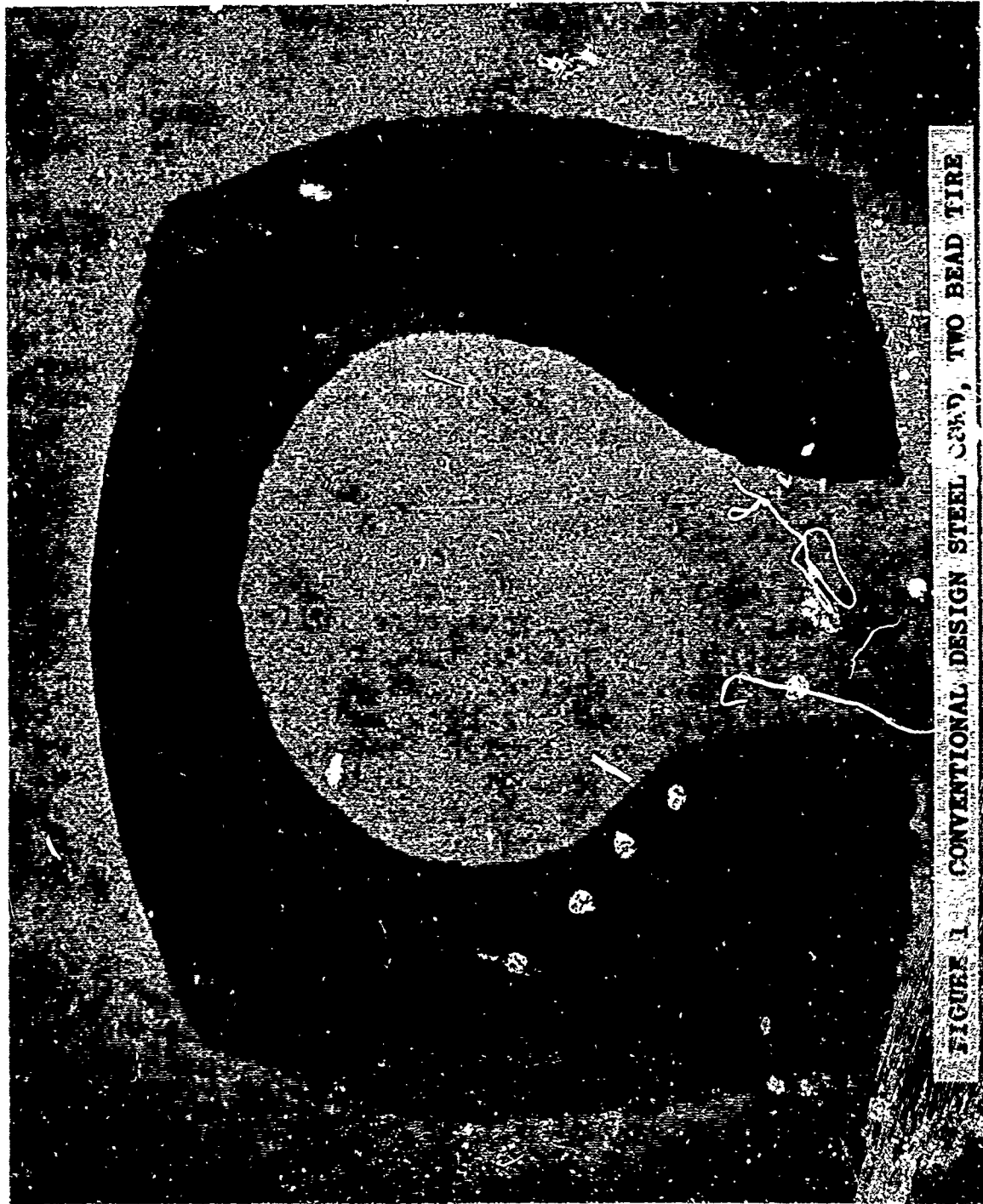


FIGURE 1 CONVENTIONAL DESIGN STEEL CORED, TWO BEAD TIRE

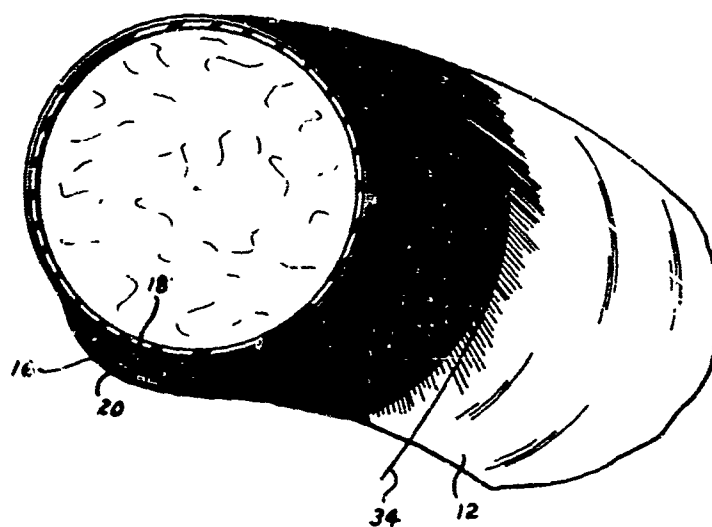
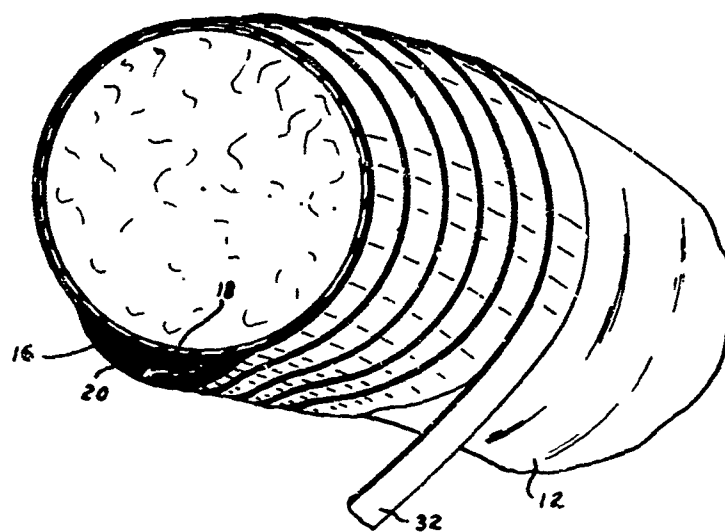


FIGURE 2 ORIGINAL CONCEPT PATENT DRAWINGS OF FILAMENT WOUND CARCASS CONFIGURATION

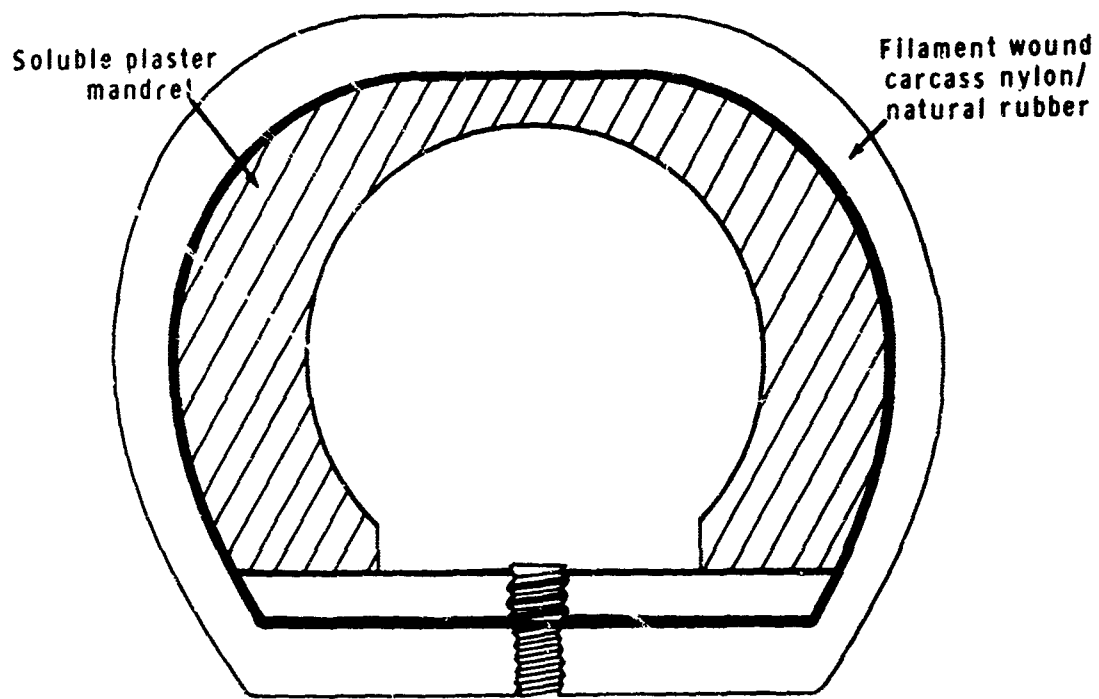


FIGURE 3 BASIC FILAMENT WOUND TIRE ASSEMBLY

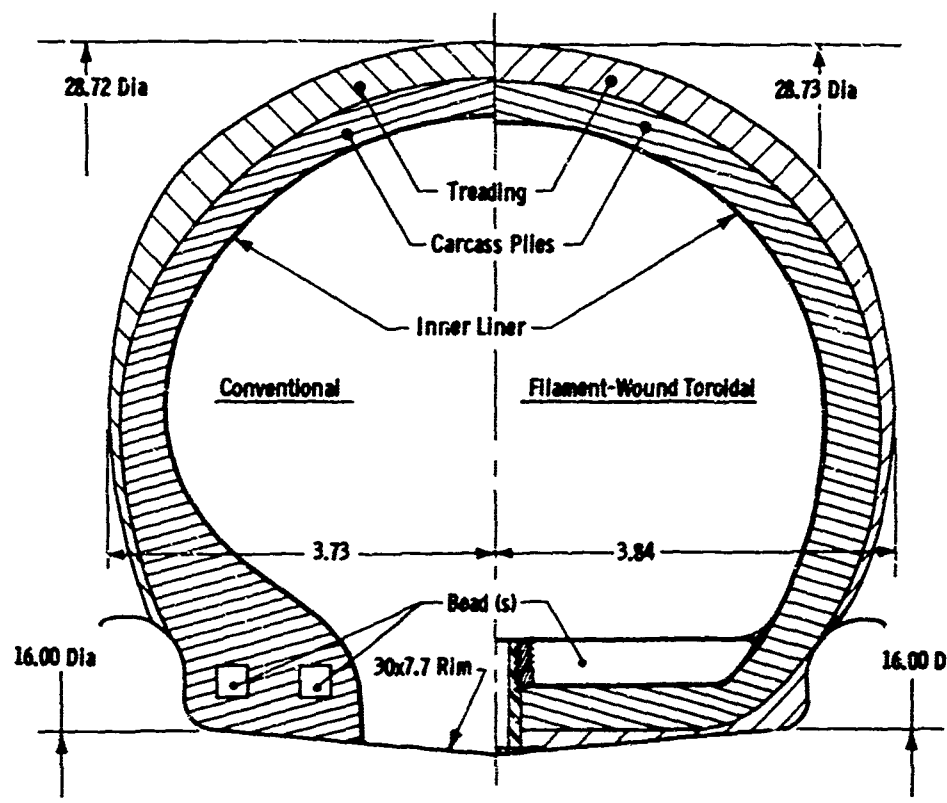


FIGURE 4 INFLATES PROFILES OF CONVENTIONAL AND FILAMENT WOUND TIRES

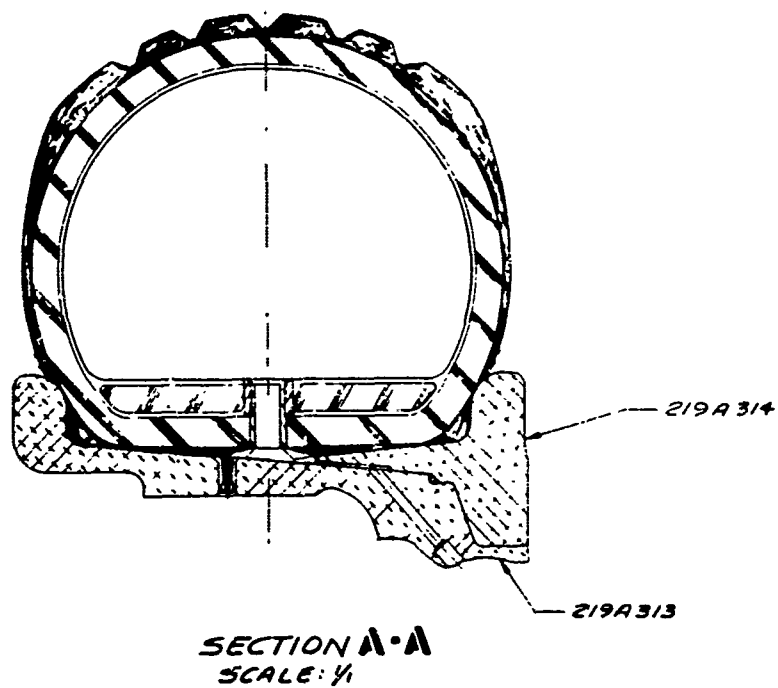
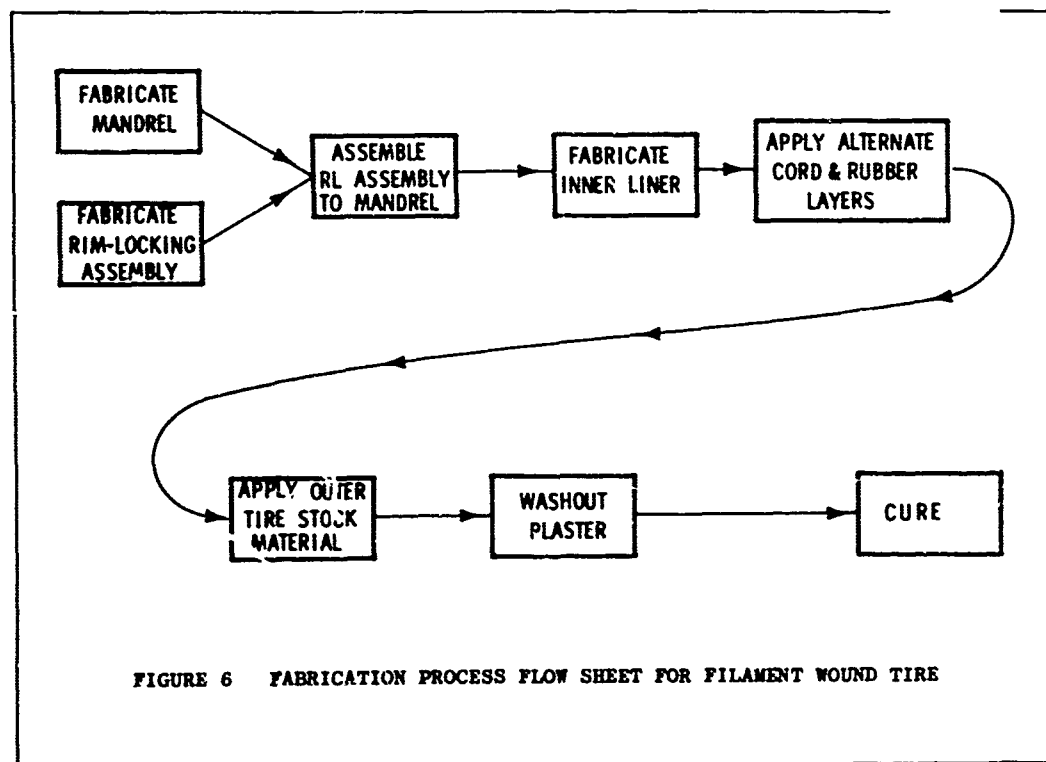


FIGURE 5 CROSS SECTION OF FILAMENT WOUND TIRE ON AN AIRCRAFT WHEEL



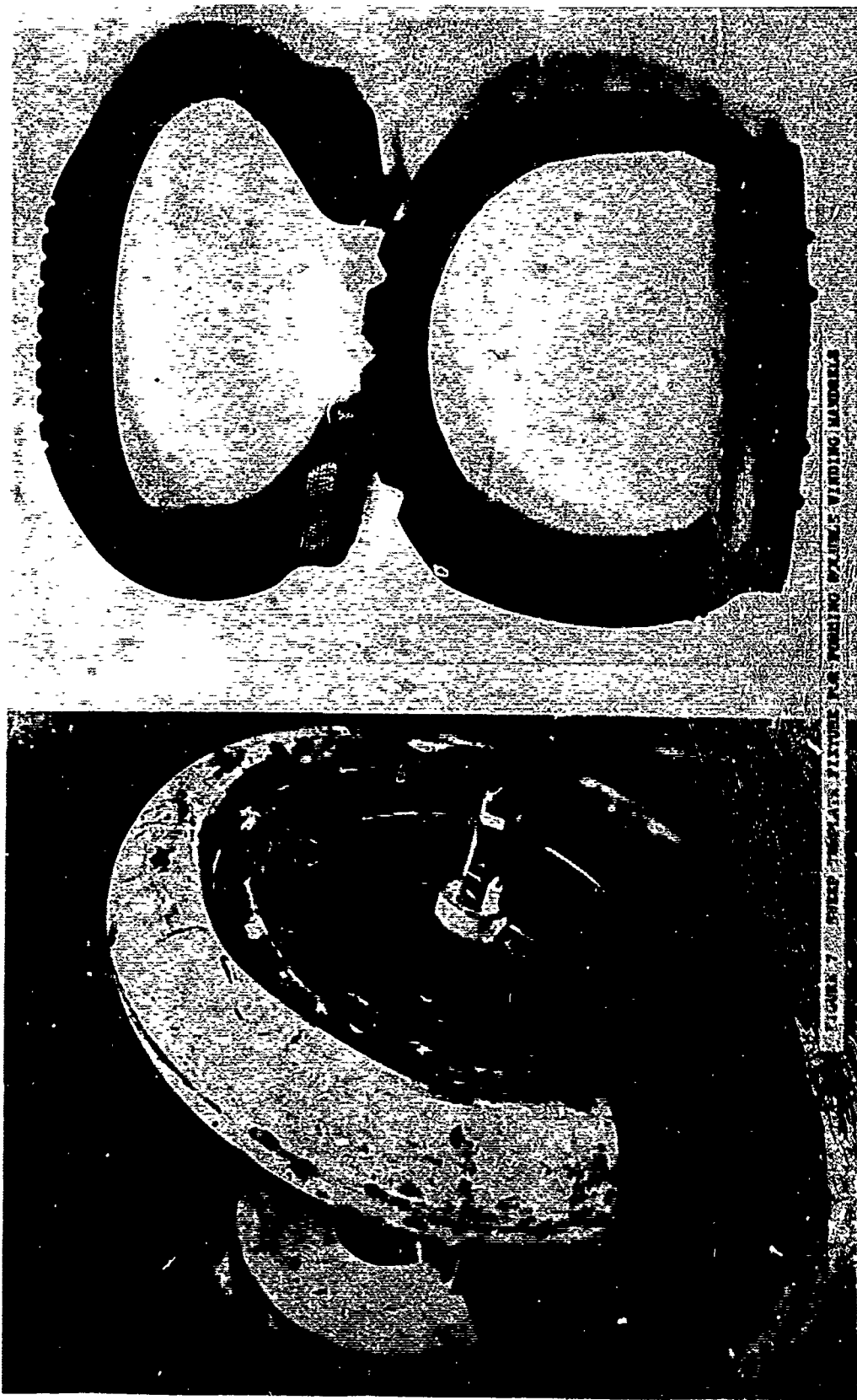
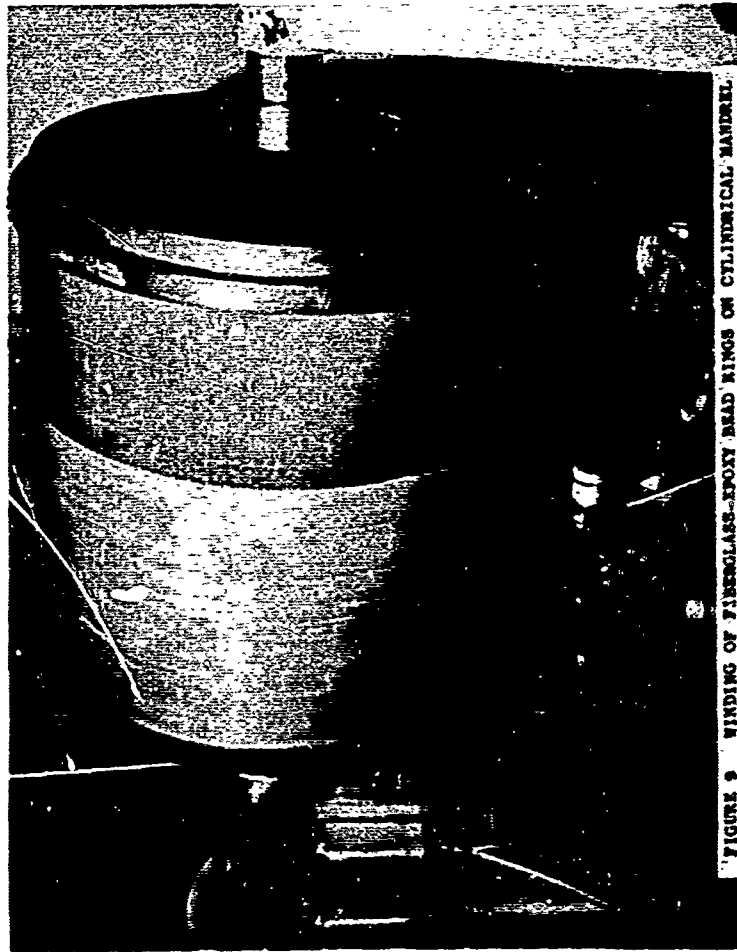
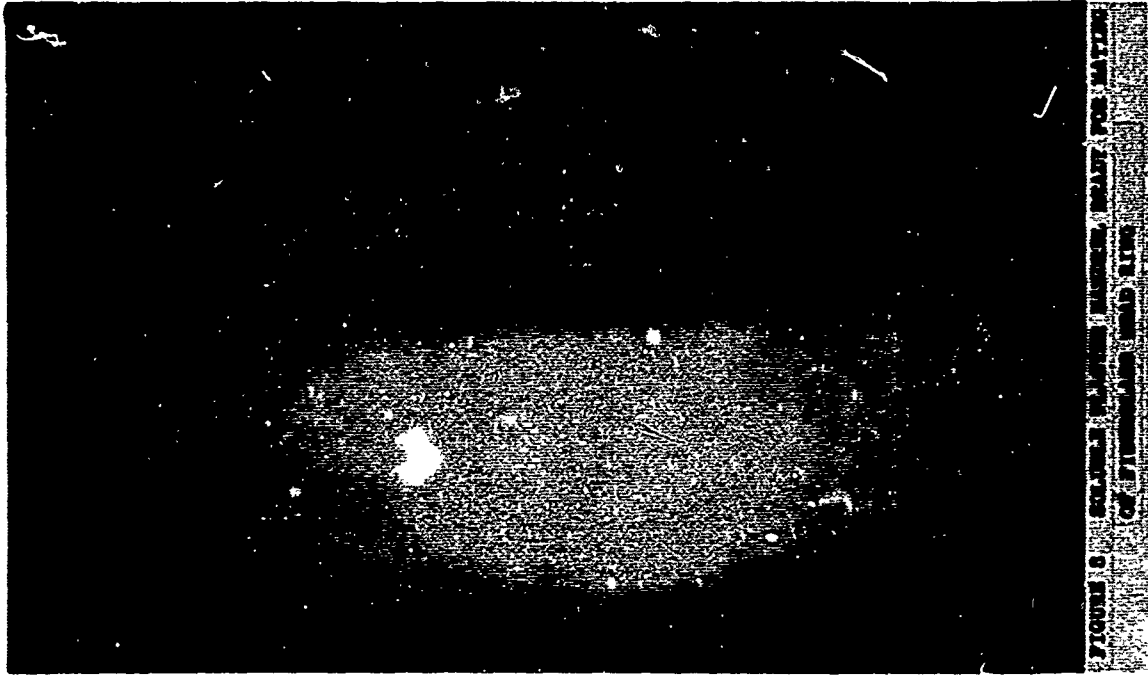


FIGURE 7. OPEN AND CLOSED STATES OF THE DEVICE



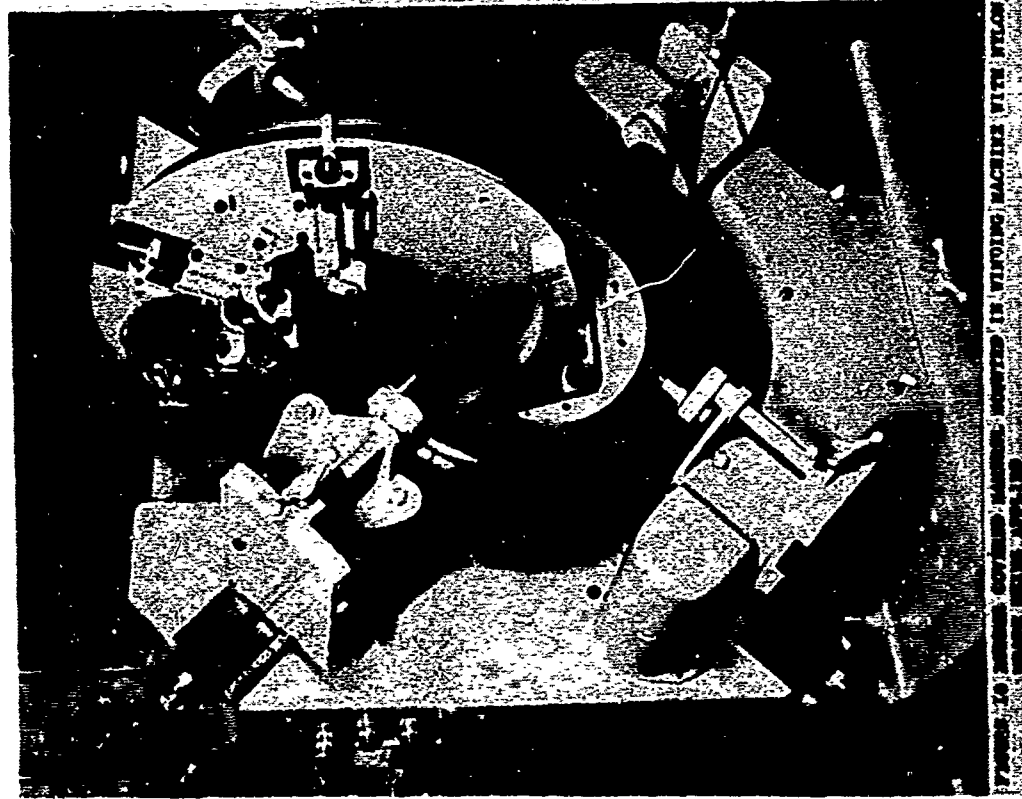


FIGURE 10. WIRE MACHINE. WIRE MACHINE IS WINDING MACHINE WITH WIRE

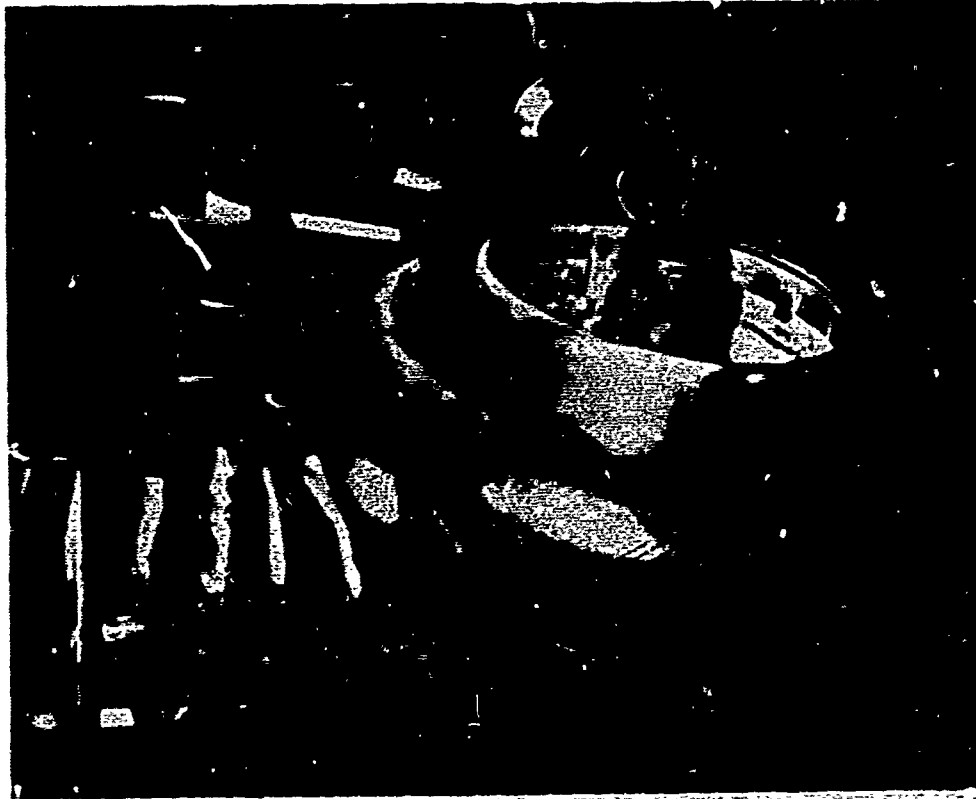
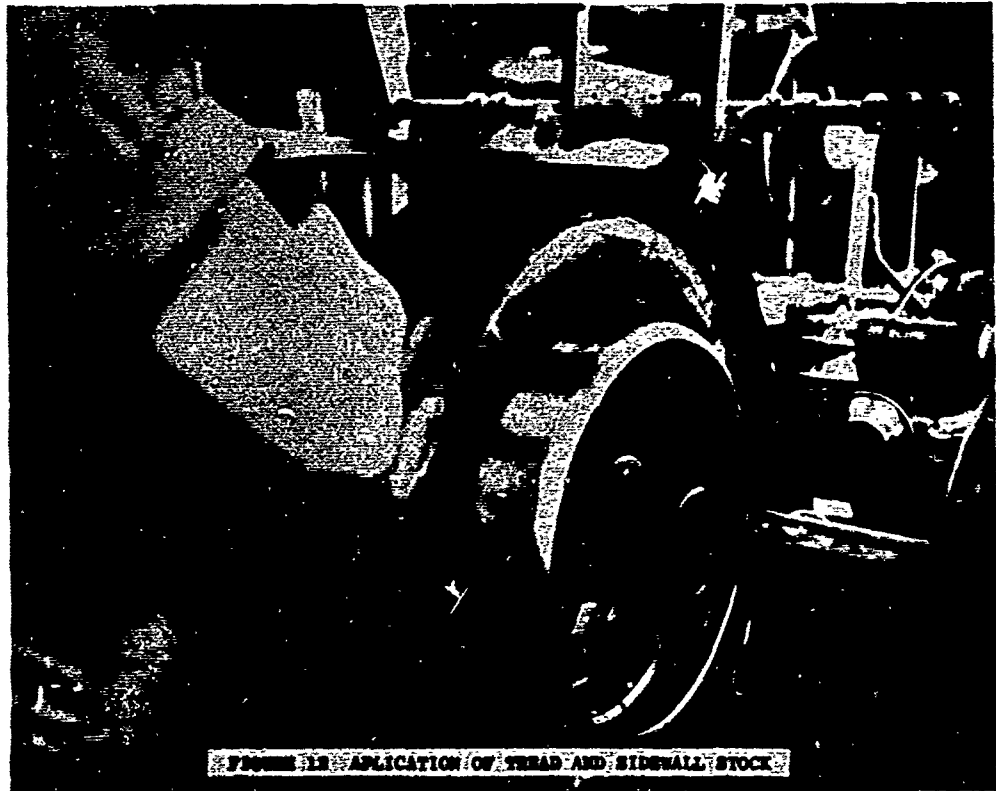
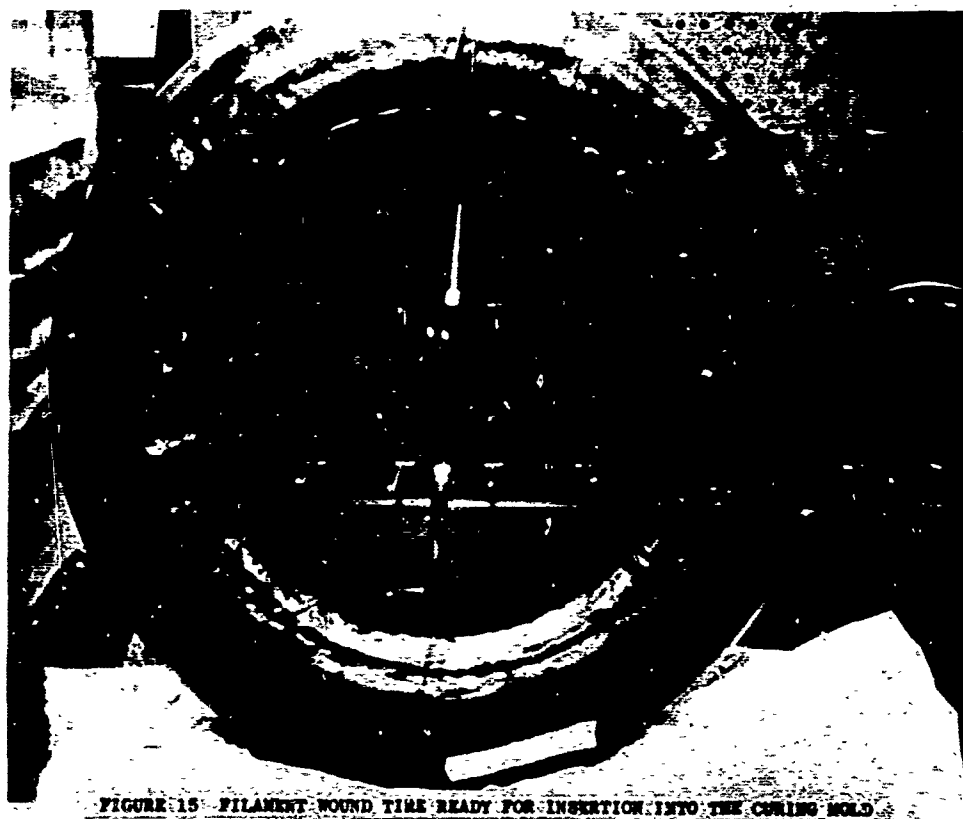
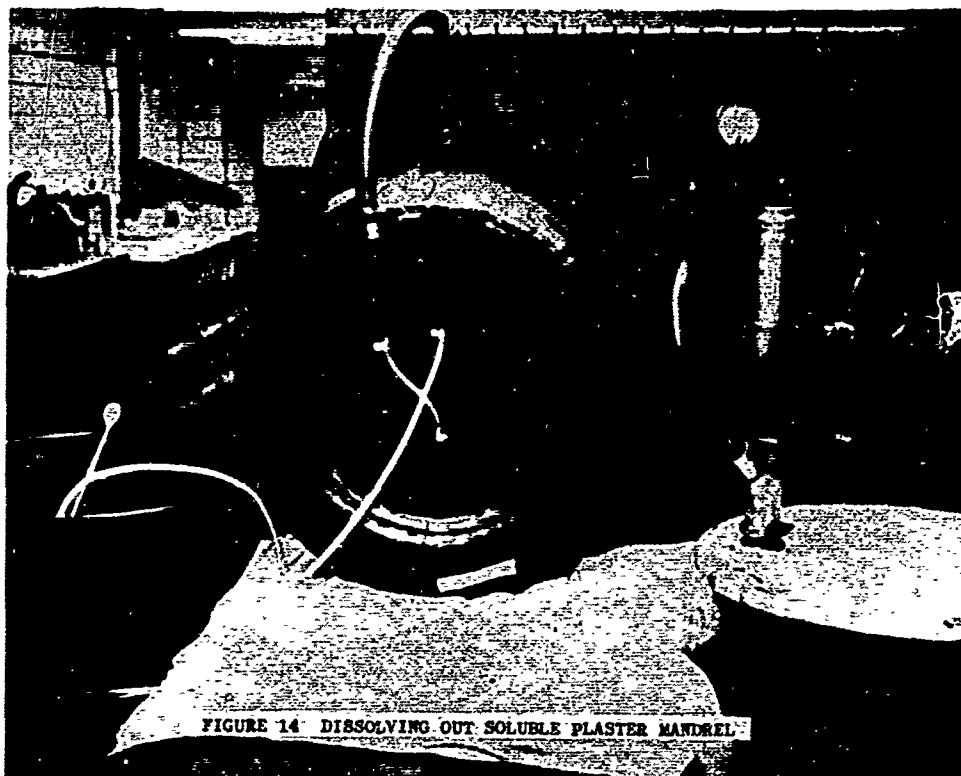
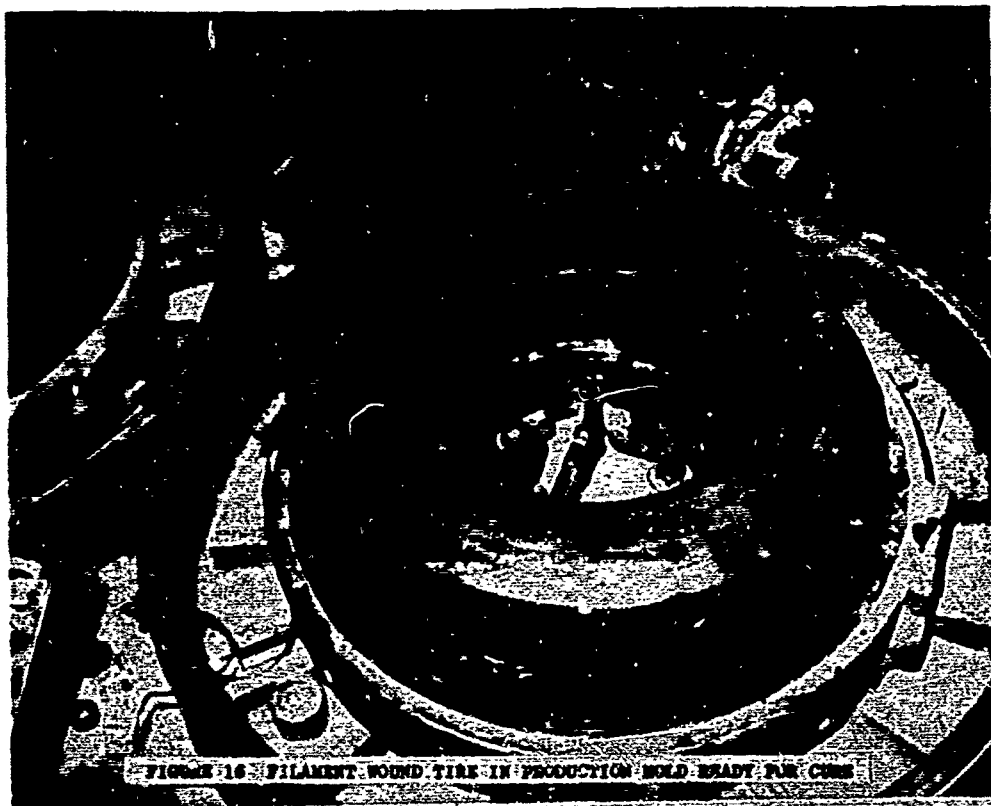
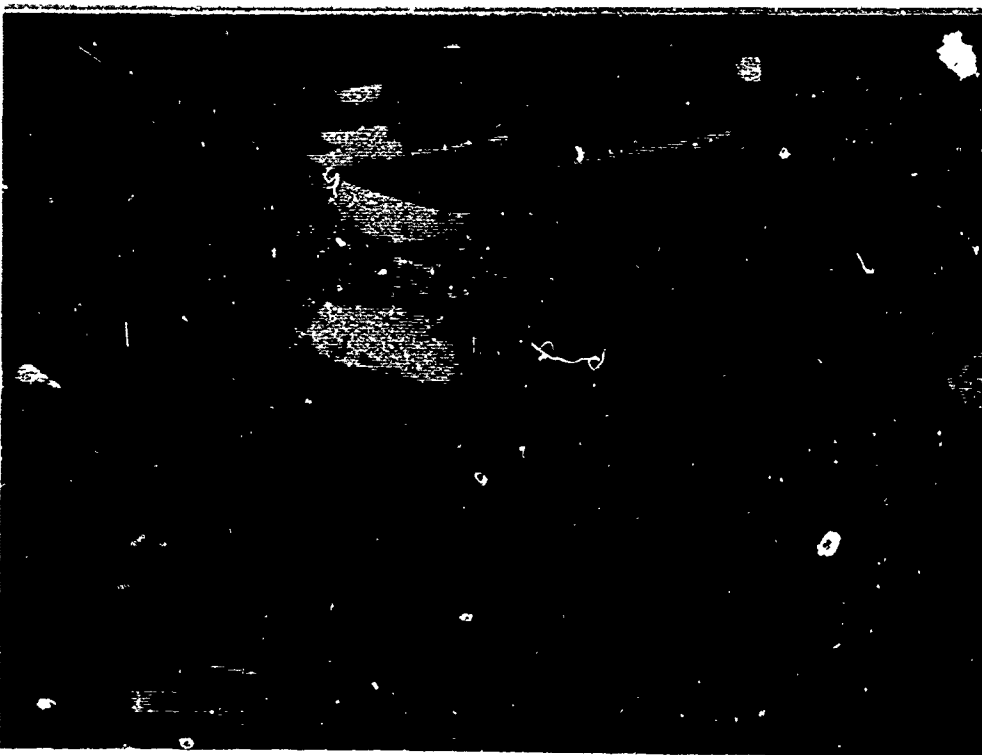


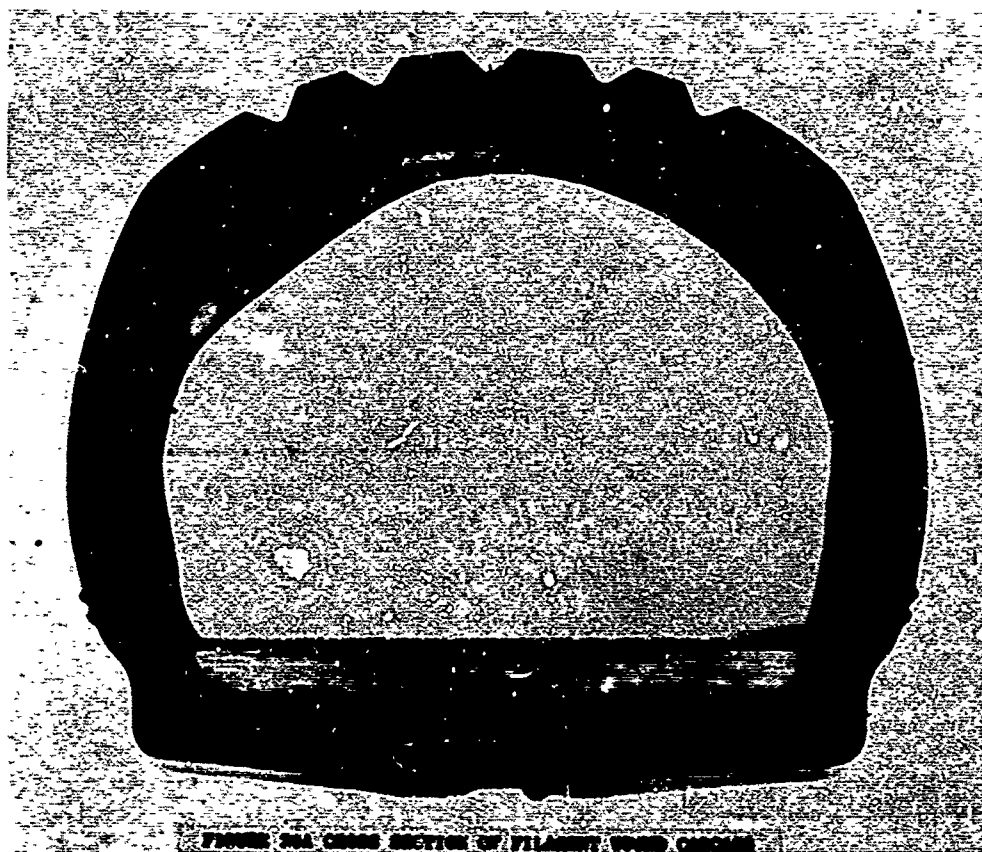
FIGURE 11. COMPLETELY BOUND CARCASS READY FOR TREAD AND SIFTALL











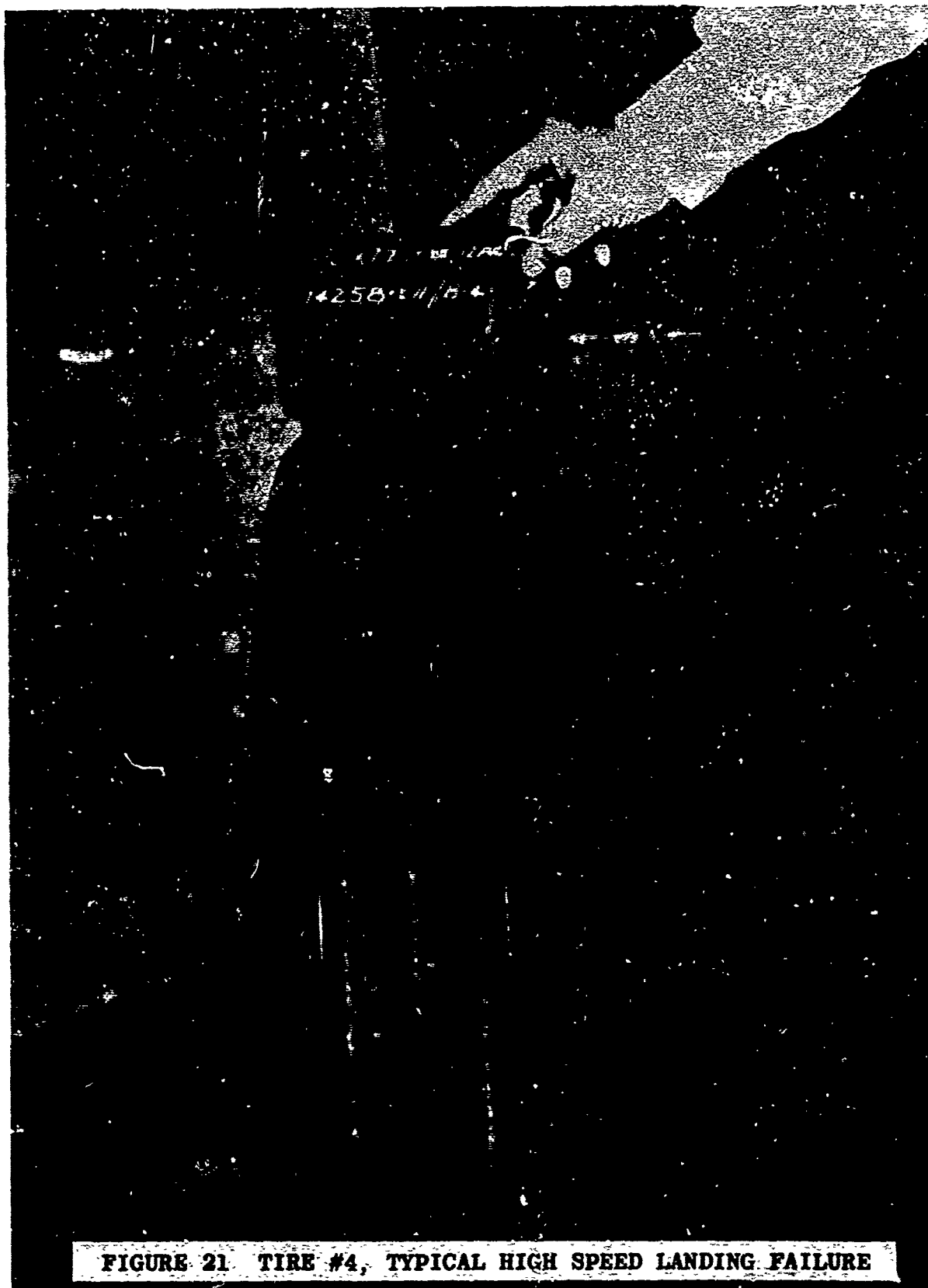


FIGURE 21. TIRE #4, TYPICAL HIGH SPEED LANDING FAILURE

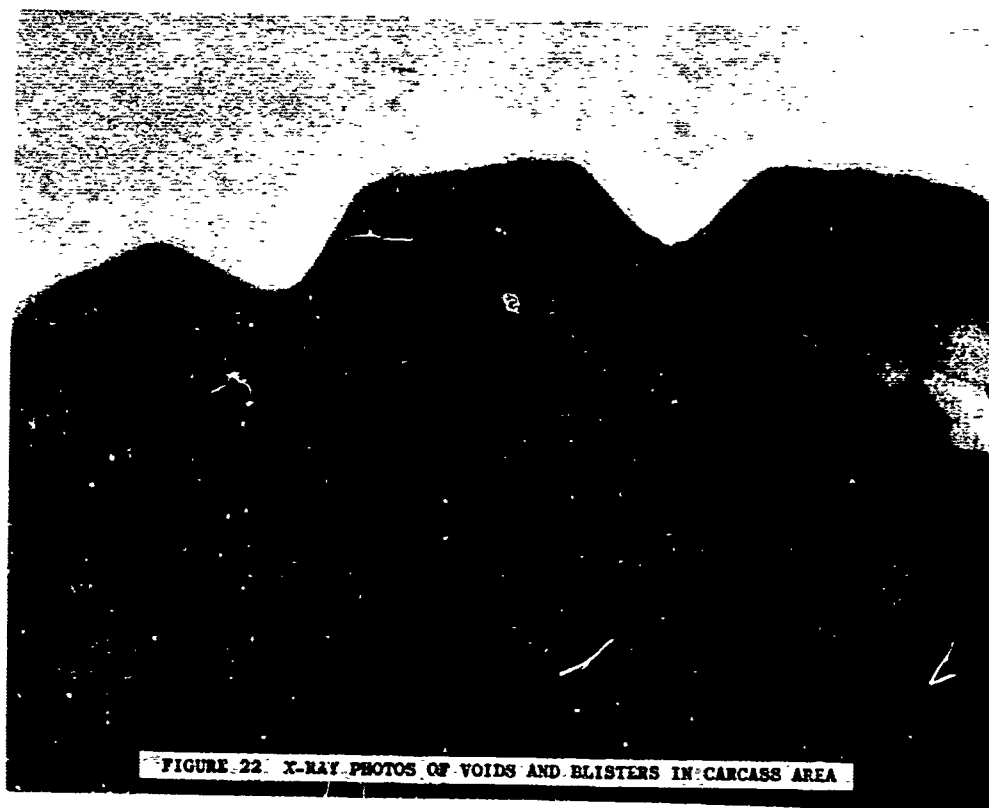


FIGURE 22. X-RAY PHOTOS OF VOIDS AND BLISTERS IN CARCASS AREA

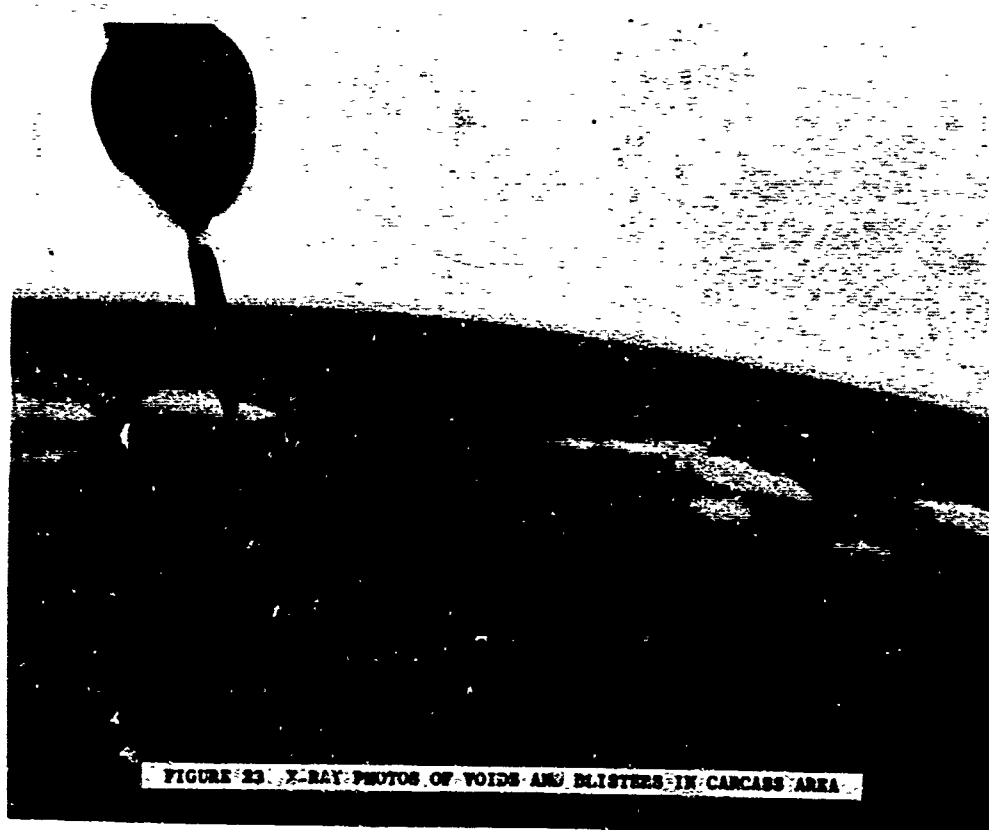


FIGURE 23. X-RAY PHOTOS OF VOIDS AND BLISTERS IN CARCASS AREA

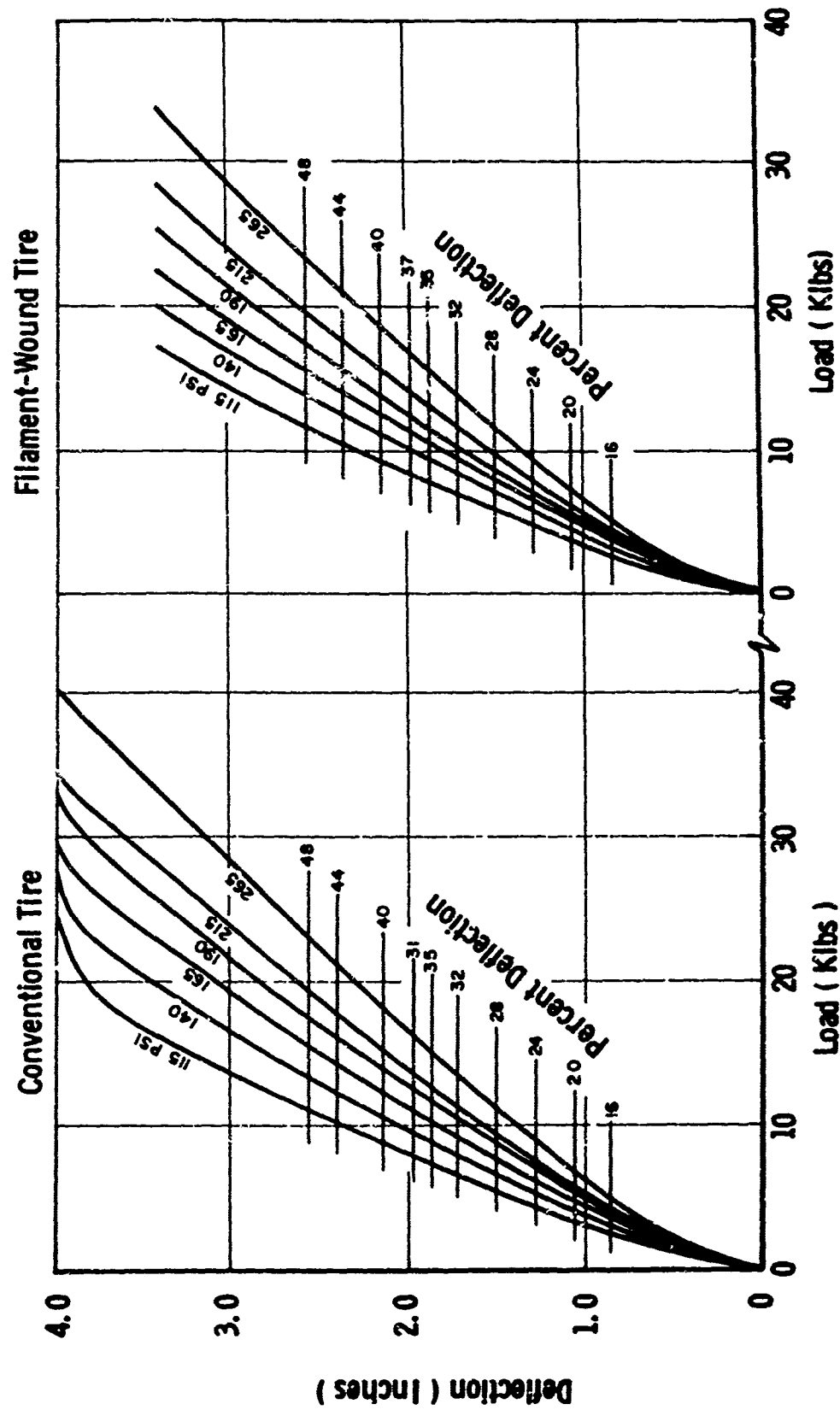


FIGURE 24 STATIC LOAD DEFLECTION CURVES OF CONTROL AND FILAMENT WOUND PROTOTYPE

Tire Chronology - Contract AF. 33(615)-2315

Tire	History
# 1	Blew during cure (punctured liner)
# 2	Multiple blows (blisters) between tread and carcass (trapped air)
# 3	Multiple blows (blisters) between tread and carcass (trapped air)
# 4	Multiple blows (blisters) between tread and carcass (trapped air) tire was repaired, lasted 4,200 mph landings and lost its tread. Tire carcass still intact.
# 5	Plaster mandrel damaged during handling at Aerojet, tire did not survive cure due to punctured liner.
# 6	Fiberglass bead ring cracked during cure, tire would not hold air when mounted on wheel. Sectioning showed carcass to be of good quality.
# 7	(Same as # 6) except tire was not sectioned.
# 8	Visually, tire looks perfect, no leaks, blisters and dimensionally good. Survived 26,200 mph landing cycles before tread chunked out. Carcass is intact, tire is repairable.
# 9	Tire blew during cure (valve and beadrings cracked due to improper mold clearances (same as # 6 and # 7)
#10	In fabrication. (Valve blew out during cure 1st 400 psig cure)
#11	Tire blew during cure due to faulty liner - liner was fabricated with overage rubber which failed to bond together at the seams (new valve concept - 400 psig cure)
#12	Prototype visually perfect, loose valve necessitated cutting of cords in carcass area to tighten locking nut. Affect of cut cords on carcass strength is not presently known.

FIGURE 25 HISTORY OF FILAMENT WOUND PROTOTYPES FABRICATED AND TESTED IN FEASIBILITY PROGRAM

STATIC TEST DATA FOR 30 x 7.7, TYPE VII TIRES

Item	Specification	Conventional	Toroidal
Size	30 x 7.7 T-VII	30 x 7.7 T-VII	30 x 7.7 T-VII
Ply rating	12	12	12
Tubeless Weight (lb)	42.5 (maximum)	39.5	42.5
Rated inflation (psi)	165	165	165
Rated load (lb)	10,000	10,000	10,000
Static unbalance	19	17	49 to 105
Burst pressure (psi)	580 (minimum)	720 (bead)	800 (crown)
Outside diameter (in.)	28.60 - 29.40	28.72	28.73
Section width (in.)	7.40 - 7.85	7.46	7.68
Shoulder width (in.)	6.95 (maximum)	5.40	5.70
at diameter (in.)	26.90	26.90	25.23
Bead seat pressure (psi)	50 - 165	120	N/A
Rated conditions:			
% Deflections	28 - 35	33.04	33.55
Inch deflection	-	1.771	1.80
Static loaded radius	-	12.59	12.57
Contact area (sq in.)	-	61.4	61.7

FIGURE 26 COMPARISON OF CONTROL AND FILAMENT WOUND TIRE DIMENSIONS TO SPECIFICATION VALUES

ADVANTAGES OR IMPROVEMENTS OVER CONVENTIONAL TIRE DESIGNS

FABRICATION

1. AUTOMATIC FABRICATION
2. IMPROVED REPRODUCIBILITY
3. UTILIZATION OF WIDER VARIETY OF RAW MATERIALS
4. ELIMINATION OF FORMING, BAGGING AND DEBAGGING OPERATION
5. IMPROVED CONTROL OVER REINFORCEMENT ORIENTATION
6. ELIMINATION OF BEAD PULL DOWN DURING CURE
7. ELIMINATION OF FATIGUE AND CHAFFING HINGE PT. IN BEAD AREA
8. RAPID TIRE FABRICATION
9. ELIMINATION OF PLY TURNUPS AROUND THE BEAD

FIGURE 27 LIST OF ADVANTAGES OR IMPROVEMENTS OVER CONVENTIONAL DESIGNS

PERFORMANCE

1. ELIMINATION OF BEAD PULL OUT DURING HIGH TEMP.
HIGH PRESS. OPERATION
2. EXTREME DEFLECTION CAPABILITIES IN TIRE
3. ELIMINATES RIM SEAL
4. MORE EFFICIENT USE OF REINFORCEMENT MATERIAL
5. MORE UNIFORM AND THINNER CROSS SECTION, GIVE LESS
HEAT BUILD UP

FIGURE 28 PERFORMANCE ADVANTAGES OVER CONVENTIONAL TIRES

MATERIALS

1. VERY LITTLE GREEN TACK REQUIRED IN ELASTOMER
2. VERY STIFF REINFORCEMENTS CAN BE USED (DUE TO ELIMINATION
OF PLY TURN UP)
3. LOW ADHESION AND LOW TEAR COMPOUNDS MAY BE USED
(BECAUSE ADHESION TO BEAD CPDS. NOT NEEDED)
(SILICONES, VITRONS, PESIN CURED BUTYLS)

FIGURE 29 FLEXIBLE MATERIALS UTILIZATION OF FILAMENT WOUND TIRE CONCEPT

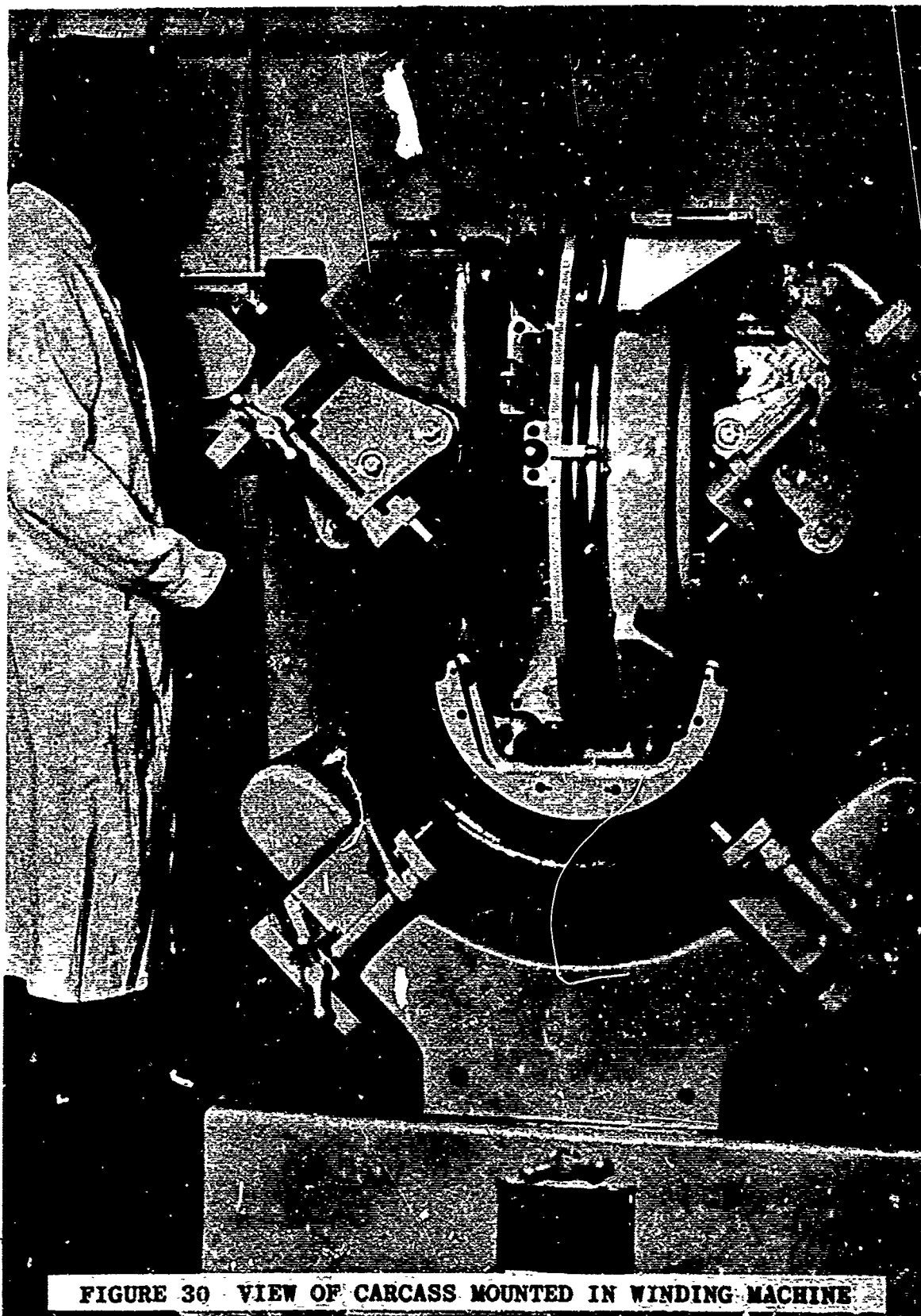


FIGURE 30 VIEW OF CARCASS MOUNTED IN WINDING MACHINE

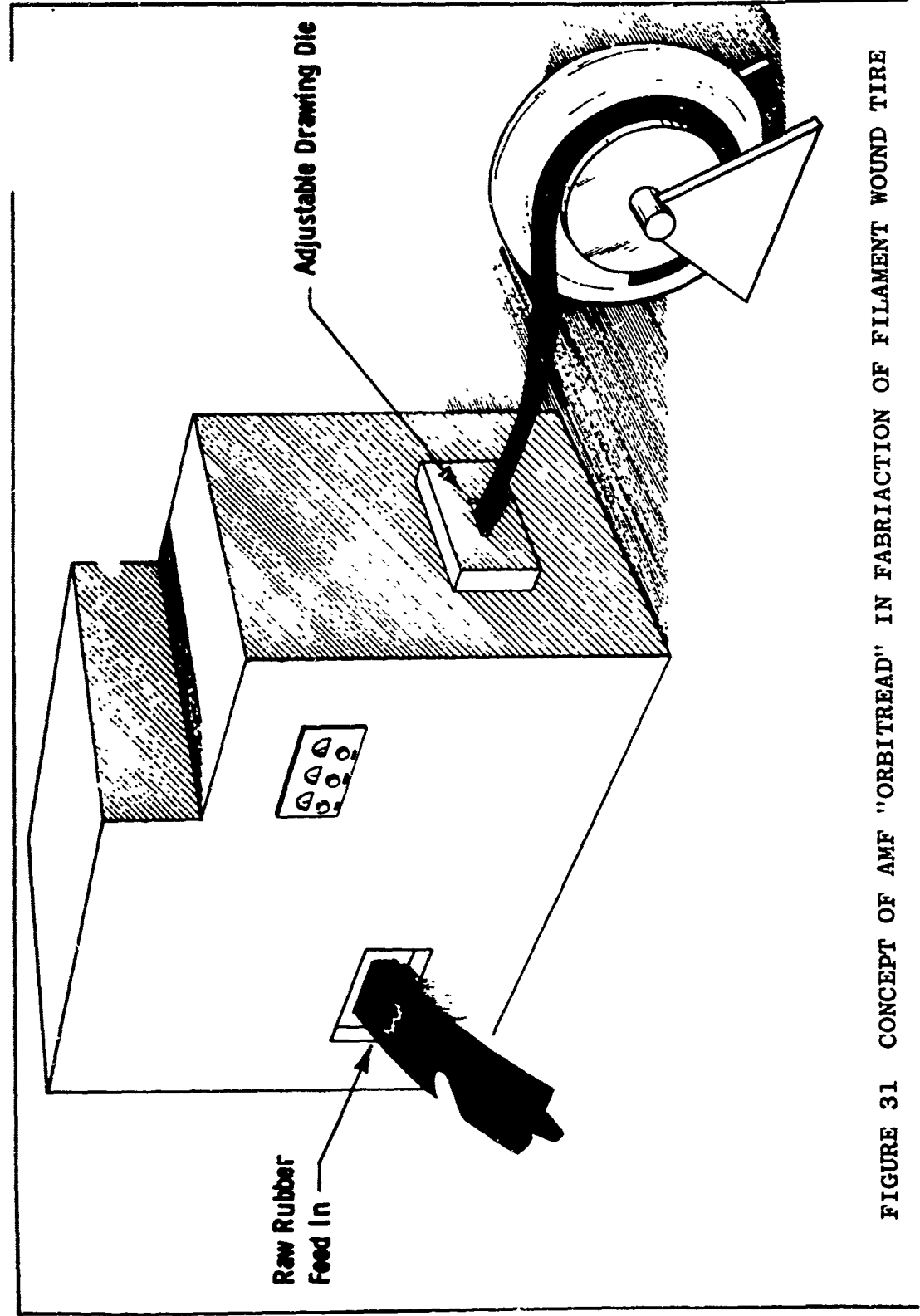


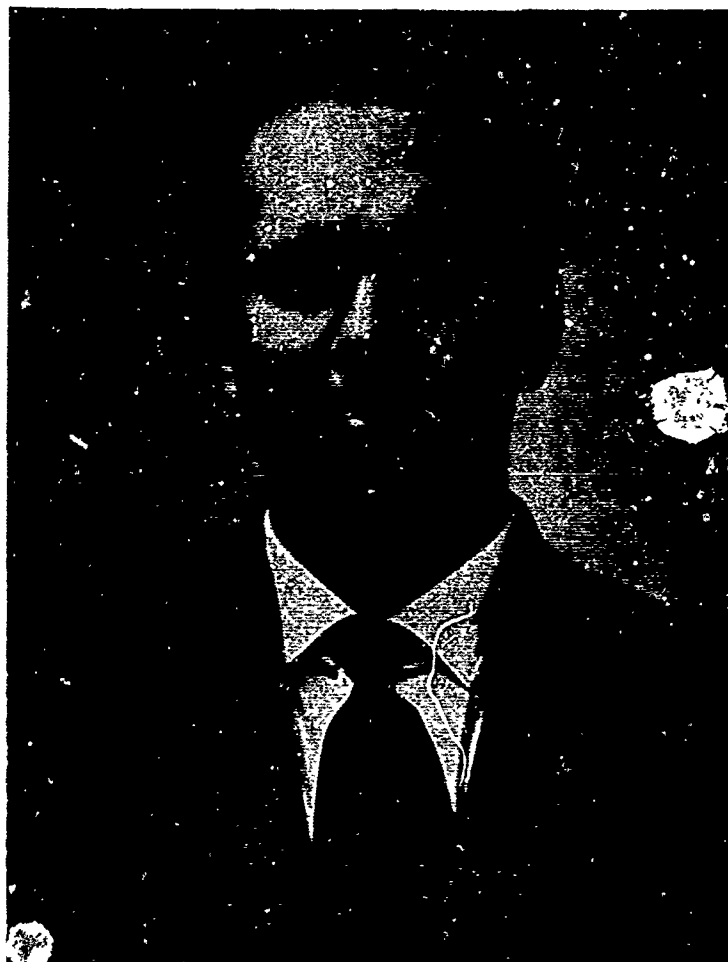
FIGURE 31 CONCEPT OF AMF "ORBITREAD" IN FABRIATION OF FILAMENT WOUND TIRE

(U) USE OF TUNED VISCOELASTIC DAMPERS
FOR REDUCTION OF VIBRATIONS IN AEROSPACE STRUCTURES

by

David I. G. Jones, Ph.D.
John P. Henderson, M.S.
George H. Bruns, 1/Lt, USAF

Strength and Dynamics Branch
Metals and Ceramics Division
Air Force Materials Laboratory
Wright-Patterson AFB, Ohio



David I. G. Jones

BIOGRAPHY

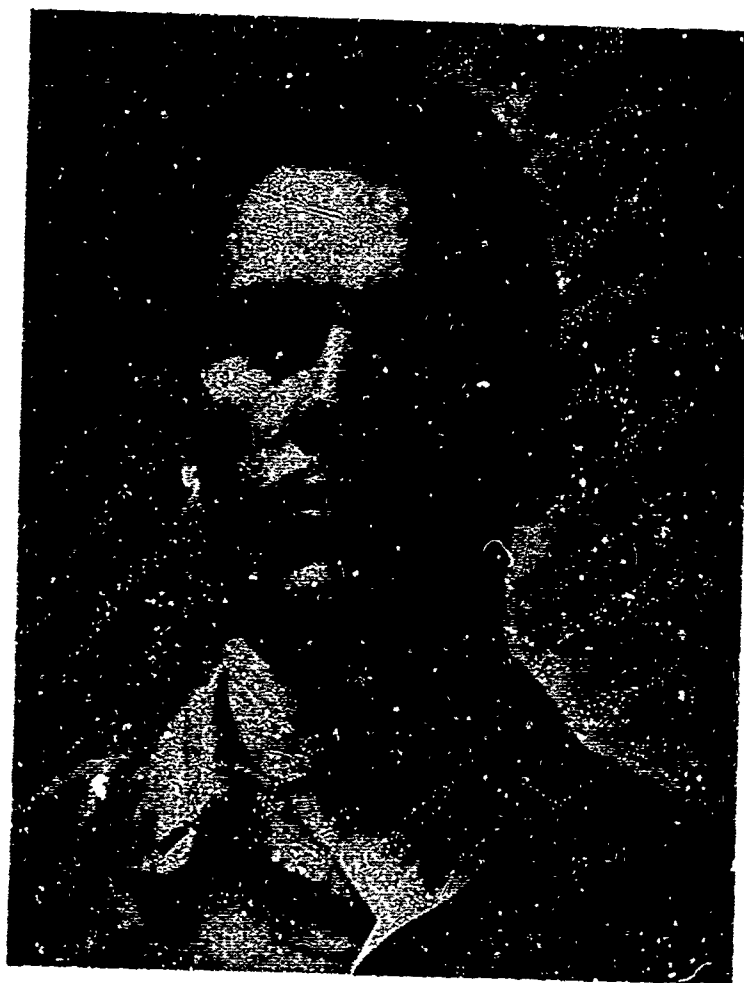
DAVID I. G. JONES was born in London, England, on 5 November 1936. He completed his High School education at Llandysul County Grammar School in Llandysul, Wales, in 1955, winning a State Scholarship to continue his education in Aeronautical Engineering, under Professor E. J. Richards, at Southampton University, Southampton, England. He received the degree of Bachelor of Science in Aeronautical Engineering with First Class Honours in 1958 and the degree of Doctor of Philosophy in Aeronautical Engineering in 1961. From January to July 1961 he completed the industrial experience requirement of his Graduate Apprenticeship in Aeronautical Engineering with Vickers - Armstrongs Ltd., Swindon, England. During this time he worked on the thermodynamics of nuclear reactor systems under contract with the United Kingdom Atomic Energy Authority. Between July 1961 and December 1963, he was a member of the Staff of the Hovercraft Division of the same company, where he developed techniques for the prediction of the internal aerodynamics of Ground Effect Vehicles and the dynamic response and damping over water and various types of terrain. Since January 1964 he has been directing an in-house research effort in the field of vibrations and damping at the Strength and Dynamics Branch of the Air Force Materials Laboratory, Wright-Patterson AFB, under the guidance of Mr. W. J. Trapp. He is a member of the Institute of Environmental Sciences.



John P. Henderson

BIOGRAPHY

JOHN P. HENDERSON was born on 3 September 1934 in Cleveland, Ohio. He graduated from Lakewood High School, Lakewood, Ohio in 1952 and received the degree of Bachelor of Science in Mechanical Engineering with Honors, from Case Institute of Technology, in 1956. From 1956 to 1957, he was a mechanical engineer at the Cincinnati Milling Machine Company. In 1957, he entered the United States Air Force as a lieutenant and, after serving as a maintenance officer in the Strategic Air Command, was assigned in 1959 to Wright Air Development Center, Wright-Patterson Air Force Base, Ohio, in the capacity of a project engineer. Since 1960, he has been engaged as a civilian engineer at Wright-Patterson Air Force Base, and has contributed to several projects including the development of ground run-up noise suppressors for jet engines and the design of a broad-band acoustic test facility. From 1962 to the present time, he has been active in research on vibrations and damping in the Air Force Materials Laboratory. In 1965 he received the degree of Master of Science from the Ohio State University through a part time study program, and is currently continuing his graduate studies. He is a member, and a past chapter president, of the Institute of Environmental Sciences.



Lt George H. Bruns

BIOGRAPHY

GEORGE H. BRUNS, III, was born in New York City on 14 December 1942. He completed his High School education at Pleasant Hill High School, Pleasant Hill, California in 1960 and went on to the United States Air Force Academy. He graduated with the degree of Bachelor of Science in 1964 and received a Commission into the United States Air Force. In 1964, he was assigned to the Strength and Dynamics Branch of the Air Force Materials Laboratory and has been conducting research in the field of vibrations and damping from that time. He has published several Air Force reports in this field. He is currently completing a part-time graduate study course at Ohio State University and will submit a thesis for the degree of Master of Science in the near future.

(U) USE OF TUNED VISCOELASTIC DAMPERS
FOR REDUCTION OF VIBRATIONS IN AEROSPACE STRUCTURES

David I. G. Jones, Ph.D.
John P. Henderson, M.S.
George H. Bruns, 1/Lt, USAF

ABSTRACT

The severe vibration levels encountered in modern aerospace vehicles as a result of the intense noise levels generated by rocket and jet engines frequently results in fatigue damage and equipment malfunction. Damping represents a useful tool for the reduction of such vibrations, and research is needed to develop both materials capable of dissipating the energy of vibration and methods of using these materials to best advantage.

Both the material and configuration aspects of this problem have been investigated at the Air Force Materials Laboratory, the main effort being concentrated on those areas which did not appear to be receiving adequate attention elsewhere. A damping technique which has shown considerable promise is the tuned viscoelastic damper. This is an offshoot of the well known classical vibration absorber. However, it is shown that the unique properties of several presently available viscoelastic materials have made it possible to design prototype tuned dampers which are not confined to operation at a single discrete frequency, but can operate over a band of frequencies suffi-

ciently wide to offer hope of application in present and future aerospace vehicles, where wide-band frequency response can often be anticipated. Analyses and experiments are briefly described which demonstrate the effectiveness of these prototype tuned dampers in simple structures and in more complex structures typical of aerospace applications. A case history of the application of this type of damper to an equipment failure problem in a modern aircraft is discussed.

SYMBOLS

A	Resonant amplification factor for structure under shaker excitation (boundaries moving)
A_1	Arbitrary constant
b	Breadth of beam. Also breadth of damper according to context.
B	Frequency ratio ω/ω_0 of applied harmonic excitation to natural frequency ω_0 of tuned damper.
B_1	Arbitrary constant
c	Constant
C_1	Arbitrary constant
Cos	Circular cosine function
Ch	Hyperbolic cosine function
D	Energy dissipated per cycle during harmonic deformation of viscoelastic material
D_1	Arbitrary constant
exp	Exponential function
E	Young's modulus
f	Frequency in cycles per second ($=\omega/2\pi$)
f_0	Natural frequency of tuned damper in cycles a second ($=\omega_0/2\pi$)
F_a	Amplitude of cyclic force generated by impedance head
$F(\eta)$	Function of loss factor η [Equation (20)]
F	Force tending to deform viscoelastic spring in tuned damper. Also force transmitted back to structure by tuned damper.
g	Acceleration due to gravity

G	Real part of shear modulus of viscoelastic material
h	Thickness of beam
h_D	Thickness of metal part of cantilever damper beam
h_0	Initial thickness of beam
\cdot	Function of ξ and x/L [Equation (6)]
i	Square root of -1
I	Second moment of area of beam cross section about neutral axis
J	$\cos \xi \operatorname{Sh} \xi - \operatorname{Ch} \xi \sin \xi$
k	Real part of stiffness of viscoelastic spring
L	Length of beam
ℓ	Length of cantilever damper beam or circumference of ring damper
m	Mass of tuned damper
M	Bending moment
M_1	Effective mass of impedance head
n	Mode number of simple structure
p	Instantaneous value of applied loading
P	Amplitude of exciting force at free end of cantilever
$P(x)$	Amplitude of loading on beam
P_n	n th term in expansion of $P(x)$ as series of undamped normal modes of simple structure
p^2	Power spectral density of input force under random excitation
Q	Resonant amplification factor for simple structure under excitation by a force (boundaries fixed in space)
R	Radius of curvature of vibrating beam $[= (d^2W/dx^2)^{-1}]$

S	Shear load carrying area for tuned damper
\sin	Circular sine function
Sh	Hyperbolic sine function
U	Maximum strain energy stored in structure during harmonic oscillation
u	Instantaneous transverse displacement relative to fixed point in space
w	Instantaneous transverse displacement of beam relative to a fixed end
$W(x)$	Amplitude of transverse displacement of beam w
\bar{W}	Root mean square displacement of beam under random excitation
x	Station along beam measured from clamped end
x_0	Particular station along beam
X	Amplitude of harmonic input displacement produced by electrodynamic shaker in shaker tests
x_r	Instantaneous relative displacement between ends of viscoelastic spring in tuned damper
$U(x)$	Amplitude of u
X_n	n th term in expansion of X as series of normal modes
x_r	Amplitude of x_r
y	Instantaneous displacement of mass m of tuned damper
z	Distance from neutral axis of beam, measured normal to beam length
Z	Function of ξ , ψ , Γ and η [Equation (5)]
Z_r	Real part of Z
Z_i	Imaginary part of Z

α	Phase angle between input displacement X and x_r for tuned damper or constant for beam on shaker
γ	Phase angle between exciting force and observed acceleration at same point of damper
Γ	kL^3/EI (Stiffness parameter)
δ	Dirac Delta function
η	Loss factor of viscoelastic material of tuned damper
η_s	Effective loss factor of beam-tuned damper system
η_o	Initial loss factor of nominally undamped structure
λ	$(\mu\omega^2/EI)^{1/4}$
ν	Mass per unit length of beam
ξ	$(\mu\omega^2L^4/EI)^{1/4}$ (frequency parameter)
ξ_n	$(\mu\omega_n^2L^4/EI)^{1/4}$ - nth eigenvalue of simple structure
π	3.14159 - - -
ρ	Density of beam material
σ	Bending stress in beam
σ_{max}	Maximum bending stress at point in beam (on surface)
$\bar{\sigma}$	Root mean square bending stress under random excitation
$\bar{\sigma}_{max}$	Root mean square surface bending stress in beam under random excitation
τ	Thickness of viscoelastic material
ϕ_n	n th normal mode of simple structure
ϕ_n''	Normalized second derivative of ϕ_n with respect to x/L
ψ	$m/\mu L$ (mass parameter)
ω	Circular excitation frequency
ω_o	Natural circular frequency of tuned damper
ω_n	Natural frequency of n th normal mode of simple structure

INTRODUCTION

The main reason for the study of damping materials and configurations in the Air Force and elsewhere is the necessity for controlling the extreme vibrational environments encountered in many modern aerospace vehicles, with a view to improving the useful operational life and reducing equipment malfunctions. Viscoelastic materials, many of which dissipate large amounts of vibrational energy during deformation, represent a very powerful tool in the hands of those concerned with damping and its application in aerospace structures.

The aim of the in-house damping research program at the A.F. Materials Laboratory has been to supplement an extensive contractual program, and the work of other independent investigators, by evaluating those damping configurations which appeared to hold promise of useful practical application in the solution of pressing acoustical fatigue and other vibration problems and which did not appear to be under adequate investigation elsewhere.

One such configuration is the tuned viscoelastic damper. This represents an offshoot of the classical vibration absorber, well known for the reduction of discrete frequency resonances. However, the highly dissipative properties of some of the newest viscoelastic materials enable one to alter the characteristics of the undamped or only lightly damped absorber to such an extent that useful frequency bandwidths are wide enough to encompass several modes of vibration of a complex structure, such as a modern aerospace structure. Several specific and practical prototype dampers have been developed in this program and will be discussed in this paper.

I. ENERGY DISSIPATION IN A TUNED DAMPER

In a preliminary investigation of the dynamic characteristics of highly dissipative tuned viscoelastic dampers, such as that shown in Figure 1, it has been demonstrated [1] [2] that the relationship between the energy D dissipated per cycle during harmonic oscillation of amplitude X (of the base to which the damper is attached) and the physical characteristics of the damper is:

$$\frac{D}{\pi k X^2} = \frac{\eta B^4}{(1-B^2)^2 + \eta^2} \quad (1)$$

where k is the real part of the complex stiffness of the damper spring, η is the loss factor of the spring and B is the ratio f/f_0 . f is the frequency of excitation and f_0 is the undamped natural frequency of the damper, i.e.

$$\omega_0 = 2\pi f_0 = (k/m)^{1/2} \quad (2)$$

where m is the mass attached to the damper spring. The theory is outlined in [2].

In order to verify Equation (1), a damper of the configuration illustrated in Figure 2 was built. The significant dimensions of the damper are given in Table 1. In the absence of end effects in the viscoelastic layers, $k = GA/\tau$ where G is the real part of the shear modulus of the material. It has been shown [1] [2] that end effects modify this relationship somewhat and reduce the value of k by about 7 percent. G varies with frequency, so that a more basic form of Equation (1) had to be used, namely:

$$\frac{D}{X^2} = \frac{\pi \eta k m^2 \omega^4}{(k - m\omega^2)^2 + k^2 \eta^2} \quad (3)$$

In the experiments [2], the damper was attached to an electrodynamic shaker. The setup is illustrated in Figure 3. The input displacement X and the energy dissipated per cycle D were measured for a number of frequencies. Allowance was made, as far as possible, for the variation of G with frequency and temperature. Some of the results are seen in Figure 4, where D/X^2 is plotted against the frequency f . The theoretical curves are taken from Equation (3), using the manufacturer's data [2] on 3M-Y9063 viscoelastic foam at 96°F and 77°F, the bounding temperatures encountered in the investigation. The experimental points

should lie inside the cross-hatched area. A measure of agreement is obtained but the calculated natural frequency of the damper seems to be overestimated. It was surmised that this was probably due to the use of inaccurate values of G in the theoretical analysis.

It is now of interest to examine Equation (1) in more detail. Graphs of $D/\omega kX^2$ against B for various values of the loss factor η have been plotted in Figure 5. It has been assumed that k and η are constants for the purpose of this investigation, although this is only an approximation to the behavior of real viscoelastic materials. It is seen that, as η increases, the frequency bandwidth over which the damper dissipates significant amounts of energy increases rapidly. It follows, therefore, that use of viscoelastic materials with high loss factors would enable one to build tuned dampers that could operate over a wide frequency range rather than at a single discrete frequency as in the case of the classical vibration absorber. We shall discuss this matter further, however, when we come to the complex multi-span structure in a later section. We shall first discuss some aspects of tuned dampers in simple structures.

II. TUNED DAMPERS IN SIMPLE STRUCTURES

(a) Response and Damping under Harmonic Excitation

In the case of a simple structure, for which the resonant frequencies are widely separated, tuned dampers can be used effectively only for a single mode, such as the first. As an example, consider a cantilever beam, excited by a force $P \exp(i\omega t)$ at the free end and having a tuned damper of complex stiffness $k(1+i\eta)$ also at the free end. The response $W(x)\exp(i\omega t)$, where the coordinate x is measured from the clamped end, is shown in [3] [4] to be:

$$(2EI/PL^3)W = H/Z \quad (4)$$

where

$$Z = \frac{\psi\xi(\text{Cos}\xi\text{Sh}\xi - \text{Ch}\xi\text{Sin}\xi)}{1 - \psi\xi^4/\Gamma(1+i\eta)} + 1 + \text{Ch}\xi\text{Cos}\xi \quad (5)$$

$$H = (\text{Sh}\xi + \text{Sin}\xi)[\text{Ch}(\xi x/L) - \text{Cos}(\xi x/L)] - (\text{Ch}\xi + \text{Cos}\xi)[\text{Sh}(\xi x/L) - \text{Sin}(\xi x/L)]/\xi^3 \quad (6)$$

$$\xi = \lambda L \quad \text{is the frequency parameter}$$

$$\Gamma = kL^3/EI \quad \text{is the stiffness parameter}$$

$$\psi = m/\mu L \quad \text{is the mass parameter}$$

and $\lambda^4 = \mu\omega^2/EI$. Now Z is a complex number which can be expressed in terms of real and imaginary parts, so that $Z = Z_r + iZ_i$ where:

$$Z_r = \frac{\psi\xi\Gamma J(\Gamma - \psi\xi^4 + \Gamma\eta^2)}{(\Gamma - \psi\xi^4)^2 + \Gamma^2\eta^2} + 1 + \text{Ch}\xi\text{Cos}\xi \quad (7)$$

$$Z_i = \frac{-\psi^2\eta\xi^5\Gamma}{(\Gamma - \psi\xi^4)^2 + \Gamma^2\eta^2} \quad (7)$$

$$\text{and } J = \text{Cos}\xi\text{Sh}\xi - \text{Ch}\xi\text{Sin}\xi$$

The amplitude of the response $W(x)$ may therefore be written in the form:

$$(2EI/PL^3) |W| = |H|/(Z_r^2 + Z_1^2)^{1/2} = |H|/|Z| \quad (9)$$

Values of $(2EI/PL^3) |W|$ have been evaluated numerically as functions of ξ for several values of Γ , ψ , η and x/L . The spectra of $(2EI/PL^3) |W|$ against ξ , shown in Figures 6 and 7, differ from the response spectra for the undamped beam in that two resonant peaks appear for the first mode. Some damping of the higher modes also occurs. When the stiffness parameter Γ was varied, these peaks varied in their relative amplitudes and the minimum amplification factor Q was obtained when Γ was such as to make the two peaks of equal amplitude. The effective loss factor η_g of the beam is defined as $(Q^2-1)^{-1/2}$ for each such peak, for the first mode only. Typical graphs of η_g against Γ are shown in Figure 8 [3] [4].

The maximum values of η_g , corresponding to the crossover points in Figure 8, are then plotted against the damper loss factor η as in Figure 9. Mode shapes at resonance were also investigated by plotting the normalized values of $|W|$ against x/L for various Γ , ψ and η . Some results are shown in Figure 10. It is seen that the mode shapes do not generally change significantly. This is because the natural frequencies are so widely separated that interference between the various modes is small.

Again, an experimental investigation to verify the theory was completed. Tuned dampers of the geometries shown in Figure 11 were constructed and attached to the end of the cantilever. The setup is illustrated in Figures 12 and 13. The fixed end of the cantilever was then vibrated at constant input acceleration on an electrodynamic shaker and the response at the free end of the beam was measured using a miniature accelerometer. Records such as that shown in Figure 14 were obtained. The length of the beam was variable so that Γ could be controlled and records were taken when the two response peaks of the first mode were of equal amplitude.

Since the tests were conducted on a shaker instead of under force excitation, a different relationship between η_g and the observed amplification factor A had to be obtained. This relationship is shown in [3] [4] to be:

$$\eta_g = 1.56(A^2 - 1)^{-1/2} \quad (10)$$

The values of η for the cantilever type tuned dampers were obtained in the usual way from response curves of acceleration against frequency measured on the damper mass m . The amplification A was measured and η calculated from the relationship $\eta = (A^2 - 1)^{-1/2}$. Values of η so calculated are plotted against the ratio of the viscoelastic material thickness τ to the cantilever damper beam thickness h_D in Figure 15. For the ring type dampers, however, the loss factor η was too high for this method to be accurate. Instead, therefore, one end of the diameter of the ring was attached to an impedance head and the other end was connected to ground as in Figure 16. A known cyclic force F_a of constant amplitude was applied by the impedance head and the resulting acceleration $-\omega^2 X$ and phase angle γ between the force and the acceleration were recorded. The value of η was calculated from the relationship:

$$\eta = \frac{F_a \sin \gamma}{M_1 (-\omega^2 X) - F_a \cos \gamma} \quad (11)$$

where M_1 is the effective mass of the impedance head [4].

Values of η so obtained are plotted in Figure 17 and compared with the manufacturer's data [5]. From all these values of η , graphs of η_s against ψ could be plotted for the cantilever and ring dampers on the cantilever beam and the results are shown in Figures 18 and 19 respectively. It is seen that the agreement between theory and experimental investigations of a clamped-clamped beam is generally acceptably good. Similar experimental investigations of a clamped-clamped beam with tuned dampers have also been carried out [3] [6] and have demonstrated equally good agreement between theory and experiment. On the basis of this verification of the theory, it is now of interest to develop the theory further to include random vibrations of simple structures.

(b) Response under Random Excitation

Some confidence having been established in the theory of tuned dampers on simple structures under harmonic excitation, we now consider random excitation. In order to avoid raising questions concerning the nature of the excitation, this particular investigation is limited to analysis of a cantilever beam, with a tuned damper at the tip and excited by a random load at the tip. The spectral density of the load is assumed to be constant between $\xi=0$ and $\xi=4$ and zero everywhere else. The cut off is introduced in order to avoid excitation of all modes of vibration apart from the first. Let \bar{P}^2 be the power spectral density of the applied load. Then, from Equation (4), the mean square response \bar{W}^2 is:

$$\bar{W}^2 (2EI/L^3)^2 = (1/2) \int_{-\infty}^{\infty} \bar{P}^2 (H/|Z|)^2 d\omega \quad (12)$$

But $\mu\omega^2 L^4/EI = \xi^4$ so that $(\mu L^4/EI)^{1/2} d\omega = 2\xi d\xi$.

$$\bar{W}^2 (\mu L^4/EI)^{1/2} (2EI/\bar{P}L^3)^2 = 2 \int_0^4 (H/|Z|)^2 \xi d\xi \quad (13)$$

i.e. the root mean square displacement is given by:

$$\bar{W} (2EI/\bar{P}L^3) (\mu L^4/EI)^{1/4} = 2^{1/2} \left[\int_0^4 (H/|Z|)^2 \xi d\xi \right]^{1/2} \quad (14)$$

The integral in Equation (14) has been evaluated numerically for several values of ψ , Γ , η and x/L . Some results are shown in Figures 20 to 23, inclusive. It is seen that, for values of ψ equal to 0.1 or more, the value of \bar{W} is comparatively insensitive to the tuning of the damper i.e. the value of Γ , over quite a wide range. For each value of ψ and η , a minimum value of \bar{W} exists and a graph of this minimum value is plotted in Figure 24 against $\eta_s^{-1/2}$, taken from Figure 9. Superimposed is a graph of \bar{W} against the same quantity for a cantilever beam of homogeneous material of loss factor η_s , to be derived in the next section. It is seen that, apart from a moderate variation due partly to computing approximations and partly to small true variations, the beam with a tuned damper behaves under random excitation in very much the same way as a homogeneous beam of the same loss factor η_s . We may therefore make use of this fact to simplify further investigation of the stresses in highly damped simple structures.

(c) Stresses in Simple Highly Damped Structures

Consider a cantilever beam of loss factor η subjected to a load $P \exp(i\omega t)$ at the free end. The response $W(x) \exp(i\omega t)$ at any point of the cantilever, measured from the fixed end, is readily obtained by expanding W and P as series of normal modes. In fact, as shown in Appendix C:

$$W = \frac{L^4}{EI} \sum_{n=1}^{\infty} \frac{P_n \phi_n(x/L)}{(1+i\eta) \xi_n^4 - \xi^4} \quad (15)$$

where n is the mode number, $\phi_n(x/L)$ is the n th normal mode, normalized at the free end, ξ_n is the n th eigenvalue of the system and $\xi^4 = \mu \omega^2 L^4 / EI$. For a cantilever beam, $\xi_1^4 = 12.36$ and $\xi_2^4 = 485.5$ so that the second and higher terms of equation (15) are negligible in comparison with the first. In that case, therefore:

$$W \left(\frac{2EI}{PL^3} \right) \doteq \frac{8\phi_1(x/L)}{12.36(1+i\eta) - \xi^4} \quad (16)$$

since $P_1 L / P = 4$ for a clamped cantilever beam. Now consider a loading of power spectral density \bar{P}^2 , constant for all frequencies (white noise). Then the mean square response \bar{W}^2 is defined by:

$$\begin{aligned} \bar{W}^2 \left(\frac{2EI}{PL^3} \right)^2 &= \frac{1}{2} \int_{-\infty}^{\infty} \frac{64 \phi_1^2(x/L) d\omega}{(12.36 - \xi^4)^2 + (12.36\eta)^2} \\ \bar{W}^2 \left(\frac{2EI}{PL^3} \right) \left(\frac{\mu L^4}{EI} \right)^{1/2} &= \int_0^{\infty} \frac{128 \phi_1^2(x/L) \xi d\xi}{(12.36 - \xi^4)^2 + (12.36\eta)^2} \end{aligned} \quad (17)$$

$$= \frac{1.64}{\eta} \left[\frac{1 + (1+\eta^2)^{1/2}}{1 + \eta^2} \right]^{1/2} \phi_1^2(x/L) \quad (18)$$

since the integral in equation (17) is standard. Finally, therefore, we may write the root mean square response in the form:

$$\bar{W} (2EI / PL^3) (\mu L^4 / EI)^{1/4} = 1.28 F(\eta) \phi_1(x/L) \quad (19)$$

$$\text{where } F(\eta) = \eta^{-1/2} \left[\frac{1 + (1+\eta^2)^{1/2}}{1 + \eta^2} \right]^{1/4} \quad (20)$$

A graph of $F(\eta)$ against η is plotted in Figure 25. From these values of $F(\eta)$, the values of $\bar{W}(2EI/\bar{P}L^3) (\mu L^4/EI)^{1/4}$ are plotted as functions of $\eta^{-1/2}$ in Figure 24.

So far, we have considered only the root mean square displacement at any point of the beam. However, the bending stress σ at any point along the beam may be derived from the well known relationship:

$$\sigma/z = M/I = E/R$$

where z is the normal distance from the neutral axis, M is the bending moment, I is the second moment of area and R is the radius of curvature equal to $(d^2W/dx^2)^{-1}$. From this relationship:

$$\begin{aligned} \sigma_{\max} &= \sigma|_{z=h/2} = (Eh/2) [d^2W(x)/dx^2] \\ &= (Eh/2) (\xi_1^4/L^4) W(L) \phi_1''(x/L) \end{aligned} \quad (21)$$

using the notation of Bishop and Johnson [7]. The root mean square value of σ_{\max} therefore becomes:

$$\begin{aligned} \bar{\sigma}_{\max} &= (Eh\xi_1^4/2L^4) (EI/\mu L^4)^{1/4} (\bar{P}L^3/2EI) 1.28F(\eta) \phi_1''(x/L) \\ &= (E^{1/4} \bar{P} \xi_1^4 b^{-1} h^{-3/2} L^{-2} \rho^{-1/4}) 3.67F(\eta) \phi_1''(x/L) \end{aligned} \quad (22)$$

since $I = bh^3/12$ and $\mu = \rho bh$. It will be noted that the form of equation (22) is such that it is essentially true, apart from a constant of proportionality, for any boundary conditions. The discussion which follows is therefore applicable to simple structures with any boundary conditions.

If it is now assumed that, for a particular beam configuration, the loss factor η is independent of the beam thickness h , all other quantities being kept constant, then it follows that $\bar{\sigma}_{\max}$ will be proportional to $h^{-3/2}$ alone. Since $h = h_0(1+\psi)$, where h_0 is the initial thickness and ψ is the fractional weight increase due to a thickness increase alone, then:

$$\bar{\sigma}_{\max}(\psi) / \bar{\sigma}_{\max}(0) = (1 + \psi)^{-3/2} \quad (23)$$

This is, in part, the principle behind the usual method adopted for overcoming acoustical fatigue problems. If ψ is increased to 0.2, a thickness increase corresponding typically to one standard metal gage, then $\bar{\sigma}_{\max}$ will be decreased by about 20 percent, as seen in Figure 26. This is often sufficient, particularly if the actual loading spectrum also diminishes with increasing excitation frequency, and damping is not then needed. If, on the other hand, a situation arises in which a stress reduction of the order of 50 percent or more is required, ψ would have to be 0.6 or more. This would often be the case for structures in which weight was extremely critical in the first instance, and which had therefore to be designed with as low a thickness as possible. The margin for error is then small and properly designed damping may be the only way of overcoming specific vibration problems without increasing weight by a prohibitive amount.

If damping is introduced by means of tuned dampers, it has already been shown that, to a degree of approximation, the same root mean square displacement is obtained as for a homogeneous beam of loss factor η_s . If η_s is read off Figure 9 for the tuned damper, therefore, Equation (22) may be used directly to determine an approximate value of $\bar{\sigma}_{\max}$. It will be noted that $\bar{\sigma}_{\max}$ is infinite if the loss factor η is zero. No meaningful discussion of the effect of damping is therefore possible unless the initial damping of the structure is known. This, of course, depends in general on many things such as the beam material, the effects of riveting and other fabrication techniques, acoustic damping and so on. However, a figure of $\eta_0 = 0.01$ for the initial structural damping is typical and will be used for the sake of definiteness. If h , E , P , b , L and ρ are now kept constant in Equation (22), then $\bar{\sigma}_{\max}$ will depend on the damping η_s alone i.e.

$$\bar{\sigma}_{\max}(\psi) / \bar{\sigma}_{\max}(0) = F(\eta_s + \eta_0) / F(\eta_0) \quad (24)$$

In order to determine ψ in Equation (24), it is assumed that η_0 and the tuned damper contribution η_s are independent. This is likely to be true if η_0 is small, as assumed, but it remains a hypothesis.

For each selected value of η_s , $F(\eta_s + \eta_0)$ is read off Figure 25 and $\bar{\sigma}_{\max}(\psi) / \bar{\sigma}_{\max}(0)$ calculated from Equation (24).

The mass ratio ψ is then determined as a function of η_s from Figure 9. Graphs of $\bar{\sigma}_{\max}(\psi)/\bar{\sigma}_{\max}(0)$ are then plotted against ψ as in Figure 26. It is seen that, for values of ψ up to about 0.1, the reduction of stress is far greater than that obtained by only increasing the beam thickness. The reason for the curves levelling off for values of ψ in excess of 0.1 is that η_s approaches the damper loss factor η at about this point and no further significant gain in η_s is then possible.

For comparison, the performance of a typical unconstrained layer damping treatment, namely Aquaplas, on a simple structure is also illustrated in Figure 26. The data represents an average of measurements taken by Mead [8] at several points in a simple structure, for which the measured value of η_0 was about 0.008. It is seen that the stress reductions for tuned dampers are greater than those for this unconstrained layer treatment for low values of ψ but, owing to the fact that unconstrained layer treatments also increase the stiffness of the structure, the tuned dampers are not so effective at the greater weight additions.

(d) Reduction of Vibrations in a Radar Antenna

An application of a tuned damper to reduce the failure rate in a typical aircraft radar antenna has recently been demonstrated. Under an unexpectedly severe operational environment, simulated in a shaker test by the random input acceleration illustrated in Figure 27, rapid failure occurred around the rim of the antenna, illustrated in Figure 28. The rim was the only area subjected to severe bending stresses and the mode of vibration was observed to be almost piston-like, with an effective pivot near the rim, with high bending stress. Failure occurred in a few minutes under the shaker excitation shown in Figure 27. Temperature rises of the order of 30°F were observed to occur in the vicinity of the electrical connector, possibly because most of the energy was dissipated at this point.

In order to better determine the nature of the problem and to seek means of avoiding failure, or at least increasing the time to failure, a sample antenna was excited harmonically on an electrodynamic shaker, as in Figure 29. A typical response spectrum, measured by a miniature accelerometer on the dish-like inner surface, is shown in Figure 30. It is seen that amplification factors of the order of 30 at a frequency of about 485 cycles per second occurred in the absence of damping additions. Most of the damping that did exist seemed to be due to actions in the electrical connector, where the high temperature rises occurred. The antenna appeared to act as a single degree of freedom system since no further response peaks were observed up to several thousand cycles per second.

The surface strains at all points apart from the rim edge were very small and all attempts to use commonly available layered damping treatments were, consequently, fruitless. In fact, a tuned damper, by virtue of the fact that the energy dissipation depends on the local acceleration level rather than the strain level, was the only possibility apart from a complete re-design of the antenna.

Tuned dampers of the type shown in Figure 31 were therefore constructed. These dampers fitted on to the electrical connector at the center of the antenna. Several viscoelastic materials and damper dimensions were tested and each individual damper configuration was tuned by varying the mass m , since this was far more convenient than varying the stiffness. A typical graph of the amplification factor A against the mass m for one of the dampers [9] is shown in Figure 32, the test being conducted at 80°F. Several such tests were carried out, over a range of temperatures from 75°F to 150°F, in an attempt

to achieve low amplification factors over as wide a range of temperatures as possible. For the optimum mass appropriate to each damper configuration, a graph of the amplification factor A against the temperature in the vicinity of the damper is shown in Figure 33. It is seen that it was possible to keep A below 12 or so over quite a wide temperature range.

For this optimized damper (using a selected viscoelastic material [9]) further tests were run under the same random excitation as for the undamped antenna. The time to failure was increased by a factor of 4 for this particular damper - antenna combination.

III. TUNED DAMPERS IN COMPLEX MULTI-SPAN STRUCTURES

Up to now, we have been concerned with the performance of tuned viscoelastic dampers in simple structures. It has been shown that, for these simple structures, vibrating in their fundamental modes, a properly tuned viscoelastic damper can perform as well as, or better than, most layered damping treatments when compared on the basis of equal weights of damping treatment. It has also been shown that if one of these dampers is properly tuned to damp the fundamental mode of a cantilever beam, then it will also contribute to the damping of the second and higher modes of vibration of the beam, the second mode being at a frequency about 6.6 times that of the fundamental. Admittedly, the effective loss factor of the damped beam vibrating in its second mode is much lower than when it is vibrating in its fundamental mode, but this can be accounted for by comparing the energy dissipated per cycle in the damper and the elastic strain energy for a given displacement of the free end in the two different modes of vibration.

The effective loss factor η_s of the beam with the damper attached may also be defined by the relationship

$$\eta_s = D / 2\pi U$$

where D is the total energy dissipated per cycle and U is the total strain energy in the damper and the beam [10]. In the case of the cantilever beam the strain energy is much greater in the second mode than in the fundamental mode (about 41 times) for the same displacement at the free end. Therefore, even if the energy dissipated per cycle remains about the same for the two modes, the effective loss factor in the second mode will be much lower. The question now arises as to whether this defeats the possibility of using dampers such as these to control the multi-modal response of complex structures. It would appear that it does not, since it frequently is not the vibration modes with high strain energies that create the problems. Consider, for example, a continuous skin-stringer type of structure typical of aircraft construction, illustrated in Figure 34. It has been shown both experimentally [11] and theoretically [12] that the most troublesome modes occur in a frequency band bounded on the low frequency side by the first "stringer twisting" mode and on the high frequency side by the first "stringer bending" mode, as sketched in Figure 35. These two limiting modes often occur at frequencies about an octave apart [12] and the strain energies associated with these modes are reasonably close to each other. In fact, the strain energy in the stringer bending mode is approximately four times that in the stringer twisting mode. It seems feasible, therefore, that a single

damper could be employed to damp all modes in the entire band of frequencies between these two limiting modes.

A detailed investigation of the effect of tuned viscoelastic dampers on the response of multi-span structures is presently in progress at the Air Force Materials Laboratory. Preliminary results, in both the theoretical and experimental phases of the investigation, support the prospect of using a single tuned damper in the center of each span to effectively reduce resonant response of several modes of vibration within the frequency band of most interest. The experimental set-up which is being used in this investigation is shown in Figure 34. A test specimen, consisting of a row of five flat panels stiffened by stringers between the panels and heavier frames at the edges, is attached through the frames to a vibration fixture, which in turn is mounted on an electromagnetic shaker. Since there are five panels in the row, there would normally be five modes in the frequency band bounded by the first stringer twisting mode and the first stringer bending mode but, due to the symmetric excitation in this test, only the symmetric modes are excited. Figure 36 shows the acceleration measured at the center of the middle panel with no dampers on the specimen and with the frames excited harmonically at an input level of 0.5 g's while the frequency is slowly swept between approximately 150 and 300 cycles a second. Preliminary amplitude and phase measurements indicate that the response peaks at 195, 210 and 260 cycles a second correspond respectively to the first stringer twisting mode (adjacent panels out of phase with each other), the intermediate symmetric mode (three center panels in phase with each other and out of phase with the end panels) and the first stringer bending mode (all panels in phase with each other).

Identical ring dampers, of the configuration shown in Figure 11, were then attached at the center of each panel, and the specimen was excited as before with a 0.5 g acceleration at the frames. The resulting response measured in the center of the middle panel is shown in Figure 37. As can be seen, the acceleration response at this point of the specimen has been reduced by a factor of more than five. Similar measurements were made for the response in the center of each of the other panels. Each panel was observed to exhibit the same general type of response, characterized by greatly reduced resonant peaks and an apparent high degree of modal overlap, with all panels vibrating in phase with each other, over all the frequency range of interest. Additional measurements have confirmed that the maximum acceleration still occurs at or near the center of each panel, when the tuned dampers are attached. Therefore the damped response spectrum shown in Figure 38 is typical of the maximum accelerations existing in the specimen and illustrates the broad band performance that can be attained with lightweight (total damper weight was about 3 percent of the weight of the skin) tuned viscoelastic dampers.

IV. CONCLUSIONS

A theory of the performance of tuned viscoelastic dampers in simple structures has been developed and experimentally verified. On the basis of this theory, bending stress levels in simple structures, with tuned dampers, under random excitation have been predicted and it has been shown that far greater stress reductions are obtained for lower weight additions than by either the often used procedure of increasing skin thickness or by use of unconstrained layer damping treatments. An application of tuned dampers in a radar antenna is described, where fatigue life in a severe vibrational environment is greatly increased.

Applications of high loss factor tuned viscoelastic dampers in complex structures exhibiting multi-modal response are also discussed. Preliminary experiments are described showing the effect of such dampers on the response of a typical model of an aerospace structure.

ACKNOWLEDGEMENTS

The experimental investigations described in this paper were carried out on equipment purchased using the Directors' Fund of the Air Force Materials Laboratory. The authors would like to extend their appreciation to Mr. W. J. Trapp, Chief of the Strength and Dynamics Branch of the Air Force Materials Laboratory for his support of the work, Mr. J. Schmermund of the Strength and Dynamics Branch for invaluable assistance with the equipment, Dr. D. J. Mead of the University of Southampton, Southampton, England for assisting us with early plans of the multi-span panels used in the experiments on complex structures, Mr. A. D. Nashif and Mr. E. D. Goens of the University of Dayton for assistance with the experimental investigation, Miss Connie Mantych for assistance with preparation of the manuscripts and Mr. DeMarey of the University of Dayton for invaluable help in preparing the figures.

REFERENCES

1. Henderson, J. P., "Energy Dissipation in a Viscoelastic Damper Utilizing a Viscoelastic Suspension", M.S. thesis, Ohio State University, Columbus, Ohio, 1964.
2. Henderson, J. P., "Energy Dissipation in a Viscoelastic Damper Utilizing a Viscoelastic Suspension", Shock and Vibration Bulletin 35, Part 7, Office of the Director of Defense, April 1966, pp 213-229. Also AFML-TR-65-403, U.S. Air Force, November 1965.
3. Jones, D. I. G., Adkins, R. L. and Nashif, A. D. "Effect of Tuned Dampers on Vibrations of Simple Structures", Paper submitted to AIAA, 1966.
4. Nashif, A. D., "Effect of Tuned Dampers on Vibrations of Cantilever Beams", AFML-TR-66-83, Air Force Materials Laboratory, Wright-Patterson AFB, Ohio (March 1966).
5. Anon. "DC-400 Vibration Damping Material", Bulletin D-104, Lord Mfg. Co., Erie, Pa. (now called LD-400).
6. Adkins, R. L. and Jones, D. I. G., "Effect of Tuned Viscoelastic Dampers on Response and Damping of a Clamped-Clamped Beam", AFML-TR-66-100, Air Force Materials Laboratory, Wright-Patterson AFB, Ohio, (April 1966).
7. Bishop, R. E. D. and Johnson, D. C., The Mechanics of Vibration, Cambridge University Press, pp 375-387, (1960).
8. Mead, D. J. and Pretlove, A. J., "An Experimental Investigation of the Damping Properties of Aquaplas Under Random and Harmonic Excitation", ASD-TDR-62-336, Air Force Materials Laboratory, Wright-Patterson AFB, Ohio, (March 1962).
9. Oberst, H. and Schommer, A., "Optimization of Viscoelastic Damping Materials for Specific Structural Composite Applications", Acoustical Fatigue in Aerospace Structures, edited by W. J. Trapp and D. M. Forney, Jr., Syracuse University Press, p 604, Figure 2, 1965.
10. Lazan, B. J. and Goodman, L. E., "Material and Interface Damping", Shock and Vibration Handbook, edited by Harris, C. M. and Crede, C. E., McGraw-Hill Book Company, New York, Ch. 36, Vol. 2, (1961).
11. Clarkson, B. L. and Ford, R. D., "Experimental Study of the Random Vibrations of an Aircraft Structure Excited by Jet Noise", WADD-TR-61-70, Air Force Materials Laboratory, Wright-Patterson AFB, Ohio, (March 1961).

12. Lin, Y. K., "Dynamic Characteristics of Continuous Skin-Stringer Panels", Acoustical Fatigue in Aerospace Structures, edited by Trapp, W. J. and Forney, D. M. Jr., Syracuse University Press, pp 163-184, (1965).
13. Soroka, W. W., "Note on The Relation of Structural and Viscous Damping", Journal of the Aeronautical Sciences, Vol. 16, pp 409, (1949).
14. Myklestad, N. O., "The Concept of Complex Damping", Journal of Applied Mechanics, Vol. 19, p 284, (1952).
15. Bishop, R. E. D., "The Treatment of Damping Forces in Vibration Theory", Journal of the Royal Aeronautical Society, Vol. 59, p 738, (Nov. 1955).
16. Snowdon, J. C., "Representation of the Mechanical Damping Possessed by Rubberlike Materials and Structures", Journal of the Acoustical Society of America, Vol. 35, No. 6, p 821, (June 1963).
17. Reed, F. E., "Dynamic Vibration Absorbers and Auxiliary Mass Dampers", Shock and Vibration Handbook, edited by Harris, C. M. and Crede, C. E., McGraw-Hill Book Company, New York, Chapter 6, (1961).
18. Snowdon, J. C., "Vibration of Cantilever Beams to which Dynamic Absorbers are Attached" Journal of the Acoustical Society of America, Vol 39, No. 5, May 1966, pp 878-886, (May 1966).
19. Rodden, W. P. and Whittier, J. S., "Damping of Shaker-Excited Beams Calculated Solely From Displacement Amplitude Measurements", Journal of the Acoustical Society of America, Vol. 34, pp 469-471, (April 1962).

TABLE I

Significant Damper Dimensions

Dimension	Symbol	Magnitude
Mass	m	1.33 Lb.
Thickness	t	0.25 ins.
Total Shear Load Supporting Area	S	2 in ²
Viscoelastic Material	3M-Y9063	See [1, 2]

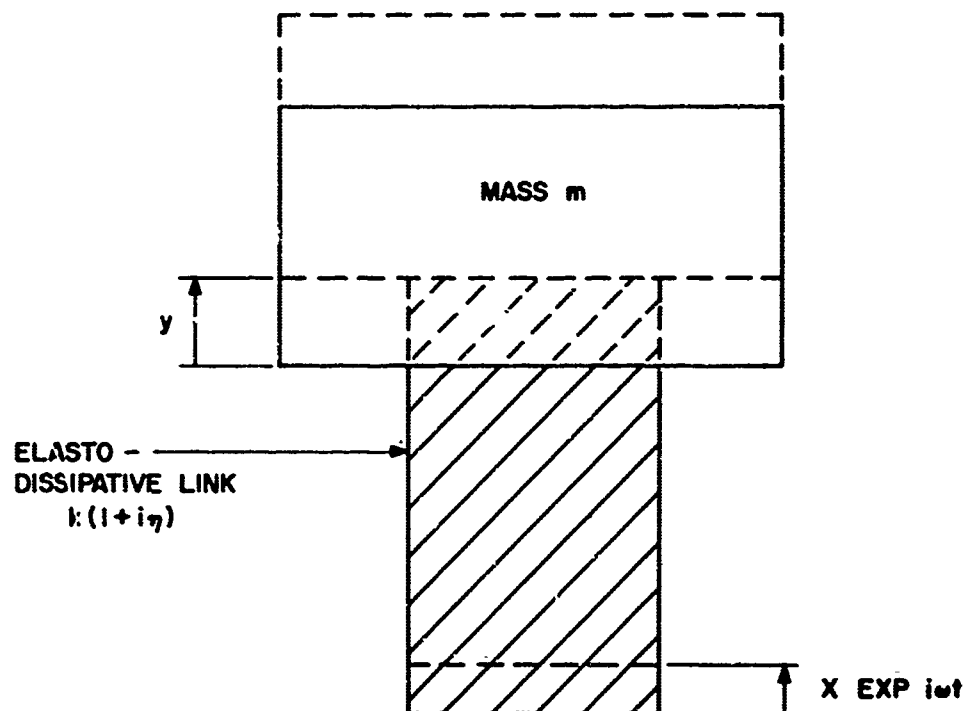


FIGURE 1 IDEALIZED TUNED DAMPER UNIT

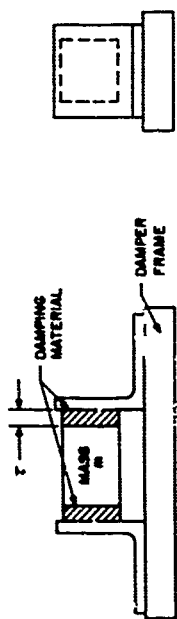


FIGURE 2 EXPERIMENTAL DAMPER CONFIGURATION

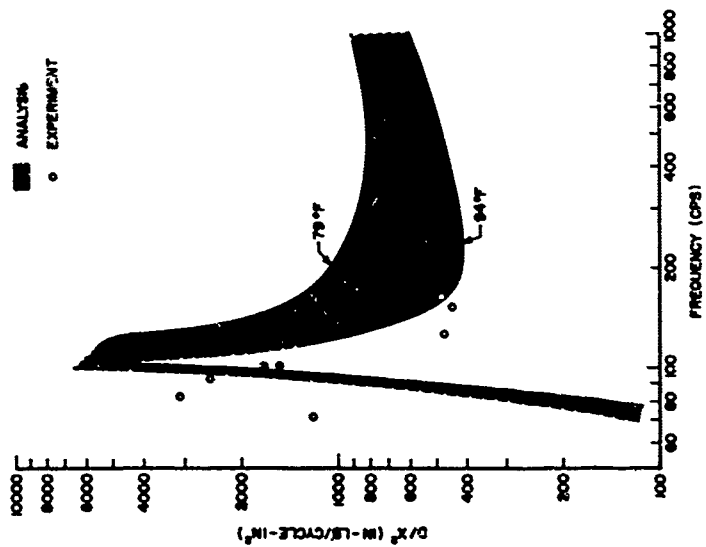


FIGURE 4 EXPERIMENTALLY MEASURED ENERGY DISSIPATION COMPARED WITH ANALYSIS

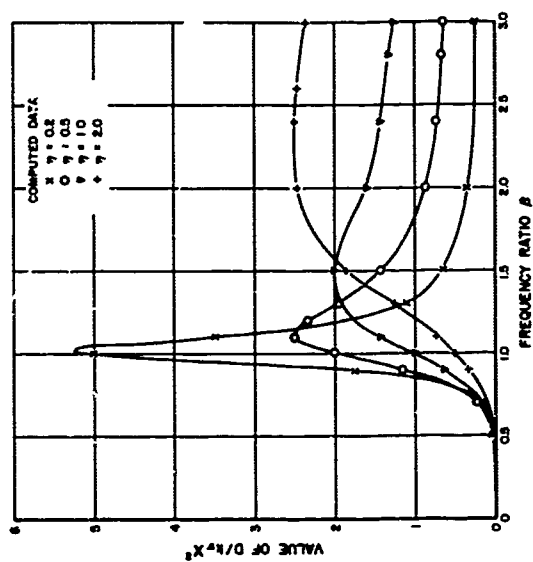
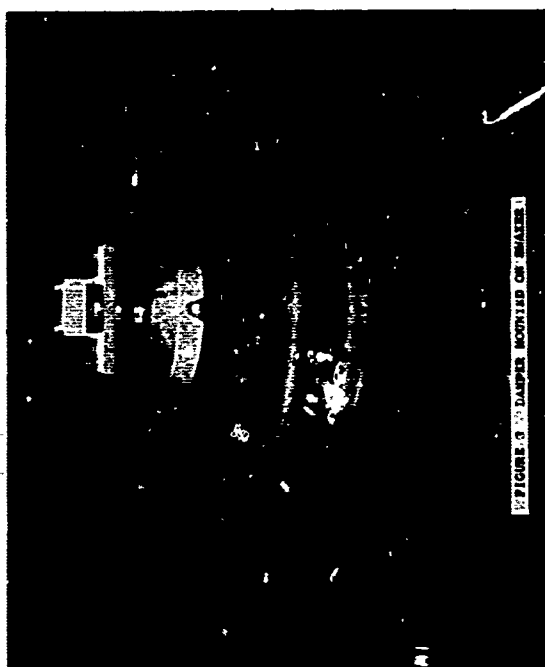


FIGURE 5 VARIATION OF ENERGY DISSIPATION WITH FREQUENCY RATIO FOR IDEAL TUNED DAMPER

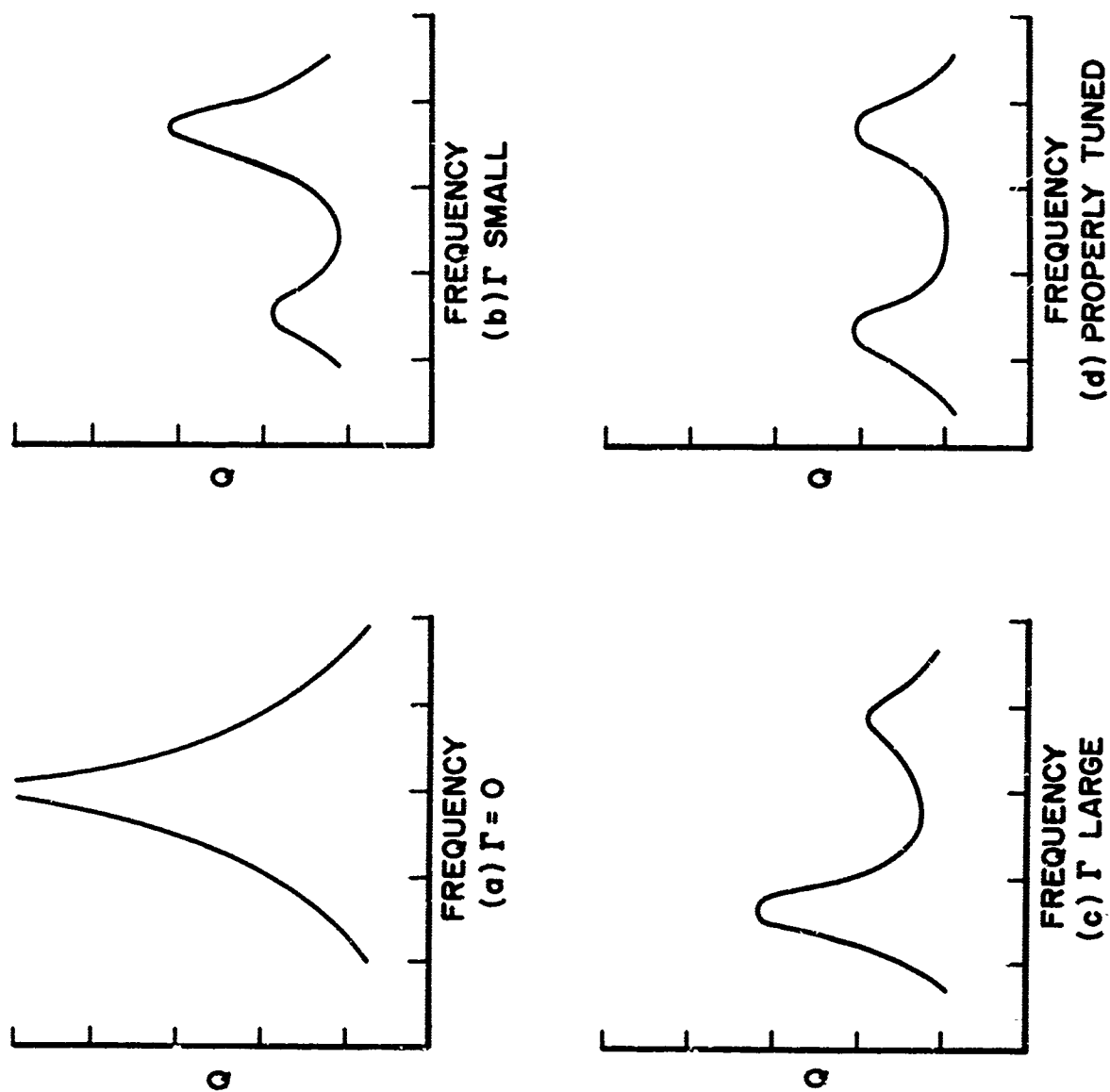


FIGURE 6 GRAPHS OF AMPLITUDE AMPLIFICATION FACTOR AGAINST FREQUENCY FOR VARIOUS STIFFNESS RATIOS

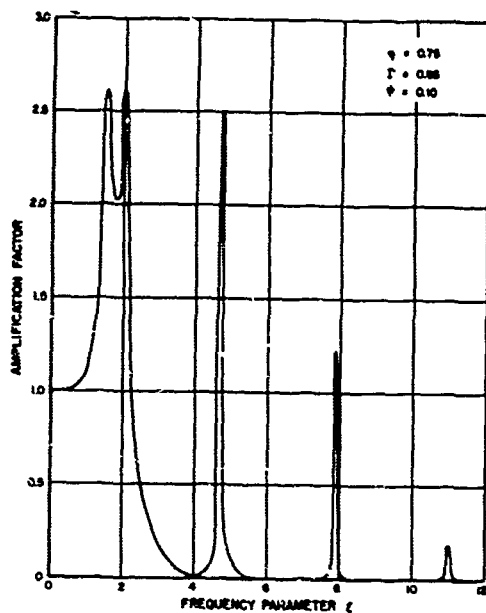


FIGURE 7 TYPICAL SPECTRUM FOR CANTILEVER BEAM WITH TUNED DAMPER

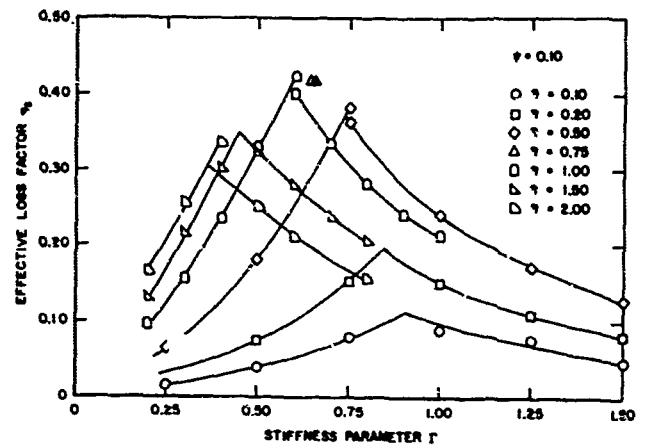


FIGURE 8 GRAPHS OF THEORETICAL VALUES OF EFFECTIVE LOSS FACTOR AGAINST STIFFNESS PARAMETER FOR BOTH RESPONSE PEAKS

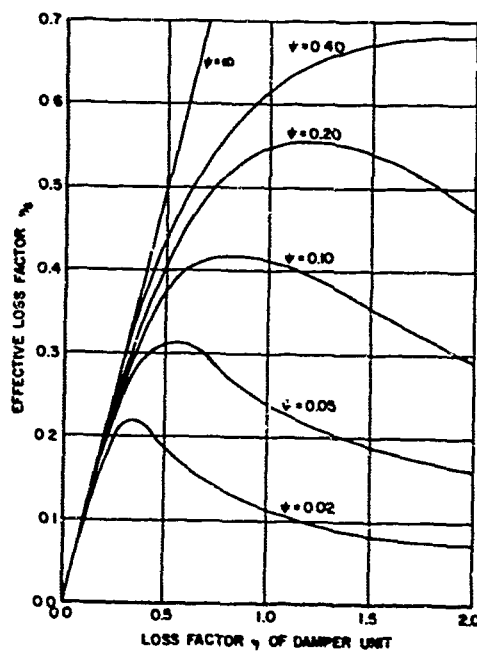


FIGURE 9 GRAPHS OF EFFECTIVE LOSS FACTOR AGAINST DAMPER LOSS FACTOR FOR VARIOUS MASS RATIOS IN CANTILEVER BEAM

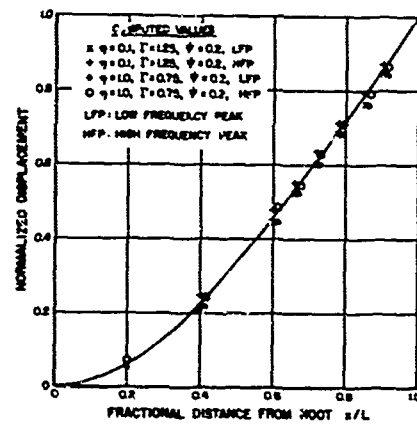


FIGURE 10 TYPICAL THEORETICAL RESONANT MODE SHAPES FOR CANTILEVER BEAM WITH TUNED DAMPER

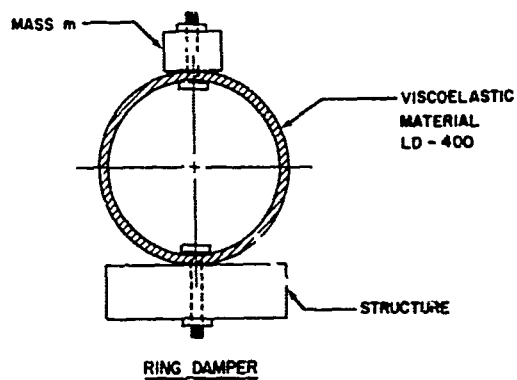
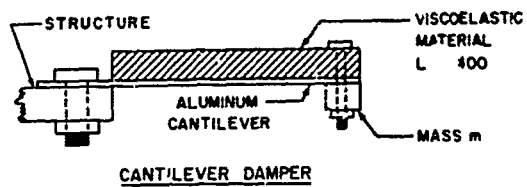


FIGURE 11 SKETCHES OF TUNED DAMPER CONFIGURATIONS

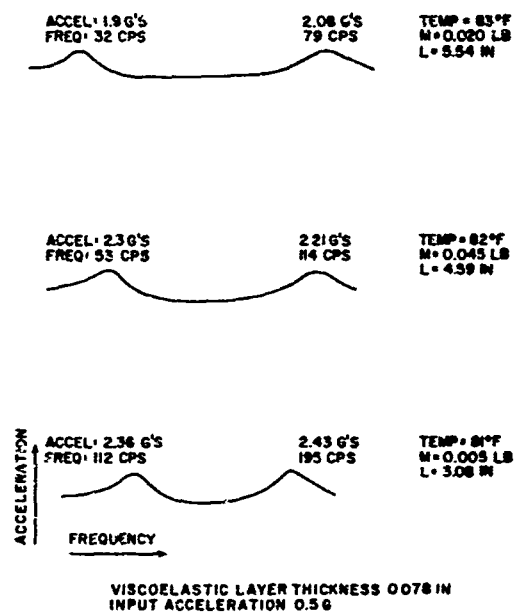
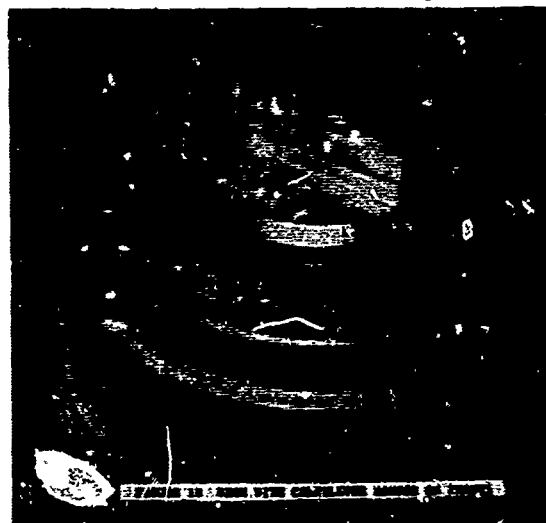


FIGURE 14 TYPICAL OUTPUT ACCELERATION AGAINST FREQUENCY SPECTRA FOR CANTILEVER BEAM WITH TUNED CANTILEVER DAMPER

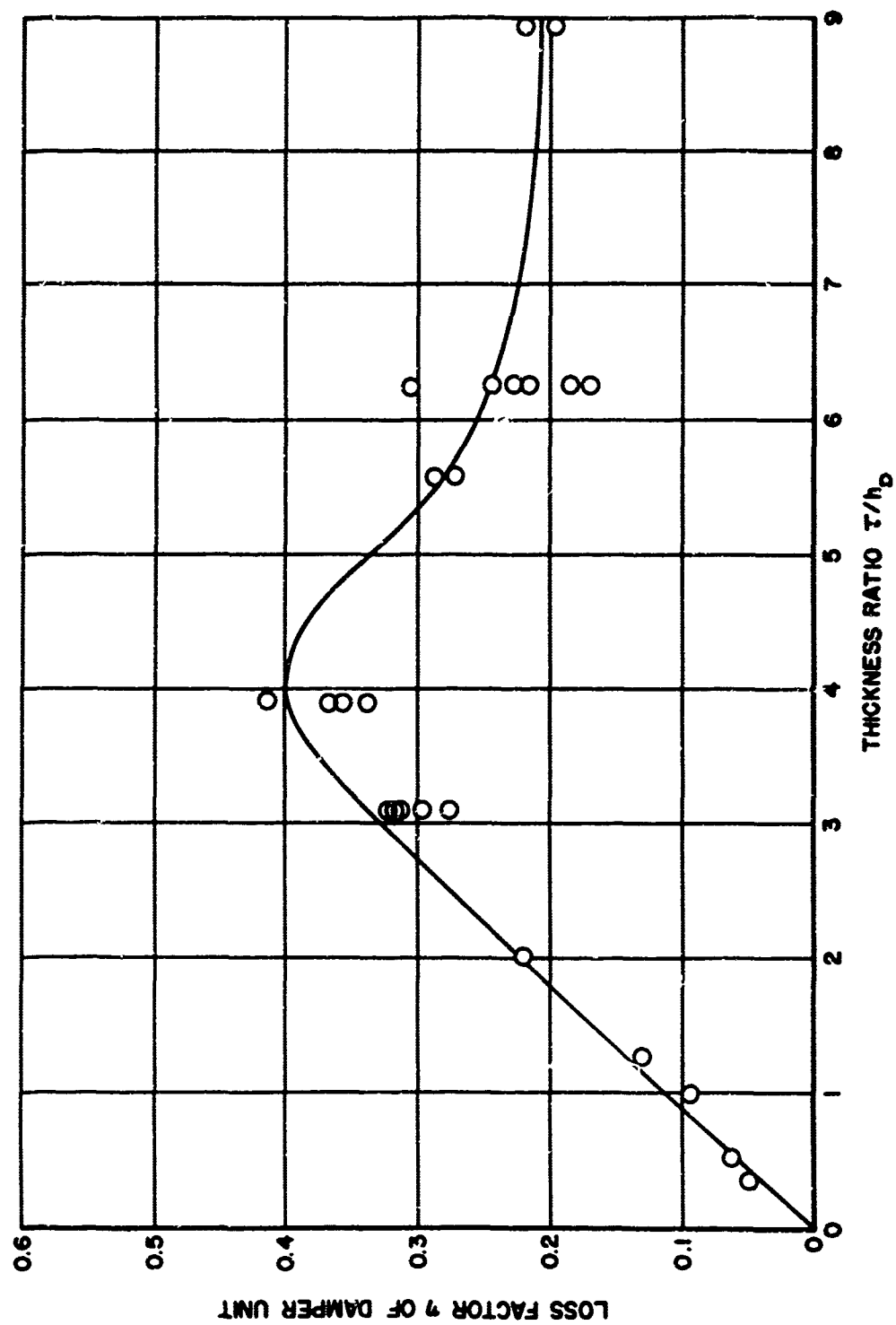


FIGURE 15 GRAPH OF CANTILEVER DAMPER LOSS FACTOR AGAINST RATIO OF VISCOELASTIC LAYER THICKNESS TO METAL BEAM THICKNESS

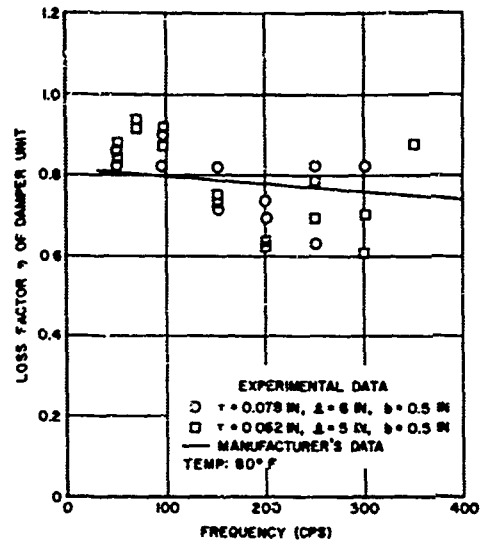
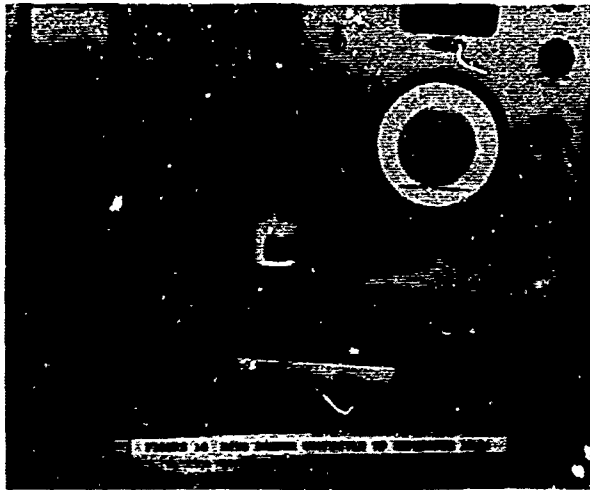


FIGURE 17: GRAPH OF RING DAMPER LOSS FACTOR AGAINST FREQUENCY

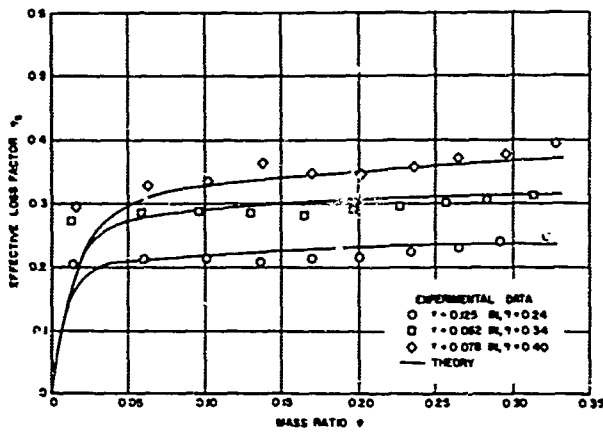


FIGURE 18: GRAPH OF EFFECTIVE LOSS FACTOR AGAINST MASS RATIO FOR CANTILEVER BEAM WITH CANTILEVER DAMPER UNIT AT END

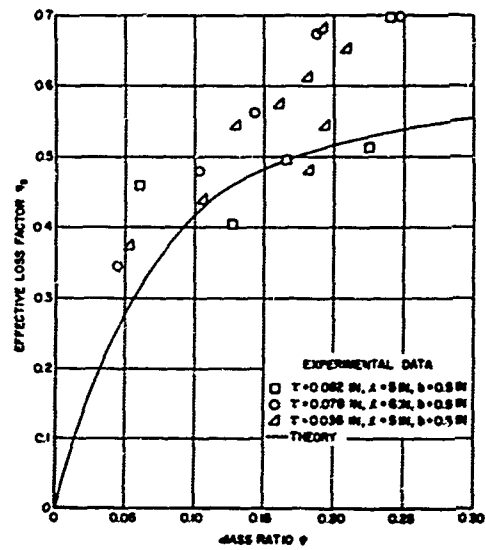


FIGURE 19: GRAPH OF EFFECTIVE LOSS FACTOR AGAINST MASS RATIO FOR CANTILEVER BEAM WITH RING DAMPER AT END

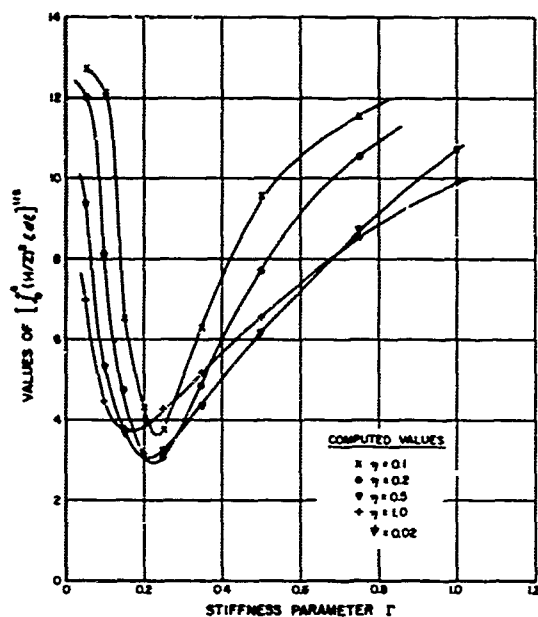


FIGURE 20 GRAPH OF NON-DIMENSIONAL ROOT MEAN SQUARE DISPLACEMENT AGAINST STIFFNESS PARAMETER ($\eta=0.02$)

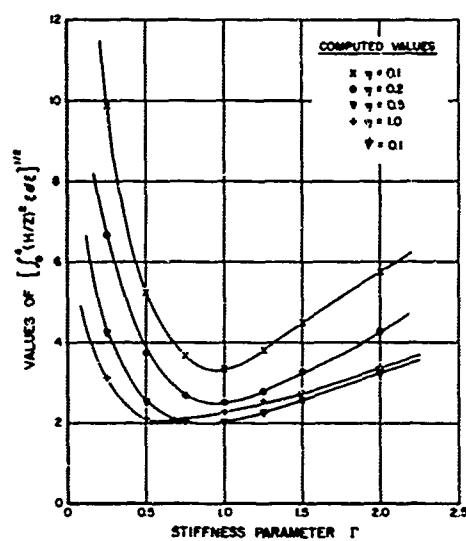


FIGURE 21 GRAPH OF NON-DIMENSIONAL ROOT MEAN SQUARE DISPLACEMENT AGAINST STIFFNESS PARAMETER ($\eta=0.1$)

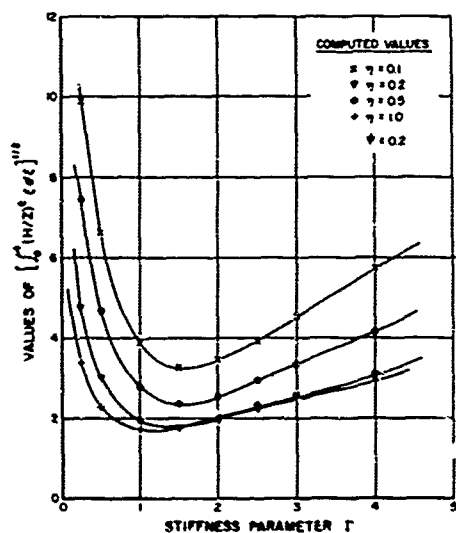


FIGURE 22 GRAPH OF NON-DIMENSIONAL ROOT MEAN SQUARE DISPLACEMENT AGAINST STIFFNESS PARAMETER ($\eta=0.2$)

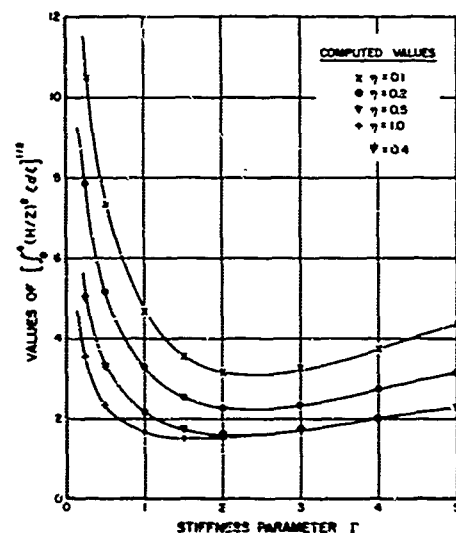


FIGURE 23 GRAPH OF NON-DIMENSIONAL ROOT MEAN SQUARE DISPLACEMENT AGAINST STIFFNESS PARAMETER ($\eta=0.4$)

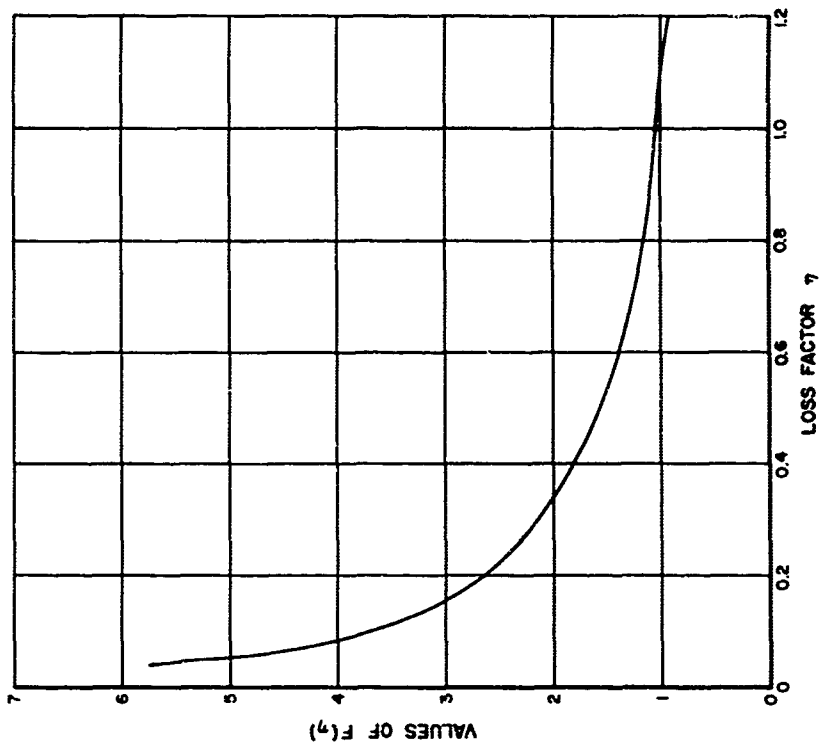


FIGURE 25 THE FUNCTION $F(\eta)$

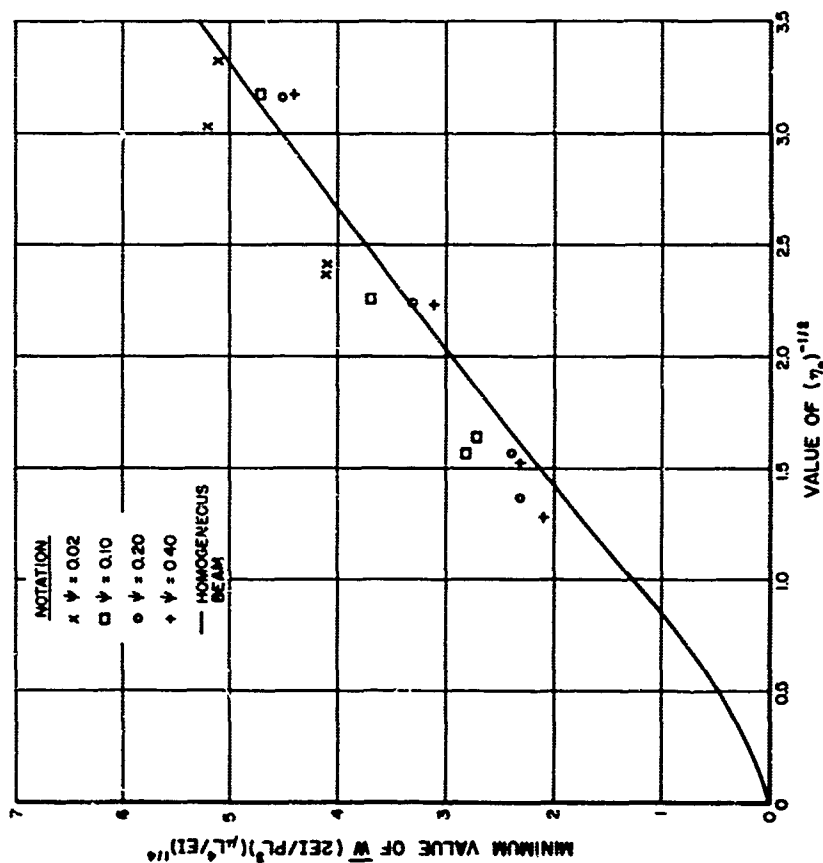


FIGURE 24 GRAPH OF NON-DIMENSIONAL ROOT MEAN SQUARE DISPLACEMENT AGAINST A FUNCTION OF THE EFFECTIVE LOSS FACTOR

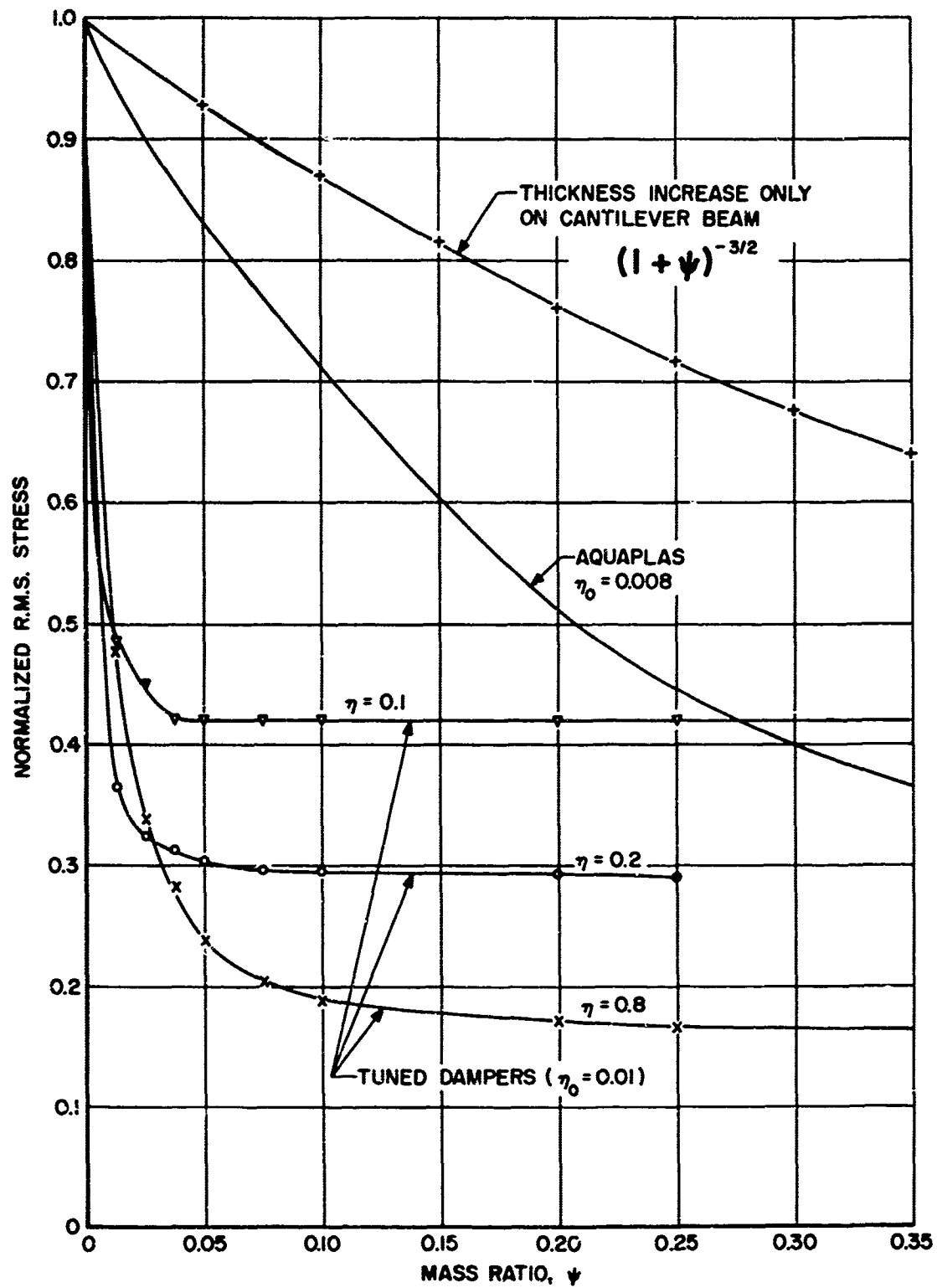


FIGURE 26 GRAPHS OF NORMALIZED STRESSES IN SIMPLE STRUCTURES AS FUNCTIONS OF MASS ADDED FOR VARIOUS DAMPING TECHNIQUES

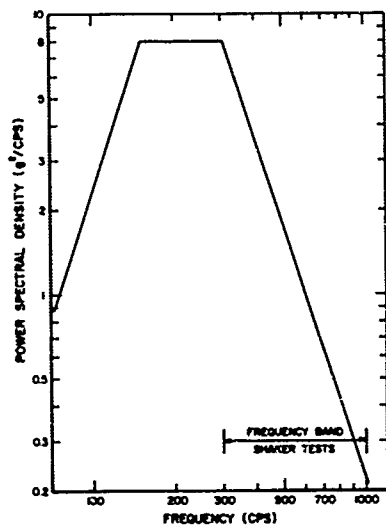


FIGURE 27 INPUT SPECTRA TO THE RADAR ANTENNA

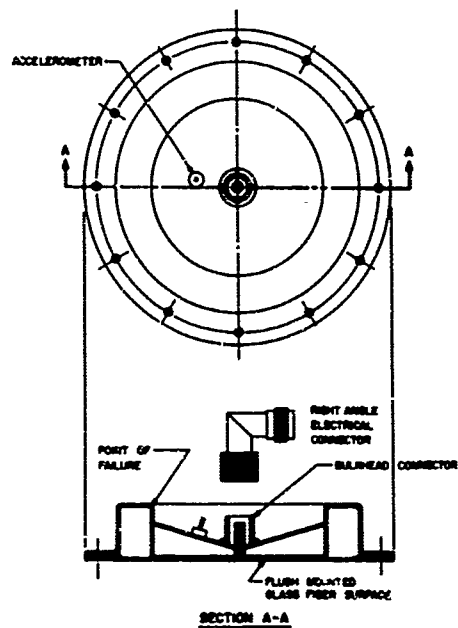
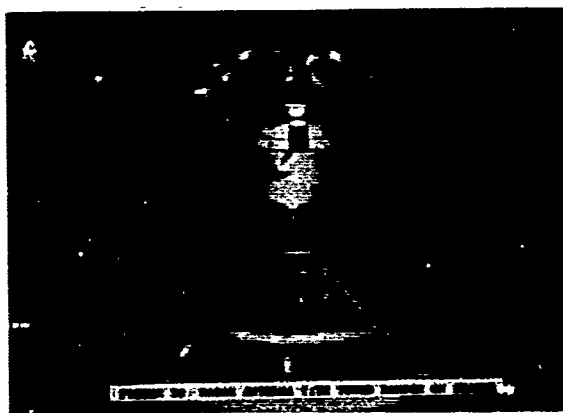


FIGURE 29 DIAGRAM OF THE RADAR ANTENNA CONFIGURATION

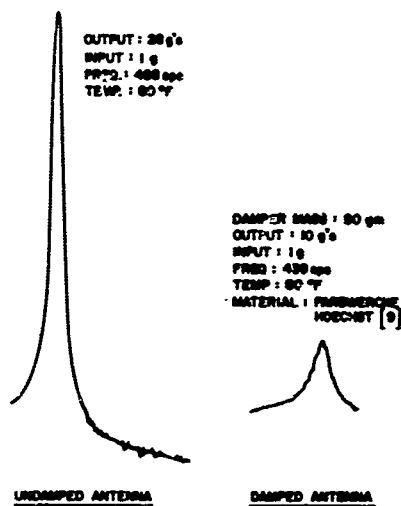


FIGURE 30 TYPICAL ACCELERATION AGAINST FREQUENCY SPECTRA OF THE ANTENNA WITHOUT DAMPING AND WITH OPTIMIZED TUNED DAMPER

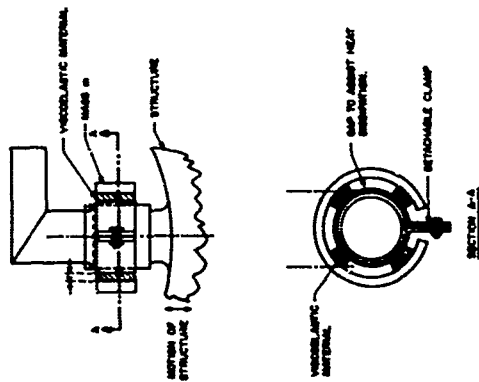


FIGURE 31 SKETCHES OF THE FIXED DAMPER USED ON THE BEAM ANTENNA

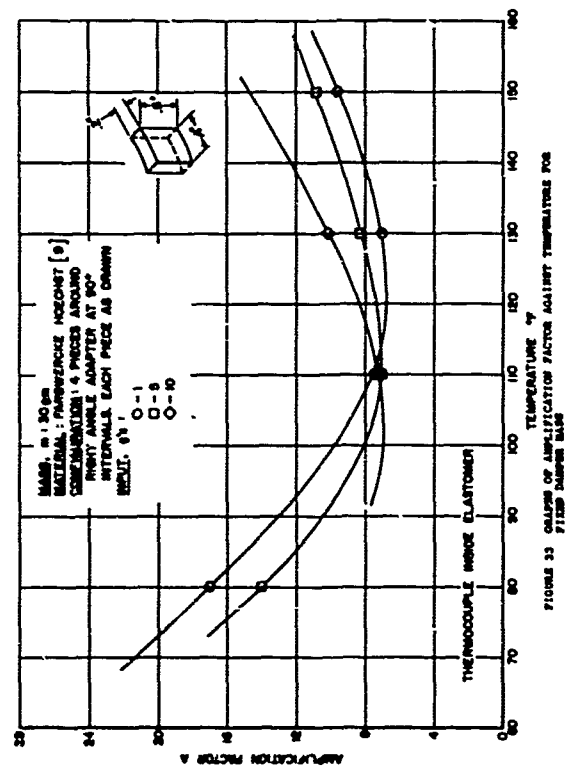


FIGURE 33 GRAPHS OF AMPLIFICATION FACTOR AGAINST TEMPERATURE FOR FIXED DAMPER WIDE

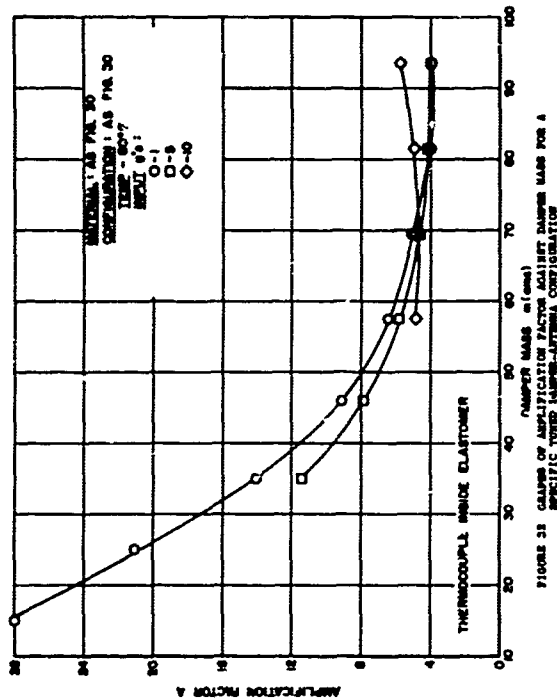


FIGURE 35 GRAPHS OF AMPLIFICATION FACTOR AGAINST FREQUENCY FOR A SPECIFIC TYPED WIDE-ANTENNA CONSTRUCTION

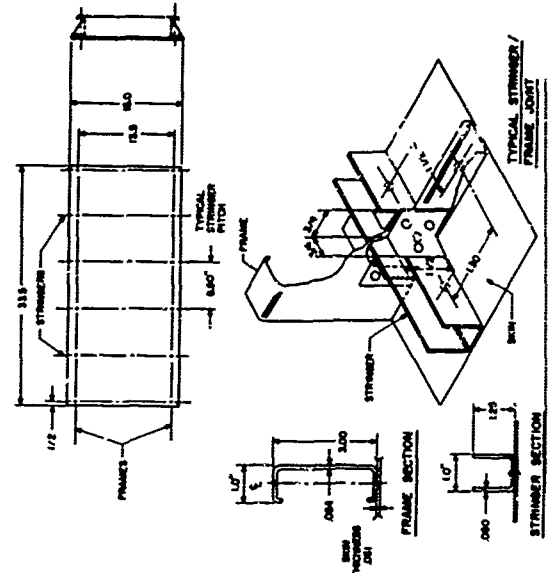


FIGURE 34 GEOMETRY OF FIVE BEAM WIDE-ANTENNA STRUCTURE

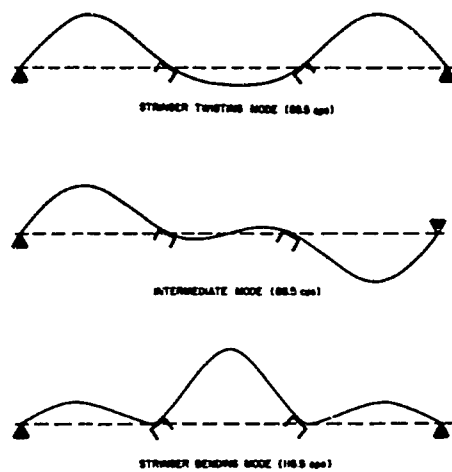


FIGURE 35 MODE SHAPES CORRESPONDING TO THREE LOWEST FREQUENCIES FOR A ROW OF PANELS WITH EQUALLY SPACED STRINGERS 12

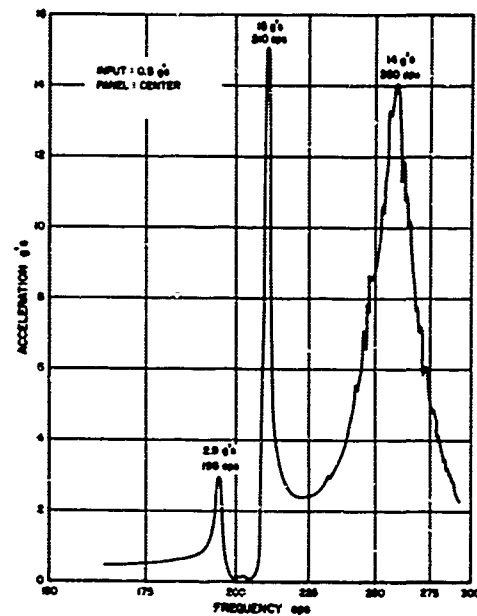
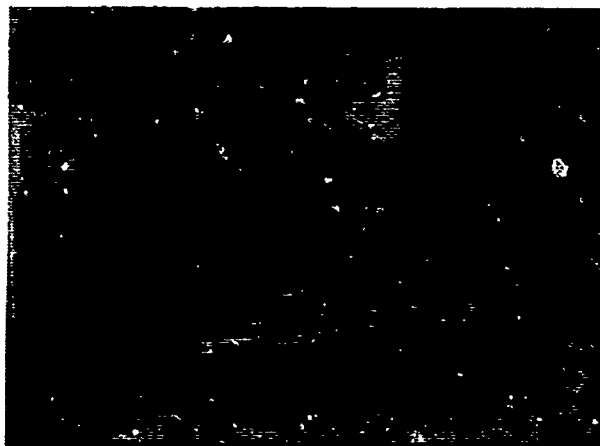


FIGURE 36 TYPICAL MEASURED ACCELERATION AGAINST FREQUENCY SPECTRUM FOR FIVE SPAR STRUCTURES WITH NO TUNED DAMPERS

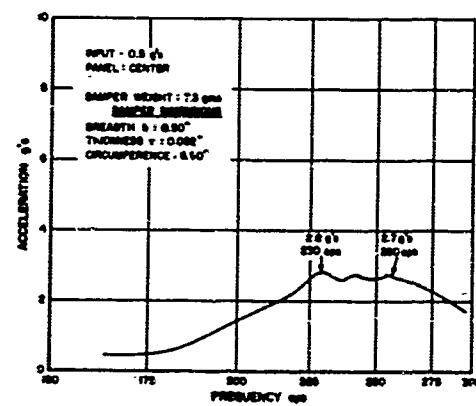


FIGURE 38 TYPICAL SPECTRUM OF MEASURED ACCELERATION AGAINST FREQUENCY FOR FIVE SPAR STRUCTURE WITH TUNED DAMPERS

(U) - PROGRESS REPORT - DEVELOPMENT OF
ADVANCED COMPOSITE STRUCTURES

by

Loris D. Whipple, Major, USAF

Air Force Materials Laboratory
Research & Technology Division
Wright-Patterson AFB, Ohio



Maj Loris D. Whipple

BIOGRAPHICAL SKETCH

of

LORIS D. WHIPPLE
Major, USAF

Major Whipple served two years in the Army Air Corps during World War II after which he returned to civilian life to complete his Bachelors Degree in Civil Engineering at Michigan State University. On returning to the service he served for seven years as a Strategic Air Command navigator on B-29, B-36 and B-47 crews. Upon completion of a two year Air Force Institute of Technology assignment to the University of California he was awarded a Masters Degree in Chemistry and subsequently served for four years as an Assistant Professor of Chemistry at the Air Force Academy in Colorado Springs. After the academy assignment he attended the Air Command and Staff College at Maxwell AFB, Alabama. During this period he completed the requirements and was awarded a Masters Degree in Business Administration from the George Washington University. He has been assigned to the Air Force Materials Laboratory at Wright-Patterson AFB, Ohio for the past three and one half years and is currently the Assistant Chief of the Advanced Filaments and Composites Division of that Laboratory.

PROGRESS REPORT - DEVELOPMENT OF ADVANCED COMPOSITE STRUCTURES

by

Loris D. Whipple, Major, USAF

Air Force Materials Laboratory
Research & Technology Division
Wright-Patterson AFB, Ohio

ABSTRACT

In this paper, the high potential payoffs of using high modulus filament reinforced composite materials in aerospace systems applications are discussed in light of Program Definition Phase studies and technical results of the Air Force Advanced Filaments and Composites Advanced Development Program efforts. The first step taken toward realizing these payoffs by demonstration with actual hardware was the initiation of structural and propulsion component development programs in the areas of aircraft structures, helicopter rotor blades, re-entry vehicles, and gas turbine engines. The results of these seven-month, first generation programs are discussed with emphasis on the analysis of the performance of the structural components. This graphically reflects the status of the entire technological development program.

This is a progress report of what may be the greatest material structures breakthrough in centuries. The materials are advanced composites. The structures are aerospace structures specifically designed to take maximum advantage of the new materials. Advanced composites are made of high modulus, high strength, low density filaments and appropriate organic or metallic matrix materials. Fiberglass composites on the other hand are made of relatively low modulus filaments and appropriate matrix materials.

Fiberglass composites have been used for years in a variety of structural applications. Perhaps the most significant is their use in primary structure rocket motor case applications such as third stage Minuteman and in both stages of Polaris missiles. Other applications have included radomes, hatches, secondary aircraft structure, decorative coverings, etc. In the majority of cases, the applications have been in areas of other than primary load bearing structures. The major materials limitation to their usage in primary structural applications has been due to the relatively low modulus of elasticity of 12×10^6 psi. This modulus characteristic shows little hope for significant improvement.

By 1961, Air Force exploratory development demonstrated that by vapor depositing boron on a fine tungsten filament core, a boron filament could be produced that had a modulus of 60×10^6 psi. Subsequent investigation of composites made with these high modulus filaments provided encouragement and impetus to the development. In 1963, the potential of advanced composites was emphasized during Project FORECAST. A Scientific Advisory Board report of July 1964 and Program Definition Phase reports of December 1964, indicated that significant payoffs could be realized by the application of advanced composites in the areas of aircraft structures, helicopter rotor blades, re-entry vehicles, and gas turbine engines. The SAB report concluded that advanced composite structures for aircraft could result in a substantial weight savings on the order of 25 to 35 per cent. The Program Definition Phase reports projected that structural weight savings in aircraft and propulsion systems ranged from 10 per cent to 50 per cent. These studies also indicated that in almost every case the systems designer could be granted relief from conventional design constraints. Thus, the need for an integrated materials/design approach was indicated. As a result of the added impetus provided by FORECAST activities, an Advanced Development Program was formulated to develop, demonstrate, and bring to the operational weapons use stage this exciting new technology. The management responsibility of the Advanced Development Program was given to the Air Force Materials Laboratory of the Research and Technology Division. After a short period of management at the staff level, a new Laboratory Division was formed in January 1965 and was delegated the responsibility to accomplish the Advanced Development Program. It is

within this new Advanced Filaments and Composites Division that the development efforts described in this paper were performed.

On the basis of the state-of-the-art provided by exploratory development efforts and the potential payoffs projected in applications studies, objectives were developed for the Advanced Development Program. The overall objective of the program is to conclusively demonstrate the high potential payoffs of application of advanced composites in aerospace structural and propulsion systems.

Program goals include:

1. Materials development which will make the use of advanced composites both reliable and cost effective.
2. The development of new design concepts and techniques which will take full advantage of the unique characteristics of advanced composite materials and minimize the disadvantages.
3. The development of fabrication and test procedures which will effectively translate the materials and design solutions into practical cost effective, reproducible structural assemblies on a quality and quantity basis.
4. The design, fabrication, and test of full-scale structural assemblies which will conclusively demonstrate the high potential payoffs possible through the use of advanced composite materials.

The approach taken to achieve these goals was to integrate the efforts of materials engineers, designers, and fabricators into a single team effort. It is this team concept that is currently being employed both in the Air Force management activities and in the participating industry activities. Too often in the past, new materials have been laboratory engineered and have been placed "on-the-shelf" for use by designers who didn't understand the materials and fabricators who couldn't handle it. The purpose of the advanced composite materials, design, and fabrication team is to not only accelerate the advancement of the technology, but also to insure that a trained, experienced high confidence level industry is ready to project the technology into usable, operational system hardware.

In the initial stages of the Advanced Development Program, emphasis was placed on improving filament materials and reducing production costs. The cost of boron (tungsten core) filament has consequently been reduced from approximately \$6000 per pound in 1963 to approximately \$800 per pound in early 1966. By September 1966, it is predicted to be

approximately \$500 per pound. Efforts to reduce the cost are continuing and include the possible introduction of new reinforcements such as silica substrate boron filaments, carbon filaments, and silicon carbide filaments.

Along with the efforts to reduce costs of materials, emphasis has been in the areas of fabrication and testing of advanced composite materials. One of the major developments has been to provide a materials form which can be efficiently and effectively used in fabricating the all important demonstrative structural hardware. The primary form used to date is a resin-preimpregnated boron filament tape. The basic tape is one-eighth inch wide and contains thirty boron filaments collimated in one layer thick flat band across the tape. All tape used in hardware fabrication to date has been impregnated with an epoxy resin. To expedite the hand layup techniques used in most of the programs to date, a three-inch wide tape was prepared by combining 24 one-eighth inch tapes. Another materials form used in the program has been widegoods produced by filament winding on a large drum. The pre-impregnated material was cut off the drum and used as a layer of oriented filaments with which composite laminates can be fabricated.

In October 1965, five seven-month component hardware development efforts were initiated. These were in the application areas of aircraft structures, helicopter rotor blades, re-entry vehicles, and gas turbine engines. The purpose of these programs was to take a first, hard look at problems involved in designing, fabricating, and testing hardware using advanced composite materials. Another purpose, and perhaps even more important, was to provide meaningful direction to the rest of the Advanced Development Program.

Each of the component development efforts included three work areas: (1) program studies, (2) technological base activities, and (3) component development. Program studies included application studies, operational analyses, and cost effectiveness studies. The supporting materials screening, fabrication, and testing was included in the technological base activities. The culmination of the efforts is found in the actual design, fabrication, and test of the component hardware. This culmination presents the component hardware development efforts in their true light as the spearhead of the overall program.

Two of the seven-month programs were in the aircraft structures area. The first of these was with General Dynamics/Fort Worth. Participating industry team members included the Illinois Institute of Technology Research Institute and Texaco Experiment, Incorporated. The specific application investigated was the F-111 horizontal stabilizer. The major seven-month demonstrative item developed was a represen-

tative primary load bearing mid-section of the stabilizer. Figure 1 is a sketch of this component. Two items were fabricated. One was for static test at the contractor's facility, and the other was for fatigue test at the Air Force Flight Dynamics Laboratory facility at Wright-Patterson Air Force Base. The configuration of the items included boron reinforced epoxy matrix skins, full-depth fiberglass honeycomb core, fiberglass closure spars along each edge, and titanium end fittings. This is a good example of the materials application philosophy of the entire Advanced Development Program which consists of using the best material from both a cost and performance basis. This philosophy has resulted in a discriminating use of advanced composites only where the great performance of these materials is essential.

Program studies showed that a weight savings of 350 pounds in an entire horizontal stabilizer assembly can be realized on a direct substitution basis using the configuration described above. Another 200 pounds of weight savings is expected, due to a redesign in internal tail structure and control assembly because of the lighter weight tail assembly. Thus, a total of 550 pounds of weight savings is possible by applying advanced composite materials and redesign in the F-111 horizontal stabilizer.

Unique test specimens were developed in the technological base activities of the program. Of particular interest were beam specimens constructed of boron-epoxy skins and aluminum honeycomb core. By using four point test loading, unidirectional boron-epoxy composite materials tensile strengths from 200,000 psi to 224,000 psi were reported.

The laminate configurations used in the skins and the resulting measured properties are examples of the data used in the computerized design techniques which determined the final skin laminate layups in the two tail components. The three-inch wide tape materials form was used to fabricate these skins.

The static test of the first tail component was extremely successful. The spectrum of loading included both subsonic configurations and supersonic configurations. The aeroelastic response of the component was 101% of design under supersonic conditions and 104% of design under subsonic conditions. The component was tested to destruction which occurred at 133% of design limit load or 89% of design ultimate for an ultimate factor of safety of 1.5. The component responded elastically to failure. As a result of the failure analysis, three possible failure modes have been postulated. A non-bonded area approximately 1" x 6" existed between the skin and the titanium spar on the compression side of the skin. The failure could have been due to compression buckle of

the skin which resulted in delamination of the joint. At another area along the failure, stress analysis and strain gage data showed that the load path near one edge of the failure was not as predicted. Consequently, the filament orientation was not optimized and failure could have initiated in this area. Strain gage data indicated that there was a more rapid transfer of load from the composite to the titanium scarf plate than had been predicted. Thus, this represents the third possible failure mode.

At the time of writing this paper, the second component has been instrumented but the scheduled fatigue test had not been accomplished. A fatigue spectrum representative of the F-111 design spectrum will be used for this test. An equivalent of four lifetimes will be applied.

The second program in the aircraft structures area was with North American Aviation, Los Angeles Division. The major component developed was a wing box (Figure 2) representative of the configuration of the T-39 wing center section. As in the horizontal stabilizer program, one of the two items was for static test at the contractor's facility, and one was for fatigue test at the Air Force Flight Dynamics Laboratory. The configuration of the items included upper and lower plates of boron-epoxy skins with aluminum honeycomb cores, fiberglass spars, and stainless steel end fittings for attachment to the test rig. Preimpregnated widegoods were used in the fabrication of the plate skins.

Program studies showed that using a conventional aluminum stringer stiffened concept as a base, 36.5% weight savings can be realized using the advanced composite design. This design is based on boron filaments with an average tensile strength of 250,000 psi. Using boron filaments with an average tensile strength of 400,000 psi, a weight savings of 42.5% is possible due to the resulting improved and more efficient composite materials.

The first wing box component was static tested to destruction. Failure of the item occurred at 69% of design ultimate considering a factor of safety of 1.5. Although this is lower than was expected, an analysis has shown that failure probably initiated at the corner of the compression face and the steel end fitting. Poisson's Ratio of the face plate had not been adequately considered in the design and excessive strain of the face plate coupled with the constraint of the steel end fitting resulted in excessive shear stress. The combination of the added shear and the compression stresses induced premature failure.

The second item has not been fatigue tested at the time of writing this paper. A fatigue spectrum representative of the T-39 design spectrum will be used for the test.

The second systems application area in the seven-month component development efforts was in the area of helicopter rotor blades. The demonstration items included a 28-inch tail rotor section, main rotor blade root end specimens, and a 6-foot main rotor blade spar. All of the items were designed and applicable to the UH-1F helicopter. Whittaker Corporation was the prime contractor with Bell Helicopter as the team member.

Figure 3 is a sketch of the tail rotor section. This aeroelastic item included boron-epoxy skins, trailing edge, and spar, aluminum honeycomb core, and stainless steel leading edge erosion cap. Filament orientation in the skins was $\pm 30^\circ$ to the span direction, unidirectional in the trailing edge member, and $\pm 10^\circ$ to the span direction in the spar. The design of the item was intended to attain the same flexure and torsional stiffness as in an all aluminum counterpart. Testing of the aeroelastic item showed it to be 36% stiffer in flexure, and 41% stiffer in torsion than the aluminum blade section. In addition, the advanced composite blade section was 25% lighter in weight than the aluminum counterpart.

Another major component designed, fabricated, and tested during the program was a 6 ft section of a boron-epoxy main rotor spar. The design was a flattened "D" section which matched the upper and lower airfoil contours of the main rotor designed during the seven-month program. The spar was fatigue tested as a free-free beam. Failure occurred after only 81,400 cycles which was far below the approximately 10^6 cycles anticipated. Subsequent testing of small specimens cut from the spar indicated that the fabrication process had not successfully produced a sound composite material. One specimen ran to destruction at 2,030 cycles and a peak load of 14,500 psi. Another specimen was tested to 8.9×10^6 cycles at a peak loading of 13,000 psi. Investigation of a cross section cut from the spar indicated that the 24-ply thick structure had not been compacted adequately during the fabrication and curing cycles. Main rotor root end specimens which were fabricated with composite laminates having filament orientations the same as the main rotor spar were successfully fatigue tested to design values.

The success of the aeroelastic tail rotor component discussed earlier and the main rotor blade root end specimens are evidence of the efficient design and fabrication techniques that are available. The premature failure of the main rotor spar section confirms the necessity of producing sound void-free composite materials which can be depended upon to perform as predicted in design.

Program studies indicate that only marginal performance improvements can be realized by applying advanced composite materials to

small helicopter rotor blades. One of the major benefits applicable to these new materials is weight savings. However, weight savings are not necessarily a benefit in the rotor blade application because of the requirement to maintain rotor inertia to a level adequate for auto rotation. Further considerations of applying these materials to other parts of the helicopter system make the weight savings characteristic of continued interest. To design and build a blade of composite materials and take advantage of the ability to tune the frequency response of the blade by selective application of high modulus reinforcement materials is perhaps the primary benefit that can be derived in the rotor blade application areas. This benefit cascades into improvements in reducing total system vibration, pilot fatigue, and increasing the life of the blade.

The third major area in the seven-month component efforts was that of gas turbine engine application. This contract was with General Electric of Evendale, Ohio. Other industry team members were Whittaker Corporation and General Technologies Corporation. Figure 4 is a sketch of the three major components considered in the program.

Program studies indicate that considerable weight savings can be realized by using advanced composites in this application area. Using today's conventional materials as a baseline, program analyses indicate that a weight savings of 15% in a direct lift engine and 18% in a cruise engine are possible by substitution of organic matrix advanced composites in the cool section of the engine. Looking farther into the future and into the hot section of the engine, by using higher temperature organic matrices and metal matrix advanced composites, a weight savings of 33% in a direct lift engine and 45% in a cruise engine are possible with redesign of the engine.

Three first stage compressor integral rotor blade and disc assemblies were fabricated from glass reinforced epoxy matrix composite material. Two additional rotors were fabricated from a boron-glass-epoxy composite. Initial tests on the glass-epoxy rotors were conducted at both vacuum and ambient conditions. Design tip speed was 1500 feet per second. A tip speed of 1220 feet per second was achieved at temperatures exceeding 275°F. Some delamination was noted at the tip and base of the blades. However, structural characteristics of the rotors were such that no damaging vibrational levels were observed. The boron reinforced rotors should reduce the delamination problem, increase the tip speed capability; and because of their inherent and higher vibrational frequencies, they should eliminate any damaging vibrational difficulties which might occur with increased speeds. The boron-glass-epoxy rotors had not been tested at the time this paper was written.

Sixteen boron-glass-epoxy fan blades were fabricated during the

program. Frequency tests showed that the boron composite blade is superior in stiffness to a titanium blade of similar design. It is also 20% lighter in weight than a hollow titanium blade which weighs 254 grams and 50% lighter than the currently used solid titanium blade which weighs 400 grams. Attachment failures showed the need to design an attachment suitable for composites rather than rely on the titanium blade dovetail configuration. Subsequent work will include additional dovetail pull tests and analysis of redesign attachment configurations.

Ten stator vanes were designed, fabricated, and tested to demonstrate needed operational stiffness and fatigue properties. The boron-glass-epoxy vanes were tested for fatigue and demonstrated that they were capable of operating indefinitely in the experimental direct-lift engine at engine design loads. Ballistic impact tests were run on the leading and trailing edges of the vanes. Although damaged, the vanes were still three times stiffer than an undamaged fiberglass vane counterpart. The boron-glass vanes also maintained a higher frequency response than the all glass vanes. No comparisons were made with metal vanes of a similar geometry.

Although these hardware items have shown that considerable payoffs can be achieved in using advanced composites in gas turbine engines, in order to realize the full potential much remains to be done particularly in the high temperature matrix areas. Metal matrix composites technology is really in its infancy, but it promises to provide the higher temperature capability that is needed.

The fourth major area in the seven-month efforts was the application of advanced composite materials in re-entry vehicles. This contract was with General Electric of Valley Forge. Hercules Powder Company was a team member. The specific demonstration component was a cylinder representing the mid-section of a re-entry vehicle. The load configuration that a typical re-entry vehicle conical midsection would experience was reduced to representative loads on the three 18-inch diameter, 24-inch long cylinders which were designed, fabricated, and tested in the program.

The basic design of the cylinders included internal stiffeners integrally wound and cured with the cylinder wall. The configuration is shown in the cutout section in Figure 5. There are three primary advantages of this design and materials combination over an aluminum substructure counterpart: (1) greater internal volume which will payoff in increased size or number of payloads and thus greater targeting flexibility per vehicle, (2) reduced weight which also permits increased payload, and (3) improved aerodynamic stability which results from decreasing the weight in the midsection, thus increasing the distance

between the center of gravity and the center of pressure.

The primary purpose of the first of the three cylinders was to check out the automated tape winding procedure and equipment. This was the only seven-month hardware program that used a fabrication technique other than hand layup. In order to conserve the relatively expensive boron filament material, this first item was wound using boron and glass. A plaster mandrel was formed and grooves were cut to accommodate the integrally wound stiffeners. One-eighth inch wide boron reinforced epoxy resin preimpregnated tape was first wound into the bottom of the grooves. A lightweight plastic filler strip was then clamped into each groove leaving sufficient space on each side to permit winding of the sidewalls of the stiffeners. After the stiffener sidewalls were wound, the first circumferential wrap was made on the main wall of the cylinder. This was followed by helical windings and final circumferential windings. After curing in the autoclave, the plaster mandrel was removed and the cylinder inspected. The first cylinder made of glass and boron tape showed considerable stiffener wall voids. Consequently, more precise control of stiffener wall thickness was desirable. Subsequent cylinders were fabricated using an eutectic metal stiffener filler which was melted and removed after the cylinder was cured. This procedure produced excellent stiffeners.

The second cylinder was designed for three loading conditions. The first was axial tension of 56,200 pounds combined with 102 psi external side pressure. The second was bending of 90,000 inch pounds. The third was axial compression of 22,000 pounds combined with 90 psi external side pressure. The cylinder was tested to at least 75% of design loads in all three cases. It was then subjected to axial tension to destruction which occurred at 59,900 pounds which was 107% of design. The failure mode was local bending caused by the end fitting which was bonded to the inside of the cylinder wall.

The third cylinder was of a more optimized design taking maximum advantage of the supporting test information acquired from 6-inch diameter cylinders designed, fabricated, and tested during the program. Designing to the same load configuration as used with cylinder number two, less stiffeners were required in number three. In addition, the end fitting was designed for and bonded to both the inner and outer surface of the cylinder wall to eliminate the introduction of local bending during test. The test sequence on the third cylinder included two runs to 100% of design under each of the three cases described earlier. The cylinder was not tested to destruction.

These initial re-entry vehicle results have been most promising. However, much remains to be done. Problems to be considered include

attaching the midsection to the rest of the vehicle, attaching the heat shield, and attaching internal subsystems to the substructure. One potential design and fabrication technique which may vastly improve the picture is to integrally wind the heat shield and substructure.

The Advanced Development Program is charged with the responsibility of conclusively demonstrating the payoffs in the use of advanced composites technology. The five seven-month component hardware development programs were the first major step toward an October 1968 conclusive demonstration. Currently, two areas are being pursued: aircraft structures, and helicopter rotor blades. By October 1968 a flightworthy item of primary structural hardware will have been designed, fabricated, and tested. Examples of items that may be included are an F-111 horizontal stabilizer ground tested and ready for flight test or a full set of helicopter rotor blades flight tested. By that time, the cost of high modulus filaments will have been reduced to a point which will hopefully make the October 1968 hardware cost effective. In addition to the dramatic hardware demonstrations, there will be a materials design, fabrication, and test handbook. With these accomplishments, advanced composite technology will be significantly closer to winning the game. The game is - - - get advanced composites flying.

This has been a very brief resume of the component hardware that has been designed, fabricated, and tested. Although these efforts by no means provide a complete story, they have provided a first, hard look at the potential application and first generation problems with which advanced composite technology is confronted. In the areas of gas turbine engine application, there is a dramatic need for increased temperature capability possible through the use of metal matrix composites. All the areas have shown a definite need for automated tape layup techniques. The hand layup techniques used could not possibly provide cost effective procedures for production of operational systems hardware. In all areas, there is a dire need for more design data; for example, there is only very limited fatigue data available. These are only examples of the multitude of problems facing the advancement of the technology.

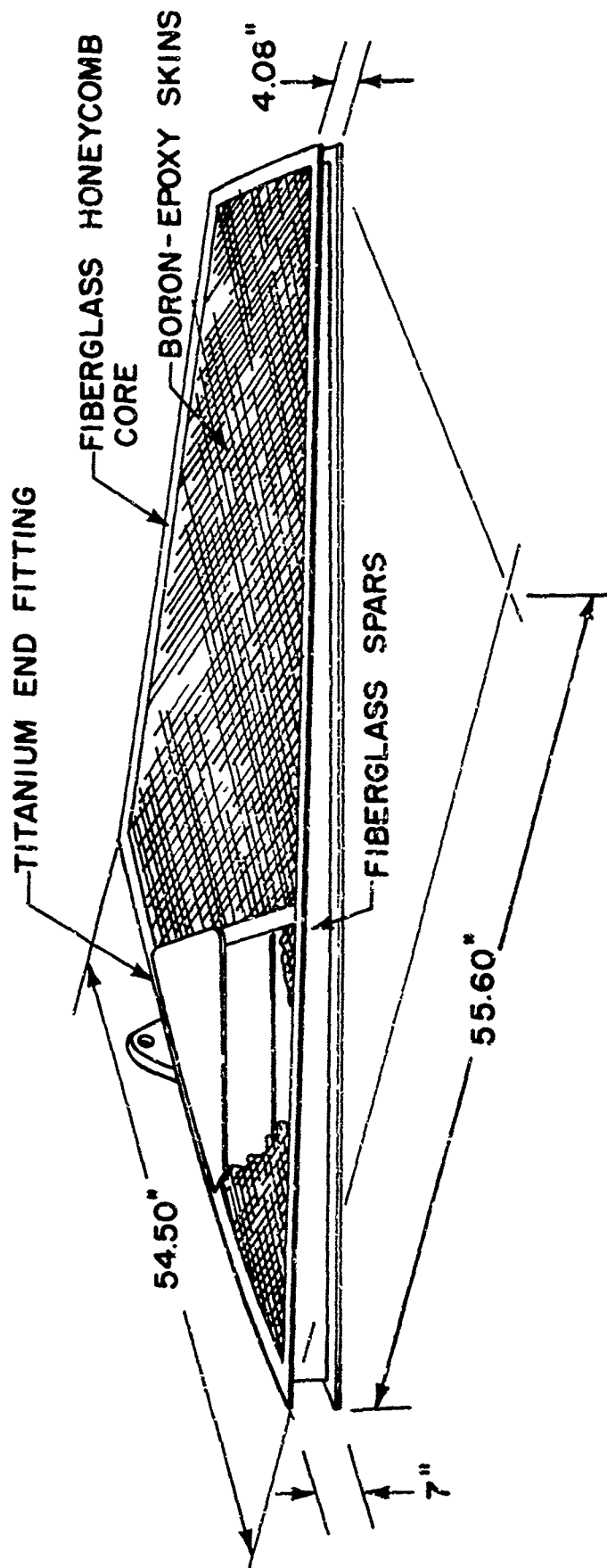


FIG.1 F-111 HORIZONTAL STABILIZER COMPONENT

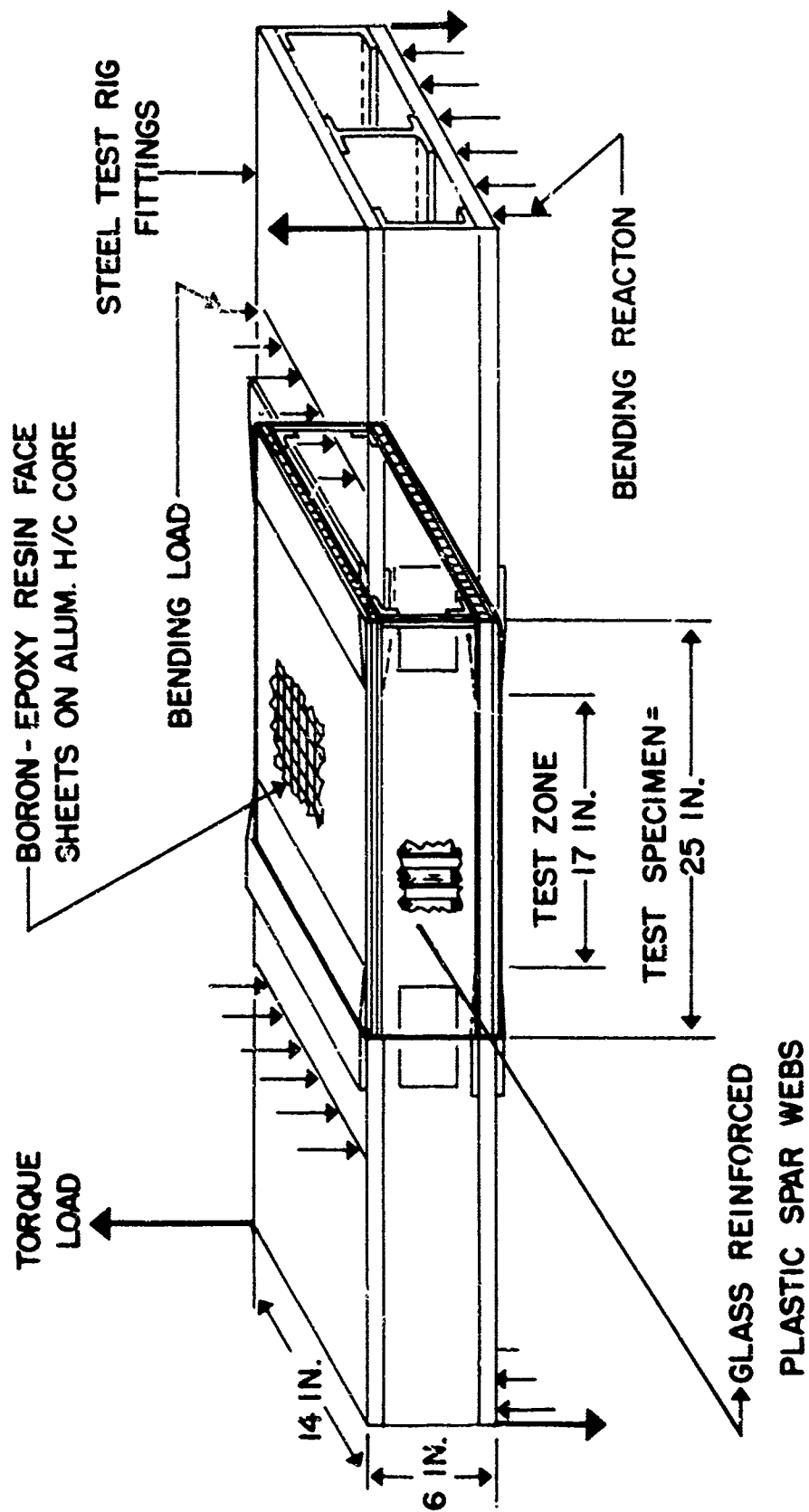


FIG.2 T-39 WING BOX COMPONENT

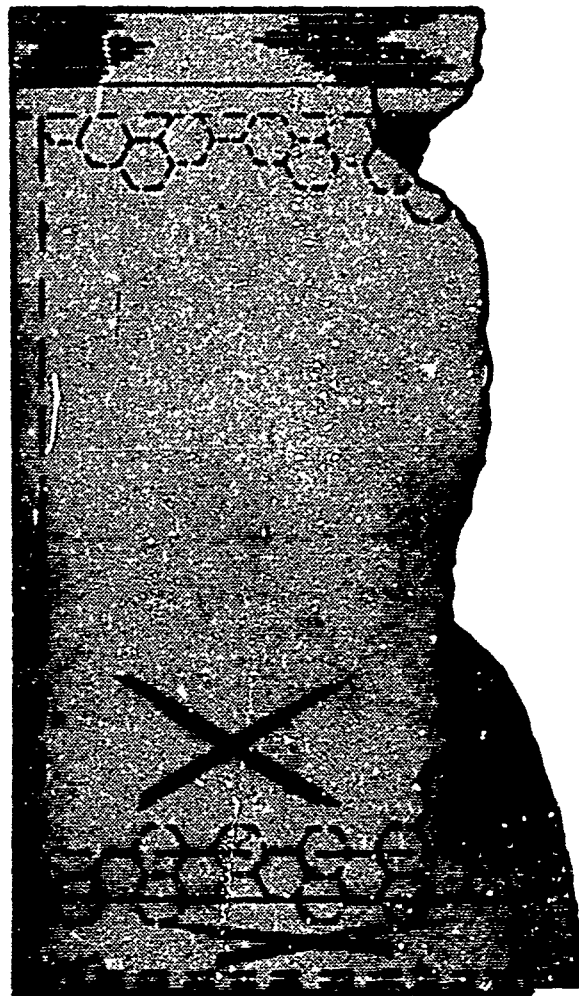
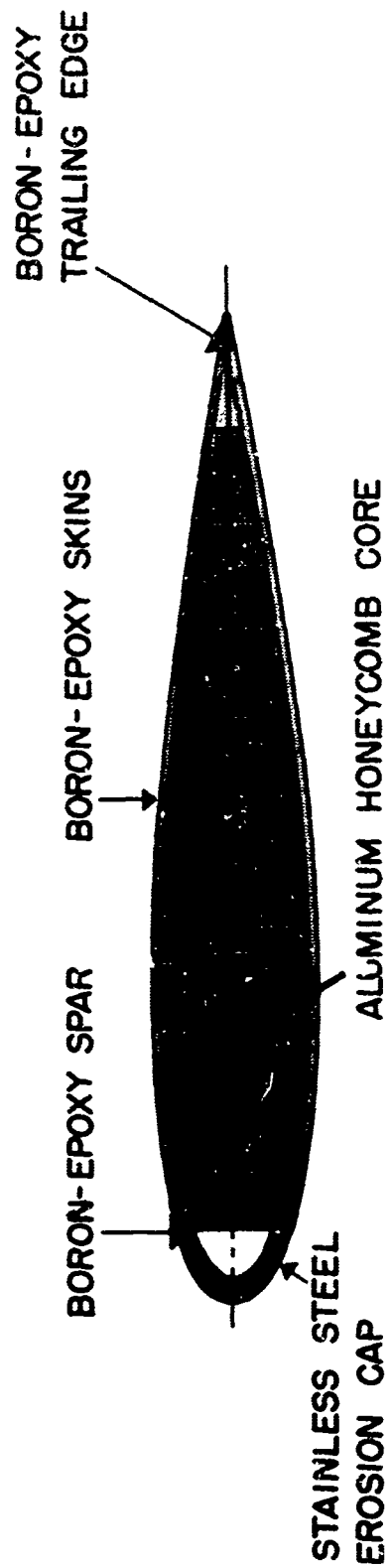


FIG. 3 AEROELASTIC TAIL ROTOR COMPONENT

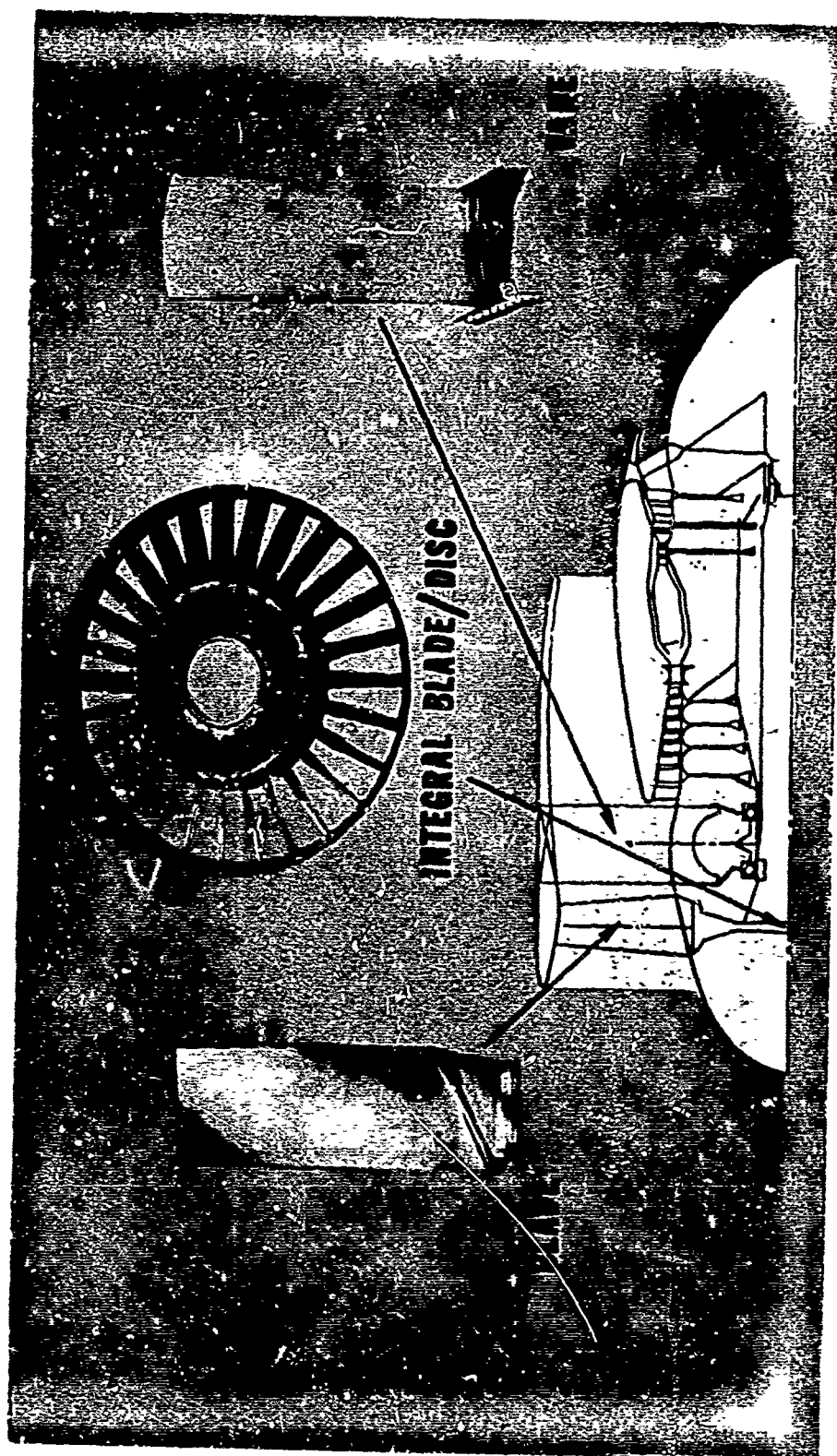
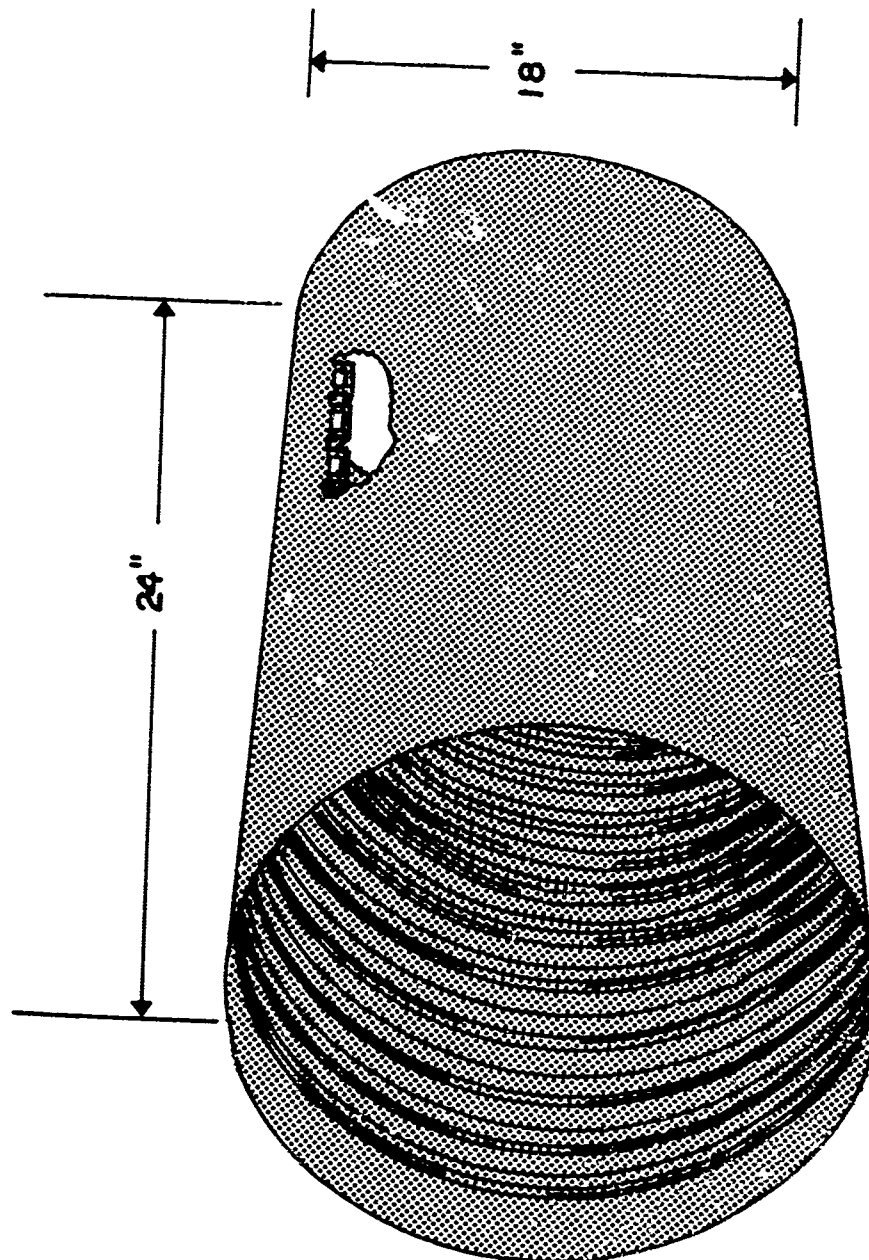


FIG. 4 GAS TURBINE ENGINE COMPONENTS



**FIG.5 TYPICAL RE-ENTRY VEHICLE
STRUCTURE**

ULTRASONIC STUDIES OF 1060 AND 6061-T6 ALUMINUM

JAMES R. ASAY & ARTHUR H. GUENTHER

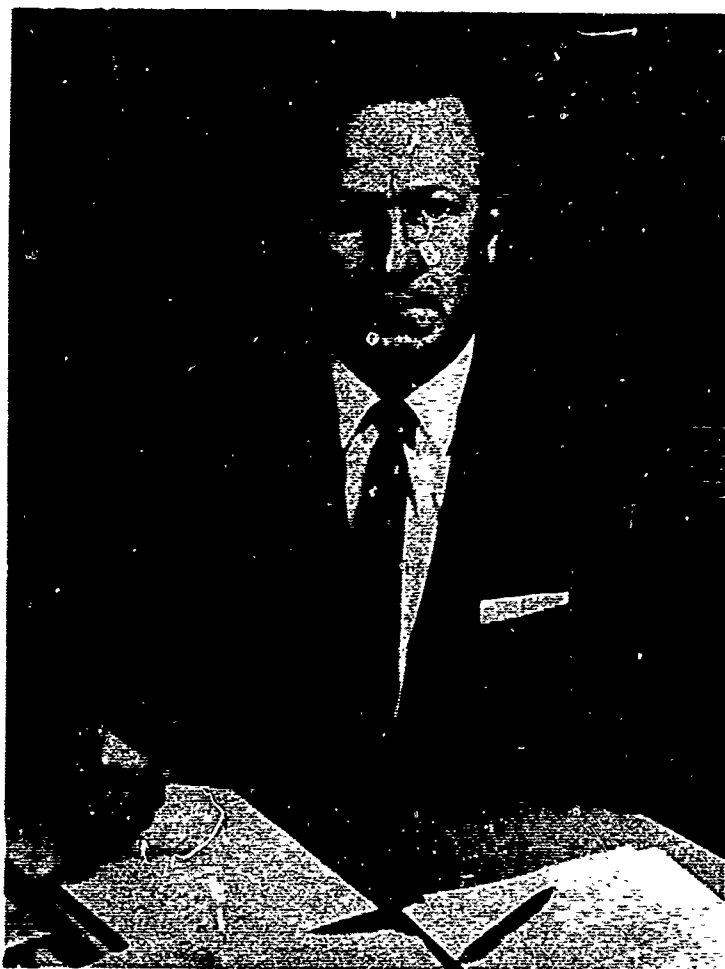
AIR FORCE WEAPONS LABORATORY
KIRTLAND APB, NEW MEXICO



James R. Asay

BIOGRAPHY

First Lieutenant James R. Asay was graduated with honors from San Jose, California in 1964 with a B.A. degree in Physics. He is currently completing the requirements for an M.S. degree in Physics at the University of New Mexico. He entered Officer's Training School in June 1964 and was awarded a commission as a Second Lieutenant in September of that year. Since then he has served as a Project Officer in the Air Force Weapons Laboratory. He has performed research leading to publication of papers relating to the applications of ultrasonic velocity measurements to material dynamic investigations.



Arthur H. Guenther

BIOGRAPHY

Dr. Arthur H. Guenther was born April 20, 1931, in Hoboken, New Jersey. He graduated from Memorial High School, West New York, New Jersey, in June, 1949. He received the B.S. degree in Chemistry from Rutgers University, New Brunswick, New Jersey, in June 1953. He was a graduate assistant and fellow at the Pennsylvania State University, University Park, Pennsylvania from September, 1953, until June, 1957. He was commissioned a 2nd Lieutenant in the United States Air Force in June, 1953, and was promoted to 1st Lieutenant in June, 1956. He received his PhD in Chemistry-Physics at the Pennsylvania State University in 1957. Dr. Guenther served as Project Officer, Physics Branch, AFSWC (1st Lt) from 1957-1959. He served as Director, Pulse Power Lab (GS-13) from 1959-1960; Director, Material Dynamics Laboratories (GS-14) from 1960-1963; Scientific Advisor, Physics Branch, AFSWC (GS-15) from 1963-1965; and Scientific Advisor and Chief, Simulation Group, Effects Branch, AFWL (PL-313) from 1965 to present. He is a member of the American Chemical Society, American Institute of Physics, Phi Lambda Upsilon and Sigma Psi. He has been coauthor of approximately 30 scientific publications in the fields of material dynamics, spectroscopy, lasers, and optics, exploding wire phenomena, and other high energy density research areas and in particular simulation of nuclear weapon effects and phenomena.

ABSTRACT

An ultrasonic pulse echo technique has been used to measure the longitudinal and shear velocities at ambient pressure in two aluminum alloys, 1060 and 6061-T6. Measurements were made from 25°C to ~ 200°C to determine the temperature dependence of the elastic constants. A Grüneisen ratio is calculated from the experimental data which is used in conjunction with the Murnaghan logarithmic representation of the equation of state to estimate the specific volume to ~ 450 kbars. Data are also presented regarding the pressure dependence of the various modes of propagation, as obtained in a uniaxial stress technique. The applied uniaxial stress ranged from ambient to ~ 11,000 psi for 6061-T6, and to ~ 3,000 psi for 1060 AL.

TABLE OF CONTENTS

	<u>Page</u>
I. INTRODUCTION	1
II. EXPERIMENTAL METHOD	3
2.1 Acoustic Circuitry	3
2.2 Uniaxial Measurements	4
2.3 Errors	5
III. RESULTS	6
3.1 Relations for Third-Order Coefficients	6
3.2 Results for 6061-T6 Aluminum	7
3.3 Results for 1060 Aluminum	9
IV. DISCUSSION	11
V. CONCLUSIONS	13

I. INTRODUCTION

The experimental investigation of the equation of state of solids at high pressures was originally initiated by Bridgman¹ employing static compressibility methods. The pressure range of investigation has been extended in recent years by dynamic approaches in which the pressure is generated by high magnitude shock waves induced in the specimen by explosive or projectile impact techniques.²

A convenient and highly precise method for investigating the equation of state of solids is through the use of ultrasonic techniques, in which acoustic velocities are measured in a solid specimen subjected to various states of stress. This approach was employed in a technique essentially established by Lazarus,³ in which different acoustic velocities (longitudinal, shear) were measured as a function of hydrostatic pressure. Such studies allow determinations of the pressure derivatives of the characteristic modes of propagation and, consequently, of the elastic constants. As illustrated recently by Anderson,⁴ precise ultrasonic measurements obtained at relatively low hydrostatic pressures (on the order of a few kilobars) can be extrapolated in certain cases to estimate the compression (ΔV) at considerably higher pressures, such as would be experienced by targets exposed to nuclear weapon environments. This compression quantity is important in equation of state considerations which relate to the behavior of materials under static high pressure or impulsive loading. Hence, this equation of state relation is of major import and plays a fundamental role in Air Force scientific investigations which study damage mechanisms and thresholds on contemporary and future operational Aerospace systems, and will directly lead to an improved basic understanding of the vulnerability and survivability of such systems.

The advantage of the ultrasonic approach is that an analytical expression for the compression can be determined solely from the acoustic measurements, without recourse to curve fitting of the coefficients in a polynomial expansion. The applicability of the technique relies, in large part, upon the precision with which the ultrasonic measurements can be made. The accuracy of such measurements has been extended in recent years to within a few parts in 10^5 , principally through the application of pulse superposition techniques developed by McSkimin.⁵

Another point regarding the applicability of ultrasonic pressure measurements concerns the stress environment to which the specimen is exposed. For the determination of most equation of state parameters, perhaps the simplest approach is to employ hydrostatic pressure. This state of stress is desirable for investigations of many materials since, as Hughes and Kelly⁶ have shown, the symmetry of the specimen is preserved under hydrostatic pressure. However, Brugger⁷ illustrates that ultrasonic measurements on a specimen subjected to uniaxial stress

can be used to calculate the third-order stiffnesses, which are defined as the isothermal strain derivatives of the isentropic second-order stiffnesses (as determined at zero external pressure). Since the pressure derivatives of the elastic moduli are functions of the third-order coefficients, the derivatives can be determined from the calculations involving these quantities. In addition, Thurston⁸ has shown that the third-order coefficients can be used to explain anharmonic mechanisms which are responsible for phenomena such as crystal stability, thermal expansion, elastic damping, Grüneisen coefficients, and harmonic mode generation, and are therefore of great applicability to the general areas of material dynamics.

Since the uniaxial stress technique relies upon complete elastic behavior of the specimen in the state of uniaxial stress, the method has been used primarily for the investigation of single crystals or for materials that do not exhibit slip properties or plastic deformation under the application of a one-dimensional stress. As Bateman⁹ et al., have pointed out, uniaxial stress often induce plastic strain or slip at relatively low pressures, and such behavior can produce much larger effects than the elastic properties of the material itself.

The purpose of the present experiment was to study the applicability of calculating the third-order coefficients in two polycrystalline aluminum alloys subjected to uniaxial stress. The alloys used for this study were 1060 Al (measured bulk density of 2.702 ± 0.002 g/cc) and 6061-T6 Al (bulk density 2.704 ± 0.003). The 1060 alloy is essentially pure aluminum (99.6% Al) which exhibits a low yield strength (~ 4000 psi) when in the annealed condition, as in the present experiments. 6061 Al is $\sim 98\%$ aluminum with minor concentrations of magnesium, chromium, silicon and copper. In the T-6 condition this alloy exhibits a yield strength of $\sim 37,000$ psi. These alloys are presently being utilized in nuclear weapons effects tests at the Nevada Test Site as control samples and as members of structural assemblies. Hence, complete understanding of their high pressure material properties is necessary from analytical and engineering standpoints.

The temperature dependence of the longitudinal and shear wave velocities was also determined for both alloys, since this information is also necessary in equation of state calculations.

II. EXPERIMENTAL METHOD

2.1 Acoustic Circuitry

The electronic circuitry used here is shown in Figure 1. A time mark generator triggers a pulse generator and at some later time, determined by the continuously variable delay line, triggers the oscilloscope.

The RF pulse generator produces a pulse a few microseconds in duration with a carrier frequency of from 0.2 to ~ 100 Mc. The input signal is applied to a transducer located on the specimen and simultaneously displayed on the oscilloscope. The time delay between the applied signal and one of the reflected echoes is determined by extrapolating between calibrated 1 μ sec time marks produced by the time mark generator. An attenuator was used to prevent overloading the amplifier when the 500-volt output signal from the oscillator was viewed.

Since the velocity, and consequently the roundtrip time, changes only slightly with applied uniaxial stress, it was necessary to precisely detect small changes in transit time. This was accomplished by using the variable time delay shown in Figure 1. By triggering the oscilloscope just before a preselected echo arrived, the echo could be viewed on an expanded time scale and small changes in transit time could easily be detected with the delay potentiometer. A change of 2 to 3 nsec in a 30 to 50 μ sec time interval could be reproducibly measured with this arrangement.

The samples were prepared as approximately 1-inch cubes and were machined flat and parallel to within ~ 0.003 mm. For the uniaxial measurements it was necessary that the corners be square to ensure one-dimensional stress in the specimen. This was achieved with various degrees of success; however, the corners were generally square to within ~ 2 minutes of the arc.

Both quartz and PZT-5 (lead zirconate titanate) transducers were used for the velocity measurements. For most of the measurements the transducers were operated at their 3-Mc fundamental frequencies. It was found that for both the longitudinal and shear modes the quartz crystals (X-cut for longitudinal measurements and AC-cut for shear measurements) produced cleaner waveforms, and were therefore used for most of the stress measurements. The disadvantage of quartz over PZT is that the generated stress fields for a given input voltage are lower because of the lower piezoelectric coefficients. However, this caused no experimental problems, since the amplified received signals were well above background noise.

Some difficulty was encountered in choosing a proper bond for attaching the transducers to the specimens. A rigid bond is necessary for the shear measurements in order to transmit the transverse motion

of the transducer to the specimen. Also, for the stress measurements a bond is necessary which will produce no adverse effects as the lateral boundaries of the specimen contract under uniaxial compression. A light viscosity silicone oil was satisfactory for the longitudinal experiments. But because of the requirement of a rigid bond, the silicone oil could not be used for shear measurements. However, an epoxy resin (Eastman 910) was satisfactory for these measurements, and the transducer could be easily removed by heating at 400°C for a few minutes. Both types of transducers were bonded to the specimen under moderate pressure.

2.2 Uniaxial Measurements

The most important consideration in the uniaxial measurements is the provision of a homogeneous uniaxial load. The system used to accomplish this is shown in Figure 2. The entire system consists of a 20-ton lab press driven by a manually operated pump. To eliminate the effect of friction in the hydraulic system, the pressure gauges used in these experiments were calibrated with 10,000 and 50,000 lb proving rings. These rings had been previously calibrated at the National Bureau of Standards and were accurate to within 0.3 percent. The pressure was maintained to within ± 20 psi throughout the pressure range of 0 to 11,000 psi.

To maintain complete alignment of the sample and piston, a ball bearing-piston arrangement was used, as shown in Figure 2. To compensate for any misalignment of the piston jacks, both the sample and piston anvil were machined flat to 0.003 mm.

Furthermore, shear forces arising because of the difference in lateral expansions of the piston and specimen can cause undesirable effects. An analysis of Bogardus¹⁰ indicates that these forces can be minimized by matching the ratio of Young's modulus to Poisson's ratio for the sample and piston surface. Measurements were therefore made with a 1/4-inch thick piece of aluminum inserted between sample surface and piston anvil. However, no definite difference from the original measurements could be detected, so it was concluded that the effect is apparently insignificant in the present study.

Since a temperature change in aluminum corresponds to a larger change in the velocity than a pressure change, it was important to maintain close temperature control during a pressure run. An enclosure around the specimen controlled the temperature variation to $\sim 0.1^\circ\text{C}$ during a set of pressure measurements. The variation in temperature from one set of measurements to another was $\sim 0.5^\circ\text{C}$. However, the present technique was not sensitive enough to detect a difference in slope resulting from a change in environment of 0.5°C so that the data were plotted together.

2.3 Errors

The estimated uncertainty for the velocity vs temperature measurements is approximately 0.25 percent. This value is obtained from uncertainties in the echo transit time (0.02%), path length (0.01%), transducer coupling (0.2%) and diffraction (0.007%, McSkimin and Andreatch¹¹). The temperature of the sample was measured to within 0.5°C, but since the slopes of the velocity-temperature curves are very small this source of error contributes only ~ 0.05 percent to the overall uncertainty. The uncertainty in transducer coupling is the largest contribution to the overall inaccuracy of the technique. This correction was obtained by measuring the transit times through various specimen thicknesses (6-38 mm) and by using different transducers and bonds.

For the uniaxial measurements, precision is highly important since it is necessary to accurately determine the change in velocity with uniaxial pressure. Since the transit time was on the order of 30 to 40 μ sec and a change of 2 to 3 nsec could reliably be detected, the precision was on the order of 1 part in 10^4 .

Uncontrollable effects lead to errors which may be greater than those discussed above and arise because of plastic yielding in the specimen, random misalignment between the piston and the sample, and random variable stress distribution. Lippincott and Duecker¹² have studied the pressure distribution in fixed-anvil systems and have shown that the pressure gradient is approximately parabolic across the stress applying face, being a maximum at the center of the face. Misalignment between specimen and piston is considered negligible in the present experiments, since the results for any one specimen were reproducible to within the stated limits of precision. Plastic flow, and possibly dislocation movement, can contribute a large error to the calculations of the third-order coefficients, since the calculations rely upon the fact that the deformation is purely elastic. This effect will be considered when discussing the results.

III. RESULTS

3.1 Relations for Third-Order Coefficients

The elastic coefficients which specify the velocity at any particular pressure can be defined as a combination of the second order constants as measured under atmospheric pressure and the third order coefficients determined under uniaxial stress. For arbitrary symmetry there are 216 third order constants.¹³ However, in the isotropic case only three of these are independent so that only three independent measurements must be made. Toupin and Bernstein¹⁴ and Thurston and Brugger¹⁵ have developed the equations of motion for the case of infinitesimal elastic deformations superimposed on a finite elastic deformation. A particular advantage to their notation is that the coefficients can be evaluated without calculating density and length changes, and hence the actual velocity of propagation. To evaluate the pressure derivatives of the effective coefficients, they introduce the concept of "natural velocity" $W(P)$, which is defined as the initial length divided by the transit time at pressure P . The actual velocity of propagation $V(P)$ can easily be determined by the relation¹⁶

$$V(P) = W(P) [l(P)/l(0)] \quad (1)$$

where $l(0)$ is the initial length and $l(P)$ is the length at pressure P , determinable from the ultrasonic measurements.

Table I illustrates the equations which relate a linear change in transit time as a function of applied pressure for both hydrostatic and uniaxial compression. The third-order coefficients v_1, v_2, v_3 correspond to the notation employed by Brugger.¹⁷ The quantity $(\rho_0 W^2)'_{P=0}$ can be evaluated from the ultrasonic data, since

$$W = W_0 + W'P$$

$$\frac{W}{W_0} = \frac{t_0}{t}, \quad W_0 = V_0 \quad (2)$$

$$(\rho_0 W^2)'_{P=0} = 2 \frac{\rho V_0^2}{P} \left(\frac{t_0}{t} - 1 \right)$$

where $\frac{t_0}{t}$ is the inverse ratio of the transit time at pressure P to that at atmospheric pressure. These equations are strictly valid only for a linear dependence of transit time with pressure, so that the quantity $\left(\frac{t_0}{t} \right) - 1$ must be linear in pressure.

Hydrostatic pressure measurements were not obtained in the present experiments and the equations are presented only for comparison purposes. However, since the third-order coefficients are primarily responsible for the change in velocity with purely elastic deformation, the pressure derivatives of the elastic constants can be expressed in terms of these quantities. Alternatively, the derivatives of the elastic constants can be calculated from the change in the actual velocity with applied hydrostatic pressures, since the symmetry is preserved under these conditions and therefore the equations for the elastic constants remain unchanged.

A particular parameter which is important to equation of state calculations is the pressure derivative of the adiabatic bulk modulus β_s , obtainable from the isothermal bulk modulus β_T . Birch¹⁸ and Toupin¹⁴ have shown that this quantity for an isotropic medium is given in the present notation by

$$\left(\frac{\partial \beta_s}{\partial P}\right)_{P=0} = - \left(\frac{9v_1 + 18v_2 + 8v_3}{9\beta_T} \right) - \frac{1}{3} \alpha \gamma T \quad (3)$$

where α is the volumetric coefficient of thermal expansion, γ is the Grüneisen ratio, and T is the absolute temperature.

3.2 6061-T6 Aluminum

Figure 3 shows the dependence of velocity on uniaxial pressure in 6061-T6 Al. The aluminum used for these measurements had been solution heat treated and artificially aged. Most of the physical measurements were taken after machining and without annealing. The data illustrated in Figure 3 correspond to shear wave propagation perpendicular to the stress. Since the degeneracy of the characteristic matrix for the undeformed material is removed by application of the uniaxial stress, the two transverse modes ($S(\parallel)$ and $S(\perp)$) have different speeds. However, as the figure shows, there is a definite scatter of points, particularly for the shear (\parallel) mode. The six slopes shown in Figure 3 for this mode were obtained on one specimen by measuring in the two perpendicular directions for each of the three sample axes. The notation used here corresponds to applied stress (M_1), propagation direction (N_1), and particle displacement (U_k) along specified axes. Considering a precision of ~ 1 part of 10^4 there is a definite separation into at least three different slopes. The effect was reproducible in that measurements for one set of conditions were reproducible after the specimen had been subjected to various other axial loadings. The effect was consistent, since other specimens exhibited a separation of the shear (\parallel) mode into approximately the same slopes. Hysteresis for all the uniaxial measurements was negligible if the maximum stress was kept below the yield strength, since the zero pressure transit time was reproduced to less than one part in 10^4 in all cases. Annealing did not produce a detectable change in the slopes, but the data in this case were limited to lower pressures because of the lower yield strength.

The shear (\perp) mode (Fig. 3) did not show a noticeable dependence upon the stress and propagation directions as the shear (\parallel) mode did. The data in the figure were obtained from a number of different specimens and for different stress directions. All of the data are within 1 part in 10^4 of the least squares lines.

The longitudinal mode gave results similar to the shear (\parallel) mode and was less dependent on sample orientation. Figure 4 indicates the behavior of velocity with uniaxial pressure for the specimen corresponding to the shear (\parallel) mode in Figure 3. Although the maximum separation of the longitudinal-pressure slopes is ~ 6 parts in 10^4 at 10,000 psi (vs ~ 3 parts in the 10^3 for the shear (\parallel) measurements), this magnitude of variation is well outside experimental uncertainty. The splitting of the slopes was also observed on other specimens, but the data are omitted from a least squares analysis on all data. The slopes α are calculated from the relation

$$\left(\frac{t}{t_0} - 1\right) = \alpha P \quad (4)$$

The maximum range of slopes is given for both the shear (\parallel) and longitudinal modes, and an average of all samples for the shear (\perp) mode.

The 6061-T6 aluminum used in these experiments exhibited a grain length on the order of 1 mm. The material also appeared to exhibit stratification on a microscopic scale. The sample corresponding to the shear (\parallel) mode in Figure 3 and the longitudinal mode of Figure 4 exhibited apparent stratification approximately perpendicular to the M_1 axis. In some of the other specimens the stratification appeared at various angles to the specimen axes. However, in these specimens the variation of the slopes for the shear (\parallel) mode likewise varied slightly from that in Figure 3.

Texture on a microscopic scale was probably induced in the material during initial rolling, and results in a nonuniform distribution of stresses for an applied uniaxial stress. In any case, the data reported here for uniaxial pressure would have to be supplemented by other information, such as the pressure derivatives of the longitudinal and shear velocities under hydrostatic pressure, in order to calculate the third-order coefficients.

The three separate curves for the shear (\parallel) mode in Figure 3 are what would be expected if the symmetry in the specimen exhibited grain orientation close, but not exactly parallel, to one of the specimen axes. If the observed splitting is a result of only this effect, the results shown here could be used to rotate the coordinate system so that each pair of the three slopes corresponded to the same value of slope. This would give the necessary angular deviation of the specimen symmetry from the three principal axes.

Metallurgical examination also indicated that the 6061 aluminum used in the present experiments exhibited a higher impurity and porosity than is common in this alloy. However, specimens obtained from two different sources were similar in microscopic detail and velocity variation vs. temperature and pressure.

Figure 5 shows the temperature dependence of the longitudinal and shear velocities in 6061-T6 aluminum. The measurements were made on a specimen 1.5 in. long, annealed at 400°C for ~ 3 hours, with both 3 Mc quartz and PZT-5 crystals for the longitudinal mode. Both solid lines in Figure 5 correspond to measurements made along the same specimen axis (which was perpendicular to the apparent stratification layers). For the longitudinal measurements, the velocities in both directions perpendicular to this axis were about 0.4 percent higher, as illustrated by the dashed line. For displacement direction parallel to the cube edge the 6 different shear modes agreed to within 0.2 percent. The data were corrected for thermal expansion using Corruccini and Gniewek's value of $6.9 \times 10^{-5}/^{\circ}\text{C} + (9.0 \times 10^{-8}/^{\circ}\text{C}^2) T$ for the volume coefficient of expansion.¹⁹ The elastic moduli were calculated from the usual relations for an isotropic medium and are shown in Table II as a function of temperature. The moduli were computed from arithmetic means of the longitudinal and shear modes, and were calculated as linear functions of temperature, since the higher order terms were insignificant to ~ 250°C.

3.3 1060 Aluminum

Figure 6 illustrates the relative change in transit time for all three velocity modes in 1060 Al. The material used here had been annealed so that the proportional limit was much lower than that in 6061-T6 aluminum. The data were therefore confined to lower pressures, leading to somewhat reduced accuracy in the slopes. However, as Figure 6 illustrates, the slope for the shear (\parallel) mode still appears to be split into two components. In Table III, the range of the two slopes for the shear (\parallel) mode in Figure 6 are listed and all the data for the shear (\parallel) and the longitudinal mode are tabulated as single slopes.

Figure 7 illustrates yielding behavior in 1060 aluminum. Both solid lines correspond to increasing pressure for two previously unstressed specimens. The dashed line for the shear (\parallel) mode corresponds to

data taken for decreasing pressure after the deviation from the straight line fit is significant. As shown, appreciable hysteresis is present (3 parts in 10^4) after yielding occurs; however, the relaxation slope is approximately the same as that for increasing pressure before the limit is exceeded. The data for the longitudinal mode were obtained to 8800 psi (the corresponding relative transit time at this pressure was 1.0091) and indicate departure from linearity at a somewhat different pressure than for the shear ($||$) mode. The data for decreasing pressure (not shown) were essentially linear to zero stress, with a slope of approximately half that for increasing pressure (the zero pressure value of $\frac{t}{t_0}$ was 1.00882).

The behavior of annealed 6061-T6 aluminum during yielding was similar to that for 1060 aluminum. The slope of the shear ($||$) mode in 6061-T6 after annealing was equal to that before annealing, but departure from linearity began at ~ 4400 psi.

The temperature dependences of longitudinal and shear velocities in 1060 aluminum are shown in Figure 8. The data did not indicate a marked dependence of the velocities with direction of propagation along the axes of the cube, as in 6061-T6 aluminum. Microscopic examination revealed elongated grain size, but the stratification was less evident than that observed in 6061-T6. The data in Figure 8 correspond to 3 Mc, but measurements from 2 to 9 Mc indicated negligible dispersion in this frequency range. Table III summarizes the results on 1060 aluminum.

IV. DISCUSSION

Since the slopes of the transit time curves for the longitudinal mode and the shear ($| |$) mode are very dependent upon the directions of propagation and particle displacement, uniaxial stress measurements are not reliable for determining third-order coefficients in polycrystalline aluminum. However, hydrostatic measurements would be useful in this respect, since as shown in Table I, ultrasonic data for hydrostatic pressure would yield two equations relating to the three unknown third-order coefficients. The slope of the shear ($| |$) mode might then be used to calculate the three coefficients. This approach would only be appropriate to first order because of the micro-anisotropy due to grain texture. The third-order coefficients in aluminum could also be determined by studying the distortion of sinusoidal ultrasonic waves into higher harmonics as a function of propagation distance.²⁰

Alternately, this technique offers the possibility of studying the effect of various stress systems upon the mechanisms of elastic and plastic deformations because of its inherent high sensitivity. In particular, the onset of yielding and the effects of grain orientation can be precisely measured.

In view of the uncertainty of using the results to calculate the third-order coefficients and hence the pressure derivative of the elastic constants, the pressure derivative of the bulk modulus can be estimated from other equation of state relations. Dugdale and MacDonald²¹ show that the Grüneisen parameter γ at zero pressure is given for a monoatomic lattice as

$$\gamma = -1 - \frac{V}{2} \left(\frac{\partial^2 P / \partial V^2}{\partial P / \partial V} \right) \quad (5)$$

which is readily reduced to

$$\gamma = -1/2 + 1/2 \left(\frac{\partial \beta_s}{\partial P} \right) \quad (6)$$

where $\beta_s = \frac{\partial \beta_s}{\partial P}$ is the adiabatic pressure derivative of the bulk modulus. The Grüneisen parameter can be expressed to a high degree of accuracy in terms of the volume coefficient of expansion α , specific heat c_p and bulk modulus as

$$\gamma = \frac{\alpha \beta_s}{\rho c_p} \quad (7)$$

This relation can also be related to the longitudinal and shear velocities in a semi-infinite, purely elastic, isotropic medium as follows:

$$\gamma = \frac{\alpha (v_l^2 - 4/3 v_t^2)}{c_p} \quad (8)$$

Using the algebraic means of these velocities in 6061 Al, Corruccini and Gniwlek's¹⁹ value of γ , and c_p ,²² a value of 2.139 is obtained for γ . The derivative β_s' is then estimated from equation (6) as 5.278.

Anderson⁴ shows that if the bulk modulus is linear in pressure the Murnaghan logarithmic equation can be used to extrapolate the relative volume to pressures on the order of the bulk modulus. This equation is given in terms of the bulk modulus and its derivative as

$$\ln \left(\frac{V}{V_0} \right) = \frac{1}{B_0} \cdot \ln \left[B_0' \left(\frac{P}{B_0} \right) + 1 \right] \quad (9)$$

Here B_0 is the isothermal bulk modulus at atmospheric pressure (related to the adiabatic modulus β_s as measured ultrasonically by $\beta_s = B_0(1 + \alpha\gamma T)$, where T is the absolute temperature) and B_0' is the corresponding pressure derivative. Anderson also shows that the assumption of linearity of the bulk modulus with pressure is generally valid for metals (the second derivative is typically on the order of 10^{-4} /kbar) and that a 1 percent error in B_0 changes the extrapolated volume at $P = B_0$ by $\sim 1/2$ percent. B_0 is given in terms of β_s as⁴

$$\begin{aligned} B_0' &= \beta_s' + \alpha\gamma \cdot \left(\frac{B_0}{\beta_s} \right) \left[1 - \frac{2}{\alpha B_0} \cdot \left(\frac{\partial B_0}{\partial T} \right)_P - 2\beta_s' \right] \\ &+ \left[\alpha\gamma \cdot \left(\frac{B_0}{\beta_s} \right) \right]^2 \left[\beta_s' - 1 - \frac{1}{\alpha^2} \left(\frac{\partial \alpha}{\partial T} \right)_P \right] \end{aligned} \quad (10)$$

The temperature dependence of the bulk modulus was obtained in the present experiments and da/dT is given in reference (19) for aluminum. A value of 5.759 for B_0 is then used in equation (9) to estimate the compression at high pressure.

Figure 9 shows the results of using the estimated pressure derivative B_0' in the Murnaghan equation. Also shown in the graph are some experimental points for 6061-T6 Al to 31 kbars determined by Lundergan and Herrmann²³, and some higher pressure points determined by Walsh et al.,²⁴ on 24 ST Al. Up to ~ 200 kbars, V/V_0 estimated from equation (9) is in particularly good agreement with the experimental points. At higher pressure the estimated curve progressively deviates from the experimental points, being ~ 2 percent high at 450 kbars. However, the agreement is good considering that the pressure derivative was derived from ultrasonic data obtained at atmospheric pressure and was not directly measured and further considering the difficulty in obtaining highly accurate equation of state data at high pressure using dynamic techniques.

At 25°C the corresponding quantities in 1060 aluminum are

$$\begin{aligned} \gamma &= 2.113 \\ \beta_s' &= 5.226 \\ B_0' &= 5.723 \end{aligned}$$

Using these results in equation (9), the curve in Figure 10 is obtained. The experimental points are those of Munson and Barker²⁵ and Anderson et al.²⁶ Again, the agreement is within 2 percent to ~ 450 kbars.

V. CONCLUSIONS

Uniaxial pressure measurements have limited applicability to the determination of third-order elastic coefficients in polycrystalline aluminum. The application of the results are restricted in part by the generation of inhomogeneous stress conditions due to grain boundary slipping and microscopic anisotropy. However, these data when supplemented with hydrostatic pressure measurements will allow a calculation of the three third-order elastic coefficients. In addition, the uniaxial stress measurements may be useful in studying the microscopic behavior of yielding.

The present study shows that in the absence of ultrasonic pressure measurements, the Dugdale-MacDonald relation may be effectively used to estimate the pressure derivative of the bulk modulus for aluminum. This derivative can then be used in the Murnaghan logarithmic equation to estimate the compression at very high pressure where direct measurements are not only difficult but less accurate and quite expensive. The comparison with experimentally determined points is good in the two alloys studied here, which illustrates the applicability of the Murnaghan equation as an appropriate relation in the equation of state of aluminum.

The data presented here demonstrates that, in the absence of experimental high-pressure measurements, ultrasonic data obtained at zero external pressure can be used in some instances to estimate high pressure behavior. The applicability of this approach depends, in large part, upon whether the material under investigation undergoes a phase transition in the pressure region of interest. However, the extrapolation can easily be checked by one or two experimental high pressure points. Thus, the technique will be useful in Air Force programs involving material dynamics research, where the amount of available material is limited, since the ultrasonic approach is non-destructive; or where high pressure data are scarce, in which case the ultrasonic approach can be used to supplement existing high pressure measurements with a concurrent increase in accuracy and reduced expenditures. The approach can likewise be used to easily obtain the complete PVT behavior of nosecone materials. This complete equation of state is necessary in vulnerability studies because of mechanical heating of a material subjected to high impulsive loading. The data will thus supplement dynamic experiments where temperature measurements are extremely difficult.

ACKNOWLEDGEMENTS

The authors are indebted to Mr. James W. Page for performing many of the measurements; to Miss Leonie D. Boehmer for computational assistance; and to Mr. Willy E. Kunzler for metrological support.

REFERENCES

1. P.W. Bridgman, The Physics of High Pressures, G. Bell and Sons, London, England (1952).
2. R.G. McQueen and S.P. Marsh, J. Appl. Phys. 31, 1253 (1960).
3. D. Lazarus, Phys. Rev. 76, 545 (1949).
4. O.L. Anderson, J. Phys. Chem. Solids 27, 547 (1966).
5. H.J. McSkimin, J. Acoust. Soc. Am 33, 12 (1961).
6. D.S. Hughes and J.L. Kelly, Phys. Rev. 92, 1145 (1953)
7. K. Brugger, J. Appl. Phys. 36, 759 (1964).
8. R.N. Thurston, Proceedings of the IEEE 53, 1320 (1965).
9. T. Bateman, W.P. Mason and H.J. McSkimin, J. Appl. Phys. 32, 928 (1961).
10. E.H. Bogardus, J. Appl. Phys. 36, 2504 (1965).
11. H.J. McSkimin and P. Andreatch, J. Appl. Phys. 35, 2161 (1964).
12. E.R. Lippencott and H.C. Duecker, Science 144, 1119 (1964).
13. R.N. Thurston, "Wave Propagation in Fluids and Normal Solids," in Physical Acoustics, Vol. 1A, W.P. Mason, Ed., New York: Academic Press, 1 - 110 (1964).
14. R.A. Toupin and B. Berstein, J. Acoust. Soc. Am. 33, 216 (1961).
15. R.N. Thurston and K. Brugger, Phys. Rev. 133, A1604 (1964).
16. H.J. McSkimin, P. Andreatch and R.N. Thurston, J. Appl. Phys. 36, 1624 (1965).
17. K. Brugger, Phys. Rev. 133, A1611 (1964).
18. F. Birch, Phys. Rev. 71, 809 (1947).
19. R.J. Corruccini and J.J. Gniewek, National Bureau of Standards, Monogr 29, (1961), as quoted in reference 4.
20. M.A. Breazeale and J. Ford, J. Appl. Phys. 36, 3486 (1965).

21. J.S. Dugdale and D.K.C. MacDonald, Phys. Rev. 39, 832 (1952).
22. D.R. Stull and G.C. Sinke, "The Thermodynamic Properties of the Elements in their Standard States," (Dow Chemical Company, 1955), as quoted in reference 23.
23. C.D. Lundergan and W. Herrmann, J. Appl. Phys. 34, 2046 (1963).
24. J.M. Walsh, M.H. Rice, R.C. McQueen and F.L. Yarger, Phys. Rev. 108, 196 (1957).
25. D.E. Munson and L.M. Barker, J. Appl. Phys. 37, 1652 (1966).
26. C.D. Anderson, D.G. Doran, and A.L. Fahrenbruck, "Equation of State of Solids: Aluminum and Teflon," Air Force Weapons Laboratory Technical Report 65-147, Kirtland AFB, New Mexico (1965).

TABLE I
ISOTROPIC MEDIUM UNDER HYDROSTATIC PRESSURE & UNIAXIAL COMPRESSION

Type of Stress	Propagation Direction \underline{N}	Mode*	Displacement Direction \underline{U}	$w = (\rho_0 v^2) P = 0$	$(\rho_0 v^2)^{-1}$
Hydrostatic pressure	arbitrary	L	to \underline{N}	$\lambda^S + 2\mu$	$-1 - \frac{1}{3B} \quad w + 3v_1 + 10v_2 + 8v_3$
Hydrostatic pressure	arbitrary	S	\perp to \underline{N}		$-1 - \frac{1}{3B} (v_1^2 + 3v_2^2 + 4v_3^2)$
Uniaxial compression	\perp to stress	L	to \underline{N}	$\lambda^S + 2\mu$	$\frac{1}{E} [\sigma(2w + 8v_3) + v_1(2\sigma - 1) + v_2(8\sigma - 2)]$
Uniaxial compression	\perp to stress	S	to \underline{N}	μ	$\frac{1}{E} [-2w + v_2(2\sigma - 1) + 2v_3(\sigma - 1)]$
Uniaxial compression	\perp to stress	S	\perp to \underline{N}	μ	$\frac{1}{E} [v_1(2w + 4v_3) + v_2(2\sigma - 1)]$

*L = Longitudinal; S = Shear; $B = \lambda^T - 2/3\mu$ = isothermal bulk modulus; $E = 3\mu B / (\lambda^T + \mu)$ = isothermal Young's modulus; $\sigma = \lambda^T / 2(\lambda^T + \mu)$ = isothermal Poisson's ratio.

TABLE II. ELASTIC PROPERTIES OF 6061-T6 ALUMINUM

Longitudinal Velocity*, v_l , mm/usec	$6.428 \pm 0.002 - (0.00091 \pm 0.00001)T$
Shear Velocity, v_t , mm/usec	$3.188 \pm 0.003 - (0.00086 \pm 0.00003)T$
Young's Modulus, E , dynes/cm ²	$7.35 \times 10^{11} - (4.16 \times 10^8)T$
Shear Modulus, μ , dynes/cm ²	$2.75 \times 10^{11} - (1.67 \times 10^8)T$
Bulk Modulus, β_g , dynes/cm ²	$7.51 \times 10^{11} - (1.70 \times 10^8)T$
Poisson's Ratio, σ	$0.336 + (0.00011)T$
Grüneisen Ratio, γ at 25°C	2.139
Uniaxial Pressure Slope, α_l , cm ² /dynes Longitudinal Mode	$(-1.17 \pm -1.72) \times 10^{-12}$
Uniaxial Pressure Slope, α_s , cm ² /dynes Shear () Mode	$(1.04 \pm 5.36) \times 10^{-12}$
Uniaxial Pressure Slope, α_s , cm ² /dynes	$(-1.927 \pm 0.005) \times 10^{-12}$

*Temperature in °C.

TABLE III. ELASTIC PROPERTIES OF 1060 ALUMINUM

Longitudinal Velocity, v_l , mm/ μ sec	$6.404 \pm 0.003 - (0.00100 \pm 0.00003)T$
Shear Velocity, v_t , mm/ μ sec	$3.18 \pm 0.002 - (0.00079 \pm 0.00003)T$
Young's Modulus, E, dynes/cm ²	$7.32 \times 10^{11} - (3.92 \times 10^8)T$
Shear Modulus, μ , dynes/cm ²	$2.74 \times 10^{11} - (1.55 \times 10^8)T$
Bulk Modulus, β , dynes/cm ²	$7.43 \times 10^{11} - (2.16 \times 10^8)T$
Poisson's Ratio, σ	$0.335 + (0.000094)T$
Grüneisen Ratio, γ at 25°C	2.113
Uniaxial Pressure Slope, α_l , cm ² /dynes Longitudinal Mode	$(-1.49 \pm 0.02) \times 10^{-12}$
Uniaxial Pressure Slope, α_s , cm ² /dynes Shear () Mode	$(1.55 \pm 3.42) \times 10^{-12}$
Uniaxial Pressure Slope, α_s , cm ² /dynes	$(-2.89 \pm 0.06) \times 10^{-12}$

* Temperature in °C.

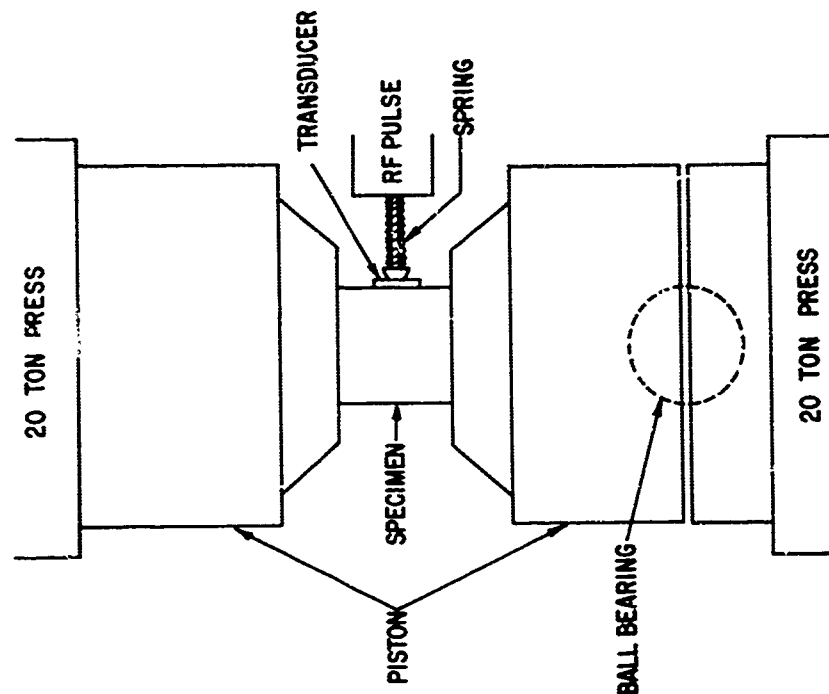


Figure 2. Stress system for applying uniaxial pressure and measuring the three velocity modes perpendicular to the stress.

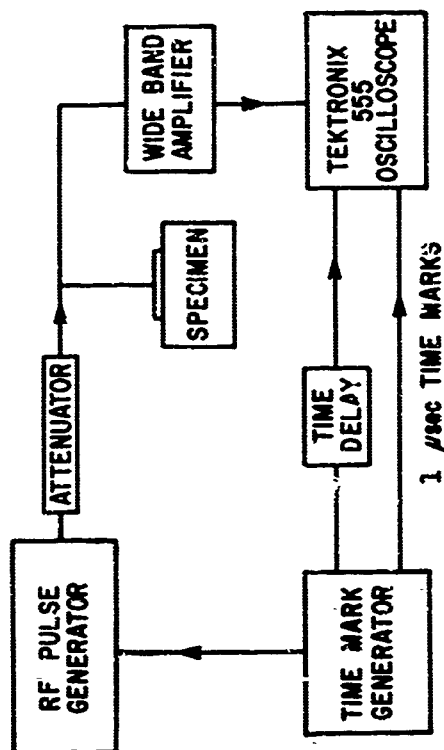


Figure 1. Block diagram of velocity measuring apparatus

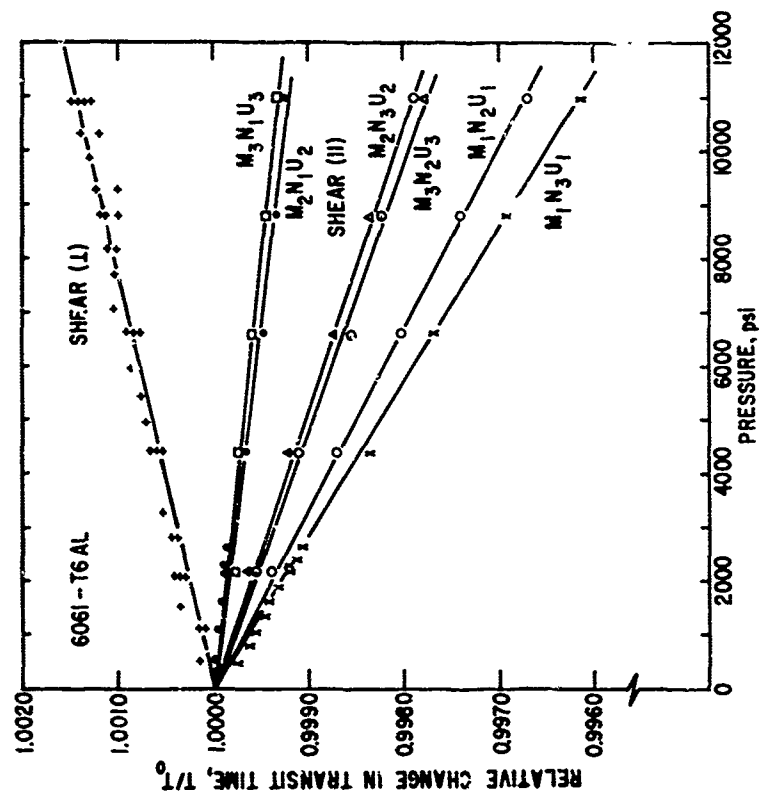


Figure 3. Relative change in transit time for the two shear modes perpendicular to the stress in 6061-T6 aluminum. The points corresponding to the shear (I) mode were obtained from one sample by applying the stress along the three orthogonal axes. The symbols $M_iN_jU_k$ are identified in the text.

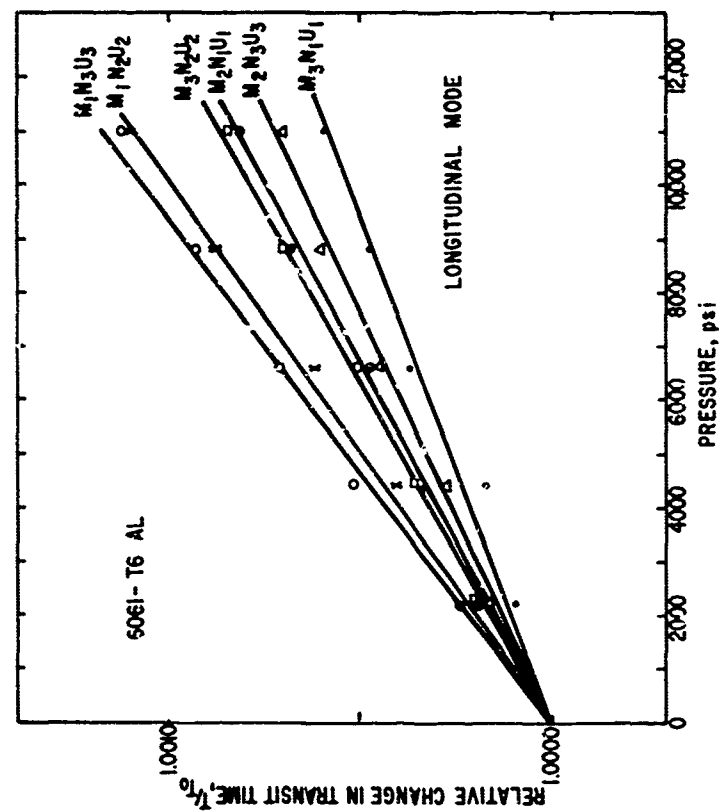


Figure 4. Relative change in transit time for the longitudinal mode in 6061-T6 aluminum. The data were obtained from the specimen corresponding to the shear (I) mode in Figure 5.

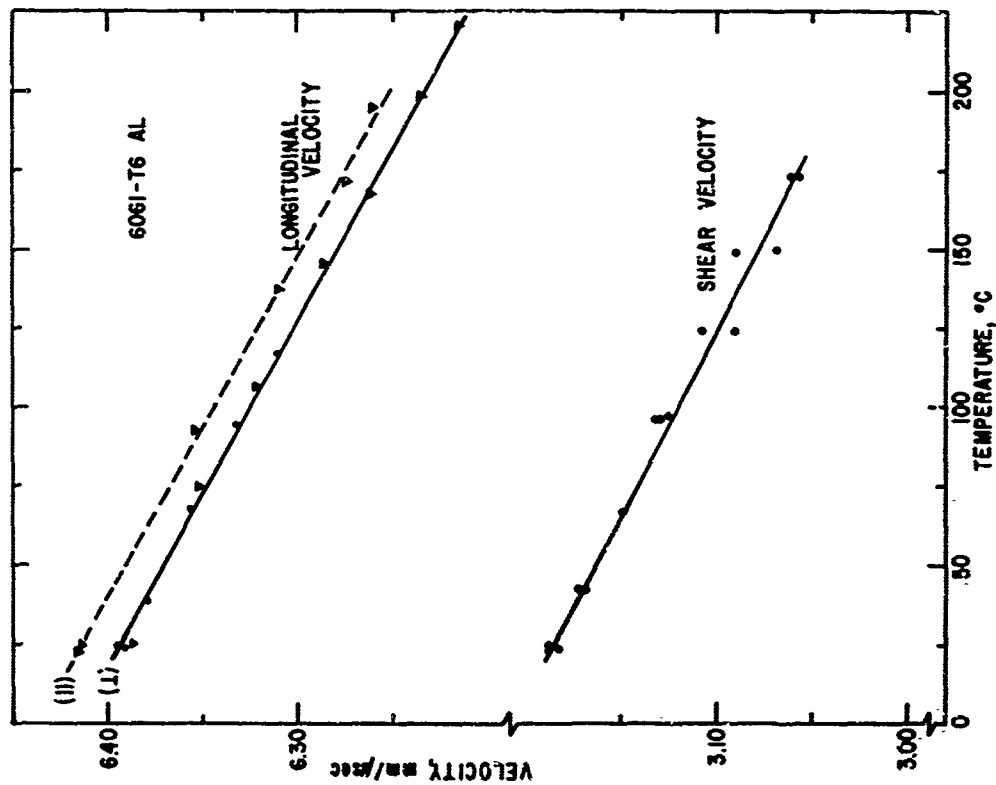


Figure 5. Longitudinal and shear velocities in 6061-T6 aluminum. The points correspond to measurements made with quartz crystals and the triangles refer to those made with PZT-5. Both solid curves correspond to velocity along the same sample axis. The dashed line (II) refers to velocity along one of the axis parallel with the stratification layers. The solid line (I) refers to measurements across the layers. All of the data are 3 Mg.

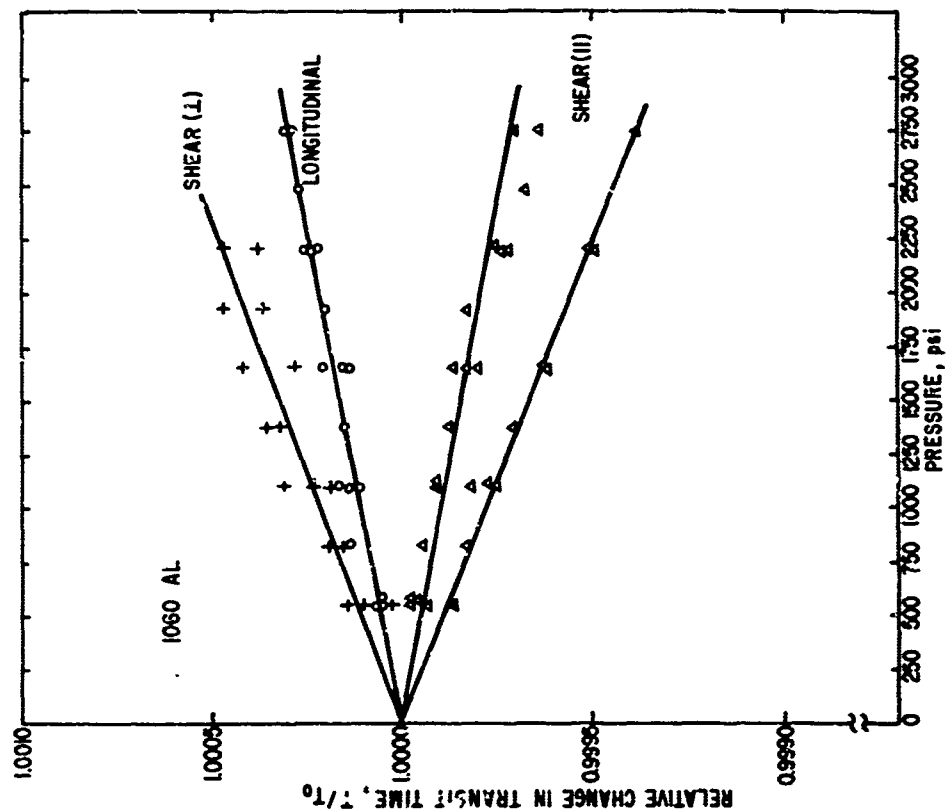


Figure 6. Relative change in transit time vs. uniaxial stress in 1060 aluminum. The data were obtained from various specimens.

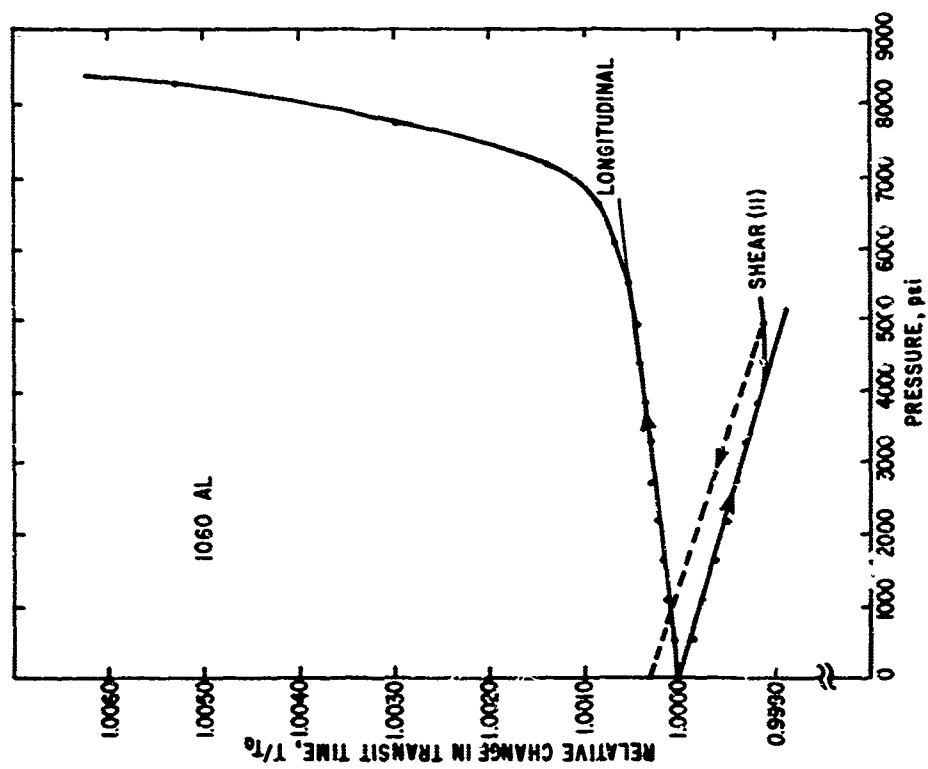


Figure 7. Yielding in 1060 aluminum. The data were obtained on two previously unstressed samples.

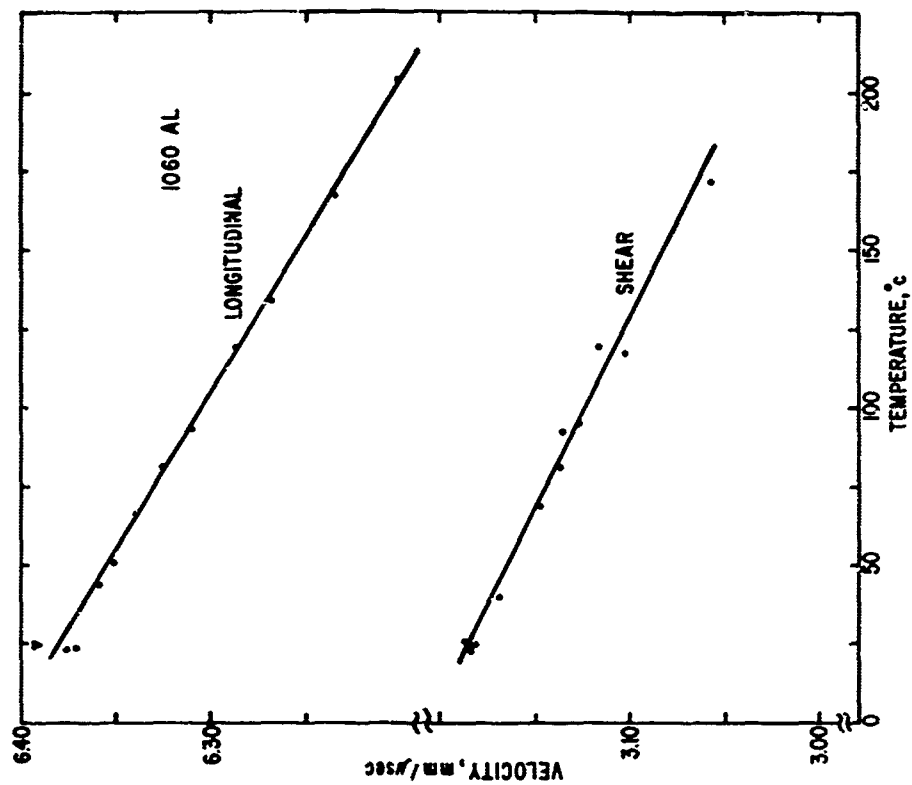


Figure 8. Longitudinal and shear velocities at 3 Mc in 1060 aluminum. The triangle corresponds to velocity determined with PZT-5; the points correspond to measurements made with quartz.

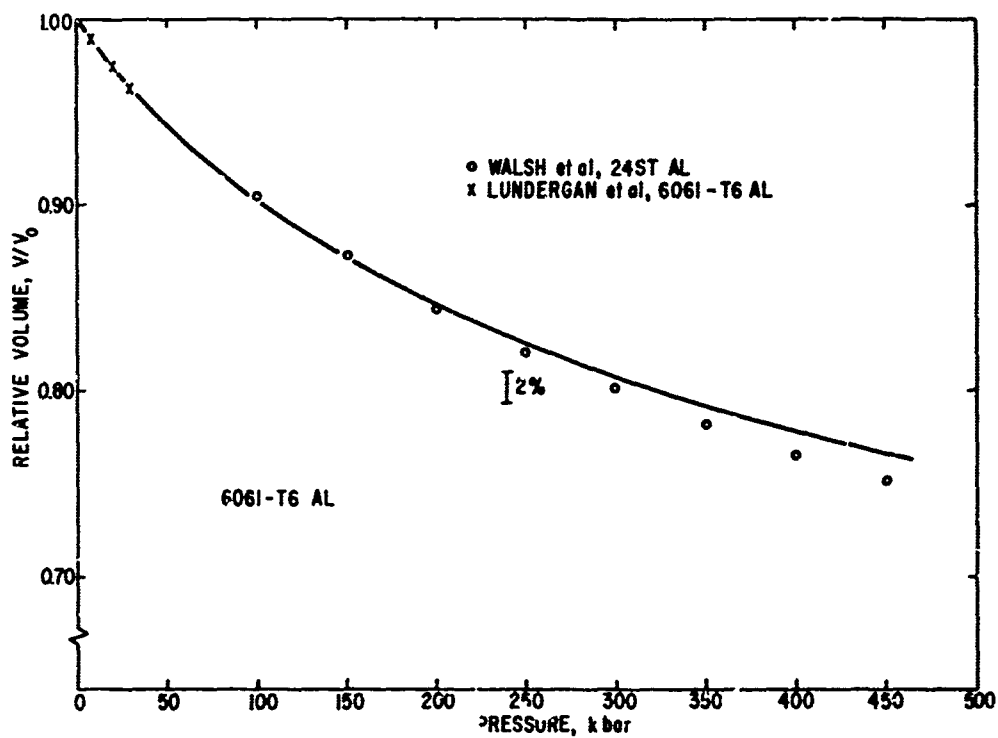


Figure 9. Relative volume in 6061-T6 aluminum. The solid curve is equation (5) evaluated with the use of equation (6).

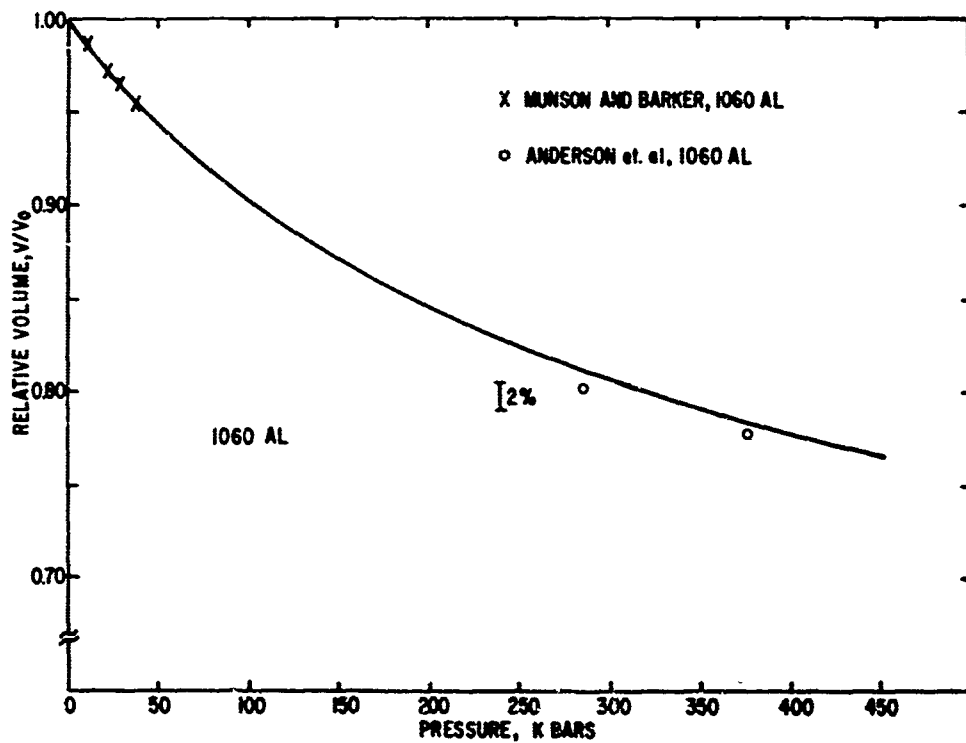


Figure 10. Relative volume in 1060 aluminum. The solid curve is equation (9) evaluated with the use of the Dargdale-MacDonald relationship (6).

AD 641 921

ERRATA SHEET

VOLUME I

PROCEEDINGS OF THE 13TH ANNUAL AIR FORCE SCIENCE AND
ENGINEERING SYMPOSIUM

27-29 September 1966

Paper #1

Author: John F. Schaefer

Title: (U) ADAPTIVE BANG-BANG CONTROL OF AN UNSTABLE
MECHANICAL SYSTEM CONTAINING AN UNKNOWN
PARAMETER

Page 7, Lines 2 & 3

Delete - 3rd line

$$\left(\bar{U}(t) = \frac{1}{t-t_{ch}} \int_{t_{ch}}^t U(t) dt \right)$$

Add - end of 2nd line continuing on 3rd line

$$\left\{ \text{that is, } \bar{U}(t) = \frac{1}{\Delta T} \int_{t-\Delta T}^t U(t) dt, \text{ where} \right. \\ \left. \Delta T \geq \text{the period of the chatter motion} \right\}.$$

Paper #3

Authors: Everett W. Dunlap

Milton B. Porter, Jr., 1st Lt, USAF

Title: (U) ACCELERATIONS ON AIRCRAFT INDUCED BY THE
EARTH'S ROTATION

Add beneath the Abstract

Since the paper was published, a more refined analysis has been made of the variations of thrust and cruise weight that are produced by the accelerations induced by the earth's rotation. The variations are altered when the precise equations for the earth's gravity are used. This refined analysis is described in an AFFTC Technical Report, FTC-TR-66-38, available on request from DDC approximately March 1967.